An Electrochemical Sensor for Forane

A Thesis submitted for the Degree of

Doctor of Philosophy in the

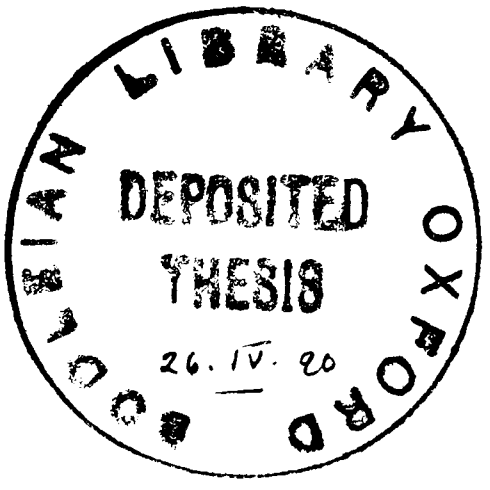
University of Oxford

by

Richard J. Northing

St. Hugh's College

Michaelmas Term 1989



For my Mother, Father and Grandfather

An Electrochemical Sensor for Forane

Abstract of a thesis submitted for the Degree of
Doctor of Philosophy
by
Richard J. Northing
St. Hugh's College, Oxford
Michaelmas Term 1989

This thesis is concerned with the development and laboratory assessment of an electrochemical sensor for the detection and measurement of the volatile inhalation anaesthetic, forane. Investigations were therefore based on the heterogeneous and homogeneous reduction of this agent in non–aqueous electrolyte.

Preliminary experiments at a mercury and other rotating disc electrodes (RDEs) revealed that the direct reduction of forane was not possible and therefore the use of an electron transfer mediator was examined. To this end, the radical anion of the polyaromatic compound, fluoranthene, (F), was investigated as a possible electro–reduction catalyst and the mediated reduction of the anaesthetic, via a catalytic process, demonstrated.

Theory was presented for the calculation of chronoamperometric and steady–state responses at the RDE resulting from one electron transfer and coupled (catalytic) homogeneous kinetic processes. The latter enabled a precise mechanism to be assigned to the F + forane process, while a comparison of the former theory with experimental chronoamperometric results was used, in conjunction with AC impedance studies, to investigate the adsorption of F at the mercury/acetonitrile interface.

A polymer modified electrode, based on the polymer poly–(11–vinylfluoranthene) was demonstrated to be effective in the heterogeneous reduction of forane but displayed only a limited lifetime. Therefore, a Clark–type membrane electrode was constructed and the detection and measurement of forane, in the absence of oxygen, demonstrated using this device. However, the sluggish response of this sensor, together with interference problems from oxygen encouraged the development of a device which utilised a channel electrode (ChE) sensing approach.

Theory was presented for the deduction of steady–state currents at the ChE resulting from coupled catalytic kinetics and this was used to demonstrate that the same mechanism for the F + forane system operated at the ChE as the RDE. The conventional ChE was then modified by the incorporation of a membrane and this sensor, which was shown to operate successfully in the presence of high concentrations of oxygen and nitrous oxide, responded linearly to forane, while displaying an excellent response time of under ten seconds. The device should find application in clinical monitoring.

ACKNOWLEDGEMENTS

I should like to express my sincere gratitude to the following:

Richard Compton, for his supervision, enthusiasm and continual supply of innovative ideas during the course of this work.

Past and present members of the Oxford Electrochemistry group and, in particular, I thank Pat Unwin, Andy Waller, Mark Laing, Virginia Maxwell, Matt Pilkington, Keith Pritchard, Richard Harland and Dave Mason for much helpful advice, support and friendship.

Clive Hahn for several useful discussions on sensor technology.

SERC, Ohmeda and St. John's College for financial support and St. Hugh's College for an Elizabeth J. Harris Graduate Scholarship.

The administrative and technical staff of the Physical Chemistry Laboratory, especially Roger Bowler and John Graham for constructing the membrane and channel sensors.

I am especially indebted to Carol Greaves whose help at the keyboard has been invaluable during the preparation of this thesis.

TABLE OF CONTENTS

Chapter One: INTRODUCTION 1.

1.1 The history of volatile inhalation anaesthetics 1.

1.2 Methods of determining anaesthetic gases 5.

1.2.1 Non–electrochemical techniques 5.

1.2.2 Electrochemical techniques 7.

1.3 The aims and objectives of this thesis 10.

Chapter Two: ELECTROCHEMICAL PRINCIPLES 12.

2.1 Electrode processes 12.

2.1.1 Electron transfer 14.

2.1.2 Mass transport 20.

2.1.2.1 Migration 20.

2.1.2.2 Convection 21.

2.1.2.3 Diffusion 21.

2.2 Diffusion–only systems 23.

2.2.1 Linear sweep/cyclic voltammetry 24.

2.2.2 AC Impedance 32.

2.3 Convective–diffusion 33.

2.3.1 The hydrodynamics of the rotating disc electrode 37.

2.3.2 The solution of the convective–diffusion equation for a transport limited process at the rotating disc electrode 40.

2.3.3 Hydrodynamic flow through a channel electrode 44.

2.3.4 Solution to the convective–diffusion equation for a transport limited process at the channel electrode 46.

2.4 The relationship between potential and current under mass transport controlled conditions 48.

2.4.1 Reversible electron transfer 48.

2.4.2 Irreversible electron transfer 50.
2.5 The use of the rotating disc and channel electrodes in the study of electrochemical reaction mechanisms 52.
2.5.1 Coupled homogeneous reactions 52.
2.5.2 Coupled heterogeneous reactions 56.
2.6 Spectroelectrochemistry 57.

Chapter Three: THEORY 59.
3.1 The rotating disc electrode 60.
3.1.1 Introduction 60.
3.1.2 The general approach 63.
3.1.2.1 Theory 63.
3.1.2.2 The method of solution 64.
3.1.3 Double potential steps 66.
3.1.4 The inclusion of homogeneous kinetics 70.
3.1.5 The inclusion of heterogeneous kinetics 75.
3.1.6 Results and discussions 76.
3.1.6.1 Simple electron transfer: single potential step chronoamperometry 76.
3.1.6.2 Simple electron transfer: double potential step chronoamperometry 78.
3.1.6.3 Homogeneous kinetics 78.
3.1.6.4 Heterogeneous kinetics 83.
3.1.7 Summary 88.
3.2 The channel electrode 90.
3.2.1 The solution of the mass transport equation to the channel electrode via the Lévêque approximation 92.
3.2.2 The solution of mass transport to the channel electrode using the backwards implicit finite–difference method 96.
3.2.2.1 The solution for a one electron transfer 98.
3.2.2.2 The inclusion of coupled homogeneous kinetics 101.

Chapter Four: EXPERIMENTAL PROCEDURE 115.

4.1 The rotating disc assembly 115.

4.1.1 Electrodes 115.

4.1.2 The cell design 116.

4.1.3 Experimental protocol 116.

4.2 The channel electrode assembly 118.

4.2.1 The channel cell 118.

4.2.2 The flow system 120.

4.3 Electrochemical techniques 122.

4.3.1 Instrumentation 122.

4.3.2 Time dependent measurements 123.

4.4 ESR experiments 124.

4.4.1 The ESR spectrometer 124.

4.4.2 The ESR channel cell 124.

4.4.3 The ESR flow system 124.

4.4.4 Spin trapping experiments 124.

4.5 Chemicals and materials 126.

4.6 Computing 126.

Chapter Five: THE ELECTROCHEMISTRY OF FLUORANTHENE 129.

5.1 An investigation of the one electron reduction of fluoranthene using double potential step chronoamperometry 130.

5.2 The mediated reduction of t–butyl bromide: an investigation using rotating disc electrode voltammetry 146.

Chapter Six: THE INHIBITION OF ELECTRON TRANSFER REACTIONS AT THE MERCURY/ACETONITRILE INTERFACE BY ADSORBED LITHIUM IONS 158.

6.1 Introduction 158.

6.2 Preliminary experiments 159.

6.3 AC impedance 166.

6.4 Cyclic voltammetry 172.

6.5 Conclusions 177.

Chapter Seven: THE ELECTRO–REDUCTION OF FORANE AT THE ROTATING DISC ELECTRODE 178.

7.1 Reduction of forane 178.

7.1.1 Mediation via the fluoranthene radical anion 179.

7.1.2 Conclusions 191.

7.2 A modified electrode for the electrochemical reduction of forane 192.

7.3 Interferences by nitrous oxide and oxygen 200.

7.3.1 Nitrous oxide 200.

7.3.2 Oxygen 206.

7.3.3 Conclusions 211.

Chapter Eight: MEMBRANE ELECTRODES FOR THE ANALYSIS OF FORANE AND NITROUS OXIDE/OXYGEN MIXTURES 212.

8.1 The detection of forane 212.

8.1.1 The forane sensor 212.

8.1.2 Forane sensing results 214.

8.1.3 Multigas analysis 218.

8.2 The nitrous oxide/oxygen sensor 220.

8.2.1 The simultaneous nitrous oxide/oxygen sensor 220.

8.2.2 The reduction of nitrous oxide and oxygen at a silver rotating disc electrode 220.

8.2.3 The reduction and sensing of gaseous nitrous oxide and oxygen using an aqueous membrane electro 223.

8.3 Summary 227.

Chapter Nine: THE MEDIATED REDUCTION OF FORANE AND NITROUS OXIDE AT THE CHANNEL ELECTRODE 231.

9.1 Preliminary experiments 231.

9.2 The mediated reduction of forane 232.

9.3 The mediated reduction of nitrous oxide 235.

Chapter Ten: AN AMPEROMETRIC SENSOR FOR FORANE BASED ON THE CHANNEL ELECTRODE 241.

10.1 The channel electrode sensor 241.

10.2 The theoretical solution of mass transport to the channel electrode sensor 243.

10.3 The reduction of forane at the channel electrode sensor 247.

10.3.1 Preliminary experiments 247.

10.3.2 The mediated reduction of forane 247.

10.3.3 Interferences by oxygen 252.

10.4 The reduction of nitrous oxide at the channel electrode sensor 258.

10.5 Potential pulsing experiments 262.

10.6 Conclusions 268.

APPENDICES

Appendix One: AC impedance 271.

Appendix Two: The Levich equation for the rotating disc electrode 280.

Appendix Three: The Levich equation for the channel electrode 282.

Appendix Four: Computer programs 284.

Appendix Five: The relationship between forward and reverse chronoamperograms 285.

Appendix Six: The Thomas algorithm 287.

Appendix Seven: The synthesis of poly(11–vinylfluoranthene) 289.

REFERENCES 291.

LIST OF TABLES

1.1 The empirical formulae of the anaesthetic gases discussed in Chapter One.

3.1 Values of k_{mech}, p and q appropriate for equations 3.33–3.35.

3.2 Values of k_{norm} and r appropriate for equations 3.36–3.38.

3.3 The definitions of k_{mech}, p_{mech}, p and q appropriate for equations 3.93–3.98.

3.4 The values of d_1 for the EC' mechanisms.

3.5 The values of d_j for the EC' mechanisms.

3.6 The values of b_1 for the EC' mechanisms.

3.7 The appropriate normalised rate constants k_{norm} for the EC' mechanism.

4.1 The source and grade of the chemicals used.

6.1 The chemical structures of the organic compounds investigated.

6.2 The reduction potentials and diffusion coefficients of the compounds studied.

6.3 The estimated and measured coverages for Type B compounds irreversibly adsorbed on a mercury electrode.

CHAPTER ONE

INTRODUCTION

The development of a sensor capable of measuring the new volatile anaesthetic, forane, is essential if this gas is to find continued safe success in clinical anaesthesia. Such a device must be able to quickly and accurately determine the concentration of the anaesthetic in a mixture of several gases and to this end, this thesis is concerned with detecting forane by amperometric means. The aim of this chapter is to explain the necessity for research into new anaesthetics, such as forane, and to introduce electrochemical sensors. The merits of these devices will be emphasised. A review of the gases which have found use in anaesthesia will also be presented and the techniques available for their determination discussed.

1.1 The History of Volatile Inhalation Anaesthetics

Credit for the first anaesthetic gas is given to Valerius Cordus, who synthesised diethyl ether in 1540. Its pain relieving qualities were observed in the same year by Paracelsus [1]. Three centuries later, this agent was used for the first time as a general anaesthetic for the relief of pain during surgery by Crawford Long [2]. Around the same time, nitrous oxide, chloroform and ethyl chloride were also finding use in anaesthesia and despite the apparent undesirable side effects and physical dangers of these agents [3–6], they remained popular in clinical use for the following century. The chemical formulae of the gases discussed here are shown in Table 1.1.

Table 1.1: The empirical formulae of the anaesthetic gases discussed in Chapter One.

	ANAESTHETIC	EMPIRICAL FORMULA
1	Diethyl ether	$CH_3CH_2OCH_2CH_3$
2	Nitrous oxide	N_2O
3	Chloroform	$HCCl_3$
4	Ethyl chloride	CH_3CH_2Cl
5	Ethylene	CH_2CH_2
6	Cyclopropane	$(CH_2)_3$
7	Divinyl ether	$CH_2CHOCHCH_2$
8	Ethyl vinyl ether	$CH_3CH_2OCHCH_2$
9	Trichloroethylene	CCl_2CHCl
10	Fluroxene	$CF_3CH_2OCHCH_2$
11	Halothane	$CHBrClCF_3$
12	Methoxyflurane	$CHCl_2CF_2OCH_3$
13	Enflurane	CHF_2OCHF_2CHFCl
14	Isoflurane	$CHF_2OCHClCF_3$

The flammable nature of diethyl ether means that its use is hard to justify in modern operating theatres [7], while evidence of hepatic toxicity explains the seldom use of chloroform [8,9], despite the appearance in the literature of work calling for a resurgence of this particular agent [10]. Ethyl chloride has several disadvantages including flammability, a narrow margin of safety and administration difficulties [11]. Nitrous oxide, however, has remained popular. It is a colourless gas with a very faint odour and sweetish taste. When inhaled in its pure form, it causes asphyxia, but in high concentrations (>80%), with sufficient oxygen present to avoid this problem, nitrous oxide induces rapid and shallow anaesthesia. The gas is a non–irritant, gives no unpleasant aftermath and is rapidly eliminated unchanged from the bloodstream on completion of anaesthesia. It is now most often employed as a background anaesthetic in conjunction with more potent additives for major surgery or in dilute mixtures with oxygen as an analgesic. A more detailed review of the physical and anaesthetic properties of nitrous oxide is provided elsewhere [12].

In the 1920's, a new era arrived in anaesthesia with ethylene [13], cyclopropane [14] and several other hydrocarbons [15] finding success in clinical anaesthesia. The anaesthetic properties of ethylene closely resemble those of nitrous oxide with the additional advantage that it is slightly more potent [13]. However the flammable nature of this agent along with the others mentioned above, means that they are rarely used today [7]. Between 1930 and 1950, there followed the discovery, testing and clinical use of a wide range of anaesthetic agents, which have since, on the whole, been discarded because of either undesirable side effects or physical dangers. These agents included divinyl ether (which is flammable, causes convulsions and is associated with a toxicity of the hepatic and renal systems [11]), ethyl vinyl ether [5] (which causes convulsions), trichloroethylene [16] (unstable to alkali and therefore difficult to administer [17]) and fluroxene [18] (non–flammable but causes seizures and is believed to metabolise in the patient [19]).

Halothane was first synthesised in 1951 by Suckling [20] and after initial trials on animals showed it to be a non–flammable, potent and safe anaesthetic [21], it was clinically evaluated on man [22], where these properties were confirmed and its great versatility became apparent [23]. Today it is the most universally used

inhalation anaesthetic [1,24]. However, soon after the introduction of halothane, certain disadvantages became apparent. Those proposed included cardiovascular depression, incompatibility with adrenalin [25] and the possibility of liver damage [26]. These have all since been confirmed [1,27,28].

Thus the search for better and safer anaesthetics continues. More recently, the fluorinated anaesthetics, methoxyflurane [29] and enflurane [30], have enjoyed limited popularity but problems with inorganic fluoride metabolates [1,31] in the former case and convulsions in the latter [32], has restricted their use. An isomer of enflurane, isoflurane (or forane) is the most recent fluorinated ether anaesthetic to be introduced [33]. While showing excellent anaesthetic properties, it underwent over 3000 initial clinical tests on human cases [34], before investigations were suspended due to reports of possible carcinogenity induced by its use in rats [35]. However, these preliminary results were not confirmed and forane is now approved for clinical use by the American Food and Drug Administration [36]. Forane is believed to be "closer to the ideal than any compound previously tested" [1].

Forane is a non–irritant, potent anaesthetic, which has a low blood/gas partition coefficient [36,37] and therefore gives rapid induction of anaesthesia. Stimulation of the central nervous system is thus minimised, while no evidence of neuromuscular irritation has been observed. Forane has been shown to be compatible with adrenalin and to have a greater hypnotic, analgesic and muscle relaxant effect than either halothane or enflurane [38], which may explain its slightly slower recovery period [39–41]. No abnormal biochemical disturbances [42] or retrograde amnesia [43] occur after forane anaesthesia. There is no significant metabolism of this compound *in vivo* [44,45] so that the plasma inorganic fluoride levels remain virtually unchanged, even after prolonged clinical anaesthesia [46]. This can be partly attributed to its low fat and blood solubilities [1] and also to the chemical inertness of forane [45,47], which appears to be greater than any other fluorinated anaesthetic currently available. Therefore, no antioxidant or stabiliser additives are required to prevent molecular breakdown and its inertness facilitates anaesthetic administration since it does not react with carbon dioxide absorbents, strong alkali or metal and it is not affected by ultra–violet light [12]. Finally,

reports suggest that forane causes no hepatic [48,49] or renal [50] functional or pathological abnormalities confirming its favorable comparison in every way with all other inhalation anaesthetics. More complete reviews of the properties of forane are given by Dobkin [1] and Eger [36,45].

It will now be useful to consider the various techniques which have been employed to monitor the administration, uptake and recovery from the anaesthetic agents discussed above. This section will be divided into two broad categories – those techniques which employ electrochemical measurements and those which utilise other non–electrochemical methods.

1.2 Methods of Determining Anaesthetic Gases

The need for continual monitoring of anaesthesia is unequivocal [51,52] and hence several techniques have been applied to this task. The merits of each method for detecting and determining an anaesthetic agent in breath gas or blood will therefore be described briefly.

1.2.1 Non–electrochemical Techniques

Mass spectrometry has a relatively long history of *in vivo* gas analysis [53] since the early work of Waldring [54], who first reported its use for arterial oxygen and carbon dioxide partial pressure (P_{O_2} and P_{CO_2}) measurements in animals. Despite this, few examples of actual human studies are apparent. Measurements are possible using invasive blood gas probes via the use of a catheter [55], non–invasive transcutaneous blood gas methods [56] and respiratory gas analysis [57]. The former technique usually employs a stainless steel catheter [58]. Flexible plastic probes have been employed [56], but problems arise due to diffusion of water vapour through the catheter walls. The catheter is covered with a silastic or teflon membrane at the tip to permit diffusion of gas molecules; tips constructed from a sintered porous substrate [59] have also been employed. This technique has been used to successfully analyse volatile anaesthetics but the waiting time between analysis is too long to

reasonably serve the needs of anaesthesiologists [60]. Transcutaneous sensors are commercially available and in clinical use [61]. Mass spectrometry has also been used successfully on–line to determine respiratory gases down to 0.1ppm [62], but despite this excellent sensitivity, the shear cost and complexity of these devices has limited their practical use.

The method by which gas chromatography is employed in determining blood–gas levels involves prior infusion of fluid, pre–equilibrated with six tracer gases, into a patients vein [63]. After allowing a period for equilibration, blood samples are removed in gas–tight glass syringes, mixed with nitrogen and an exact volume of this gas mixture injected into a gas chromatograph [64]. Unknown arterial concentrations can be determined by interpolation of the data obtained for the tracer gases [65] and remarkably precise results have been found using this approach [66]. However, this technique is time consuming and limited to only a few blood samples in each experiment and has so far been limited in use to specialised respiratory function tests [61].

Oxygen was observed to quench the fluorescence of inorganic adsorbents in the 1930's [67] and this property has since been exploited to measure both dissolved oxygen [68] and carbon dioxide [69] using *in vivo* fibre optic intravascular sensors. Fibre optical fluorosensors have recently been reported to be successful in the simultaneous measurement of halothane and oxygen [70]. The sensor works on the principle that these test gases reduce the intensity of the fluorescent light emitted from a photoexcited polycyclic aromatic molecule such as anthracene. Advantageously, this technology can be incorporated into a catheter probe. However these sensors are still undeveloped [61], and further progress may be hindered by their slow response times (≈ 2 minutes) [70].

Two commercially available detectors for monitoring anaesthetic gases work on the principle of the adsorption of, for example, halothane on a quartz crystal [71] and the characteristic IR absorption of an anaesthetic gas [72]. Other noteworthy analytical techniques for the determination of breath and blood gas include UV [73] and NMR spectroscopy [74] and surface plasma resonance [75]. Lastly, a recent article describes the continuous detection of respiratory anaesthetic gases using ion

mobility spectroscopy [76]. This appears to be a superior technique for the determination of trace levels of volatile halogenated anaesthetics and therefore may have applications to the study of recovery over a period of hours. However responses plateau at practical concentrations restricting its on–line monitoring capability.

The aim of this discussion is to highlight the wide range of sensing devices available, to consider the strengths as well as the flaws of each and to emphasise the importance of sensitive and selective continuous monitoring. These are both qualities associated with electrochemical sensors, which have the additional merits of reliability, ease of use and economy of construction and maintenance [61].

1.2.2 Electrochemical Techniques

Amperometric electrochemical sensors employ the principle of destroying the gas to be detected at a working electrode (WE). This electrode is held at a potential (measured against a reference electrode (RE)) which is sufficiently extreme to electrochemically reduce (or oxidise) all the gas which reaches it. The Faradaic current flowing between the WE and counter electrode (CE) is a function of the gas species concentration. For simplicity, the RE and CE are sometimes combined although the precise potential of the WE cannot then be deduced.

Practical sensors employing this approach are constructed by trapping a thin layer of electrolyte solution over the electrodes using a gas permeable membrane. The gas under investigation can therefore diffuse rapidly through the membrane and electrolyte to the WE. Reasonably fast response times might therefore be expected using these devices. The concentration of gas reaching the WE, $[gas]_0$, is a function of the gas concentration external to the membrane, $[gas]_*$ [61]. The first design to employ this technology was devised by Stow [77] and measured P_{CO_2} [78], although it is accepted that the first successful amperometric sensor was that of Clark [79], which was used to record P_{O_2} of blood. This is shown schematically in Figure 1.1. Severinghaus [80] used similar technology to construct a successful carbon dioxide sensor. Although these designs have been incorporated into catheter probes [81], transcutaneous [82], conjunctional [83] and respiratory [84] sensors, as well as atmospheric trace gas detectors [85,86], amperometric devices have progressed very

little since the original Clark electrode [84].

An "interference" effect was observed by several workers [87,88] when a Clark–type sensor was used to measure oxygen in the presence of nitrous oxide (N_2O). N_2O is known to be electrochemically inert on the platinum and gold WE's used in these devices but Albery and workers discovered that silver (from the Ag/AgCl RE) plated out on the WE and that N_2O can be reduced on this material [84]. These observations were utilised in the development of an amperometric sensor that could measure P_{O_2} and P_{N_2O} simultaneously in blood or gas samples [89,90]. Identical circumstances led to the development of a sensor for determining halothane. Once again, spurious interferences were observed from an oxygen electrode, this time when measurements were collected in the presence of halothane [91,92]. The anaesthetic was shown to be electroactive on silver [93] and a sensor thus constructed, as illustrated in Figure 1.2, which could simultaneously measure oxygen, nitrous oxide and halothane [94]. The latter, however, can only be quantitatively reduced on silver in the absence of oxygen [93] and this sensor therefore utilises a metallised membrane (made by depositing gold or silver on teflon using vacuum evaporation) in order to both measure and filter oxygen. The device operates in a pulsed amperometric mode [95] to enhance sensitivity and to avoid electrode contamination by reaction products [90].

To date, no report of any electroactivity of forane at any electrode or in any solvent system has appeared in the literature, and therefore no electrochemical sensor for its detection exists. This inertness is not unexpected in the light of the chemical properties described in section 1.1 [36,37], together with the known tendency of alkyl halides, in general, to display a high overpotential to electrochemical reduction [96–98]. Work in this thesis will therefore study the electroactivity of forane using conventional electrode/solvent systems and also examine the possibility of performing an indirect electron transfer either homogeneously, using a mediator in solution, or heterogeneously, using a chemically modified electrode. Quantitative voltammetric behaviour will be shown to lead to the development of an amperometric sensor for forane, possessing all the benefits mentioned above.

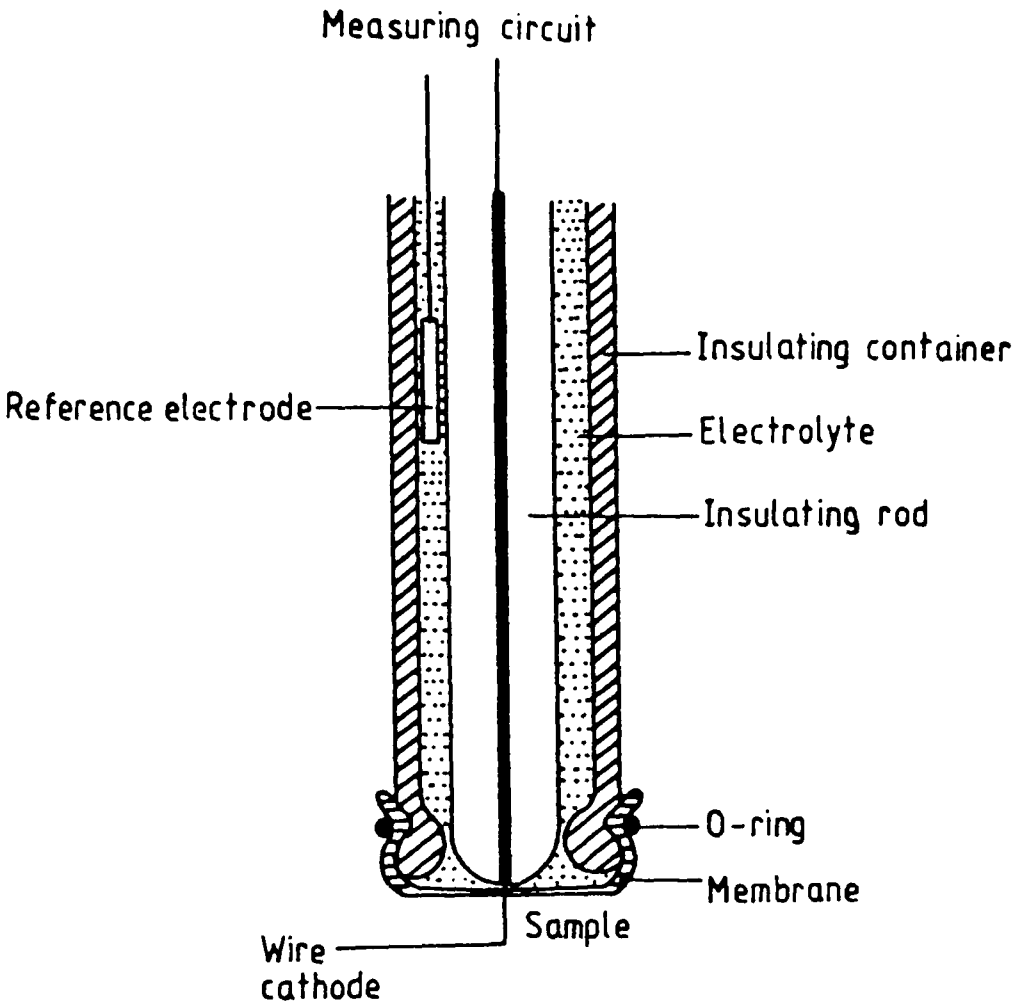


Figure 1.1: A schematic outline of a practical Clark P_{O_2} sensor.

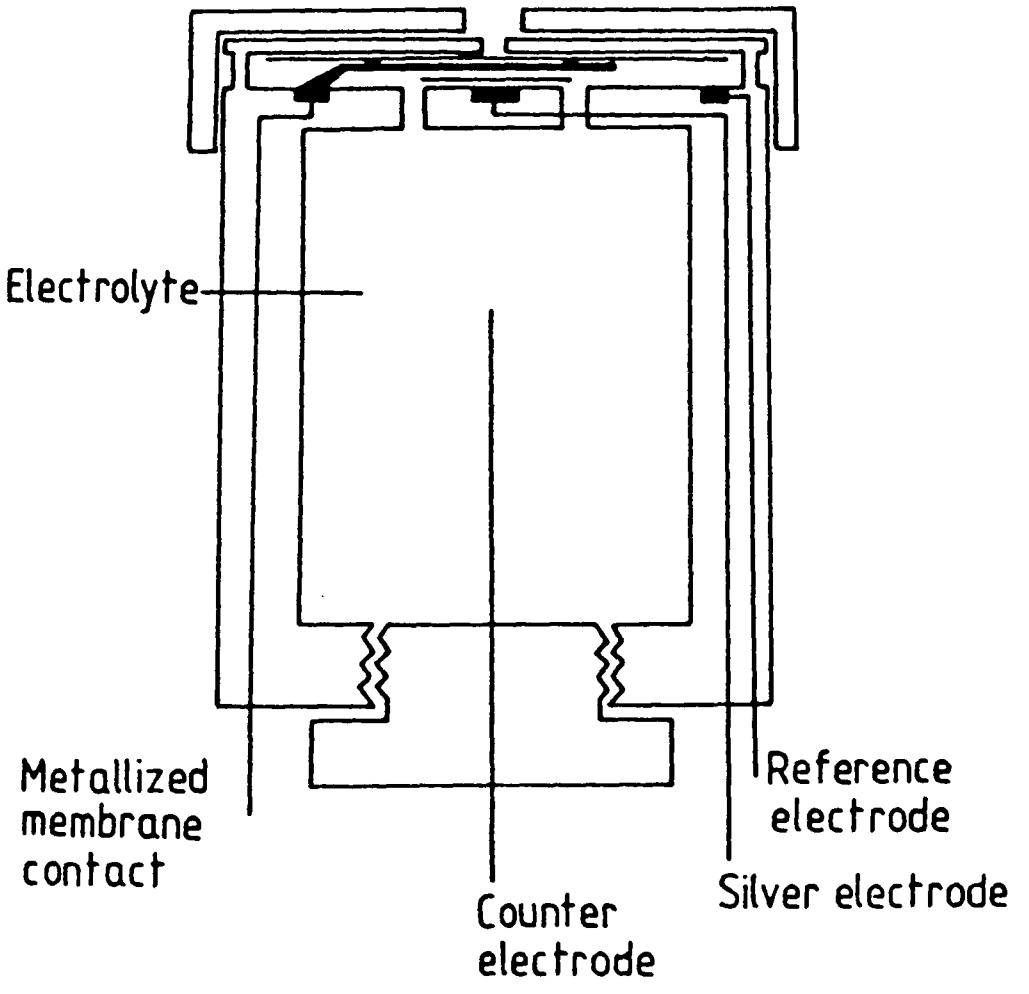


Figure 1.2: Schematic view of the composite sandwich electrode of Albery *et al.*

1.3 The Aims and Objectives of this Thesis

The aim of this thesis is the development and laboratory assessment of an amperometric sensor for the detection of the volatile anaesthetic, forane. This, therefore, involves in the investigation of both the heterogeneous and homogeneous reduction of this agent.

Chapter Two introduces the fundamental principles of electrochemistry via a discussion of mass transport and heterogeneous electron transfer. The range of electro– and spectroelectro–chemical techniques employed in this thesis are also described. The particular merits of hydrodynamic electrodes are proposed and theoretical descriptions of mass transport to the channel (ChE) and rotating disc (RDE) electrodes are presented.

Theory is described in Chapter Three which solves the convective–diffusion equations appropriate for the ChE and RDE. A general numerical strategy is presented for the calculation of chronoamperometric and steady–state RDE problems which involve coupled homogeneous and heterogeneous kinetics. Two approaches to the theoretical solution of steady–state ChE problems are introduced and particular emphasis is placed on those reactions involving homogeneous complications.

The experimental details of the techniques, instrumentation and chemicals used throughout this thesis are given in Chapter Four.

The electrochemistry of the polycyclic aromatic compound, fluoranthene (F), is examined at the RDE in Chapter Five and the experimental results obtained are compared with the theoretical predictions of Chapter Three for i) simple electron transfer, ii) coupled heterogeneous and iii) coupled homogeneous processes. F is shown to adsorb onto the mercury electrode and this property is investigated further in Chapter Six, where lithium ions are demonstrated to displace the adsorbed organic moiety, forming a thick solvated layer which inhibits heterogeneous electron transfer to solution phase F.

In Chapter Seven, forane is shown to be electroinactive on all conventional electrode materials. However, electron transfer to the anaesthetic via the radical

anion of fluoranthene is demonstrated, when the latter is attached to polymer backbone and immobilised on an electrode, or when electrogenerated in bulk solution.

The homogeneous approach is incorporated into a Clark–type membrane electrode sensor in Chapter Eight, where the detection and measurement of forane, in the absence of O_2 is demonstrated using this device.

Chapters Nine and Ten are concerned with the development of a practical amperometric ChE sensor for forane. Chapter Nine confirms that the homogeneous reduction of forane, using the radical anion of fluoranthene as an electrogenerated mediator, follows the same mechanism at the ChE as determined at the RDE in Chapter Seven. This work is extended in Chapter Ten to the construction of a workable ChE sensor, which is assessed in the presence of other species likely to be present in a clinical environment.

CHAPTER TWO

ELECTROCHEMICAL PRINCIPLES

The application of electrochemical techniques to the investigation of electrode reaction mechanisms and kinetics will be discussed in this chapter. Two classes of reaction will be of primary interest: i) electrode processes which involve homogeneous reactions coupled to electron transfer, ii) reactions involving adsorption at the electrode/solution interface. The preference for defined and calculable mass transport in the study of both types of reaction will be discussed and thus hydrodynamic electrodes introduced. Mass transport to the two hydrodynamic electrodes employed in this work will be described in detail and solutions given to the convective–diffusion equations for a transport–limited reaction. In addition, a comparison with investigations carried out in quiescent solution will be included.

2.1 Electrode Processes

In its simplest form, an electrochemical cell consists of two electrodes dipping into an electrolyte solution which forms a contact between the two electrodes. When the two electrodes are connected to a current source of sufficiently high voltage, then current will flow through the cell, causing an electrochemical reaction to occur at each electrode. This process is known as electrolysis. Under normal circumstances the reaction occurring at one electrode only, the working electrode (WE), is of specific interest; the other electrode is now referred to as the counter electrode (CE).

In order to measure the precise voltage which is being applied to the WE a third electrode, the reference electrode (RE), is employed.

Consider the simple reaction taking place at the WE :

$$O + ne^- \longrightarrow R. \qquad 2.1$$

The current flowing between the CE and RE is generally a function of the applied potential. The study of this current–voltage relationship is known as voltammetry and clearly factors which affect the current will be of fundamental importance to such investigations. The current will be directly related to the rate of the electrode reaction, which is in turn governed by the rates of processes such as:

1. mass transport from bulk solution.
2. electron transfer at the electrode surface.
3. homogeneous or heterogeneous chemical steps preceding or following electron transfer.
4. heterogeneous surface processes. i.e. adsorption and/or desorption.
5. removal of product back to bulk solution.

The inter–relationship between each of these processes must be fully evaluated in order to determine the mechanism of an electrode reaction. In particular, it should be noted that the efficiency of electron tunneling falls approximately exponentially with distance and that electron transfer is thought to occur within about 10Å of the electrode surface (a more detailed discussion of electron tunneling appears in Chapter Six). Therefore knowledge of the concentration of electroactive material at the electrode surface ($[O]_0$) is of the upmost importance; this is rarely the same as that of the bulk solution ($[O]_\infty$). A rigorous treatment of the various modes of transport adopted by an electroactive species through a solution can however enable the calculation of $[O]_0$ from $[O]_\infty$. This will be discussed in sections 2.1.2 and 2.3.

Returning to the very simple reaction of equation 2.1, then, in the absence of any complications, the electrode reaction rate, and therefore current, will depend on the relative kinetics of steps 1.,2. and 5. Each process must therefore be considered in detail.

2.1.1 Electron Transfer

$$O + ne^- \longrightarrow R \qquad 2.1$$

The rate of such an electrode reaction can be expressed by the number of moles of substance, N, which react in unit time per unit area:

$$-\frac{\partial N_O}{\partial t} = \frac{\partial N_R}{\partial t} = k_f [O]_o - k_b [R]_o. \qquad 2.2$$

k_f and k_b are the forward and backward heterogeneous rate constants measured in units of cms^{-1} and can be related to the applied potential by [99]:

$$k_f = k^0 \exp\left[\frac{-\alpha n F (E - E^0)}{RT}\right] \qquad 2.3a$$

$$k_b = k^0 \exp\left[\frac{(1-\alpha) n F (E - E^0)}{RT}\right] \qquad 2.3b$$

where E refers to the potential measured and E^0 the standard potential of the couple in question, k^0 is the standard heterogeneous rate constant and α is the cathodic transfer coefficient, a constant with a value between 0 and 1 (usually approximated to 0.5), which describes the potential dependence of the free energy of the transition state for the electron transfer. The rate of the electrochemical reaction can be found by combining equations 2.2 and 2.3 :

$$i_d = nFk^0 \{ [O]_0 \exp\left[-\frac{\alpha n F (E - E^0)}{RT}\right] - [R]_0 \exp\left[\frac{(1-\alpha) n F (E - E^0)}{RT}\right] \} \qquad 2.4$$

$$\text{or} \quad i_d = i_c + i_a$$

where i_d is the current density (Acm^{-2}) and i_c and i_a represent the cathodic and anodic components of the current respectively. Current density is therefore shown to be a function of the difference between the applied potential and the standard

electrode potential for the same reaction.

At equilibrium, no electrochemical reaction occurs, no net current flows and $[O]_0$ will be equal to $[O]_\infty$. Therefore $i_c = i_a$ and :

$$nFk^0[O]_0 \exp\left[-\frac{\alpha nF(E_e - E^0)}{RT}\right] = nFk^0[R]_0 \exp\left[\frac{(1-\alpha)\ nF(E_e - E^0)}{RT}\right] \qquad 2.5$$

or by rearranging to give the Nernst equation [99]:

$$E_e = E^0 + \frac{RT}{nF} \ln\frac{[O]_\infty}{[R]_\infty} \qquad 2.6$$

where E_e is the equilibrium potential. Strictly activities rather than concentrations should be employed here but the activity coefficients are in effect included in the formal rate constants used.

The rate of an electron transfer reaction is very sensitive to changes in the electrode potential and it is therefore more useful to consider the equilibrium potential as a reference and work in a non equilibrium environment. To this end, the overpotential, η, is defined as:

$$\eta = E - E_e \qquad 2.7$$

$$\text{or} \quad \eta = E - E^0 - \frac{RT}{nF} \ln\frac{[O]_\infty}{[R]_\infty} \qquad 2.8$$

Equation 2.4 may now be rewritten to give the net current density as:

$$i_d = nfk^0 \left\{ [O]_0 \left[\frac{[R]_\infty}{[O]_\infty}\right]^\alpha \exp\left[-\frac{\alpha n F \eta}{RT}\right] - [R]_0 \left[\frac{[O]_\infty}{[R]_\infty}\right]^{1-\alpha} \exp\left[\frac{(1-\alpha) nF\eta}{RT}\right] \right\} \qquad 2.9$$

which is an exact form of the Butler – Volmer equation [99], normally presented as:

$$i_d = i_c + i_a = i_0 \left[\exp\left[\frac{(1-\alpha)\,nF\eta}{RT} \right] - \exp\left[-\frac{\alpha n F \eta}{RT} \right] \right] \qquad 2.10$$

The terms in the square brackets represent the anodic (negative) and cathodic (positive) contributions to the overall current and the exchange current density, i_0, is a scaling factor which depends on the values of k^0, $[O]_\infty$ and $[R]_\infty$. Figure 2.1 shows how the current varies with overpotential, revealing the asymmetry caused by $\alpha \neq 0.5$ and the scaling effect of i_0. It should be noted here however that this assumes $[O]_0 = [O]_\infty$; that is, that there is no change in reactant concentration close to the electrode. The remainder of this section shows how this will only be justified at low overpotentials.

Consider small values of η, such that $-RT/\alpha nF << \eta << RT/\alpha nF$, then the exponential terms of equation 2.10 can be written as Taylor expansion and combined, yielding:

$$i_d = \frac{i_0\, nF\eta}{RT} \qquad 2.11$$

An Ohmic resistance of the electrode/solution interface can be defined by rearranging equation 2.11 thus:

$$R_{ct} = \frac{RT}{nF\, i_o} \qquad 2.12$$

where R_{ct} is the charge transfer resistance, so that:

$$i_0 = \frac{\eta}{R_{ct}} \qquad 2.13$$

The exchange current is therefore a measure of the ease with which a given electrode reaction proceeds. High values of i_0 means that there is a low resistance to charge transfer – so called reversible systems, while low values correspond to a high resistance – irreversible systems. i_0 has been found experimentally to vary not only

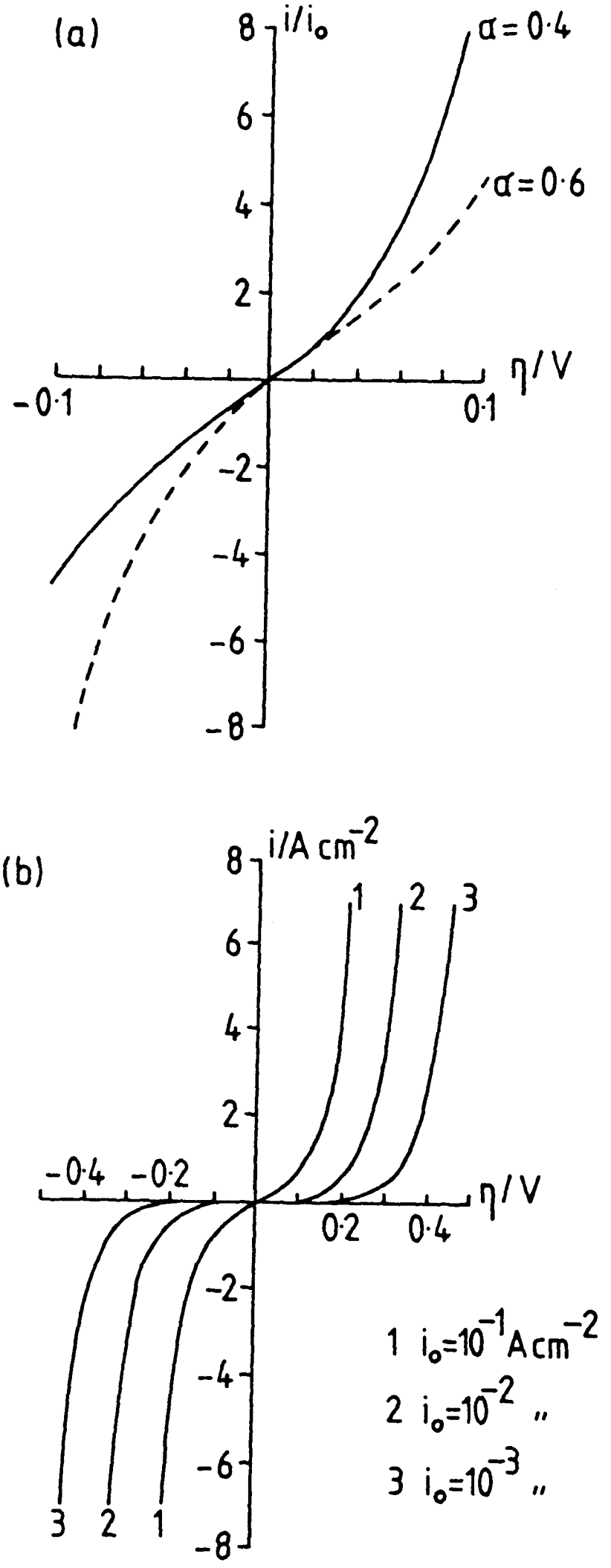


Figure 2.1: Current – voltage characteristics predicted by equation 2.10. (a) shows the effect of α on the symmetry of this plot and (b) the scaling effect of i_0.

from system to system but also for the same system on different electrode materials. The choice of electrode material can hence be important in analytical investigations.

Figure 2.2 shows that in practice, the linear approximation is only valid for $|\eta| \leq 10/n$ mV. Considering the full Butler – Volmer equation at large positive or negative overpotentials, then one or other of the exponentials dominate and the limiting relationships become for large negative overpotentials:

$$i_d = -i_0 \exp[-\alpha n F \eta / RT] \qquad 2.14a$$

and for large positive overpotentials:

$$i_d = i_0 \exp[(1-\alpha) n F \eta / RT] \qquad 2.14b$$

These equations may be rewritten into the more usual Tafel form [100]:

$$\eta = \frac{2.3RT}{\alpha n F} [\log i_0 - \log i_d] \qquad \eta < 0 \qquad 2.15a$$

and

$$\eta = \frac{2.3RT}{(1-\alpha)\, nF} [\log i_0 + \log i_d] \qquad \eta > 0 \qquad 2.15b$$

Plots of log i_d versus η are called Tafel plots and contain information about the exchange current density i_0 and the transfer coefficient α. Figure 2.3 shows a Tafel plot for $\alpha = 0.5$.

Hence, as the overpotential is increased in either direction, the current will increase exponentially. This results in an increasing consumption of the electroactive material at the electrode surface (particularly if i_0 is large), so that a point is eventually reached where the rate of electron transfer is limited by the rate of transport from the bulk of solution to the electrode. Mass transport of bulk solution therefore needs to be considered.

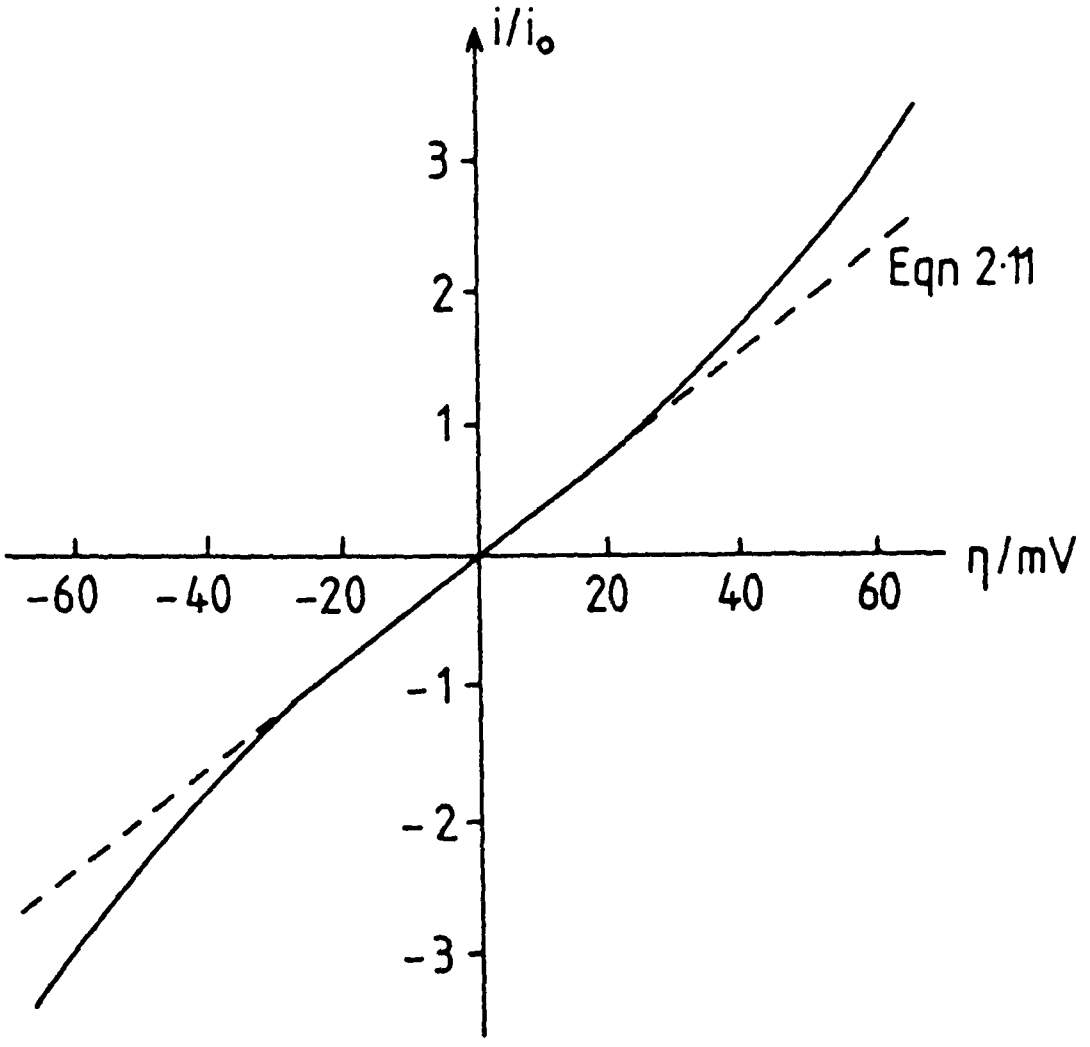


Figure 2.2: The linear approximation to the Butler – Volmer equation.

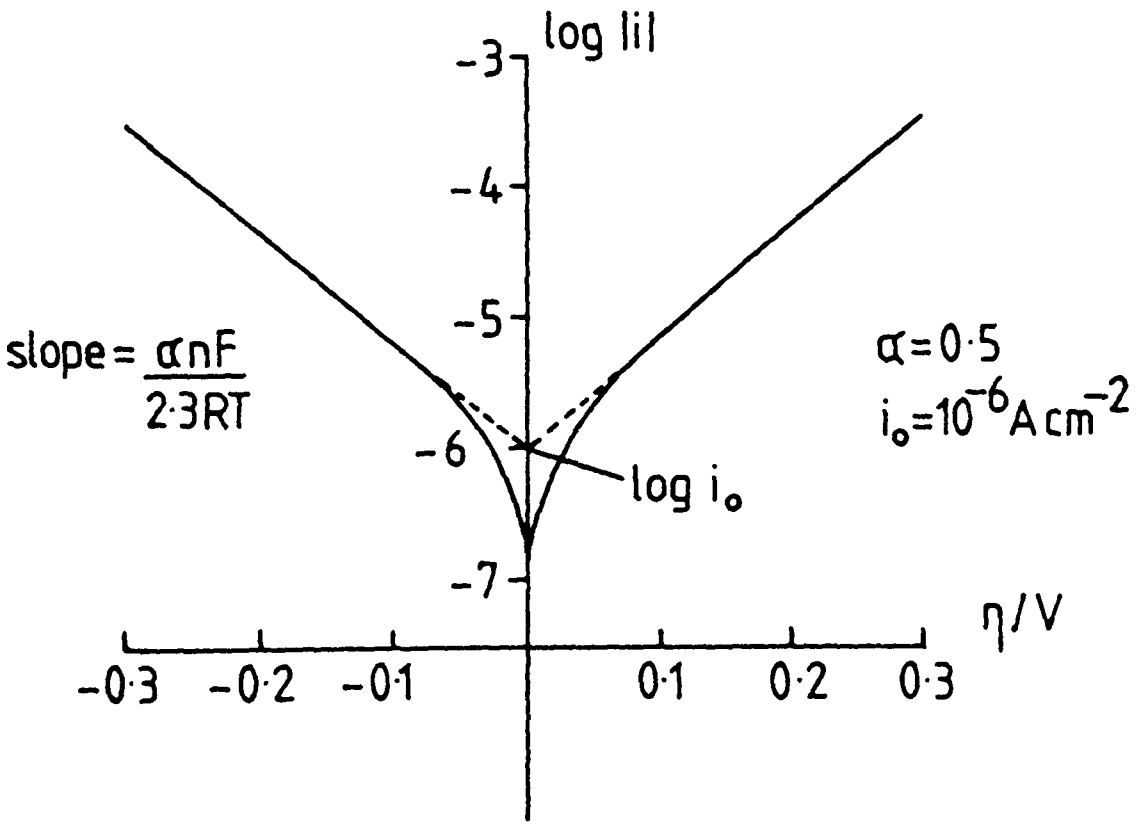


Figure 2.3: Tafel plots for the anodic and cathodic branches of the current – overpotential curve.

2.1.2 Mass Transport

At a sufficiently extreme potential, the heterogeneous electron transfer can be driven fast enough so that the electrode reaction rate (current) is limited only by the rate at which the electroactive material can be delivered to the electrode. Several detailed reviews of mass transport through solution to a solid electrode appear in the literature [101–104]. Three main processes operate: migration, diffusion and convection, and the relative importance of each will be shown to be experimentally controllable.

The flux, j_o, of a solute species reaching an electrode is described by the sum of the three modes of mass transport :

$$j_o = j_c + j_d + j_m \qquad 2.16$$

where j_c is the flux due to convection, j_d is the flux due to diffusion and j_m is the flux due to migration. Each process will now be examined in more detail.

2.1.2.1 *Migration*

This occurs when a charged particle is placed in an electric field; thus negatively charged ions will be attracted to a positive electrode and positive ions to a negative electrode. The flux due to migration of a given ion is proportional to its charge, concentration and to the electric field gradient:

$$j_m = -\frac{zF}{RT} Dc \frac{\partial E}{\partial z} \qquad 2.17$$

where z is the charge on the ion, $\frac{\partial E}{\partial z}$ the electric field gradient and c the concentration ($molcm^{-3}$). Migration is invariably a complicating factor in an electrochemical system and therefore needs to be suppressed. Since the force leading to migration is purely electrostatic, the charge may be carried by any ion in the solution. Therefore, if a large concentration of ionic, electroinactive background electrolyte is present, only a small, negligible part of the current will be due to

migration of the electroactive material.

2.1.2.2 *Convection*

This is a result of the movement of a fluid by mechanical means (forced convection) or by natural means due to the presence of temperature or density gradients (natural convection). In contrast to migration (and diffusion) where solute molecules more through a "stationary" solution, convection describes the transport of a solution as a whole. The flux due to convection is given by:

$$j_c = \vec{v}\, c \qquad 2.18$$

where $\vec{v}$ is the fluid velocity vector.

When a liquid flows past the surface of a solid body, the layer of fluid immediately adjacent to the surface remains motionless. The stationary layer or boundary layer is very narrow -- of the order of several molecules thick -- and is caused by viscous forces alone. Although the boundary layer occupies only an extremely small volume, it exerts a significant influence on the motion of the fluid. Detailed analysis shows that the thickness of the hydrodynamic boundary layer, δ_b, can be related to the characteristic length of a system, l, by the Reynolds number:

$$\frac{\delta_b}{l} \approx \frac{1}{\sqrt{Re}} \qquad 2.19$$

Thus δ_b is smaller than the characteristic dimension of the body by a factor approximately equal to the square root of the Reynolds number.

The transition from viscous flow in the boundary layer to laminar flow in the bulk fluid is smooth and gradual. The quantity, δ_b, represents the thickness of the region across which the principal change in the velocity from zero to its maximum, bulk value occurs.

2.1.2.3 *Diffusion*

This occurs when a gradient of chemical potential exists in the solution. It is

therefore not the result of any physical force but rather a thermodynamic response as the solution maximises its entropy. In the electrochemical cell, diffusion results from concentration gradients of the electroactive species and affects charged and uncharged species equally. Quantitative treatment of diffusion is provided by Fick's First and Second Laws, which deal with the space and time dependence of diffusion respectively. These may be represented mathematically by:

Fick's First Law

$$j_d = -D\frac{\partial c}{\partial z} \qquad 2.20$$

Fick's Second Law

$$\frac{\partial c}{\partial t} = D\frac{\partial^2 c}{\partial z^2} \qquad 2.21$$

where j_d is the flux of the material in the z direction (measured in $molcm^{-2}s^{-1}$) and D is the diffusion coefficient (cm^2s^{-1}).

The diffusion coefficient is an exponential function of temperature [105]:

$$D = D_0 \exp\left[\frac{-E_d}{RT}\right] \qquad 2.22$$

where E_d is the activation energy for diffusion or the energy required to surmount the barrier a given species must overcome in diffusing from one site to another and D_0 is the diffusion coefficient at some reference temperature. Most importantly, D therefore increases with temperature – about 2% per degree for an aqueous solution. Hence the temperature of any electrochemical experiment must be constant and measurable if diffusion is to be a controllable factor.

It is now possible to redefine equation 2.16 as:

$$j_o = \vec{v}[O] - D_0\frac{\partial[O]}{\partial z} - \frac{zF}{RT} D_0 [O] \frac{\partial E}{\partial z} \qquad 2.23$$

or in the presence of a high concentration of inert electrolyte:

$$j_0 = \vec{v}[O] - D_0 \frac{\partial [O]}{\partial z} \qquad 2.24$$

In three dimensions:

$$\vec{j} = \vec{v}[O] - D_0 \nabla [O] \qquad 2.25$$

or in terms of time and space:

$$\frac{\partial [O]}{\partial t} = -\nabla \vec{j} \qquad 2.26$$

$$\frac{\partial [O]}{\partial t} = D_0 \nabla^2 [O] - \vec{v} \nabla [O] \qquad 2.27$$

and as we can now see, two experimental strategies emerge for the study of electrode reactions:

(a) quiescent solutions, with no forced convection.

(b) convective – diffusion systems.

2.2 Diffusion–only Systems

Equation 2.27 reveals that if no convection is employed then diffusion remains the only means of mass transport of a reactant to the electrode. The sole approach for electrode reaction investigation is therefore to measure j_0 at the interface as a function of time, after a large step or oscillation in concentration of O at the solid surface. Such steps or oscillations in [O] are easily performed at an electrode since $[O]_0$ may be readily controlled by the applied potential. Studies in the time domain – transient techniques – are therefore feasible. An instantaneous perturbation of the electrode potential (or current) results in a corresponding perturbation in j_0 and the

system is then monitored as it relaxes back to a new steady state. Chronoamperometry and chronopotentiometry are typical examples of such techniques [106].

Alternatively, a periodically varying perturbation of current or potential may be applied to the system, and its response measured as a function of the perturbation. Cyclic [107] and a.c. voltammetry [108] are both examples of this experimental approach. Collection of data over a wide range of times or frequencies means that mechanistic and kinetic analysis is feasible using these techniques.

When the size of the electrode is reduced so that one dimension is of the order of 10^{-6}m, then two dimensional diffusion becomes significant. Steady–state measurements are then possible under diffusion–only conditions. This has led to the recent popularity in the investigation of electrode reactions at microelectrodes [109]. However, restrictions on the size of the electrode and the rate of mass transport (controlled by varying the microdimension) may limit the general applicability of this method for mechanistic and kinetic studies, although the use of these electrodes for detecting and monitoring purposes has already been proposed [110].

2.2.1 Linear Sweep/Cyclic Voltammetry

In these techniques, the potential of a stationary electrode is varied linearly with time using the sequence shown in Figure 2.4. Figure 2.5 shows a typical linear sweep voltammogram (LSV) current–voltage curve for a reversible charge transfer process obtained for the various scan rates indicated. Features of significance, which are labelled, are the peak current (i_p), the peak potential (E_p), the reversible potential ($E_{rev} = E^0$ at 298 K vs. S.H.E.) and the half–wave potential ($E_{1/2}$). This notation is also applicable to the cyclic voltammogram (CV) shown in Figure 2.6. However here, processes occurring during the cathodic scan are superscripted (red) and those which take place after the potential has been reversed, (ox) [107].

The LSV of Figure 2.5 assumes that initially only O is present in solution and that the sweep in the negative direction causes the reversible electrode reduction:

$$O + ne^- \rightleftharpoons R$$

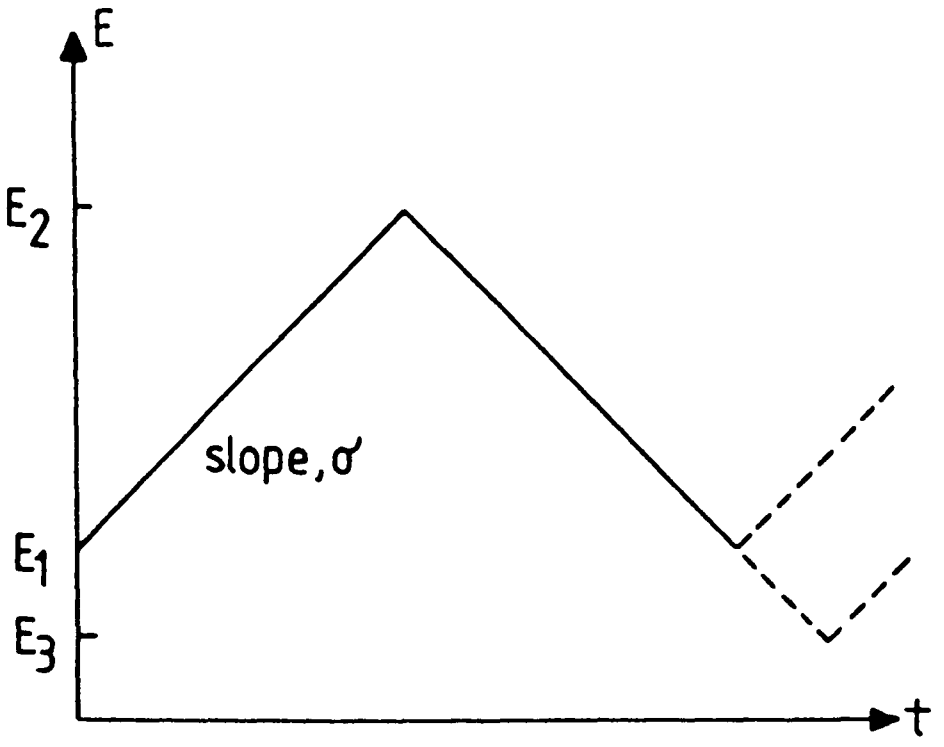


Figure 2.4: Potential – time profile for sweep voltammetry.

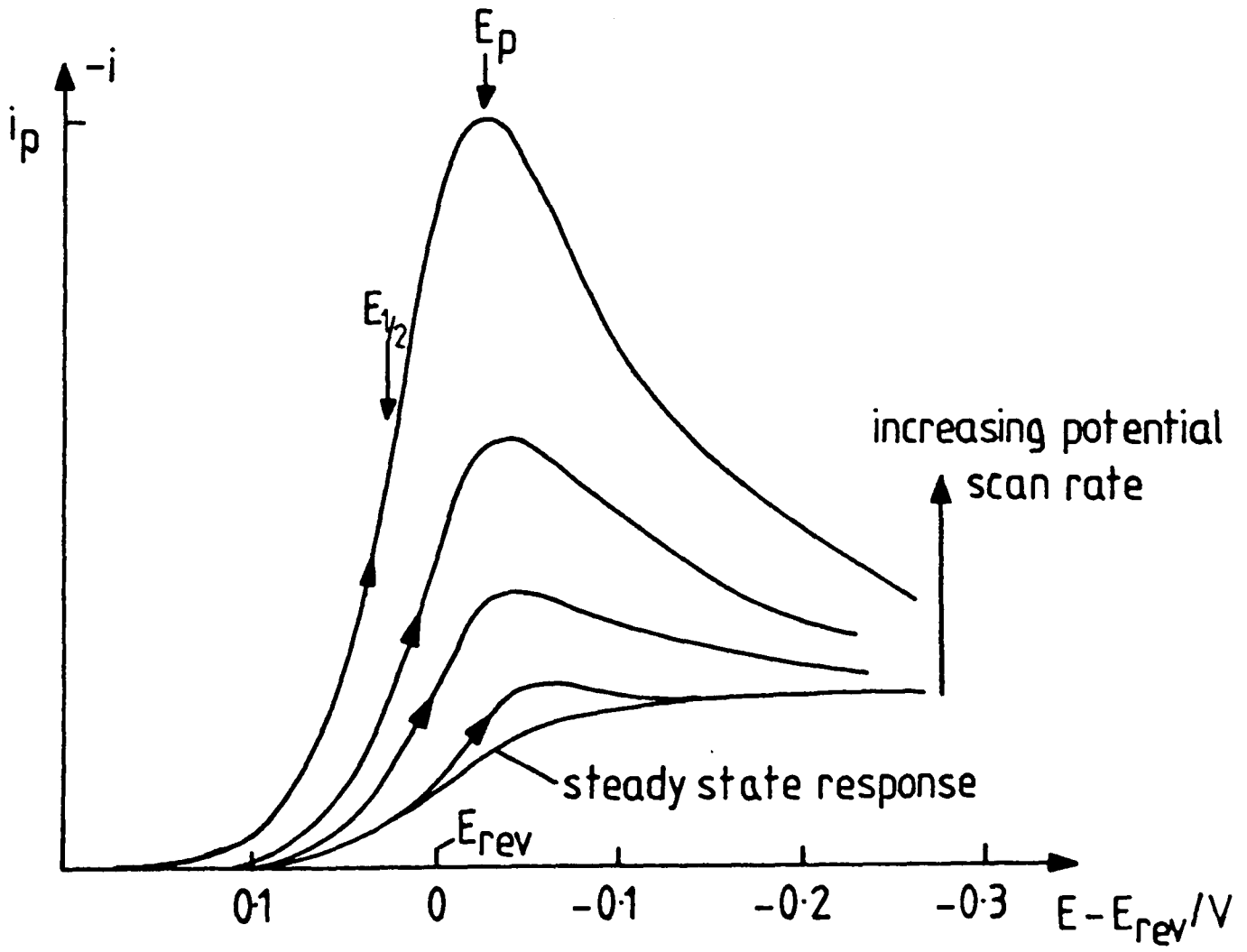


Figure 2.5: A series of linear sweep voltammograms at several potential scan rates.

At very slow scan rates, the voltammogram appears like a steady–state curve, but as the sweep rate is increased, a peak of increasing height develops; this behavior is readily explained by consideration of the concentration profiles of O as a function of potential. Natural convection maintains a constant concentration of reactant in the bulk of solution but in the region near to the electrode (within the diffusion layer – see section 2.3) the concentration gradients of O and R are steep and essentially linear. The ratio of $[O]_0/[R]_0$ for the reversible reaction can be found from the Nernst equation:

$$\left[\frac{[O]_0}{[R]_0}\right](t) = \exp\left[\frac{nF}{RT}\{E(t) - E_{rev}\}\right] \qquad 2.28$$

and hence as the potential scans more negative, so the surface concentration of the reactant progressively decreases. The reactant therefore diffuses towards the electrode and the product away. As the scan progresses, the concentration gradients, and likewise the current, increase until a potential is reached (E_p) where mass transfer is at its maximum. At more negative potentials, the current begins to fall as a consequence of the depletion of [O] in the vicinity of the electrode. Now essentially all reactant which reaches the electrode is immediately reduced and the current is diffusion controlled. The variation of the concentration profiles with time during a LSV is shown in Figure 2.7. This overall behaviour gives rise to the peak shaped current – voltage curves of Figure 2.5. Faster scans cause steeper concentration gradients and thus larger values of i_p.

In the case of the return sweep, applicable for a CV, at slow scan rates the pseudo steady–state nature means that the i–E response of the backward sweep directly tracks the forward one. For faster sweeps, however, the reduction initially continues producing R until E_{rev} is reached when an oxidation process takes over. Similar arguments apply for this process, as for the forward sweep, so that on increasing the potential, the anodic current peaks at E_p^{ox}, before returning to the initial baseline. For a reversible process, the shape of the wave is virtually identical in both directions, although the baseline is less well defined for the reverse sweep.

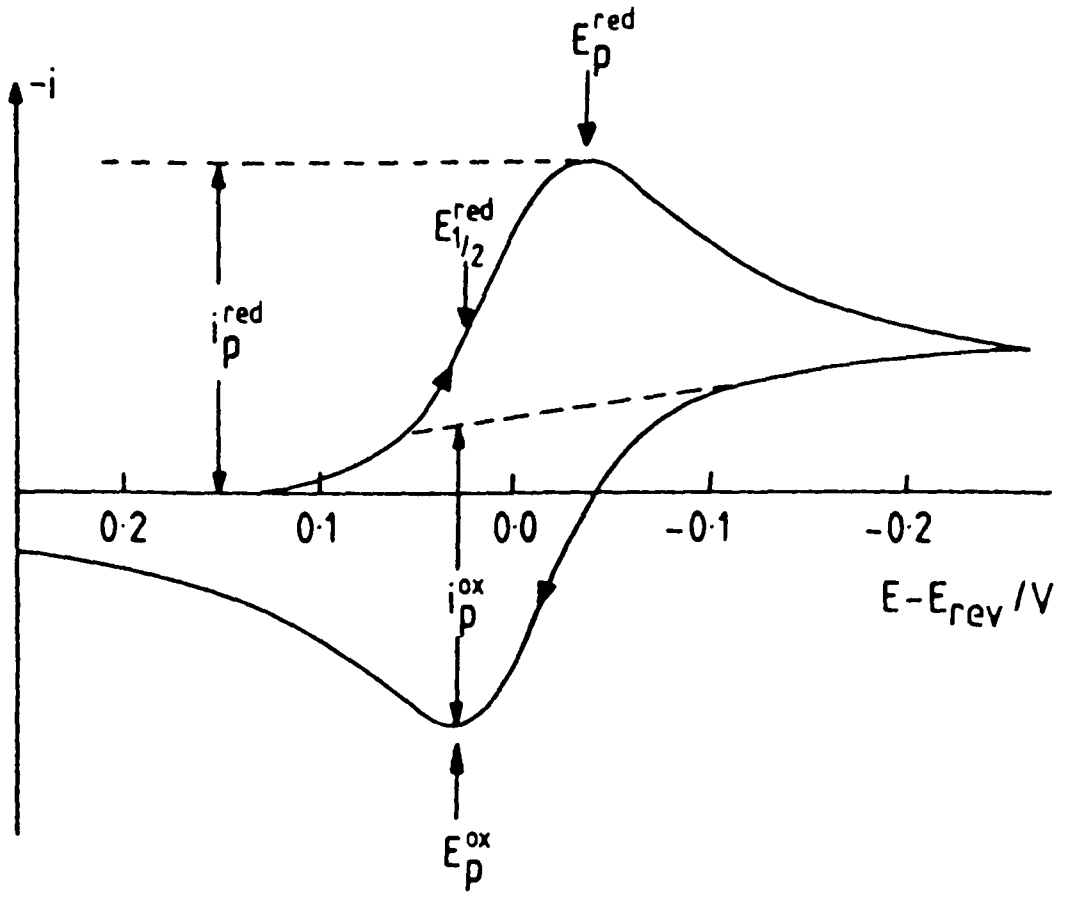


Figure 2.6: Cyclic voltammogram for the reversible process $O + ne \rightleftharpoons R$. Initially only O present in solution.

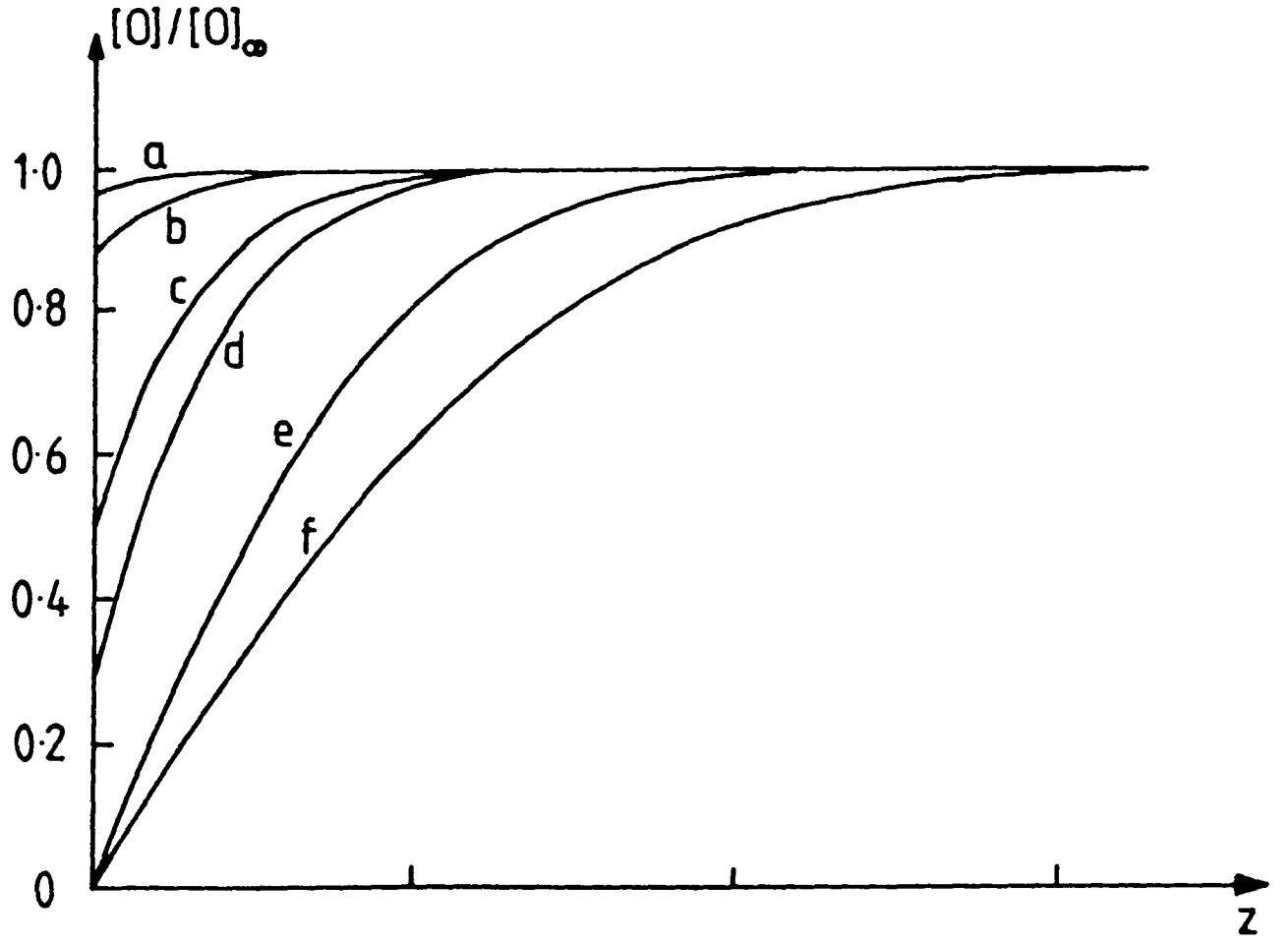


Figure 2.7: Concentration – distance profiles for O during a linear sweep experiment. a) E_{rev}+90mV, b) E_{rev}+50mV, c) E_{rev}, d) E_{rev}–28mV, e) E_{rev}–128mV, f) E_{rev}–280mV.

Considering a planar stationary electrode, where semi–infinite linear (planar) diffusion is the only form of mass transport in operation, then the mathematical description of the i–E response during a CV can be found from Fick's Second Law [111–113]:

$$\frac{\partial[O]}{\partial t} = \frac{\partial^2[O]}{\partial z^2} \quad \text{and} \quad \frac{\partial[R]}{\partial t} = \frac{\partial^2[R]}{\partial z^2} \qquad 2.29$$

When initially only reactant O is present in solution and assuming $D_O = D_R = D$, then the initial and boundary conditions are:

$$t = 0, \quad z > 0, \quad [O] = [O]_\infty \quad [R] = 0 \qquad 2.30\ \text{i}$$

$$t > 0, \quad z = \infty, \quad [O] = [O]_\infty \quad [R] = 0 \qquad \text{ii}$$

$$t > 0, \quad z = 0, \quad D\left[\frac{\partial[O]}{\partial z}\right] = -D\left[\frac{\partial[R]}{\partial z}\right],$$

$$\left[\frac{[O]_0}{[R]_0}\right] = \exp\left[\frac{nF}{RT}(E - E_{rev})\right]$$

$$\text{and} \quad i = -nFAD\,\frac{\partial[O]_0}{\partial z} \qquad \text{iii}$$

For a sweep rate σ:

$$0 < t < \lambda \qquad E = E_1 - \sigma t \qquad 2.31$$

$$t > \lambda \qquad E = E_1 - 2\sigma\lambda + \sigma t \qquad 2.32$$

where E_1 is the initial potential and λ is the time at which the scanning potential is reversed.

The solution of this problem is made difficult by the time dependent potential term, but it has been shown that for planar diffusion:

$$i_p = -0.4463\,[O]_\infty A\left[\frac{n^3 F^3}{RT}\right]^{1/2}\sigma^{1/2}D^{1/2} \qquad 2.33$$

where A is the area of the electrode (cm^2). This is commonly known as the Randles–Sevcik equation [111,112]. Also:

$$E_p - E_{rev} = -1.109 \frac{RT}{nF} \qquad 2.34$$

and

$$E_p - E_{1/2} = -2.20 \frac{RT}{nF} \qquad 2.35$$

Hence CVs may be used as a diagnostic test for a reversible process, since at 25°C [114]:

1. $E_p^{ox} - E_p^{red} = 59/n \text{ mV}$ 2.36 i
2. $|E_p - E_{1/2}| = 59/n \text{ mV}$ ii

3. $|i_p^{ox} / i_p^{red}| = 1$ iii
4. $i_p \alpha \sigma^{1/2}$ iv
5. E_p is independent of σ v

For a totally <u>irreversible</u> system:

$$O + ne^- \xrightarrow{k_f} R$$

the initial boundary conditions (2.30 i and ii) are identical to those for the reversible case. However iii now becomes:

$$t > 0, \qquad z = 0 \qquad \frac{1}{nFA} = D\left[\frac{\partial [O]_0}{\partial z}\right] = k_f [O]_0 \qquad 2.37$$

where

$$k_f = k_0 \exp\left[\frac{-\alpha nF}{RT} (E - E_{rev})\right]$$

These differential equations have been solved to yield the following equation for the peak current at 25°C [113,115]:

$$i_p = 2.99 \times 10^5 (\alpha n)^{1/2} [O]_\infty A D^{1/2} \sigma^{1/2} \qquad 2.38$$

and the relationships between the potentials as:

$$E_p - E_{rev} = \frac{-RT}{\alpha n F}\left[0.780 + \ln\left[\frac{D}{k_0}^{1/2}\right] + \ln\left[\frac{\alpha n F \sigma}{RT}\right]^{1/2}\right] \qquad 2.39$$

and

$$E_p - E_{1/2} = 1.857\,\frac{RT}{\alpha n F} = \frac{47.7}{\alpha n}\ mV \qquad 2.40$$

Therefore the diagnostic tests for a totally irreversible process are:

1. No reverse peak (could also be caused be fast following chemical reaction)
2. $i_p^{rev}\ \alpha\ \sigma^{1/2}$
3. E_p^{red} shifts by $30/\alpha n$ mV per decade increase in σ
4. $|E_p - E_{1/2}| = 47.7/\alpha n$ mV

Cyclic voltammetry can also be employed as a means of investigating adsorption and desorption [116,117]. When the adsorbed species only are electroactive in the potential range of interest, then a symmetrical CV similar to the one shown in Figure 2.8 can be obtained. The peaks are sharp, rising essentially from zero current to a peak value and then falling once again to zero. There is little or no peak separation. Symmetry arises because only a fixed amount of reactant O is present on the electrode surface and the values of i_p, E_p and peak width depend on the type of adsorption isotherms involved and the relative strengths of adsorption of O and R.

The area under the cathodic peak corresponds to the charge associated with the reduction of the adsorbed layer, enabling the surface excess of O, Γ_o, to be determined [118]:

$$i_p = \frac{n^2F^2}{4RT}\ \sigma A \Gamma_o \qquad 2.41\ i$$

For the irreversible case [117], the forward peak ceases to be symmetric and there is no reverse peak. Now [118]:

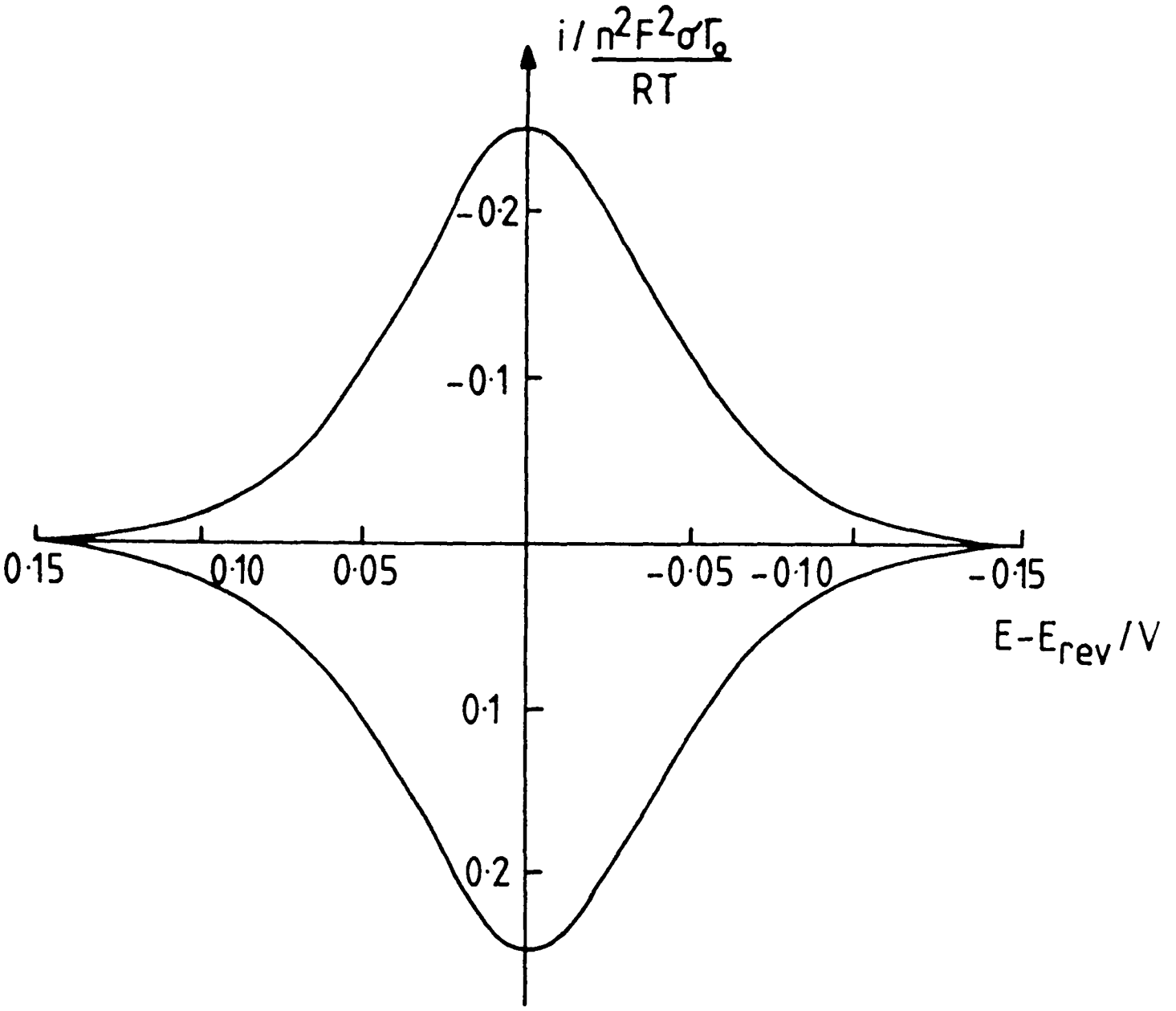


Figure 2.8: Cyclic voltammogram for the reduction of adsorbed O and reoxidation of the product. Free energies of adsorption of O and R are equal.

$$i_p = \frac{n^2 F^2 \alpha\sigma A\Gamma_0}{2.718\ RT} \qquad \text{ii}$$

Cyclic voltammetry has also been used in the investigation of polymer modified electrodes [119] – where a reactant is attached to the electrode by chemical means. These behave very similarly to adsorption systems, voltammetric analysis therefore proceeds as outlined above and for fast electron transfer within the polymer coat, the peak current varies linearly with scan rate [120,121].

In conclusion, LSV and CV are excellent means of examining a system for the first time, recording voltammograms over a wide range of potentials and sweep rates to provide qualitative information. Studying the variation of peak height with scan rate can identify the roles of adsorption, diffusion and coupled homogeneous reactions [122–123], as well as determining the reversibility of a given system. However, it should be noted that the use of these techniques in providing quantitative kinetic detail is limited by the analytical measurement of i_p and E_p alone.

2.2.2 AC Impedance

When a sinusoidal perturbation of potential is applied to an electrochemical system then it is, in principle, possible to separate the capacitive and resistive components of the current by their phase differences in the response signal. This method – AC impedance, is hence important for double layer studies as well as the investigation of electrode kinetics [108]. The underlying theory which governs impedance studies is explained in Appendix One, from which it can be seen that:

1. At a potential where no electrochemical reaction is taking place, the smooth electrode/solution interface can be represented by a series RC circuit. The impedance is given by:

$$Z = R + \frac{1}{jwC} \qquad 2.42$$

and the Argand diagram (Figure 2.9) has axes: real = Z' = R and imaginary = Z'' = $1/wC$, where $j = \sqrt{(-1)}$, w is the frequency (rad s^{-1}), R is the resistance (Ω) and C is the capacitance (F).

2. At a potential corresponding to a simple one electron transfer, the equivalent circuit is shown in Figure 2.10. Here the notation is C_{dl} for the double layer capacitance, R_{ct} for the charge transfer resistance, Z_W for the Warburg impedance (a resistance due to mass transfer effects) and R_u for the uncompensated solution resistance. This is known as Randles equivalent circuit [124]. $R_{ct} = \frac{RT}{nFi_o}$ and $Z_W \alpha w^{1/2}$. Two extreme frequency regions are of interest:

a. Low frequency – the system reaches equilibrium and mass transport control exists. Thus, $R_{ct} << Z_W$ and C_{dl} is unimportant.

b. High frequency – no equilibrium is attained and the reaction is kinetically controlled. Under these conditions, $R_{ct} >> Z_W$ and C_{dl} is crucial.

A typical plot of Z' versus Z'' for this system is shown in Figure 2.11. σ_c is defined in Appendix One.

Equivalent circuits can be drawn for processes which involve, for example, adsorption and coupled homogeneous reactions – very often semi–circles appear on the Argand diagram corresponding to successive steps in the reaction mechanism. AC impedance studies have therefore found considerable application to the study of electrode reactions [108] and corrosion [125,126]. In particular, this technique has been employed in the investigation of electrode surfaces [127] and adsorption processes [128,129]. In this thesis, AC impedance will be used as a means of determining the surface roughness of a given electrode.

2.3 Convective–diffusion

These systems make use of forced convection as a mode of mass transport and it follows from equation 2.27 that both time dependent and steady–state measurements are feasible. Variation of the fluid velocity vector $\vec{v}$ may now be

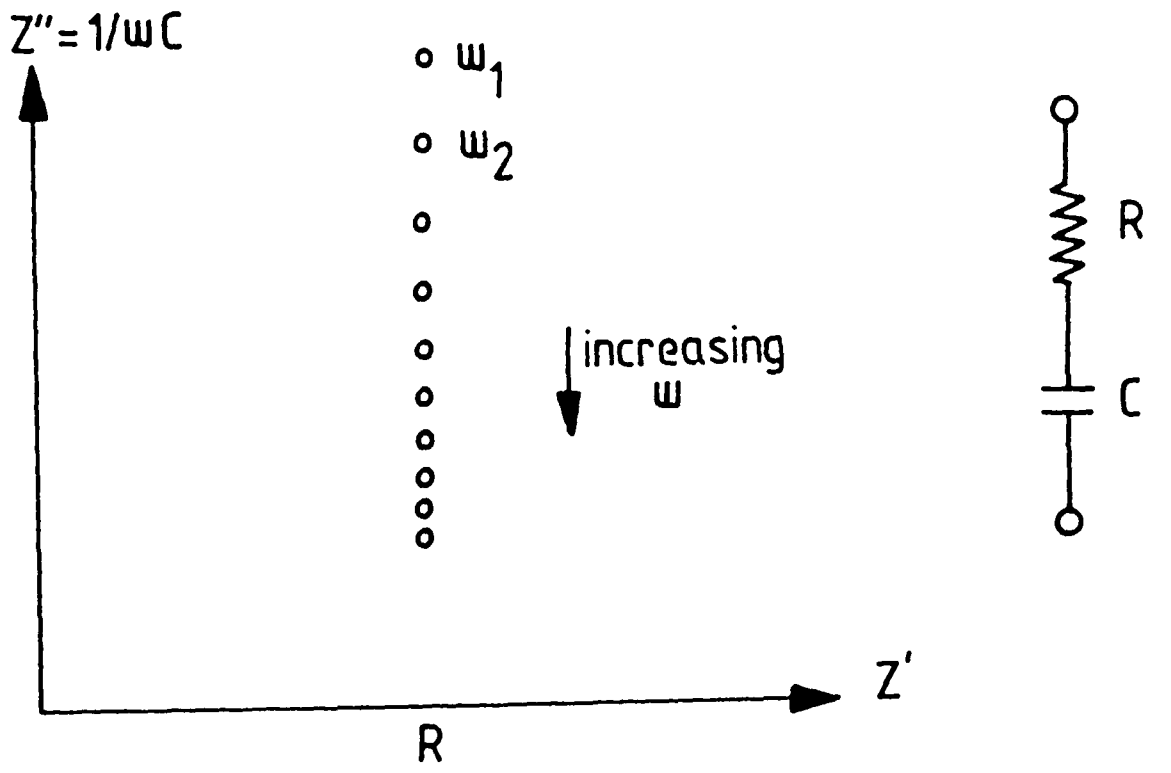


Figure 2.9: Complex plane diagram for a series RC circuit.

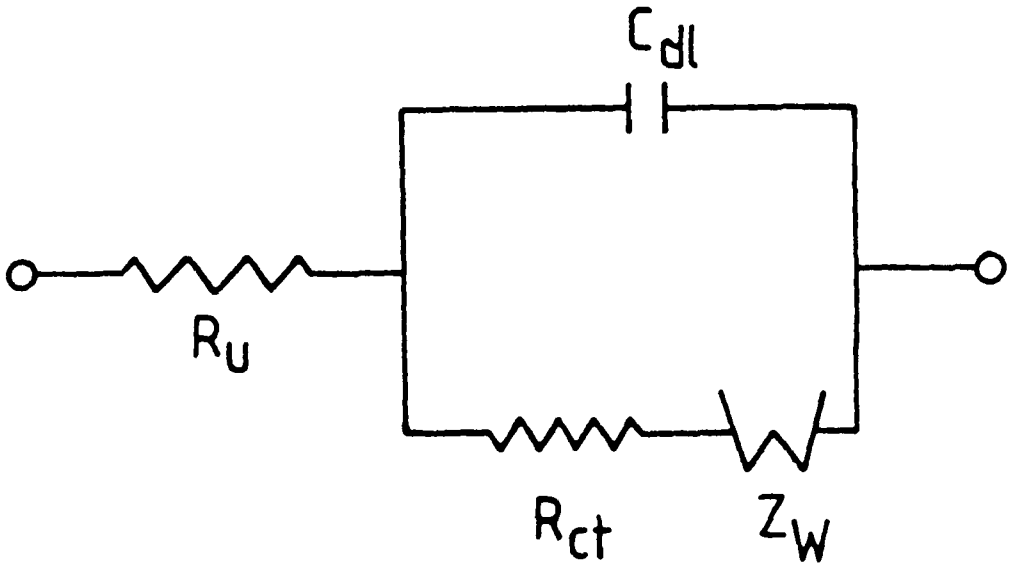


Figure 2.10: Randles equivalent circuit.

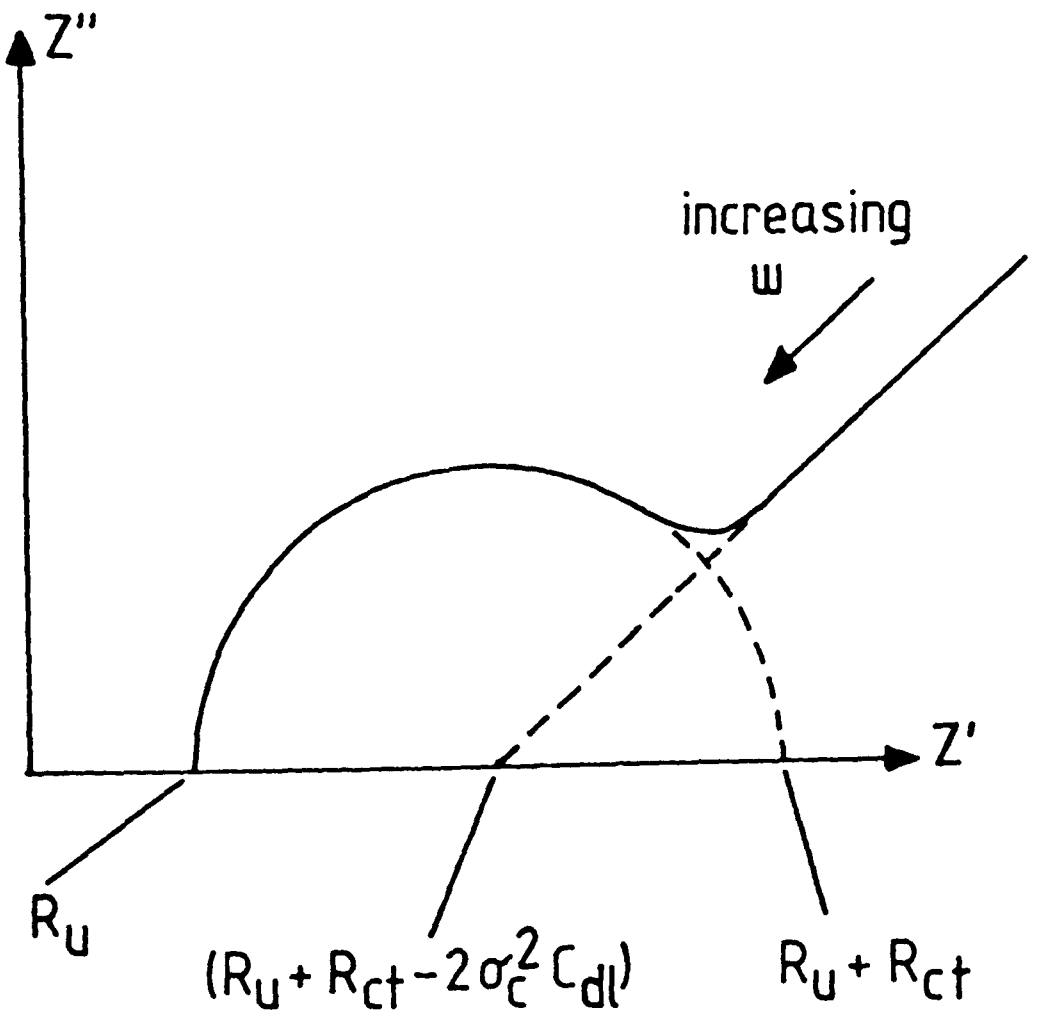


Figure 2.11: Complex plane impedance plot for the circuit of Figure 2.10.

employed as a method of changing the rate of mass transport and the problem of irregular natural convection has thus been removed, allowing experiments to run over a longer time scale. Since the rate of transport is higher than that in a stationary solution, sensitivity is greatly enhanced and the constant renewal of electroactive material at the electrode surface improves reproducibility. Electrochemical systems employing forced convection are termed hydrodynamic electrodes and they play the most significant role in the investigation of electrode processes [130,131].

By definition, forced convection is present in these systems and therefore the electrolyte solution must move with respect to the electrode. This may arise from: 1) movement of the electrode 2) agitation of solution, or from 3) flowing the solution past a stationary electrode. The best known example of the first kind of hydrodynamic electrode is the pioneering use by Heyrovsky of the Dropping Mercury Electrode (DME) in classical polarography [132]. This however is limited in application to liquid metal working electrodes only. More useful examples of electrodes of this class (which employ solid electrodes) are the rotating disc [104], rotating hemisphere [133,134], rotating cone [135], rotating ring [136] and rotating cylinder [137] electrodes. The vibrating wire electrode [138] is an example of a hydrodynamic electrode which uses agitation of the solution as a means to achieve a forced convection system and the tube [139], channel [140], annular duct [141], wall–jet [142], wall–tube [143], stationary disc in laminar uniform flow [144], stationary disc in radial flow [145] and wedge [146] electrodes are all examples of type 3).

The possibilities for electrode configuration and flow pattern appear endless, but if the system is to be used as an investigative tool, then the velocity vector $\vec{v}$ must be well defined and the convective – diffusion equation for a particular geometry solvable for the boundary conditions imposed by all conceivable methods employed.

The first consideration requires that flow is restricted to being laminar and fully developed i.e. the solution advances in separate non–mixing layers in an ordered manner [147]. Few convective–diffusion systems are amenable to exact

treatment; the rotating wire and vibrating wire electrodes are examples where the mass transport is well defined and reproducible but not calculable. However, the rotating disc electrode (RDE), rotating ring disc electrode (RRDE) and flow through channel between parallel or concentric tubes are cases where exact solutions can be obtained [131]. Experimental work described in this thesis utilises the RDE and channel electrode (ChE) and therefore further consideration will focus on these two hydrodynamic electrodes alone.

In section 2.1.2.2, the concept of a hydrodynamic boundary layer close to the solid/solution interface was discussed and similarly, consideration of the presence of such a layer in a convective–diffusion system is imperative. The solution can be divided into two regions: 1) a region of constant concentration $[O]_\infty$ far from the electrode surface where convection is the important part of mass transport and, 2) a region of rapidly changing concentration in the immediate vicinity of the surface where diffusion is important. Within this layer the concentration of electroactive solute shows a rapid change from its bulk to electrode surface value. The region 2) therefore represents a very thin fluid layer which is exactly analogous to the hydrodynamic boundary layer [131], and just as viscosity is the significant factor in determining the value for δ_b, so molecular diffusion is critical to the layer adjacent to the reaction surface [131]. Region 2) is therefore called the diffusion layer and has a thickness δ_d. The hydrodynamic and diffusion boundary layers can be related by [148]:

$$\delta_d = \left[\frac{D}{\nu}\right]^{1/3} \delta_b \qquad 2.43$$

and since D is normally of the order of 10^3 times smaller than ν, viscosity, δ_d will be approximately 10% of δ_b [148,103].

2.3.1 The Hydrodynamics of the Rotating Disc Electrode

The rotating disc electrode consists of a disc of electrode material embedded concentrically into a cylindrical sheath of insulator. The radius of the disc should be small compared to that of the insulating mantle. This is illustrated in Figure 2.12.

When such an electrode is rotated in a large volume of solution, a well–defined flow pattern is established; solution is sucked up to the electrode in a pump–like action, spun around with the electrode and then thrown out radially. Laminar flow is maintained so long as the Reynolds number for the RDE [149], defined as $Re = Wr^2/\nu$ where W is the rotation speed in Hz, r is the radius of the electrode and ν is the kinematic viscosity (cm^2s^{-1}), does not exceed a critical value in the region of $2x10^5$.

The theoretical description of this behaviour, describing the motion of the liquid near a disc of infinite radius, rotating with a constant angular velocity w (rad s^{-1}) with laminar flow was first given by von Karman [150]. A more precise calculation was made by Cochran [151] in 1934 and further information is provided in the book by Levich [103].

If a dimensionless variable g is defined as:

$$g = \left[\frac{w}{\nu}\right]^{1/2} z \qquad 2.44$$

where z is the distance normal to the electrode surface, then the corresponding velocities in polar coordinates are:

$$V_r = r w\, F(g) \qquad 2.45$$

$$V_\varphi = r w\, G(g) \qquad 2.46$$

$$V_z = -(w/\nu)^{1/2}\, H(g) \qquad 2.47$$

These functions are plotted in Figure 2.13. Figure 2.14 shows a 3–dimensional schematic representation of the flow in the vicinity of the RDE. These Figures illustrate that at the surface (i.e. $z = 0$), $G(g) = 1$ and $F(g) = H(g) = 0$, i.e. the fluid spins around with the disc.

Moving away from the surface (increasing z), the centrifugal force of the rotating disc begins to force the fluid outwards so that V_r increases, while the rotational motion, V_φ, decreases. The solution which is forced outwards radially from the disc is replenished by the flow in the V_z direction towards the disc. In the

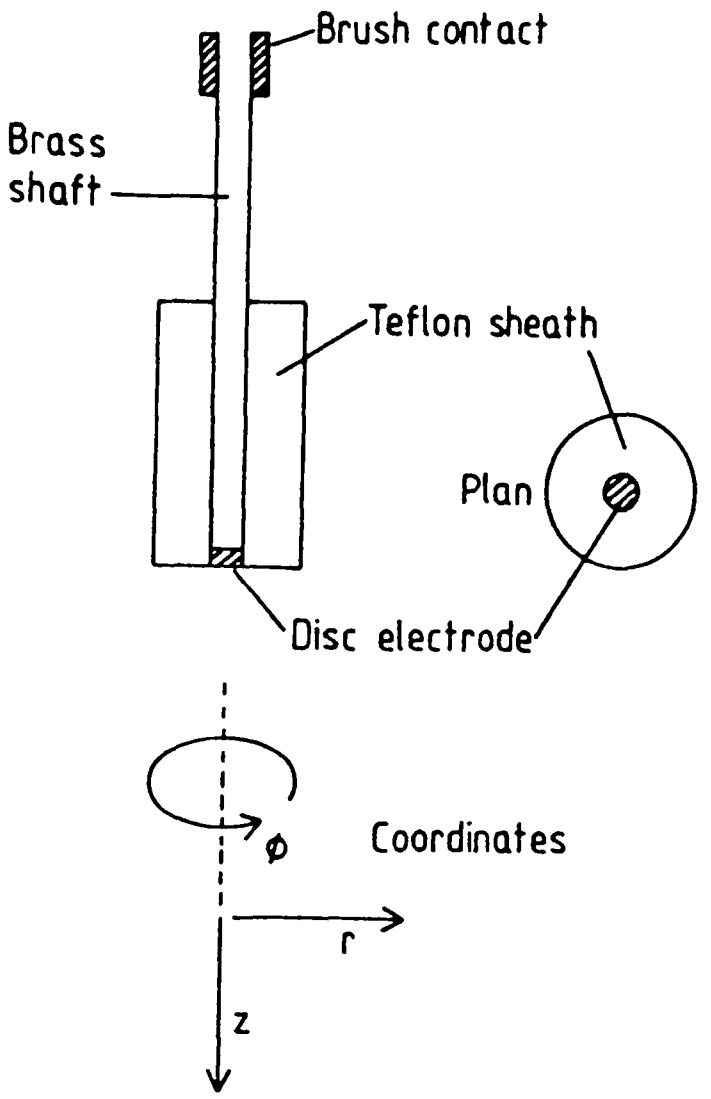


Figure 2.12: Schematic diagram and coordinate system for the RDE.

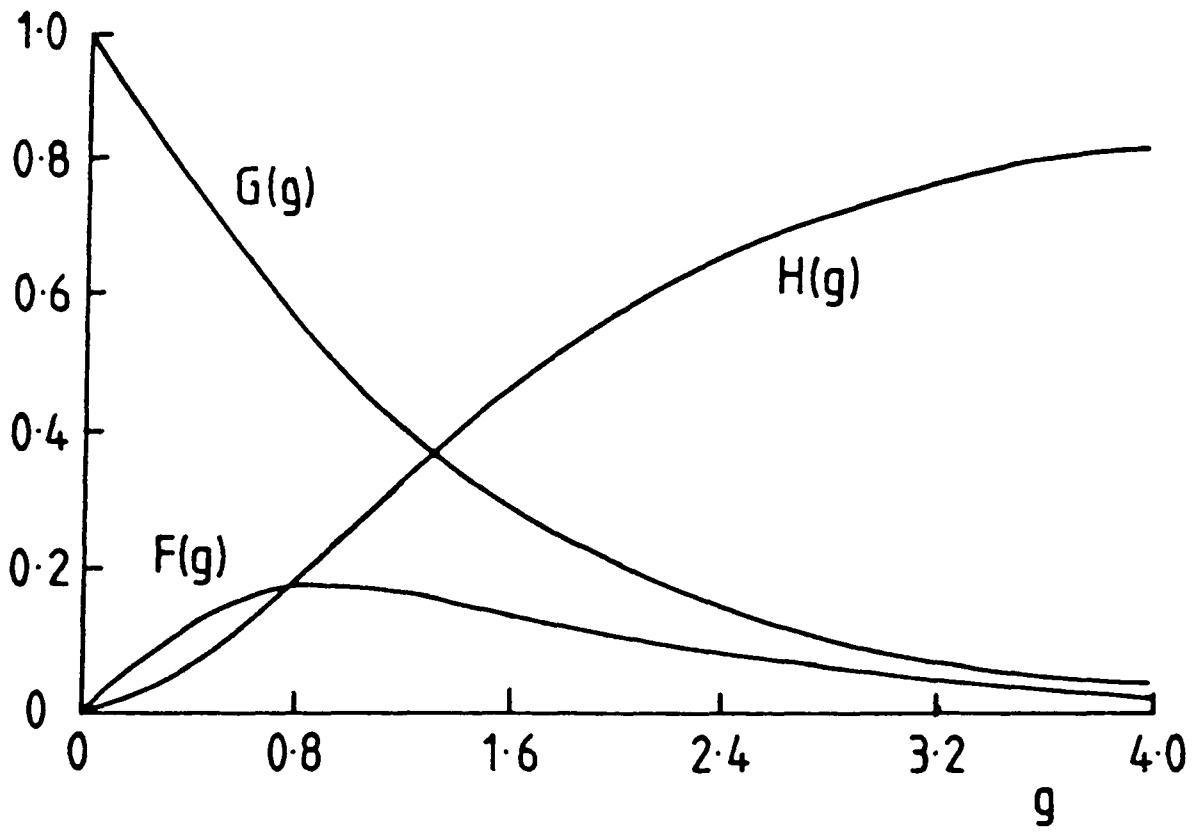


Figure 2.13: Dimensionless representation of the variation of the velocity components as a function of distance from the electrode surface.

bulk solution, V_z increases with z, reaching a maximum value of $V_z \quad (z \rightarrow \infty) = -0.8845\ (w\nu)^{1/2}$ (the negative indicating flow towards the disc) whereas the radial and rotational motions diminish so that V_r and V_φ tend to zero. Inspection of V_z shows that it is independent of r and φ so that at any plane parallel to the disc surface, the upward velocity is the same. The rotating disc is therefore said to be uniformly accessible [152].

The hydrodynamic boundary layer at the RDE, i.e. the thickness of the thin layer of solution dragged around by the disc, is defined by the point at which the function G(g) is 5% of its value at the disc surface [149]:

$$\delta_b = 3.6\ (\nu/w)^{1/2} \qquad 2.48$$

The theory outlined above applies only to systems where an infinite disc rotates in an infinite medium and the applicability of such results to practical RDEs must therefore be questioned. However, it has been shown that if the disc has a radius which is much greater than the hydrodynamic boundary layer then the effect of the finite size of the disc (i.e. its edge) has no noticeable effect on the pattern of flow used above [149,153]. The experimental conditions under which the RDE can be employed have been reviewed by several workers [154–156].

2.3.2 The Solution of the Convective–Diffusion Equation for a Transport–Limited Process at the Rotating Disc Electrode

Combination of equations 2.45, 2.46 and 2.47 with equation 2.27 reveals that the convective–diffusion equation describing, under laminar flow conditions, the variation of the concentration of the species O with time and space in the vicinity of the RDE may be written:

$$\frac{d[O]}{dt} = D_o\left[\frac{\partial^2[O]}{\partial r^2} + \frac{1}{r}\frac{\partial[O]}{\partial r} + \frac{1}{r^2}\frac{\partial^2[O]}{\partial \varphi^2} + \frac{\partial^2[O]}{\partial z^2}\right] - \left[V_r\frac{\partial[O]}{\partial r} + V_\varphi\frac{\partial[O]}{\partial \varphi} + V_z\frac{\partial[O]}{\partial z}\right] \qquad 2.49$$

This equation may however be simplified considerably because:

1. The cylindrical symmetry of the system requires that [O] is not a function of φ and hence all derivatives in φ can be removed

2. A steady–state situation is often (but not always, see Chapters Five and Six) experimentally favoured.

Therefore equation 2.49 becomes:

$$\frac{d[O]}{dt} = 0 = D_o\left[\frac{\partial^2[O]}{\partial r^2} + \frac{1}{r}\frac{\partial[O]}{\partial r} + \frac{\partial[O]]}{\partial z^2}\right] - \left[V_r\frac{\partial[O]}{\partial r} + V_z\frac{\partial[O]]}{\partial z}\right] \qquad 2.50$$

Consideration of the boundary conditions relevant to the case where [O] is consumed under transport–limiting control at the electrode surface:

$$z = \infty \qquad [O] \rightarrow [O]_\infty \qquad 2.51 \text{ i}$$

$$r = \infty \qquad [O] \rightarrow [O]_\infty \qquad \text{ii}$$

$$z = 0 \qquad [O] = 0 \qquad \text{iii}$$

$$r = 0 \qquad \frac{\partial[O]}{\partial r} = 0 \qquad \text{iv}$$

and assuming that the convective–diffusive transport to the disc is uniform, then equation 2.50 reduces to:

$$D_o\frac{\partial^2[O]}{\partial z^2} = V_z\frac{\partial[O]}{\partial z} \qquad 2.52$$

Using the first term of Cochran's exact solution for V_z [151]:

$$V_z = -0.5102\, w^{3/2}\nu^{-1/2}\, z^2 \qquad 2.53$$

where w is the rotation speed in rad s^{-1}, then the convective–diffusion equation for the RDE becomes:

$$D_o \frac{\partial^2[O]}{\partial z^2} = C\, z^2 \frac{\partial[O]}{\partial z} \qquad 2.54$$

where $C = 0.510\, w^{3/2}\, \nu^{-1/2} = 8.032\, W^{3/2}\, \nu^{-1/2}$.

The use of the approximate equation 2.53, however, is only valid for systems characterised by large ($\approx 10^3$) Schmidt numbers, Sc, where $Sc = \nu/D$ – i.e. when the concentration changes take place very close to the disc surface. This is certainly applicable to most electrochemical systems where typically $\nu = 0.004$ cm^2s^{-1} (the kinematic viscosity of acetonitrile at 25°C) and $D \approx 10^{-5}$ cm^2s^{-1}.

The concept of a diffusion layer, inside which diffusion is the primary mode of mass transport, was outlined in section 2.3. At the rotating disc, the thickness of this layer is given by [131]:

$$\delta_d = \frac{1.6\,1\ \nu^{1/6}\ D^{1/3}}{W^{1/2}} \qquad 2.55$$

and Figure 2.15 illustrates how the concentration of the electroactive material [O] varies across this imaginary boundary. The flux of material through the diffusion layer can be expressed in terms of a mass transfer coefficient, k_m, so that the flux at the disc surface, j_s, is:

$$j_s = k_m\, ([O]_\infty - [O]_0) \qquad 2.56$$

The mass transport coefficient is related to the transport–limited current, i_{lim}, (obtained when the potential is held such that $[O]_0 = 0$) by:

$$k_m = \frac{i_{l\,im}}{nF[O]_\infty A} \qquad 2.57$$

where A is the area of the disc.

The combination of equations 2.55, 2.56 and 2.57 produces the Levich equation for the RDE [103,157], which relates the transport–limited current to the rotation

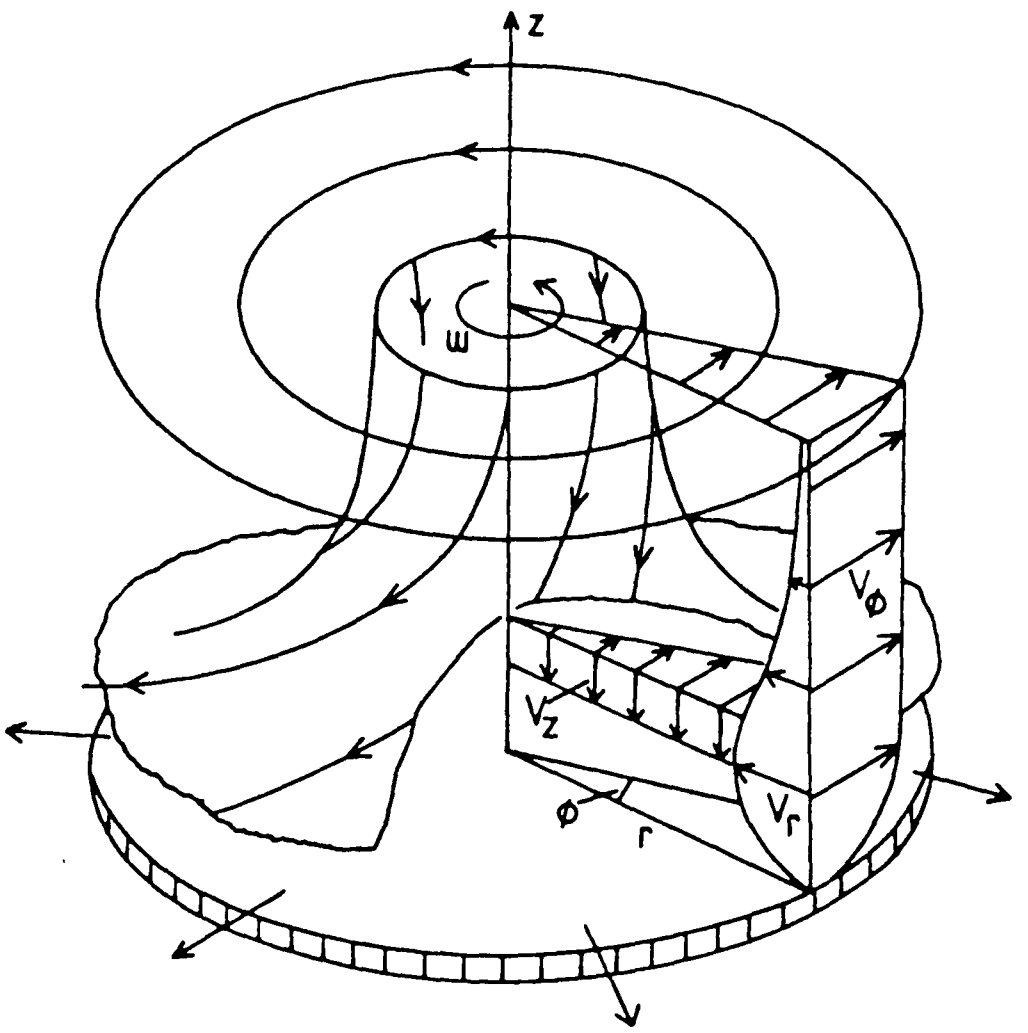


Figure 2.14: Laminar flow pattern in the vicinity of the RDE.

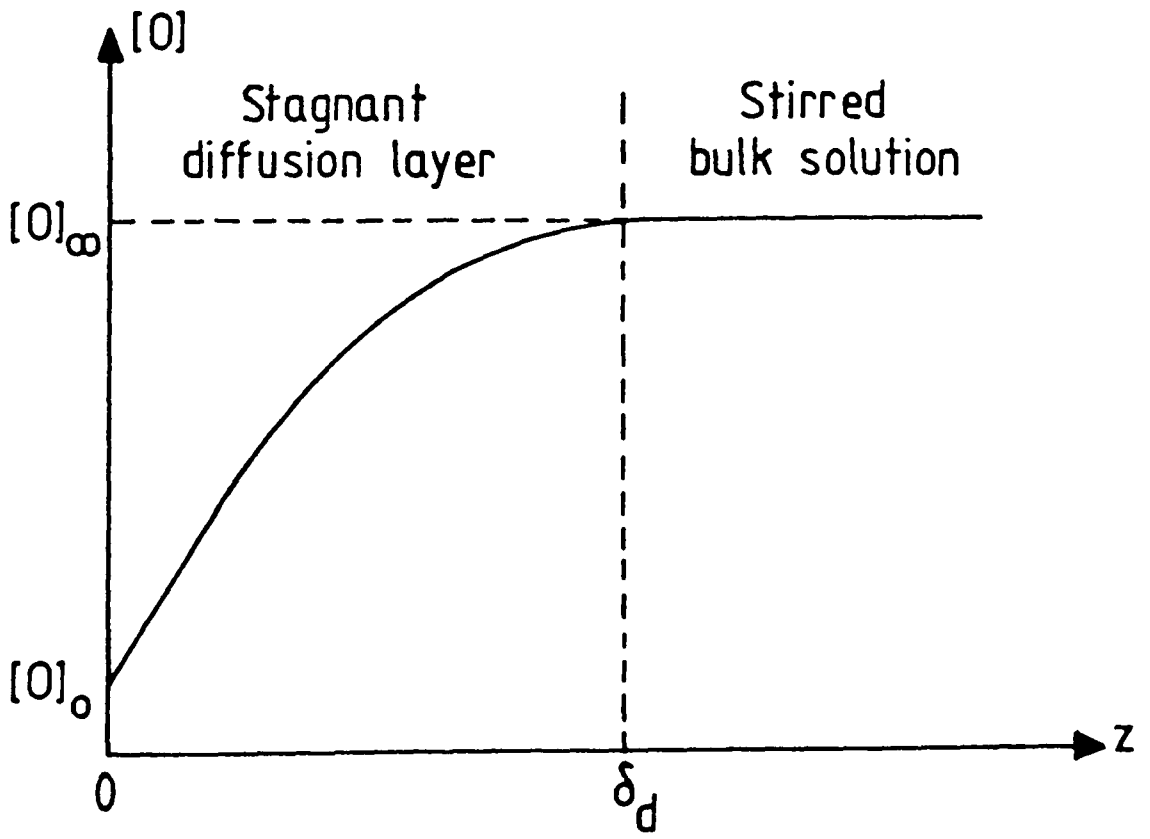


Figure 2.15: Concentration profile of O near the RDE surface.

speed (in Hz):

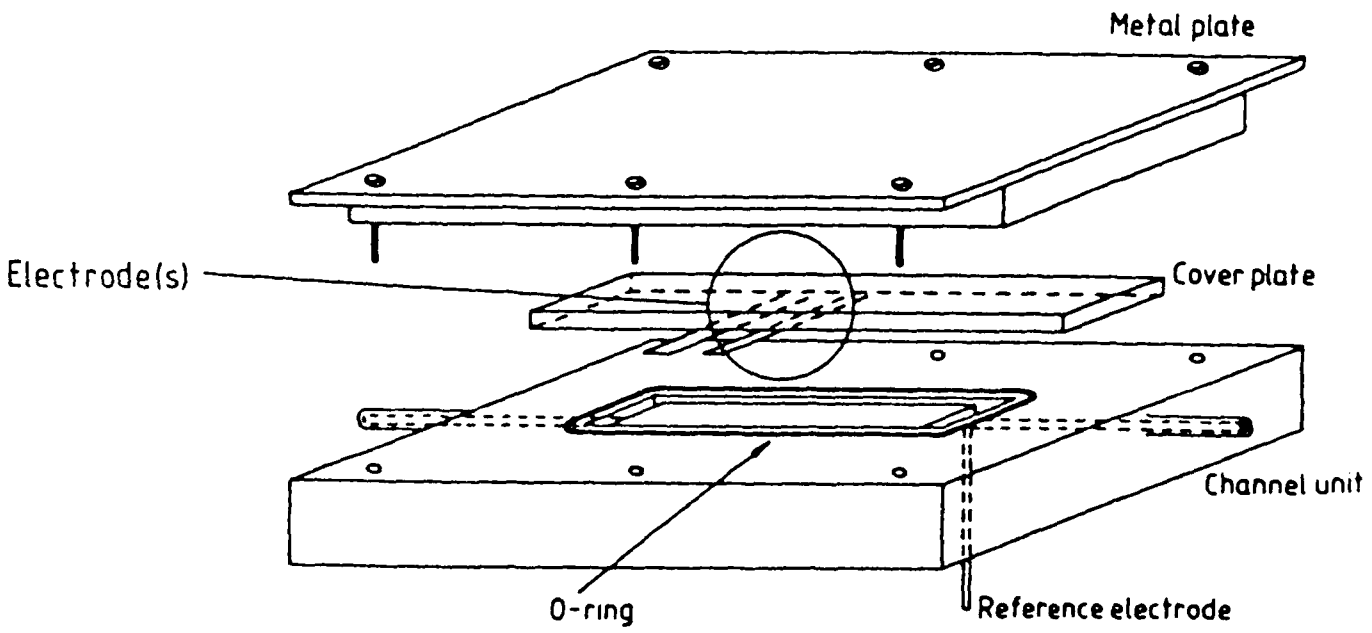
$$i_{lim} = 1.554\ n\ A\ F\ D^{2/3}\ \nu^{-1/6}\ [O]_{\infty}\ W^{1/2} \qquad 2.58$$

The exact derivation of this equation is given in Appendix Two.

Equations 2.53, and therefore 2.58, utilise the first term only in Cochran's infinite series of V_z [151]. The relationship between i_{lim} and W has since been established numerically by considering the first two terms of this series (by Gregory and Riddiford [154]) and for high Sc, an expression using all the terms has been derived analytically (by Newman [158]). Both results confirm the dependence of i_{lim} on W as shown in equation 2.58 [159] and a comparison between these three solutions [160] has shown that for $Sc > 10^3$, the Levich treatment is accurate to within 3%.

2.3.3 Hydrodynamic Flow through a Channel Electrode

A hydrodynamic system which utilises solution flow rather than electrode movement – namely the channel electrode – will now be considered. The channel electrode (ChE) essentially consists of a rectangular electrode embedded in one side of a rectangular duct through which the solution flows. This is shown schematically in Figure 2.16, alongside the coordinate system employed in the ChE. The ChE is considered to be infinite in the y direction so that laminar flow is two dimensional in the x and z coordinates. Laminar flow is achieved [161] provided that the Reynolds number, $Re = \frac{v_0 h}{\nu}$, is less than 10^3; this criterion is obeyed under virtually all practical conditions. The pattern of flow is almost flat when the solution enters the cell , but the solution in the vicinity of the cell walls is retarded (as described in section 2.1.2.2) compared to that of the centre. At a short distance l_{crit} down the ChE, the resulting hydrodynamic boundary layers merge and a steady–state parabolic flow pattern is achieved [162]. This is shown in Figure 2.17. The velocity profile is characterised by:



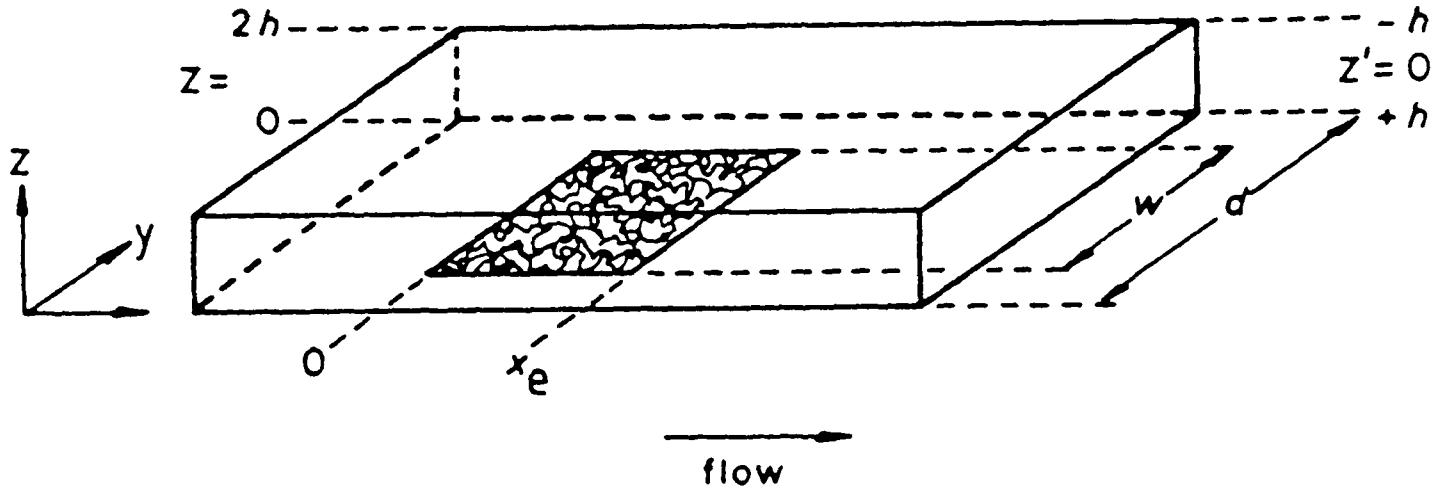


Figure 2.16: A schematic diagram of the ChE and the appropriate coordinate system.

$$v_x = v_0 \left[1 - \left[\frac{z'}{h}\right]^2\right] \qquad 2.59$$

$$v_z = v_y = 0 \qquad 2.60$$

where v_0 is the solution velocity in the centre of the channel.

The entrance length required to satisfy this condition is given by [162]:

$$\frac{l_{crit}}{2h} = 2 \times 10^{-2}\ Re \qquad 2.61$$

2.3.4 The Solution to the Convective–Diffusion Equation for a Transport–Limited Process at the Channel Electrode.

Substituting equations 2.59 and 2.60 into the general convective–diffusion equation (equation 2.27) under steady–state conditions gives (in three–dimensions):

$$D_0 \nabla^2[O] = v_0 \left[1 - \left[\frac{z'}{h}\right]^2 \frac{\partial[O]}{\partial x}\right] \qquad 2.62$$

In solving this equation for the transport controlled reaction of O at the electrode, Levich [103] assumed that diffusion in the x and y directions was negligible. This is reasonable since diffusion in the direction of fluid flow (x) will be insignificant when compared to convection (v_x) and electrode diffusional side–edge effects are minimised for sufficiently wide electrodes.

Equation 2.62 therefore reduces to:

$$D_0 \frac{\partial^2[O]}{\partial z^2} = v_0 \left[1 - \left[\frac{z'}{h}\right]^2\right] \frac{\partial[O]}{\partial x} \qquad 2.63$$

When the appropriate boundary conditions for this system are applied:

$0 \leq x \leq 1, z = 0$: $[O] = 0$ 2.64 i

$x < 0$: $[O] = [O]_\infty$ ii

$z \to \infty$: $[O] = [O]_\infty$ iii

then the solution of equation 2.63 proceeds via the approximation of Léveque [163] (initially proposed for the heat transfer in pipes):

$$v_x = v_0 \left[1 - \left[\frac{z'}{h}\right]^2\right] = 2\, v_0 \left[1 - \frac{z'}{h}\right] \qquad 2.65$$

This assumes that the parabolic nature of the velocity profile v_x is linear and is therefore only valid in the vicinity of the electrode or channel walls where all concentration changes must occur. The convection time along the channel must therefore be much faster than the diffusion time across it, i.e. $(D_o x_e / v_0 h^2) << 1$ [164].

Using the Léveque approximation, the Levich equation for the limiting current at the ChE is:

$$i_{lim} = 0.925\, n\, F\, w_e\, [O]_\infty \left[\frac{V_f\ D_o^2\ x_e^2}{h^2\ d}\right]^{1/3} \qquad 2.66$$

where V_f is the volume flow rate of the solution in the cell:

$$V_f = \frac{4}{3}\, d\, h\, v_0 \qquad 2.67$$

A precise derivation of this equation is presented in Appendix Three.

Although the validity of equation 2.66 has been demonstrated under most experimental conditions [139], deviations have been observed at low flow rates [165,166]. These may be attributed to the significance of natural convection, lateral diffusion and thin layer behaviour. Modifications to equation 2.66 have been proposed [167] to account for lateral diffusion [167] and also design considerations for practical ChEs given so that such contributions can be made negligible [168]. In

summary, for all electrode geometries and flow rates where the Léveque approximation is valid [169], lateral diffusion effects can be ignored [168], mass transport to the ChE is essentially two–dimensional in character [170] and the Levich equation is applicable [171].

In section 2.3.2, the diffusion layer at the RDE was shown to be independent of the radius of the electrode (equation 2.55) and the electrode was therefore described as uniformly accessible. The diffusion layer at the ChE, however, depends on $x^{1/3}$, where x is the distance along the electrode and this configuration is therefore described as non–uniformly accessible (Figure 2.18). The relative merits of these two electrodes have been compared elsewhere [160,172].

2.4 The Relationship between Potential and Current under Mass Transport Control

The current potential response at a hydrodynamic electrode can be expressed in terms of a mass–corrected Tafel equation [173].

2.4.1 Reversible Electron Transfer

In section 2.1.1, it was shown that if the standard rate constant for the simple reaction:

$$O + ne^- \underset{k_b}{\overset{k_f}{\rightleftharpoons}} R \qquad 2.68$$

is large, then the i–E relationship at all rotation speeds or flow rates will appear reversible. The complete relationship can be obtained by manipulation of the Nernst equation:

$$E - E^0 = \frac{2.3RT}{nF} \log \frac{[O]_0}{[R]_0} \qquad 2.69$$

and the equation given in section 2.3.2, which relates current density to the mass transfer coefficient. For the cathodic current this is given by:

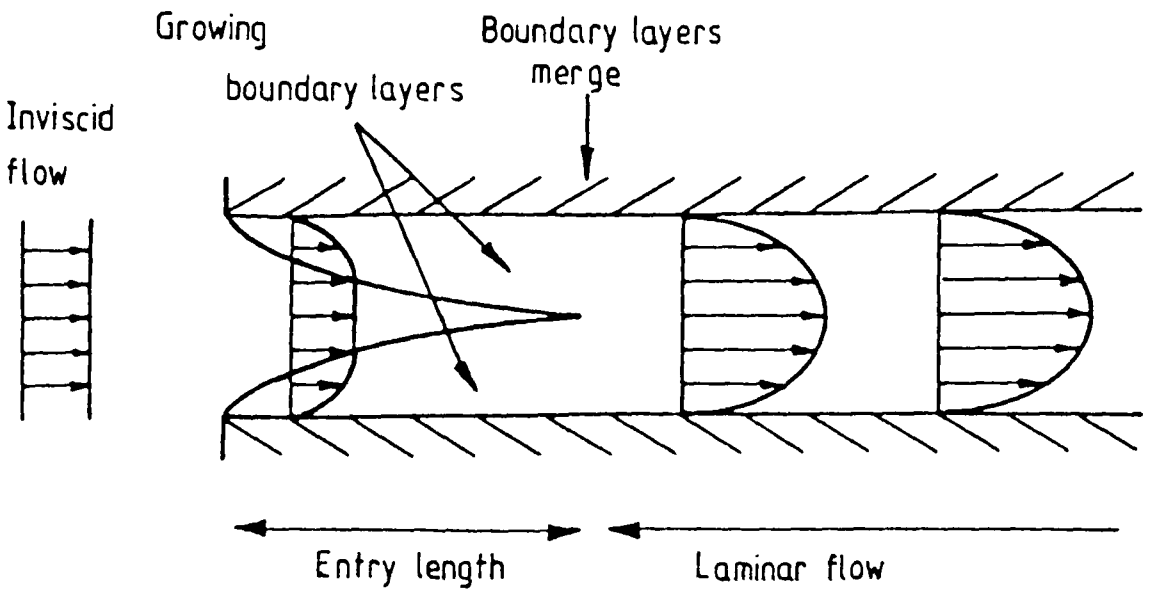


Figure 2.17: Development of the boundary layers for solution flowing through the ChE.

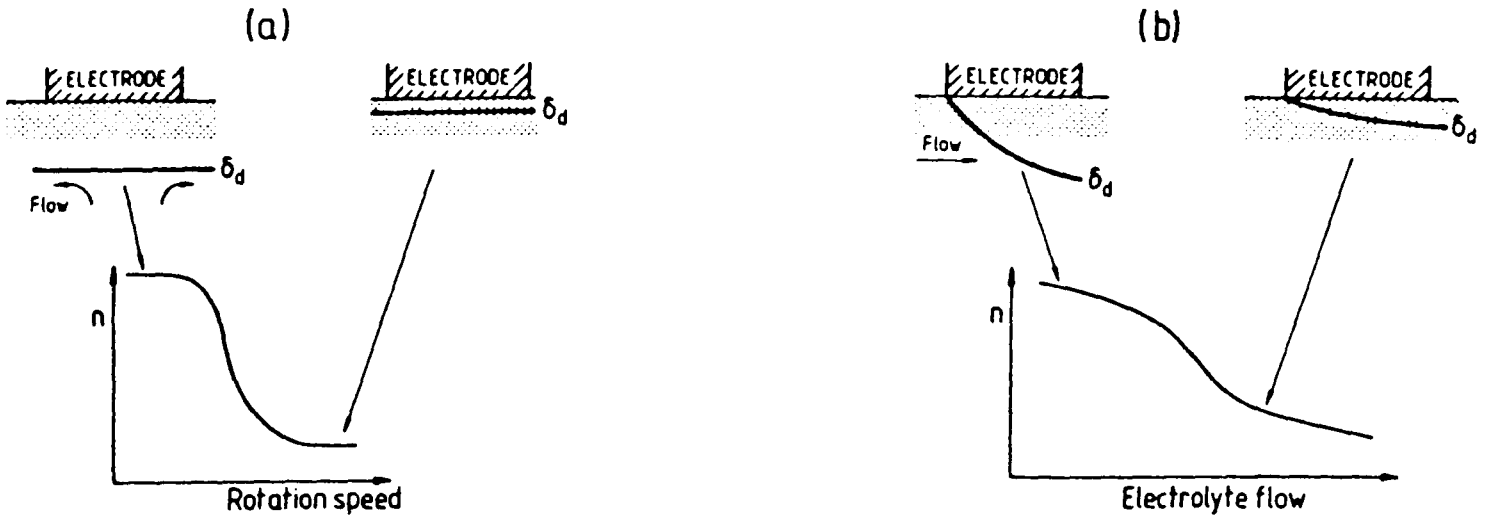


Figure 2.18: Diffusion layers at the a) RDE and b) ChE illustrating how the number of electrons transferred (n) varies with the rate of mass transport at each electrode.

$$i_d = nFk_m ([O]_\infty - [O]_0) \qquad 2.70$$

and for the anodic current, by:

$$i_d = nFk_m ([R]_\infty - [R]_0) \qquad 2.71$$

The reaction scheme can now be pictured as:

$$[O]_\infty \underset{k_m}{\overset{k_m}{\rightleftharpoons}} [O]_0 + ne^- \underset{k_b}{\overset{k_f}{\rightleftharpoons}} [R]_0 \qquad 2.72$$

At the limiting current for this reaction, $[O]_0 = 0$ and therefore equation 2.70 becomes:

$$i_{lim} = nFk_m [O]_\infty \qquad 2.73$$

Since $[R]_\infty = 0$, then the resulting equation governing the i–E relationship for a reversible process becomes:

$$E - E^0 = \frac{2.3RT}{nF} \log \frac{i_{lim} - i_d}{i_d} \qquad 2.74$$

2.4.2 Irreversible Electron Transfer

In the case of an irreversible electron transfer:

$$O + ne^- \xrightarrow{k_f} R$$

the back reaction can be ignored so that $k_b = 0$. The current at the electrode will therefore be governed by the forward rate constant, so that:

$$i_d = nFk_f [O]_0 \qquad 2.75$$

and the current was related in section 2.3.2 to the rate of mass transport using the mass transport coefficient, k_m, such that:

$$i_d = nFk_m ([O]_\infty - [O]_0) \qquad 2.76$$

The reaction may now be represented in terms of two rate processes involving mass transport and electron transfer:

$$[O]_\infty \underset{k_m}{\overset{k_m}{\rightleftharpoons}} [O]_0 + ne^- \xrightarrow{k_f} [R]_0$$

Therefore the combination of equation 2.75 and 2.76 yields:

$$[O]_0 = \frac{k_m \ [O]_\infty}{k_f + k_m}$$

$$\text{or} \quad i_d = nFk_f \frac{k_m \ [O]}{k_f + k_m} \qquad 2.77$$

However, at the transport controlled limiting current, $[O]_0 = 0$ and therefore:

$$i_{lim} = nFk_m [O]_\infty \qquad 2.78$$

$$\text{and} \quad \frac{1}{i_d} - \frac{1}{i_{lim}} = \frac{1}{nFk_f \ [O]_\infty} \qquad 2.79$$

Hence combining equation 2.79 with equation 2.3a gives:

$$\log\left[\frac{1}{i} - \frac{1}{i_{lim}}\right] = \frac{\alpha nF \ (E - E^0)}{2.3RT} - \log k^0 - \log [O]_\infty - \log (nFA) \qquad 2.80$$

where A is the area of the electrode. A Tafel plot of $\log\left[\frac{1}{i} - \frac{1}{i_{lim}}\right]$ versus E therefore

enables the value of αn to be found from the slope.

2.5 The Use of the Rotating Disc Electrode and Channel Electrode in the Study of Electrochemical Reaction mechanisms

The preceding sections have demonstrated the importance of well defined hydrodynamics in the study of electrode reactions and the relevant relationships between current, potential and mass transport have been derived for the RDE and ChE. These results have been illustrated for a very simple reaction; electrode processes are rarely as simple as this and consequently complications due to coupled chemical steps and surface phenomena often need to be considered. Fortunately, the use of mass transport as an experimental variable can not only give a guide to reaction mechanism, but additionally provide quantitative kinetic detail.

The aim of this section is to distinguish between reactions taking place in the solution (homogeneous reactions) from those occurring at the electrode/solution interface (heterogeneous), and to briefly discuss the use of the RDE and ChE in the investigations of these processes. The notation of Testa and Reinmuth [174] will be employed: i.e. electrode reactions will be labelled E and chemical steps C.

2.5.1 Coupled Homogeneous Reactions

The simplest forms of this kind of reaction are the CE and EC mechanisms, where a homogeneous chemical step proceeds or follows an electron transfer. The CE mechanism is as shown below:

$$\text{C:} \qquad Y \underset{k_{-1}}{\overset{k_1}{\rightleftharpoons}} A \qquad K = k_1/k_{-1}$$

$$\text{E:} \qquad A + e^- \longrightarrow B$$

The dependence of i_{lim} and the half–wave potential, $E_{1/2}$ ($i\{E_{1/2}\} = i_{lim}/2$), on the rate of mass transport (W for the RDE, V_f for ChE) are illustrated for the case of the RDE in Figure 2.19. i_{lim} is increasingly lower than that expected for a simple E

reaction as W is increased. This is because the precursor of the electroactive material Y spends increasingly less time in the vicinity of the electrode surface for complete conversion to the electroactive form, A. The relative rate of mass transport compared to the rates of A and B will effect the extent to which i_{lim} is perturbed from the value expected for a simple E process, and provided the former is sufficiently fast to distinguish this shift then the rate constants for the preceding C step may be determined [175].

The additional free energy barrier to reduction caused by the chemical step results in the cathodic shift observed in the $E_{1/2}$ – log W plot. Mechanistic discrimination is possible from quantitative analysis of this behaviour when E^0 (for the A/B couple) is known under conditions where kinetic complications are negligible [176].

The EC mechanism is defined as:

$$\text{E:} \qquad A + e^- \longrightarrow B$$

$$\text{C:} \qquad B \xrightarrow{k} C$$

where C is electroinactive in the potential range of interest. Here, the chemical step has no influence on i_{lim} and therefore the variation of the limiting current with $W^{1/2}$ is identical to that observed for a simple electron transfer. This is shown in Figure 2.20.

However, the chemical step manifests itself in the $E_{1/2}$ – W behaviour, the decomposition of B producing an anodic shift in the reduction potential [177]. Once again, analysis of this shift can provide mechanistic information and a value for the rate constant, k [176].

The application of these basic principles means that identification of more complex reactions such as E_{qr} [178,179], E_i [178,179], EC_2 [180,181], C_2E [182,183] and EC' [184,185] is possible at hydrodynamic electrodes using steady–state measurements, which have therefore been of considerable significance in the study of electrode mechanisms [130,131,186].

In this thesis, steady–state measurements alone will be employed for the

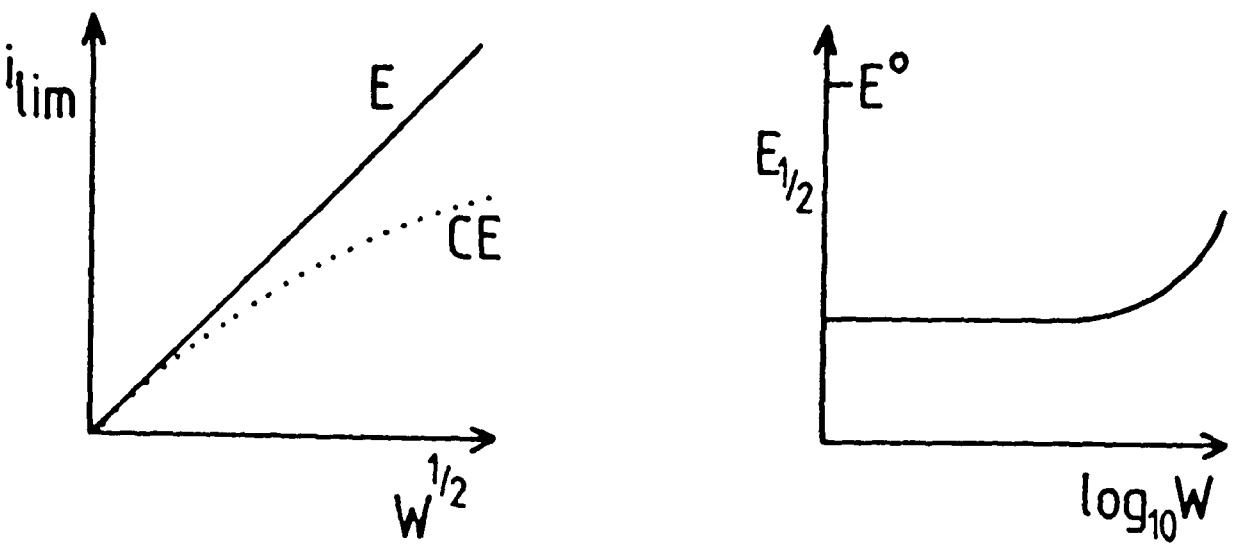


Figure 2.19: The variation of i_{lim} and $E_{1/2}$ with the rate of mass transport for a CE process at the RDE.

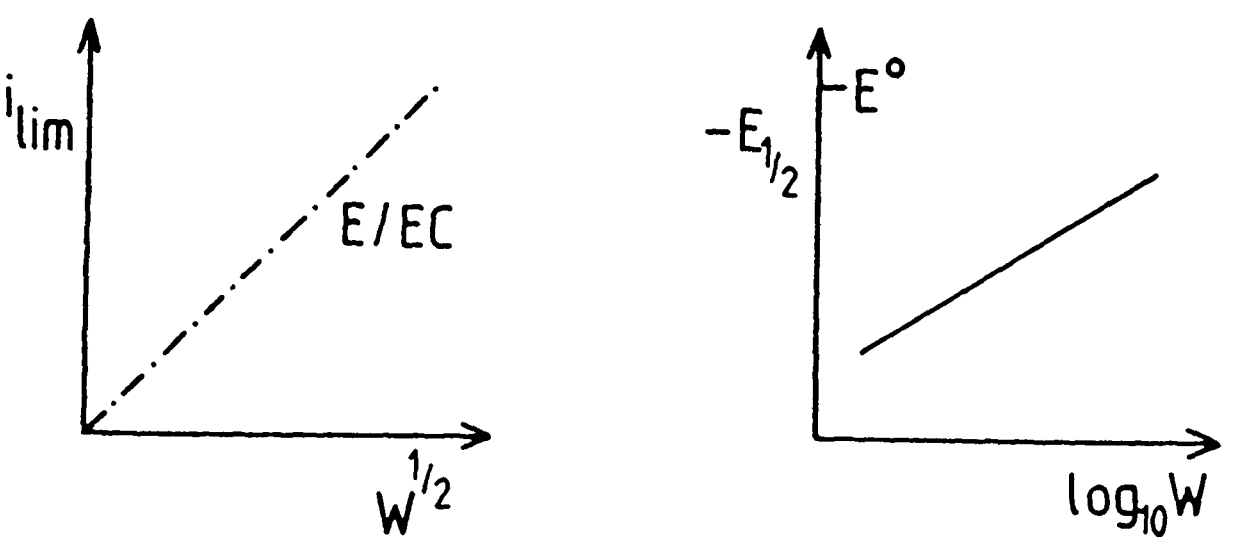


Figure 2.20: The variation of i_{lim} and $E_{1/2}$ with the rate of mass transport for an EC process at the RDE.

investigation of electrode processes which involve coupled homogeneous kinetics. It is however worth noting at this point that there are natural limitations on the information which this methodology can provide. In particular, mechanistic diagnosis using electrochemistry has recently reached levels where, say, the various details of a given reaction pathway, rather than general mechanistic discrimination, is of interest [187]; steady–state analysis is often not the best probe for determining such information. Secondly, the range of chemical constants which are accessible using steady–state techniques are invariably limited by the rotation speeds or flow rates which are practically attainable [131]. Hence, one further advantage of hydrodynamic electrodes is exploited, and time–dependent measurements are employed. In addition, mechanistic and kinetic detail can be found and/or confirmed using other electrochemical or spectroelectrochemical techniques [188]. The ECE/DISP1 system [189] provides an excellent illustration of this point. The reaction scheme is as follows:

1.	E:	$A + e^- \rightleftharpoons B$	
2.	C:	$B \underset{k_{-1}}{\overset{k_1}{\rightleftharpoons}} C$	$K = [C] / [B]$
3.	E:	$C + e^- \rightleftharpoons D$	
4.	DISP	$B + C \longrightarrow D + A$	

Three limiting mechanisms, summarised below, have been identified [190]:

Mechanism	Rate determining step	2nd electron transfer
ECE	(2)	(3) heterogeneous
DISP1	(2)	(4) homogeneous
DISP2	(4)	(4) homogeneous

The second order dependence with respect to [B] means that the DISP2 mechanism may be readily distinguished from the other two mechanisms using steady–state measurements at the RDE or ChE [191,192]. This distinction has been

made using both measurements of $E_{1/2}$ and i_{lim} with W (or V_f) [181,193] as well as with other conventional electrochemical techniques such as LSV, CV [191,194,195] and single potential step chronoamperometry [196,197].

The discrimination between ECE and DISP1, however, has proved much more difficult [194]. Steady–state measurements at the RDE, ChE and wall–jet electrode (WJE) [189,198,199] are all unsuccessful in resolving the ECE/DISP1 competing reaction mechanisms at present levels of experimental accuracy, although discrimination has been achieved when an independent value for k_1/k_{-1} can be found using, for example, spectroelectrochemical means [189]. The degree of experimental precision required to resolve the two mechanisms has also resulted in the failure of LSV (both peak potential [194] and peak current [190] – scan rate analysis) in ECE/DISP1 discrimination. However, the use of double potential step chronoamperometry to analyse systems where the kinetics of step (2) are compatible with the time scale of the experiment, has been demonstrated by several workers to successfully discriminate between the two mechanisms [194,200,201].

This example illustrates that through the use of transient techniques, the hydrodynamic electrode can still prove to be a powerful probe of electrode reactions when steady–state measurements in isolation provide insufficient mechanistic detail.

2.5.2 Coupled Heterogeneous Reactions

By definition, steady–state techniques are also relatively insensitive in the analysis of electrode adsorption phenomena [130]. An example where such measurements have been successful is the heterogeneous catalytic reaction concerning oxygen reduction at metal electrodes. A non–electrochemical regeneration mechanism operates which is heterogeneous in nature and involves the adsorbed product [202]. The reaction is therefore of the type:

$$\text{E} \qquad A + ne^- \longrightarrow B$$

$$\text{M} \qquad B \xrightarrow{k_h} A$$

For a first order regeneration mechanism the effect will be to shift the Levich plot of

i_{lim} vs. $W^{1/2}$ up the y axis by a constant amount. Therefore at the RDE the intercept is given by:

$$i_{lim} = n\,F\,A\,k_h\,[B] \qquad 2.81$$

and rate constants in the range $10^{-3} \leq k_h \leq 10^{-1}$ cms^{-1} can be determined. The rotating ring disc electrode has been exploited for these studies [203–205].

The use of transient techniques however can provide more detail in the investigation of heterogeneous processes [130]. The simplest case to consider of a reaction involving adsorption is that where only the adsorbed form(s) of O (and/or R) is electroactive in the potential range under examination. The analysis of such a system is straight forward since mass transport effects can be ignored and measurements made in stationary solution. Hence many examples are to be found in the literature where LSV, CV [107], AC impedance [108], thin layer coulometry [206] and potential step techniques [106] have been used to study adsorption, desorption and nucleation. Non–electrochemical techniques have also been employed [188].

However the solution species (O and R) are often also electroactive and may themselves be involved in homogeneous reactions; therefore such systems are amenable to studies using hydrodynamic electrodes employing transient measurements. Double potential step chronoamperometry at the RDE has been used to measure the kinetics of adsorption of bromine onto polycrystalline platinum electrodes [207] and transient techniques have been proposed as a method for studying adsorption at double channel electrodes [208,209].

2.6 Spectroelectrochemistry

The electrochemical techniques which have been described so far rely on measuring potential or current as a function of experimental parameters such as time, sweep rate or the rate of mass transport. In particular, the measurement of

current has been used to determine the rate of an electrode reaction. Such measurements however lack molecular specificity so that when information on the identity of a reaction intermediate or product is required, to say elucidate a reaction mechanism, a non–electrochemical technique must be employed [210,211]. Section 2.5.1 described how in–situ ESR [189] has been used to investigate successfully the ECE/DISP1 problem and such spectroscopic techniques have become increasingly favoured in recent electrochemistry.

The particular merits of in–situ techniques are that in addition to identifying reaction intermediates, the time dependent concentration profiles of these and other radical species can be monitored. Studies of surface properties such as adsorbate orientation, ordering and coverage are also possible [212–214]. Hence many examples can be found in the literature of the use of UV–visible, IR, Raman, ESR and other in–situ techniques [188]. Work covered here however will be restricted to the use of in–situ ESR as a tool for confirming mechanistic detail and kinetic analysis.

ESR has been proven as an excellent technique for the identification and investigation of species containing unpaired electrons i.e. radicals, radical cations and anions, and certain transition metal species. If radicals involved in an electrochemical experiment can be produced in the ESR cavity without perturbing the sensitivity of the spectrometer then this technique can be used to study the intermediates and products of the electrode reaction. To this end, several in–situ ESR cells have been developed: channel and tubular electrodes are the principal examples of systems which do not significantly effect the sensitivity of the spectrometer and also have well defined hydrodynamics [215,216].

In combination with conventional electrochemical techniques, ESR is particularly useful since it provides not only unambiguous intermediate and product identification, but also probes the entire concentration profiles (x,t) of these species near the electrode. Hence analysis of transient ESR data can yield kinetic information, helping to solve problems such as the assignment of an ECE or DISP1 [189,217] process as well as a number of other mechanisms [218,219].

CHAPTER THREE

THEORY

In this chapter, theory is presented for the mathematical description of mass transport to both the rotating disc and channel electrodes. A general computational strategy is detailed for the calculation of chronoamperometric responses arising from single and double potential step experiments at the RDE. The method is amenable to the inclusion of both heterogeneous and homogeneous coupled kinetics. Theoretical results are provided for the catalytic mechanism (EC') which reveal that steady–state measurements in isolation are sufficient to discriminate between similar variants of this general mechanistic pathway.

Calculation of the transport–limited current/flow rate behaviour for the EC' mechanism at the channel electrode proceeds using two contrasting approaches:

1. by modification of the appropriate convective–diffusion equations via the Lévêque approximation, replacing concentration gradients in the direction of flow by their average values, and

2. by maintaining the full parabolic nature of the velocity profile.

These two methods of solution are shown to be in good agreement with the existing theory, and with each other, when kinetic processes are fast. Lastly, steady–state working curves, generated for the RDE and ChE using these theories, are compared.

3.1 The Rotating Disc Electrode

3.1.1 Introduction

The considerable application which RDEs have found in the investigation of electrode processes comprising electron transfers coupled to homogeneous and heterogeneous chemical reactions was discussed in Chapter Two. It was shown that usually studies involved steady–state measurements: the variation of either the transport–limited current [220–222] or the half–wave potential [223–225] with electrode rotation speed being used for mechanistic deductions and to provide quantitative kinetic detail. However, the limitations to the information which these techniques can convey were also outlined. In particular, steady–state methods may be insensitive to the various nuances existing within one general mechanism and to the investigation of heterogeneous processes.

Time dependent measurements, providing a more complete and accurate mechanistic description, can, at least partly, overcome these problems. The combination of a large perturbation method [187] (e.g. chronoamperometry) with the controlled hydrodynamics of the RDE is particularly useful since both steady–state and time dependent characteristics can be determined with one measurement. Chronoamperometric experiments involve changing the potential of the working electrode instantaneously and recording the resultant current–time response. In the simplest of these experiments – single potential step chronoamperometry (SPSC) – the potential is "stepped" from a value where no current flows to a new potential corresponding to a reduction (oxidation) at the mass transport controlled rate.

In stationary solution, Fick's Second Law can be solved with the appropriate boundary conditions, to describe the current–time behaviour. For example, consider a reaction free from kinetic complications at a planar electrode:

$$A + e^- \rightleftharpoons B$$

then the exact form of the i–t transient is given by the Cottrell equation [150]:

$$i = \frac{nFAD^{1/2}[A]_{\infty}}{1.77t^{1/2}} \qquad 3.1$$

Homogeneous reaction kinetics have also been introduced [226,227].

Early work concerned with the current response to a potential step at the RDE was largely theoretical and proceeded analytically by dropping the highest order convective term [228], neglecting convection completely [229] or assuming a linear concentration profile within a time dependent boundary layer [184]. These treatments were however applied essentially to reactions free from kinetic complications. The work of Bruckenstein and Prager [184] was later found to give the best agreement with the rigorous numerical simulation, in Cartesian space, of the problem by Prater and Bard [230]. More recently, Pons [231] has solved the problem for simple electron transfer using the orthogonal collocation (OC) method. This work was not however extended to cover coupled chemical reactions. RDE chronoamperometry has not therefore been hitherto applied to the study of complex electrode mechanisms.

The theoretical analysis of the steady–state behaviour at the RDE has been based almost exclusively [223,232] on the reaction layer approximation [176,182,233–235] and theories are therefore only applicable to fast kinetic processes. A method for solving this problem without making any assumptions about the rapidity of the chemical steps is therefore desirable.

In this chapter, a general strategy is presented for calculating the current response to single and double potential steps for mechanistically complex reactions. Consideration of the resultant current transients at suitably long times enables the deduction of the steady–state response. Here, its applicability in theoretically discriminating between several subtle nuances of one particular electrode reaction mechanism, involving coupled homogeneous kinetics, will be examined and assessed. The inclusion of heterogeneous kinetics will also be presented.

The theoretical approach employed makes use of the spatial transformation first suggested by Hale [236,237] for the calculation of RDE chronopotentiometry. This effects the equivalent of a non–linear space grid to permit efficient numerical

calculations which are computed using an explicit finite–difference method. It has been demonstrated [238, 239] that, for a number of electrode processes, a similar approach in the numerical simulation of the chronoamperometric response to a potential step at a plane electrode in a stationary solution, leads to a considerable saving in computer time. Albery [130] has also recently drawn attention to the merits of this approach and used it in the solution of steady–state rotating ring–disc problems, where it appears to be no less successful than, for example, the cartesian hopscotch–finite–difference simulations of Feldberg [240]. The considerable generality of this approach has already been demonstrated [201,207,241–243].

More sophisticated finite difference methods, such as OC, have been applied to solve various electrochemical problems, both at the RDE under steady–state conditions [221,222,244–248] and at stationary electrodes in various time–dependent modes [249–254], but these numerical techniques have not been used in the solution of anything more complex than the case of a simple reversible electron transfer when the RDE is operated under non–steady–state conditions [231]. This may be related to the fact that for a successful solution of a particular electrochemical problem via OC, "an initial guess of the concentration profiles is needed" [246] and "initial guesses of the dependent variables are often important to get good results" [248]. Clearly, when the concentration profiles change rapidly with time, as during the chronoamperometric cases considered here, modelling the concentration profiles using OC may be quite difficult.

It will be shown in this chapter that the explicit finite–difference/Hale transformation approach to the solution of chronoamperometry and limiting current/rotation speed behaviour offers both simplicity and flexibility in that changes in mechanism are readily incorporated through minor changes to the main program. The limitations of the method are those of any finite–difference approach, namely that problems arise when information is required either at very short times or when very fast kinetics are involved. In particular, when homogeneous reactions become fast, a large number of grid points in both the spatial and time domains are required. The major advantage of the Hale transform method over simple finite–difference techniques, with uniform grids representing real space, is that the

method concentrates the calculation on the region close to the electrode where the largest concentration variations occur.

3.1.2 The General Approach

3.1.2.1 *Theory*

In this section, the general approach will be developed with reference to the specific case of the current response due to a single potential step, for an electrode reaction free from complications of coupled chemical kinetics. The validity of this is tested later in the chapter by comparison of the results with existing theory.

The time dependent convective–diffusion equation describing mass transport to the RDE was shown in Chapter Two for the reaction:

$$A + e^- \rightleftharpoons B$$

to be:

$$\frac{\partial[A]}{\partial t} = D_A \frac{\partial^2[A]}{\partial z^2} + Cz^2 \frac{\partial[A]}{\partial z} \qquad 3.2$$

where z is the distance normal to the electrode surface and D_A is the diffusion coefficient of the electroactive species, A, which is assumed to be kinetically stable. The term Cz^2 describes the convective flow close to and normal to the electrode: $C = 8.032\ W^{3/2}\ \nu^{-1/2}$ where W is the RDE rotation speed in Hz and ν is the kinematic viscosity in cm^2s^{-1}.

The form of equation 3.2 assumes that the RDE may be considered uniformly accessible (section 2.3.1) at all times. For the case of a simple electron transfer, this has been established as a valid assumption by a number of workers [184,230,231,255]. In particular, the results of the theoretical treatment of Bruckenstein and Prager [184], based on equation 3.2, were shown to be in excellent agreement with chronoamperometric data (for currents up to five times the steady–state value) obtained for the reduction of cupric ions from an aqueous potassium chloride solution at a gold RDE, when a potential step was applied to the transport–limited current region.

Equation 3.2 may be cast into non–dimensional form [205] by writing:

$$w = (C/D)^{1/3}\, z \qquad 3.3$$

$$t^* = (C^2\, D)^{1/3}\, t \qquad 3.4$$

and

$$a = [A]/[A]_\infty \qquad 3.5$$

so that

$$\frac{\partial a}{\partial t^*} = \frac{\partial^2 a}{\partial w^2} + w^2 \frac{\partial a}{\partial w} \qquad 3.6$$

Hale showed [236,237] that the substitution:

$$x = \frac{\int_0^w \exp\,(-\,w^3/3)\; dw}{\int_\infty^w \exp\,(-\,w^3/3)\; dw} \qquad 3.7$$

transforms RDE problems from real, infinite space ($0 < w < \infty$) to Hale, finite space ($0 < x < 1$). Equation 3.7 uses the description of the rotating disc diffusion layer (see equation 2.55) originally formulated by Levich [255] for a simple electron transfer under steady–state conditions. Equation 3.6 now becomes:

$$\frac{\partial a}{\partial t^*} = \frac{\exp\,(-\,2w^3/3)}{A} \frac{\partial^2 a}{\partial x^2} \qquad 3.9$$

where

$$A = \left[\int_0^\infty \exp\,(-\,w^3/3)\; dw \right]^2 = 1.65894. \qquad 3.10$$

Notice that the two terms corresponding to convection and diffusion have been reduced by the transformation to one term, simplifying the means by which the equation can be solved.

3.1.2.2 *The Method of Solution*

The simulation of the transient response to a perturbation of some existing concentration distribution proceeds by dividing up – 1) the transposed spatial

coordinate ($0 < x < 1$) into N boxes defined by the (N+1) grid points {0,1,2,3,..,N–1,N} and, 2) the time interval under consideration ($0 < t^* < 1$) into lM intervals such that:

$$dt^* = M^{-1} \qquad 3.11$$

Choosing a(m,n) to denote the concentration at the point $x = n/N$ and time $t^* = m/M$, the changes in concentration, da(m,n) are computed by means of the following equation:

$$a\,(m+1,n) = a\,(m,n) + da\,(m,n) \qquad 3.12$$

where

$$da(m,n) = \frac{[dt^*N^2\exp(-2w^3/3)]}{A}.[a(m,n-1) - 2a(m,n) + a(m,n+1)] \qquad 3.13$$

Computationally, values of w appropriate to each value of x are calculated from the following differential equation:

$$\frac{dw}{dx} = \exp\,(w^3/3)\left[\int_0^{\infty} \exp\,(-w^3/3)\,dw\right] \qquad 3.14$$

using the third–order Runge–Kutta method [256].

In order to carry out the calculations defined above, the initial and boundary conditions must be specified for each type of mechanism and experiment. Thus, the current–time response, following a potential step from a region where no current flows to one which would correspond to the transport–limited current under steady–state conditions (SPSC), can be calculated using the following, for a simple electron transfer:

$$m = 0 \qquad a(0,n) = 1 \qquad 3.15\ i$$

$$m > 0 \qquad a(m,0) = 0 \qquad ii$$

The current flowing at a time, t*, may be readily deduced as being:

$$i(t^*) = \frac{n_e F A D^{2/3} C^{1/3} \exp(-N^{-3}/3) j(m)}{A^{1/2}} \qquad 3.16$$

where

$$j(m) = [a(m,1) - a(m,0)].N \qquad 3.17$$

and n_e is the number of electrons involved in the electrode reaction, A is the area of the electrode and F is the Faraday constant. Provided that a moderate number of boxes (>20) are used for the simulation, the term $[\exp(-N^{-3}/3)]$ in equation 3.16 can be taken as effectively equal to unity. The current flowing at time t* is often also conveniently represented by the effective number of electrons transferred, n_{eff}, normalised to the value of the steady–state current.

For a given value of N, the size of dt* follows automatically from the stability criterion applicable to an explicit finite–difference method [257]:

$$S = N^2\, dt^* < 0.5 \qquad 3.18$$

Following the recommendations of other workers [160,230,257,258], a value of dt* was chosen so that $0.4 < S < 0.5$ was always obeyed.

3.1.3 Double Potential Steps

Minor extension of this theory permits the deduction of the current–time response to a double potential step (DPSC). The potential sequence employed is shown in Figure 3.1 and once again the electrode process is assumed free from complicating homogeneous or heterogeneous kinetics. Thus, during the step from E_1 to E_2, a species A is reduced (oxidised) at a transport–limited rate to B while during the step from E_2 to E_3 this is reversed [207,259] i.e.:

$$\text{"Forward step"} \quad A + e^- \longrightarrow B$$

$$\text{"Reverse step"} \quad B - e^- \longrightarrow A$$

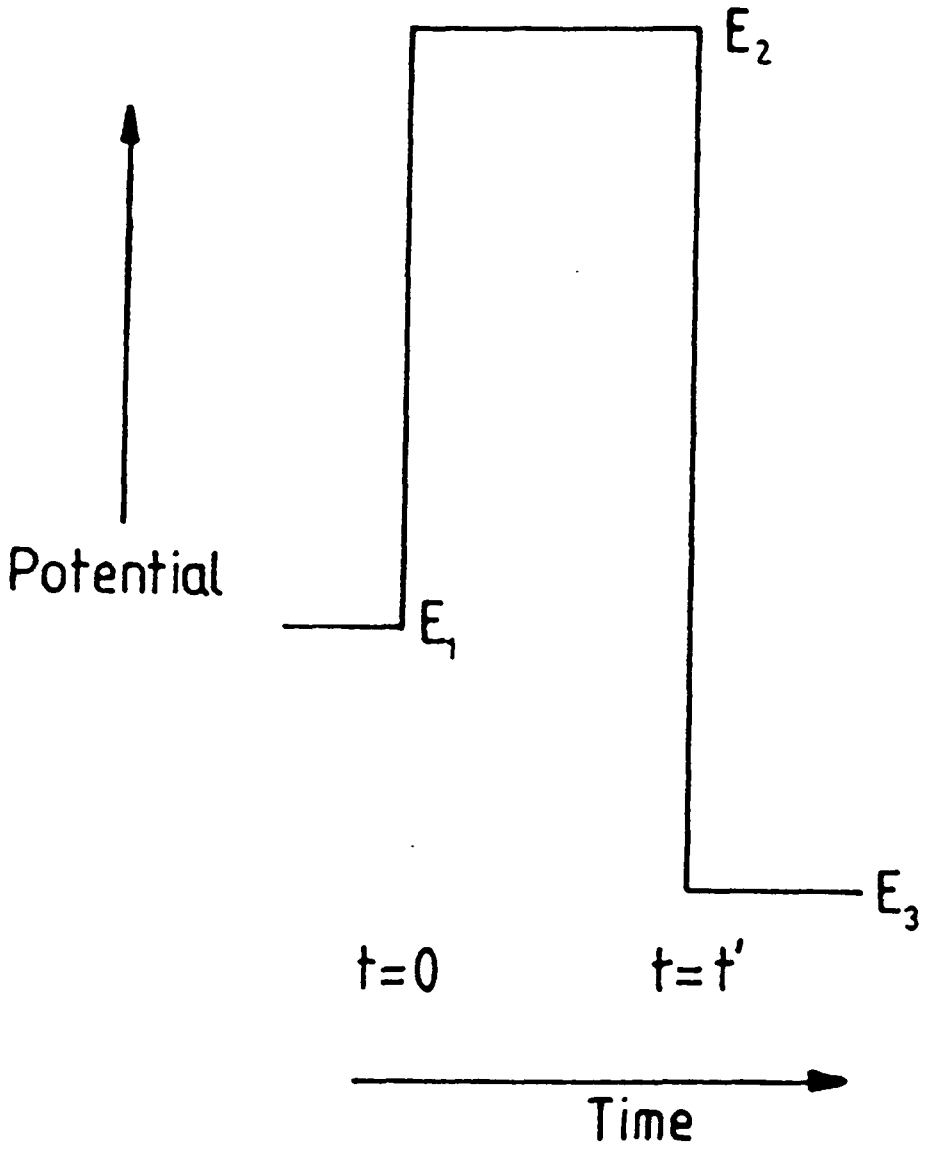


Figure 3.1: The potentials E_1, E_2 and E_3 defining a double potential step experiment.

As before, the dimensionless convective–diffusion equation may be written:

$$\frac{\partial h}{\partial t^*_H} = \frac{\partial^2 h}{\partial w_H^2} + w_H^2 \frac{\partial h}{\partial w_H} \qquad 3.19$$

where $h = [H]/[H]_\infty$ and H is either A or B.

w_H and t^*_H are given by:

$$w_H = (C/D_H)^{1/3} z \qquad 3.20$$

$$t^*_H = (C^2 D_H)^{1/3} t \qquad 3.21$$

and D_H is the diffusion coefficient of H.

Upon applying the Hale transformation, equation 3.19 becomes:

$$\frac{\partial h}{\partial t^*_H} = \frac{\exp\ (-2w_H^3/3)}{A} \frac{\partial^2 h}{\partial x_H^2} \qquad 3.22$$

Concentration profiles can be computed from:

$$h\ (m+1,n_H) = h\ (m,n_H) + dh\ (m,n_H) \qquad 3.23$$

where

$$dh(m,n_H) = \left[\frac{dt^*_H\ N_H^2\ \exp(-2w_H^3/3)}{A}\right] [h(m,n_H-1) - 2h(m,n_H) + h(m,n_H+1)] \qquad 3.24$$

During the first potential step B is being generated from A. The concentration profiles of A and B are "linked" both physically and mathematically by means of:

$$\left[D_A \frac{\partial a}{\partial z}\right]_{z=0} = -\left[D_B \frac{\partial b}{\partial z}\right]_{z=0} \qquad 3.25$$

which expresses the fact that the flux of A to the electrode surface is equal to the flux of B away from it. Transforming to Hale space, equation 3.25 becomes:

$$\left[D_A^{2/3}\frac{\partial a}{\partial w_A}\right]_{w=0} = \left[D_B^{2/3}\frac{\partial b}{\partial w_B}\right]_{w=0} \qquad 3.26$$

For the "forward" step ($0 < m/M < t'$), then the surface concentration of A will be zero. The initial and boundary conditions may therefore now be written in the following computationally compatible forms, where $t_A^{*\prime}$ is the normalised time corresponding to t':

$$m = 0 \qquad a(0,n_A) = 1 \qquad 3.27\ \text{i}$$

$$b(0,n_B) = 0 \qquad \text{ii}$$

$$0 < m/M < t_A^{*\prime} \qquad a(m,0_A) = 0 \qquad 3.28\ \text{i}$$

$$a(m,N_A) = 1 \qquad \text{ii}$$

$$b(m,0_B) = [D_A/D_B]^{2/3}a(m,1_A) + b(m,1_B) \qquad \text{iii}$$

$$b(m,N_B) = 0 \qquad \text{iv}$$

$$m/M > t_A^{*\prime} \qquad b(m,0_B) = 0 \qquad 3.29\ \text{i}$$

$$b(m,N_B) = 0 \qquad \text{ii}$$

$$a(m,0_A) = [D_B/D_A]^{2/3}b(m,1_B) + a(m,1_A) \qquad \text{iii}$$

$$a(m,N_A) = 1 \qquad \text{iv}$$

and transients may be evolved by sequentially updating the concentrations in the A and B Hale grids according to the usual concentration change expressions given by equations 3.23 and 3.24. The current flowing at time t* is given by:

$$i(t^*) = \frac{nFAD_H^{2/3}C^{1/3}\ \exp\ (-N_H^{-3}/3).j_H(m)}{A^{1/2}} \qquad 3.30$$

where:

$$j_H(m) = \{h(m,1_H) - h(m,0_H)\}\ N_H \qquad 3.31$$

Once again, in computing these transients, the stability requirement given in equation 3.18 was always observed [257].

3.1.4 The Inclusion of Homogeneous Kinetics

In this section, the theory is extended to include coupled homogeneous kinetics. This will be illustrated by modelling the kinetics associated with the so–called catalytic mechanism (EC') and its nuances.

In this general class of mechanistic pathways [187,260–271], an electrogenerated species (the "mediator") reduces or oxidises some other solution species (the "substrate") with the regeneration of the original electroactive material, which can thus undergo further reaction at the electrode [241,243,272]. The simple catalytic mechanism (EC'pure) is defined by the following scheme:

$$A + e^- \rightleftharpoons B \qquad 3.32\ i$$

$$B + Y \longrightarrow A + \text{products} \qquad ii$$

This mechanism is often studied with the substrate Y present at a much higher concentration than the mediator B so that the kinetic step ii may be taken as first order [182,184,273]. However, the analysis presented here will be valid for all relative concentrations of the two species.

A closely related process involves a pre–equilibrium before the product–forming irreversible step:

$$A + e^- \rightleftharpoons B \qquad iii$$

$$B + Y \rightleftharpoons A + \text{intermediate} \qquad iv$$

$$\text{intermediate} \longrightarrow \text{products} \qquad v$$

where reaction (iv) is described by the the equilibrium constant K_{iv}:

$$K_{iv} = \frac{[A]\ [\text{intermediate}]}{[B]\ [Y]}$$

This mechanism is defined EC'pre–eqm. The process may be regarded as a "self limiting" catalytic reaction, because if the concentration of A is raised to enhance the catalytic turnover of Y into products, the consequential shift of the equilibrium

in step (iv) is to produce a smaller catalytic response than would occur if the simple EC' mechanism operated. Such a mechanism is thought to operate, for example, in the oxidation of certain carboxylates (Y in the above scheme) mediated by the cation radical (B) of tris–(p–bromophenyl)amine (A) [272,274].

Another conceivable complication is that a disproportionation step is involved:

$$A + e^- \rightleftharpoons B \qquad \text{vi}$$

$$B + B \rightleftharpoons A + C \qquad \text{vii}$$

followed by either:

$$C + Y \longrightarrow A + \text{products} \qquad \text{viii}$$

or

$$C + Y \longrightarrow B + \text{products} \qquad \text{ix}$$

The mechanisms are denoted as EC'dispA and EC'dispB respectively and each may be divided further into two subcases since either the product forming step or the disproportionation step may be rate–limiting. In the former case, the notation EC'dispA1 or EC'dispB1 is applied, while in the second case the labels EC'dispA2 or EC'dispB2 are used.

The appropriate mass transport equations for these six mechanisms are:

$$\frac{\partial a}{\partial t^*} = D\frac{\partial^2 a}{\partial z^2} + Cz^2\frac{\partial a}{\partial z} + k_{mech}\, p_a q_a \qquad 3.33$$

$$\frac{\partial b}{\partial t^*} = D\frac{\partial^2 b}{\partial z^2} + Cz^2\frac{\partial b}{\partial z} - k_{mech}\, p_b q_b \qquad 3.34$$

$$\frac{\partial y}{\partial t^*} = D\frac{\partial^2 y}{\partial z^2} + Cz^2\frac{\partial y}{\partial z} - k_{mech}\, p_y q_y \qquad 3.35$$

where $b = [B]/[A]_\infty$, $y = [Y]/[Y]_\infty$ and the relevant rate constants (k_{mech}), concentrations (p) and bulk concentrations (q) are given in Table 3.1. Solution of

equations 3.33 to 3.35 proceeds by applying the Hale transformation (equation 3.7). The resultant convective–diffusion equations in Hale space are:

$$\frac{\partial a}{\partial t^*} = \frac{\exp\ (-2w^3/3)}{A} \frac{\partial^2 a}{\partial x^2} + k_{norm}\, p_a r_a \qquad 3.36$$

$$\frac{\partial b}{\partial t^*} = \frac{\exp\ (-2w^3/3)}{A} \frac{\partial^2 b}{\partial x^2} - k_{norm}\, p_b r_b \qquad 3.37$$

$$\frac{\partial y}{\partial t^*} = \frac{\exp\ (-2w^3/3)}{A} \frac{\partial^2 y}{\partial x^2} - k_{norm}\, p_y r_y \qquad 3.38$$

where the normalised rate constants (k_{norm}) and the bulk concentration ratios (r) are given in Table 3.2.

The boundary conditions for a single potential step, where the current changes from zero to the transport–limited value, for each mechanism, are:

$t = 0$:	$a = 1$	$b = 0$	$y = 1$	3.39 i
$t > 0$, $x = 1$:	$a = 1$	$b = 0$	$y = 1$	ii
$x = 0$:	$a = 0$	$b = 1$	$\frac{\partial y}{\partial x} = 0$	iii

The time evolution of the current is then found from concentration profiles determined using:

$$h\ (m+1,n) = h\ (m,n) + dh\ (m,n) \qquad 3.40$$

where h = a, b or y, and:

$$da\ (m,n) = [dt^*N^2 \exp(-2w^3/3)]\ [a(m,n-1) - 2a(m,n) + a(m,n+1)] + k_{norm}\, p_a(m,n)\, r_a\, dt^* \qquad 3.41$$

$$db\ (m,n) = [dt^*N^2 \exp(-2w^3/3)]\ [b(m,n-1) - 2b(m,n) + b(m,n+1)] - k_{norm}\, p_b(m,n)\, r_b\, dt^* \qquad 3.42$$

Table 3.1: Values of k_{mech}, p and q appropriate for equations 3.33–3.35.

MECHANISM	k_{mech}	p_a	p_b	p_y	q_a	q_b	q_y
EC'pure	k_{ii}	yb	yb	yb	$[Y]_\infty$	$[Y]_\infty$	$[A]_\infty$
EC'preeqm	$K_{iv}k_v$	$\frac{yb}{a}$	$\frac{yb}{a}$	$\frac{yb}{a}$	$\frac{[Y]_\infty}{[A]_\infty}$	$\frac{[Y]_\infty}{[A]_\infty}$	1
EC'dispA1	$K_{vii}k_{viii}$	$\frac{2b^2y}{a}$	$\frac{2b^2y}{a}$	$\frac{b^2y}{a}$	$[Y]_\infty$	$[Y]_\infty$	$[A]_\infty$
EC'dispA2	k_{vii}	$2b^2$	$2b^2$	*	$[A]_\infty$	$[A]_\infty$	*
EC'dispB1	$K_{vii}k_{ix}$	$\frac{b^2y}{a}$	$\frac{b^2y}{a}$	$\frac{b^2y}{a}$	$[Y]_\infty$	$[Y]_\infty$	$[A]_\infty$
EC'dispB2	k_{vii}	b^2	b^2	*	$[A]_\infty$	$[A]_\infty$	*

* y concentration profile not required for this calculation.

Table 3.2: Values of k_{norm} and r appropriate for equations 3.36–3.38.

MECHANISM	k_{norm}	$r_y^{\ddagger}$
EC'pure	$k_{ii}\, C^{-2/3}\, D^{-1/3}\, [Y]_\infty$	$\frac{[A]_\infty}{[Y]_\infty}$
EC'preeqm	$K_{iv}k_v\, C^{-2/3}\, D^{-1/3}\, \frac{[Y]_\infty}{[A]_\infty}$	$\frac{[A]_\infty}{[Y]_\infty}$
EC'dispA1	$K_{vii}k_{viii}\, C^{-2/3}\, D^{-1/3}\, [Y]_\infty$	$\frac{[A]_\infty}{[Y]_\infty}$
EC'dispA2	$k_{vii}\, C^{-2/3}\, D^{1/3}\, [A]_\infty$	*
EC'dispB1	$K_{vii}k_{ix}\, C^{-2/3}\, D^{1/3}\, [Y]_\infty$	$\frac{[A]_\infty}{[Y]_\infty}$
EC'dispB2	$k_{vii}\, C^{-2/3}\, D^{1/3}\, [A]_\infty$	*

* y concentration profile not required for this calculation.

‡ $r_a = r_b = 1$ for each mechanism listed above.

$$dy\,(m,n) = [dt^{*}N^{2}\exp(-2w^{3}/3)]\,[y(m,n-1) - 2y(m,n) + y(m,n+1)] - k_{norm}\,p_{y}(m,n)\,r_{y}\,dt \qquad 3.43$$

i.e. three one dimensional arrays of N+1 grids points corresponding to a, b and y are set up, and upon calculating the changes in "a" for a step of M^{-1} in t^{*}, the changes in "b" and "y" are computed.

The boundary conditions (equation 3.39) are incorporated into the numerical calculation by means of the following:

$$m = 0 \qquad a\,(0,n) = 1 \qquad b\,(0,n) = 0 \qquad y = (0,n) = 1 \qquad 3.44\ \text{i}$$

$$m > 0 \qquad a\,(m,N) = 1 \qquad b\,(m,N) = 0 \qquad y\,(m,N) = 1 \qquad \text{ii}$$

$$a\,(m,0) = 0 \qquad b\,(m,0) = 1 \qquad y\,(m,0) = y\,(m,1) \qquad \text{iii}$$

The three arrays are sequentially updated during computation and the current calculated using equations 3.16 and 3.17.

For simplicity, the theory presented in this section has considered only SPSC and it has been assumed that species A, B and Y have equal diffusion coefficients. In section 3.1.3, the straightforward manipulation of the theory required to consider both double potential steps and unequal diffusion coefficients was presented; this can readily be incorporated into cases where coupled homogeneous kinetics exist so that both DPSC and where $D_A \neq D_B$ can be modelled. The computationally compatible initial and boundary conditions then become:

$$m = 0 \qquad a\,(0,n_A) = 1 \qquad b\,(0,n_B) = 0 \qquad y\,(0,n_A) = 1 \qquad 3.45\ \text{i}$$

$$0 < m/M < t_{A}^{*}{}' \qquad a\,(m,0_A) = 0 \qquad a\,(m,N_A) = 1 \qquad \text{ii}$$

$$b\,(m,0_B) = [D_A/D_B]^{2/3}a\,(m,1_A) + b\,(m,1_B) \qquad \text{iii}$$

$$b\,(m,N_B) = 0 \qquad \text{iv}$$

$$y\,(m,0_A) = y\,(m,1_A) \qquad y\,(m,N_A) = 1 \qquad \text{v}$$

$$m/M > t_A^{*\prime} \quad a(m,0_A) = [D_B/D_A]^{2/3} b(m,1_B) + a(m,1_A) \qquad \text{vi}$$

$$a(m,N_A) = 1 \qquad \text{vii}$$

$$b(m,0_B) = 0 \qquad b(m,N_B) = 0 \qquad \text{viii}$$

$$y(m,0_A) = y(m,1_A) \qquad y(m,N_A) = 1 \qquad \text{ix}$$

and the only assumption is that $D_A = D_Y$.

3.1.5 The Inclusion of Heterogeneous Kinetics

The ease with which heterogeneous kinetics can be included into the theoretical approach presented here will be illustrated by considering an electrode process where electron transfer ($A + e^- \longrightarrow B$) is preceded by the first order adsorption of A. The result of this adsorption is to change the concentration of A at the electrode surface; finite heterogeneous kinetics will prevent all of A from being instantaneously reduced (oxidised) at the electrode so that the boundary condition $a(m,0_A) = 0$ of equation 3.26 is no longer valid. However, calculation of the new boundary condition within the Hale formulation is straightforward.

The finite first–order kinetics restrict the flux of material reaching the electrode to:

$$D_A \frac{da}{dz} = k'[A]_{z=0} \qquad 3.46$$

where k' is the rate constant of the chemical step. For computational purposes, the boundary conditions now become:

$$m = 0 \qquad a(0,n_A) = 1 \qquad b(0,n_B) = 0 \qquad 3.47\ \text{i}$$

$$0 < m/M < t_A^{*\prime} \qquad a(m,0_A) = \frac{D_A\ a\ (m,1_A)}{(D_A + k'dz)} \qquad \text{ii}$$

$$a(m,N_A) = 1 \qquad \text{iii}$$

$$b(m,0_B) = [D_A/D_B]^{2/3} a(m,1_A) + b(m,1_B) \qquad \text{iv}$$

$$b(m,N_B) = 0 \qquad \text{v}$$

$$m/M > t_A^{*\prime} \qquad b\,(m,0_B) = 0 \qquad \text{vi}$$

$$b\,(m,N_B) = 0 \qquad \text{vii}$$

$$a\,(m,0_A) = [D_B/D_A]^{2/3} b\,(m,1_B) + a\,(m,1_A) \qquad \text{viii}$$

$$a\,(m,N_A) = 1 \qquad \text{ix}$$

Other than the change in this boundary condition, the computation proceeds exactly as for the case where there are no kinetic complications. In performing these calculations, the stability criterion for an explicit finite–difference method given by equation 3.17 was always maintained and therefore values of N are dt* were chosen so that $0.4 < S < 0.5$ [257].

3.1.6 Results and Discussions

In this section, the results of the calculations described above are presented and interpreted.

3.1.6.1 *Simple Electron Transfer: SPSC*

The chronoamperogram for a transport–limited electron transfer was calculated in order to validate the theoretical procedure described in section 3.1.2. Figure 3.2 shows the resultant transient normalised to the steady–state current, obtained using the FORTRAN program given in Appendix 4a, with N = 20 and M = 1000. On decreasing N from 20 to 10, it was found that the predicted currents, for $t^* > 0.1$ were changed by less than 1% confirming that these results are free from artefacts due to assumptions about N. The data in Figure 3.2 are indistinguishable from those of the numerical simulation of Prater and Bard [220], which were performed in Cartesian space. In addition, excellent agreement is also found with the approximate analytical treatment of Bruckenstein and Prager [184], who derived the following equation:

$$t^* = 0.347 \left[\frac{1}{2} \ln\left[\frac{1-R^3}{(1-R)^3}\right] + \sqrt{3}\left[\frac{\pi}{6} - \tan^{-1}\left[\frac{2R+1}{\sqrt{3}}\right]\right]\right] \qquad 3.48$$

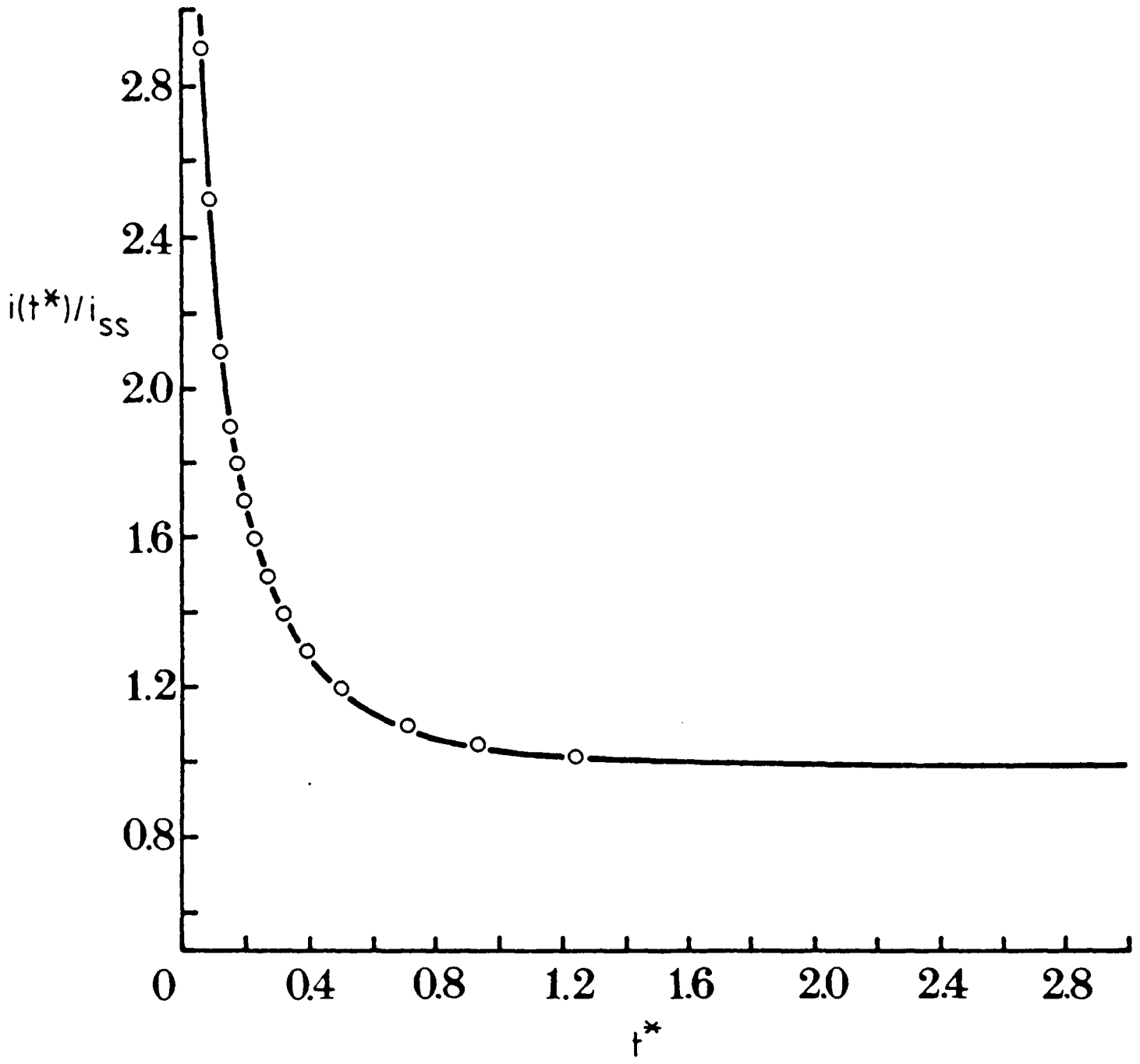


Figure 3.2: Computed chronoamperometric transient for an E process resulting from a single potential step at a RDE. The open circles represent points calculated using the approximate theory of Bruckenstein.

where $$R = \frac{i\,(t^* \rightarrow \infty)}{i\,(t^*)} \qquad 3.49$$

This has been shown to relate in a satisfactory manner to experiment [184]. The open circles in Figure 3.2 are points determined using equation 3.48.

The validity of the numerical strategy presented here for computing RDE SPSC transients can therefore be concluded.

3.1.6.2 *Simple Electron Transfer: DPSC*

The precise form of the potential sequence to be examined can be understood by reference to Figure 3.1, where it should be recognised that the solution contains only one electroactive species, A. Also the potentials E_2 and E_3 are of sufficient magnitude and applied for enough time that steady–state transport–limited currents for the reductive and oxidative processes are established.

As for the previous section, transients calculated using the method described in section 3.1.3 (using the program in Appendix 4b) were insensitive to the particular value of N chosen, provided that N was sufficiently large. Once again, N = 20 (m = 1000) was perfectly adequate. The "forward" transient is calculated identically to that presented in Figure 3.2 and therefore is indistinguishable from previous work. A typical reverse transient, also normalised to the transport–limited current, is shown in Figure 3.3. This is believed to be the first calculation of this problem.

For the "special" case where $D_A = D_B$, the transients shown in Figures 3.2 and 3.3 are in fact related. The algebraic difference between the current on the "forward" transient (at a {real} time, t, after the start of the transient), $i_f(t)$ and the current on the "reverse" transient at the corresponding time, t, (after the start of this second transient), i_r (t–t'), is equal to the steady–state current, i_{ss}, which flows at the potential E_2. t' and E_2 are defined in Figure 3.1. This observation is proved mathematically in Appendix Five.

3.1.6.3 *Homogeneous Kinetics*

In any numerical approximation method, the production of stable and truly

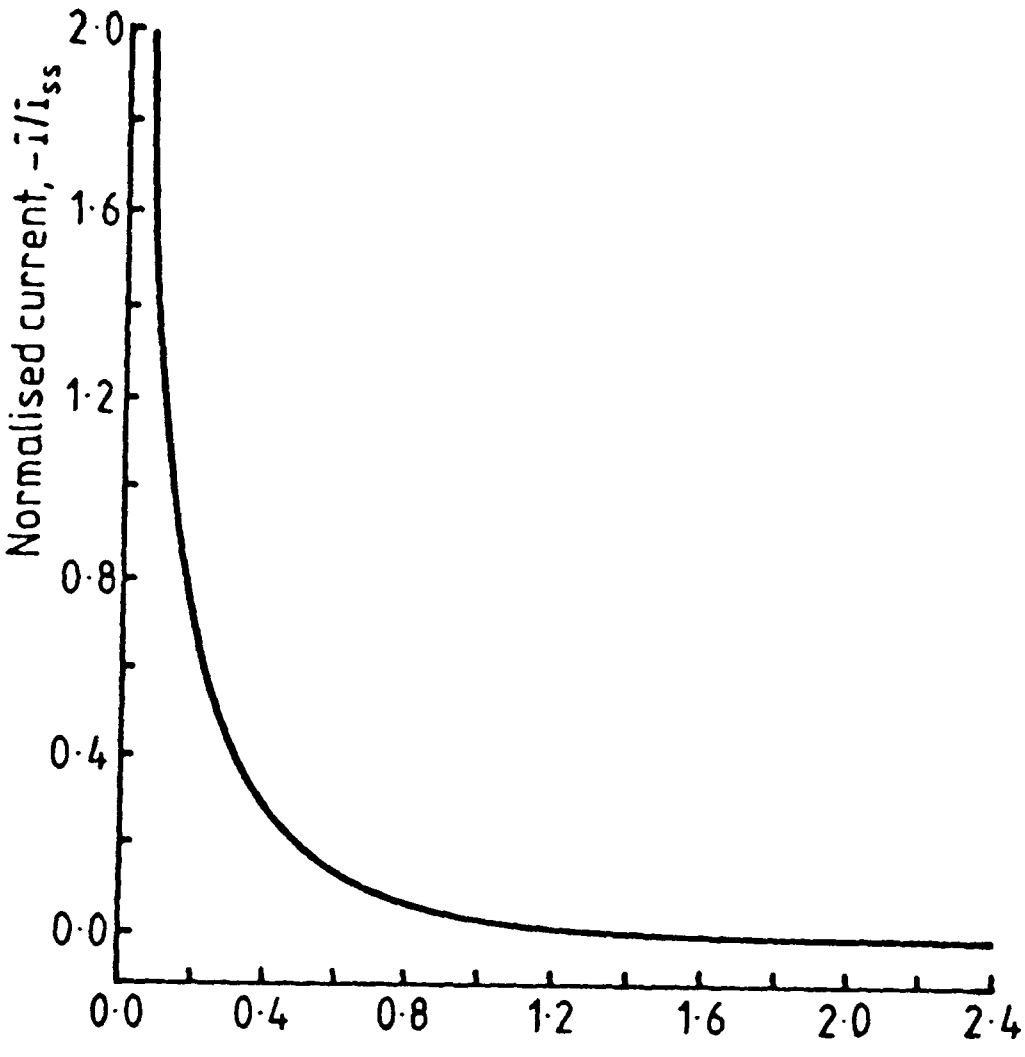


Figure 3.3: The "reverse" current transient corresponding to a potential step from E_2 to E_3 (= E_1), calculated under the assumption that there are no kinetic complications.

converged results is essential. For the simple electron transfer processes already illustrated, a value of n = 20 was clearly sufficient to meet this requirement. However, when coupled homogeneous kinetics are included into the problem, the concentration profiles of reactant and products change more rapidly and therefore need to be determined more precisely in order to model electrode processes accurately. Hence larger values of N and M are necessary. Remembering that N^2dt^* must be < 0.5, any two–fold increase in N requires a four–fold increase in M resulting in an eight–fold overall increase in computer time. In particular, when the homogeneous rate constant is large, the value of N must also be high. The relationship between N and normalised rate constant has been considered quantitatively for EC, ECE and DISP processes by Unwin [160]. However here with a value of N = 200 and $dt^* = 1x10^{-5}$ convergence was achieved, even for the fastest rate constants considered (see Chapters Five, Seven and Eight) and these values, which were not computationally prohibitive were therefore used throughout.

Figure 3.4 shows a typical transient, generated from the theory presented in section 3.1.5 for an EC'pure process with k_{norm}(EC'pure) = 1.0 and $[A]_\infty/[Y]_\infty$ = 0.235. This was calculated using the FORTRAN program given in Appendix 4c. The final steady–state portion of such transients allows the deduction of the "working curves" shown in Figure 3.5 for $[A]_\infty/[Y]_\infty$ = 0.1, 1.0 and 10.0. Here it is assumed that $D_A = D_B = D_Y$. Also shown in this figure are the results of Prater and Bard [275], who used numerical simulation in cartesian space to tackle the same problem. Excellent agreement is observed under all conditions, validating the explicit finite–difference/ Hale transformation approach adopted here.

The special case which arises when [Y] >> [B] and pseudo first–order kinetics can be assumed, was discussed in the introduction to the catalytic mechanism. The working curve for this instance is shown in Figure 3.6 along with the behaviour calculated from the "reaction layer" theory for this mechanism, which is given by [276]:

$$n_{eff} = 0.6435\, D^{-1/6}\, W^{-1/2}\, \nu^{1/6}\, (k_{ii}\, [Y]_\infty)^{1/2} \qquad 3.50$$

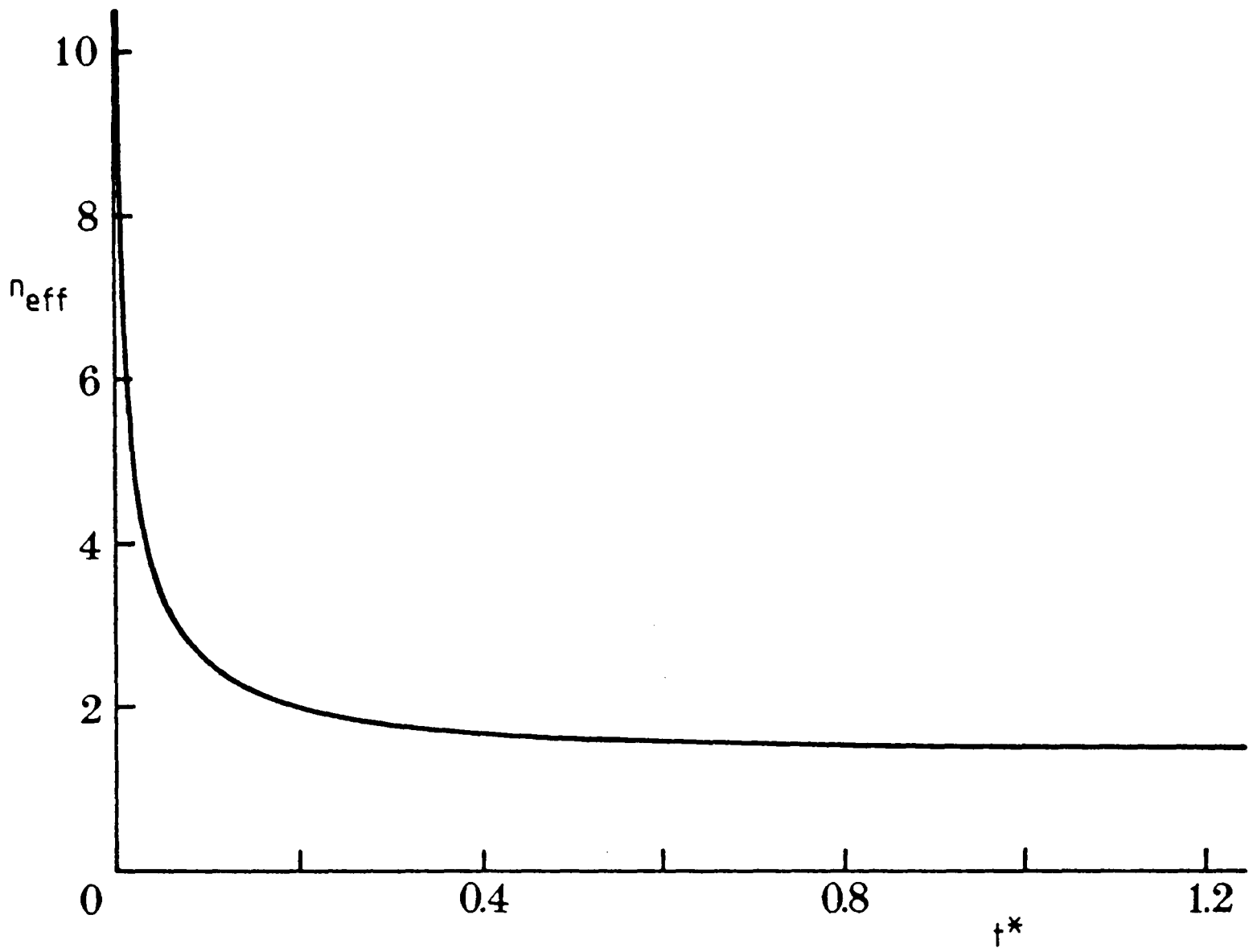


Figure 3.4: Computed single potential step chronoamperometric transient for the EC'pure mechanism. k_{norm}(EC'pure) = 1.0 and $[A]_\infty/[Y]_\infty = 0.235$.

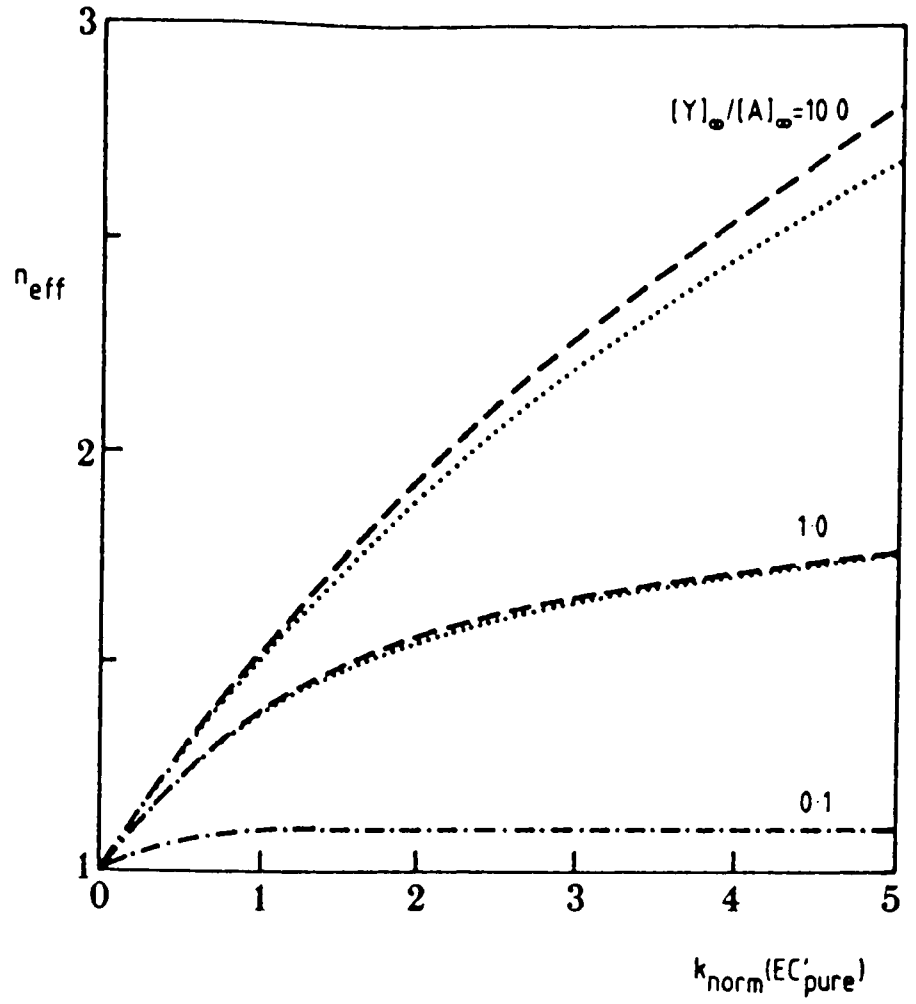


Figure 3.5: Steady–state working curves for the EC'pure mechanism calculated using the explicit finite difference/Hale transformation method (.....). The results of Prater and Bard are also shown (– – – –).

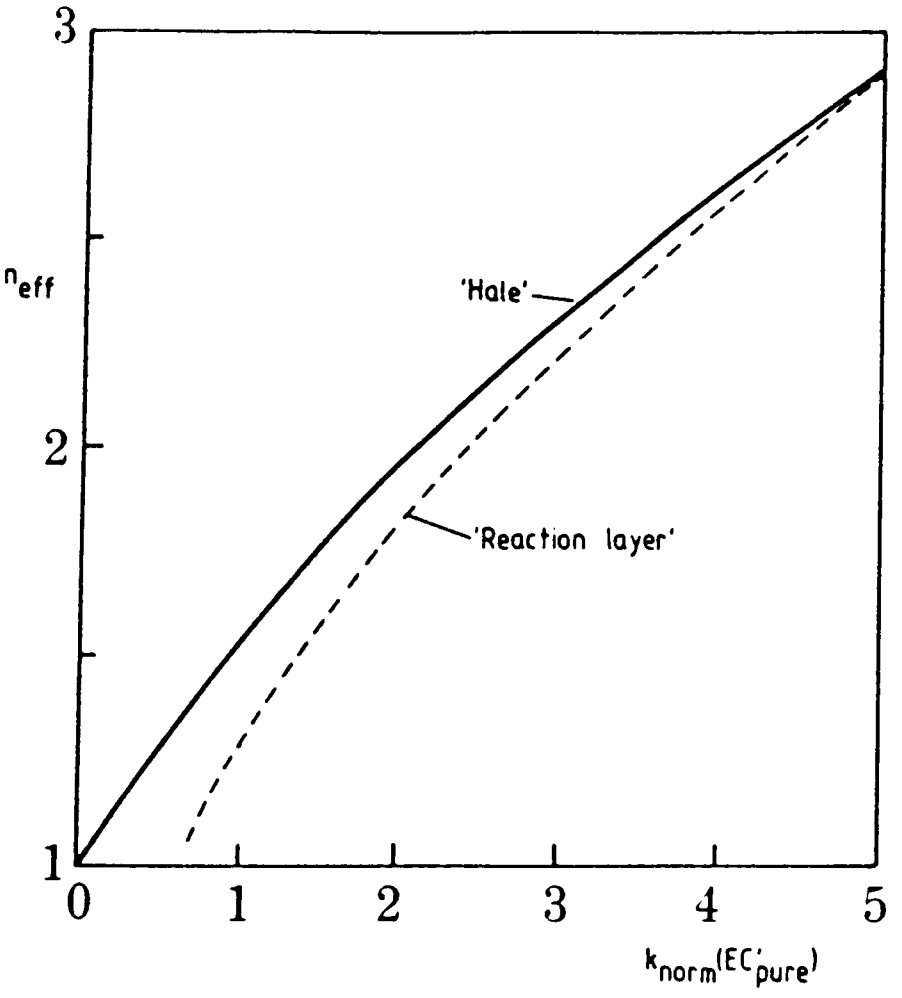


Figure 3.6: Steady–state working curve for the EC'pure mechanism, where pseudo–first–order kinetics have been assumed (_____). The curve calculated using the reaction layer theory is also shown (– – – –).

This latter approach is valid for fast rate constants and low rotation speeds (i.e. $W(D/\nu)^{1/3} << 3k_{ii}[Y]_\infty$) where the reaction layer thickness is much narrower than the diffusion layer thickness and a limiting kinetic current independent of rotation speed is found. This corresponds to the high k_{norm} section of the "working curve" where good agreement between the analytical and numerical theories is apparent. However, when $k_{ii}[Y]_\infty/W$ becomes small, the analytical theory breaks down and approaches the transport–limited current ($n_{eff} = 1$). Here, where the kinetics are slow, the numerical/Hale approach is at its best.

Working curves, calculated in an identical manner to those above, are shown in Figures 3.7 to 3.9 for the EC'preeqm, EC'dispA1 and EC'dispB1 mechanisms. Figure 3.10 shows the working curve appropriate for both the EC'dispA2 and EC'dispB2 nuances, since the Y species is absent from the current determining equations for these processes, this curve is independent of $[A]_\infty/[Y]_\infty$.

Inspection of Figures 3.5 to 3.10 reveals that the n_{eff} versus normalised rate constant behaviour is sufficiently different that all of the mechanistic varieties might be distinguished on the basis of steady–state measurements alone, provided that a suitably wide range of rotation speeds is employed. The range of 1 – 50Hz, which is experimentally accessible and convenient may be adequate for these purposes. Hence, chronoamperometric analysis may not be essential but could be employed in the confirmation of mechanistic and kinetic results.

3.1.6.4 *Heterogeneous Kinetics*

Figure 3.11 illustrates the effect of finite first–order heterogeneous kinetics on the "forward" transient when the potential is stepped from a potential where no current flows to one which gives rise to the transport–limited current. The FORTRAN program used to generate this data is given in Appendix 4d. Results are plotted here in terms of real current, i, and real time, t. In the calculation of these transients a value of n = 100 (and correspondingly m = 25,000) was found to be sufficient to provide converged data. Values of W = 9Hz, $D_A = 9.0\times10^{-6}$, $D_B = 1.82\times10^{-5}$ cm^2s^{-1} and $[A]_\infty = 2.86\times10^{-3}$ $moldm^{-3}$ were used for these calculations. Notice that in the limit of fast kinetics, the transients converge, giving the same

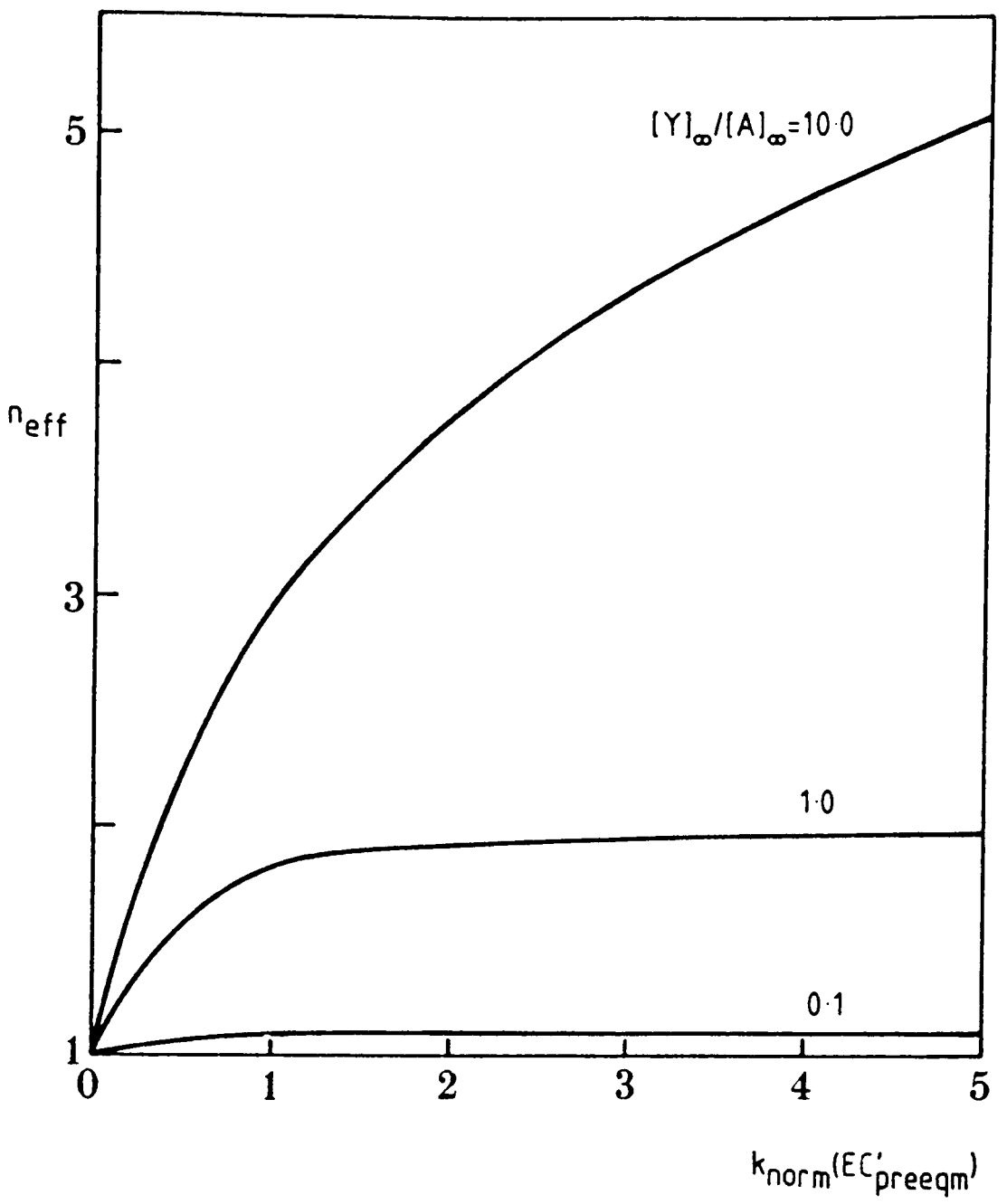


Figure 3.7: Steady–state working curves for the EC'preeqm mechanism.

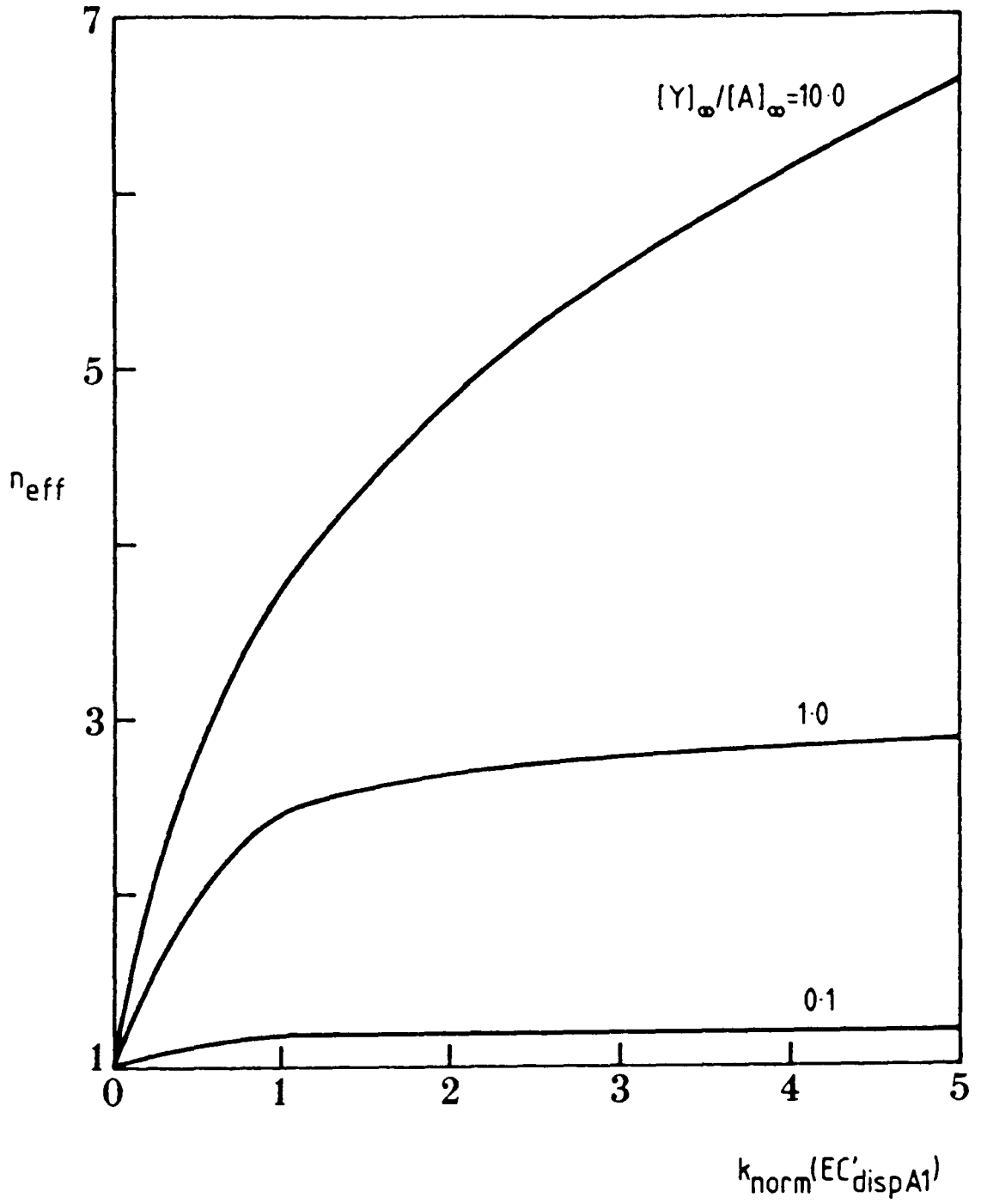


Figure 3.8: Steady–state working curves for the EC'dispA1 mechanism.

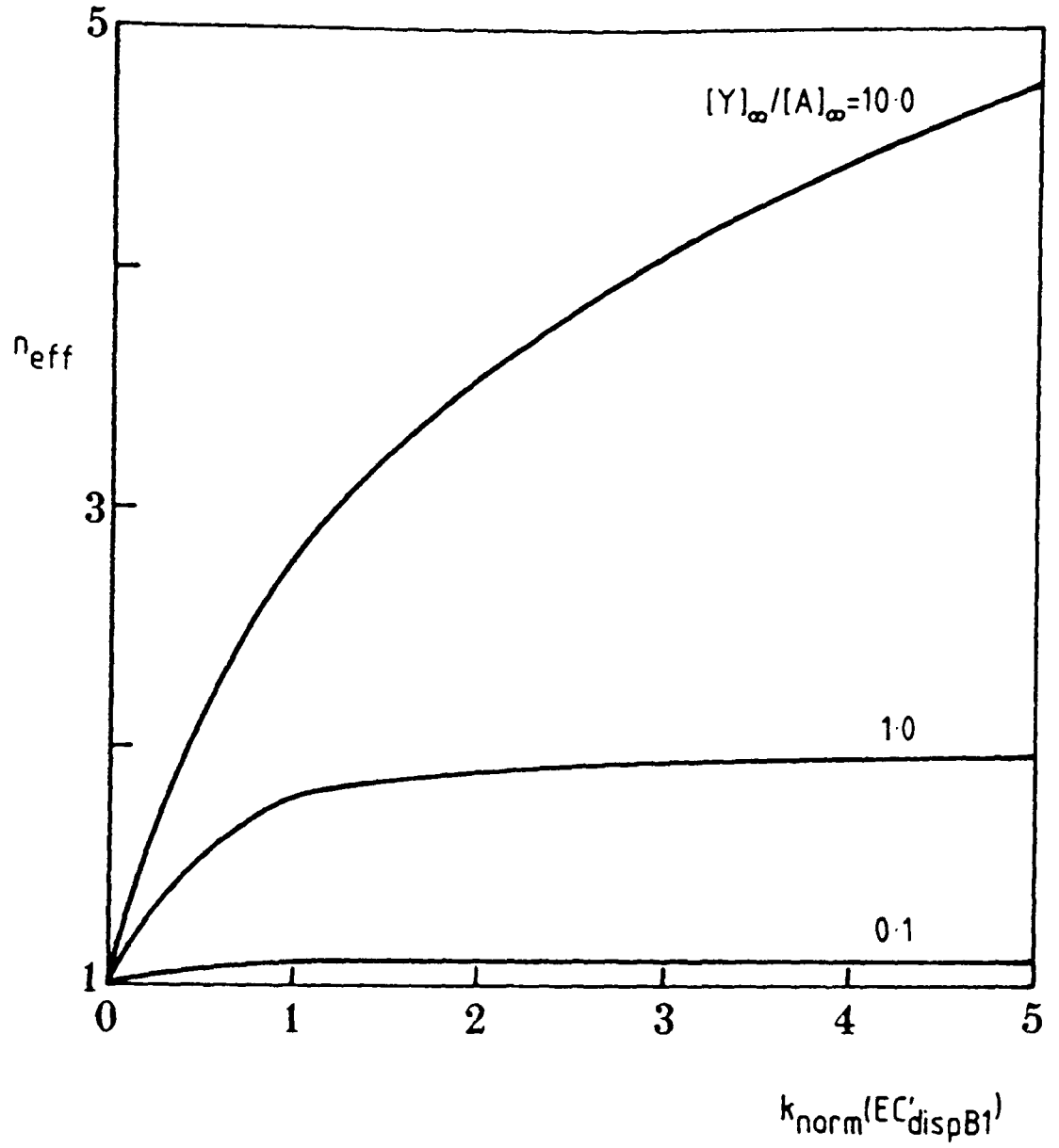


Figure 3.9: Steady–state working curves for the EC'dispB1 mechanism.

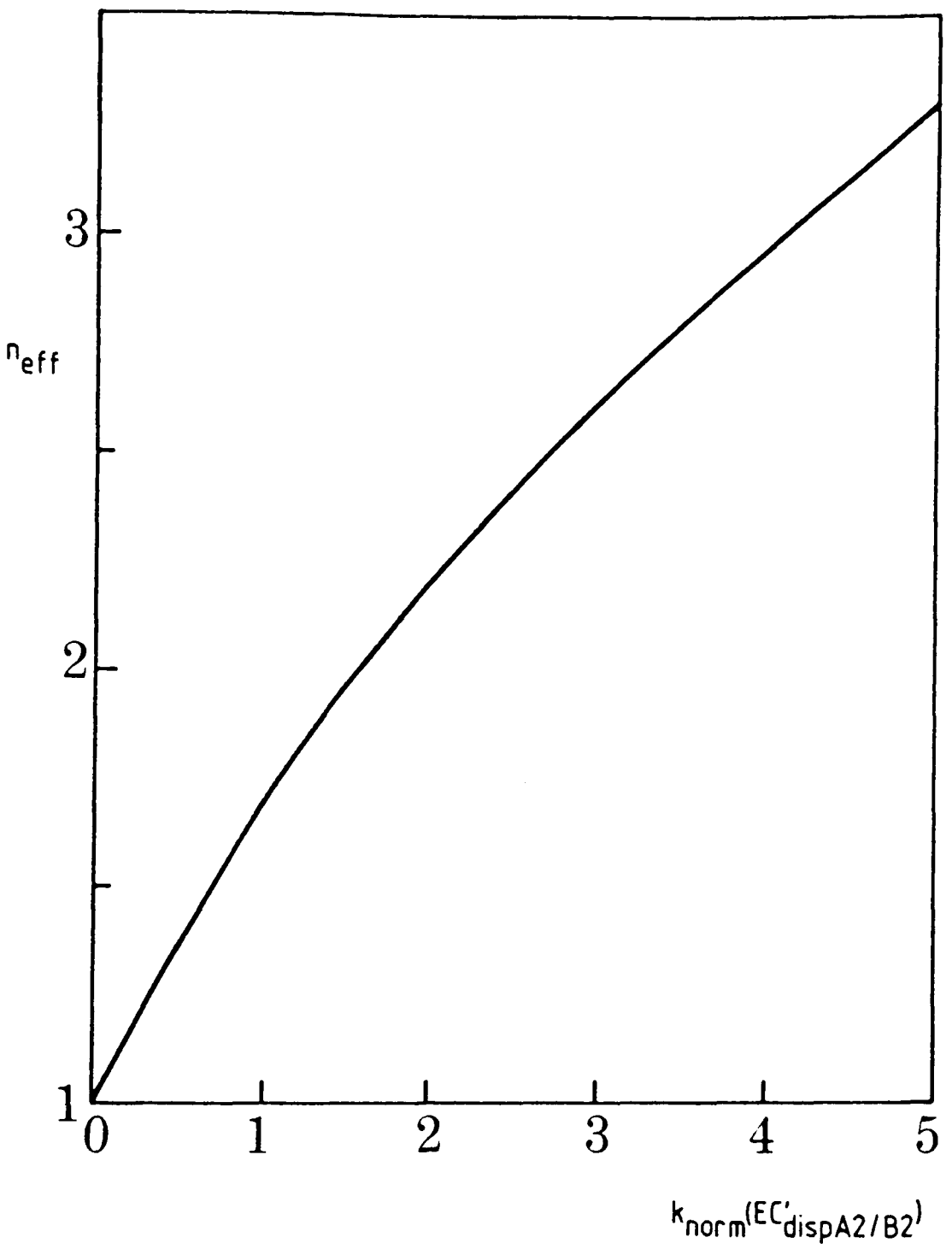


Figure 3.10: Steady–state working curve deduced for the EC'dispA2 and EC'dispB2 mechanisms. This curve is independent of $[A]_\infty / [Y]_\infty$.

result as in the absence of any kinetic complications (as shown in Figure 3.2). Also, at low rate constants, the transient becomes "flattened", there is less current at short times and correspondingly more at long times than the case of fast kinetics. This is a result of the finite kinetics preventing the instantaneous reduction (oxidation) of all A at the electrode surface. These observations are in complete agreement with the work of Harland [207], who using the explicit finite–difference/Hale transformation approach, included a heterogeneous kinetic step into the "reverse" transient. This theory was shown to be entirely consistent with experimental results and thus a definitive mechanism for the reduction of bromine at polycrystalline platinum electrodes was proposed, whereby the electrode reaction is preceded by the adsorption of bromine; this step was shown to be first order with a heterogeneous rate constant of approximately $200s^{-1}$.

The "reverse" transients calculated here use the same boundary conditions as those calculated for the "no kinetics" case and are hence indistinguishable from those in Figure 3.3. The mathematical relationship between the "forward" and "reverse" transients discussed in section 3.1.6.2 however will no longer be valid, except for very fast kinetics ($k' > 5000cms^{-1}$).

3.1.7 Summary

In summary, the explicit finite–difference/Hale transformation approach provides a computationally economical method for calculating both transient and steady–state RDE phenomena. Where comparison is possible, agreement with existing theory is excellent. The inclusion of homogeneous and heterogeneous coupled kinetics is uncomplicated and the method can also be easily extended to satisfactorily take account of reactions which involve species with appreciably different diffusion coefficients. This has previously proved to be difficult [241]. For the EC' and related mechanisms, steady–state measurements in isolation have been shown to discriminate between the variants of the main mechanistic theme.

The only apparent limitation of this approach is that when the rate of coupled reactions rises, the computing time required for the simulation increases markedly.

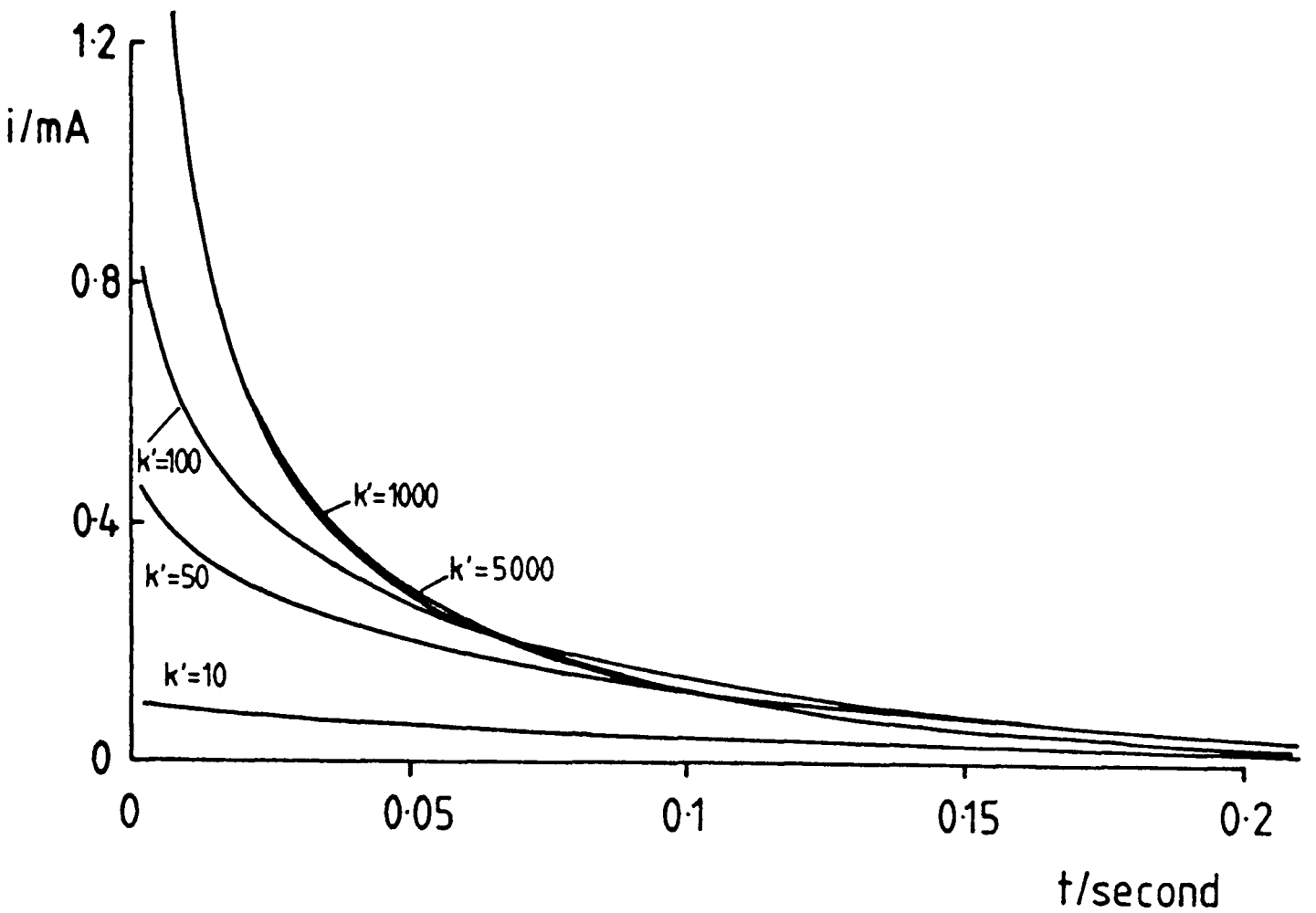


Figure 3.11: Computed "forward" transients for a CE process in which the chemical step is heterogeneous. The effect of first–order heterogeneous kinetics with rate constants k' = 10, 50, 100, 1000 and 5000 cm s^{-1} are illustrated. The parameters used were W = 9.0Hz, D_A = 9.4×10^{-6} cm^2s^{-1}, D_B = 1.82×10^{-5} cm^2s^{-1} and $[A]_\infty$ = 2.86×10^{-3} $moldm^{-3}$.

However, problems in simulating fast electrode reaction mechanisms are not confined to explicit methods, but are also associated with implicit methods and OC. Despite this, the computer time required to perform the necessary calculations here was not prohibitive for either heterogeneous or homogeneous processes. Additionally, the success of this approach is illustrated by its application to the study of a wide range of RDE problems in the current literature [201,207,241–243,272,277].

3.2 The Channel Electrode

The channel electrode has been recently developed into a popular and powerful hydrodynamic electrode, both for analytical purposes and for the mechanistic investigation of electrode reactions which involve coupled homogeneous kinetics [186,215,278]. A full description of a typical channel cell, together with the appropriate coordinate system was given in sections 2.3.3 and 2.3.4, where it was shown that, in the absence of any kinetic complications and in the presence of sufficient supporting electrolyte to suppress migration, mass transport to the electrode is given by the following time dependent convective–diffusion equation:

$$A + ne^- \rightleftharpoons B$$

$$\frac{\partial[A]}{\partial t} = D_A \frac{\partial^2[A]}{\partial z^2} - v_x \frac{\partial[A]}{\partial x} \qquad 3.51$$

The velocity profile in the x direction, v_x, is parabolic provided that the flow is laminar and fully developed [161]; i.e. the lead–in criterion [162] given in equation 2.61 is obeyed. Then quantitatively:

$$v_x = v_0 [1 - (z'/h)^2] \qquad 3.52$$

which, as discussed in section 2.3.4, assumes that the width of the electrode, w_e, is

sufficiently less than the width of the channel, d, for edge effects to be negligible, that h << d and that diffusion in directions other than normal to the electrode surface can be ignored. These approximations were shown to be valid for practical electrodes [169].

Two approaches to the solution of the problem stated by equations 3.51 and 3.52 have been adopted. The first proceeds by invoking the Lévêque approximation [163] which linearises the parabolic velocity profile near the electrode surface:

$$v_x \approx 2v_0 [1 - (z'/h)] = 2v_0 z/h \qquad 3.53$$

The solution then proceeds analytically [139,164,185,279–281] or numerically [169] and a considerable variety of channel electrode problems have been solved by this method. However, solutions only apply to electrodes of certain geometries and to flow rates constrained within certain bounds, so that the concentration changes induced by the electrode are confined to be close to its surface and are thus located in a region of space where equation 3.53 is a reasonable approximation. Despite these limitations, the method has been shown to be amenable to the inclusion of coupled homogeneous kinetics [279] and the resulting theory used to explore the subtlest of differences between similar mechanisms [189,217,282].

Alternatively, Anderson [283–289] has tackled various steady–state, kinetically uncomplicated, channel electrode problems by retaining the full parabolic term in equation 3.51. This dictates the adoption of numerical methods, and the suitability of the explicit (forward difference), Crank–Nicholson (central difference) and implicit (backward difference) finite–difference methods have been investigated for the calculation of the transport–limited current resulting from a simple electron transfer at a channel electrode [283].

These two approaches to the solution of equations 3.51 and 3.52 will therefore now considered in greater detail and applied to problems relevant to this thesis by extending the theories to include coupled homogeneous (EC') kinetics.

3.2.1 The Solution of the Mass Transport Equation to the Channel Electrode via the Lévêque Approximation

In addition to approximating the parabolic velocity profile in the region of the electrode as linear, a further simplification in respect to equation 3.51 has been adopted by Singh and Dutt [290]. This involves replacing the concentration gradient in the x direction by its so–called "average value" [290], so that for the electrode process:

$$A + ne^- \rightleftharpoons B$$

it is possible to write:

$$\frac{\partial[A]}{\partial x} = \left[\frac{[A] - [A]_\infty}{x_e}\right] \qquad 3.54$$

and

$$\frac{\partial[B]}{\partial x} = \frac{[B]}{x_e} \qquad 3.55$$

This reduces equation 3.51 to an ordinary differential equation (in x) and various time–dependent phenomena have already been deduced from the latter since the introduction of this approximation facilitates the use of straightforward analytical methods [291–294]. However, the question arises as to whether the approach has a sound physical basis since it approximates the channel electrode to a uniformly accessible electrode, i.e. one with a uniform diffusion layer thickness across the whole of the electrode surface. With this in mind, the method has been thoroughly assessed by comparison with existing rigorous theory, both at the level of the Lévêque approximation [281,282,295] and using the full parabolic description of equation 3.51 [160]. Agreement was found to be very good for both steady–state and time–dependent problems by Compton *et al* [282] who "presented a sufficiently broad number of successful examples of the application of the Singh and Dutt approximation so as to encourage its adoption in the theoretical description of convective–diffusion problems at the channel (and tubular) electrodes". This

approach was shown to "work best when the concentrations in the vicinity of the electrode are not too different from the concentration averaged over the length of the electrode" [282] and the applicability of these (Lévêque and Singh and Dutt) approximations to solving channel electrode problems, under such conditions, can therefore be concluded.

This approach will now be demonstrated for the calculation of the transport–limited current/flow rate behaviour at a channel electrode for the particular case of an EC'preeqm mechanism. The mass transport within a channel cell for the species involved in this electrode reaction can be described by the following time dependent convective–diffusion equations:

$$\frac{\partial[A]}{\partial t} = D\frac{\partial^2[A]}{\partial z^2} - v_x\frac{\partial[A]}{\partial x} + k_v K_{iv}\frac{[B]\ [Y]}{[A]} \qquad 3.56$$

$$\frac{\partial[B]}{\partial t} = D\frac{\partial^2[B]}{\partial z^2} - v_x\frac{\partial[B]}{\partial x} - k_v K_{iv}\frac{[B]\ [Y]}{[A]} \qquad 3.57$$

$$\frac{\partial[Y]}{\partial t} = D\frac{\partial^2[Y]}{\partial z^2} - v_x\frac{\partial[Y]}{\partial x} - k_v K_{iv}\frac{[B]\ [Y]}{[A]} \qquad 3.58$$

upon applying the Lévêque approximation [163] and using the following variables, equations 3.56, 3.57 and 3.58 may be normalised:

$$\chi = x\ /\ x_e \qquad 3.59$$

$$\epsilon = (3\bar{U}/hDx_e)^{1/3}\ z \qquad 3.60$$

$$\tau = (9\bar{U}^2D/x_e^2h^2)^{1/3}\ t \qquad 3.61$$

$$a = [A]/[A]_\infty \quad b = [B]/[B]_\infty \quad y = [Y]/[Y]_\infty \qquad 3.62$$

$$k'_{pe} = k_v K_{iv}\,([Y]_\infty/[A]_\infty)\,(h^2x_e^2/9\bar{U}^2D)^{1/3} \qquad 3.63$$

where $\bar{U} = {}^2/_3 v_0$, i.e. the mean solution velocity.

The resulting equations are:

$$\frac{\partial a}{\partial \tau} = \frac{\partial^2 a}{\partial \epsilon^2} - \epsilon \frac{\partial a}{\partial \chi} + k'_{pe} \frac{ba}{y} \qquad 3.64$$

$$\frac{\partial b}{\partial \tau} = \frac{\partial^2 b}{\partial \epsilon^2} - \epsilon \frac{\partial b}{\partial \chi} - k'_{pe} \frac{ba}{y} \qquad 3.65$$

$$\frac{\partial y}{\partial \tau} = \frac{\partial^2 y}{\partial \epsilon^2} - \epsilon \frac{\partial y}{\partial \chi} - k'_{pe} \frac{ba}{y} \frac{[A]_\infty}{[Y]_\infty} \qquad 3.66$$

The concentration gradients in the x–direction are now replaced by their average values using the Singh and Dutt approximation given by equations 3.54 and 3.55 so that:

$$\frac{\partial a}{\partial \chi} = a - 1, \quad \frac{\partial b}{\partial \chi} = b, \quad \frac{\partial y}{\partial \chi} = y - 1 \qquad 3.67$$

The problem is therefore reduced to one dimension with respect ϵ, enabling the concentration profiles of all three species to be calculated using a straightforward numerical technique. Thus distance (in ϵ space) between the electrode surface and the opposite channel wall is divided into N grid points, the distance between each point given by:

$$\epsilon_{wall}/(N-1) = [3\bar{U}/hDx_e]^{1/3} [2h/(N-1)] \qquad 3.68$$

Likewise, increments of normalised time are considered, where $\partial\tau = 1/M$, so that the concentration at the nth point at a time $\tau = m/M$ is represented by c (n,m). The steady–state concentrations of the various species are then obtained by replacing the coupled differential equations $(3.64 - 3.66)$, with their finite difference equivalents. Computing their evolution in time, after a potential step (at $\tau = 0$) from a potential at which no current flows to one corresponding to the transport–limited current, yields the required steady–state profiles.

The appropriate initial and boundary conditions are:

$$m = 0 \qquad a\,(n,0) = 1 \qquad b\,(n,0) = 0 \qquad y\,(n,0) = 1 \qquad 3.69\ \text{i}$$

$$\text{for } n = 1,2,3,\ldots,N$$

$$m > 0 \qquad a\,(1,m) = 0 \qquad b\,(1,m) = 1 \qquad y\,(1,m) = y\,(2,m) \qquad \text{ii}$$

$$b\,(2,m) = 1 - a\,(2,m) \qquad a\,(N-1,m) = a\,(N,m) = 1 \qquad \text{iii}$$

$$b\,(N-1,m) = b\,(N,m) = 0 \qquad y\,(N-1,m) = y\,(N,m) = 1 \qquad \text{iv}$$

The conditions for $m = 0$ correspond to the unperturbed concentrations prevailing through all space before the step. The first three conditions for $m > 0$ express the fact the the flux of [A] to the electrode is transport–limited and the flux of [Y] through the electrode must, by Fick's First Law be zero. The next boundary condition matches the flux of [A] to the electrode to [B] leaving it and finally the last three conditions indicate zero flux of all species through the wall of the channel opposite the electrode. In all calculations, for the parameters chosen, the concentration at these points ($n = N-1, N$) were found to be indistinguishable from the "bulk" values and this is crucial to the success of the method. Therefore the concentrations at these two points have been put equal to their bulk values in the boundary conditions above.

The evolution of the three concentration profiles may be computed from the following:

$$h\,(n,m+1) = h\,(n,m) + \Delta h\,(n,m) \qquad 3.70$$

$$\text{and} \quad \Delta h\,(n,m) = M^{-1}\Big[\{D_H[h\,(n-1,m) - 2h\,(n,m) + h\,(n+1,m)]/[\epsilon_{wall}/N]^2\} - \{n\,\epsilon_{wall} Z/N\} + \{k'_{pe} b\,(n,m)\,y\,(n,m)\,H/a\,(n,m)\}\Big] \qquad 3.71$$

where for:

$$h = a \qquad Z = a\,(j,m) - 1 \qquad \text{and} \quad H = 1 \qquad 3.72\ \text{i}$$

$$h = b \qquad Z = b\ (j,m) \qquad \text{and} \qquad H = -1 \qquad \text{ii}$$

$$h = y \qquad Z = y\ (j,m) - 1 \qquad \text{and} \qquad H = -[A]_{\infty}/[Y]_{\infty} \qquad \text{iii}$$

Typical values required for convergence (to 0.1%) of this data and for evolution to steady–state were $N = 201$, $d\tau = 0.0001$ and $m = 70{,}000$. The FORTRAN program used to solve equations 3.70–3.72 and thus calculate this data is given in Appendix 4e.

In this thesis, the theory presented above is used to model the theoretical ESR signal (S) – current – flow rate (V_f) behaviour for an EC'preeqm mechanism under transport–limited conditions at the ESR in–situ channel cell. The ESR signal, due to [B] can be found by summing b (n,m) from n = 1 to 201 and the current assessed from the quantity a(1,m) – a(2,m). In each case the quantity was normalised relative to the respective value obtained for the "no kinetics" case, i.e. $k'_{pe} = 0$. The behaviour of S and i upon flow rate (through it influencing ϵ_{wall}) and $[A]_{\infty}/[Y]_{\infty}$ was thus determined. Figure 3.12 shows that a theoretical plot of ln (S/i) against ln (V_f) obtained this way gives the predicted slope, for a stable radical of –2/3 [219,296,297].

3.2.2. The Solution of Mass Transport to the Channel Electrode using the Backwards Implicit Method

In solving the problem of mass transport to the channel electrode, by retaining the full parabolic nature of equation 3.52, Anderson was forced to use numerical methods [283,284,298]. In particular, the backwards implicit finite–difference (BIFD) method was found to be optimal [283]. The method is economical in computer time since, whereas alternative methods involve matrix calculations based on a two–dimensional grid representing the (x,z) space, the BIFD method only involves vector calculations [283]. The calculation proceeds "downstream", each vector enabling the calculation of the next, starting from the vector defining the boundary conditions specified for upstream of the electrode. In addition, computation is independent of the value at the upstream edge of the electrode, (0,0), which can otherwise be problematic, since a definition of this point as either

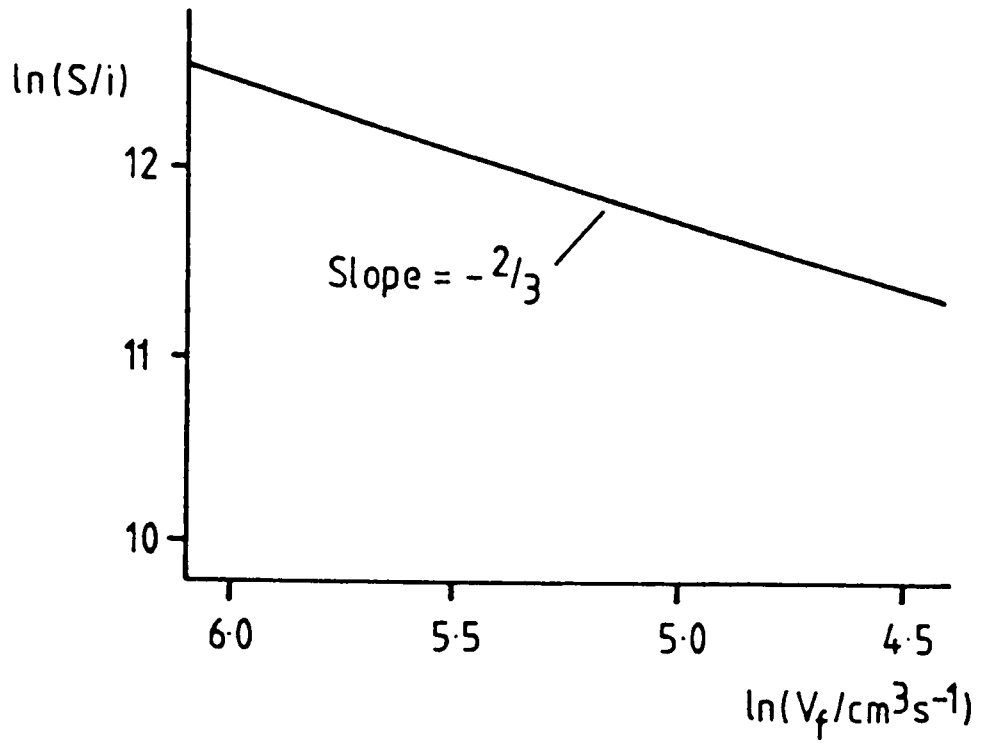


Figure 3.12: Theoretical plot of ln (S/i) (arbitrary units) versus ln (V_f) calculated using the Singh and Dutt approximation and revealing the expected slope, for a stable radical, of $-2/3$.

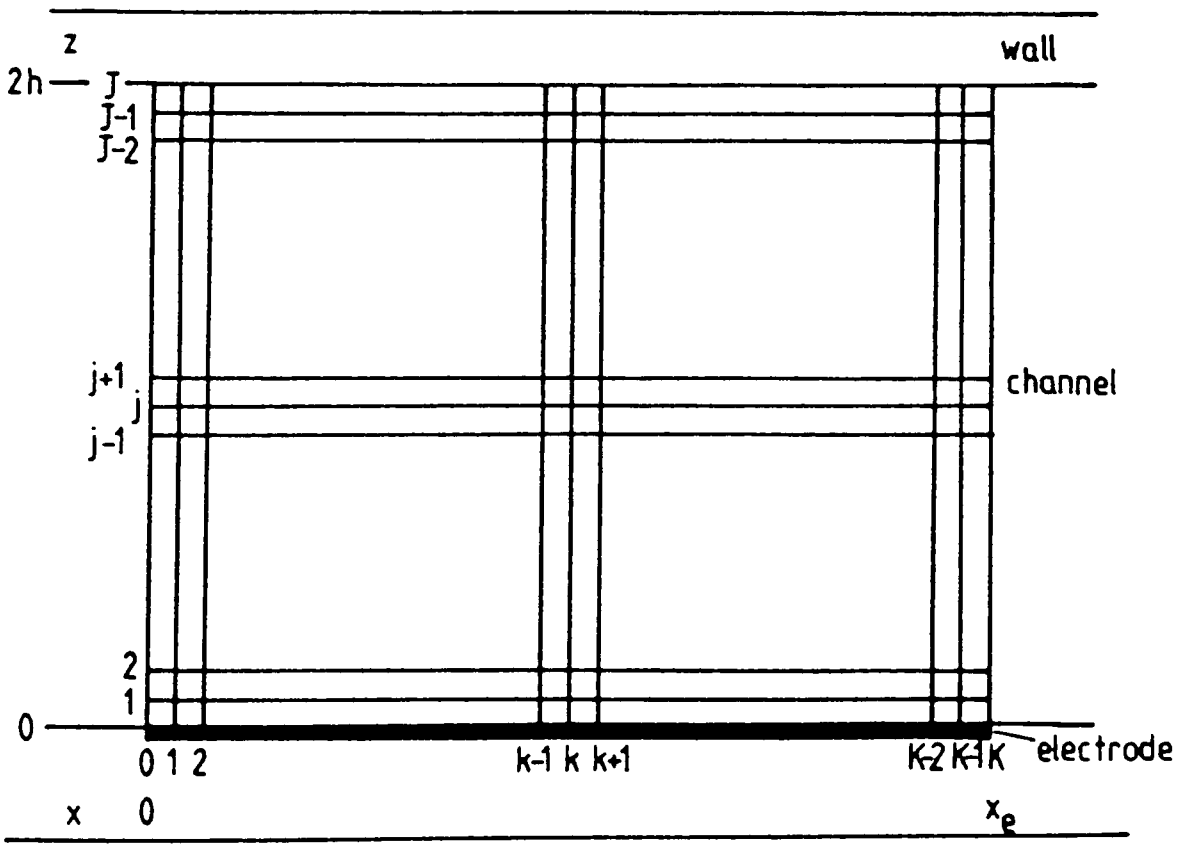


Figure 3.13: The finite difference grid.

wall or electrode is necessary. Consider, for example, the calculation of a transport–limited current; if (0,0) is electrode, then the concentration at this point must be zero, corresponding to complete conversion of electroactive material arriving at the electrode. If however (0,0) is "upstream" wall then the concentration must be the bulk upstream value so that the flux of electroactive material through the channel wall is zero. Alternative numerical strategies to the BIFD method such as the explicit finite–difference and Crank–Nicholson methods may give answers which are dependent on this choice and can therefore be regarded as less satisfactory [283]. Other problems associated with these methods, such as the stability criterion [257,258] imposed by the explicit finite–difference method and the more complicated programming required to implement the Crank–Nicholson approach [283] also indicate that the BIFD method should be favoured to solve channel electrode problems.

3.2.2.1 *The Solution for a One Electron Transfer*

The BIFD method, investigated by Anderson and Moldoveanu [283–289,298] for the calculation of the transport–limited current arising from a simple electron transfer at a channel electrode, will be demonstrated here. Consider the electron transfer:

$$A + ne^- \rightleftharpoons B$$

then the steady–state convective–diffusion equation for A is:

$$D_A \frac{\partial^2[A]}{\partial z^2} = v_0(1 - (z'/h)^2)\frac{\partial[A]}{\partial x} \qquad 3.73$$

The basis of the BIFD method involves setting up a finite difference grid over the region of interest, the x–z plane in the vicinity of the electrode, as shown in Figure 3.13. Increments in the x–direction are Δx and in the z–direction Δz. Then:

$$z_j = j\Delta z \qquad j = 0,1,\ldots,J \qquad \text{where } \Delta z = 2h/J \qquad 3.74$$

$$x_k = k\Delta x \qquad k = 0,1,\ldots,K \qquad \text{where } \Delta x = x_e/K \qquad 3.75$$

The derivatives in equation 3.73 are replaced by their finite difference equivalents:

$$\frac{\partial g^A}{\partial x} = \frac{g^A{}_{j,k+1} - g^A{}_{j,k}}{\Delta x} \qquad 3.76$$

and

$$\frac{\partial^2 g^A}{\partial z^2} = \frac{g^A{}_{j-1,k+1} - 2g^A{}_{j,k+1} + g^A{}_{j+1,k+1}}{(\Delta z)^2} \qquad 3.77$$

where $g^A = [A]/[A]_\infty$.

Substitution of equations 3.76 and 3.77 into equation 3.73 gives:

$$\left[\frac{D}{(\Delta z)^2}\right](g^A{}_{j-1,k+1} - 2g^A{}_{j,k+1} + g^A{}_{j+1,k+1}) = (g^A{}_{j,k+1} - g^A{}_{j,k})\left[\frac{D}{\lambda_j(\Delta z)^2}\right] \qquad 3.78$$

where

$$\lambda_j = \frac{D\Delta x \;\; (2h)^3 d}{6V_f \, j\,(\Delta z)^3(2h - j\Delta z)} \qquad 3.79$$

and V_f is the average volume flow rate. The appropriate initial and boundary conditions for the calculation of the transport–limited current are:

$x = 0$	$[A] = [A]_\infty$	$g^A{}_{j,0} = 1$	3.80 i
$z = 0$	$[A] = 0$	$g^A{}_{0,k} = 0$	ii
$z = 2h$	$\frac{\partial [A]}{\partial z} = 0$	$g^A{}_{J,k} = g^A{}_{J-1,k}$	iii

Here, the boundary condition iii stipulates that the flux of electroactive material through the "far " wall of the channel is zero. Thus:

$$g^{A}_{1,k} = (2\lambda_1 + 1)g^{A}_{1,k+1} - \lambda_1 g^{A}_{2,k+1} \qquad 3.81$$

$$g^{A}_{j,k} = -\lambda_j g^{A}_{j-1,k+1} + (2\lambda_j + 1)g^{A}_{j,k+1} - \lambda_j g^{A}_{j+1,k+1} \quad j = 2,3,\ldots, J-2 \qquad 3.82$$

$$g^{A}_{J-1,k} = -\lambda_{J-1} g^{A}_{J-2,k+1} + (\lambda_{J-1} + 1)g^{A}_{J-1,k+1} \qquad 3.83$$

These (J–1) simultaneous equations may be expressed as a (J–1) x (J–1) tridiagonal matrix equation:

$$\{d\} = [T]\{u\} \qquad 3.84$$

i.e.

$$\begin{bmatrix} d_1 \\ d_2 \\ . \\ . \\ . \\ d_j \\ . \\ . \\ . \\ d_{J-2} \\ d_{J-1} \end{bmatrix} = \begin{bmatrix} b_1 & c_1 & 0 & & & & & \\ a_2 & b_2 & c_2 & 0 & & & & \\ . & . & . & & & & & \\ & . & . & . & & & & \\ & & . & . & . & & & \\ 0 & & a_j & b_j & c_j & 0 & & \\ & & & . & . & . & & \\ & & & & . & . & . & \\ & & & & & a_{J-2} & b_{J-2} & c_{J-2} \\ & & & & & 0 & a_{J-1} & b_{J-1} \end{bmatrix} \begin{bmatrix} u_1 \\ u_2 \\ . \\ . \\ . \\ u_j \\ . \\ . \\ . \\ u_{J-2} \\ u_{J-1} \end{bmatrix}$$

where

$$d_j = g^{A}_{j,k} \qquad j = 1,2,\ldots,J-1 \qquad 3.85$$

$$u_j = g^{A}_{j,k+1} \qquad j = 1,2,\ldots,J-1 \qquad 3.86$$

$$a_j = -\lambda_j \qquad j = 2,3,\ldots,J-1 \qquad 3.87$$

$$b_j = (2\lambda_j + 1) \qquad j = 1,2,\ldots,J-2 \qquad 3.88$$

$$b_{J-1} = \lambda_{J-1} + 1 \qquad 3.89$$

$$c_j = -\lambda_j \qquad j = 1,2\ldots,J-2 \qquad 3.90$$

The tridiagonal form of the matrix [T] enables the vector $\{u\}_k$ to be found from the known vector $\{d\}_k$ using the Thomas Algorithm (see Appendix Six) [299,300]. The boundary condition given in equation 3.80 i supplies the vector $\{d\}_{k=0}$ from which $\{u\}_{k=0}$ is calculated. This in turn is equal to the new vector $\{d\}_{k=1}$ which is used to calculate $\{u\}_{k=1}$. This then proceeds "down" the electrode until $\{u\}_K$ is obtained. Thus all the values $g^{A}_{j,k}$ (j = 1,2,..., J–1, k = 1,2,...,K) are evaluated. The expression for the transport–limited current at the electrode, i_{lim}, takes the

form:

$$i_{lim} = w_e F D_A [A]_\infty \sum_{k=1}^{K} \left[\frac{g^A{}_{1,k} - g^A{}_{0,k}}{\Delta z} \right] \Delta x \qquad 3.91$$

but since the boundary condition as given in equation 3.80 ii shows, $g^A{}_{0,k} = 0$, this expression becomes:

$$i_{lim} = w_e F D_A [A]_\infty \frac{\Delta x}{\Delta z} \sum_{k=1}^{K} g^A{}_{1,k} \qquad 3.92$$

The FORTRAN given program in Appendix 4f was written to solve these equations (equations 3.84–3.92) and calculate the transport–limited current at the channel electrode. Convergence was examined by varying J and K. For a typical channel cell i.e. a 4mm by 4mm square electrode located in a duct 6mm wide by 0.4mm deep, then the highest values of J and K will result from the fastest flow rates employed (since the average diffusion layer will be thinner necessitating a finer grid in the z direction). However, for the fastest flow rates considered ($3x10^{-1}cm^3s^{-1}$), a grid of J = 200 and K = 500 was found to give convergence to 0.1%. Using these values, results obtained for the flow rate and electrode geometry dependence of the transport–limited current were identical to those reported by Anderson [283].

In addition to using this approach for calculating the transport–limited current at macro electrodes [283,284], the BIFD method has been extensively applied to micro electrode arrays [285–288]. However, as it stands, it is only applicable to a simple E process. The extension of the theory to consider channel electrode reactions which include coupled homogeneous kinetics will therefore be presented in the following section.

3.2.2.2 *The Inclusion of Coupled Homogeneous Kinetics*

Compton *et al* [193] recently illustrated how the BIFD method can be applied to the theoretical description of channel electrode processes involving heterogeneous electron transfers coupled with homogeneous kinetics. Specifically, the EC, ECE,

DISP1 and DISP2 mechanisms were examined and it was shown how both the limiting current and full current–voltage characteristics associated with these reactions are calculated. This approach will be extended here to enable the calculation of the transport–limited current/flow rate behaviour for an EC' reaction at a channel electrode.

When electrode reaction mechanisms involving more than one species are examined, then the necessary modifications to the theory presented in section 3.2.2.1 need consideration. The appropriate steady–state convective–diffusion equations for the various EC' mechanisms discussed in section 3.1.4 are:

$$0 = D_A \frac{\partial^2[A]}{\partial z^2} - v_x \frac{\partial[A]}{\partial x} + k_{mech}\, p_{mech} \qquad 3.93$$

$$0 = D_B \frac{\partial^2[B]}{\partial z^2} - v_x \frac{\partial[B]}{\partial x} - k_{mech}\, p_{mech} \qquad 3.94$$

$$0 = D_Y \frac{\partial^2[Y]}{\partial z^2} - v_x \frac{\partial[Y]}{\partial x} - k_{mech}\, p_{mech} \qquad 3.95$$

and normalisation of the concentration gives:

$$0 = D_A \frac{\partial^2 g^A}{\partial z^2} - v_x \frac{\partial g^A}{\partial x} + k_{mech}\, p_A q_A \qquad 3.96$$

$$0 = D_B \frac{\partial^2 g^B}{\partial z^2} - v_x \frac{\partial g^B}{\partial x} - k_{mech}\, p_B q_B \qquad 3.97$$

$$0 = D_Y \frac{\partial^2 g^Y}{\partial z^2} - v_x \frac{\partial g^Y}{\partial x} - k_{mech}\, p_Y q_Y \qquad 3.98$$

where k_{mech}, p_{mech}, p and q are defined in Table 3.3.

Concentrations of each species, H, present along a finite difference grid parallel to the z axis are described by vectors $\{u\}_k^H$. Adjacent vectors $\{u\}_k^H$ and $\{u\}_{k+1}^H$ are related by a set of (J–1) simultaneous equations. These are obtained for each species

Table 3.3: The definitions of k_{mech}, p_{mech}, p and q appropriate for equations 3.93–3.98.

MECHANISM	k_{mech}	p_{mech}	$p_a^{\ddagger}$	p_y	$q_a^{\ddagger}$	q_y
EC'pure	k_{ii}	$[Y][B]$	yb	yb	$[Y]_\infty$	$[A]_\infty$
EC'preeqm	$K_{iv}k_v$	$\frac{[Y][B]}{[A]}$	$\frac{yb}{a}$	$\frac{yb}{a}$	$\frac{[Y]_\infty}{[A]_\infty}$	1
EC'dispA1	$K_{vii}k_{viii}$	$\frac{2[B]^2[Y]}{[A]}$	$\frac{2b^2y}{a}$	$\frac{b^2y}{a}$	$[Y]_\infty$	$[A]_\infty$
EC'dispA2	k_{vii}	$2[B]^2$	$2b^2$	*	$[A]_\infty$	*
EC'dispB1	$K_{vii}k_{ix}$	$\frac{[B]^2[Y]}{[A]}$	$\frac{b^2y}{a}$	$\frac{b^2y}{a}$	$[Y]_\infty$	$[A]_\infty$
EC'dispB2	k_{vii}	$[B]^2$	b^2	*	$[A]_\infty$	*

* y concentration profile not required for this calculation.

‡ $p_a = p_b$, $q_a = q_b$

present from the appropriate convective–diffusion equations, using the approximations in equations 3.76 and 3.77.

In all cases, the (J–1) simultaneous equations can be expressed by the matrix equation:

$$\{d\}^H = [T]^H \{u\}^H$$

where, once again, $[T]^H$ is the tridiagonal matrix described by equation 3.84.

For all of the EC' reaction nuances:

$$g^H = [H]/[H]_\infty \qquad 3.99$$

$$u_j^H = g_{j,k+1}^H \qquad j = 1,2,...,J-1 \qquad 3.100$$

$$a_j^H = -\lambda_j^H \qquad j = 2,3,...,J-1 \qquad 3.101$$

$$b_j^H = (2\lambda_j^H + 1) \qquad j = 2,3,...,J-2 \qquad 3.102$$

$$b_{J-1}^H = \lambda_{J-1}^H + 1 \qquad 3.103$$

$$c_j^H = -\lambda_j^H \qquad j = 1,2,...,J-2 \qquad 3.104$$

where

$$\lambda_j^H = \frac{D_H \, \Delta x \, (2h)^3 d}{6V_f \, j(\Delta z)^3(2h - j\Delta z)} \qquad 3.105$$

The boundary conditions relevant to the evaluation of the effective number of electrons transferred under transport–limited conditions are:

$$x = 0 \qquad g^A = 1 \qquad g^B = 0 \qquad g^Y = 1 \qquad \text{3.106 i}$$

$$z = 0 \qquad g^A = 0 \qquad \frac{\partial g^B}{\partial z} = -\frac{\partial g^A}{\partial z} \qquad \frac{\partial g^A}{\partial z} = 0 \qquad \text{ii}$$

$$z = 2h \qquad \frac{\partial g^A}{\partial z} = 0 \qquad \frac{\partial g^B}{\partial z} = 0 \qquad \frac{\partial g^Y}{\partial z} = 0 \qquad \text{iii}$$

These conditions result in d_j and b_1 becoming dependent on the mechanism being modelled and their appropriate values for the EC' nuances are given in Tables 3.4,

Table 3.4: The values of d_1 for the EC' mechanisms.

MECHANISM	H	d_1
EC'pure	A	$g^{A}_{1,k} + (D_A^{-1}(\Delta z)^2 \lambda_1^A k_{ii} g^{B}_{1,k} g^{Y}_{1,k} [Y]_\infty)$
	B	$g^{B}_{1,k} - (D_B^{-1}(\Delta z)^2 \lambda_1^B k_{ii} g^{B}_{1,k} g^{Y}_{1,k} [Y]_\infty) + \lambda_1^B g^{A}_{1,k+1}$
	Y	$g^{Y}_{1,k} - (D_Y^{-1}(\Delta z)^2 \lambda_1^Y k_{ii} g^{B}_{1,k} g^{Y}_{1,k} [A]_\infty)$
EC'preeqm	A	$g^{A}_{1,k} + (D_A^{-1}(\Delta z)^2 \lambda_1^A k_v K_{iv} \left[\frac{g^{B}_{1,k} g^{Y}_{1,k}}{g^{A}_{1,k}}\right] \frac{[Y]}{[A]_\infty})$
	B	$g^{B}_{1,k} - (D_B^{-1}(\Delta z)^2 \lambda_1^B k_v K_{iv} \left[\frac{g^{B}_{1,k} g^{Y}_{1,k}}{g^{A}_{1,k}}\right] \frac{[Y]}{[A]_\infty}) + \lambda_1^B g^{A}_{1,k+1}$
	Y	$g^{Y}_{1,k} - (D_Y^{-1}(\Delta z)^2 \lambda_1^Y k_v K_{iv} \left[\frac{g^{B}_{1,k} g^{Y}_{1,k}}{g^{A}_{1,k}}\right])$
EC'dispA1	A	$g^{A}_{1,k} + (D_A^{-1}(\Delta z)^2 \lambda_1^A k_{viii} K_{vii} \left[\frac{2(g^{B}_{1,k})^2 g^{Y}_{1,k}}{g^{A}_{1,k}}\right] [Y]_\infty)$
	B	$g^{B}_{1,k} - (D_B^{-1}(\Delta z)^2 \lambda_1^B k_{viii} K_{vii} \left[\frac{2(g^{B}_{1,k})^2 g^{Y}_{1,k}}{g^{A}_{1,k}}\right] [Y]_\infty) + \lambda_1^B g^{A}_{1,k+1}$
	Y	$g^{Y}_{1,k} - (D_Y^{-1}(\Delta z)^2 \lambda_1^Y k_{viii} K_{vii} \left[\frac{2(g^{B}_{1,k})^2 g^{Y}_{1,k}}{g^{A}_{1,k}}\right] [A]_\infty)$

Table 3.5: The values of d_j for the EC' mechanisms.

MECHANISM	H	d_j (j = 2,3,...,J−1)
EC'pure	A	$g^{A}_{j,k} + (D_A^{-1}(\Delta z)^2 \lambda^{A}_{j} k_{ii} g^{B}_{j,k} g^{Y}_{j,k} [Y]_\infty)$
	B	$g^{B}_{j,k} - (D_B^{-1}(\Delta z)^2 \lambda^{B}_{j} k_{ii} g^{B}_{j,k} g^{Y}_{j,k} [Y]_\infty)$
	Y	$g^{Y}_{j,k} - (D_Y^{-1}(\Delta z)^2 \lambda^{Y}_{j} k_{ii} g^{B}_{j,k} g^{Y}_{j,k} [A]_\infty)$
EC'preeqm	A	$g^{A}_{j,k} + (D_A^{-1}(\Delta z)^2 \lambda^{A}_{j} k_v K_{iv} \left[\frac{g^{B}_{j,k} g^{Y}_{j,k}}{g^{A}_{j,k}}\right] \frac{[Y]}{[A]_\infty})$
	B	$g^{B}_{j,k} - (D_B^{-1}(\Delta z)^2 \lambda^{B}_{j} k_v K_{iv} \left[\frac{g^{B}_{j,k} g^{Y}_{j,k}}{g^{A}_{j,k}}\right] \frac{[Y]}{[A]_\infty})$
	Y	$g^{Y}_{j,k} - (D_Y^{-1}(\Delta z)^2 \lambda^{Y}_{j} k_v K_{iv} \left[\frac{g^{B}_{j,k} g^{Y}_{j,k}}{g^{A}_{j,k}}\right])$
EC'dispA1	A	$g^{A}_{j,k} + (D_A^{-1}(\Delta z)^2 \lambda^{A}_{j} k_{viii} K_{vii} \left[\frac{2(g^{B}_{j,k})^2 g^{Y}_{j,k}}{g^{A}_{j,k}}\right] [Y]_\infty)$
	B	$g^{B}_{j,k} - (D_B^{-1}(\Delta z)^2 \lambda^{B}_{j} k_{viii} K_{vii} \left[\frac{2(g^{B}_{j,k})^2 g^{Y}_{j,k}}{g^{A}_{j,k}}\right] [Y]_\infty)$
	Y	$g^{Y}_{j,k} - (D_Y^{-1}(\Delta z)^2 \lambda^{Y}_{j} k_{viii} K_{vii} \left[\frac{2(g^{B}_{j,k})^2 g^{Y}_{j,k}}{g^{A}_{j,k}}\right] [A]_\infty)$

3.5 and 3.6. For simplicity, these values are illustrated for the EC'pure, EC'preeqm and EC'dispA1 mechanisms only. However consideration of Table 3.3 and equations 3.81 to 3.83 means that these values are easily deducible for the other mechanisms.

Upon applying this general theory, three matrix elements result, one for each of H = A,B and Y. The matrix equation for B is dependent on $g^{A}_{j,k+1}$ because of the boundary condition 3.106 ii, so that the equations are solved for each column of the grid, in the order of A, followed by B and Y. The current is once again found using equation 3.92.

Using the program given in Appendix 4g this theory was solved, enabling the calculation of the transport–limiting current with flow rate behaviour as a function of normalised rate constant, k_{norm} [189,193,217]. The value of this latter parameter for each mechanism is given in Table 3.7. Convergence was again examined by varying J and K. The inclusion of kinetics means that the concentration gradients are steeper than in the simple one electron transfer case, and hence, accurate modelling requires the use of a finer grid, which in turn necessitates an increase in J and/or K. Over the entire range of flow rates ($3x10^{-1}$ – 10^{-3} cm^3s^{-1}) and rate constants (k_{norm} (EC'preeqm) of 0 – 120) employed, the data converged to 0.1% when J = 200 and K = 2000. Double precision calculations were employed to avoid the rounding errors which arise in single precision.

Typical working curves of n_{eff} versus k_{norm}, calculated this way, are shown in Figures 3.14 and 3.15 for the EC'pure and EC'preeqm mechanisms. The curves are sufficiently different that limiting current measurements alone are adequate to discriminate between these two mechanisms. Also shown in Figure 3.14 is the data determined analytically under the Lévêque approximation by Matsuda *et al* [185] for the case where $[Y]_{\infty} >> [A]_{\infty}$. Excellent agreement is seen. In generating these working curves, Matsuda compares the effective number of electrons transferred under transport–limited conditions to the following parameter:

$$k_{norm}(EC'pure)_{ChE} = (k_{ii}/D^{1/3})^{1/2} (hx_e/3\bar{U})^{1/3} \qquad 3.107$$

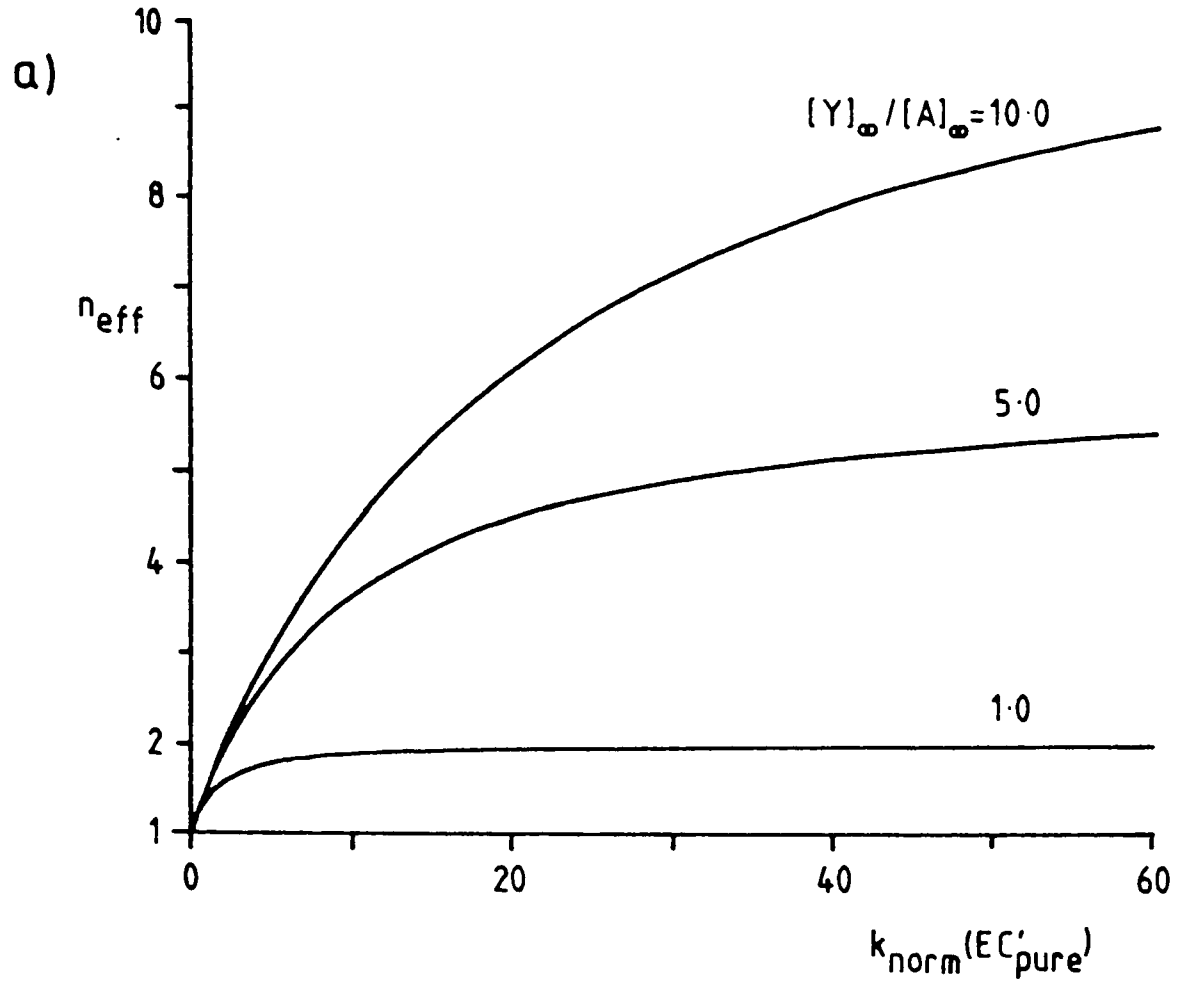
In a recent publication, Unwin [172] relates the diffusion layer thickness at the

Table 3.6: The values of b_1 for the EC' mechanisms.

MECHANISM	H	b_1
All EC'	A	$1 + 2\lambda_1^A$
mechanisms	B	$1 + \lambda_1^B$
	C	$1 + \lambda_1^Y$

Table 3.7: The appropriate normalised rate constant k_{norm} for the EC' mechanisms.

MECHANISM	k_{norm}
EC'pure	$k_{ii}\,[Y]_\infty\,(h^2x_e^2/4v_0^2D)^{1/3}$
EC'preeqm	$k_v\,K_{iv}\,[Y]_\infty/[A]_\infty\,(h^2x_e^2/4v_0^2D)^{1/3}$
EC'dispA1	$2k_{viii}\,K_{vii}\,[Y]_\infty\,(h^2x_e^2/4v_0^2D)^{1/3}$
EC'dispA2	$2k_{vii}\,[A]_\infty\,(h^2x_e^2/4v_0^2D)^{1/3}$
EC'dispB1	$k_{ix}\,K_{vii}\,[Y]_\infty\,(h^2x_e^2/4v_0^2D)^{1/3}$
EC'dispB2	$k_{vii}\,[A]_\infty\,(h^2x_e^2/4v_0^2D)^{1/3}$



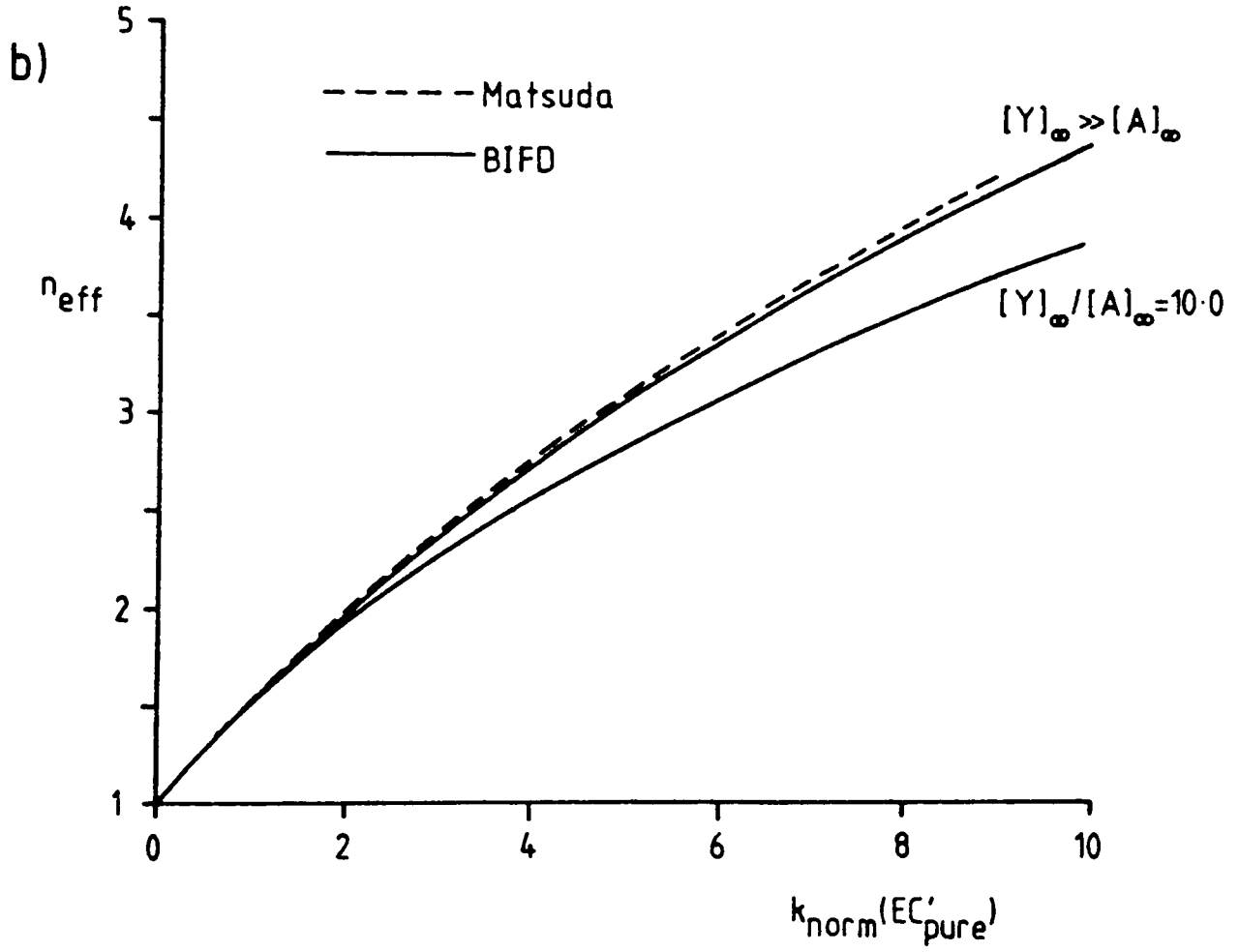


Figure 3.14: Working curves for the EC'pure mechanism calculated using the BIFD method, a) shows curves for $[Y]_\infty/[A]_\infty$ = 10.0, 5.0 and 1.0 and b) compares this data with that of Matsuda for the case where $[Y]_\infty >> [A]_\infty$.

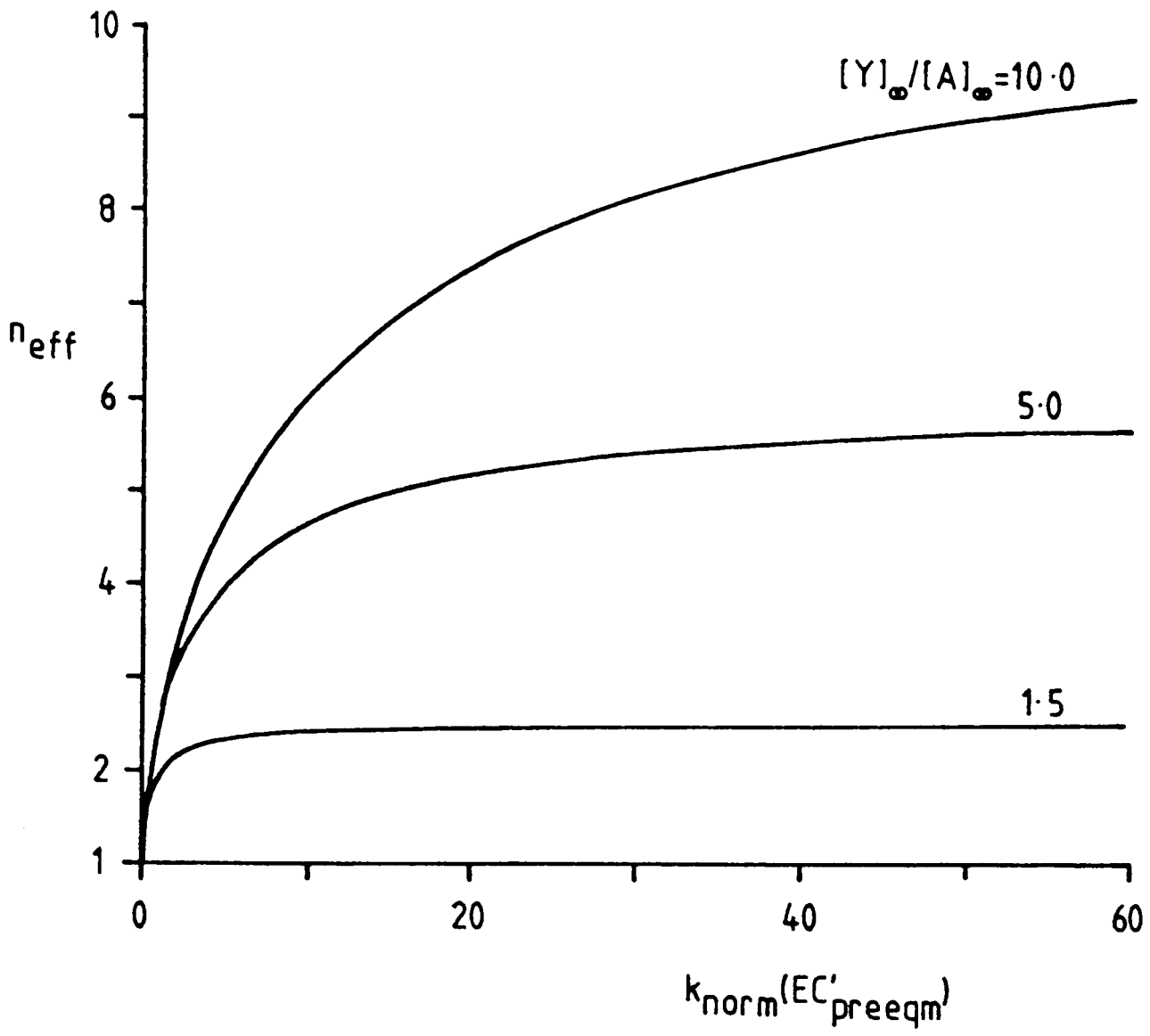


Figure 3.15: Steady–state working curves for the EC'preeqm mechanism.

RDE, δ_d, to the average diffusion layer thickness at the ChE, x_d, using the relationship:

$$\frac{x_d}{\delta_d} = \frac{0.858\ (hDx_e/\bar{U})^{1/3}}{0.643\ w^{-1/2}\nu^{1/6}D^{1/3}} = 1.0 \qquad 3.108$$

which enables the transformation of working curves deduced for one electrode into those relating to the other. Combination of equations 3.107 and 3.108 with the corresponding k_{norm} parameter at the RDE:

$$k_{norm}(EC'pure)_{RDE} = (k_{ii}/(8.032)^{2/3}w^{-1}(\nu/D)^{1/3} \qquad 3.109$$

gives:

$$k_{norm}(EC'pure)_{ChE} = \left[\frac{0.643\ x\ (8.032)^{1/3}}{0.858\ x\ 3^{1/3}}\right] (k_{norm}(EC'pure)_{RDE})^{1/2} \qquad 3.110$$

Figure 3.16 shows n_{eff} plotted against $k_{norm}(EC'pure)_{ChE}$ from the calculation of Matsuda and also using the right hand side of equation 3.110, the ChE parameter "deduced" from the RDE (calculated in section 3.1.6.3) calculation using equation 3.108. A perfect match can be observed, which not only confirms the good agreement between existing theory for the ChE (under the Lévêque approximation) and the explicit finite difference/Hale approach, but also shows that the latter is entirely consistent with the BIFD ChE theory presented here for the EC'pure mechanism.

Figure 3.17 compares the BIFD calculations with results obtained for the EC'preeqm mechanism using the Singh and Dutt approximation. When the kinetics are fast, good agreement is seen, validating the general use of this approach under such conditions.

In conclusion, it is desirable to solve channel electrode problems with as few approximations as possible and the BIFD method has been shown to be an accurate and computationally economical means of performing this. The inclusion of coupled homogeneous kinetics is relatively straightforward and data can be obtained without limitation on the electrode geometry and rate constants considered. However, the

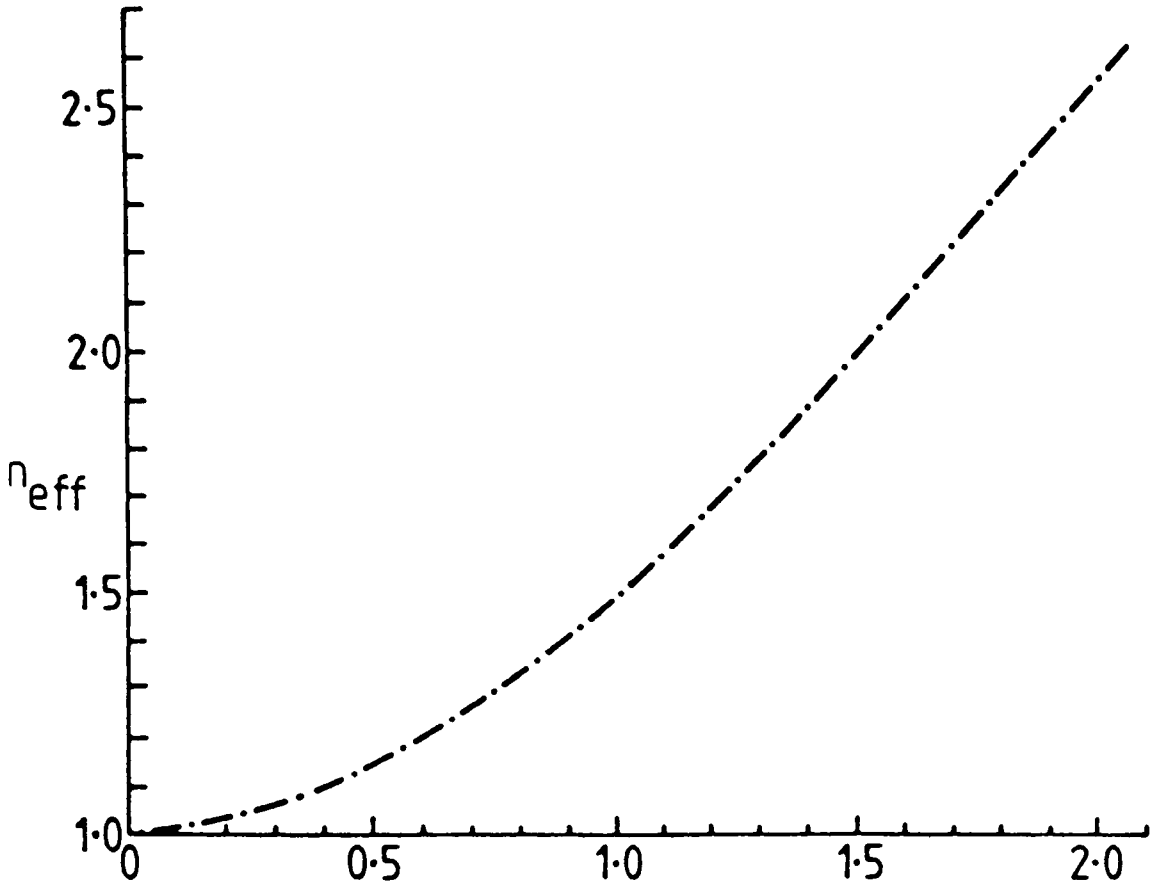


Figure 3.16: Working curve for an EC'pure mechanism ($[Y]_\infty >> [A]_\infty$) at the ChE; (– – – –) derived rigorously by Matsuda, (.....) calculated via equation 3.108 from the corresponding behaviour at the RDE, deduced in section 3.1.6.3.

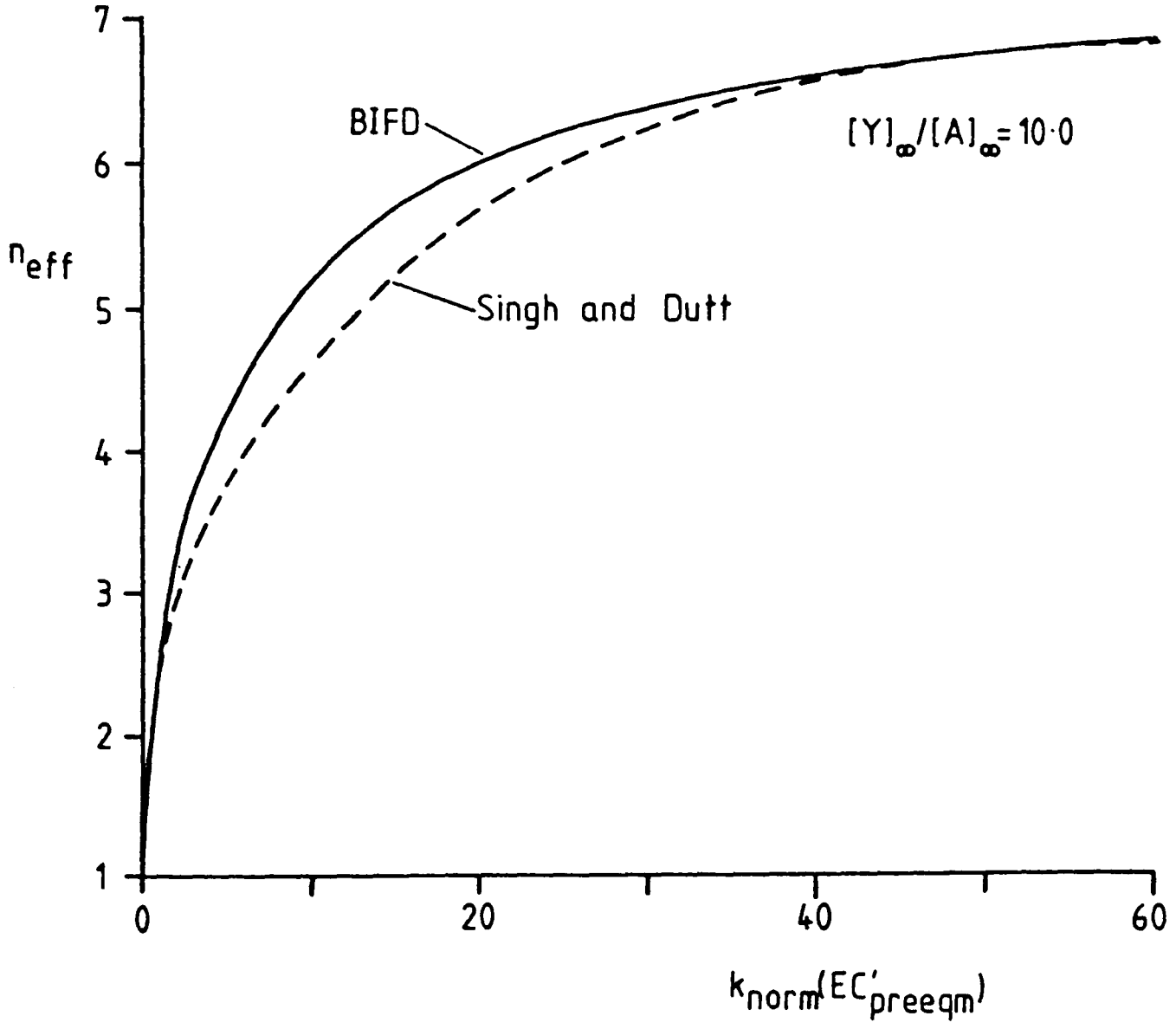


Figure 3.17: A comparison between steady–state working curves for an EC'preeqm process at the ChE calculated using the Singh and Dutt and BIFD methods.

Singh and Dutt Approximation of averaging the concentration gradient in the direction of flow is clearly attractive and, for a wide range of kinetic parameters, accurate.

CHAPTER FOUR

EXPERIMENTAL PROCEDURE

This chapter surveys the experimental techniques employed throughout this thesis. Details are given on the RDE assembly and on the design of the ChE cells and associated flow systems. The preparation of electrodes, electrochemical instrumentation and computing procedures are also described. Finally, the sources and grades of the chemicals used are provided.

4.1 The Rotating Disc Assembly

4.1.1 Electrodes

Copper, platinum and silver RDEs, each surrounded by a cylindrical teflon insulating mantle (o.d. ≈ 20mm), were obtained from Oxford Electrodes (Oxford, U.K.). These electrodes were polished to a mirror–like finish using a succession of finer (25 – 0.25μm) diamond lapping compounds ("Hyprez Sprays", Engis Ltd., Maidstone, U.K.) in conjunction with a Kent Mark II (Engis Ltd.) polishing machine. Residual polishing solvent was removed by washing the electrodes in an ultrasonic bath (Sernat Ltd., St. Albans, U.K.). Mercury plated electrodes were prepared by electroplating copper RDEs in an aqueous solution of $HgNO_3$ (0.15 $moldm^{-3}$) and KCN (0.12 $moldm^{-3}$) [301], for five minutes using a 4V battery as a potential source. The electrode surface was then washed with demineralised water before applying a tiny drop of triply distilled mercury to leave a smooth flat finish [301]. After polishing or plating, the exact dimensions of each electrode were

measured, prior to use, using a travelling microscope capable of resolving to 10^{-2}mm. The diameters of the RDEs were thus determined to be: 7.02±0.02mm (Pt), 7.29±0.02mm (Ag) and either 6.92±0.02mm or 5.95±0.02mm (Hg).

Throughout all RDE experiments, a saturated calomel electrode (SCE, Radiometer Electrodes, Copenhagen, Denmark) served as the reference and a graphite rod was used as a counter electrode (CE). The graphite rod had a surface area of at least ten times that of the working electrode (WE) [302] and was separated from the bulk solution by a glass sinter jacket (40μm pore size) which isolated the working electrode from any products formed at the counter electrode.

4.1.2 The Cell Design

The electrochemical cell, pictured in Figure 4.1, consisted of a double walled glass vessel of volume approximately 120 cm^3 covered with a teflon lid which supported a glass luggin probe. The reference electrode (RE) was placed inside the luggin to minimise the "ohmic drop" between the RE and WE [303–306]. Where required, this was further reduced by replacing the potentiostat and scan generator (described in section 4.3.1) with a Solartron Instruments (Farnborough, Hants. U.K.) 1286 Electrochemical Interface, which enabled positive feedback ohmic drop compensation to be used. The vessel was designed with a side–arm to carry the CE jacket which fitted tightly in position using a ground glass joint. A small input near the base of the vessel allowed gases to be bubbled through the solution providing a means of deoxygenation and saturation of the solution with test gases. Thermostatting to 25±0.1^{0}C was possible by circulating water from a thermostat tank, by pump, between the inner and outer walls of the cell.

4.1.3 Experimental Protocol

Where applicable, solutions were deoxygenated prior to use by bubbling through nitrogen [307] (BOC "White spot") which had been prepurified by passage over B.T.S. catalyst and calcium chloride granules. Additionally, this nitrogen was mixed with the gases to be analysed (for example, N_2O or O_2) via regulating flow meters (G.A. Platon Ltd., Basingstoke, U.K.) to deliver to the solution the required

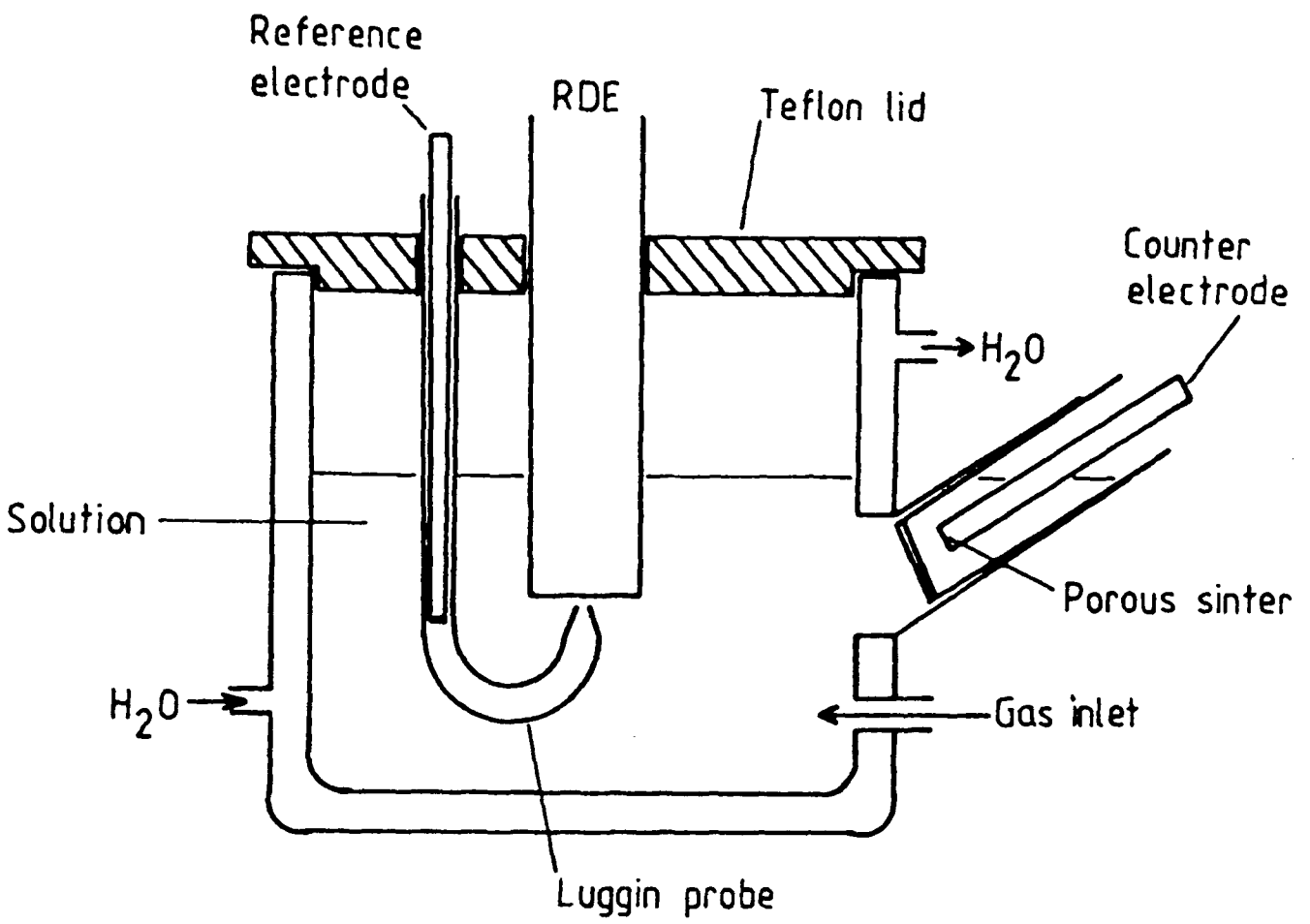


Figure 4.1: The electrochemical cell used for three–electrode RDE experiments.

percentage of each gas. Such gas mixtures also served as the carrier gas for forane which was introduced from a vaporiser (BOC Health Care, Steeton, West Yorkshire, U.K.) permitting the generation of 0–5% forane : carrier gas mixtures. PVC tubing with an internal diameter of 6mm was used to transport these gases; the vaporiser to reaction cell distance was kept to a minimum to reduce the possible absorption of forane by the tubing walls [36].

The discs were rotated using an Oxford Electrodes rotating disc assembly and motor controller which permitted rotation speeds in the range of $0 - 50$Hz to be accessed. The motor controller employed proportional feedback to maintain a precise and stable rotation speed (± 0.02 Hz). The use of an external voltage input facility on the motor controller in conjunction with a DC voltage pulse generator (Oxford Electrodes) enabled the rotation speeds to be stepped smoothly and rapidly (as fast as 0.004s) [308]. The feedback voltage was directly proportional to the rotation speed of the motor, and therefore steps in the latter were monitored by recording this voltage on a Gould (Gould Electronics Ltd., Ilford, Essex, U.K.) digital storage oscilloscope (0S4000).

4.2 The Channel Electrode Assembly

4.2.1 The Channel Cell

The entire flow cell, shown in Figure 4.2, was constructed from teflon to prevent chemical attack from organic solvents and comprised of a channel unit and coverplate, which were clamped together using steel bolts and a steel plate. The channel was 30.0mm long, 6.0mm wide and had an approximate depth of 0.4mm. This latter dimension could be adjusted by adding teflon spacers between the channel unit and the coverplate, and was therefore calibrated each time the cell was assembled. The precise depth was found from the slope of a Levich plot ($i_{lim} - V_f^{1/3}$ as explained in section 2.3.4) for the one electron reduction of an electroactive species with a known diffusion coefficient. Deeper duct sections at each end of the channel served to equalise the pressure across the width of the channel, facilitating

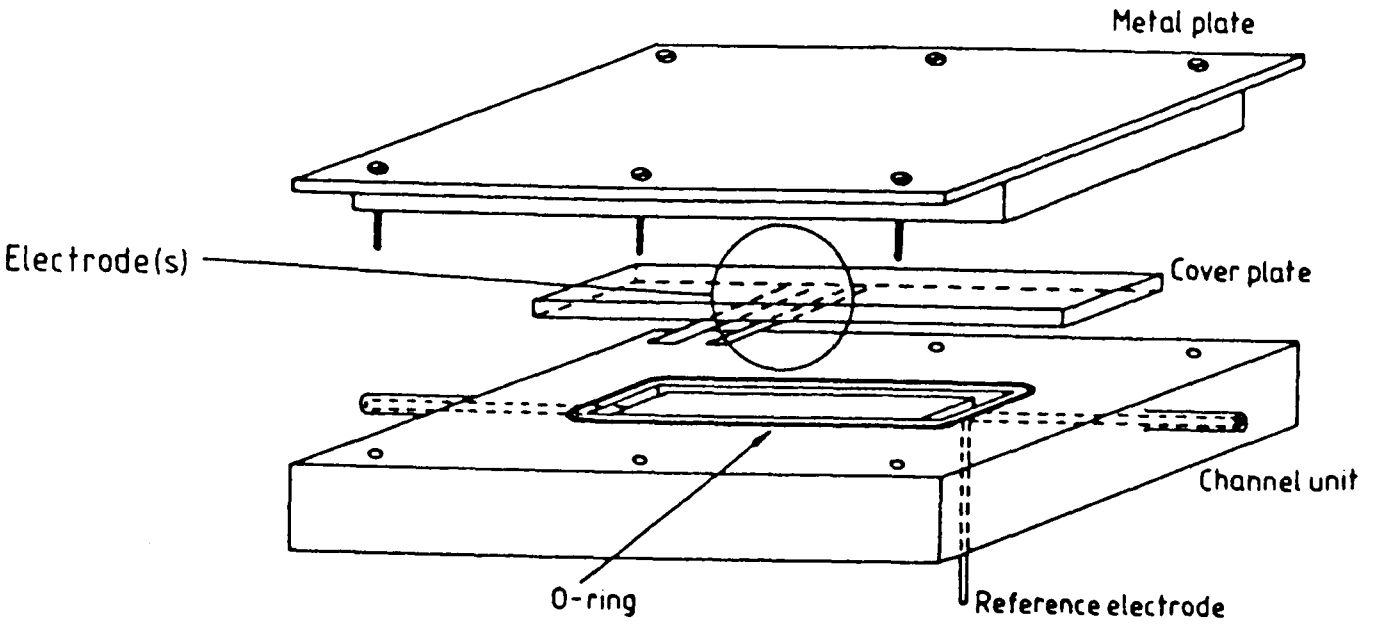


Figure 4.2: The ChE flow cell.

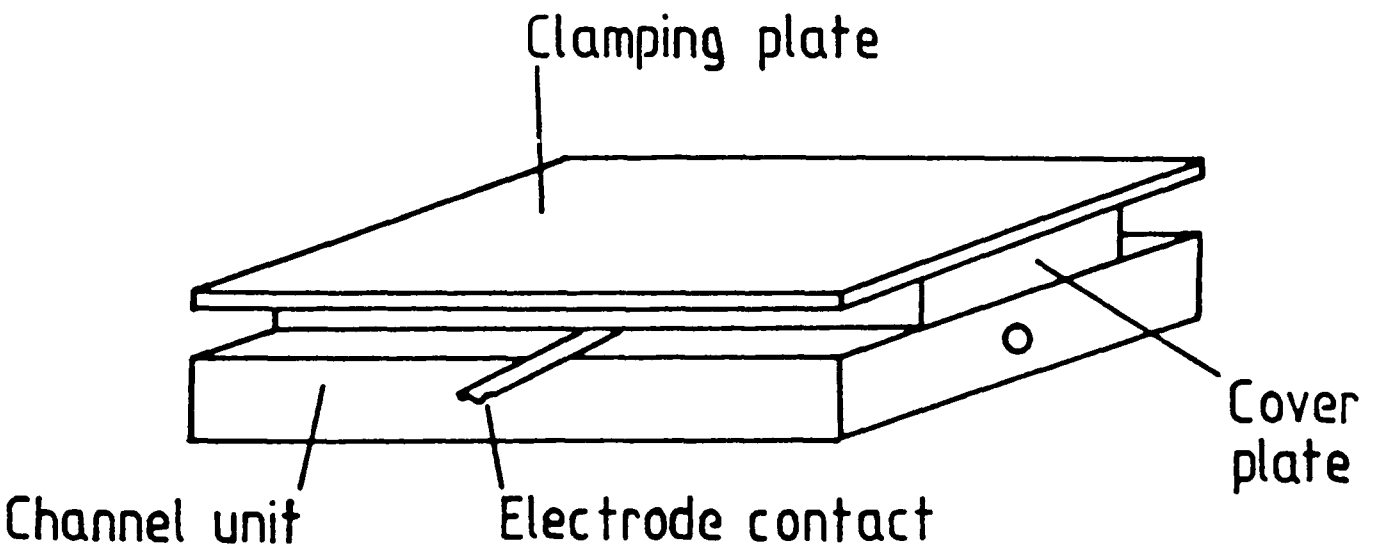


Figure 4.3: The assembled ChE flow cell and electrode contact.

laminar flow.

Copper foil strips, < 1mm wide were used as working electrodes; these were cut from thin (0.0125mm) copper (99.9%) sheets (Goodfellow, Camb., U.K.). These electrodes were cemented to the channel coverplate using a low melting point cosmetic depilatory wax (Vychem Ltd., Dorset, U.K.) which was found to be an adhesive which combined a strong bond to teflon with an inertness to decomposition from solvent. Prior to use, these copper strips were carefully polished flat using a succession of finer diamond lapping compounds and electroplated with mercury, exactly as for the RDE (described in section 4.1.1). A tiny drop of triply distilled mercury was then added to the strip, forming a smooth, flat mercury electrode. The ends of the foil strip extended beyond the edge of the coverplate (Figure 4.3) enabling electrical contact with the electrode. The exact dimensions of the mercury WE were measured using the travelling microscope before the cell was sealed.

The electrode was positioned on the coverplate so that once the cell was assembled and sealed, it was located sufficiently downstream of the entrance duct that the entry length requirement for laminar flow (expressed in equation 2.61) was fulfilled [162]. Additionally, the edges of the electrode were masked using teflon tape so that flow was essentially two dimensional and lateral edge effects were minimised [169].

A silver wire located in the upstream entrance to the channel served as a pseudo–reference electrode. A combination of mechanical pressure (applied using the steel plate and bolts) and a silicone rubber 'O' ring around the channel proved to be an efficient means of preventing leakage from the cell.

4.2.2 The Flow System

In the flow system (shown schematically in Figure 4.4), electrolyte solution flowed from a reservoir through 1.5mm bore teflon tubing ("Altex", Anachem, Luton, U.K.) into the channel where it passed over the electrode and then on through a capillary to waste. The reservoir was a 500cm^3 three necked round bottomed flask which was connected to the flow system via a Youngs Tap. Standard "Altex" connectors attached the tubing to the reservoir while the tubing was

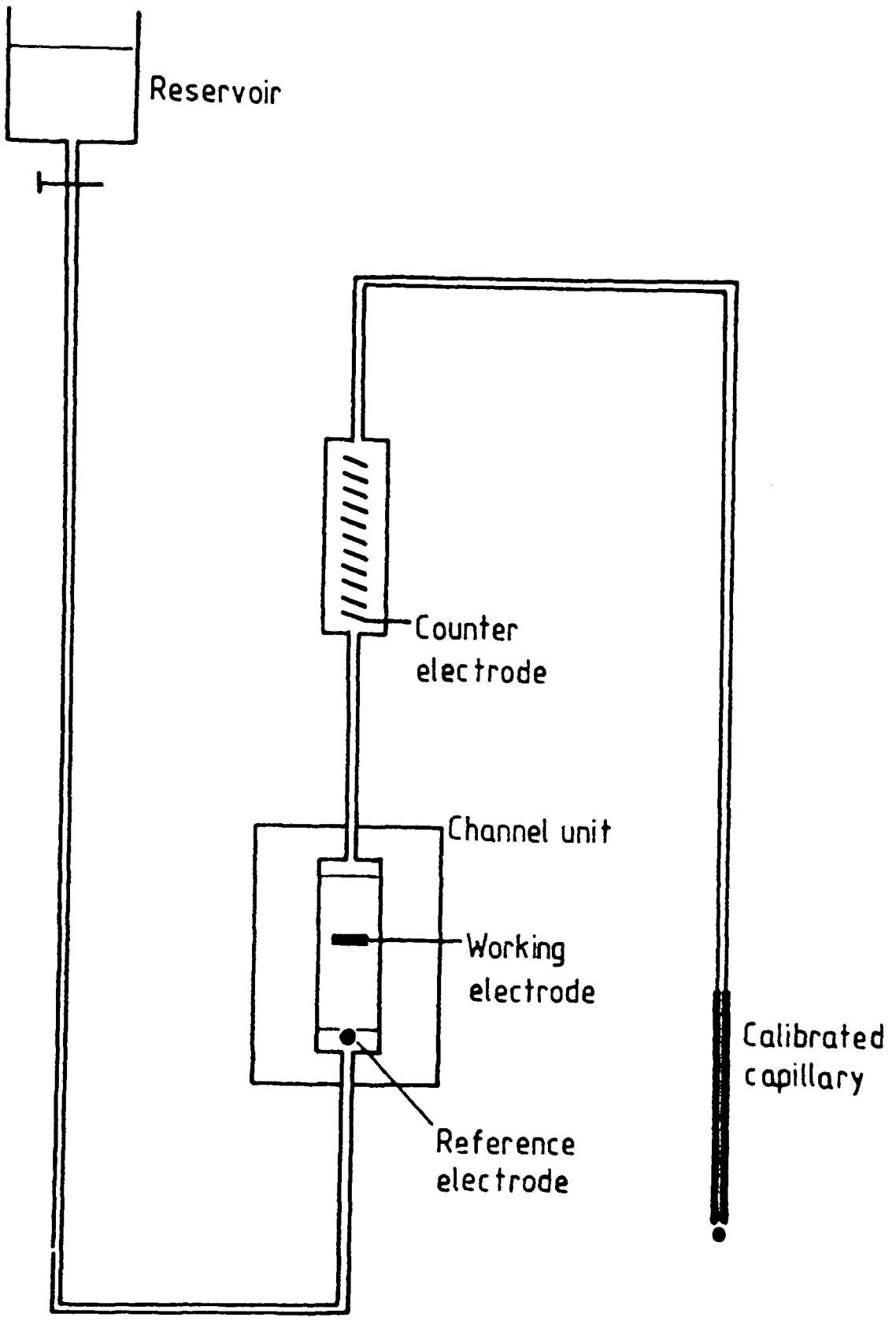


Figure 4.4: A schematic diagram of the gravity feed flow system employed.

connected to both the channel and capillary using silicone rubber tubing. An outer PVC tube (i.d. 6mm) purged with prepurified nitrogen prevented the ingress of oxygen into the solution [309]. This nitrogen was also bubbled through the reservoir to both deoxygenate the electrolyte solution [307] and to deliver gases such as forane or N_2O.

Solution flow was achieved by gravity feed [131], employing flow rates in the range 10^{-1} to 10^{-3} cm^3s^{-1}; these were adjusted by varying the height between the reservoir solution head and the exit tip of the capillary. A wide flow rate range was obtained by using capillaries with various bores. The flow rate dependence on reservoir height and capillary bore was calibrated frequently and flow rates accurate to three significant figures could thus be measured.

The CE was constructed from 8cm x 4cm platinum gauze, coiled into a spiral and sealed into an open–ended glass cylinder. This was located immediately downstream of the cell ensuring that CE products were flushed to waste.

The ChE cell was supported with the channel duct vertical and the solution exit at the top so that any air bubbles could easily escape, and their interference effect was thus minimised.

4.3 Electrochemical Techniques

4.3.1 Instrumentation

The potential applied between the WE and RE was controlled using an Oxford Electrodes potentiostat. This was employed in conjunction with an Oxford Electrodes linear potential scan generator for the measurement of current–potential characteristics. The latter enabled scan rates in the range of 1 – 2000 mVs^{-1} to be used. This equipment was also used in conjunction with a DC voltage source and differentiating operational amplifier (both Oxford Electrodes), for all double electrode experiments where the "ring" potential was fixed while the "disc" potential was scanned [310]. For sensing experiments, where the response to a potential step was required, the scan generator was replaced by an Oxford

Electrodes square wave generator. This permitted step frequencies in the range of 10^{-2} to 5 x 10^{3}Hz to be used. Data was recorded on a Gould Series 50000 x/y chart recorder with a time–base facility, and potentials and currents were checked independently using a Thurlby 1503 Digital Multimeter.

4.3.2 Time Dependent Measurements

The potential sequence used for recording double potential step chronoamperometry data was applied using the Oxford Electrodes square wave generator [207] in conjunction with the 1286 Electrochemical Interface. The latter enabled positive feedback ohmic drop compensation to be employed during the chronoamperometric measurements. The current transients thus generated were recorded using a purpose built digital transient recorder controlled by an IBM XT personal computer. This permitted the sampling of points as often as up to 10μs with a maximum of 2000 data points and a current resolution of approximately 0.38μA. One hundred transients were thus recorded during one experimental "run" and an average transient then calculated. The raw data was then transferred from the IBM PC to the Oxford University Computer Service VAX/VMS cluster by means of KERMIT 2.30 communications software [207].

AC impedance experiments were performed using the cell and electrodes described for the RDE experiments; the same procedure was adopted for deoxygenation, which continued throughout the experiment, and data was recorded at a stationary electrode. Measurements were carried out using a Solartron Instruments 1250 Frequency Response Analyser [311] in conjunction with the 1286 Electrochemical Interface. These were controlled via a BBC microcomputer. Thus frequency modulation in the range of $1x10^{-5}$ to $6.55x10^{4}$ Hz could be employed using amplitudes between 0 and 10V. Again, positive feedback ohmic drop compensation was utilised for these measurements. Results were recorded on the microcomputer and plotted using a Hewlett Packard 7470A plotter.

Linear sweep and cyclic voltammetry were carried out using the RDE assembly, potentiostat and potential scan generator. Solutions were degassed with N_2, as described for the RDE, prior to use.

4.4 ESR Experiments

4.4.1 The ESR Spectrometer

ESR measurements were carried out using a Bruker ER200D spectrometer, fitted with a 9 inch magnet, a rectangular TE_{102} cavity and a field–frequency lock. The working electrode was placed at the centre of the cavity and its orientation finely adjusted for maximum sensitivity [312].

4.4.2 The ESR Channel Cell

Both the channel cell and cover plate were constructed from silica [313]. A 4.0 x 4.0mm copper electrode was prepared from copper foil (section 4.2.1) and attached to the coverplate using araldite (Ciba Geigy, Camb., U.K.). This was then polished with diamond lapping compounds and a mercury surface prepared as described above for the RDE. A small tail, left on the centre of one side of the electrode, was bent at right–angles and introduced through a hole in the coverplate. This provided an electrical contact.

The channel cell itself (Heracus Ltd., Byfleet, Surrey, U.K.) is shown in Figure 4.5. The channel was 30mm long, 6.0mm wide and had a depth of 0.4mm, ducts at each end served to equalise the pressure as discussed in section 4.2.1. The two halves of the cell were successfully sealed together using low melting point wax [313].

A clean polished silver wire located upstream of the cell was used as a pseudo–reference electrode and a counter electrode of platinum gauze was positioned downstream of the cell.

4.4.3 The ESR Flow System

The flow system employed for the in–situ electrochemical ESR measurements was identical to that described in section 4.2.2. and shown in Figure 4.4.

4.4.4 Spin Trapping Experiments

Spin trapping experiments were carried out ex–situ using the rotating disc equipment described in section 4.1. Samples were then transferred to the ESR

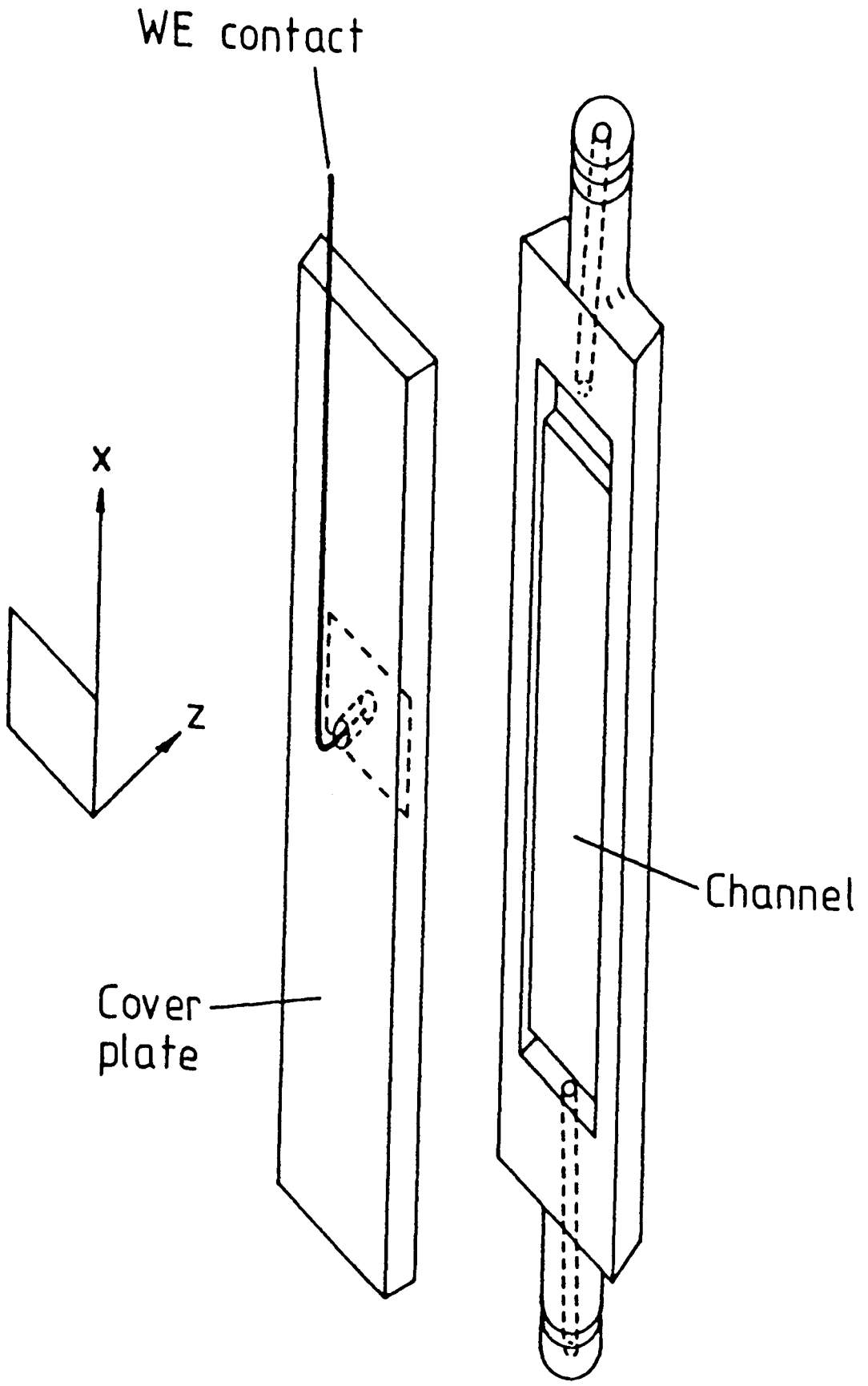


Figure 4.5: The silica in–situ ESR flow cell.

spectrometer and spectra recorded in the conventional manner [296].

4.5 Chemicals and Materials

The sources and grades of the chemicals used were as listed in Table 4.1. The solvent used for all non–aqueous electrochemistry was acetonitrile and this was dried for 24 hours immediately prior to use over pre–baked molecular sieves (size 4A, $^1/_8$" pellets). Where the absence of trace water ($< 1x10^{-4}$ moldm^{-3}) was essential, this was purified further by refluxing for two hours over calcium hydride [314]. The dry acetonitrile was then removed using a Schlenke apparatus and stored under a nitrogen atmosphere over activated molecular sieves. This procedure involved collecting the distillate in a glass vessel, which had previously been evacuated and filled three times with nitrogen. The vessel was then sealed with a Suba Seal rubber stopper. Dichloromethane was also refluxed for two hours with calcium hydride and distilled before use. Tetrabutylammonium perchlorate (TBAP) was recrystallised once from an ethanol : petroleum ether (boiling point 40–60^{0}C) (40:60 v/v) mixture.

Aqueous solutions were made up using water purified from an Elgostat (High Wycombe, Bucks., U.K.) UHQ apparatus which provided water of resistivity $> 10^7$ Ωcm.

PTFE ("Ohmeda", BOC Health Care) and high density polyethylene (HDPE, Fluorocarbon Company Ltd., Stretford, Manchester, U.K.) were investigated as possible membrane materials. 5.0μm pore size sheets ($\approx$ 25μm thick) of the former material were used and 12.5μm pore HDPE sheets ($\approx$ 30 μm thick) were studied.

4.6 Computing

All programs were written in FORTRAN 77 and executed on the Oxford University Computing Service VAX/VMS mainframe. Interpolation and fitting of

Table 4.1: The source and grade of the chemicals used.

CHEMICAL	SOURCE	GRADE
Acetonitrile	Fisons	Dried distilled
Anthraquinone	BDH	99.0%
Azo–iso–butyronitrile	BDH	98.0%
t–Butyl bromide	Koch–light	Puriss
t–Butyl–α–phenylnitrone	Aldrich	99.0%
Calcium chloride	Fisons	98.0%
Calcium hydride	Aldrich	$\geq$95%
Crystal violet	Aldrich	96%
2,3 Dichloro–5,6–dicyano–1,4–benzoquinone	Aldrich	98%
Dichloromethane	BDH	Analar
p–Dinitrobenzene	Aldrich	98%
Ethanol	J. Burrough	99.9%
Fluoranthene	Fluka	Purum
Forane	Anaquest Ltd.	Medical grade
Lithium perchlorate	Fluka	99%
Mercurous nitrate	BDH	Analar
Mercury	BDH	Aristar
Nitrogen	BOC	"White spot", >99.9%
Nitrous oxide	BOC	99.5%
Oxygen	BOC	99.5%
Petroleum ether	BDH	Analar
Potassium chloride	BDH	Analar
Potassium cyanide	BDH	Analar
Potassium hydroxide	BDH	Analar
Pyromellitic anhydride	Aldrich	97%
Tetrabutylammonium perchlorate	Fluka	Purum
Tetrabutylammonium tetrafluoroborate	Fluka	Purum
Tetrachloro–1,4–benzoquinone	Aldrich	99%
Tetracyanoethylene	Aldrich	98%
Tetraethylammonium perchlorate	Fluka	Purum
Tetramethylammonium perchlorate	Fluka	Purum
Tributyl tin chloride	Aldrich	96%

data was computed with the aid of standard NAG routines and graphical output (to a Calcomp CC1044 plotter) was achieved using SIMPLOT plotting procedures.

CHAPTER FIVE

THE ELECTROCHEMISTRY OF FLUORANTHENE

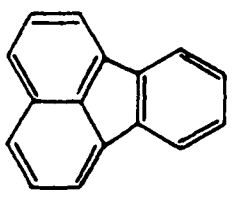
The electron transfer between a metallic electrode and the anaesthetic, forane, will be shown in Chapters Seven, Eight, Nine and Ten to be achievable only via a homogeneous mediator, namely the radical anion of fluoranthene. Anions of polycyclic aromatic hydrocarbons have been demonstrated previously as possible electro–reduction catalysts [120,315–321].

This chapter is thus concerned with the one electron reduction of fluoranthene in non–aqueous solvent. This is examined using double potential step chronoamperometry at a mercury RDE and the results are compared with the theory presented in Chapter Three. At times prior to the attainment of steady–state, the current is shown to exceed that of the theoretical transient. This is attributed to fluoranthene adsorption. Capacity measurements of the electrode/solution interface, determined using AC impedance, support this. The reverse transient is found to be in exact agreement with the theoretical prediction.

Experimental evidence is also presented which demonstrates that the radical anion of fluoranthene can be employed successfully as an electrogenerated mediator. t–butyl bromide is used as a model substrate. Comparison of the resultant data with the working curves generated in Chapter Three for the various nuances of the EC' mechanism enables a precise mechanism for the process to be evaluated. The discrimination between these similar pathways using steady–state analysis alone is thus confirmed and the theory presented in Chapter Three validated.

5.1 An Investigation of the One Electron Reduction of Fluoranthene using Double Potential Step Chronoamperometry

In this section, the simple one electron reduction of fluoranthene, F,

F = 

will be examined using, in the first instance, steady–state RDE voltammetry, and later chronoamperometric methods. The latter work will be compared with the theory presented in section 3.1.3 and used to validate, or otherwise, the use of the explicit finite–difference/Hale transformation approach for a one electron transfer (E) process.

The electrochemistry of F has been studied previously by Peover and Dietz [315,316], who reported that in several aprotic solvents, the species undergoes two one–electron reductions. In acetonitrile, the half wave potentials of these two processes are quoted as –1.75V and –2.25V (vs. SCE) on a platinum electrode. The first reduction, believed to be a completely reversible process, forms the radical anion of fluoranthene, $F^{\cdot -}$, while the addition of a second electron produces the dianion, F^{2-}. This latter reduction is thought to be electrochemically irreversible as a result of the reaction between F^{2-} and a proton, possibly from the solvent [315,316]. Despite thorough examination of the fluoranthene/aprotic solvent system with respect to this and related chemistry, no quantitative analysis of the reduction of F in any solvent appears in the literature.

As a preliminary, the reduction of F in acetonitrile/0.1 moldm^{-3} TBAP as supporting electrolyte was studied under steady–state conditions at a mercury plated RDE. A typical current–voltage curve is shown in Figure 5.1, where two reduction waves can be seen. Transport–limited currents for the first wave were measured as a function of rotation speed and found to obey the Levich equation (equation 2.58) for a simple one electron process, with a fluoranthene diffusion coefficient, D_F, of 2.28 ± 0.03 x10^{-5}cm^{2}s^{-1}. The Levich plot is shown in Figure 5.2. Mass transport corrected Tafel analysis (see section 2.4) gave a Tafel slope of 57 ±

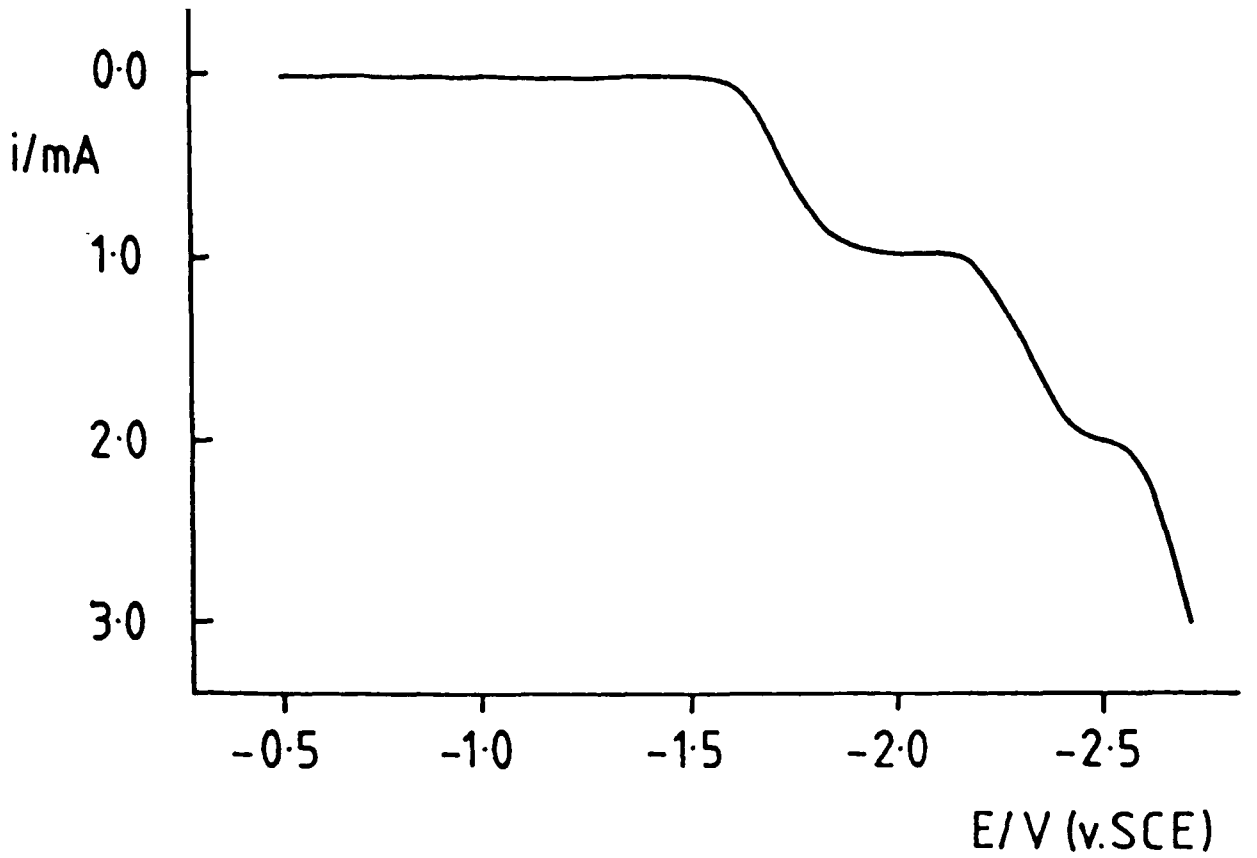


Figure 5.1: RDE voltammogram for the reduction, at a mercury electrode, of 3.0×10^{-3} moldm^{-3} fluoranthene in acetonitrile containing 0.1 moldm^{-3} TBAP. W = 16.0Hz.

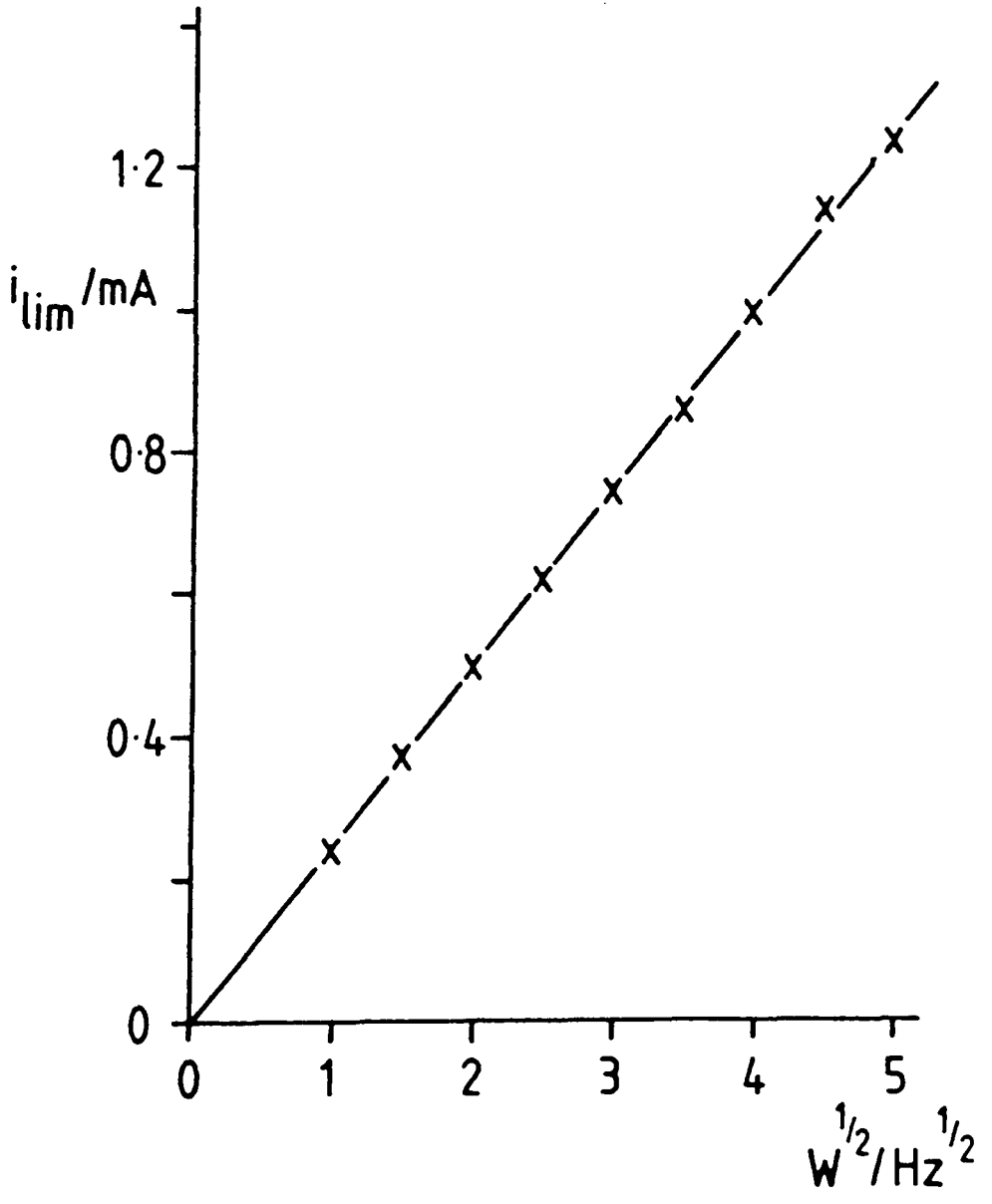


Figure 5.2: Levich plot of i_{lim} versus $W^{1/2}$ for the reduction of 3.0×10^{-3} moldm^{-3} fluoranthene.

2mV/dec., showing the one electron process:

$$F + e^- \longrightarrow F^{\cdot -}$$

to be electrochemically reversible, with $E_{1/2} = -1.80 \pm 0.02V$ (vs. SCE).

The theory presented in sections 3.1.2 and 3.1.3 enables the current–time response to both single and double potential steps at the RDE to be modelled for a one electron process. Therefore chronoamperometric results, determined from a solution containing c.a. $1x10^{-3}moldm^{-3}$ F and 0.1 $moldm^{-3}$ TBAP, will now be considered. The results were obtained using a potential sequence of the type defined in Figure 3.1, with $E_1 = E_3 = -1.50V$ (a potential where no current flows) and $E_2 = -2.00V$ (a potential corresponding to the transport–limited current for the reduction of F to $F^{\cdot -}$). The frequency of the potential pulsing was 0.05Hz which was sufficient for a true steady–state current, i_{ss}, to be established at E_2. At E_1 and E_3, the steady–state current is effectively zero, since F is the only electroactive species in solution.

Transients were recorded using the digital transient recorder described in section 4.3.2 (averaging 100 transients), as a function of rotation speed. Rotation speeds in the range 2.25 to 10Hz were employed. This range was governed by the accuracy of the motor controller and the presence of trace electroactive solution species (e.g. O_2 and H_2O), which give rise to a more significant background current, at low rotation speeds, and, at higher rotation speeds, an increasing double layer [322]:Faradaic charge ratio [259]. Trace solution species were minimised by using distilled acetonitrile and by degassing vigorously with N_2 throughout the experiment. A mercury RDE was used for these measurements and positive feedback ohmic drop compensation was employed throughout. Data was transferred from the IBM PC to the VAX/VMS mainframe (section 4.5) using the FORTRAN program listed in Appendix 4a.

The analysis of the reverse transients, which correspond to the reoxidation of electrogenerated $F^{\cdot -}$ located in the diffusion layer, back to F, will be considered first. The theoretical curve shown in Figure 3.3 illustrates that the transient should be a

unique function of t_B^*, which is related to real time through equation 3.21. This transformation requires a value for the diffusion coefficient of the radical anion of fluoranthene, $D_{F^{\cdot-}}$. This is, however, unknown. Consequently, experimental transients were fitted to the theoretical working curve by trial and error, assuming different values of $D_{F^{\cdot-}}$. Least squares analysis then gave the "best" value for the diffusion coefficient. Diffusion coefficients in the range of $2.0x10^{-5}$ to $3.0x10^{-5}cm^2s^{-1}$ at intervals of $0.25x10^{-5}cm^2s^{-1}$ were tried and as Figure 5.3 illustrates, excellent agreement was found between theory and experiments, at several rotation speeds, for $D_{F^{\cdot-}} = 2.75x10^{-5}cm^2s^{-1}$.

In generating the plots for least squares analysis, experimental data obtained for real times shorter than 0.05s were ignored, so as to exclude contributions to the transient current arising from double layer charging [322]. Experiments performed in the absence of F using 0.1 $moldm^{-3}$ TBAP/acetonitrile and an identical potential sequence, showed that the double layer charging current had fallen to below $2\mu A$ by 0.02s. This is shown on Figure 5.4. The agreement evident in Figure 5.3 is taken as implying that the reverse transient corresponds to a simple one electron oxidation of $F^{\cdot-}$ to F, uncomplicated by any other (heterogeneous or homogeneous) processes.

In conclusion, the theory presented in section 3.1.3 is in good agreement with this experiment and can be used to generate a value for $D_{F^{\cdot-}}$, which is shown to be $2.75\pm0.13\ x10^{-5}cm^2s^{-1}$.

Results obtained through the measurement of the forward transient will be examined next. Figure 5.5 shows a typical such transient, determined using a solution containing $1.0x10^{-3}moldm^{-3}$ F and a rotation speed of 4Hz. Also shown is the transient predicted theoretically using the theory presented in section 3.1.2 for a one electron process. This was calculated using the value of $D_F = 2.28x10^{-5}cm^2s^{-1}$ deduced above by means of Levich analysis of the rotation speed dependence of the steady–state reduction current. It is evident from this figure that the agreement between theory and experiment is poor, especially given the good agreement found for the reverse transients. A similar disparity was observed at all rotation speeds examined. In particular, inspection of Figure 5.5 shows the experimental current to exceed the theoretical at times before the steady–state is reached. Whilst part of

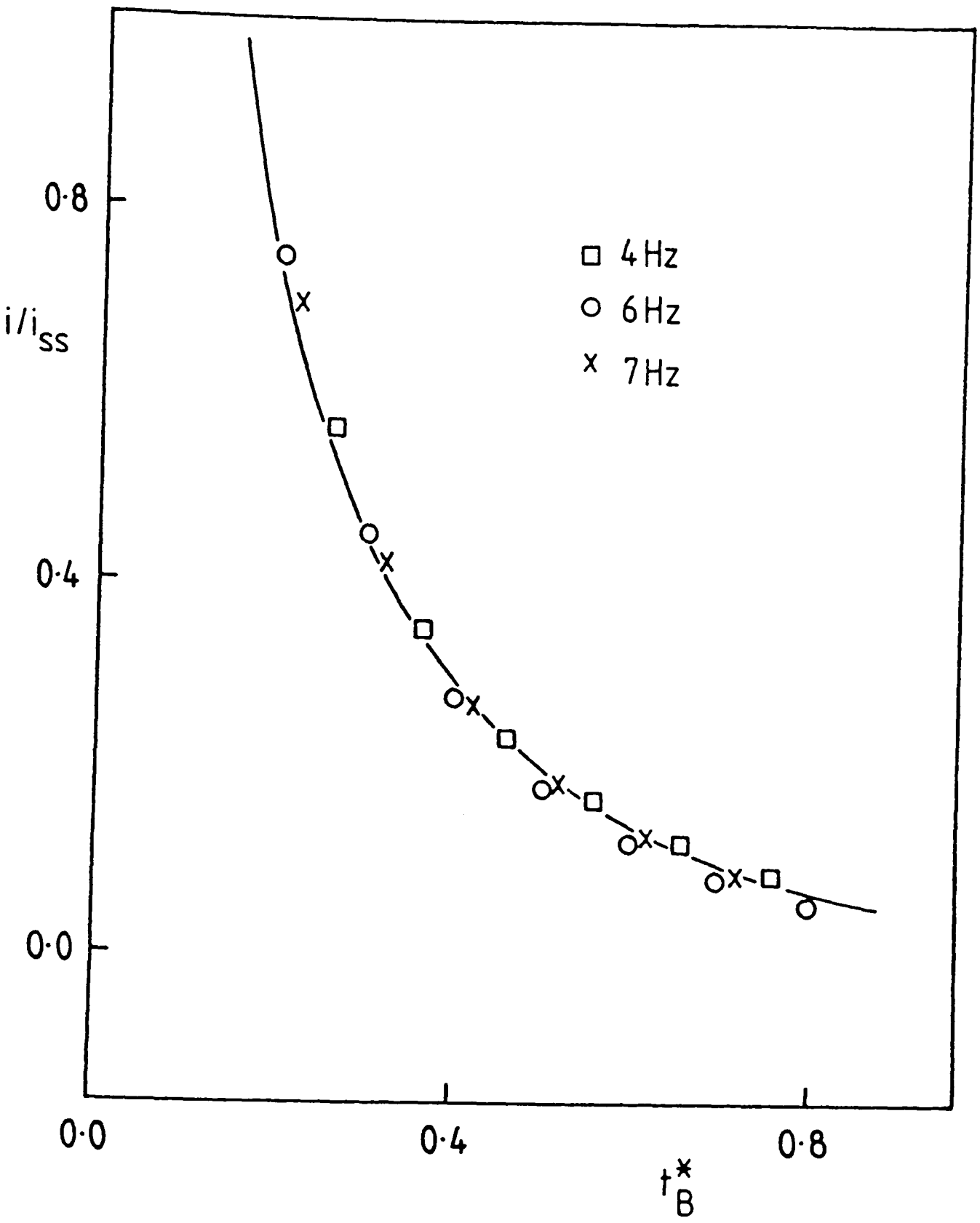


Figure 5.3: The "reverse" transient produced by a potential step from E_2 to E_3. The solid line shows the theoretical behaviour for a simple E process assuming $D_{F^{\cdot-}} = 2.75\times 10^{-5}$ cm^2s^{-1} and the experimental points relate to a 1.26×10^{-3} $moldm^{-3}$ solution of fluoranthene in acetonitrile.

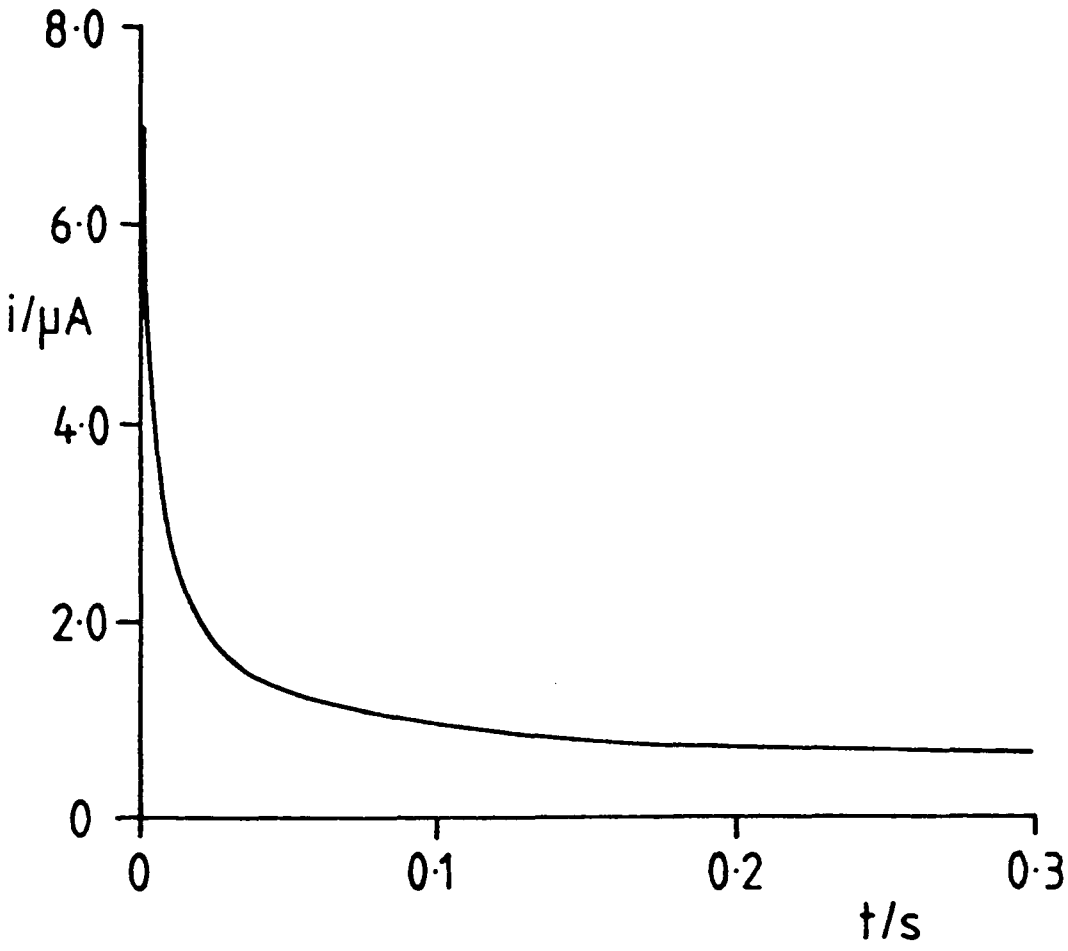


Figure 5.4: Transient produced by a potential step from E_2 to E_3, obtained from a solution containing 0.1 moldm^{-3} TBAP in acetonitrile only.

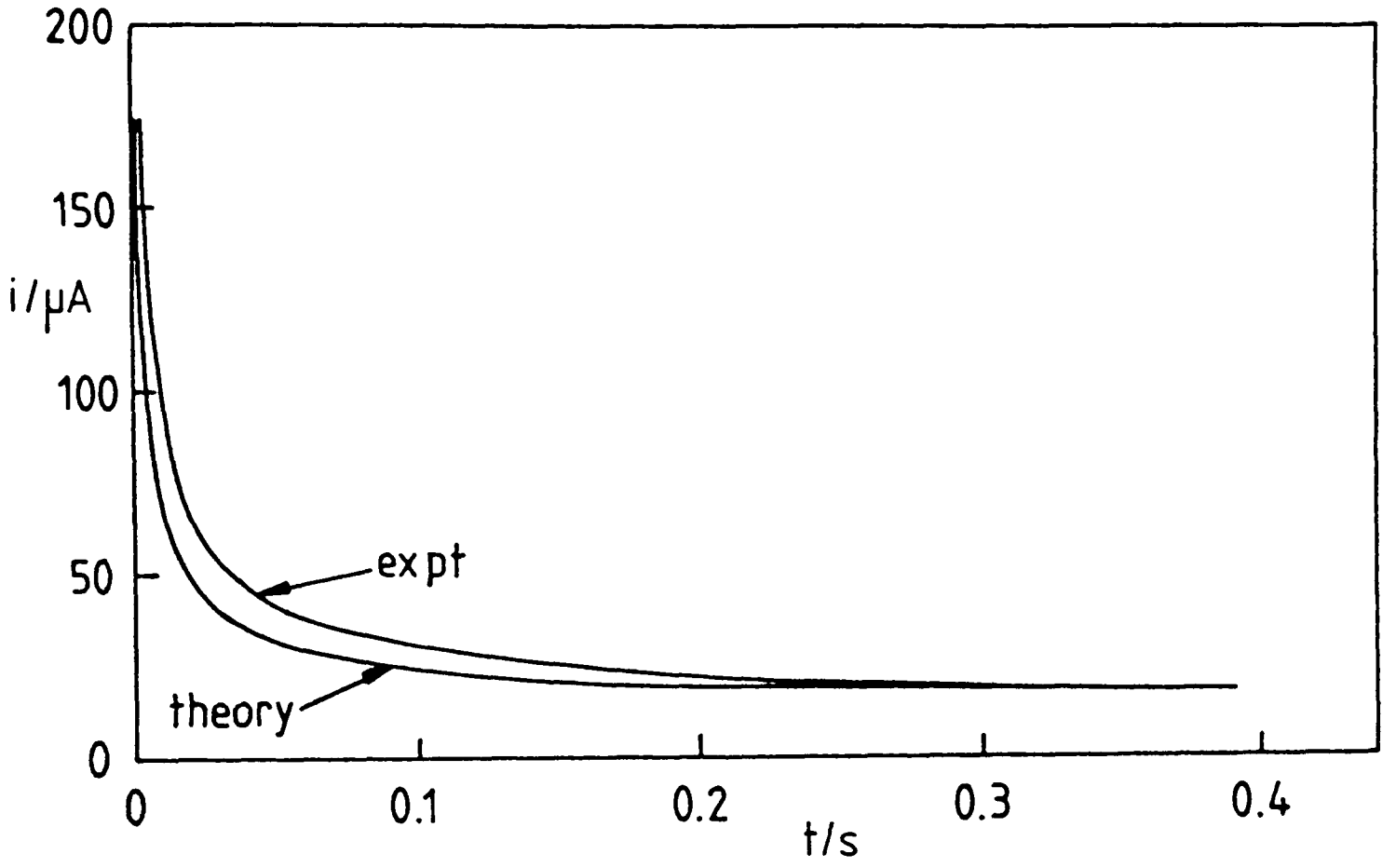


Figure 5.5: An experimental "forward" transient measured at a rotation speed of 4.0Hz using a solution containing 1.0×10^{-3} moldm^{-3} fluoranthene, together with the theoretical behaviour predicted for the case where there is no adsorption of fluoranthene.

this excess charge passed can be attributed to double layer charging [322], experiments carried out in background electrolyte alone showed that currents due to the latter had decayed to below 2μA by 0.025s and thus, this could not be the source of the extra current at longer times. Moreover, integration of the current transients revealed that the total charge passed during steps from –1.5V to –2.0V in the absence of F could contribute less than 10% of the excess charge (over theory) seen in the presence of F. In addition, a negligible current observed when no F was present and good agreement between the experimental and theoretical steady–state currents confirmed the purity of the solution, and removed any suspicion that coupled homogeneous kinetics may be responsible for the excess charge.

The theory presented in section 3.1.5 modelled the chronoamperometric response resulting from an electron transfer preceded by a finite rate of adsorption of the electroactive material [207]. Figure 5.6 compares the experimental data of the forward transient with this theory for several values of k', the heterogeneous rate constant. This figure illustrates clearly that the reduction of F is neither preceded nor controlled by its adsorption via a first order heterogeneous process, since this would result in a smaller current at times before the steady–state is reached.

The excess current observed in Figure 5.5 was thus attributed to the reduction of fluoranthene adsorbed onto the electrode surface. It was estimated that a surface coverage of 3.7×10^{14} molecules cm^{-2} was required to produce the extra current flowing, assuming a one electron reduction of the adsorbed material. In calculating this surface coverage, it was also assumed that the electrode was "smooth" so that the geometrical area of the electrode could be used in this estimate.

An independent check on the conclusion of F adsorption was sought from AC impedance spectroscopy. Initial experiments were performed using the mercury plated copper electrode in 0.1 $moldm^{-3}$ TBAP/acetonitrile only. Figure 5.7 shows the observed complex plane impedance plot measured at –1.5V, using frequencies in the range of 1Hz to 65kHz and an amplitude of 5mV. This is suggestive of a constant phase angle admittance in series with a small uncompensated solution resistance. The former can be attributed to the interfacial capacity of a "rough" electrode. The effects of surface roughness have been characterised in terms of the

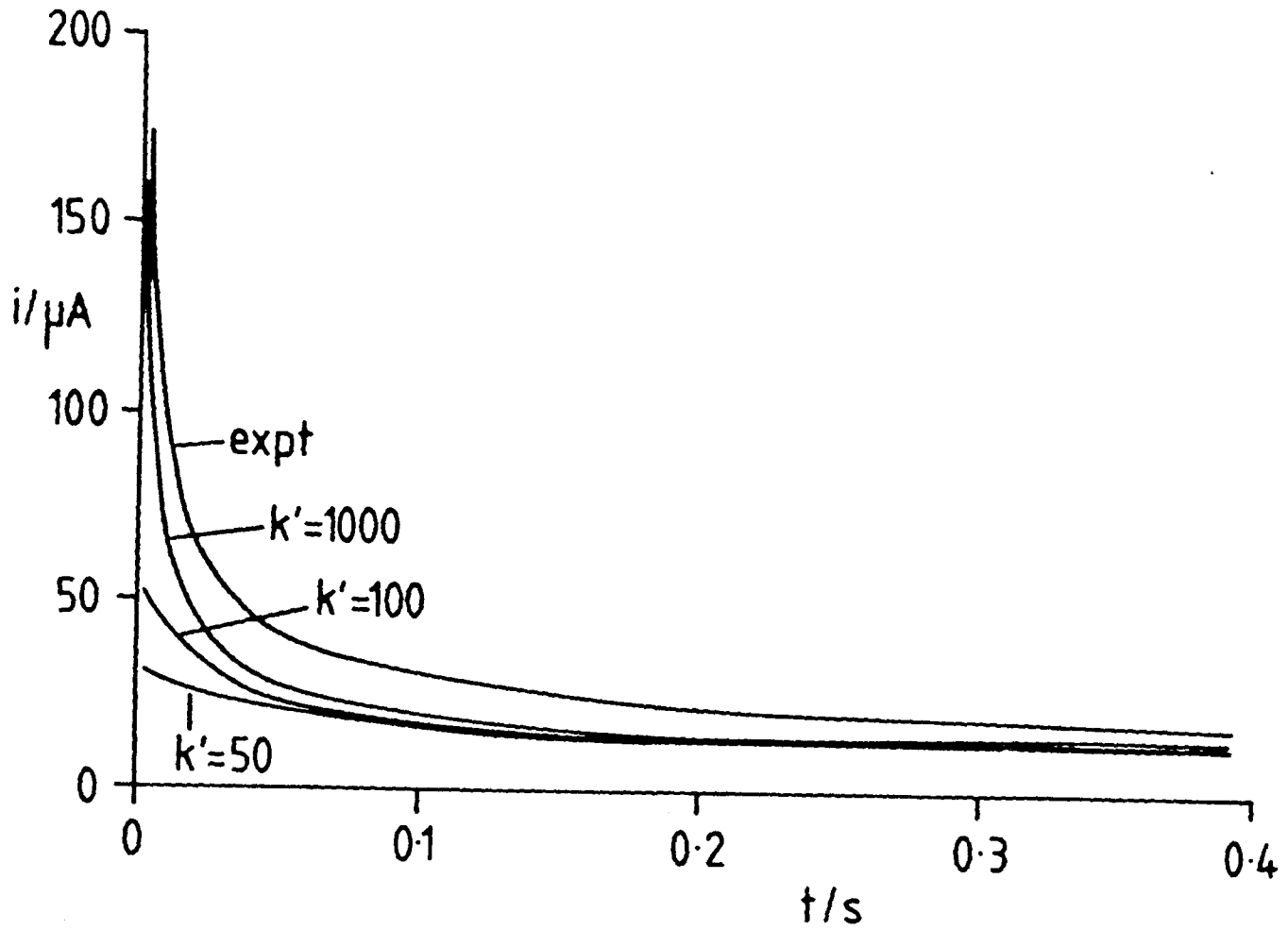


Figure 5.6: The experimental transient shown in Figure 5.5, together with theoretical transients for the case where electron transfer is preceded by the first–order adsorption of fluoranthene. Heterogeneous rate constant $k' = 50$, 100 and 1000 cm s^{-1}.

effective fractal dimension, D^f, of the surface [323–327]. For a perfectly smooth electrode, $D^f = 2$, but for real, solid electrodes, $2 < D^f < 3$, and it has been estimated that the fractal geometry of the electrolyte/electrode interface generates [323–327] a constant phase impedance:

$$Z^{-1} = \sigma'(jw)^{\alpha_i} \qquad 5.1$$

or

$$Z = \sigma'^{-1} w^{-\alpha_i}\{\cos(\alpha_i\pi/2) - j\sin(\alpha_i\pi/2)\} \qquad 5.2$$

where σ' is a frequency independent real constant, w is the frequency ($rads^{-1}$) and $j = \sqrt{(-1)}$. The exponent, α_i, is fractional and its experimental value for ideally polarizable electrodes is between $^1/_2$ and 1. Thus perfectly smooth electrodes are characterised by $\alpha_i = 1$, and show ideal capacitive behaviour, resulting in a complex plane impedance plot, which is parallel to the imaginary axis but displaced from it by an amount corresponding to the uncompensated solution resistance, i.e.:

$$Z = R_u + \frac{1}{jwC} \qquad 5.3$$

In general, it has been suggested, that $\alpha_i = 1/(D^f - 1)$ [323–326] from which it may be seen that the case of $D^f = 3$ gives $\alpha_i = {}^1/_2$, which is the result previously deduced for porous electrodes [328,329]. Equation 5.2 shows that the general case produces a straight line complex impedance plot, inclined at an angle of $\alpha_i\pi/2$ to the horizontal.

Examination of the data in Figure 5.7 gives $\alpha_i = 0.95 \pm 0.02$ both from direct measurement of the angle of inclination of the straight line to the horizontal and from plotting $\log(Z'')$ versus $\log w$ as suggested by equation 5.2 (see Appendix One). This is shown in Figure 5.8. The fractal dimension, D^f, of the surface was thus deduced to be 2.06 ± 0.03, confirming the mercury plated electrode to be smooth as expected.

The data of Figure 5.7 also allowed the capacity of the plated

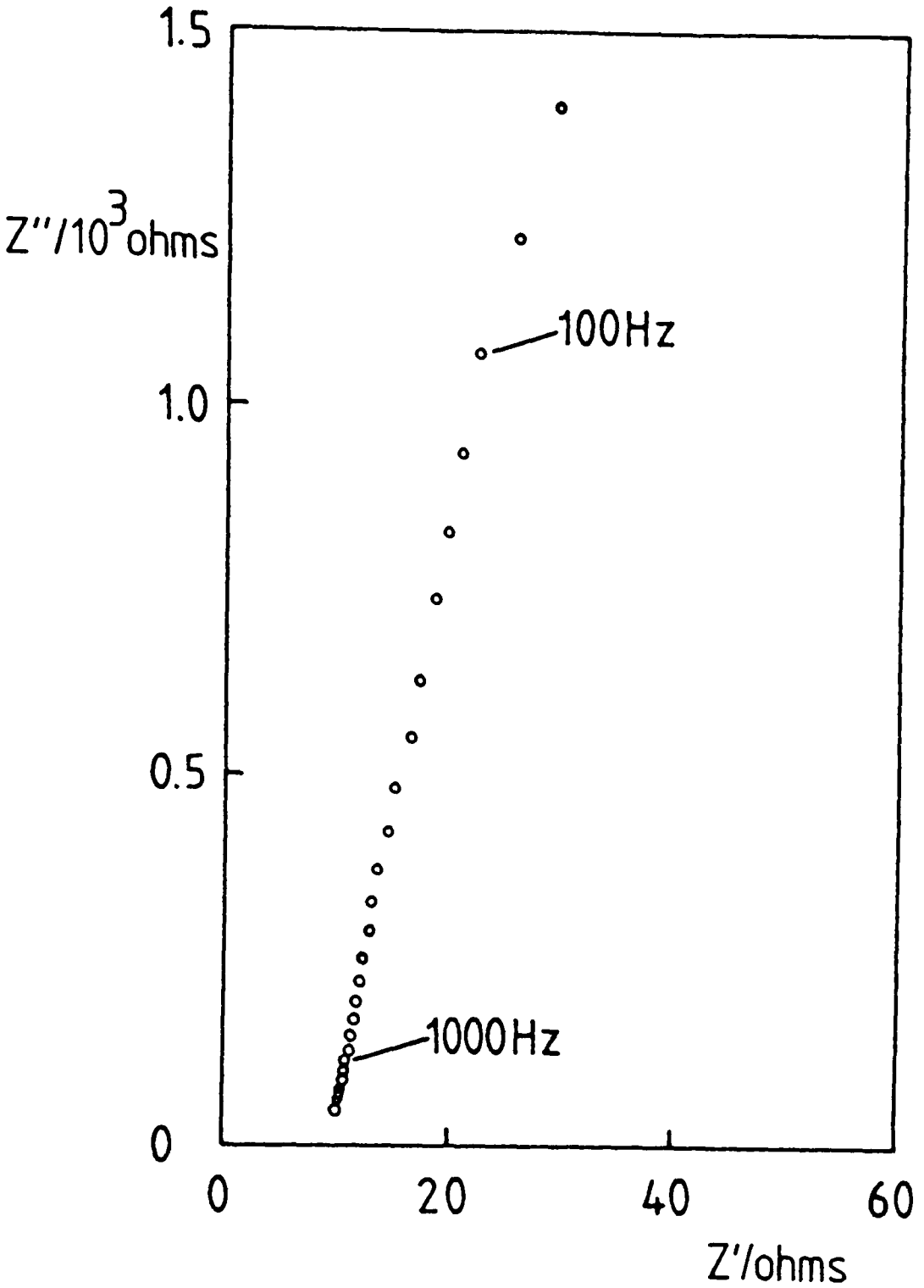


Figure 5.7: The complex plane impedance plot of a mercury RDE in 0.1 moldm^{-3} TBAP/acetonitrile measured at –1.50V v.SCE. The impedance is defined as $Z = Z' - jZ''$.

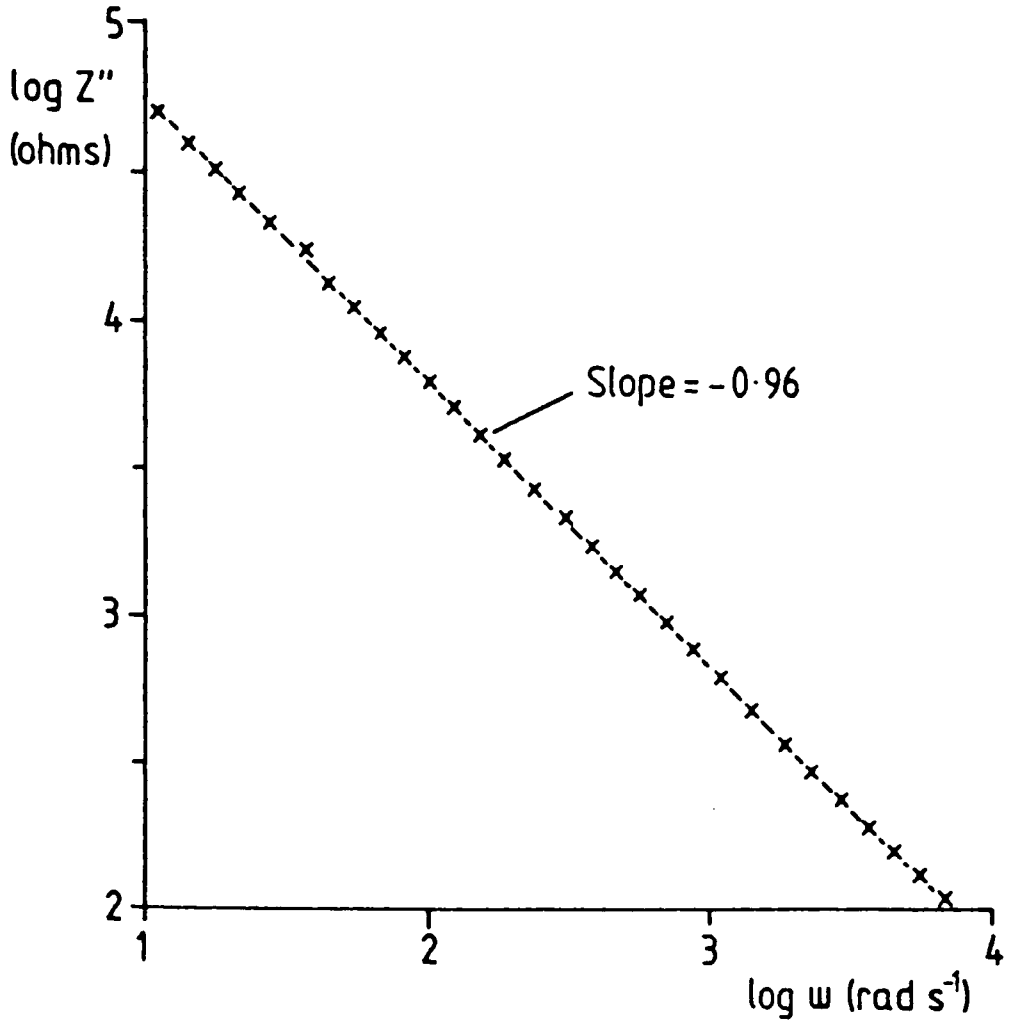


Figure 5.8: Plot of log Z'' versus log w for the impedance data of Figure 5.7.

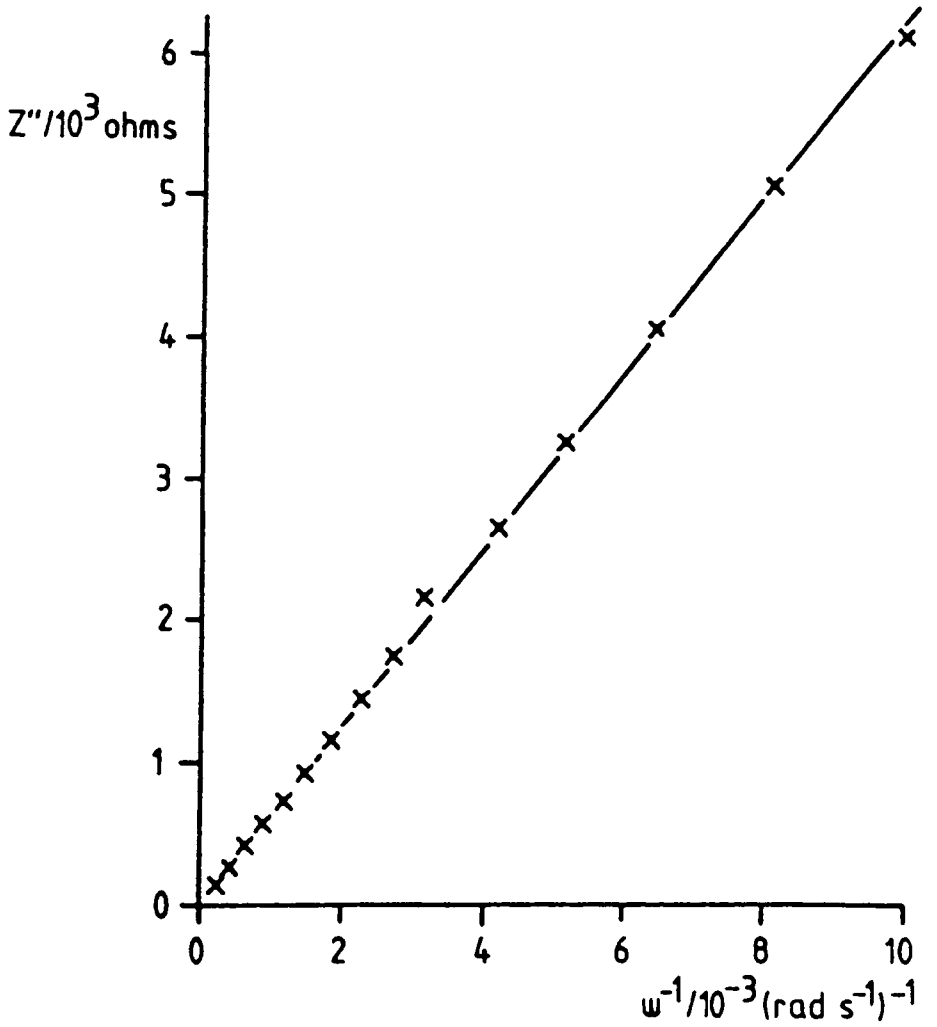


Figure 5.9: Plot of Z'' versus w^{-1} for the impedance data shown in Figure 5.7.

electrode/acetonitrile (0.1 moldm^{-3} TBAP) solution interface to be deduced by plotting Z'' versus w^{-1} (shown in Figure 5.9). It had a value of 5.7 μFcm^{-2} at –1.5V. Measurements carried out over the potential range –0.5 to –2.0V gave the same fractal dimension as at –1.5V but an interfacial capacity which varied as shown in Figure 5.10. This data may suggest that perchlorate anions (ClO_4^-) are adsorbed at –0.5V but tetrabutylammonium cations (TBA^+) at –1.5V. Interestingly, when 2.0x10^{-3} moldm^{-3} F was added, the capacity at –1.5V decreased to 3.9 μFcm^{-2}, consistent with the adsorption of F at this potential as deduced from the RDE chronoamperometry. One further point of note was that upon transferring the electrode from a solution containing F, to one without, a capacity indicative of adsorbed TBA^+ was regained suggesting that F is reversibly adsorbed on mercury. This inference was reinforced by the observation that cyclic voltammograms on such transferred electrodes showed no indication of adsorbed material [118] over the potential range –0.5 to –2.9V.

RDE chronoamperograms were then recorded for various concentrations of F and the corresponding surface coverage deduced from the excess charge between the theoretical and experimental transients. For each concentration, the amount adsorbed was found to be independent of the rotation speed used to record the current transient. This was taken as further evidence in favour of interpreting the excess charge to be due to the reduction of adsorbed F. The resultant isotherm, shown in Figure 5.11, displays two plateaux, separated by an abrupt transition. The higher coverage corresponds to the higher F concentration. This may be attributed to the adsorption of F via two different "faces". Figure 5.12 shows how the shape of the F molecule may be approximated by a rectangular block, the dimensions of which may be found from the known covalent and van der Waals radii [206,330] of the constituent atoms. It is possible to calculate the surface coverage of F by assuming that it is adsorbed by one of three faces, A, B or C defined in Figure 5.12, and that the "blocks" are packed immediately adjacent to each other. The resulting coverages for faces A and B are shown in Figure 5.11. The agreement with experiment is remarkably good and it may be reasonably assumed that at concentrations below $\approx$ 3x10^{-4} moldm^{-3}, F is adsorbed as a monolayer on mercury

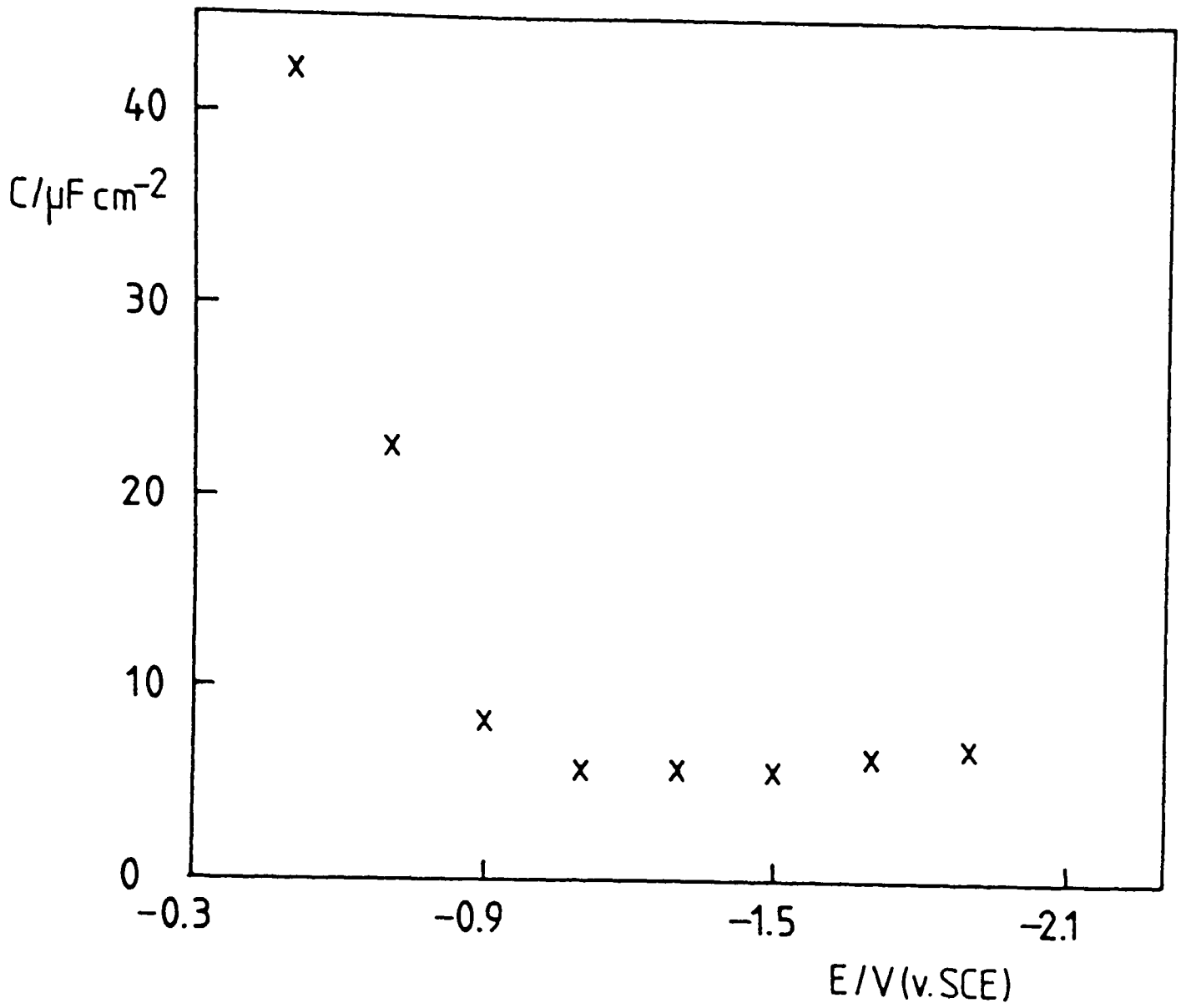


Figure 5.10: The potential dependence of the capacity of the mercury/acetonitrile (+ 0.1 moldm^{-3} TBAP) interface.

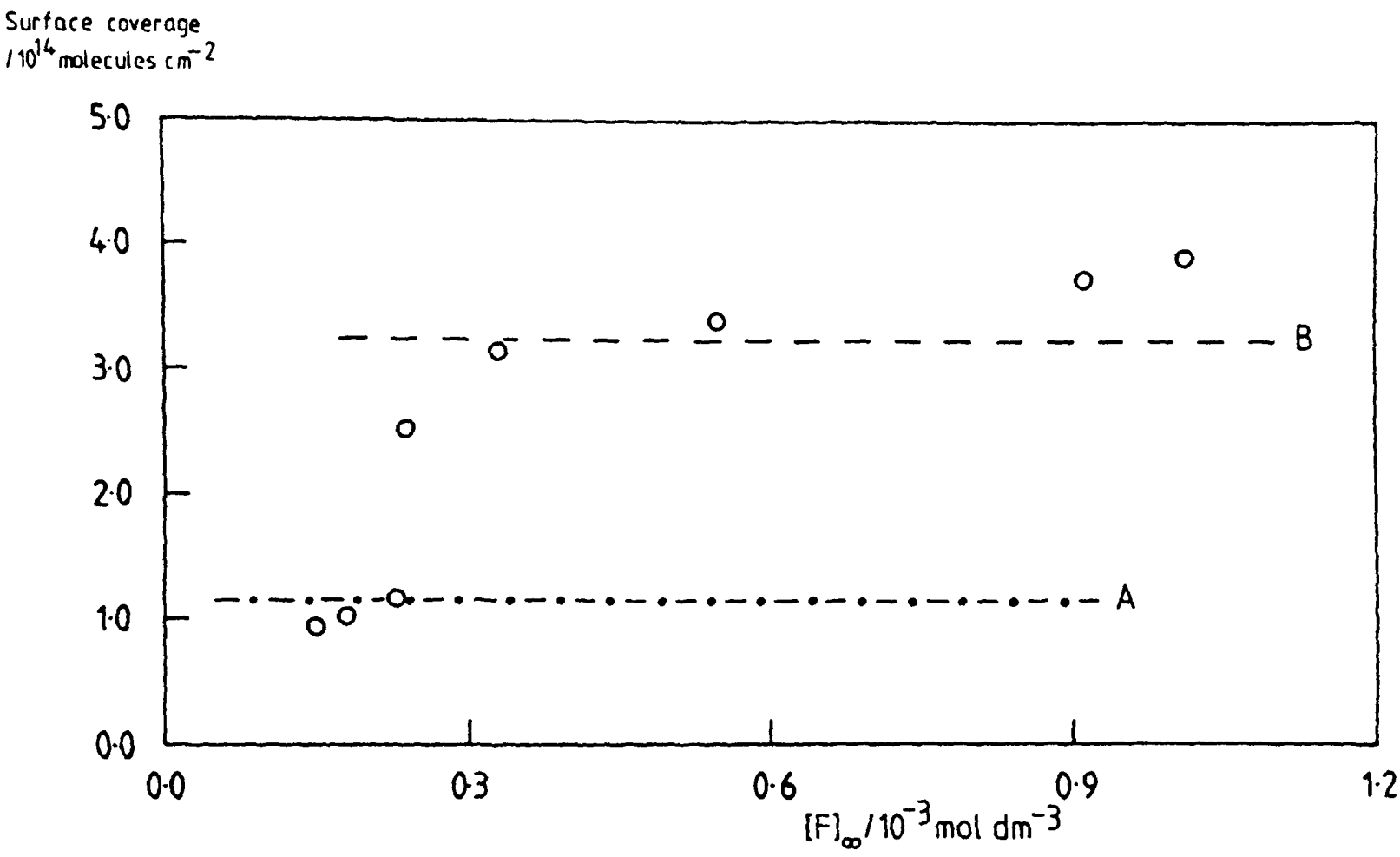


Figure 5.11: The isotherm for the adsorption of fluoranthene from 0.1 moldm^{-3} TBAP/acetonitrile onto the mercury electrode at –1.5V v.SCE as deduced by RDE chronoamperometry.

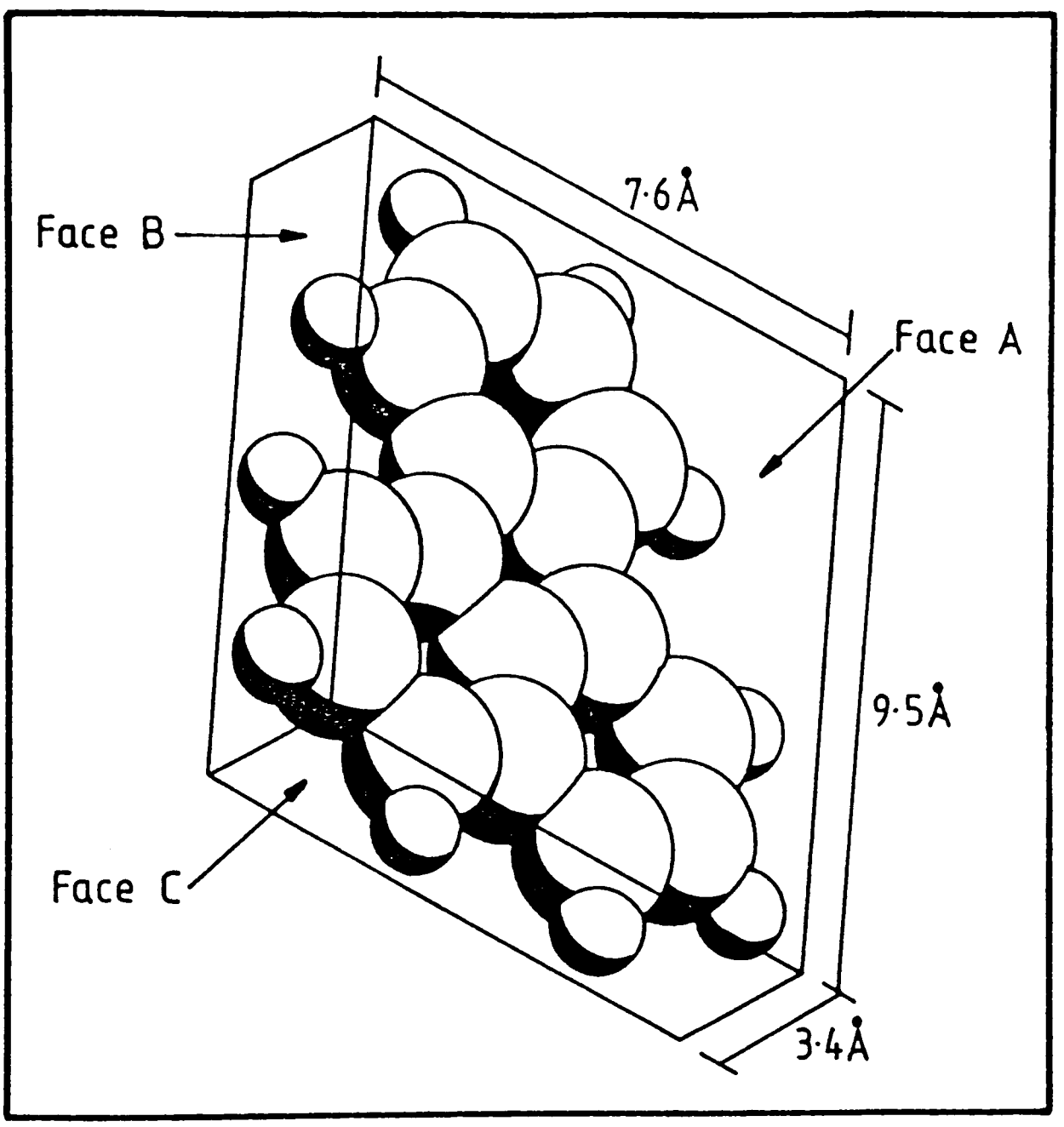


Figure 5.12: Representation of the fluoranthene molecule by a rectangular box of dimensions defined by the known van der Waals radii of the constituent atoms.

via face A, but that above this concentration, adsorption is via face B. Moreover, the small increase in coverage away from line "B" at high concentrations might tentatively be assigned to a further reorientation.

This behaviour is not unexpected in the light of similar orientational transitions suggested for aromatic molecules adsorbed on mercury [331], platinum [206,332,333] and other metal electrodes [334]. These have been deduced using various experimental techniques [335] including Auger electron spectroscopy [212,336], IR reflectance spectroscopy [213], Surface Enhanced Raman Scattering [214] and, in particular, thin layer coulometry [206]. Adsorbate orientation and the mode of surface bonding [337] are matters of fundamental and practical importance because of their influence on the nature of electrocatalytic oxidation and reduction products [338–341] and have been the subject of recent reviews by Hubbard [335,337].

In comparison with the techniques mentioned above, the particular merits of RDE chronoamperometry lie firstly in its simplicity and convenience, and secondly, in the fact that it can be used to deduce the isotherm for material reversibly adsorbed on an electrode. No other reports of orientational transitions by F appear in the literature.

In conclusion, the theory presented in Chapter Three is in excellent agreement with experiment for the case of the reverse transient resulting from an E process at a RDE. A value for the diffusion coefficient of $F^{\cdot -}$ is thus determined to be 2.75 ± 0.13 $\times 10^{-5}$ $cm^2 s^{-1}$. For the case of the forward transient, which results from stepping the electrode to a potential corresponding to the steady–state reduction of F, the disparity between theory and experiment is used to provide quantitative information about a F adsorption isotherm.

5.2 The Mediated Reduction of t–Butyl Bromide: an Investigation using Rotating Disc Electrode Voltammetry

The need for a homogeneous catalyst to mediate electron transfer to forane

was discussed in the introduction of this chapter, where the use of the radical anion of fluoranthene was proposed. The mediated reduction of t–butyl bromide (Bu^tBr) in acetonitrile/0.1 $moldm^{-3}$ TBAP using $F^{\cdot -}$ as an electrogenerated mediator will therefore be examined next. Several reviews of the electrochemistry of alkyl halides appear in the literature [96–98,342] and Bu^tBr has been shown to be electroactive on mercury. The reduction takes place at –2.3V (vs. SCE) [342,343]. This therefore is sufficiently negative of the half–wave potential for the reduction of F to ensure that the two voltammetric waves do not interfere or overlap. One further point of interest is that the reduction of simple aliphatic monohalides such as Bu^tBr is thought to proceed via rapid dissociative electron capture [344–347].

In addition to confirming, or otherwise, the success of $F^{\cdot -}$ as an electron transfer catalyst, the $F^{\cdot -}/Bu^tBr$ system may also be used as an experimental test of the theory described in section 3.1.4 for the calculation of chronoamperograms and steady–state working curves resulting from a process involving a heterogeneous electron transfer coupled with catalytic homogeneous kinetics.

The reduction of $3.0x10^{-3}$ $moldm^{-3}$ F was once again recorded as a function of rotation speed, this time in the presence of Bu^tBr. Figure 5.13 shows typical voltammograms thus obtained, both in the absence of Bu^tBr and in the presence of increasing concentration of this substrate. A catalytic process of some kind is clearly taking place. The determination of which, if any, of the mechanisms presented in section 3.1.4 is appropriate for this reaction, will therefore be discussed below.

Figure 5.14 shows typical limiting current versus rotation speed behaviour for different concentrations of Bu^tBr. Such plots enabled the deduction of n_{eff} as a function of rotation speed and concentration of mediator ($F^{\cdot -}$), A and substrate (Bu^tBr), Y. The normalised rate constants for the various catalytic mechanisms, given in Table 3.2, reveal that n_{eff} is most naturally plotted against W^{-1}. A typical plot is shown in Figure 5.15 where the concentration of F is adjusted while $[Bu^tBr]_\infty$ is held constant. Two significant features are apparent. Firstly, at high rotation speeds, n_{eff} approaches unity, as required for a catalytic process involving a one electron electrochemical step. Secondly, a systematic dependence of n_{eff} on $[F]_\infty$ is apparent. This quantity appears insensitive to $[Bu^tBr]_\infty$. This latter observation

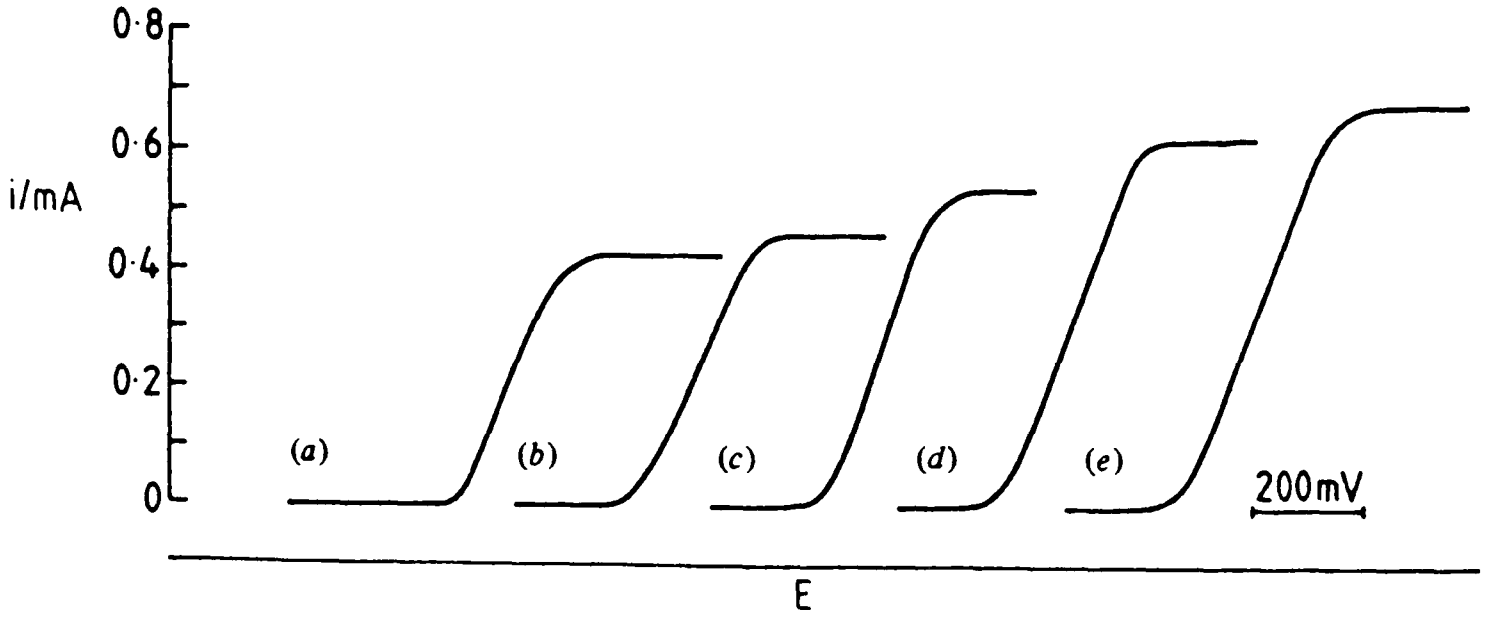


Figure 5.13: Voltammograms for the reduction of 3.0×10^{-3} moldm^{-3} fluoranthene and a) 0, b) 0.11, c) 0.22, d) 0.89, e) 1.78 $\times10^{-3}$moldm^{-3} t–butylbromide.

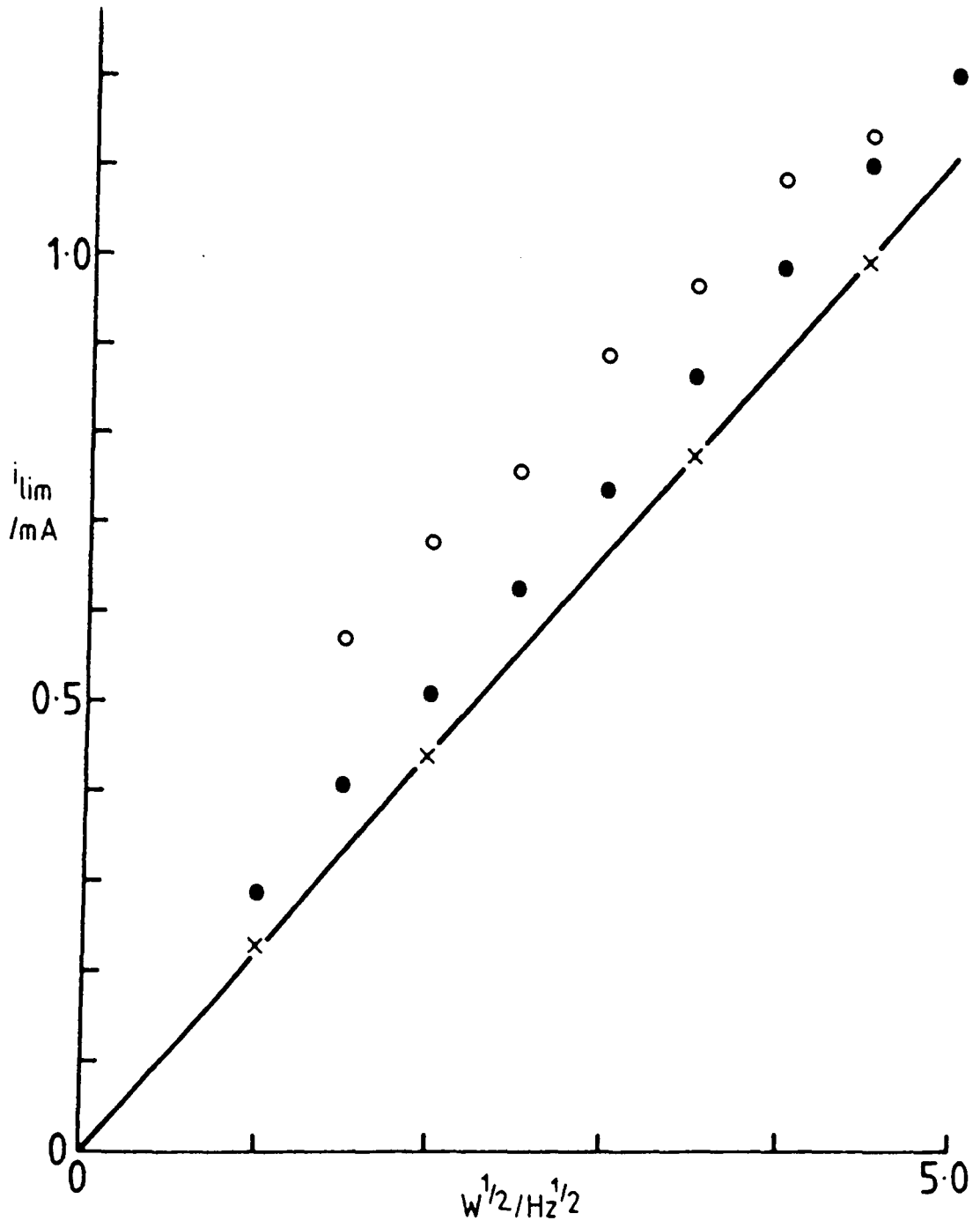


Figure 5.14: The variation of i_{lim} with $W^{1/2}$ for the reduction of 3.0×10^{-3} fluoranthene in the presence of ×, 0; ●, 1.1×10^{-4}; o, 17.8×10^{-4} moldm^{-3} t–butylbromide.

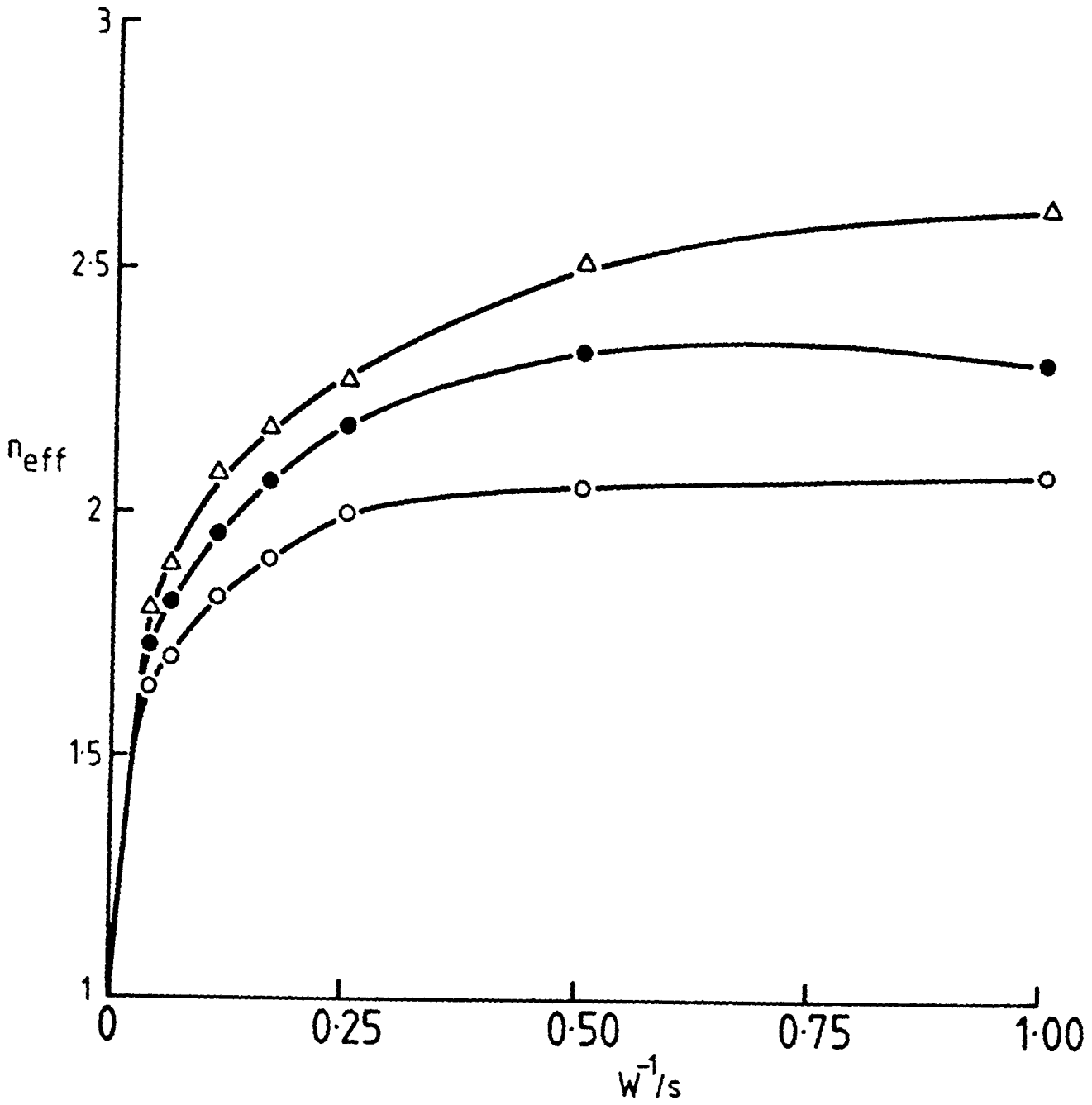


Figure 5.15: The dependence of n_{eff} on W^{-1} for the reduction of o, 1.0; ●, 2.0; Δ, 3.0 $\times 10^{-3}$moldm^{-3} fluoranthene in the presence of 1.78×10^{-3} moldm^{-3} t--butylbromide.

hints to EC'dispA2 or EC'dispB2 as likely candidate mechanisms since the theory presented in section 3.1.4 shows that for these two mechanisms alone, n_{eff} is a unique function of k_{norm} (EC'dispA2) or k_{norm} (EC'dispB2) which are dependent on $[A]_\infty$ but not $[Y]_\infty$.

Confirmation of the reaction mechanism taking place was found using the "working curves" of n_{eff} versus k_{norm}, generated as described in Chapter Three for the various EC' mechanistic variants. Thus, the possibility of the simple EC'pure mechanism being appropriate for this example is considered first. The concentrations of F and Bu^tBr used were sufficiently comparable that the full analysis (i.e. without the first order approximation) was necessary. Working curves were therefore calculated for the relevant values of $[A]_\infty$ and $[Y]_\infty$, and from these values of k_{norm} (EC'pure) were extrapolated using the appropriate observed values of n_{eff}. Table 3.2 shows that k_{norm} (EC'pure) is related to W and $[Y]_\infty$ by:

$$k_{norm}\,(EC'pure) = k_{ii}\, C^{-2/3} D^{-1/3}\, [Y]_\infty \qquad 5.4$$

where $C = 8.023\ W^{3/2}\nu^{1/3}$, and hence, if the simple EC' mechanism holds, then straight lines through the origin should result if k_{norm} is plotted against W^{-1}. The results are shown in Figure 5.16, where it can be seen that this behaviour is not apparent and the mechanism may therefore be discounted. This conclusion was confirmed by taking the least squares "best" slopes from plots such as Figure 5.16 and plotting them against $[Bu^tBr]_\infty$ for different values of $[F]_\infty$. A linear dependence of the former should be seen, together with an independence of the latter, if an appropriate choice of mechanism has been made. In fact, a systematic dependence on $[F]_\infty$ was clear, which is not unexpected in the light of Figure 5.15, and this was taken as further evidence for rejecting the EC'pure mechanism as a possible reaction pathway.

The same protocol as applied to the analysis in terms of the EC'pure mechanism was applied to each of EC'preeqm, EC' dispA1 and EC' dispB1 in turn. In each case, a poor dependence of k_{norm} on W^{-1} was found, and moreover, least squares fitting of these plots to determine the "best" slopes revealed a systematic

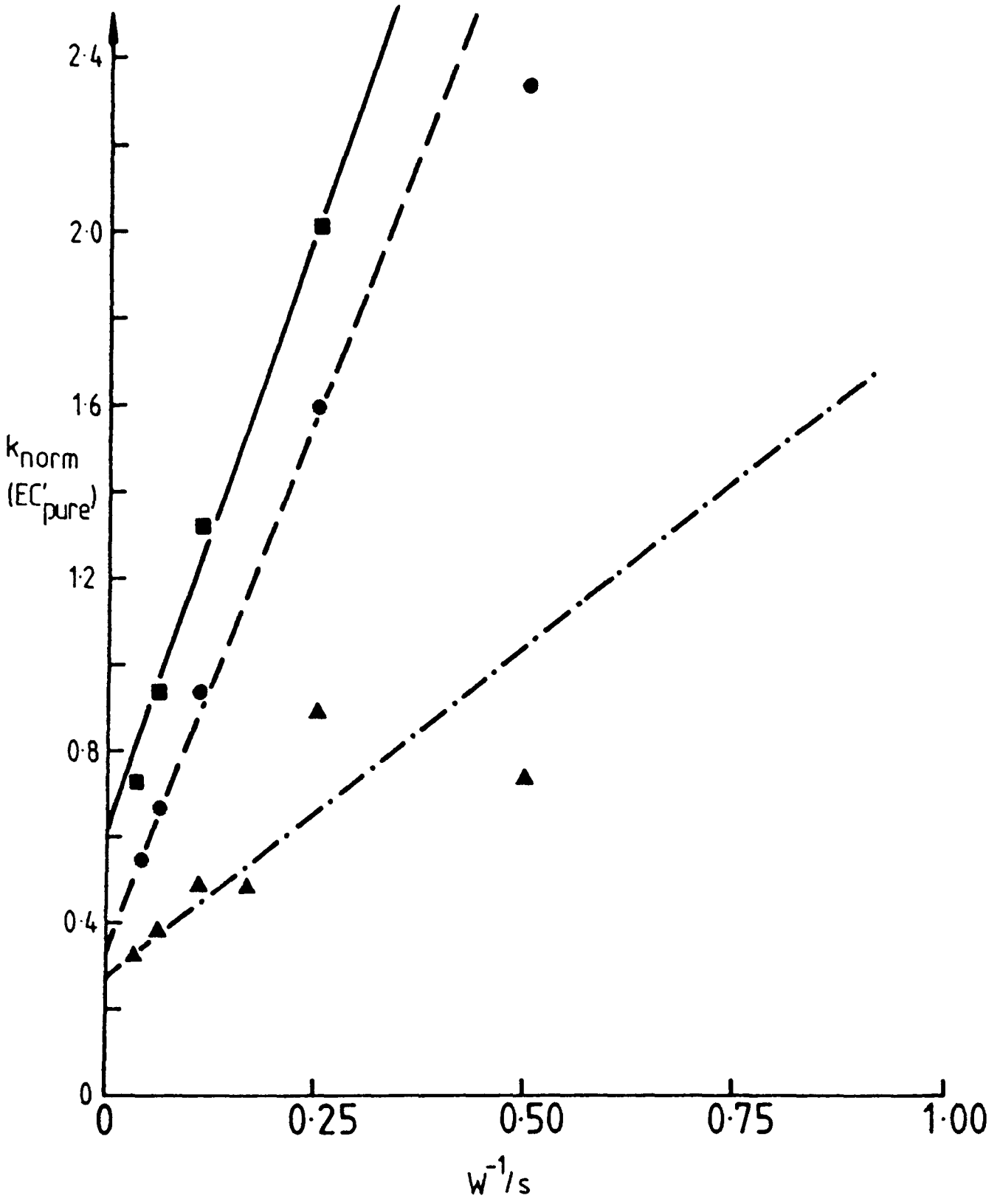


Figure 5.16: Typical plots of k_{norm}(EC'pure) versus W^{-1} for 3.0×10^{-3} moldm^{-3} fluoranthene and ▲, 0.22; ●, 0.89; ■, 1.78 $\times10^{-3}$moldm^{-3} t–butylbromide.

trend in $[A]_\infty$. Comparison with Table 3.2 then immediately rules out these mechanisms.

In contrast, satisfactory k_{norm} versus W^{-1} plots and the correct functional dependence predicted by Table 3.2 resulted from an interpretation in terms of the EC'dispA2 and EC'dispB2 mechanisms. Thus Figure 5.17 shows a typical plot of k_{norm} (EC'dispA2) (or EC'dispB2) against W^{-1}. A good straight line fit through the origin is apparent. Figures 5.18 and 5.19 show that Wk_{norm}(EC'dispA2) (or Wk_{norm}(EC'dispB2)) is independent of the bulk concentration of Bu^tBr, but proportional to the bulk concentration of F. The mechanism of reduction was concluded to be either EC'dispA2 or EC'dispB2, i.e.:

$$F + e^- \rightleftharpoons F^{\cdot -} \qquad \text{(vi)}$$

$$F^{\cdot -} + F^{\cdot -} \rightleftharpoons F + F^{2-} \qquad \text{(vii)}$$

$$F^{2-} + Bu^tBr$$

(viii) → $F + Bu^{t-} + Br^-$ — EC'dispA2

(ix) → $F^{\cdot -} + Bu^{t\cdot} + Br^-$ — EC'dispB2

where step (vii) is rate limiting.

However, it is apparent from Table 3.2 that the two mechanisms cannot be distinguished by RDE voltammetry alone, and since they differ only in steps (viii) and (ix), non–kinetic criteria must be brought to bear on the problem. This might take the form of product analysis, which in this example would involve looking for products derived from either the t–butyl carbanion or the corresponding radical. Alternatively, spin trapping [297,348] the t–butyl radical was attempted here and its intermediacy confirmed (or otherwise) by means of ESR spectroscopy.

Spin trapping experiments were carried out using the spin trap t–butyl–α–phenylnitrone (BPN) [296] to intercept any radical intermediate generated when the mercury RDE was held at potential corresponding to the

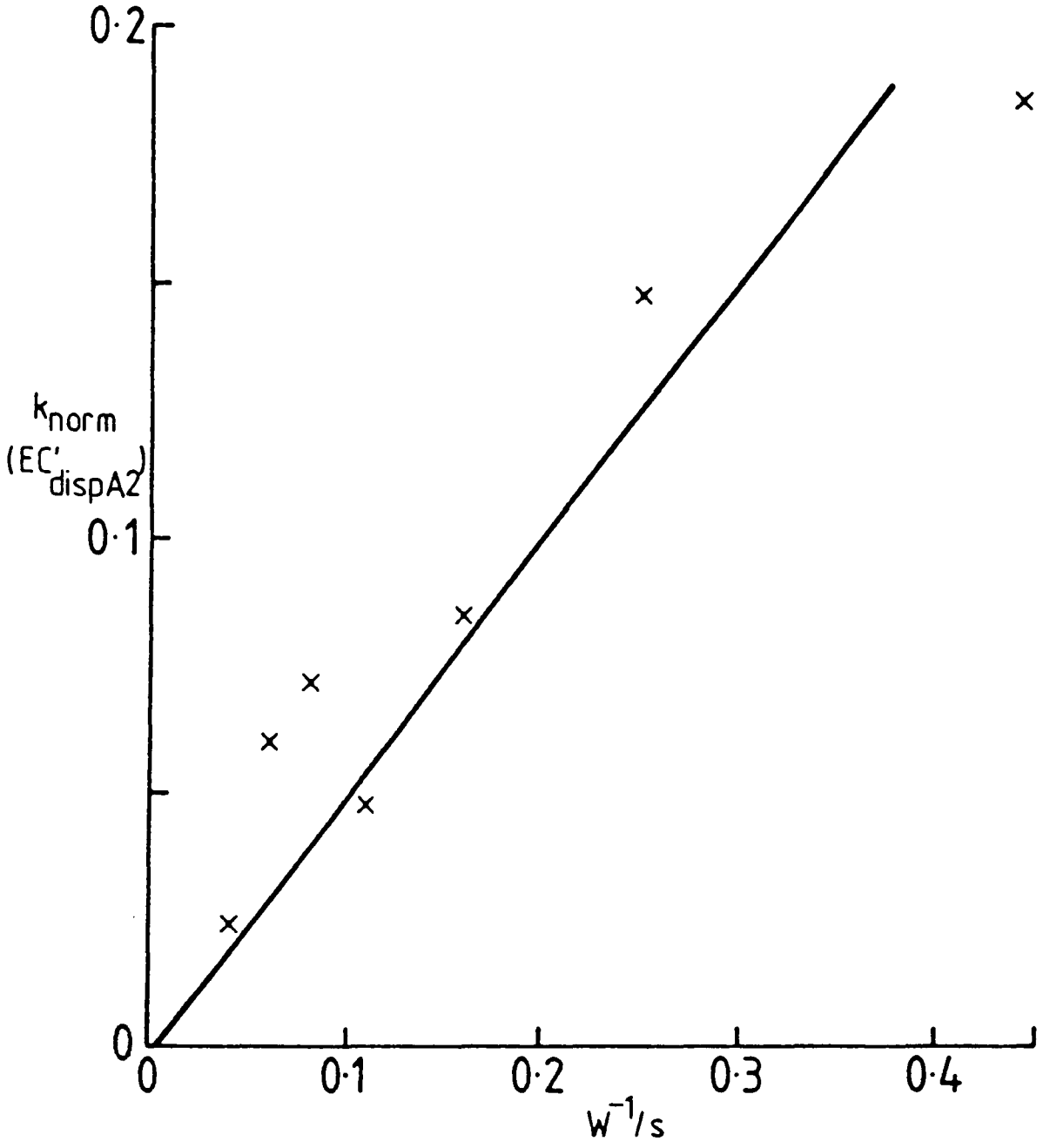


Figure 5.17: A typical plot of k_{norm}(EC'dispA2) as a function of W^{-1} for $[F]_\infty = 3.0\times 10^{-3}$ moldm^{-3} and $[Bu^tBr]_\infty = 0.22\times 10^{-3}$ moldm^{-3}.

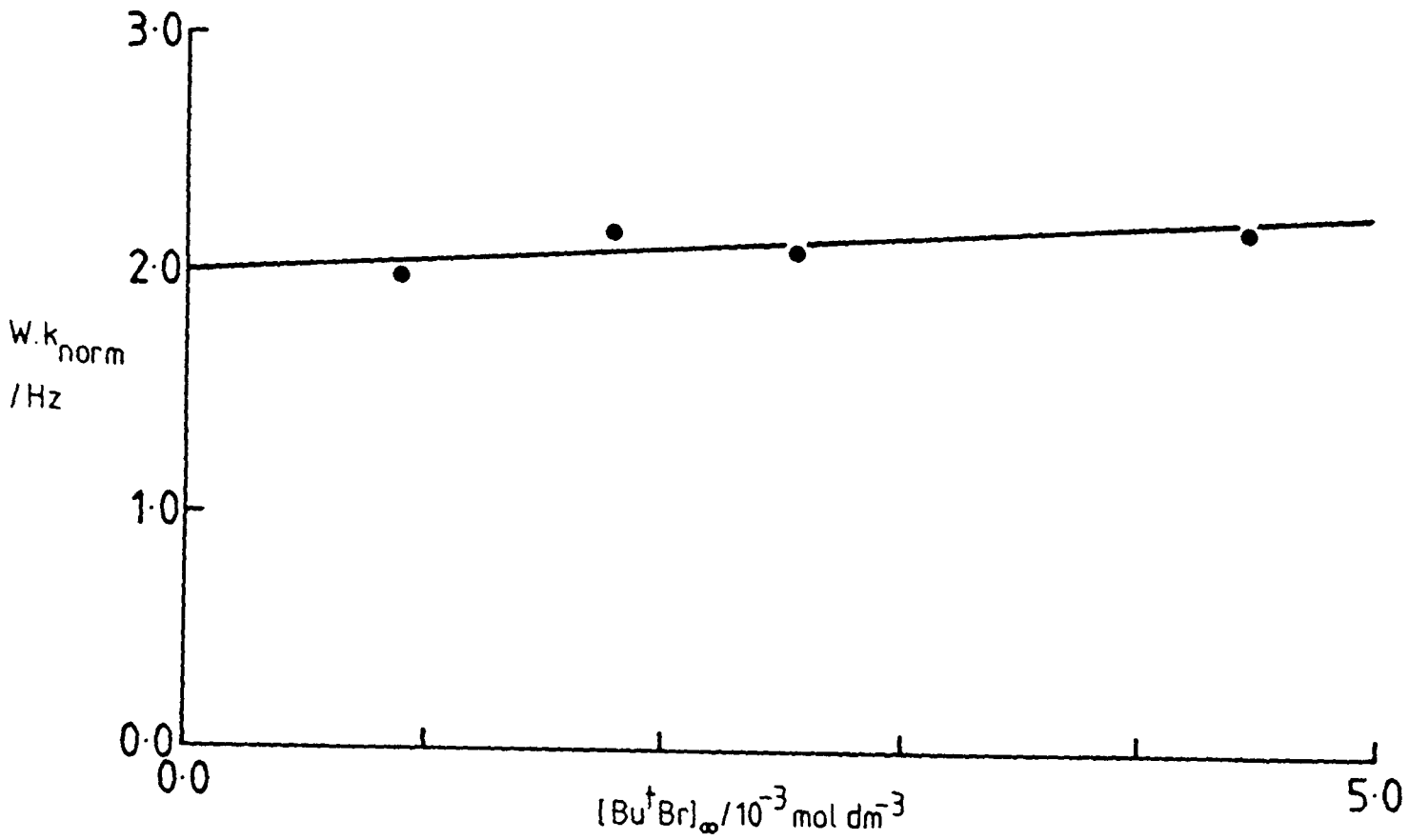


Figure 5.18: A plot showing that the product Wk_{norm}(EC'dispA2) or (EC'dispB2) is essentially independent of $[Bu^tBr]_\infty$.

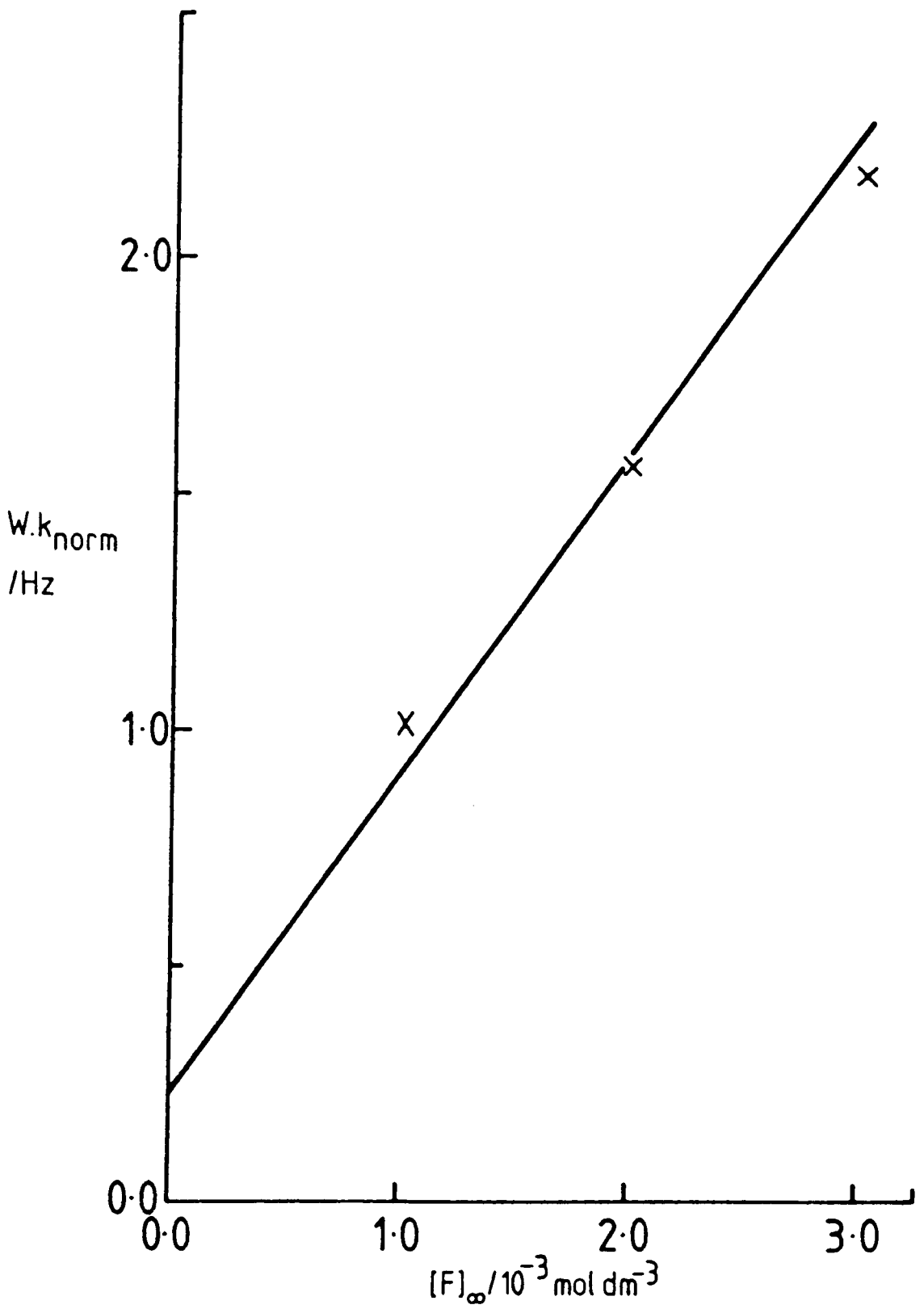
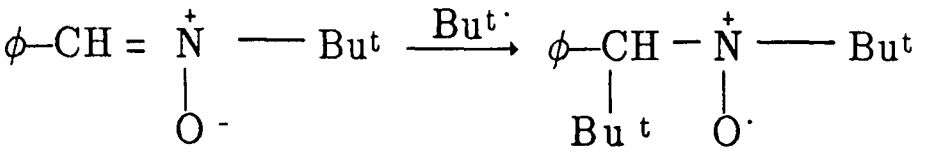


Figure 5.19: A plot showing the linear dependence of the product Wk_{norm}(EC'dispA2) or (EC'dispB2) on $[F]_\infty$.

transport–limited current for the catalytic reduction of Bu^tBr. The experiment was carried out in 0.1 moldm^{-3} tetrabutylammonium tetrafluoroborate/acetonitrile with the spin trap present at a concentration of 0.05 moldm^{-3} [296]. Samples were periodically removed from the RDE vessel and transferred to the ESR spectrometer. In this way, an ESR spectrum of a doublet of triplets was observed after electrolysis for approximately one hour and was attributed to the t–butyl adduct of BPN:



(BPN)

This spectrum gave a nitrogen coupling constant of 15.70±0.05G. Confirmation of the nature of the trapped radical was achieved by generating and trapping the radical by an independent method. Tributyltin chloride is known [348] to supply the required radical on broad–band UV irradiation. A solution of Bu^t_3SnCl (1.0×10^{-3} moldm^{-3}) and 0.1 moldm^{-3} BPN was prepared and on irradiation (using a Wotan XBO 900 W/2 Xenon arc lamp via a Jarrel–Ash 82–410 grating monochromator at 40mW/cm power and around 300nm irradiation), in the absence of oxygen, a spectrum was recorded with a closely similar nitrogen coupling constant to that reported above. The mechanism operating has therefore been shown to produce t–butyl radicals and can be confirmed as EC'dispB2.

The gradient of Figure 5.19, together with the relationship between k_{norm} and $[A]_\infty$ for the EC'dispB2 process:

$$k_{norm}\,(\text{EC'dispB2}) = k_{vii}\,C^{-2/3}D^{-1/3}\,[A]_\infty \qquad 5.5$$

enabled a value for $k_{vii} = 0.44\pm0.20s^{-1}$ to be deduced.

As a general conclusion to this experimental work and to the theory presented in section 3.1.4 for the inclusion of coupled homogeneous kinetics, RDE voltammetry in isolation has been demonstrated to be capable of unravelling the mechanistic subtleties of the EC' mechanism. In particular, all of the various

nuances described for the catalytic process can be distinguished in this way with the exception of EC'dispA2 and EC'dispB2, where either product analysis or spectroelectrochemical methods must also be employed. Thus, the homogeneous reduction of Bu^tBr, using $F^{\cdot -}$ as an electrogenerated catalyst, was shown to proceed via an EC'dispB2 mechanism, with a rate constant for the slow disproportionation (step ($_{vii}$)) of $0.44 \pm 0.2\ s^{-1}$.

CHAPTER SIX

THE INHIBITION OF ELECTRON TRANSFER REACTIONS AT THE MERCURY/ACETONITRILE INTERFACE BY ADSORBED LITHIUM IONS

In this chapter, the electro–reduction of fluoranthene at a mercury electrode in acetonitrile solution is further investigated and, in particular, is shown to be inhibited by trace levels (approximately 10^{-3}moldm^{-3}) of lithium ions. A similar phenomenon is also observed when the work is extended to investigate the reductions of seven other electroactive organic compounds. AC impedance measurements are used to study the adsorption of solvated lithium ions at the mercury/acetonitrile interface, while the adsorption of the electroactive species under consideration is examined using cyclic voltammetry.

6.1 Introduction

In Chapter Five, conclusive evidence for the monolayer adsorption of fluoranthene molecules on mercury electrodes was presented. It has long been recognised that the adsorption of such neutral organic species at the electrode–solution interface can dramatically influence the rate of transfer of electrons between metallic electrodes and electroactive solution material [349–356]. This transfer, of course, proceeds via quantum mechanical tunneling across the interface and, in particular, the work of Gierst [355] and of Weaver [356] has shown that, when the solution species cannot penetrate into the film of adsorbed material, the modification in the tunneling rate depends exponentially on the tunneling

distance:

$$k_d / k_0 \ \alpha \ \exp(-d/r) \qquad 6.1$$

Here, k_d is the rate constant for electron transfer when a film of thickness d (Å) is present, k_0 is the corresponding rate constant in the absence of any film and r (Å) is a constant, typically with a value of about 1 Å [355–357].

Fluoranthene molecules were shown to adsorb reversibly from acetonitrile solution onto mercury electrodes (in Chapter Five) and specifically, it was demonstrated that the molecular orientation on the surface depended on the solution concentration of F [259]. Such measurements have similarities with the thin layer voltammetric studies of Soriaga and Hubbard [206,332,337,358–360], which have been extensively applied to study the irreversible specific adsorption of a wide range of organic species as a function of their structure, supporting electrolyte, solute concentration, solvent and temperature.

The adsorption/desorption properties of F at a mercury electrode are studied in this chapter using steady–state RDE methods in conjunction with cyclic voltammetry and AC impedance spectroscopy. Additionally, the inhibition of electron transfer resulting from a thick layer of solvated lithium ions at the mercury/acetonitrile interface will also be examined.

6.2 Preliminary Experiments

Preliminary rotating disc measurements were conducted on the eight organic species of interest. These were: fluoranthene, crystal violet (CRV), anthraquinone (AQ), 2,3–dichloro–5,6–dicyano–1,4–benzoquinone (DCDCBQ), pyromellitic anhydride (PMA), tetrachloro–1,4–benzoquinone (TCBQ), p–dinitrobenzene (DNB) and tetracyanoethylene (TCE). The structures of these compounds are shown in Table 6.1. Reduction of AQ, CRV, F and DNB at mercury showed reversible waves (Tafel slope $\approx$ 59mV/dec) with the half wave potentials reported in

Table 6.1: The chemical structures of the organic compounds investigated.

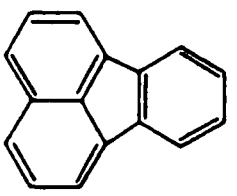
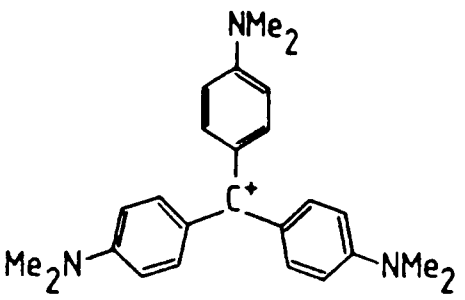
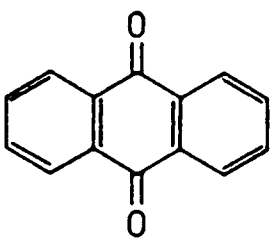
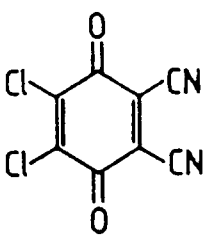
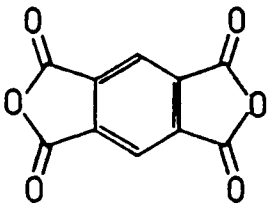
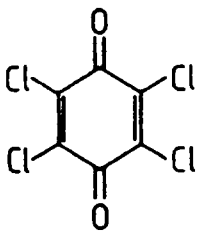
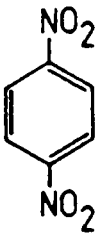
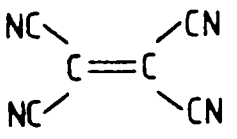
ORGANIC COMPOUND	STRUCTURE
Fluoranthene	
Crystal violet	
Anthraquinone	
2,3–Dichloro–5,6–dicyano–1,4–benzoquinone	
Pyromellitic anhydride	
Tetrachloro–1,4–benzoquinone	
p–Dinitrobenzene	
Tetracyanoethylene	

Table 6.2. Good agreement with the literature was found. The other four compounds are reduced at potentials positive of –0.5V (vs. SCE) and the onset of these reductions are therefore masked by the oxidation of the mercury electrode. Current–voltage "curves" of these compounds thus merely displayed a plateau corresponding to a transport limited current. The half–wave potentials found for the reversible reductions of DCDCBQ, PMA, TCBQ and TCE at a platinum RDE are given in Table 6.2. Agreement with the literature values was once again good.

The limiting currents and their rotation speed dependence, observed for all species, were analysed using the Levich equation and found to be consistent with one electron reductions and the diffusion coefficients cited in Table 6.2.

The effect of lithium ions (Li^+) on these reductions will be considered next. Figure 6.1 shows the result of the presence of 10^{-3} moldm^{-3} $LiClO_4$ on the reduction of F ($3.0x10^{-3}$moldm^{-3}) at a mercury plated RDE. The complete inhibition of the electro–reduction is evident. Corresponding behaviour was found for the reduction of AQ, PMA and DNB (all $3.0x10^{-3}$moldm^{-3}) at mercury. Figure 6.2 shows the case for CRV. It is apparent that at potentials positive of about –2.55V (vs. SCE), the voltammogram is identical, with or without the presence of Li^+, but that an inhibition is observed at more negative potentials, prior to the onset of solvent decomposition at around –3.0V. TCBQ, TCE and DCDCBQ behaved similarly except that the potential required for inhibition was different for each species: –2.60V for TCBQ, –2.50V for TCE and –2.80V for DCDCBQ. These values quoted correspond to the potential at which the current had fallen to half its limiting value. In the following cases, F, AQ, PMA and DNB are therefore referred to as "type A" compounds and CRV, TCBQ, TCE and DCDCBQ as "type B".

For Li^+ concentrations ($[Li^+]_\infty$) below 10^{-3} moldm^{-3}, partial inhibition of all eight reductions was observed. In these cases, the voltammograms showed transport–limited currents of a magnitude between zero and the value observed in the absence of Li^+. Figure 6.3 shows how the "effective" number of electrons transferred (at the limiting current: –2.0V for F and –2.80V for CRV) depends on $[Li^+]_\infty$ for the reduction of $3.0x10^{-3}$moldm^{-3} F and CRV. It can be seen that the critical concentration of $LiClO_4$ required to induce inhibition of electron transfer is

Table 6.2: The reduction potentials and diffusion coefficients of the compounds studied.

COMPOUND	MEASURED VALUES		LITERATURE VALUES		REFs
(Electrode)	$E_{1/2}$*/V	D/cm^{2}s^{-1}	$E_{1/2}$/V	D/cm^{2}s^{-1}	
AQ(Ag)	–0.90	2.40x10^{-5}	–0.89	2.20x10^{-5}	[361,362]
CRV(Hg)	–0.50	1.30x10^{-5}	–0.59	1.30x10^{-5}	[363]
DCDCBQ(Pt)	+0.50	1.62x10^{-5}	+0.51	–	[361]
DCDCBQ(Hg)	–	1.60x10^{-5}	–	–	–
DNB(Hg)	–0.75	2.20x10^{-6}	–0.70‡	–	[364,365]
F(Hg)	–1.80	2.28x10^{-5}	–1.75+	2.30x10^{-5}	[243,315]
PMA(Pt)	–0.50	1.17x10^{-5}	–0.55	–	[366]
PMA(Hg)	–	1.50x10^{-5}	–	–	–
TCBQ(Pt)	–0.05	1.65x10^{-5}	+0.01	1.79x10^{-5}	[296,361]
TCBQ(Hg)	–	1.70x10^{-5}	–	1.79x10^{-5}	[296,361]
TCE(Pt)	+0.15	2.16x10^{-5}	+0.24	1.91x10^{-5}	[366,367]
TCE(Hg)	–	2.10x10^{-5}	–	1.91x10^{-5}	[366,367]

* Half wave potentials measured relative to the SCE

‡ Measured in dimethylformamide as solvent

+ Measured at a platinum electrode

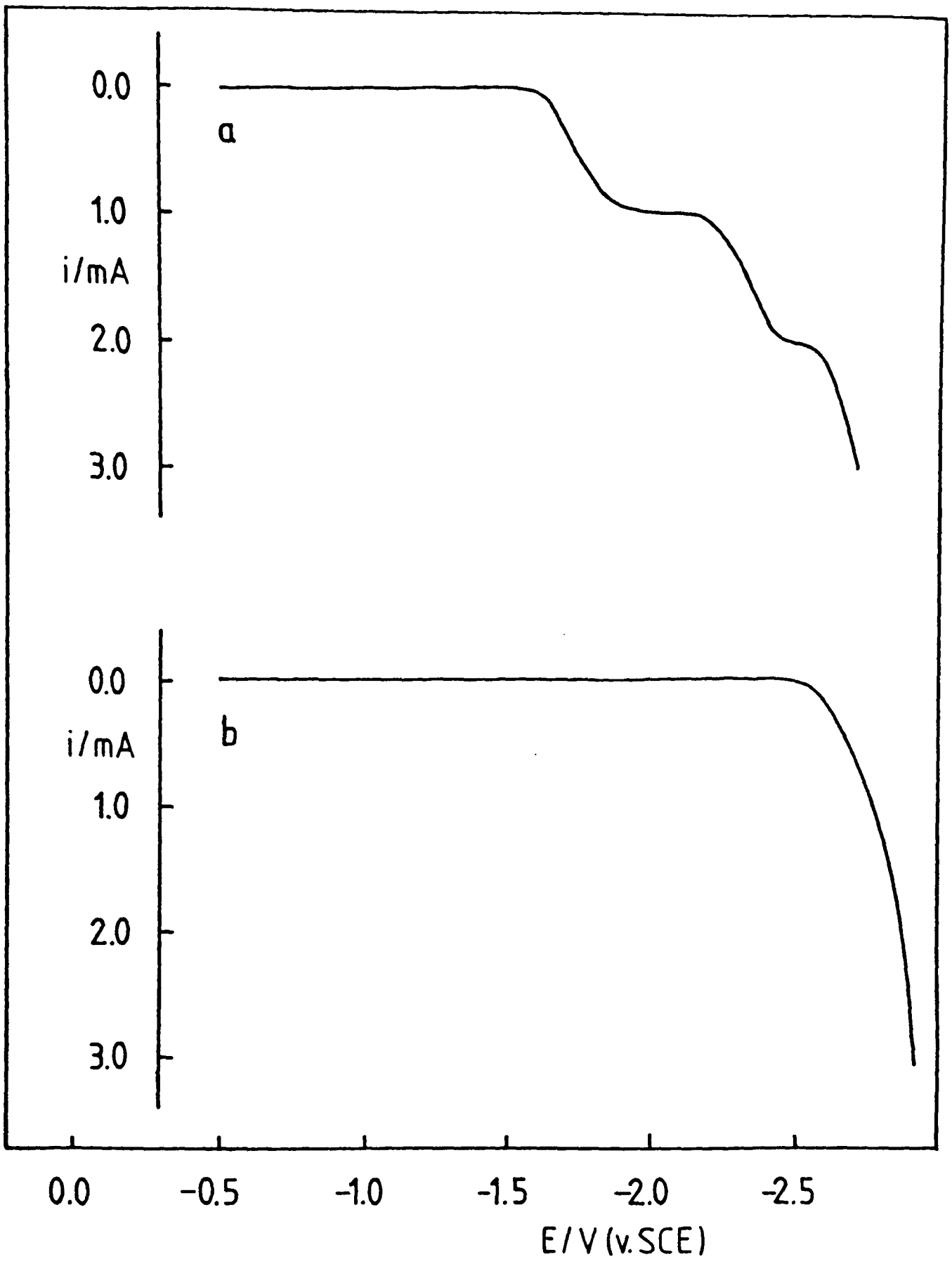


Figure 6.1: RDE voltammograms for the reduction of 3.0×10^{-3} moldm^{-3} fluoranthene in acetonitrile containing a) 0.1 moldm^{-3} TBAP and b) 0.1 moldm^{-3} TBAP + 10^{-3} moldm^{-3} $LiClO_4$. Both voltammograms were recorded at 16.0Hz.

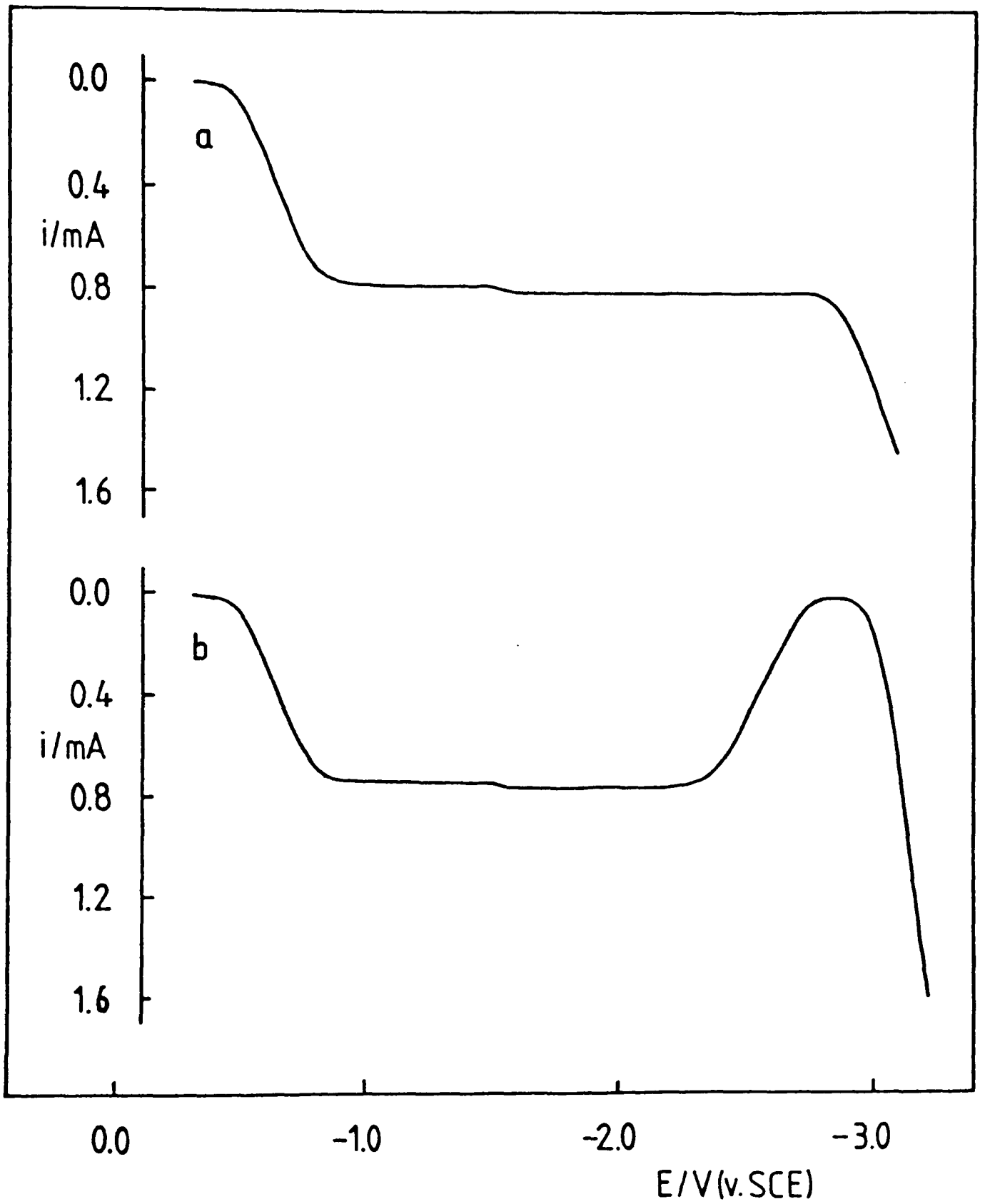


Figure 6.2: RDE voltammograms for the reduction of 3.5×10^{-3} moldm^{-3} crystal violet in acetonitrile containing a) 0.1 moldm^{-3} TBAP and b) 0.1 moldm^{-3} TBAP + 10^{-3} moldm^{-3} $LiClO_4$. Both voltammograms were recorded at 16.0Hz.

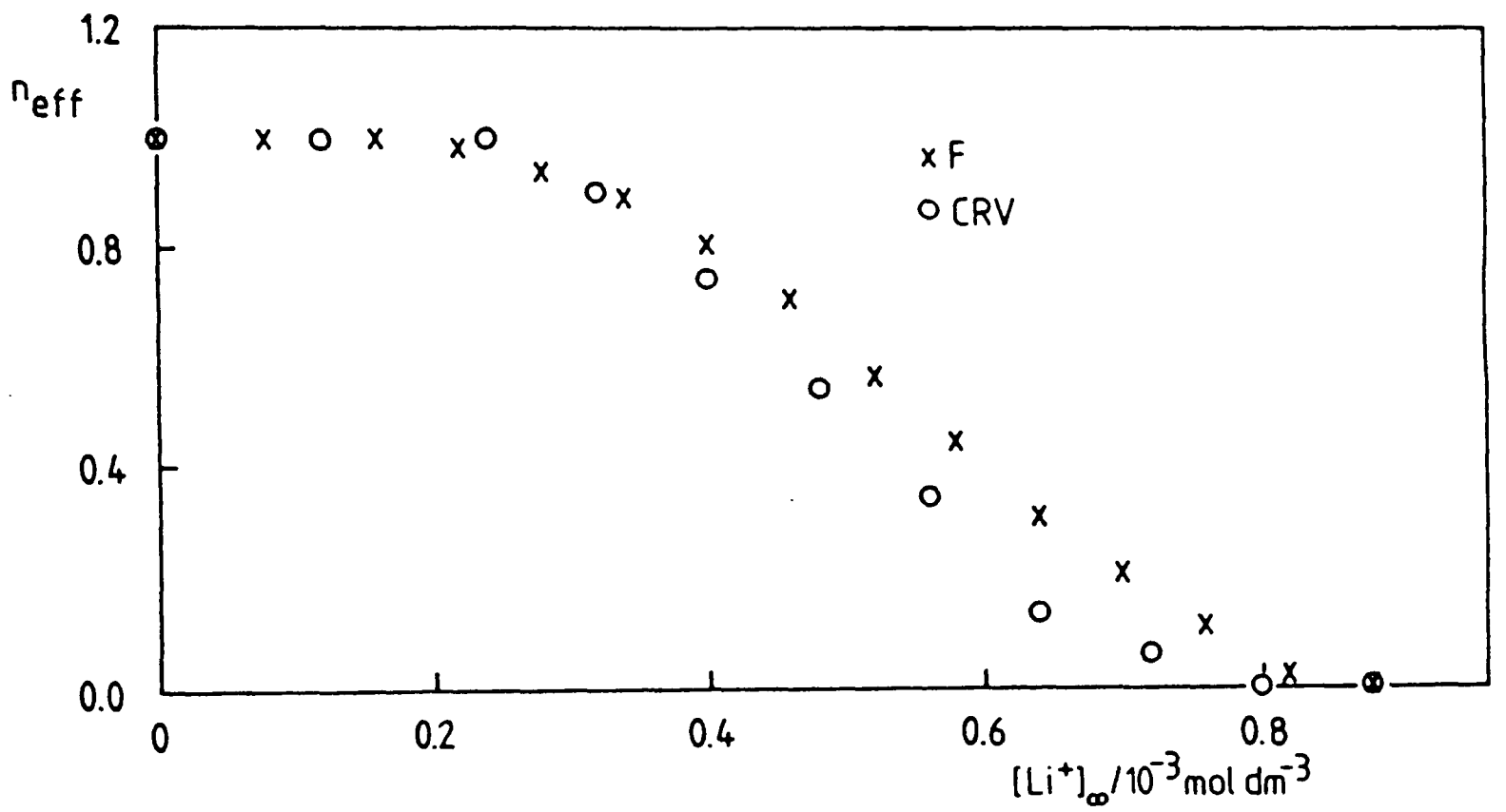


Figure 6.3: The effective number of electrons transferred in the reduction of fluoranthene (3.0×10^{-3} moldm^{-3}) at –2.20V v.SCE (×) and crystal violet (3.5×10^{-3} moldm^{-3}) at –2.70V v.SCE (o), as a function of $[Li]_\infty$. The data was found to be independent of W.

essentially independent of the nature of the electroactive species. Figures 6.4 and 6.5 show that this critical concentration is directly proportional to the concentration of supporting electrolyte (TBAP), but independent of the amount of electroactive material. This hints that the cause of the observed inhibition is the replacement, at the mercury/acetonitrile interface, of TBA^+ by Li^+ ions.

6.3 AC Impedance Studies

This hypothesis was tested further by means of AC impedance measurements. The complex plane impedance plot, measured at a mercury plated electrode potentiostatted at –1.5V in 0.1moldm^{-3} TBAP/acetonitrile, was shown in Figure 5.7 and the determination of the "smoothness" of the electrode and the capacity of the electrode–solution interface from such data was discussed in section 5.1. Figure 6.6 shows how the capacity determined in this way varies with potential for two concentrations of supporting electrolyte. These results, which are in excellent agreement with a previous study [368], may be attributed to a transition between the adsorption of perchlorate ions at potentials relatively positive of the potential of zero charge and the adsorption of tetrabutylammonium ions at negative ones. AC experiments, in which $LiClO_4$ was added to the acetonitrile/0.1moldm^{-3} TBAP solution, showed that although the shape of the impedance plots were qualitatively unchanged, there was a large decrease in the interfacial capacity at concentrations of Li^+ previously observed to cause inhibition of electron transfer at the interface. For $[Li^+]_\infty > 10^{-3}$moldm^{-3}, a capacity of 0.7μFcm^{-2} was measured and found to be essentially potential independent within the limits defined by solvent reduction ($\approx$ –3.0V) and electrode oxidation ($\approx$ –0.5V). This suggests that Li^+, and not ClO_4^-, is adsorbed throughout this potential range, i.e. that the potential of zero charge, in this medium, lies positive of –0.5V. Figure 6.7 shows how the interfacial capacity, measured at –1.5V, varies as $[Li^+]_\infty$ is increased in the presence of 0.1 and 0.05moldm^{-3} TBAP.

AC experiments were next conducted using a solution containing

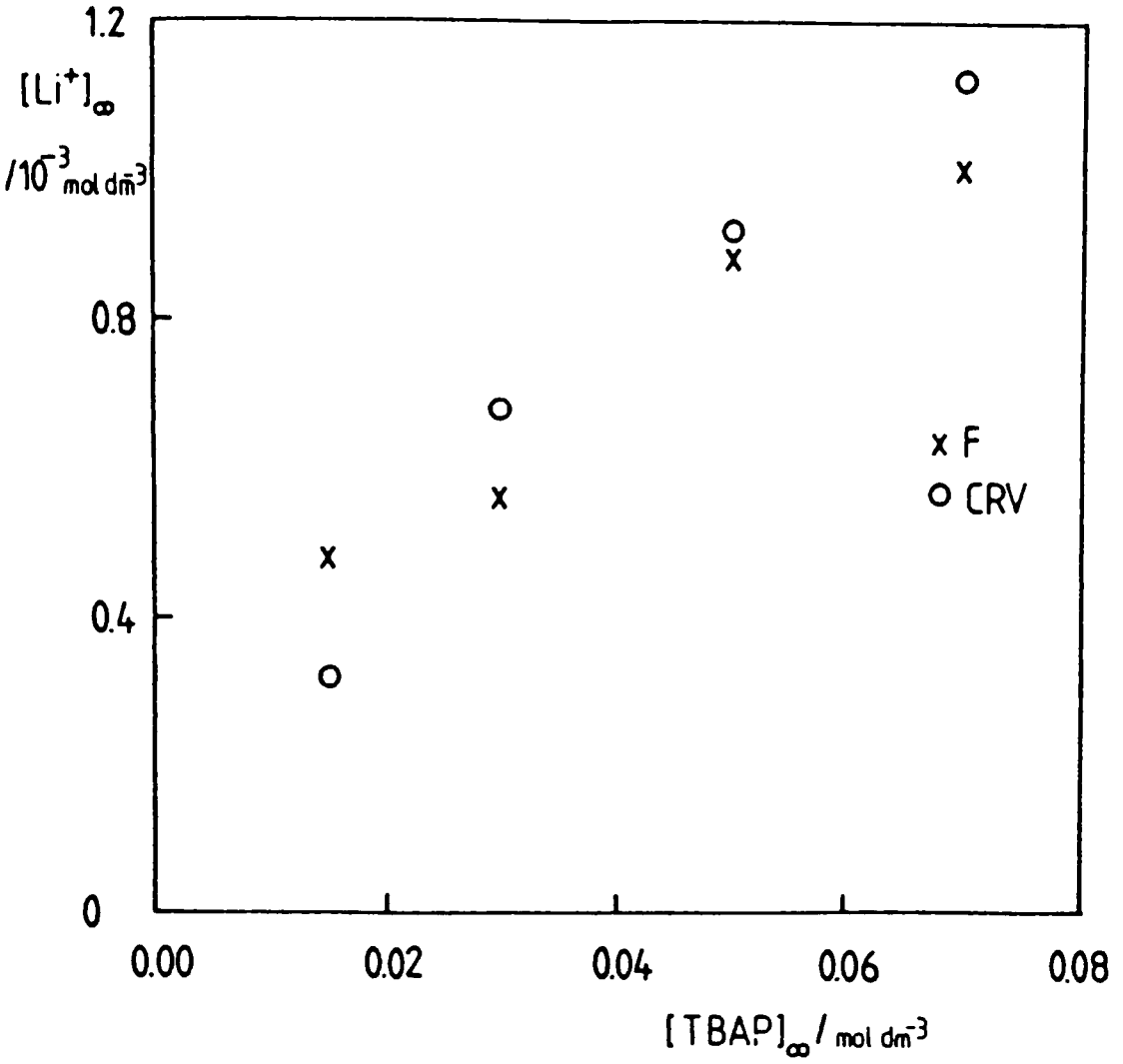


Figure 6.4: The dependence of $[Li^+]_\infty$ required for the complete inhibition of electron transfer to fluoranthene (×) or crystal violet (o), on $[TBAP]_\infty$. The experimental conditions were as specified in Figure 6.4 and once again the data was independent of W.

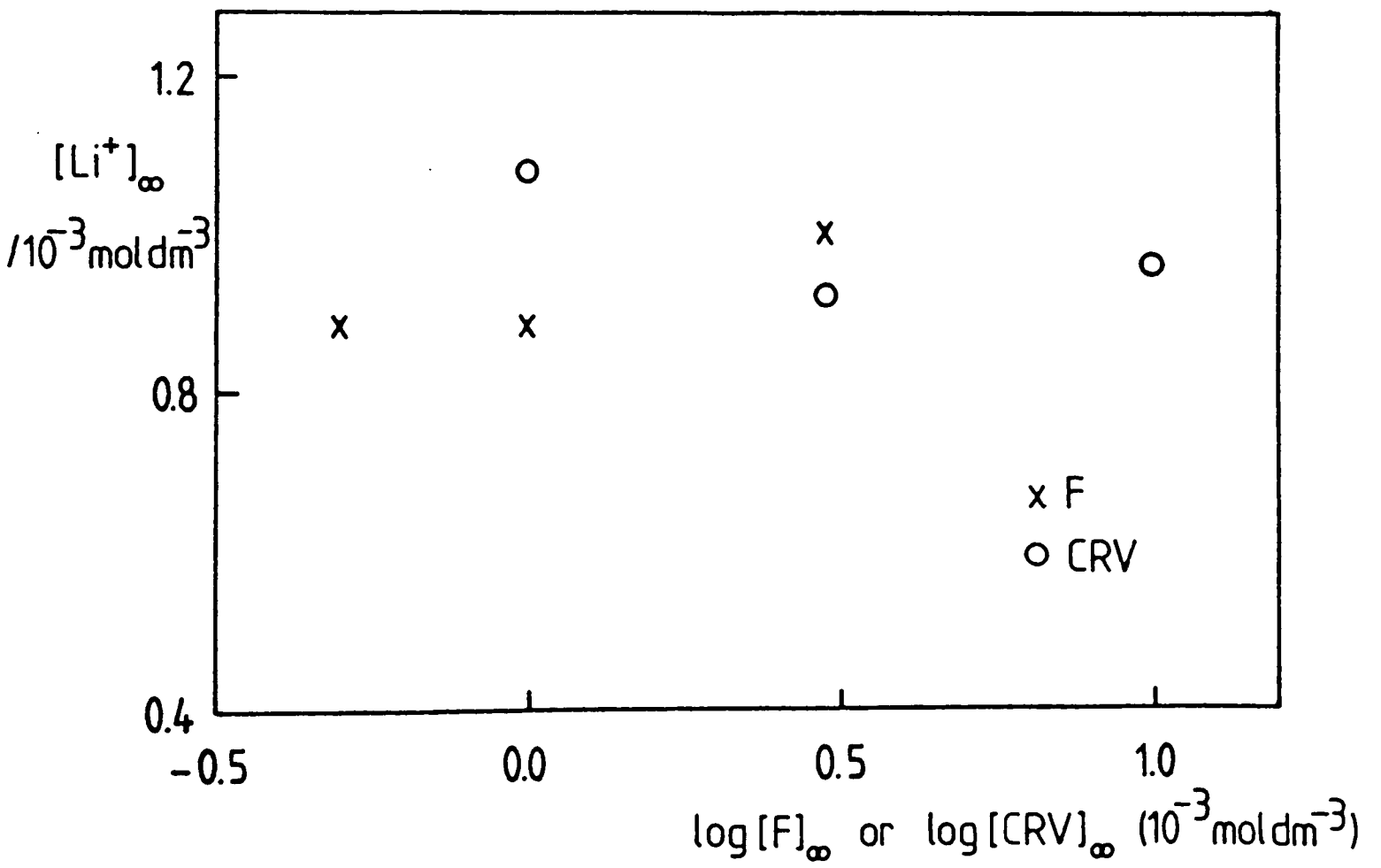


Figure 6.5: $[Li^+]_\infty$ required for the complete inhibition of electron transfer to fluoranthene (×) or crystal violet (o) in 0.05 moldm^{-3} TBAP, on the concentration of the electroactive species. The experimental conditions were as specified in Figure 6.4 and the data was independent of W.

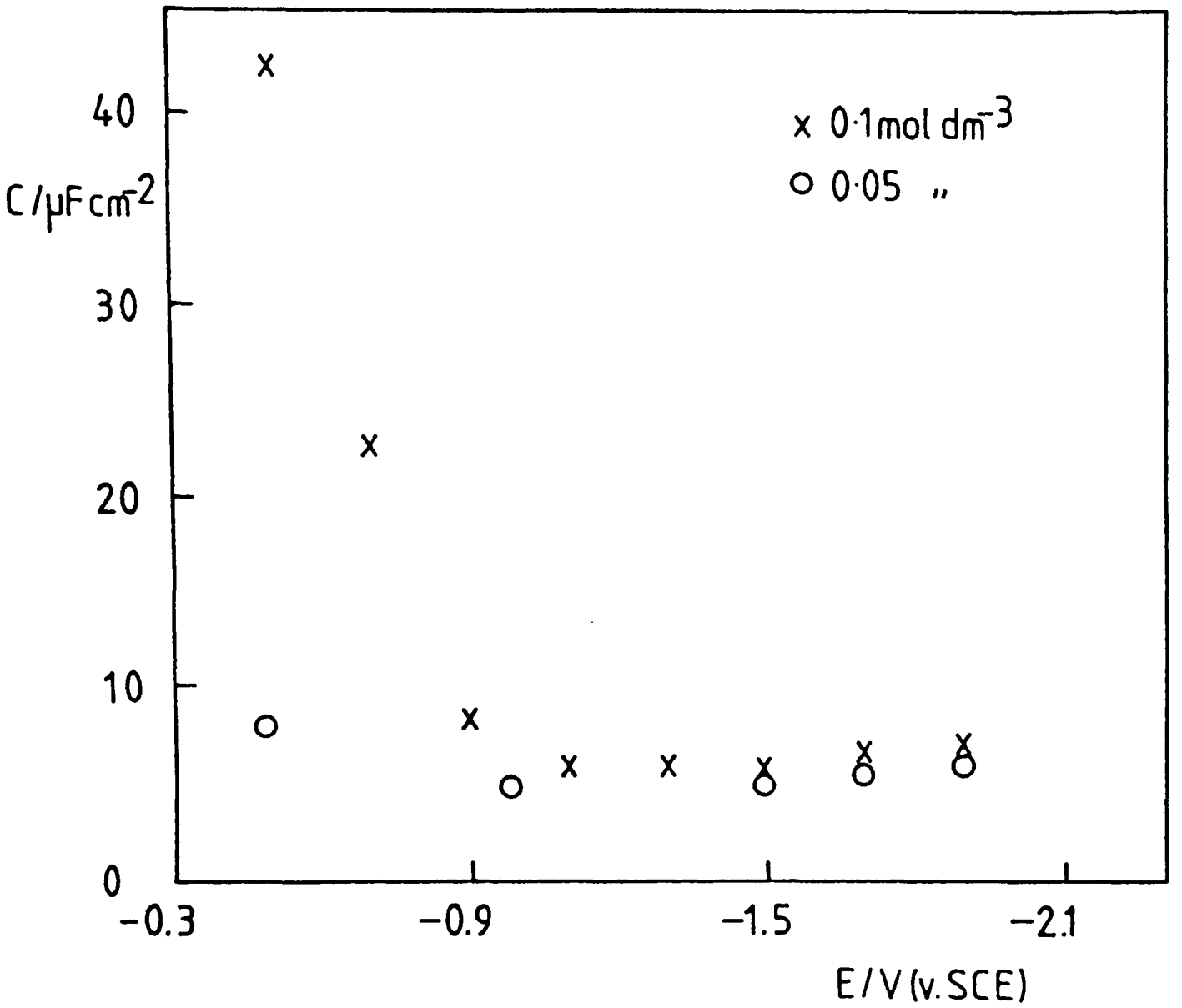


Figure 6.6: The potential dependence of the capacitance of the mercury/acetonitrile interface with 0.1 (×) and 0.05 (o) moldm^{-3} TBAP as electrolyte.

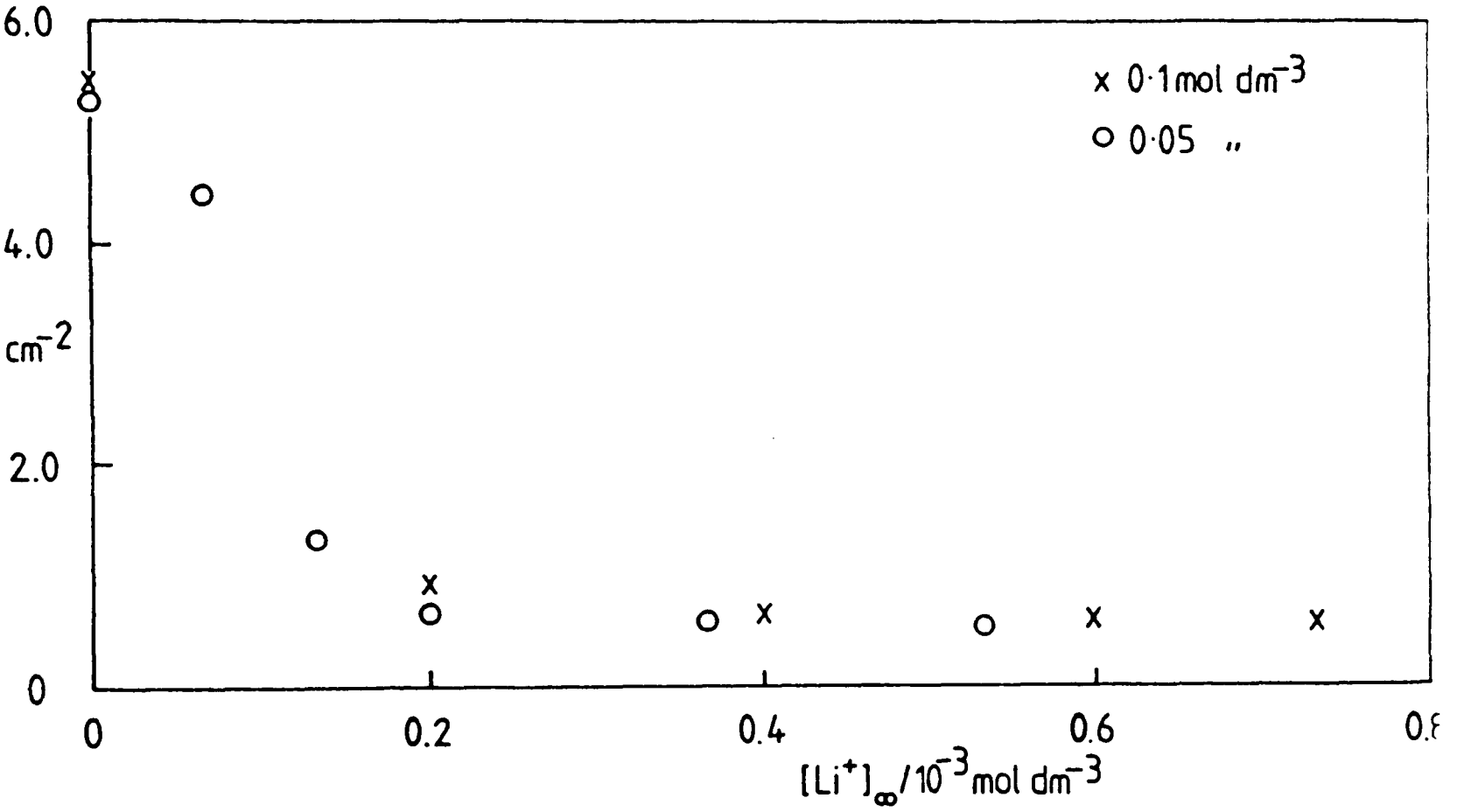


Figure 6.7: The interfacial capacity (at −1.50V v.SCE) of a mercury RDE in TBAP/acetonitrile, as a function of $[Li^+]_\infty$.

$3.0x10^{-3}moldm^{-3}$ F in acetonitrile/0.05 $moldm^{-3}$ TBAP. At an electrode potential of –1.5V the interface again behaved in a purely capacitive manner and, as described in section 5.1, the value for the electrode/solution interfacial capacity of $3.9\mu Fcm^{-2}$, thus determined, was attributed to the adsorption of F at this potential. However, upon the addition of $2.0x10^{-3}moldm^{-3}$ $LiClO_4$, the capacitance decreased to a potential independent (over the range –0.5 to –2.8V) value of $0.7\mu Fcm^{-2}$, as measured in the absence of F.

Further AC experiments were conducted on a solution containing $3.0x10^{-3}moldm^{-3}$ CRV in acetonitrile/0.05$moldm^{-3}$ TBAP as a function of potential and $[Li^+]_\infty$. Figure 6.8 shows a typical impedance spectrum obtained at –1.8V in the absence of Li^+. The semi–circular shape is attributable to the reduction of CRV observed to be taking place at potentials negative of –0.05V. The equivalent circuit is thus a Faradaic resistance in parallel with the double layer capacitance (see section 2.2.2). A slight shift of the semi–circle along the real axis is apparent and this may be attributed to a small uncompensated solution resistance (R_u) (see Appendix One). Identical AC behaviour to that described for –1.80V was found at –2.70V in Li^+ free solutions. On the addition of Li^+ ($2.0x10^{-3}moldm^{-3}$) the behaviour at –1.80V was unchanged, but at the more negative potential the system returned to being essentially capacitative. A value of $0.65\mu Fcm^{-2}$ was calculated for the interfacial capacity. This is in close agreement with the value obtained for the mercury/acetonitrile/Li^+ interface in the absence of CRV ($0.7\mu Fcm^{-2}$).

These observations are all consistent with the adsorption of Li^+ ions at the mercury/acetonitrile interface. Assuming the adsorbed layer to behave as a parallel plate capacitor, it is possible to calculate from Figure 6.7 that the thickness of the layer is about 30Å for $[Li^+] = 2.0x10^{-3}moldm^{-3}$, if a value of 2.0 is assigned to the relative dielectric constant of the solvent at the interface (as compared to a bulk value of 36.5 [368]). Substantial ordering of the solvent molecules at the interface is indicated. Application of equation 6.1 suggests that such a thick film, assuming that it could not be penetrated by the electroactive species, would produce a reduction in the electron tunneling rate constant of the order of some 15 orders of magnitude – entirely consistent with the observed inhibiting effects of Li^+ described above. A

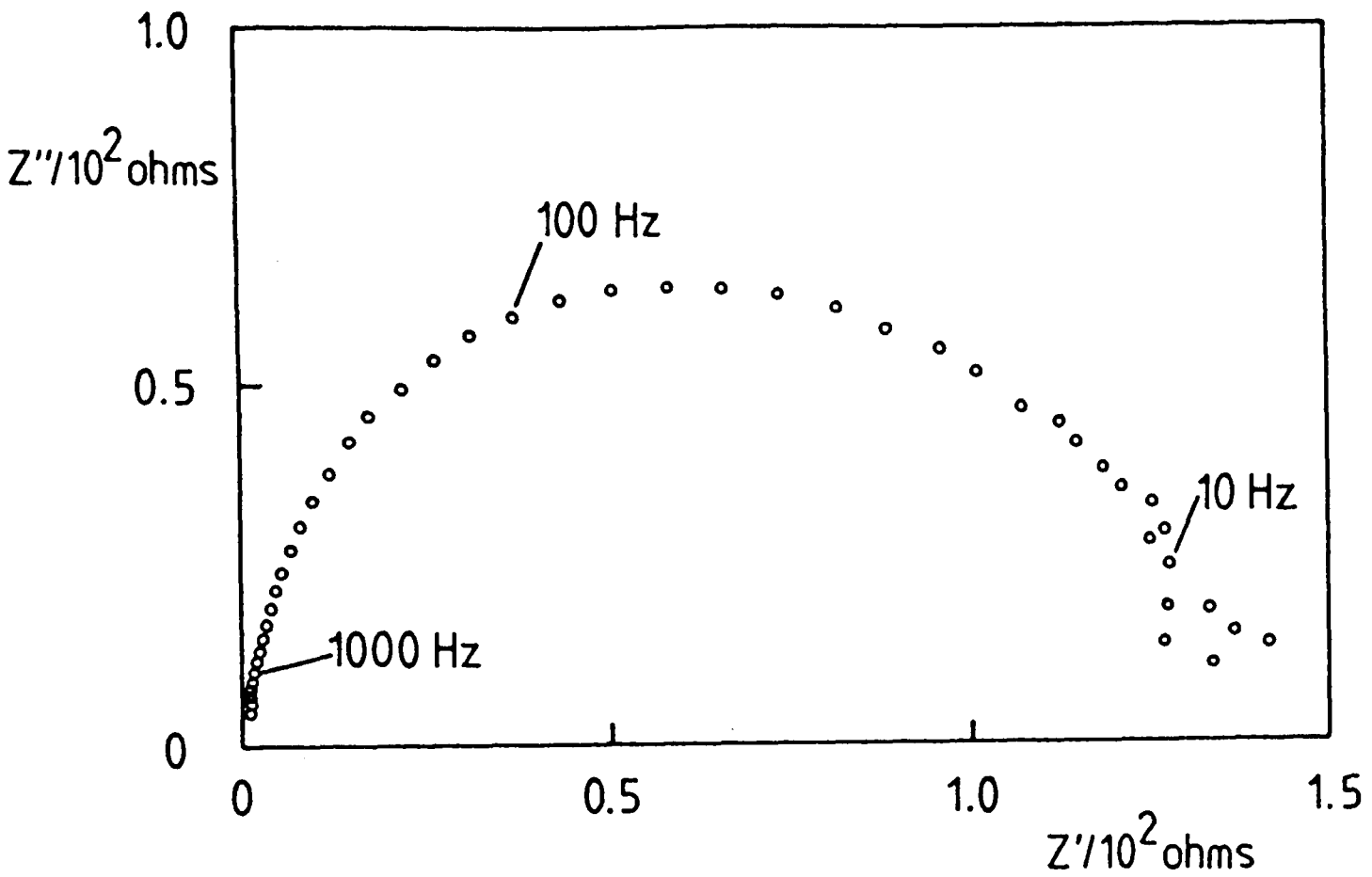


Figure 6.8: The complex plane impedance plot of a mercury RDE in 0.05 moldm^{-3} TBAP/acetonitrile solution containing 3.0×10^{-3} moldm^{-3} crystal violet, measured at –1.80V v.SCE.

similar effect has been reported at the mercury/water interface, where Li^+ ions have been shown, using Tafel analysis and impedance techniques, to influence the kinetics of electrode reactions [369–373].

6.4 Cyclic Voltammetry

Comparison of Figures 6.6 and 6.7 suggests that Li^+ is adsorbed at the mercury/acetonitrile interface at all measurable potentials negative of –0.5V. It is therefore necessary to account for the relative behaviour of the type A and type B compounds. In Chapter Five, F was shown to be weakly adsorbed on mercury and this is now suggested to be the case for all the type A systems studied, while the type B systems are strongly chemisorbed to the surface. Thus Li^+ ions can readily replace type A compounds at all potentials of interest and complete inhibition of the reduction is seen. In contrast, the competition between adsorption of Li^+ ions and type B compounds is such that the former are only adsorbed at rather negative potentials – more negative than the half wave potential for type B reduction. Thus the characteristic off – on – off behaviour of Figure 6.2 is seen as the electrode potential is swept negative.

The variation within the type B compounds of the potential of the onset of inhibition therefore reflects the relative strength of chemisorption of the organic species. This hypothesis was tested by means of experiments in which a mercury electrode was exposed to a solution containing the organic species of interest, then removed from the solution, rinsed with acetonitrile and transferred to a solution containing only acetonitrile/0.1 $moldm^{-3}$ TBAP. The emersion took place under potentiostatic conditions at a potential positive of the reduction potential of the particular species (typically –0.5V). Cyclic voltammograms were then recorded in the "blank" solution. Figures 6.9 and 6.10 show the results of this procedure for CRV. A cyclic voltammogram of a solution containing $3.0x10^{-3}moldm^{-3}$ CRV is shown in Figure 6.9; a typical reversible response ($E_p^{ox} - E_p^{red} \approx 59$ mV) is apparent. Figure 6.10 shows the same electrode after transfer. A single, irreversible reduction

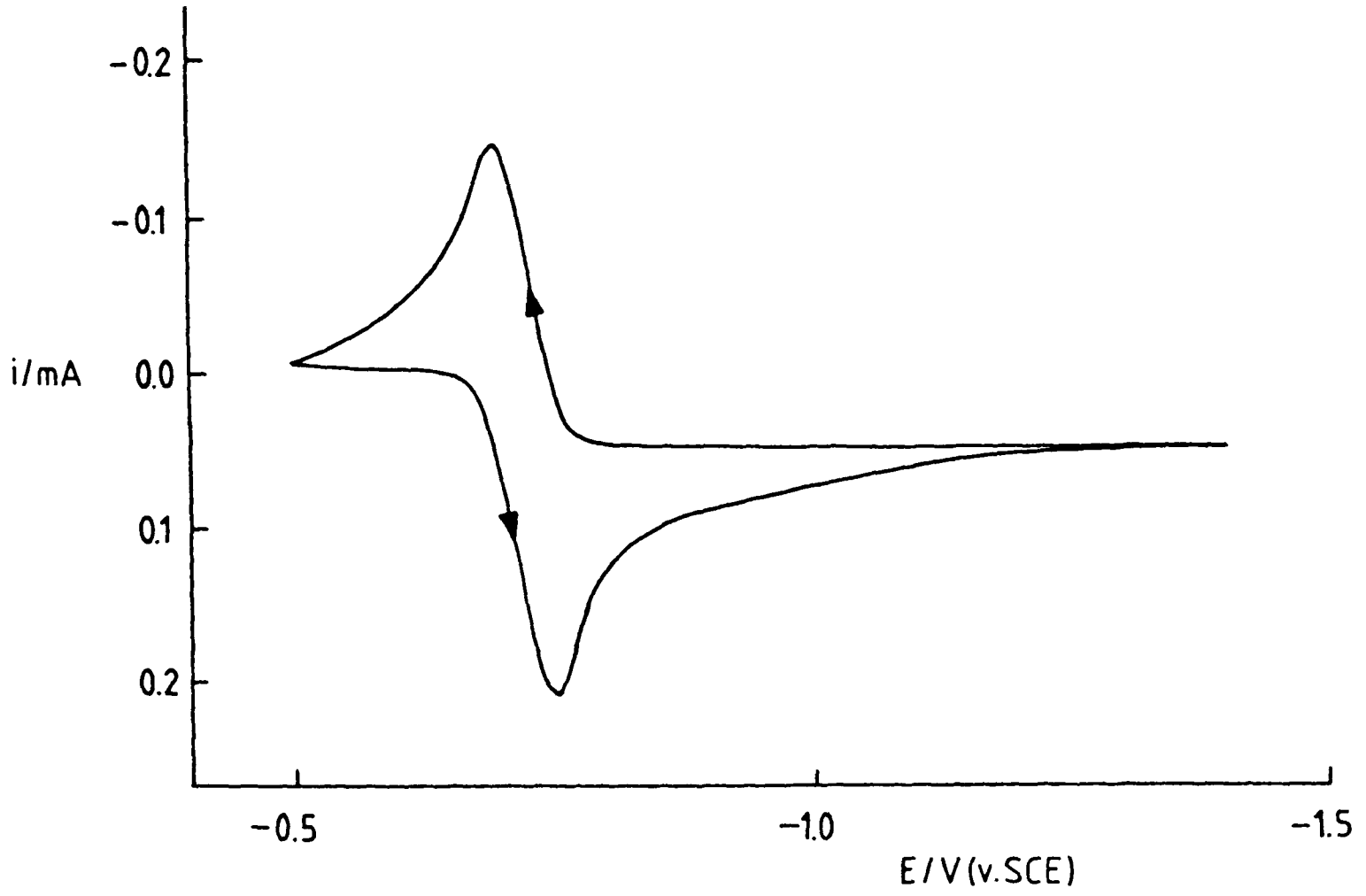


Figure 6.9: A cyclic voltammogram of 3.0×10^{-3} moldm^{-3} crystal violet in acetonitrile/0.1 moldm^{-3} TBAP recorded at a mercury electrode using a scan rate of 100 mVs^{-1}.

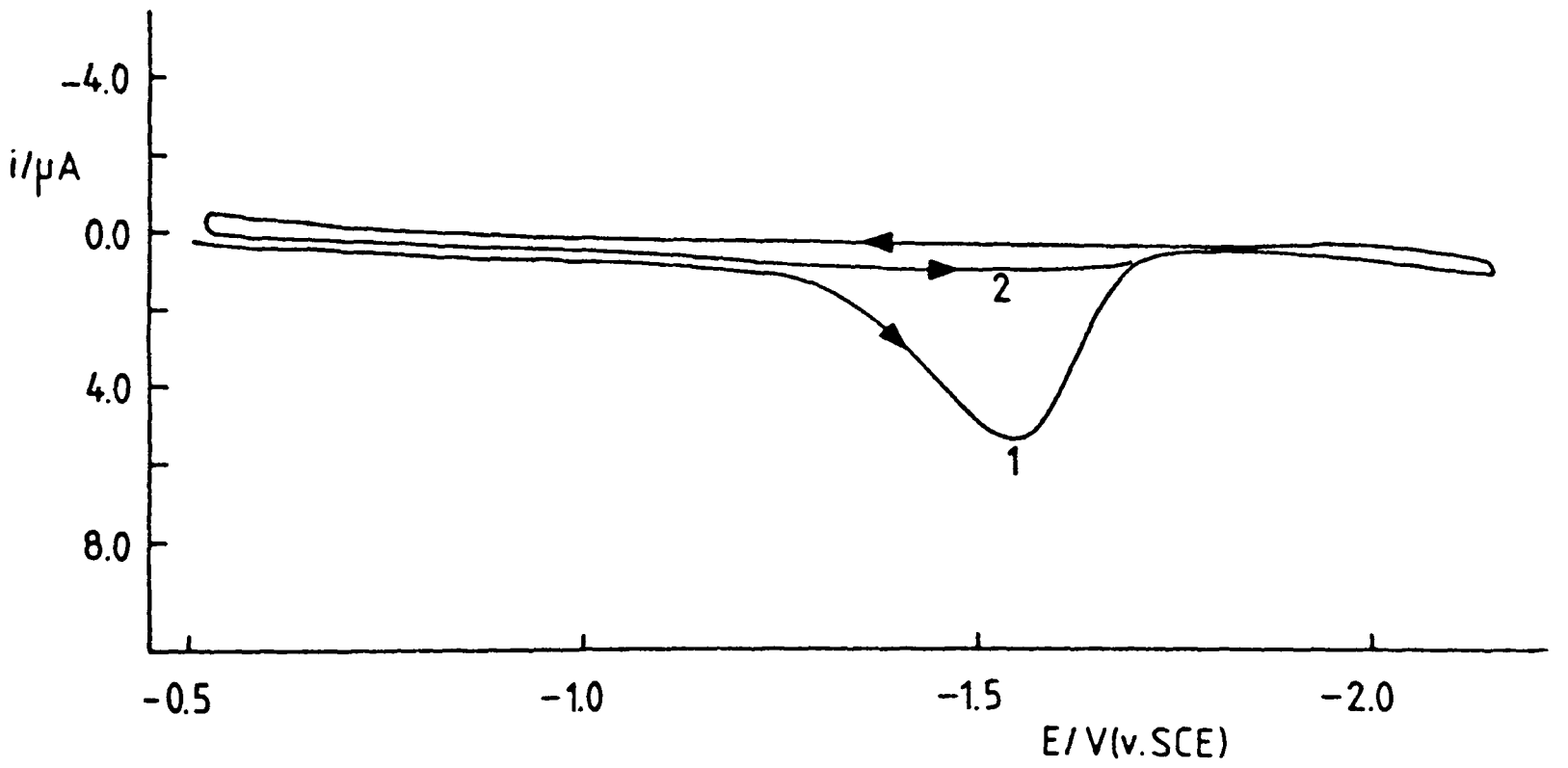


Figure 6.10: A cyclic voltammogram of crystal violet adsorbed on a mercury electrode in acetonitrile/0.1 moldm^{-3} TBAP. A scan rate of 100 mVs^{-1} was used. The first and second cycles are labelled.

peak can be seen, with a peak potential of –1.55V. The reduction occurs at a potential quite negative of that illustrated in Figure 6.9, and is attributed to the reduction of adsorbed CRV. The difference in these reduction potentials represents partly the stabilisation of the organic moiety by the mercury surface and partly the overpotential required for the reduction of the bound molecule. It follows that the reduction seen in Figure 6.9 (and also 6.2a) involving solution phase CRV ($CRV_{(s)}$) takes place in the presence of an adsorbed layer of CRV which is itself unreactive at the potential required for the reduction of $CRV_{(s)}$.

Calculation of the charge passed in the cyclic voltammogram of Figure 6.10 enables an estimate of the surface coverage of CRV to be made. Assuming the electrode to be perfectly flat, a value of 44.7±1.5 $Å^2$ was calculated for the area occupied by one molecule. This compares well with a value of 40.0 $Å^2$ calculated for an "endwise" area of CRV from the known covalent and van der Waals radii of the constituent atoms of the molecule [206,330].

Type B compounds <u>all</u> behaved in a qualitatively similar manner to CRV and cyclic voltammograms of the adsorbed molecules were obtained in each case which showed an irreversible reduction on the first cathodic scan. The same analysis as applied to CRV gave coverages that were consistent with the "endwise" adsorption of each species as shown in Table 6.3. The postulated strong adsorption of the type B compounds was thus verified. Moreover, the adsorption, as revealed by emersion cyclic voltammetry experiments, was found to be unchanged (and show the same coverage) in the presence of Li^+, even if the emersion took place at potentials where inhibition of the electron transfer to the organic compounds of interest was known to occur, including those potentials at which the reduction of unabsorbed organic species would take place. Thus the lithium ion layer must adsorb on top of adsorbed organic material. In addition, the electroreduction of each of the type B compounds in the solution phase must take place in the presence of the chemisorbed compound.

Emersion experiments on the type A compounds showed entirely different behaviour. In the cases of AQ, F and PMA no reduction attributable to chemisorbed material was seen despite the fact that F, at least, undergoes monolayer adsorption at mercury as demonstrated by means of RDE

Table 6.3: Estimated and measured coverages for Type B compounds irreversibly adsorbed as a monolayer on a mercury electrode.

COMPOUND (E_p) †	MEASURED COVERAGE ($Å^2$)	ESTIMATED COVERAGE ($Å^2$)
CRV(–1.55V)	44.7	40.0
TCE(–1.40V)	20.3	19.0
TCBQ(–1.75V)	34.9	31.3
DCDCBQ(–1.50V)	38.6	35.4
DNB(–1.40V)	22.0	25.0

† Peak potential for the reduction of the chemisorbed material.

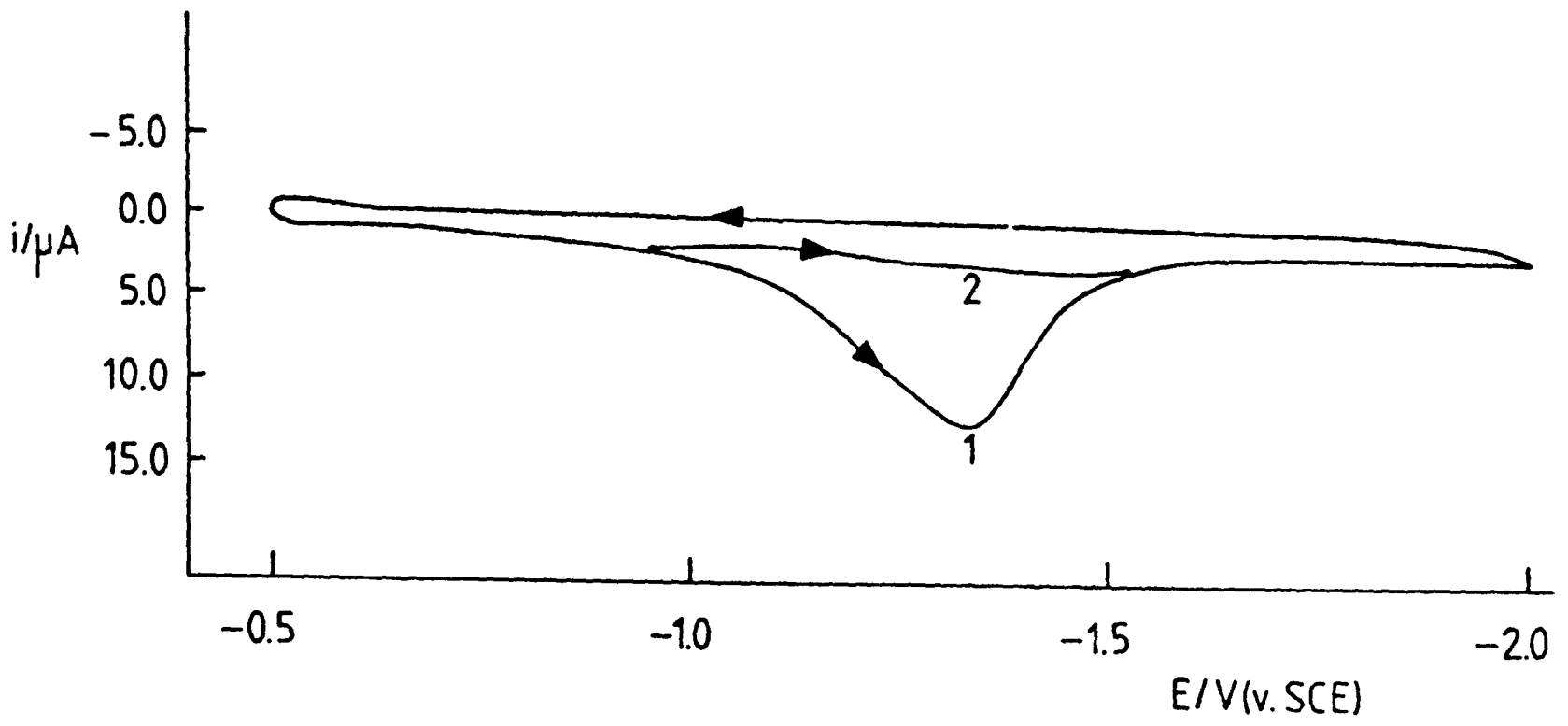


Figure 6.11: A cyclic voltammogram of p–dinitrobenzene adsorbed on a mercury electrode in acetonitrile/0.1 moldm^{-3} TBAP. A scan rate of 100 mVs^{-1} was used. The first and second cycles are labelled.

chronoamperometry, in Chapter Five. It may be concluded that F adsorption is weak and that the layer cannot survive the transfer and/or becomes desorbed in the "blank" environment. Type A species therefore undergo only weak, or no, adsorption at mercury. DNB was an exception (see Figure 6.11) in that whilst displaying type A behaviour, a cyclic voltammogram of material chemisorbed onto an emersed electrode could nevertheless be seen. DNB must therefore be sufficiently strongly chemisorbed to survive transfer and emersion, yet not so tightly bound as to not be expelled by Li^+ ions, at potentials positive of –0.70V.

6.5 Conclusions

Trace levels of lithium ions (approximately $10^{-3}moldm^{-3}$) have been shown to have a dramatic inhibitory effect on the rate of reduction of the eight species of interest. The use of AC impedance methods to characterise the mercury/acetonitrile interface reveals that in the presence of sufficient Li^+ ions to inhibit electron transfer, a low interfacial capacity consistent with a thick layer of adsorbed ions and oriented solvent molecules is observed. The inhibition is shown only to occur at potentials and concentrations at which Li^+ is adsorbed and is thus rationalised in terms of equation 6.1. The increased distance between electrode and electroactive solution species caused by this layer produces an approximate reduction of about 10^{15} in the rate of electron tunneling.

Type A compounds (F, AQ and PMA) are shown to be weakly bound to the mercury surface and their electro–reduction at mercury is inhibited by Li^+ at all potentials. Type B compounds (CRV, TCE, TCBQ and DCDCBQ) adsorb more strongly and inhibition occurs only at potentials appreciably negative of the reduction potential of the compound.

CHAPTER SEVEN

THE ELECTRO–REDUCTION OF FORANE AT THE ROTATING DISC ELECTRODE

In this chapter, forane is shown to be electro–inactive on all conventional electrode materials and thus the need for a mediated reduction of this anaesthetic is demonstrated. The radical anion of fluoranthene is shown to be capable of bringing about the reduction of forane both in homogeneous solution and when the mediator is attached to a polymer backbone and immobilised on an electrode surface. The former process is analysed using RDE voltammetry and in–situ ESR measurements while the reduction of forane at a polymer modified electrode is demonstrated, using cyclic voltammetry, to be limited by the stability of the polymer coat. Possible interferences to the $F^{\cdot -}$/forane current response from other gases present in a clinical environment, are also investigated.

7.1 Reduction of Forane

Preliminary experiments were undertaken to examine the electroactivity, or otherwise, of forane at a range of conventional electrode materials. Rotating disc voltammetry showed that the gas was inert towards reduction at silver, gold, platinum and mercury electrodes in both aqueous and non–aqueous solvents (acetonitrile and dimethylformamide). On mercury, in dimethylformamide, a reduction was observed at around –3.0V (vs. SCE), but this is too close to the potential of solvent decomposition as to preclude any analytical applications. This

inertness is not surprising in the light of the chemical properties of forane discussed in Chapter One [47]. Attention was therefore directed towards finding a suitable mediator for the electron transfer. In Chapter Five, the radical anion of fluoranthene was shown to be effective in catalysing the reduction of t–butyl bromide in acetonitrile solution and therefore the extension of this, to mediate the reduction of forane, is examined here.

7.1.1 Mediation via the Fluoranthene Radical Anion

Figure 7.1 shows typical rotating disc voltammograms of $3.0x10^{-3}moldm^{-3}$ F in the presence of increasing quantities of forane. A catalytic process is clearly taking place and the mediated reduction of forane by $F^{\cdot -}$ can be inferred. Forane concentrations were calibrated gravimetrically. Thus, the limiting reduction current, obtained using $3.0x10^{-3}moldm^{-3}$ F as mediator, was measured for a range of known forane concentrations, made up from weighed samples of the liquid anaesthetic. Measurement of i_{lim} at each concentration was repeated five times and the resultant calibration curve is shown on Figure 7.2. Limiting currents, obtained using the same ($3.0x10^{-3}moldm^{-3}$ F) mediator were then determined for solutions saturated with (0 – 5%) forane via the vapouriser described in Chapter Four. The concentration at any particular ratio of carrier gas : forane was then found from the calibration curve determined above and shown in Figure 7.2.

The limiting current–rotation speed data obtained from voltammograms such as those in Figure 7.1 is shown in Figure 7.3 and comparison of these results with the behaviour observed in the absence of forane enables the effective number of electrons transferred at each rotation speed to be deduced. In Chapters Three and Five, n_{eff} was shown to be most naturally plotted against W^{-1} and a representative plot of this type is illustrated in Figure 7.4 for varying forane concentrations at constant ($3.3x10^{-3}moldm^{-3}$) $[F]_{\infty}$. Two significant features are apparent. Firstly, at high rotation speeds n_{eff} approaches unity. This was also observed for the F/Bu^{t}Br system (see Figure 5.15) and is an obvious fundamental requirement for a catalytic process involving a one electron electrochemical step. Secondly, a systematic dependence of n_{eff} on $[Y]_{\infty}$ is observed. This immediately rules out EC'dispA2 and

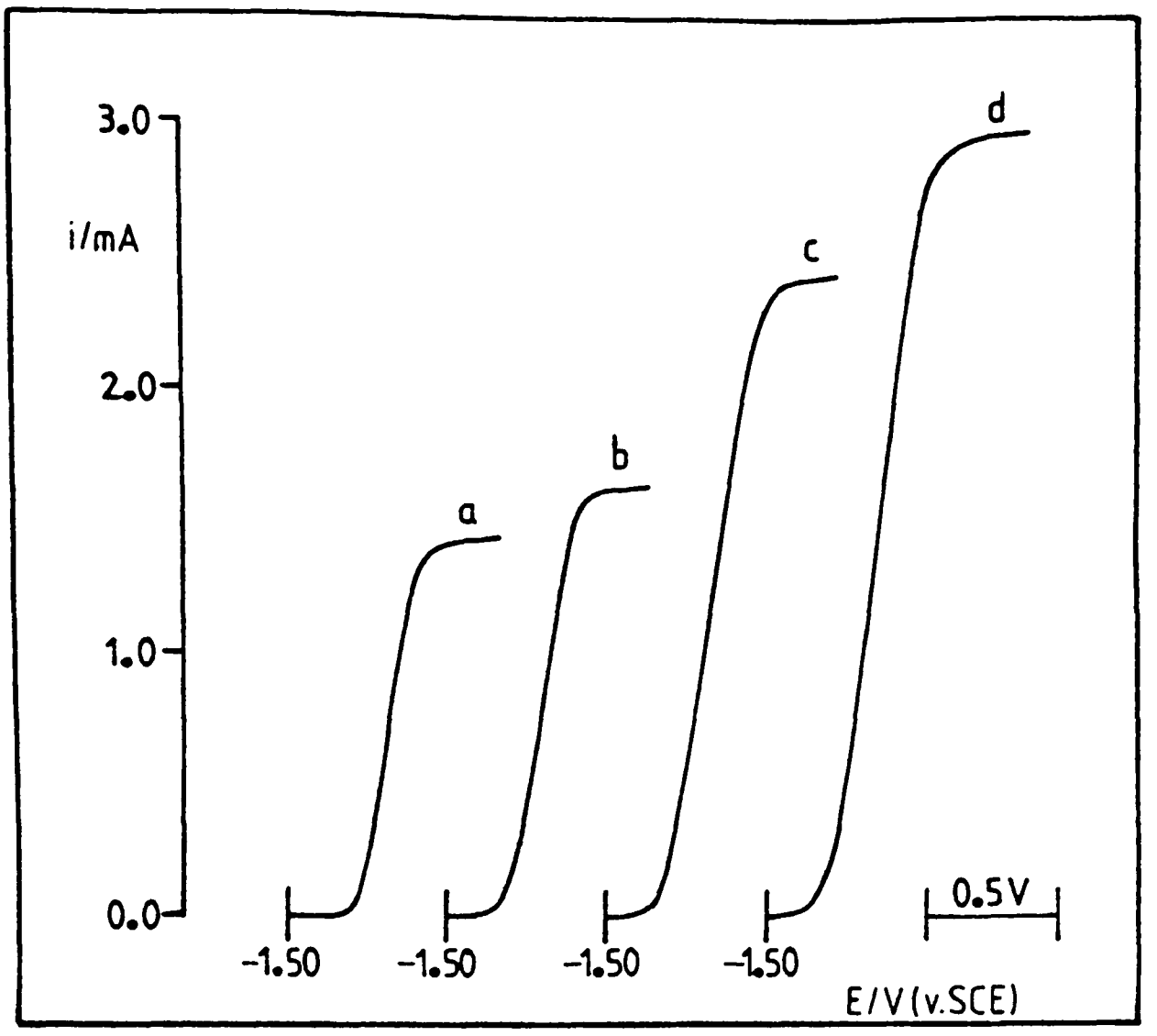


Figure 7.1: RDE voltammograms for the reduction of 3.0×10^{-3} moldm^{-3} fluoranthene in acetonitrile/0.1 moldm^{-3} TBAP in the presence of a) 0.0, b) 1.7, c) 3.3, d) 5.0 $\times10^{-3}$moldm^{-3} forane. All data were obtained at W = 16.0Hz.

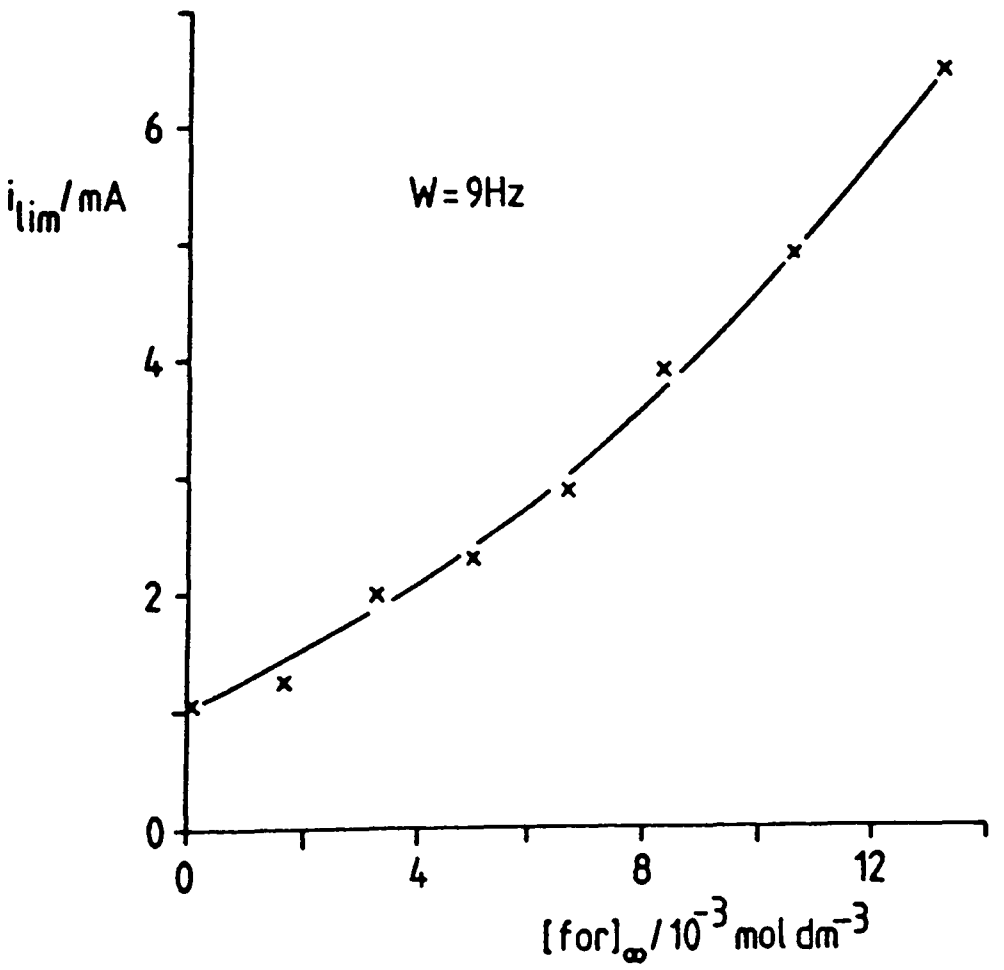


Figure 7.2: Calibration curve of i_{lim} versus $[forane]_\infty$. Data obtained using $[F]_\infty = 3.3\times10^{-3}$ moldm^{-3}.

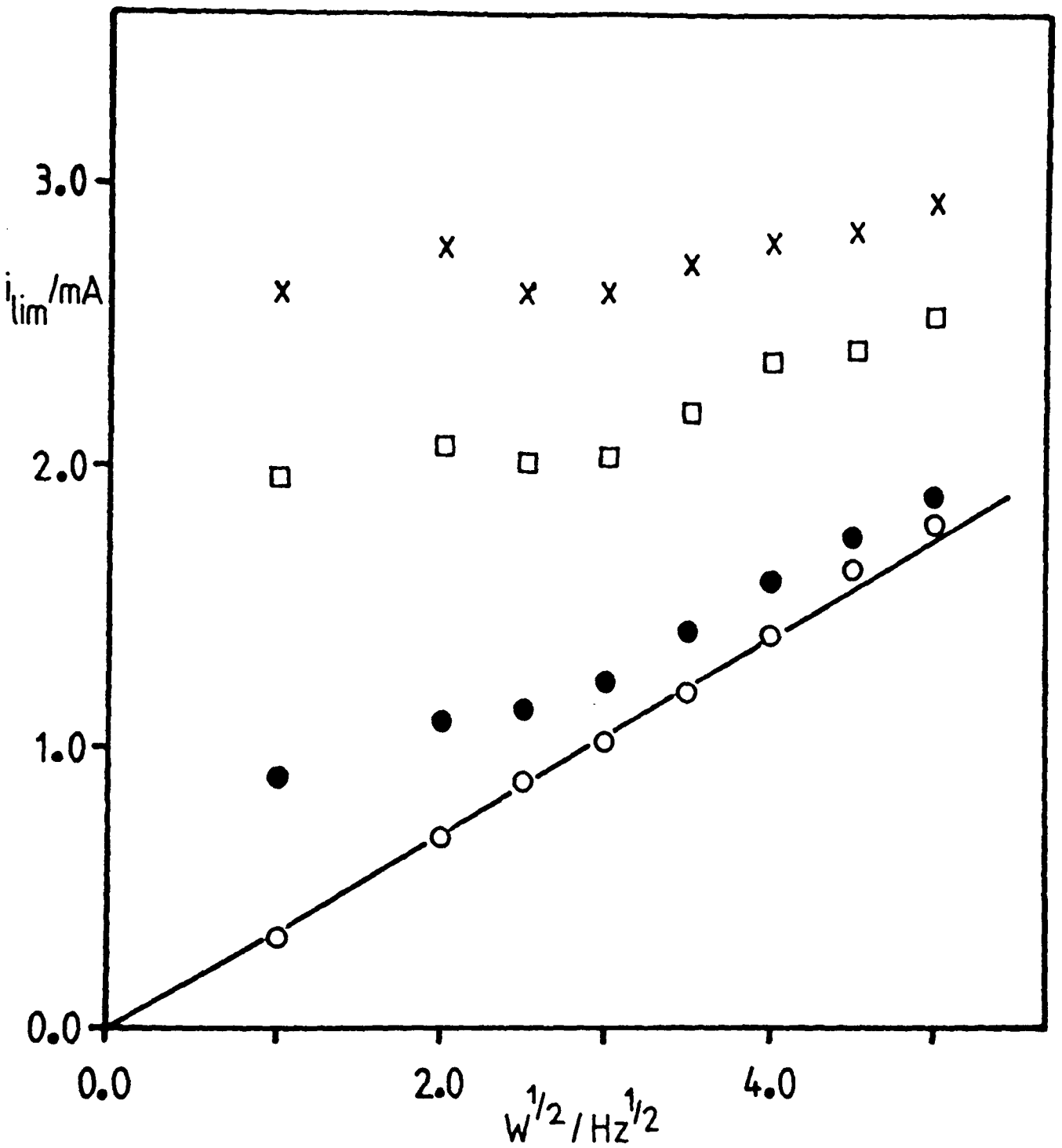


Figure 7.3: The W dependence of i_{lim} for the reduction of 3.0×10^{-3} moldm^{-3} fluoranthene in the presence of (o) 0.0, (●) 1.7, (□) 3.3, (×) 5.0 $\times10^{-3}$moldm^{-3} forane.

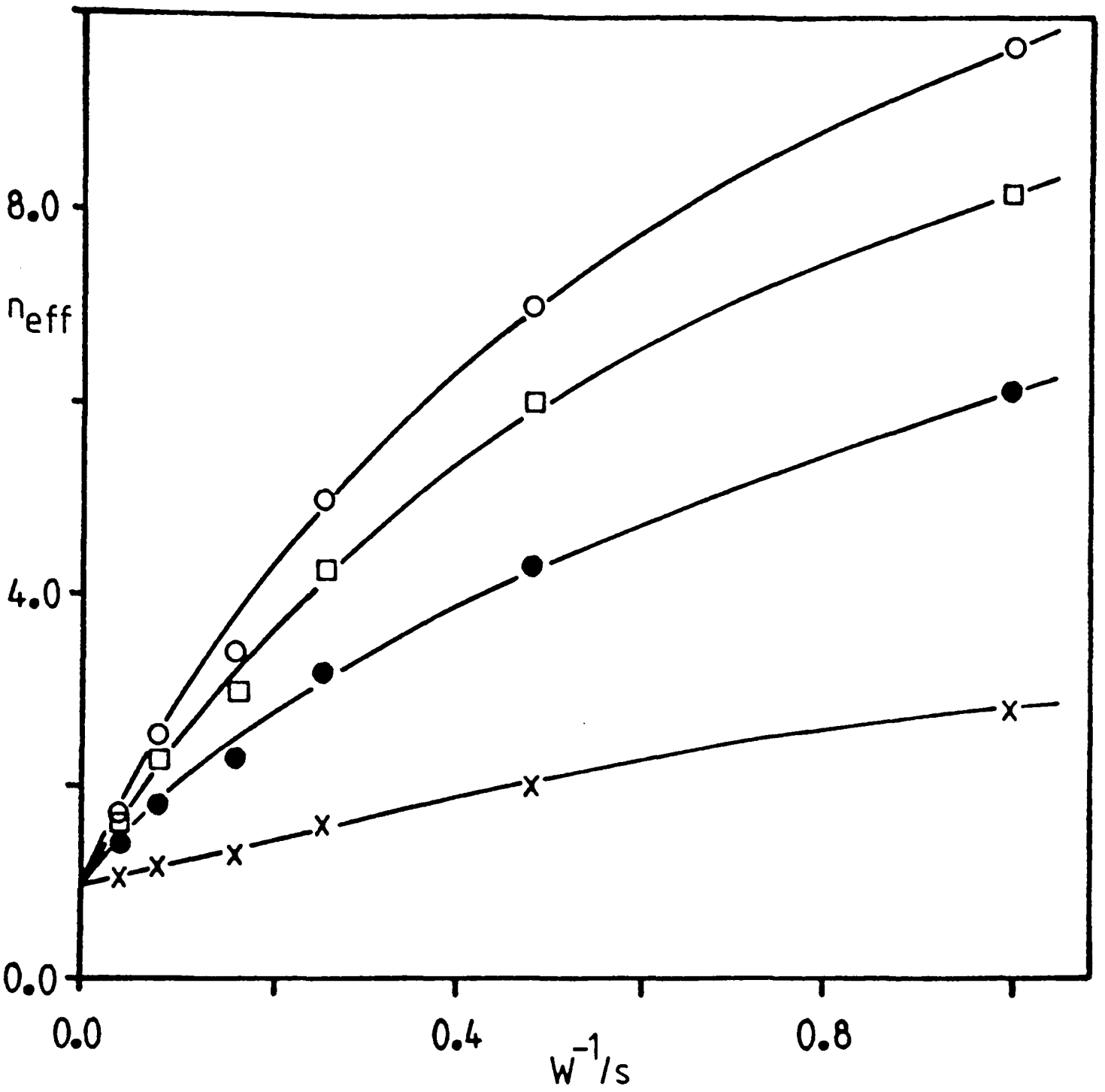


Figure 7.4: n_{eff}, deduced from data such as those in Figure 7.3, as a function of W^{-1}. Forane concentrations were (×) 1.7, (●) 3.3, (□) 5.0, (o) 6.7 $\times 10^{-3}$moldm^{-3}.

EC'dispB2 as possible reaction mechanisms, since it was demonstrated in Chapter Three that for these mechanisms, n_{eff} is a unique function of k_{norm}(EC'dispA2) or k_{norm}(EC'dispB2) which, in turn, are dependent on $[A]_\infty$ alone, and not on $[Y]_\infty$.

The determination of which, if any, of the EC' mechanisms, proposed in Chapter Three, is appropriate for this example will be presented next. The simple EC'pure mechanism is considered first. Extrapolation of the relevant "working curves", generated using the experimental ratios of $[A]_\infty/[Y]_\infty$, enabled values of k_{norm}(EC'pure) to be deduced as a function of rotation speed. A linear dependence of k_{norm}(EC'pure) on W^{-1} was not found and therefore after inspection of Table 3.2, the simple EC'pure mechanism was ruled out as a candidate reaction pathway.

The same protocol as adopted for the EC'pure mechanism was used for the analysis in terms of the EC'dispA1 and EC'dispB1 mechanisms where in each case a non–linear dependence of k_{norm}(EC'dispA1) or k_{norm}(EC'dispB1) on W^{-1} was found. Moreover, if least squares fitting was used to generate "best" values for these normalised rate constant – W^{-1} slopes, a systematic (inverse) dependence on $[F]_\infty$ was observed in each case. Comparison with Table 3.2 then immediately rules out these two mechanisms. To confirm the earlier rejection of the EC'disp2 mechanisms, a similar analysis was performed in terms of these pathways. k_{norm} was found not to vary linearly with W^{-1} and the mechanisms were thus shown to be inappropriate for the catalytic system under investigation. Illustrative examples of k_{norm} versus W^{-1} plots are shown in Figure 7.5 for the EC'pure mechanism.

In contrast, satisfactory analysis resulted from an interpretation in terms of the EC'preeqm mechanism. Figure 7.6 shows values of k_{norm}(EC'preeqm), deduced from experimentally measured n_{eff} values and the relevant "working curves", plotted against W^{-1}. Excellent straight lines through the origin were obtained suggesting that the choice of mechanism is correct in this case. This was further confirmed by plotting the least squares slopes of the lines from such plots against the ratio $[Y]_\infty/[A]_\infty$. The equation defining the normalised rate constant appropriate for this mechanism:

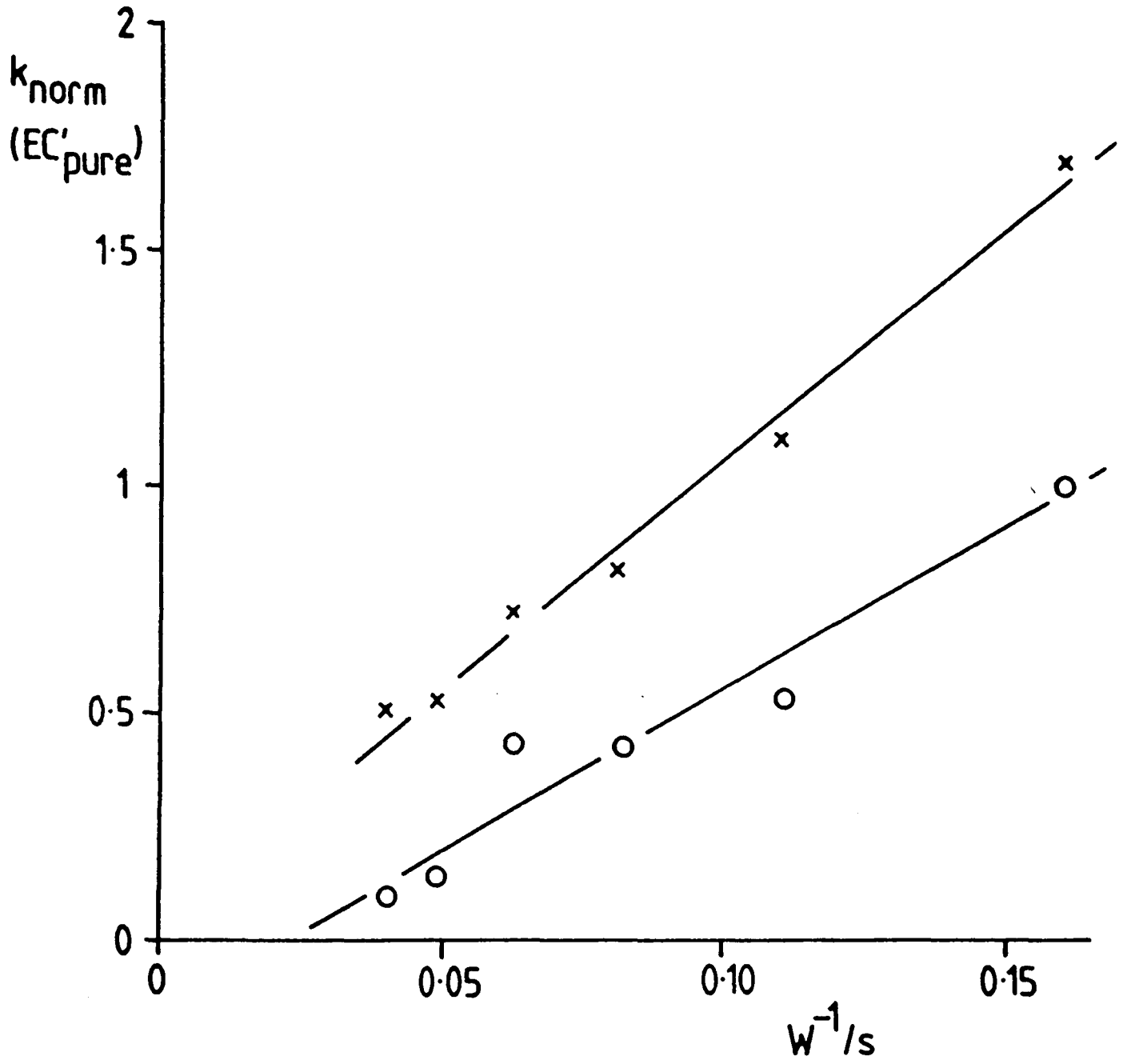


Figure 7.5: Values of k_{norm}(EC'pure), deduced from the measured n_{eff} values and the relevant working curves, plotted against W^{-1}. $[forane]_{\infty}$ = 1.70× 10^{-3} moldm^{-3} and $[F]_{\infty}$ = (×) 1.28, (o) 3.03 ×10^{-3}moldm^{-3}.

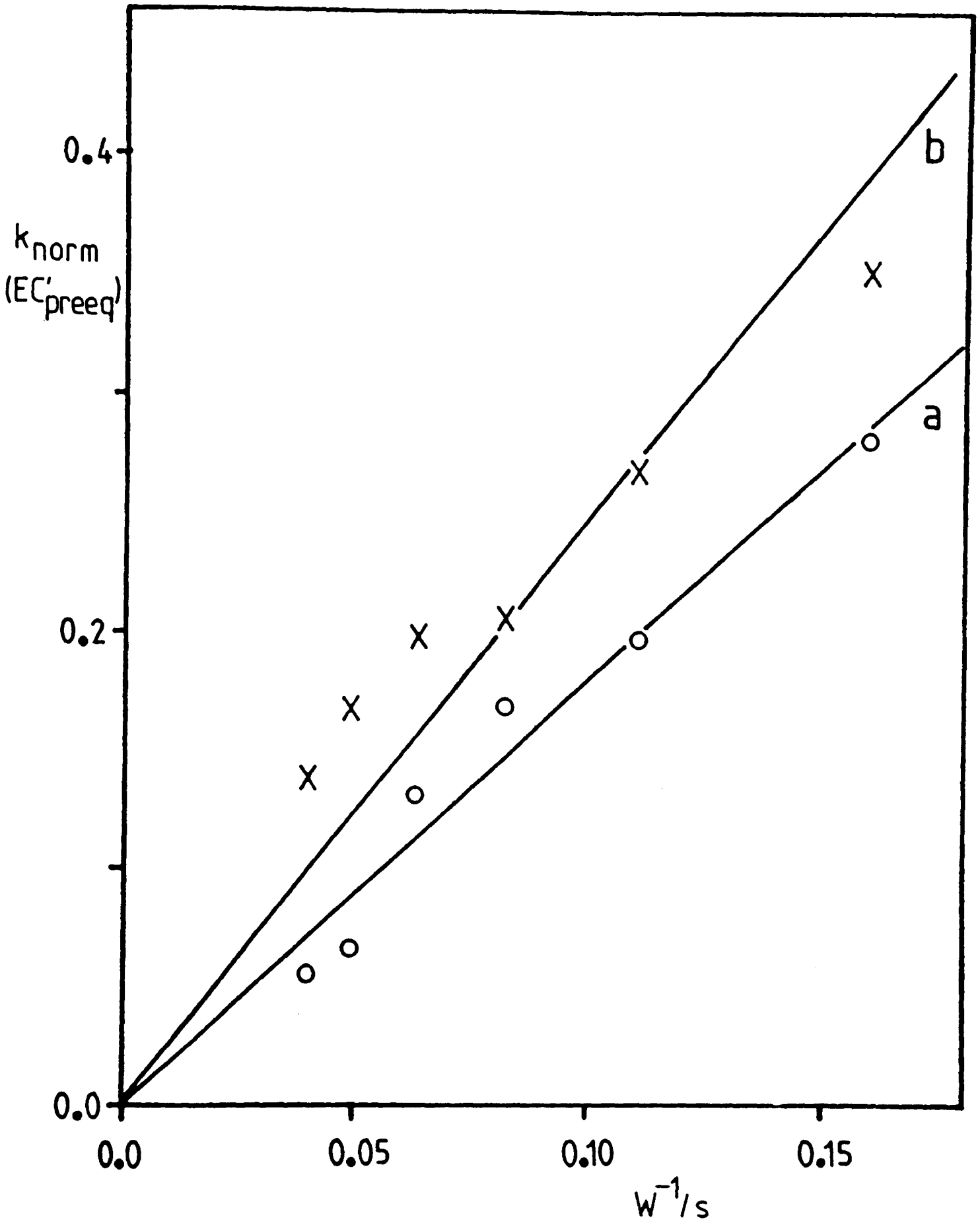
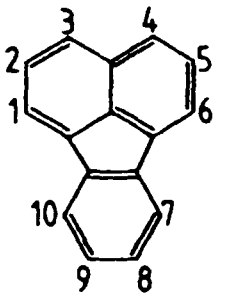


Figure 7.6: Values of k_{norm}(EC'preeqm), deduced from the measured n_{eff} values and the relevant working curves, plotted against W^{-1}. $[F]_\infty/[forane]_\infty$ = (a) 1.78, (b) 1.29.

$$k_{norm}(EC'preeqm) = \frac{k_v\ K_{iv}}{8.032^{3/2}\ W}\left[\frac{\nu}{D}\right]^{1/3}\frac{[Y]_\infty}{[A]_\infty} \qquad 7.1$$

reveals that this should be a straight line passing through the origin. The line obtained is shown in Figure 7.7. It is reasonable to conclude that the pre–equilibrium mechanism is operating in this reaction. Figure 7.7 allows a value for the rate constant $k_vK_{iv} = 25.9\pm1.2s^{-1}$ to be deduced.

The mechanistic conclusion reached in the last paragraph was investigated independently by means of in–situ ESR ChE experiments. Reduction of $2.93x10^{-3}moldm^{-3}$ fluoranthene in the absence of forane in an in–situ flow cell (in $0.1moldm^{-3}$ TBAP/acetonitrile) produced the spectrum shown in Figure 7.8. Analysis of this gave hyperfine coupling constants in close agreement with those reported by Gerson and Hammons [374] : $a_H(1,6) = 4.04G$, $a_H(3,4) = 5.26G$, $a_H(8,9) = 1.21G$, obtained for the fluoranthene radical anion through the reduction of the parent compound with potassium. The numbering of protons in the fluoranthene molecule is defined below:



The ESR signal (S) was studied as a function of the current and the flow rate. It was found that a plot of $\ln(S/i)$ against $\ln(V_f)$ had a slope of $-2/3$ as shown in Figure 7.9 and this reveals that the radical is stable on the timescale of the experiment [313]. The same behaviour was then investigated in the presence of $3.60x10^{-3}moldm^{-3}$ forane. The results are depicted in Figure 7.10. A reduction in ESR signal intensity for a given generating current and flow rate is apparent, indicating a reaction of the radical anion with the anaesthetic. Using the theory presented in section 3.2.1, the signal–current–flow rate behaviour was modelled for an EC'preeqm mechanism with $k_vK_{iv} = 25.9s^{-1}$. Excellent agreement is displayed between theory and experiment in Figure 7.10 and this is taken as independent confirmation of the reaction mechanism deduced using RDE voltammetry.

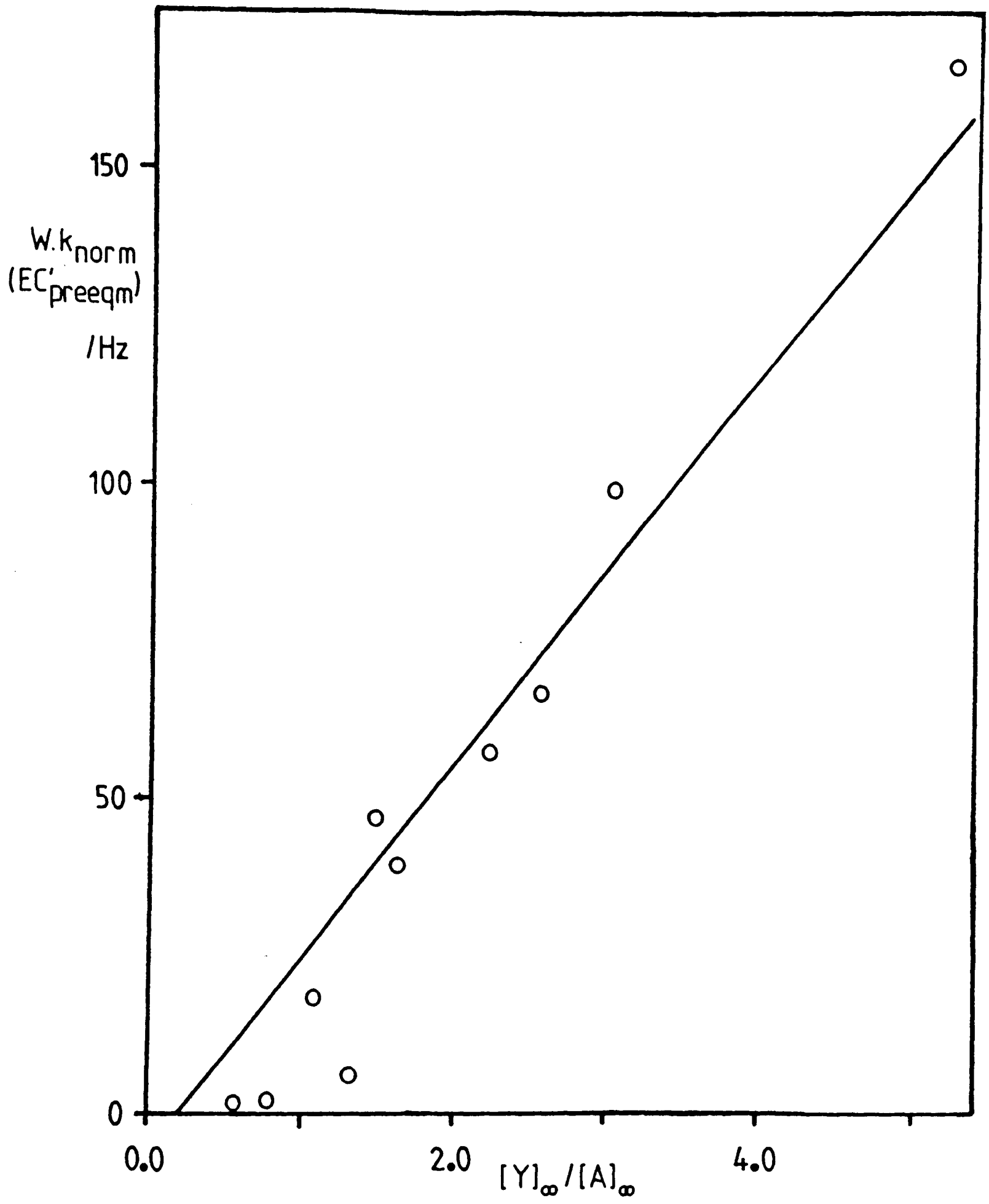


Figure 7.7: The gradients of plots such as those in Figure 7.6 plotted against the ratio $[\text{forane}]_\infty/[Y]_\infty$, showing the good linear dependence between these terms as required by the pre–equilibrium mechanism.

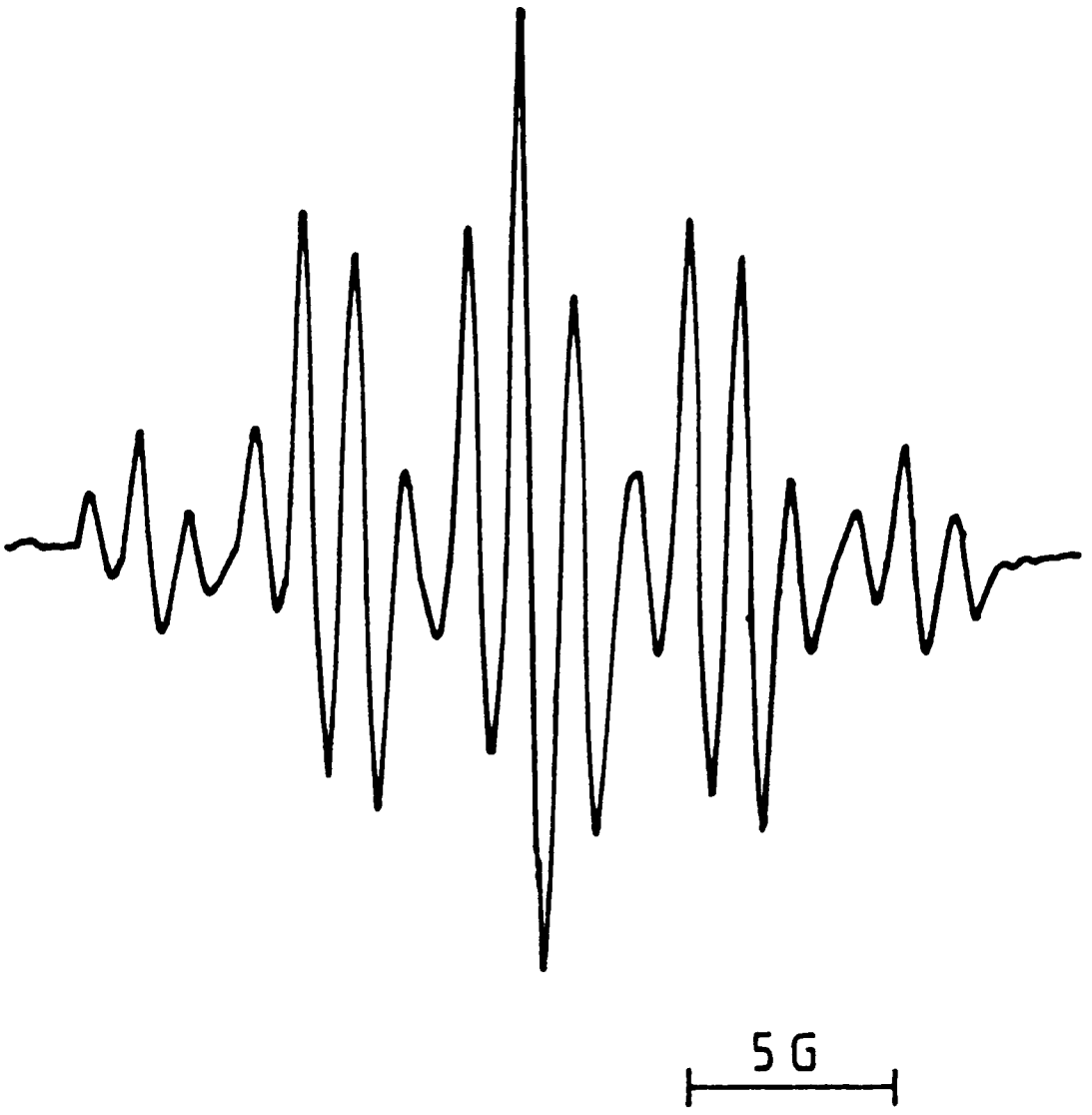


Figure 7.8: The ESR spectrum obtained from the reduction of fluoranthene in acetonitrile/TBAP at the channel flow cell and attributed to the stable radical anion of fluoranthene.

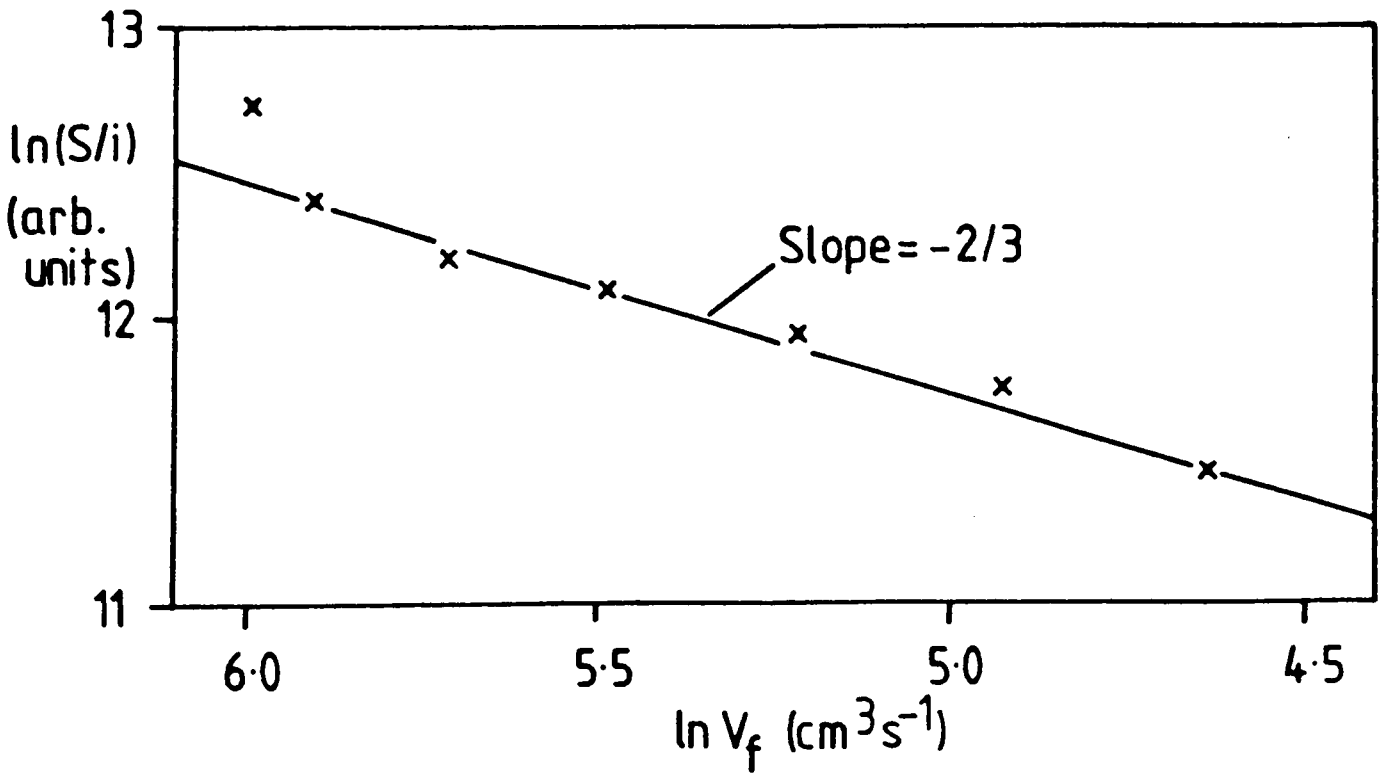


Figure 7.9: A plot of ln (S/i) (arbitrary units) versus ln V_f (×) for the reduction of fluoranthene in the in situ ESR channel cell. The slope of $-2/3$ confirms that the radical anion of fluoranthene is stable on the timescale of the experiment.

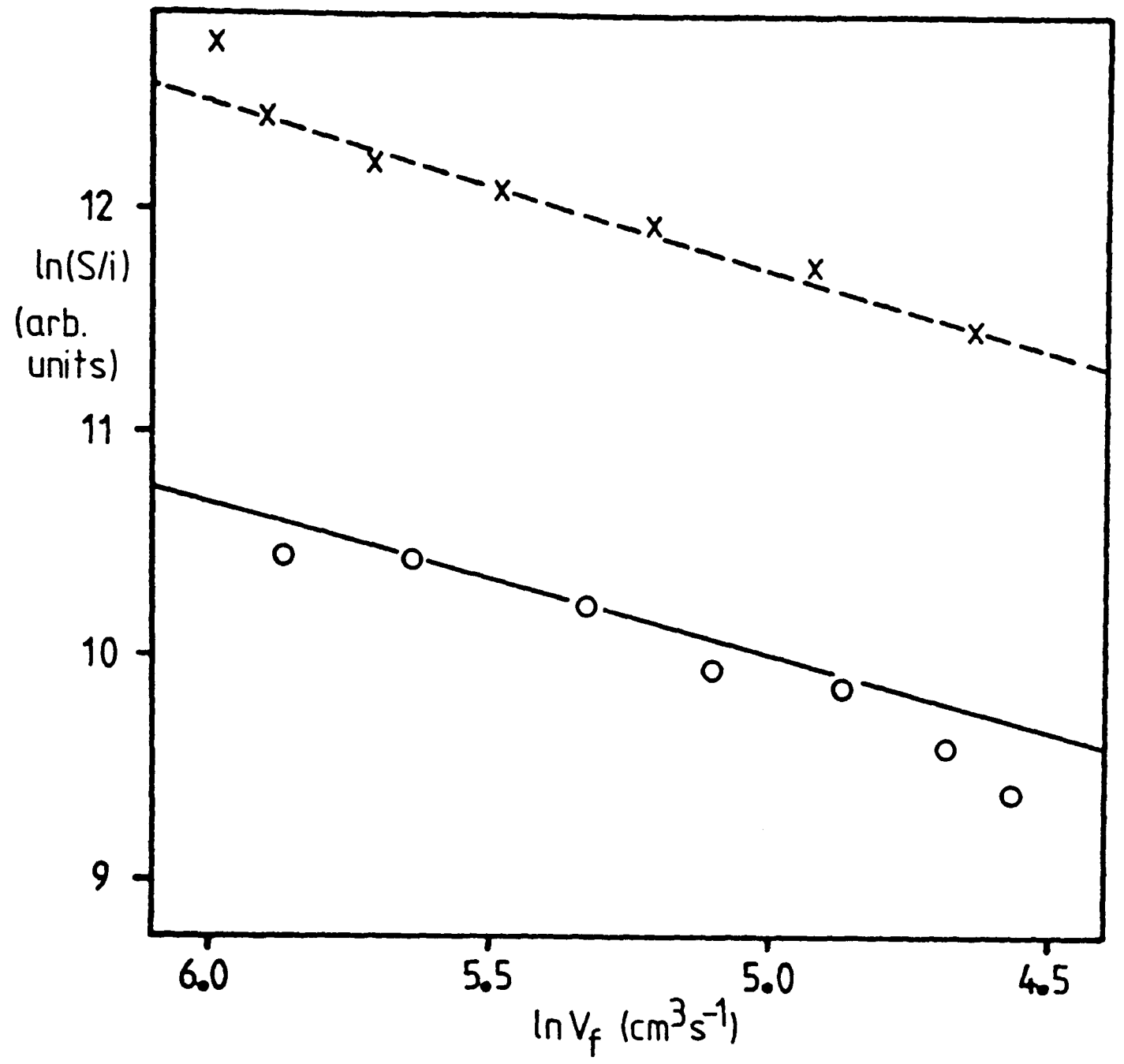


Figure 7.10: Variation of (S/i) with V_f for fluoranthene radical anions in the presence of (o) 3.06×10^{-3} moldm^{-3} forane. The solid line represents that calculated from assuming a pre–equilibrium mechanism with a rate constant of 25.9 s^{-1}.

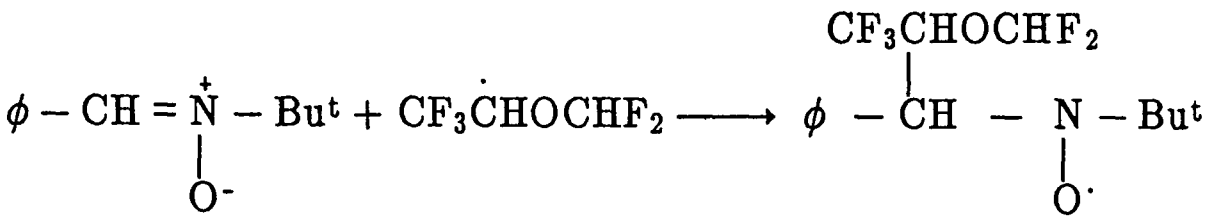
This agreement is worthy of further note. The computational method employed in this calculation proceeds by modification of the appropriate convective–diffusion equations (for the EC'preeqm mechanism at a ChE) via the approximations proposed by Singh and Dutt [290–294]. The complete strategy is presented in Chapter Three, section 3.2.1. The problem of mass transport to the ChE is thus simplified so that previously untreated reactions, for example the EC'preeqm mechanism, can be considered. Compton [282] showed that these approximations are excellent for the calculation of variables depending on concentration, or concentration gradients in the vicinity of the electrode, but less satisfactory for applications where the complete concentration profile is required, for example in spectroelectrochemistry or for second and higher order kinetics. That the Singh and Dutt approximation can be applied successfully here, confirms prior assumptions that the kinetics are sufficiently fast so only the concentrations of radicals near the electrode surface need consideration.

The reduction mechanism deduced above shows that the process involves the transfer of one electron to forane, forming its radical anion, which then decomposes with loss of Cl^-, to give the radical $CF_3\dot{C}HOCHF_2$. The presence of an equilibrium prior to the decomposition step is not unexpected in the light of the relative stability reported for the radical anions of polyhalogenated aliphatic compounds [375,376]. Thus, radical anions of compounds such as CBr_4 and CCl_4 have been shown to have a "fleeting existence" [377], with sufficient stability to effect the course of electron transfer reactions. This is in contrast to the monohalides which undergo rapid dissociative electron capture [346,347,375,378] and may, at least partly, explain the different mechanisms observed between the mediated reduction, by $F^{\cdot -}$, of Bu^tBr and forane.

The intensity of the ESR signal of $CF_3\dot{C}HOCHF_2$ was weak, showing that this radical is an intermediate, and not the product of the reaction, as implied by steps iv and v of equation 3.32. The radical is likely to react via further reduction with the possible formation of the olefin $CF_2{=}CHOCHF_2$ and fluoride ion. The literature confirms this as the most likely reduction pathway for vicinal polyhalides [96,98]. To detail further the reduction mechanism in operation here, a spin–trapping [348]

of the intermediate radical was attempted and its involvement in the overall reaction scheme thus established.

Spin–trapping experiments were once again carried out using BPN. A $3.0x10^{-3}moldm^{-3}$ solution of F and $0.05moldm^{-3}$ BPN in acetonitrile/$0.1moldm^{-3}$ tetrabutylammonium tetrafluoroborate was saturated with forane (approximately $15x10^{-3}moldm^{-3}$) and this was reduced at the mercury plated RDE (at –2.0V) for a period of one hour. Samples were removed from the rotating disc vessel periodically and transferred to the ESR spectrometer. In this way a spectrum consisting of a triplet of doublets, attributed to hyperfine interactions with the nitrogen and the α–hydrogen in the spin adduct, was observed. The following coupling constants were measured: $a_N = 14.25\pm0.10G$ and $a_N = 2.71\pm0.10G$. The spectrum was thus attributed [296] to the $CF_3\dot{C}HOCHF_2$ adduct of BPN.



These observations again support the assignment of an EC'preeqm mechanism.

Cyclic voltammetry was employed to determine whether an irreversible reaction between $F^{\cdot -}$ and $CF_3\dot{C}HOCHF_2$ occurred during the homogeneous reduction of forane. The presence of such a step would remove mediator from bulk solution [319] and therefore restrict the lifetime of an amperometric sensor based on the F/forane chemistry. Figure 7.11 shows the cyclic voltammogram obtained from an acetonitrile/$0.1moldm^{-3}$ TBAP solution containing $3.0x10^{-3}moldm^{-3}$ F and $15x10^{-3}dm^{-3}$ forane. This voltammogram remained unchanged upon prolonged cycling, for up to five hours, showing that $F^{\cdot -}$ is not consumed during the catalytic reduction of forane and confirming the absence of this irreversible reaction.

7.1.2 Conclusions

Electron transfer to forane has been demonstrated using $F^{\cdot -}$ in acetonitrile as an electrogenerated homogeneous mediator. The reduction is shown, using RDE

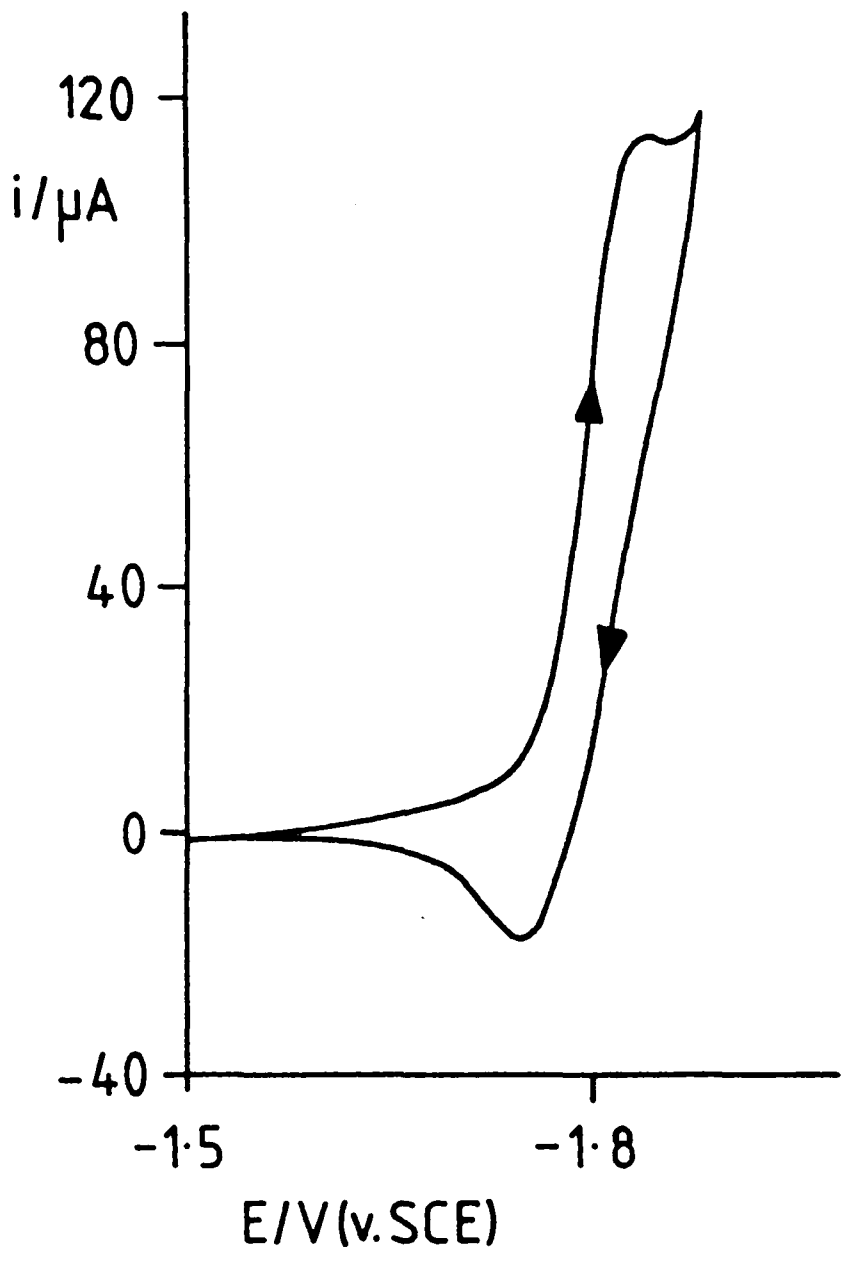


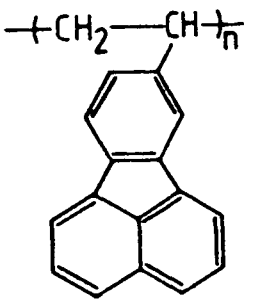
Figure 7.11: Cyclic voltammogram obtained from a mercury electrode in a solution containing 3.0×10^{-3} moldm^{-3} fluoranthene, 15.0×10^{-3} moldm^{-3} forane and 0.1 moldm^{-3} TBAP/acetonitrile. A scan rate of 100 mVs^{-1} was employed and the shape and size of the voltammogram remained unchanged upon continual cycling for five hours.

voltammetry in conjunction with in–situ ESR ChE experiments, to proceed via a EC'preeqm mechanism. Decomposition of the radical anion of forane with the loss of Cl^- forms the most likely product, the $CF_3\dot{C}HOCHF_2$ radical. This is detected using spin–trapping ESR experiments.

The demonstration of the electroactivity of this anaesthetic gas should therefore facilitate the development of an amperometric electrochemical sensor for this agent.

7.2 A Modified Electrode for the Electrochemical Reduction of Forane

The experiments described above demonstrate clearly that $F^{\cdot -}$ can mediate the reduction of forane in homogeneous solution. Given this success, we were encouraged to develop a polymer modified electrode for the reduction of the anaesthetic based on the above observations. Such an electrode constitutes an electrode of a conventional material, whose behaviour is deliberately altered through the immobilisation of a suitably chosen species onto its surface [379–381]. To this end, poly–(11–vinylfluoranthene) (PVF):

PVF = 

was synthesized by the free radical polymerisation of 11–vinylfluoranthene. The latter was kindly prepared from F by G.W.J. Fleet, J.C. Son and B.P. Bashyal (Dyson Perrins Laboratory, Oxford), using the procedure reported in Appendix Seven., via 11–acetylfluoranthene and 11–(1–hydroxy)ethyl–fluoranthene.

PVF was obtained in quantitative yield by refluxing a $5x10^{-3}moldm^{-3}$ solution of the vinyl monomer in dichloromethane for two hours at 40°C using azo–iso–butyronitrile ($5.0x10^{-5}moldm^{-3}$) as an initiator [120]. The polymer was characterised by G.C. Eastmond (Department of Chemistry, Liverpool University) using gas phase chromatography (GPC) with tetrahydrofuran as the solvent, and

shown to have a molecular weight of around 30,000. Considerable effort was paid to obtaining stable, relatively even polymer films. The optimal procedure was found to involve evaporation, at room temperature, of a small quantity (approximately $5x10^{-3}cm^3$) of a solution of PVF in dichloromethane ($0.5x10^{-3}gcm^{-3}$) from a platinum RDE. Films so produced were estimated to have a thickness of 10^{-5}cm, assuming that the density of the deposited film is similar to that of the bulk polymer (1.1 gcm^{-3}).

Figure 7.12 shows a typical cyclic voltammogram obtained for the PVF modified platinum electrode in acetonitrile with $0.1moldm^{-3}$ TBAP as supporting electrolyte and in the absence of forane. The scan rate used was $100mVs^{-1}$. The shape of the voltammogram is indicative of an electrochemically reversible process. The Faradaic process may be attributed to the one electron reduction of the pendant F moieties within the polymer since, firstly, the charge passed during the cyclic voltammogram corresponds quantitatively (within 10%) with that expected from the known amount of PVF deposited on the surface, and secondly, the mean of the potential of the forward (reduction) peak and the reverse (oxidation) peak is -1.82 ± 0.04V, which is close to the reduction of solution phase F (–1.80V, section 5.1). The peak current for the reduction of the polymer coat was found to vary directly with scan rate, as illustrated in Figure 7.13, and this is indicative of fast electron transfer within the coat [381]. Further information about the rate of charge injection into the coat was obtained by potential step experiments in which the electrode potential was stepped from –1.50V to –2.00V (vs. SCE). A typical current transient is shown in Figure 7.14. Analysis of these transients showed that at short times, the kinetics of the charge transfer process within the coat could be described by a simple model, in which the charge diffuses randomly among the different centres in the coat. This is shown in Figure 7.15. The current is then given by [382]:

$$\frac{i}{FA} = [D_c[F]_c/x_p(\pi\tau_p)^{1/2}][1 + 2\sum_{n=1}^{\infty}(-1)^n\exp(-n^2/\tau_p)] \qquad 7.2$$

where D_c is the diffusion constant, x_p is the film thickness, $[F]_c$ is the concentration

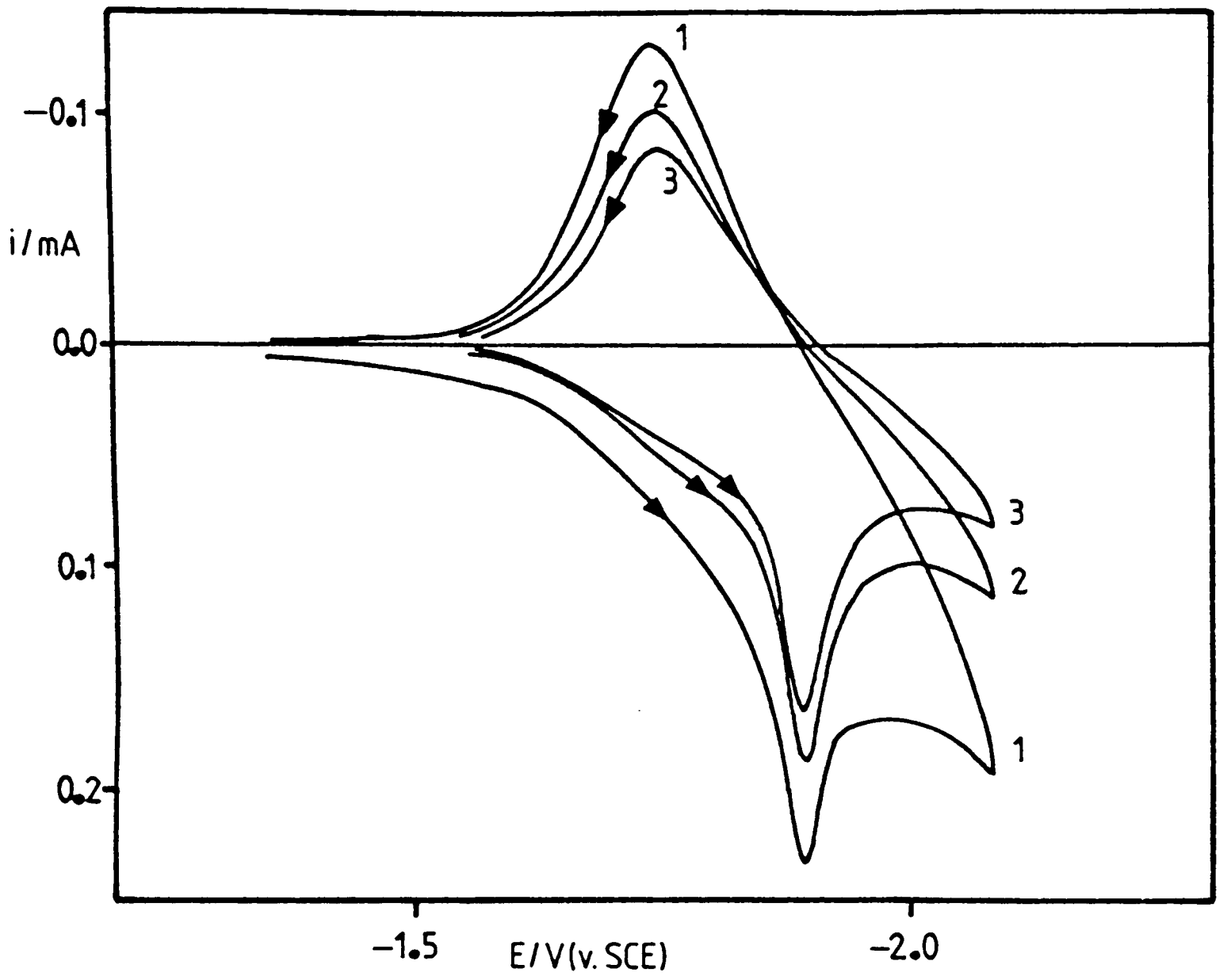


Figure 7.12: A cyclic voltammogram for the reduction of a poly(11–vinylfluoranthene) modified electrode in acetonitrile/0.1 moldm^{-3} TBAP.

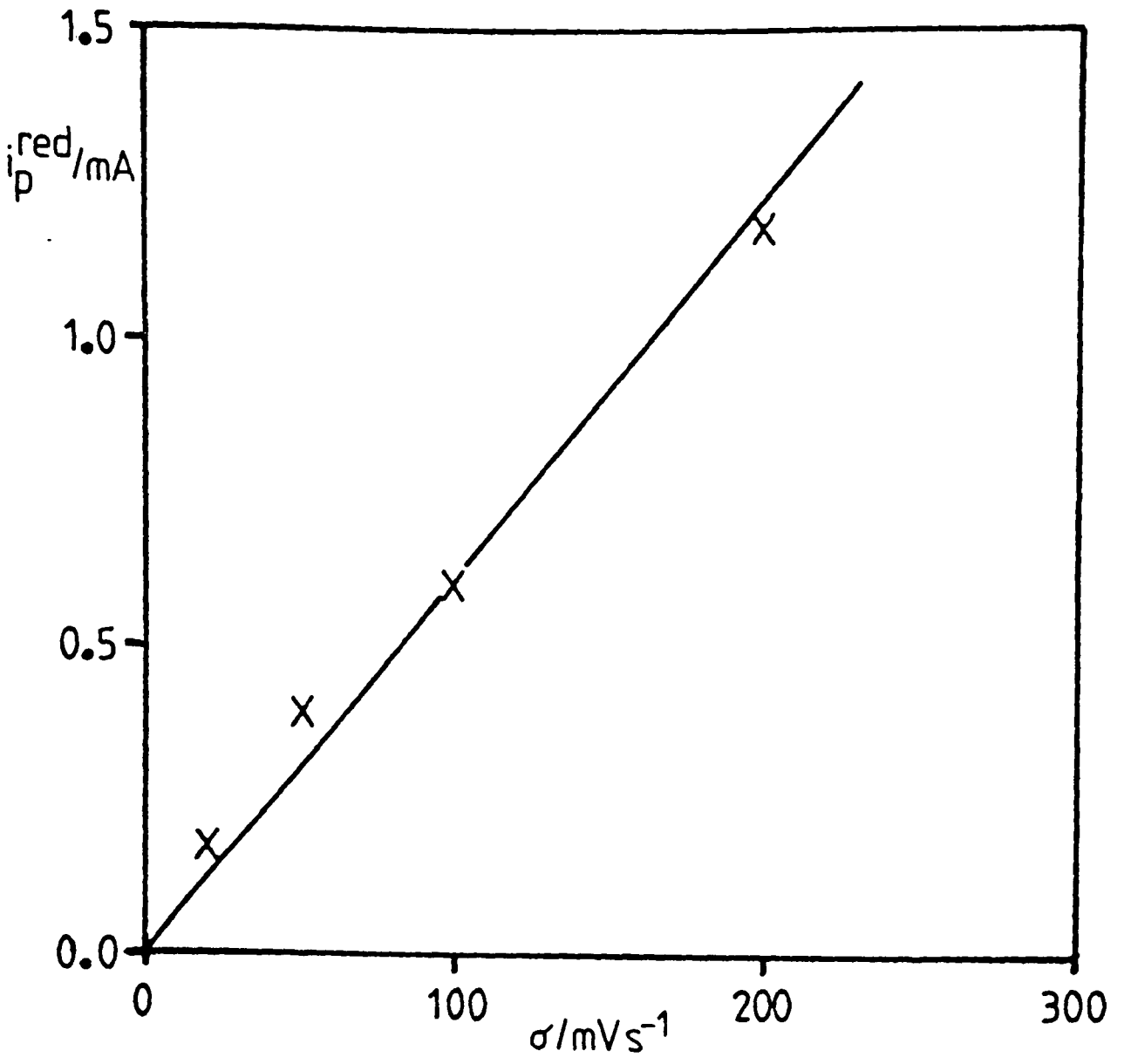


Figure 7.13: Variation of the peak current with scan rate.

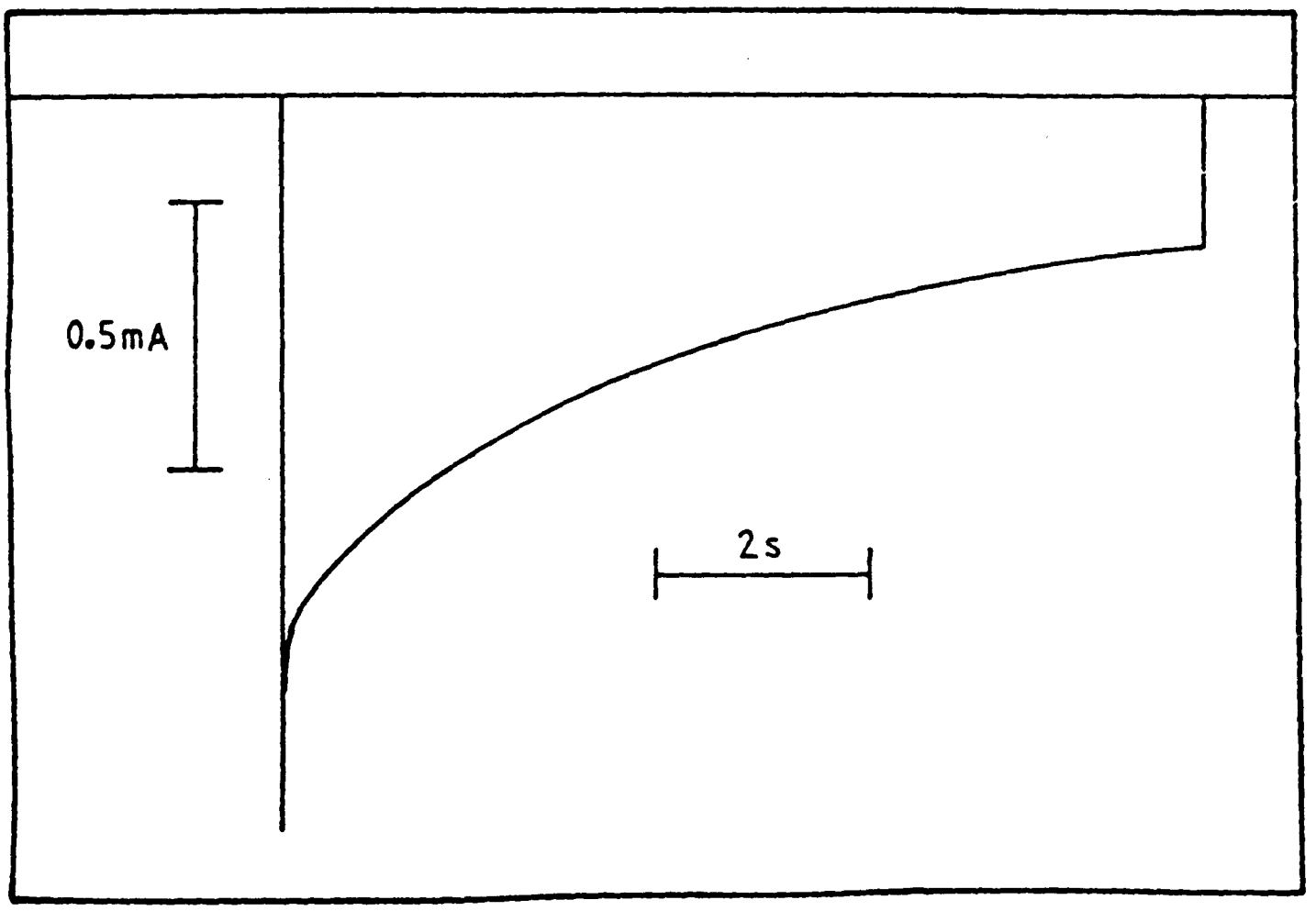


Figure 7.14: A current transient obtained by stepping the potential of the modified electrode from –1.50V to –2.00V v.SCE.

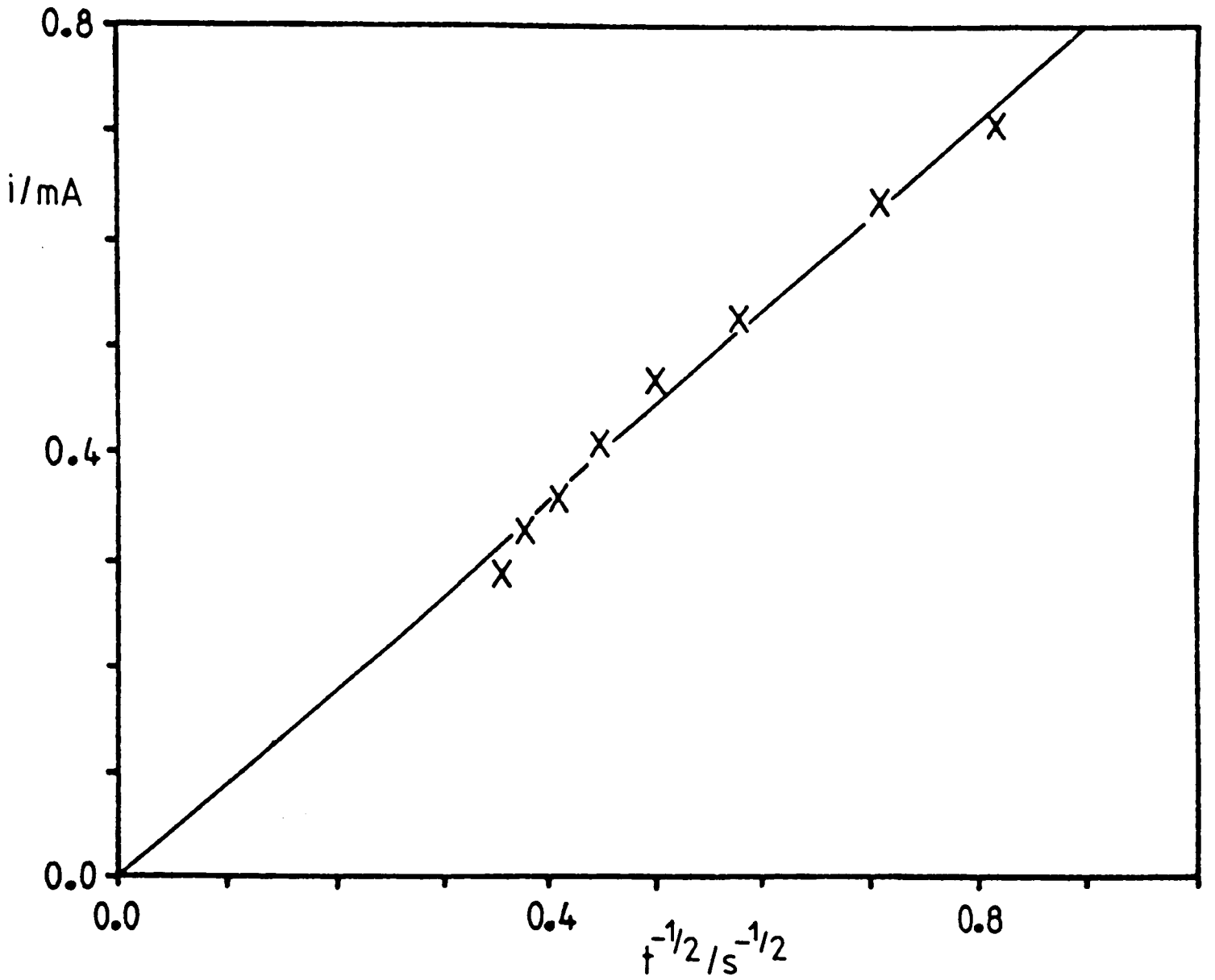
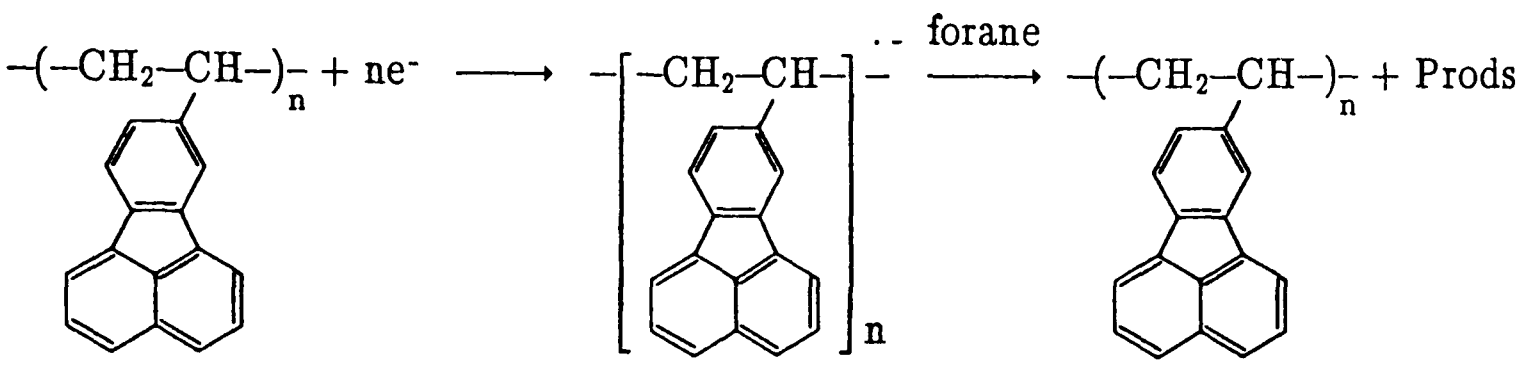


Figure 7.15: Analysis of the current transient in Figure 7.14 shows that it obeys equation 7.2 at short times.

of fluoranthene moieties within the coat and $\tau_p = D_c t/x_p^2$, where t is time. The gradient of the line in Figure 7.15 gave a value of $9x10^{-11}cm^2s^{-1}$ for D_c.

Figure 7.16 shows a cyclic voltammogram obtained under the same conditions as Figure 7.12 except for the presence of $15x10^{-3}moldm^{-3}$ forane. Typical "catalytic" behaviour is apparent, the reduction peak is considerably enhanced in size whilst the oxidation peak is significantly reduced [274] and it may be concluded that the following process is taking place:



However, the utility of such a modified electrode in the practical sensing of forane is restricted by the observation that the polymer coats showed only limited stability, so that on prolonged potential cycling, desorption of the polymer occurred and after approximately 40 cycles, no recordable voltammogram remained. Loss of material was most pronounced during the earlier potential cycles, as can be seen in Figure 7.12. Preliminary attempts to enhance the coat stability were made by changing the supporting electrolyte, since the instability results from a competition between polymer desorption on the one hand and migration of charge compensating counter ions into the coat, as a response to the injection of charge into the polymer film, on the other. However, changing the supporting electrolyte from TBAP to tetramethylammonium or tetraethylammonium perchlorate produced no significant improvement.

To summarise, the deposition of a thin layer of PVF onto a platinum electrode produces a modified electrode which is capable of reducing the anaesthetic gas, forane. One merit of an electrochemical amperometric sensor based on a polymer modified electrode would be the anticipated fast response times attainable using such a device. However, this advantage is of little significance in comparison to the limited stability which the coat displays and therefore a sensor based on the

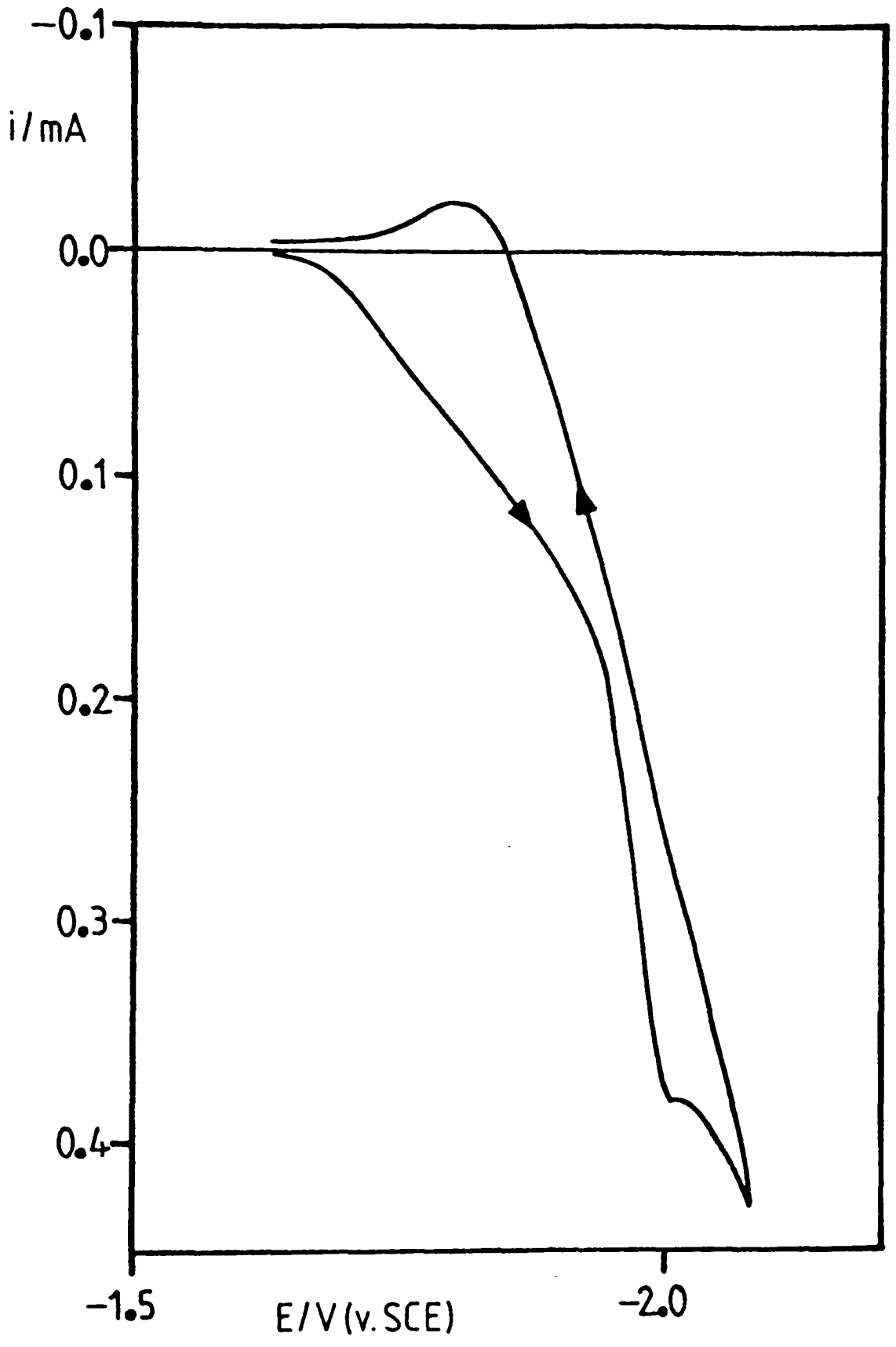


Figure 7.16: A cyclic voltammogram for the reduction of a poly(11–vinylfluoranthene) modified electrode in acetonitrile/0.1 moldm^{-3} TBAP + 15.0× 10^{-3} moldm^{-3} forane.

reduction of forane by $F^{\cdot -}$ in homogeneous solution appears favourable. The remainder of this thesis is thus concerned with the development and testing of an amperometric sensor based on homogeneous mediated electron transfer to forane.

7.3 Interferences by Nitrous Oxide and Oxygen

It is worth emphasising, from the viewpoint of developing a practical clinical sensor, that there may be interferences from other species present in the environment in which the device is to be used. For example, typical proportions of gases employed in closed circuit anaesthesia are: 79% nitrous oxide, 20% oxygen and 1% forane [1]. The determination of the electroactivity of these gases, either directly at a mercury electrode, or via homogeneous mediation from $F^{\cdot -}$ is therefore essential. Thus the aim of the following section is to examine the electrochemical properties of both N_2O and O_2.

7.3.1 Nitrous Oxide

Nitrous oxide has been reduced directly on silver in aqueous media [84], but no work in the literature reports electroactivity on other conventional electrode materials. Rotating disc voltammetry in acetonitrile/0.1moldm^{-3} TBAP confirmed that N_2O is electroinactive on gold and platinum. However, a reduction was observed on both silver and mercury electrodes. The reduction occurred at $\approx$–2.8V (vs. SCE) in each instance and therefore the onset of solvent decomposition obscured the full current voltage curve and prevented the evaluation of any quantitative information.

Experiments revealed however, that N_2O can be reduced indirectly by $F^{\cdot -}$. Figure 7.17 shows a current–voltage curve for the reduction of 3.0x10^{-3}moldm^{-3} F at a mercury electrode, in acetonitrile/0.1moldm^{-3} TBAP and also the catalytic response observed when increasing concentrations of N_2O ($[N_2O]_\infty$) are added. The mechanism for this process was determined using the same strategy as applied for the $F^{\cdot -}$/Bu^{t}Br and $F^{\cdot -}$/forane systems in section 5.2 and 7.1 respectively. Thus,

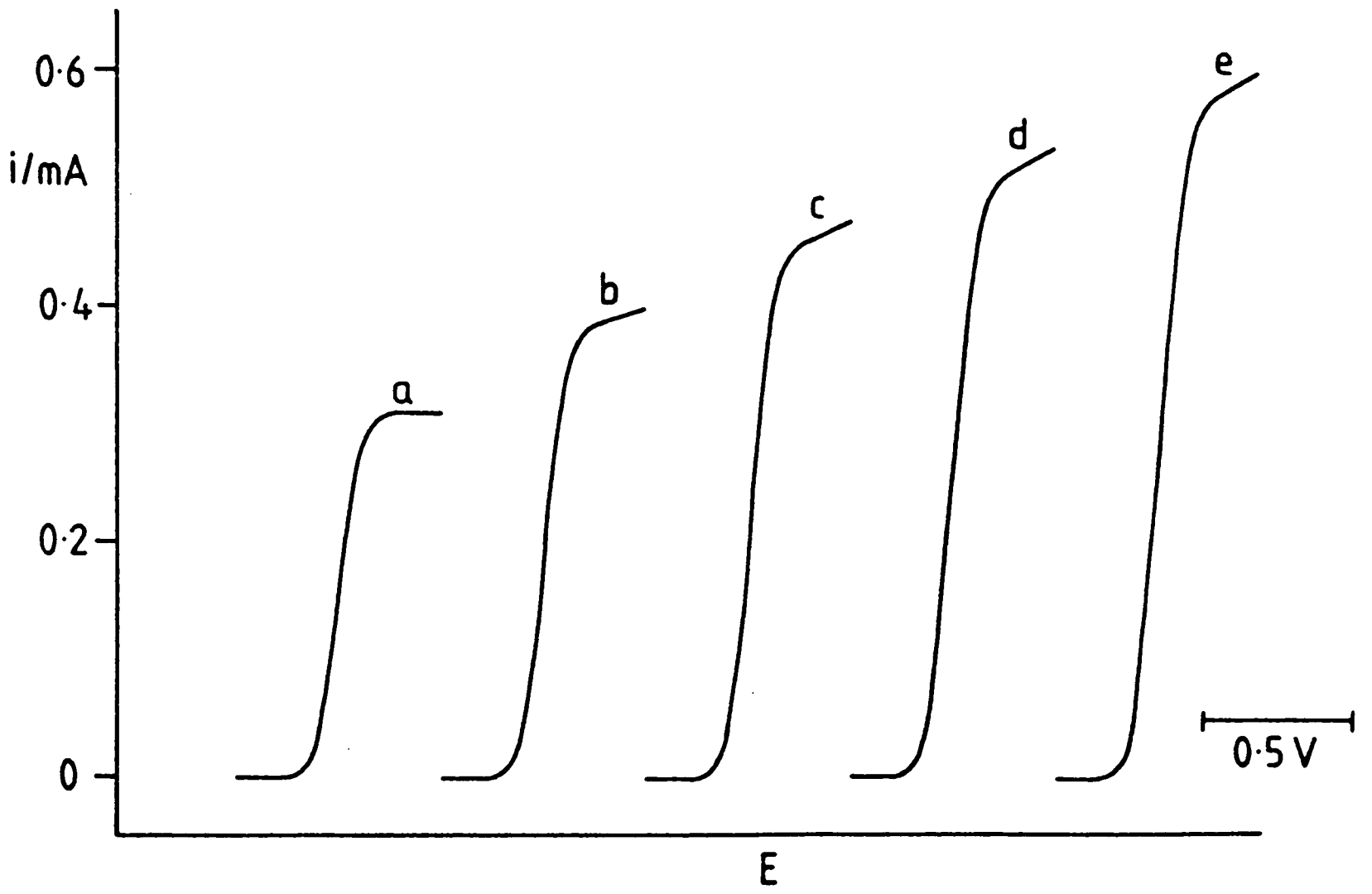


Figure 7.17: RDE voltammograms for the reduction at a mercury electrode of 1.0×10^{-3} moldm^{-3} fluoranthene in the presence of a) 0.0, b) 0.031, c) 0.063, d) 0.094, e) 0.125 moldm^{-3} nitrous oxide. All data were recorded at 16.0Hz.

limiting currents were recorded as a function of rotation speed and the ratio of $[F]_\infty$:$[N_2O]_\infty$ ($[A]_\infty$:$[Y]_\infty$), and the effective number of electrons transferred, determined. Figure 7.18 shows n_{eff} plotted against W^{-1} for various values of $[N_2O]_\infty$ and it can be seen that the former increases with increasing $[N_2O]_\infty$. Examination of Table 3.2 then suggests that EC'dispA2 and EC'dispB2 can be rejected as candidate mechanisms since these would produce n_{eff} values which were independent of $[Y]_\infty$. Working curves for the remaining mechanisms were then calculated using the theory presented in Chapter Three for the appropriate values of $[A]_\infty/[Y]_\infty$. These enabled plots of k_{norm} versus W^{-1} to be deduced for each mechanism. Non–linear plots were obtained for the EC'preeqm, EC'dispA1 and EC'dispB1 mechanisms and these were therefore also rejected. However linear plots passing through the origin (shown in Figure 7.19) were found for the EC'pure mechanism which was thus proposed as the EC' reaction pathway appropriate for this example. Moreover, Figure 7.20 shows that when the slopes of such graphs were plotted against $[N_2O]_\infty$, a linear dependence was also observed, confirming the choice of mechanism and enabling a value of $k_{ii} = 115.9 \pm 4.5 s^{-1}$ to be determined for the rate constant of the catalytic step. The mediated reduction of N_2O by the radical anion of fluoranthene therefore proceeds via an EC'pure mechanism.

At potentials corresponding to the transport–limited current for the mediated reduction of N_2O, tiny bubbles of nitrogen (the product of this reduction [84]) formed at the electrode surface. The velocity of the RDE however swept the bubbles clear of the electrode so that the latter was not obscured by their presence [94].

The question now arises as to what response can be expected when both N_2O and forane are present in solution. The reduction of both of these substrates by electrogenerated $F^{\cdot -}$ has been demonstrated. Figure 7.21 shows the n_{eff} data obtained from an acetonitrile/0.1moldm^{-3} TBAP solution containing 3.0×10^{-3}moldm^{-3} F, 3.3×10^{-3}moldm^{-3} forane and increasing concentrations of N_2O. At high rotation speeds, n_{eff} approaches unity, confirming that a catalytic process involving a one electron electrochemical step is still in operation. Modification of the theory presented in Chapter Three to include the two catalytic processes observed for the $F^{\cdot -}$/forane and $F^{\cdot -}/N_2O$ systems, assuming the kinetics to be additive, is

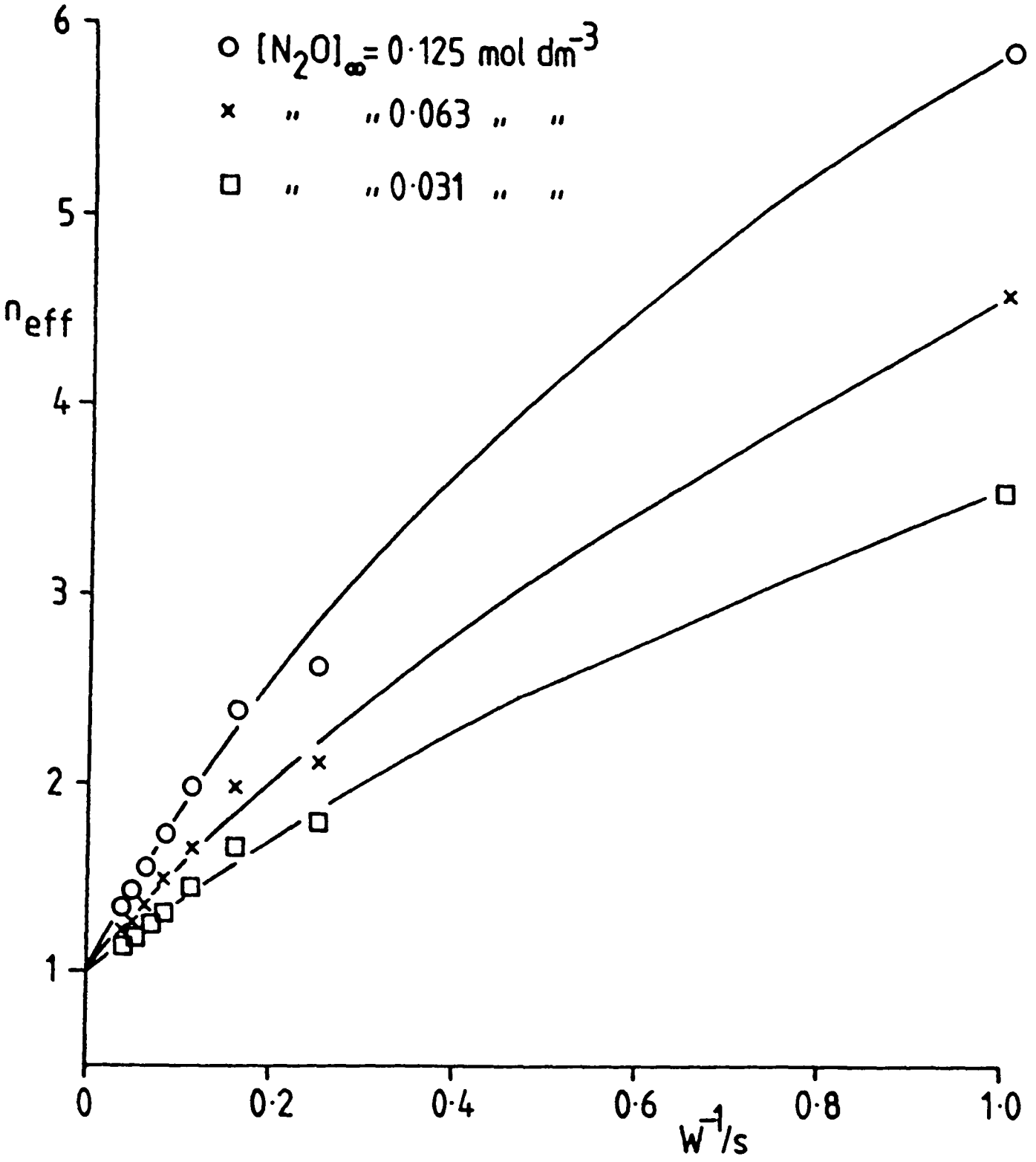


Figure 7.18: n_{eff} for the reduction of fluoranthene in acetonitrile/0.1 moldm^{-3} TBAP in the presence of nitrous oxide, plotted against W^{-1}.

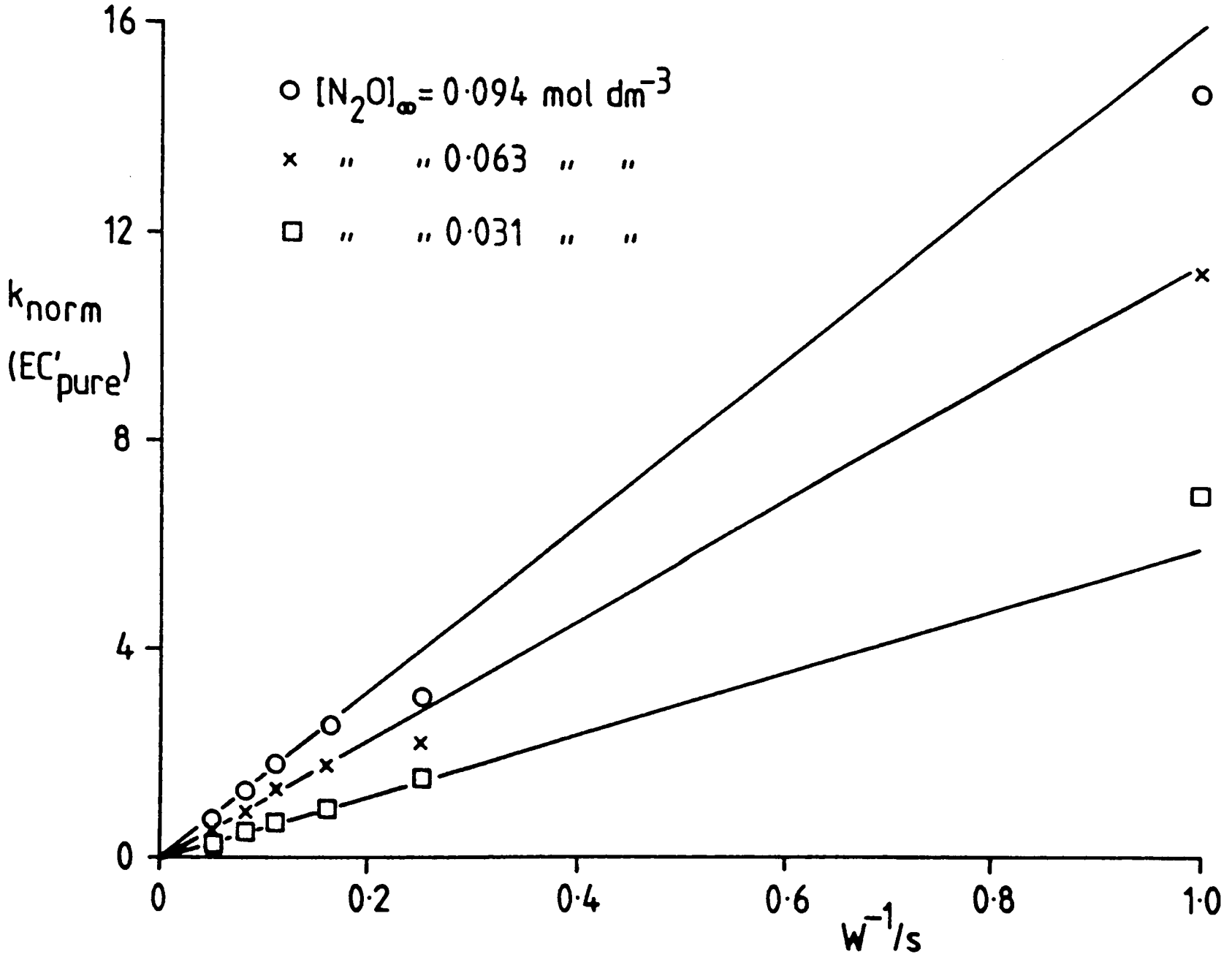


Figure 7.19: Values of k_{norm}(EC'pure), deduced from the measured values of n_{eff} and the relevant working curves, plotted against W^{-1}. $[F]_\infty = 0.5 \times 10^{-3}$ moldm^{-3}.

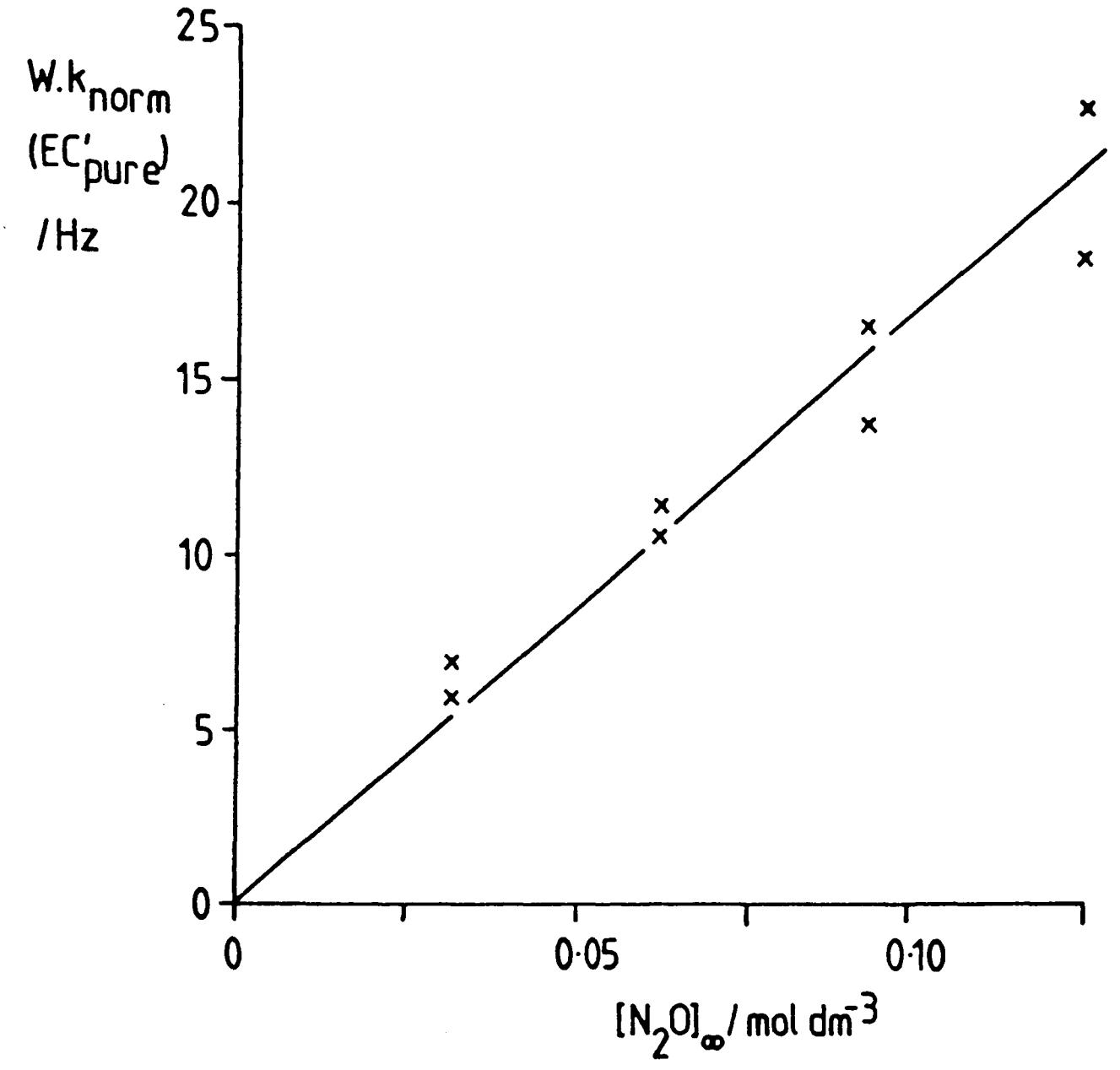


Figure 7.20: The product Wk_{norm}(EC'pure) plotted against $[N_2O]_\infty$, showing the good linear relationship between these terms as required for the EC'pure mechanism.

straightforward since the rate constant and reaction pathway has already been deduced for each. Comparison of theory with experiment proceeded by normalising the effective number of electrons transferred for the overall (N_2O and forane) process to the number transferred with forane only as a substrate. Thus working curves of n'_{eff} against $W^{1/2}$, shown in Figure 7.22 where:

$$n'_{eff} = \frac{n_{eff}\ (\text{forane} + N_2O)}{n_{eff}\ (\text{forane})} \qquad 7.3$$

were calculated in this way. The experimental data of Figure 7.21 is also displayed on this plot and good agreement can be observed between this and the theory. Thus when both N_2O and forane are present the overall mediated electro–reduction process between $F^{\cdot -}$ and these two substrates can be considered as the sum of the two individual homogeneous catalysed processes. Therefore measured n_{eff} values can be interpreted in terms of $[\text{forane}]_\infty$ and $[N_2O]_\infty$. Then, providing $[N_2O]_\infty$ is known, $[\text{forane}]_\infty$ can be readily deduced from any given value of n_{eff}.

7.3.2 Oxygen

The direct electroactivity of oxygen on a mercury electrode in acetonitrile/0.1moldm^{-3} TBAP was demonstrated using cyclic voltammetry. The resulting voltammogram is shown in Figure 7.23 and is in excellent agreement with previous studies [383,384]. Rotating disc experiments also produced a single reduction wave with $E_{1/2} = -0.75 \pm 0.03$V and no further reduction was observed upon scanning to more negative potentials. The Levich plot of i_{lim} versus $W^{1/2}$ for this wave is shown in Figure 7.24, and assuming the reduction to be a one electron process [383,384] then a value for the diffusion coefficient of O_2, $D_{O_2} = 5.4 \pm 0.2 \times 10^{-5}$cm^{2}s^{-1} was deduced from this plot. This compares with the literature value of 5.7×10^{-5}cm^{2}s^{-1} [385].

The one electron nature of this reduction process was confirmed, or otherwise, by means of a rotation speed step experiment, which has been demonstrated to yield the diffusion coefficient of an electroactive species without prior knowledge of the concentration of the species or number of electrons involved [308]. The potential of a

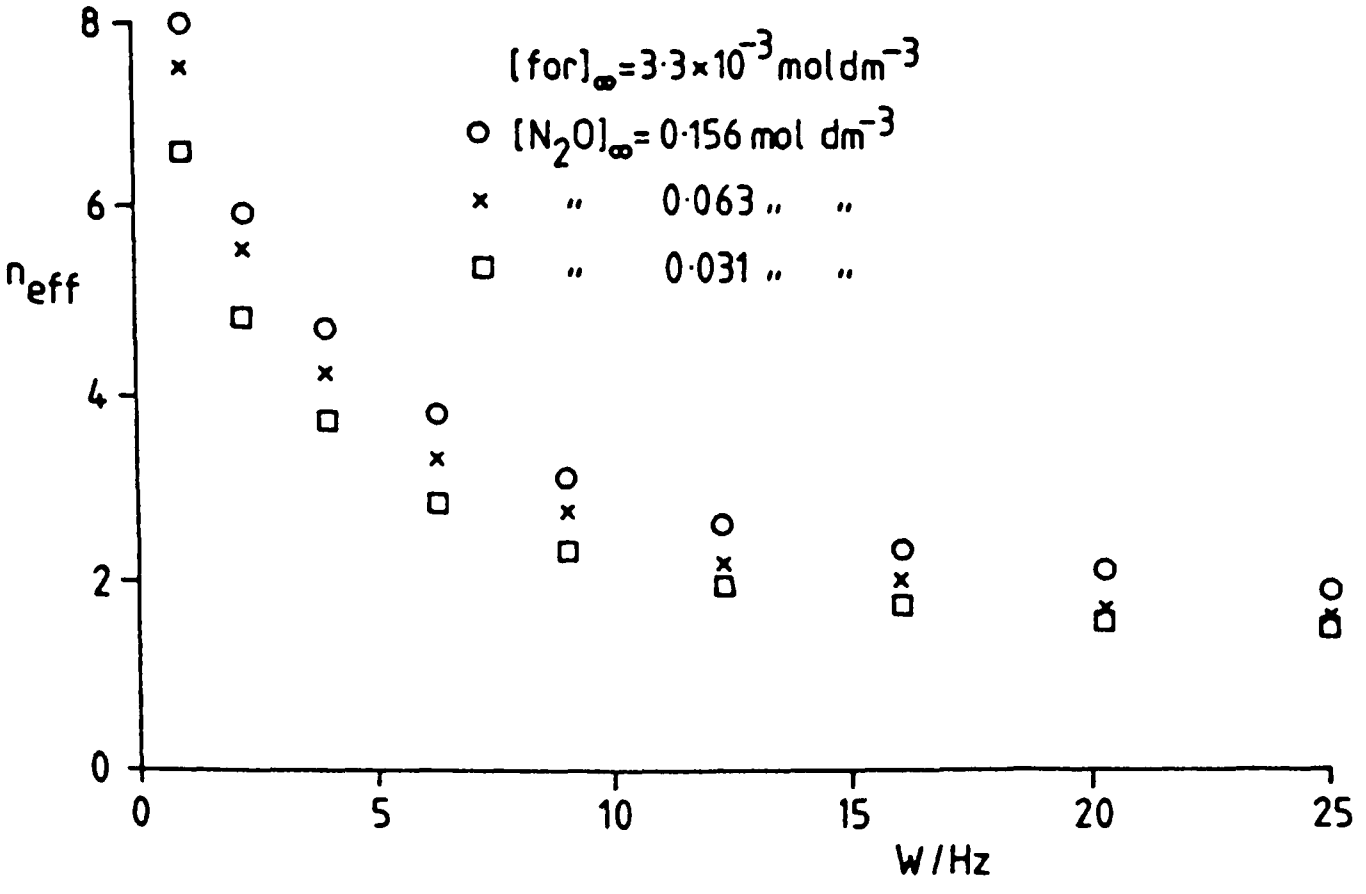


Figure 7.21: n_{eff} versus W for the reduction of 3.0×10^{-3} moldm^{-3} fluoranthene in 0.1 moldm^{-3} TBAP/acetonitrile in the presence of both forane and nitrous oxide.

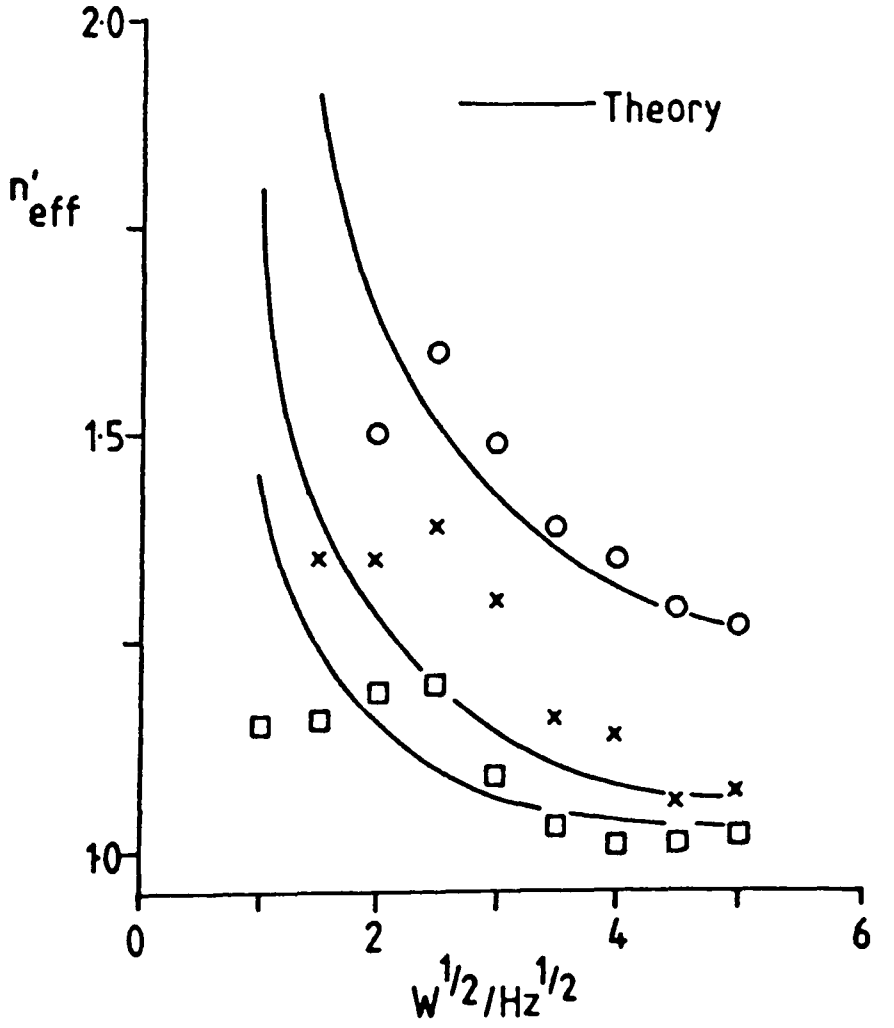


Figure 7.22: Theoretical (solid line) and experimental values of n'_{eff} plotted against $W^{1/2}$ for the reduction of 3.0×10^{-3} moldm^{-3} fluoranthene in the presence of 3.3×10^{-3} moldm^{-3} forane and (□) 0.025, (×) 0.063, (o) 0.156 moldm^{-3} nitrous oxide.

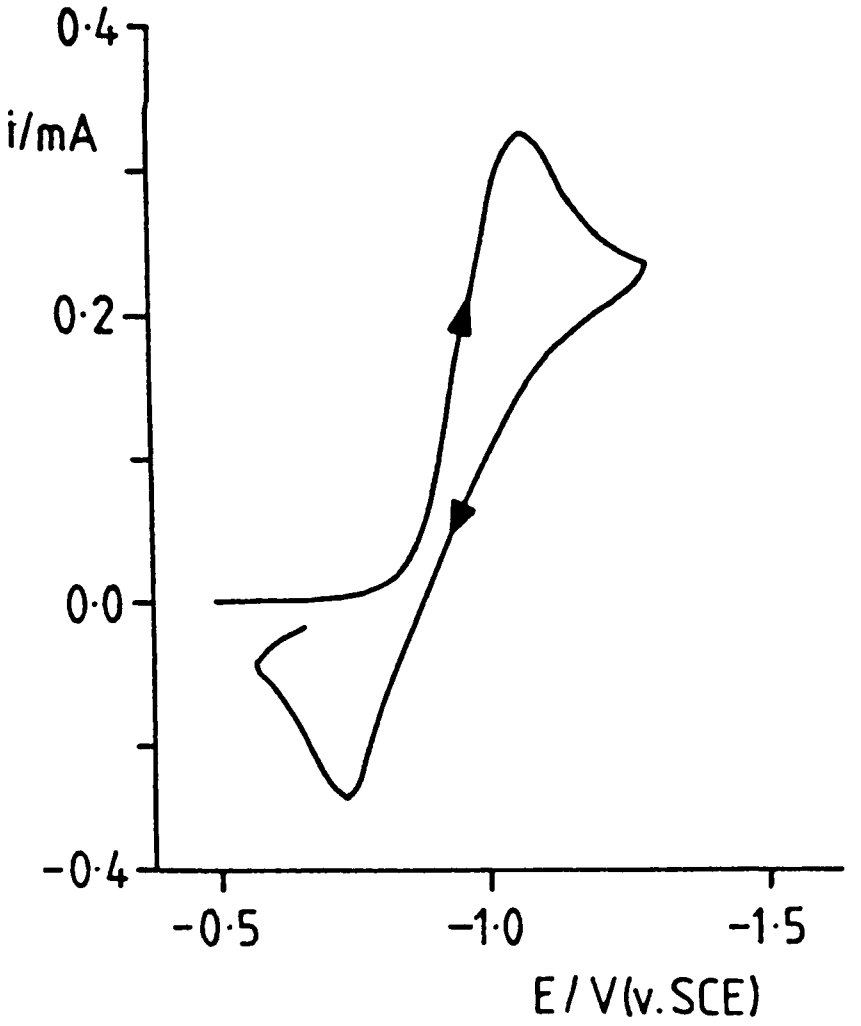


Figure 7.23: Cyclic voltammogram of 8.1×10^{-3} moldm^{-3} oxygen in acetonitrile/0.1 moldm^{-3} TBAP recorded at a mercury electrode using a scan rate of 100 mVs^{-1}.

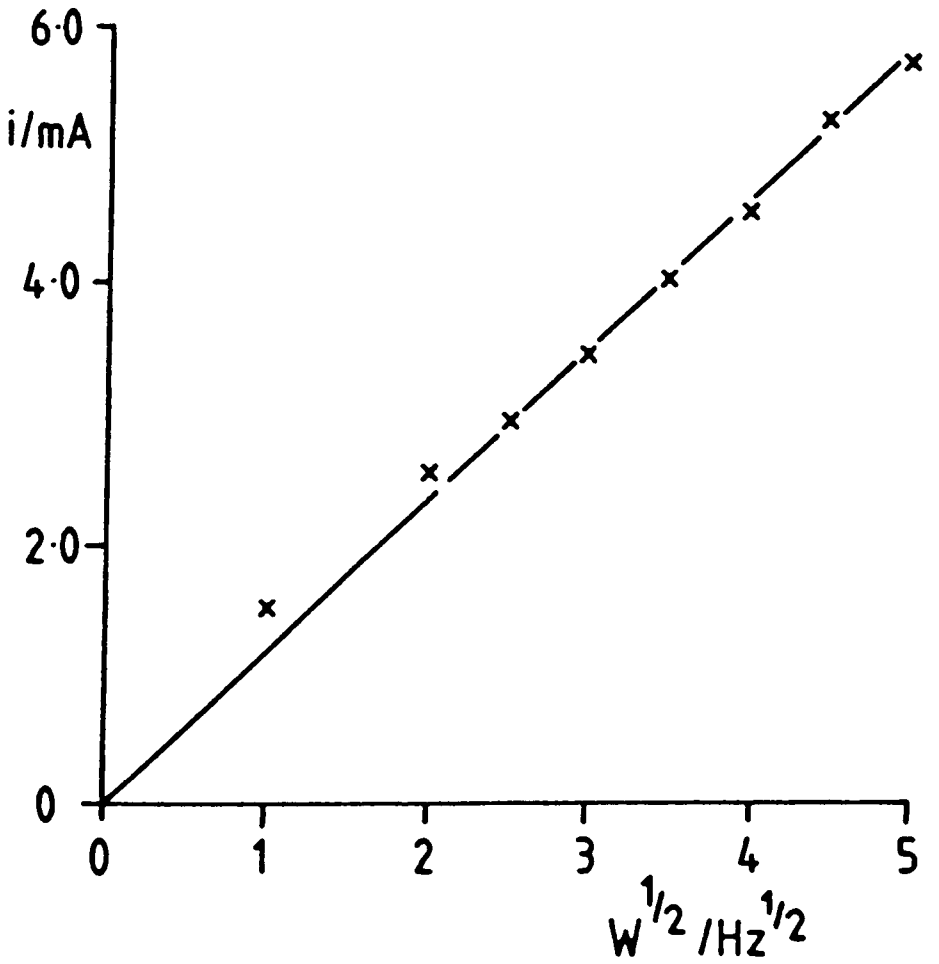


Figure 7.24: Levich plot of i_{lim} versus $W^{1/2}$ for the reduction of 8.1×10^{-3} moldm^{-3} oxygen in 0.1 moldm^{-3} TBAP/acetonitrile at a mercury RDE.

mercury RDE in acetonitrile/0.1moldm^{-3} TBAP saturated with O_2 was fixed on the limiting current of the oxygen wave and the current–time response, resulting from a step in the rotation speed, was recorded. Rotation speed steps employed were 2 → 4Hz, 3 → 5Hz and 4 → 6Hz. A typical transient, recorded using a 1 → 2Hz step, is shown in Figure 7.25. The diffusion coefficient was then determined using the expression:

$$\left[\frac{\nu}{D}\right]^{1/3} = B_q\,(W_\infty t_q - 0.04) - 1.0 \qquad 7.4$$

where W_∞ is the final rotation speed and t_q is the response time for the current to reach a fraction q of its total change. The corresponding values of B_q are:

q	0.3	0.5	0.7
B_q	20.6	12.9	8.7

The mean value for D_{O_2} was found to be 5.7±0.8x10^{-5}cm^{2}s^{-1}. This is in good agreement with the value deduced from the Levich analysis and also with D_{O_2} in acetonitrile from the literature [385]; the one electron reduction of O_2:

$$O_2 + e^- \rightleftharpoons O_2^{\cdot -}$$

can therefore be concluded as the process in operation.

Superoxide, the product of the above reaction, has been shown to act as an electron transfer reductant of fairly high reactivity [386,387] and, in particular, the cleavage of carbon/halogen bonds in aprotic solvent has been demonstrated [388]. The electro–reduction of an acetonitrile/0.1moldm^{-3} TBAP solution containing oxygen, forane and N_2O was therefore investigated using RDE voltammetry. Over a wide concentration range of forane (1–15x10^{-3}moldm^{-3}) and N_2O (1–15x10^{-3}moldm^{-3}), the reduction of oxygen remained unaffected by the presence of these substrates and the same limiting current–rotation speed data was obtained (as illustrated in Figure 7.24) for a solution containing only oxygen. In addition, this

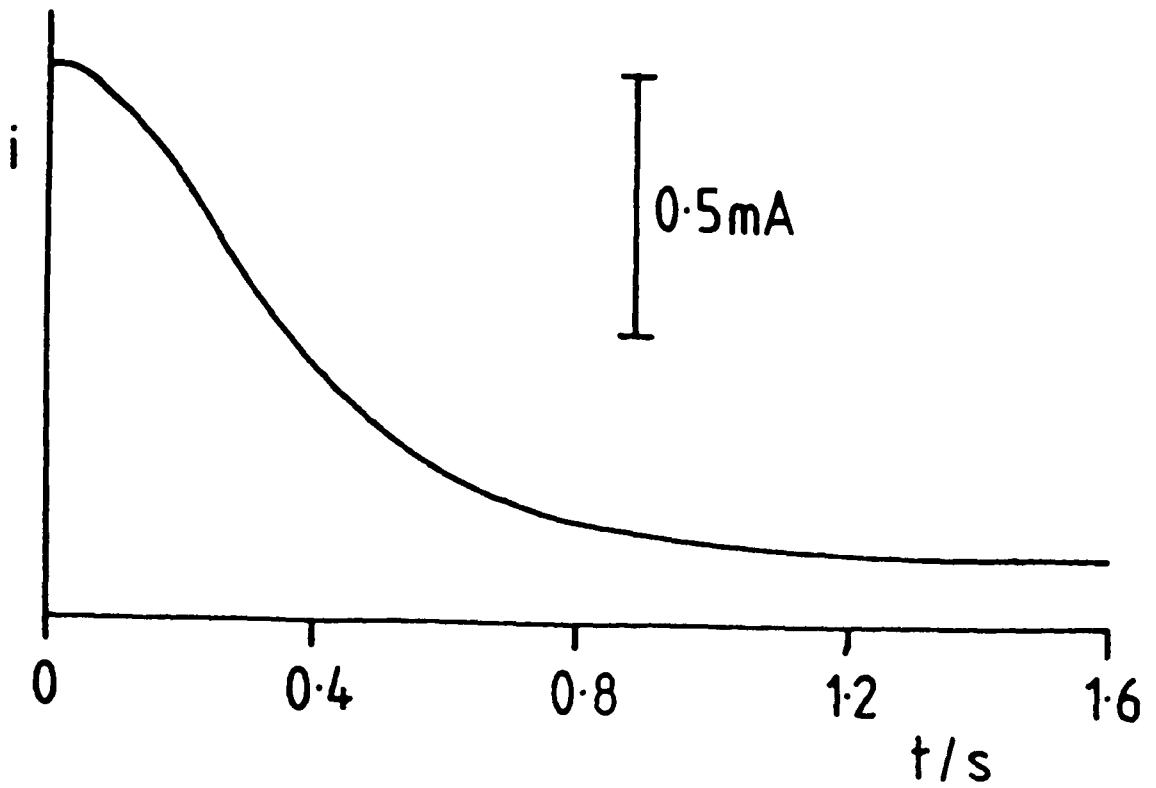


Figure 7.25: Current transient resulting from a step in the RDE rotation speed from 1.0 to 2.0 Hz. The experimental conditions were as defined in Figure 7.24.

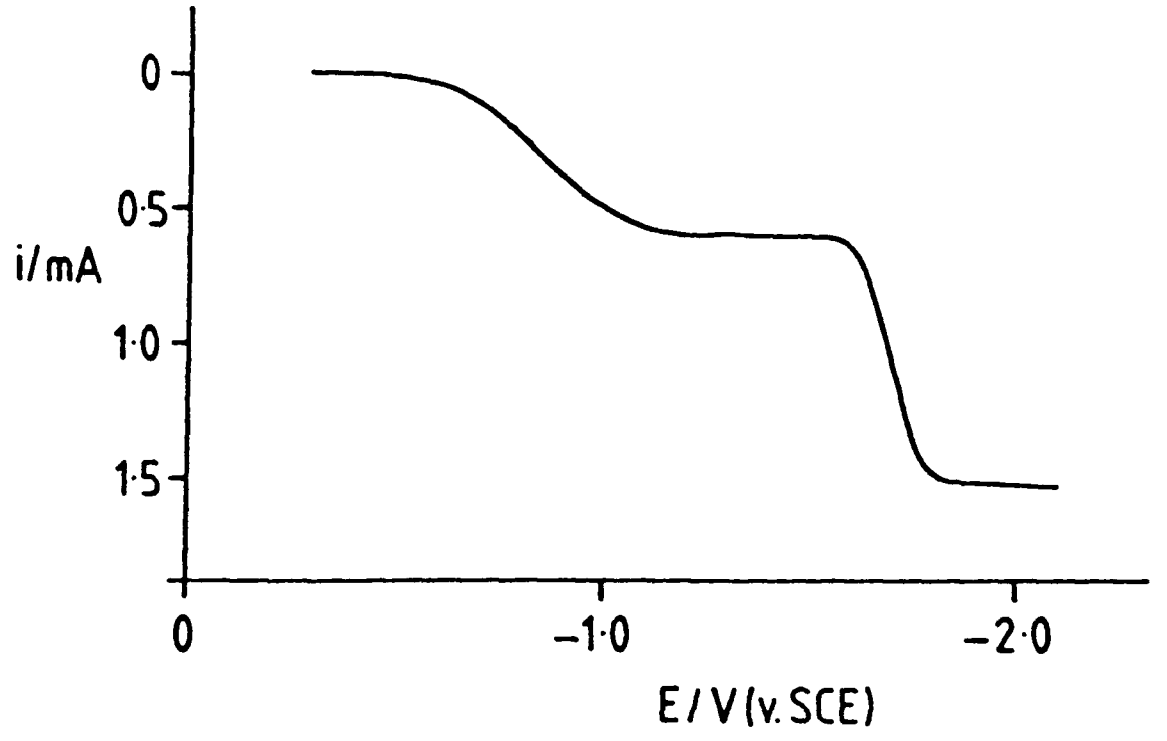


Figure 7.26: A RDE voltammogram obtained from an acetonitrile/0.1 moldm^{-3} TBAP solution containing 3.0×10^{-3} moldm^{-3} fluoranthene and 2.9×10^{-3} moldm^{-3} oxygen. A mercury RDE was employed and W = 9.0Hz.

Levich behaviour was maintained when the reduction of a solution containing oxygen and $3.0x10^{-3}moldm^{-3}$ F was investigated. This is shown in Figure 7.26 where it can be seen that the baseline for the $F/F^{\cdot -}$ reduction process is no longer at zero ampères, but instead, corresponds to the limiting current for the $O_2/O_2^{\cdot -}$ process. Levich analysis of the two waves, however, revealed that the limiting currents were additive and no interference between the two reduction processes can be concluded.

7.3.3 Conclusions

The aim of the above section was to elucidate whether N_2O or O_2 will interfere with the amperometric response of a F based forane sensor. O_2 was shown to be directly reducible on a mercury electrode in acetonitrile solution. However, the half–wave potential of the reduction is sufficiently positive of that of F to ensure no overlapping of the respective current–voltage response. Superoxide ions produced via the one electron reduction of O_2, were found not to react with forane or N_2O. The mediated reduction of N_2O by $F^{\cdot -}$ was demonstrated and the addition of the kinetics of this process to those of the $F^{\cdot -}$/forane system enabled the response in the presence of both substrates to be theoretically modelled. Thus $[forane]_\infty$ can to be deduced when a known $[N_2O]_\infty$ is present.

The conversion of this chemistry, deduced at the RDE, into the development of a practical forane sensing device can now therefore be undertaken. Such a device can be envisaged as akin to a Clark oxygen electrode in which forane diffuses through a membrane, isolating electrochemical detection from the gas phase, into an acetonitrile/TBAP/F electrolyte, where the homogeneous mediated reduction and sensing at a mercury electrode takes place. A second amperometric sensor, of the kind described by Albery *et al* [84], would be used to simultaneously measure $[O_2]$ and $[N_2O]$, enabling [forane] to be deduced (by subtraction of the N_2O response) from the catalytic current measured by the former device. This approach is therefore investigated in the following chapters.

CHAPTER EIGHT

MEMBRANE ELECTRODES FOR THE ANALYSIS OF FORANE AND NITROUS OXIDE/OXYGEN MIXTURES

In this chapter, the amperometric detection of forane, O_2 and N_2O is investigated using Clark–type membrane electrodes [79]. This approach was chosen because analogous devices have been demonstrated previously to be convenient and effective in the clinical measurement of a wide range of other gases [61,94]. Two such devices are examined here: 1) a forane sensor based on the mediated reduction of this anaesthetic via electron transfer from electrogenerated $F^{\cdot -}$ in acetonitrile solution, and 2) an aqueous, silver electrode sensor for the simultaneous determination of N_2O and O_2. The purpose of this second device is to provide continual measurements of $[N_2O]$ and $[O_2]$ which can be subtracted from the response of the forane sensor to yield a "corrected" value for measurements of forane in the presence of N_2O and/or O_2.

8.1 The Detection of Forane

8.1.1 The Forane Sensor

The design of the forane sensor is outlined in Figure 8.1. The cylindrical body (o.d. 21mm, length 250mm) was machined from nylon and the inner (o.d. 10mm, length 156mm) and outer cavities filled with an electrolyte solution of 3.0×10^{-3}moldm^{-3} F and 0.1moldm^{-3} TBAP in acetonitrile. A series of outlet holes (diameter 0.1mm) ensured solution contact between the electrolyte "reservoir" and

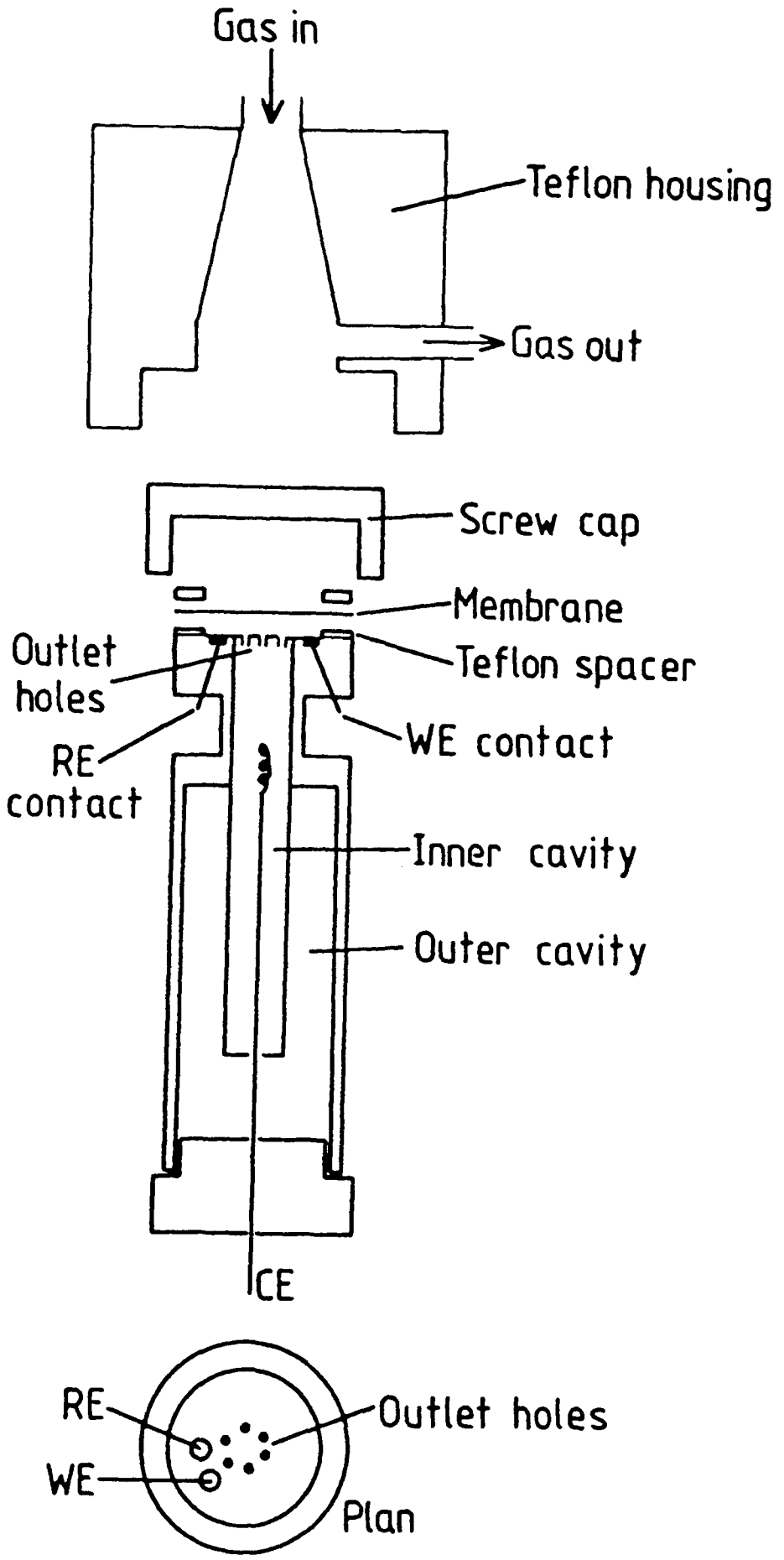


Figure 8.1: A schematic diagram of the Clark–type membrane sensor and housing used for forane detection.

the electrode elements. These consisted of a copper disc cathode (1.8mm diameter), which was electroplated with mercury using the procedure described in Chapter Four and a silver pseudo reference electrode (diameter 1.1mm). Both electrodes were set flush into the outer, exposed surface of the nylon cylinder. A platinum wire counter electrode (diameter 0.5mm) was inserted into the internal electrolyte reservoir through a nylon screw–in stopper which sealed the outer cavity.

The membrane (described later in sections 8.1.2 and 8.1.3) was held in position by a nylon cap which screwed "finger tight" onto the outer body of the sensor. A thin teflon spacer separated the membrane from the mercury working electrode, forming a tight seal and enabling the spread of a uniform electrolyte layer $\approx 30\mu$m thick. The cap of the sensor fitted tightly into the teflon housing apparatus, also shown in Figure 8.1, which was plumbed into the carrier gas/vaporiser line. Thus 0–5% forane:carrier gas mixtures could be delivered to the outer surface of the sensor membrane. All studies were conducted at room temperature.

8.1.2 Forane Sensing Results

Preliminary experiments were performed with the reservoir electrolyte solution purged of O_2 by degassing this with nitrogen as described in Chapter Four, and a teflon membrane, 25μm thick with 5μm pores was employed. The cyclic voltammogram, obtained using the above sensor containing $3.0\text{x}10^{-3}\text{moldm}^{-3}$ F in 0.1moldm^{-3} TBAP/acetonitrile, in the absence of forane is shown in Figure 8.2. The scan rate used was 100mVs^{-1}. The shape of the voltammogram is indicative of an electrochemically reversible process. The mean of the potentials of the forward (reduction) and reverse (oxidation) peaks was -1.75 ± 0.03V (vs. silver pseudo reference) which is close to the value of –1.80V (vs. SCE) for the reduction of F to $F^{\cdot -}$ observed at the RDE. This voltammogram was therefore attributed to the one electron reduction/oxidation of fluoranthene.

Figure 8.3 shows the voltammogram obtained under identical conditions to Figure 8.2, except for the delivery of a gas mixture containing 5% forane to the sensor membrane. Typical catalytic behaviour is apparent, the reduction peak is considerably enhanced in size whilst the oxidation peak is reduced [274]. This

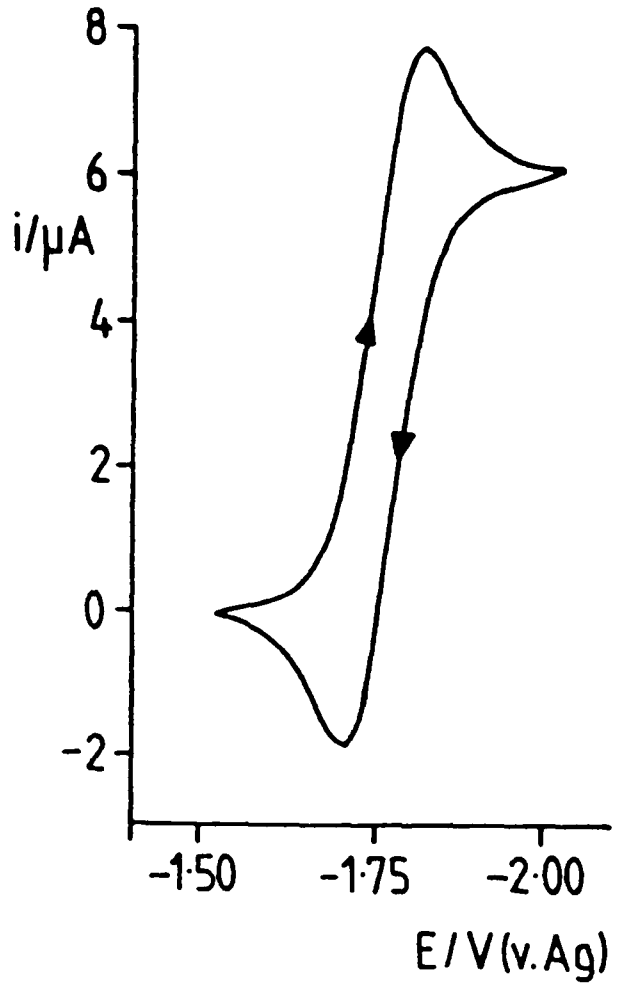


Figure 8.2: Cyclic voltammogram of 3.0×10^{-3} moldm^{-3} fluoranthene in acetonitrile/0.1 moldm^{-3} TBAP obtained from the sensor illustrated in Figure 8.1, using a scan rate of 100 mVs^{-1}.

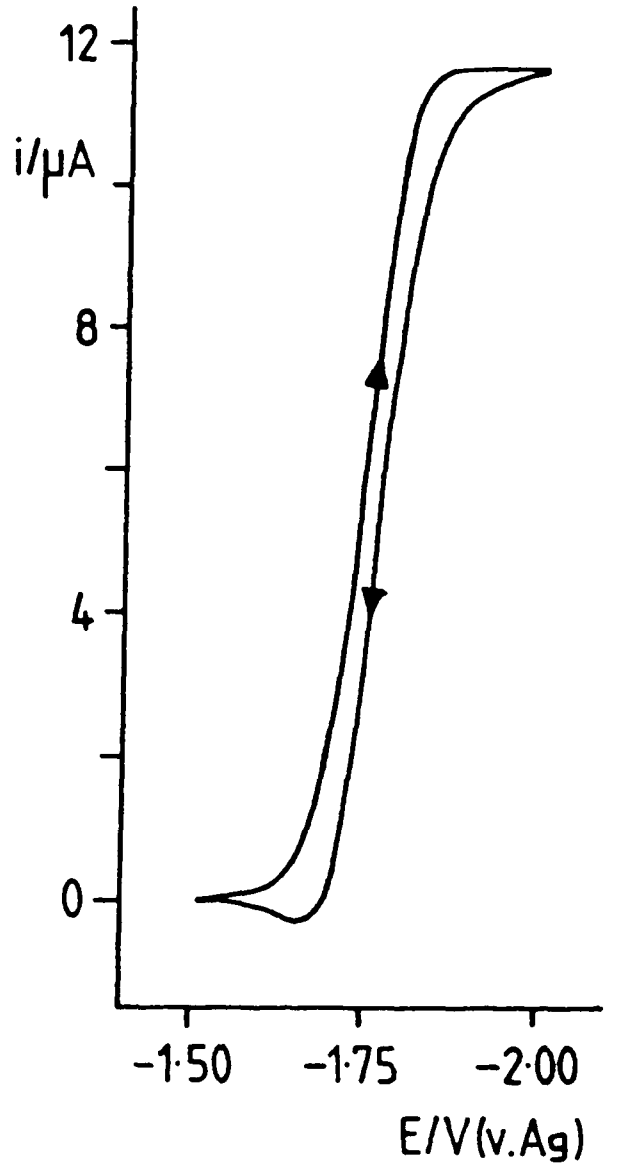


Figure 8.3: Cyclic voltammogram of 3.0×10^{-3} moldm^{-3} fluoranthene in acetonitrile/0.1 moldm^{-3} TBAP obtained from the sensor illustrated in Figure 8.1 with delivery of 5% forane to the membrane. A scan rate of 100 mVs^{-1} was used.

confirms that the anaesthetic is reaching the electrolyte and that the mediated reduction of forane is taking place.

However, the delivery of a 5% forane/N_2 gas mixture for up to four minutes was required in order for sufficient forane to diffuse through the membrane to obtain such results as shown in Figure 8.3. Moreover, when the vaporiser setting was returned to 0% forane, a delay of approximately three minutes was required before the voltammogram settled back to that expected in the absence of anaesthetic (i.e. as shown in Figure 8.2). It was concluded that the diffusion rate of forane through the 5μm pore teflon membrane was too slow [389] to meet the requirements here for an amperometric sensor with a reasonably fast response time. Additionally, after approximately twenty–four hours, the membrane began to leach acetonitrile, yielding non–reproducible results and eventually resulting in complete failure. Therefore an alternative membrane material was sought. In particular, high density polyethylene (HDPE) membranes (30μm thick, 12.5μm pores) were found to combine good forane diffusional properties with a resistance to attack from acetonitrile [390]. Sensors thus constructed lasted indefinitely without any apparent electrolyte leaching. Cyclic voltammograms in the presence of forane, similar to that in Figure 8.3 were thus obtained after delivery of the anaesthetic for approximately thirty seconds and favourably, the response returned to that of Figure 8.2 after a similar period following readjustment of the vaporiser to 0% forane.

Forane detection by a voltammetric method has therefore been demonstrated. However, the merits of pulsing the potential of the working electrode, namely increased sensitivity and decreased contamination by reaction products, were discussed in Chapters One and Two and previous amperometric sensors have successfully utilised this relatively straightforward approach [90,94]. Figure 8.4 shows the current–time response obtained when the potential of the mercury electrode was stepped from –1.40V to –2.00V (vs. silver pseudo reference) for various forane concentrations. This corresponds to a step from a potential where no current flows to a potential which causes the transport–limited reduction of F to $F^{\cdot-}$. A pulse frequency of 0.025Hz was employed. The resultant currents after the attainment of steady–state are plotted against [forane] in Figure 8.5. An excellent

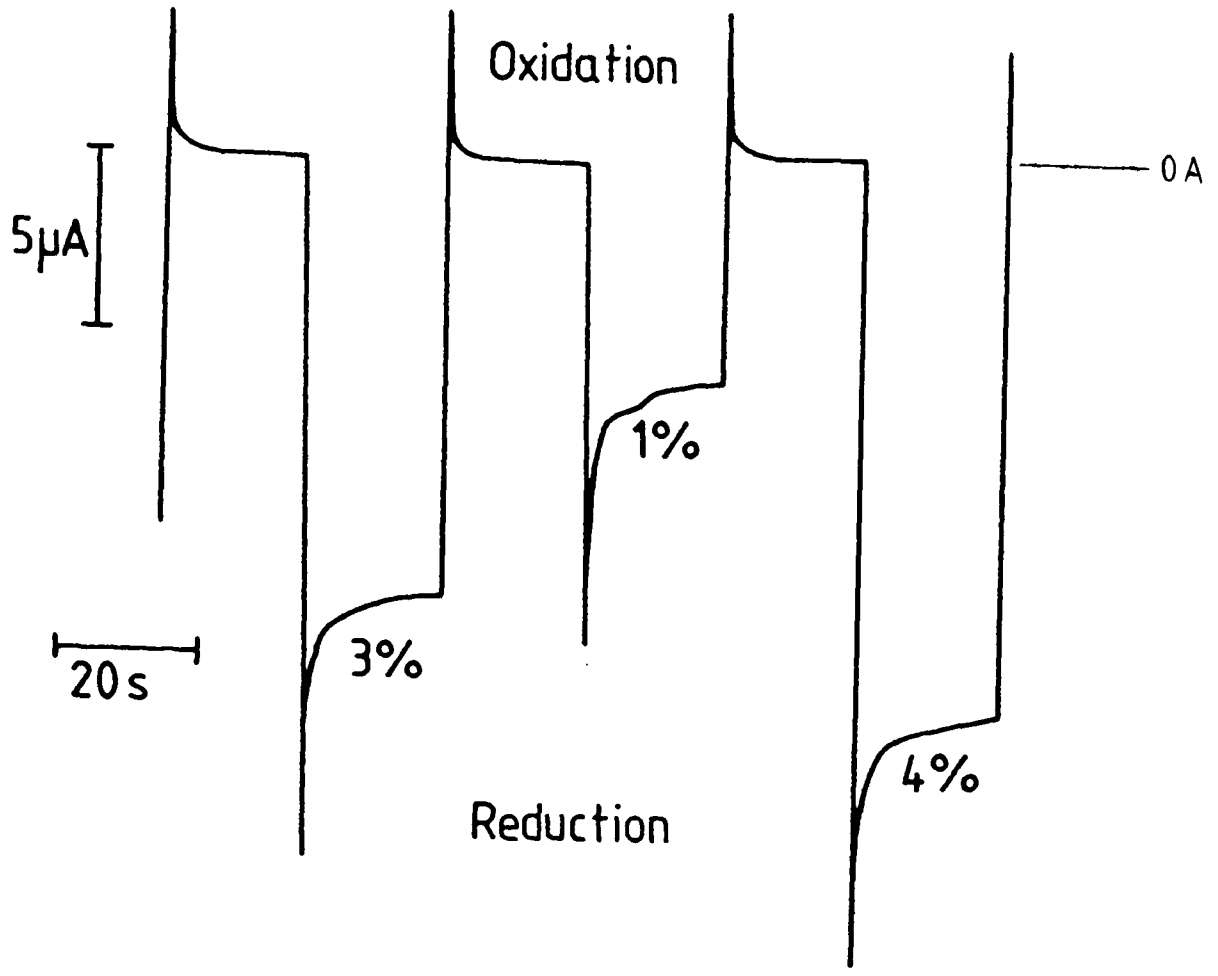


Figure 8.4: Current transient response of the membrane sensor for various forane concentrations, resulting from potential steps between –1.40V and –2.00V v.Ag.

linear relationship is observed. The transients shown in Figure 8.4 demonstrate that the response time of this device is approximately twenty seconds. This compares with response times of around ten seconds obtained previously from N_2O, O_2 and halothane amperometric sensors [90,94].

To conclude, forane detection is possible via amperometric membrane electrode means, using $F^{\cdot -}$ to homogeneously mediate the reduction of the anaesthetic and preliminary results confirm that data determined at the RDE can be reproduced using this device. 12.5μm pore HDPE is a good membrane material for use in such a sensor.

8.1.3 Multigas Analysis

The results described above, obtained using a modified Clark–type amperometric electrode, are encouraging with respect to the development of a forane sensor for use in the clinical environment. However, data was recorded in the absence of any other gases. A second amperometric sensor for the simultaneous detection of N_2O and O_2 will be discussed in section 8.2 of this chapter. This device could be plumbed into the carrier gas line and therefore used to determine [N_2O] and [O_2] which reach the membrane of the forane sensor via this source. This would enable the current response of the forane detector to be corrected (by subtraction of the N_2O and O_2 responses), using the approaches presented in Chapter Seven, to determine [forane] in the overall gas mixture. The envisaged flow system of carrier gas/forane/N_2O/O_2 would then be along the lines of that shown schematically in Figure 8.6.

The data presented in the previous section was recorded while the reservoir solution was being degassed with N_2. When this ceased, this solution became saturated with air and the current measured at the working electrode then corresponded to the reduction of both F and dissolved O_2 from the electrolyte. The concentration of O_2 dissolved in the reservoir solution cannot be determined and thus practical forane sensing using this device is only possible with continual degassing of the reservoir electrolyte solution. The utility of a practical sensor for use in respiratory analysis along the lines of a Clark–type membrane is thus

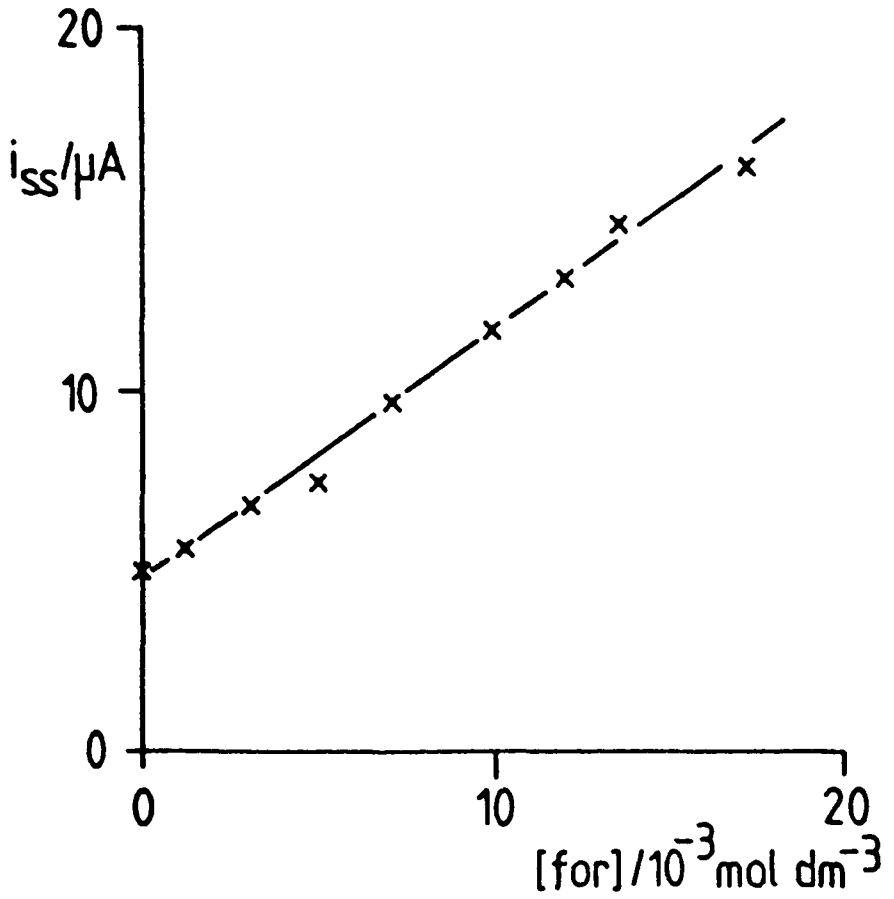


Figure 8.5: Steady–state current, determined from transients such as those shown in Figure 8.4, plotted against $[forane]_{\infty}$.

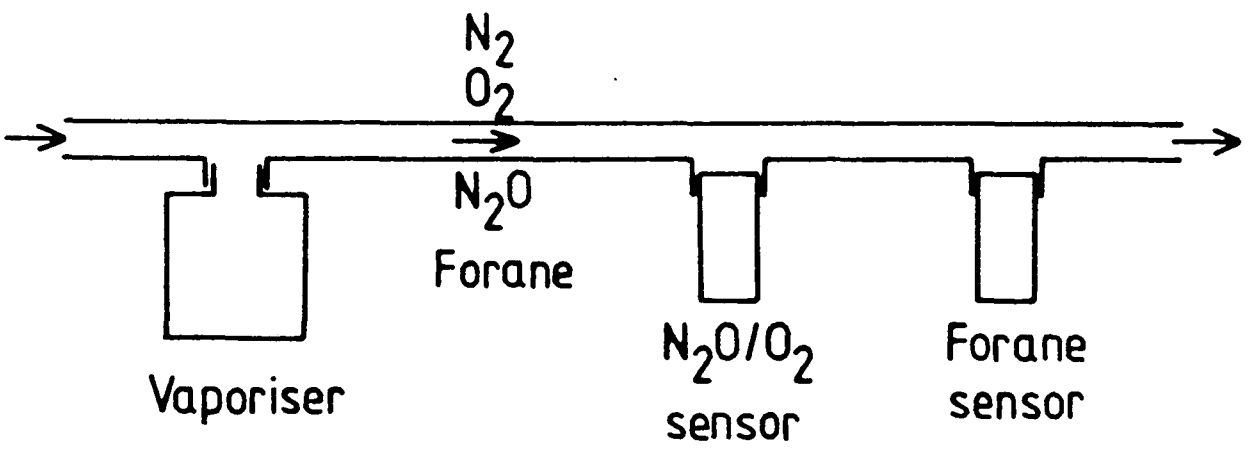


Figure 8.6: A schematic diagram of the possible vaporiser – sensor(s) gas flow system.

restricted by this problem. In addition, the response time of this device of around 10–20 seconds is tending to be slow for clinical convenience [61] where a response in under ten seconds is ideal for breath by breath analysis.

8.2 The Nitrous Oxide/Oxygen Sensor

The presence of N_2O and O_2 in the working clinical environment of any forane sensor is almost inevitable [1], and therefore the simultaneous measurement of the concentrations of these gases is essential to the successful operation of such a device. An amperometric membrane electrode sensor for the determination of N_2O and O_2 has been developed by Albery *et al* using a silver electrode in aqueous media [84,89,90] and the intended use of this device in this work is anticipated to provide the required $[N_2O]$ and $[O_2]$ information. To this end, the following section describes the construction and testing of a sensor based on these previous findings.

8.2.1 The Simultaneous Nitrous Oxide/Oxygen Sensor

The sensor constructed was similar to that described in section 8.2 and is illustrated in Figure 8.7. The working electrode was silver (diameter 1.2mm), a silver pseudo reference electrode (diameter 1.1mm) was used and an aqueous solution of 1.0moldm^{-3} KOH/0.1moldm^{-3} KCl served as supporting electrolyte. 12.5μm pore HDPE was once again used as the membrane material and a platinum wire, inserted into the reservoir solution, again served as the counter electrode.

8.2.2 The Reduction of Nitrous Oxide and Oxygen at a Silver Rotating Disc Electrode

Preliminary experiments examined the electroactivity of N_2O and O_2 at a silver RDE in 1.0moldm^{-3} KOH/0.1moldm^{-3} KCl. Reductions for each gas, shown in Figures 8.8 and 8.9 were observed with $E_{1/2}(O_2) \approx -0.38 \pm 0.02$V and $E_{1/2}(N_2O) \approx -1.20 \pm 0.02$V (versus SCE) and Levich analysis of the resulting limiting current–$W^{1/2}$ data was consistent with $D_{O_2} = 1.60 \pm 0.03 \times 10^{-5}$cm^{2}s^{-1} (four electron

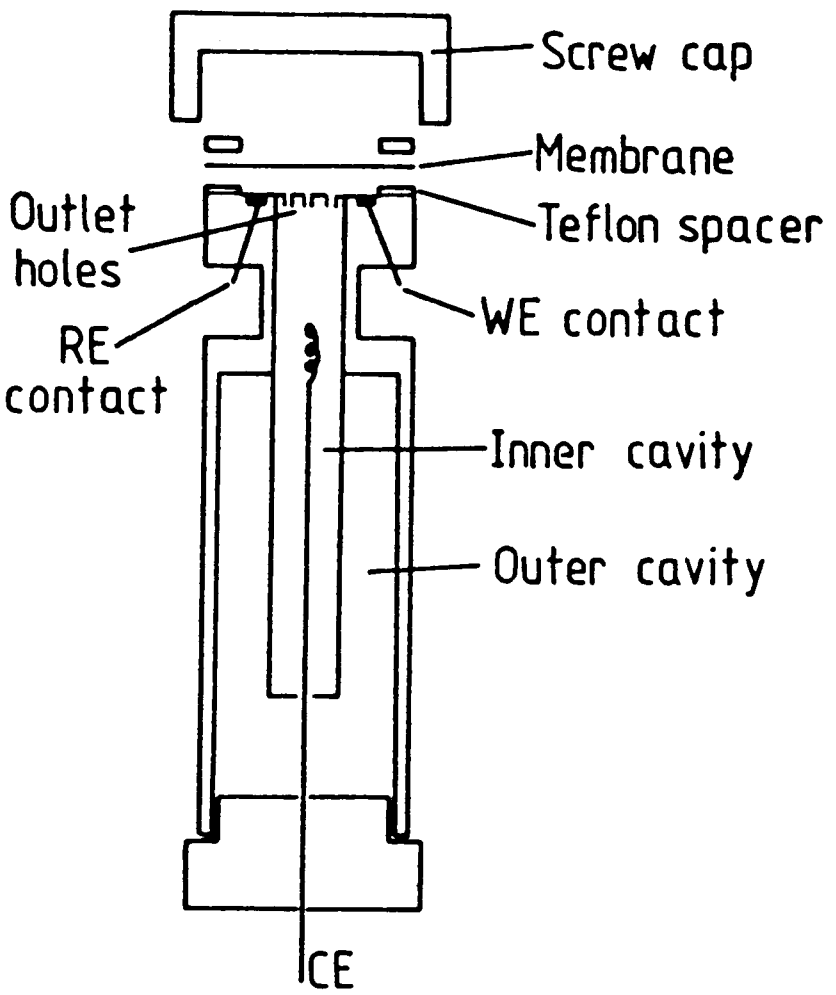


Figure 8.7: The simultaneous nitrous oxide/oxygen membrane sensor.

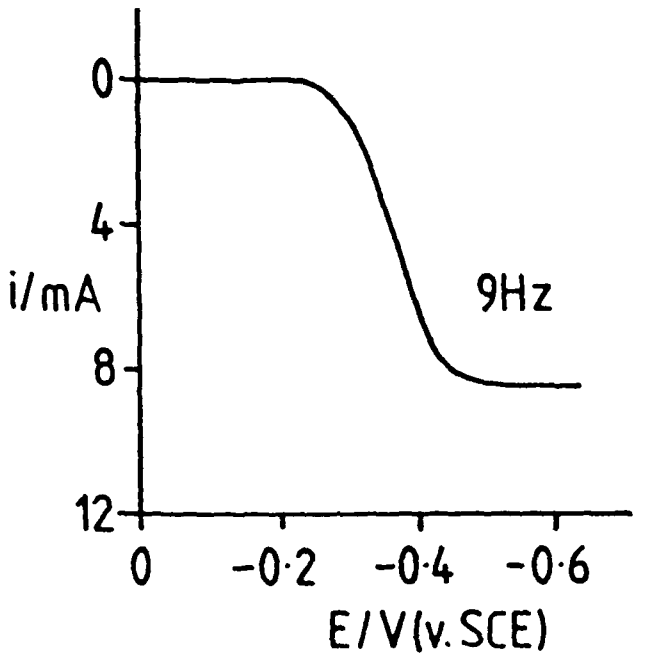


Figure 8.8: RDE voltammogram for the reduction of 8.0×10^{-3} moldm^{-3} oxygen in 1.0 moldm^{-3} KOH/0.1 moldm^{-3} KCl at a silver electrode.

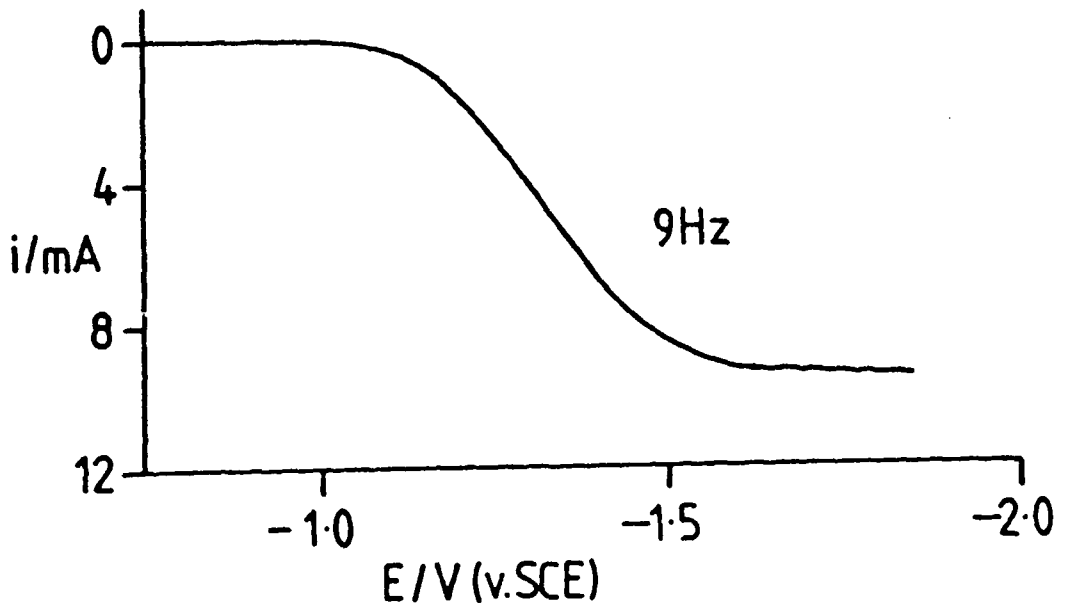


Figure 8.9: RDE voltammogram for the reduction of 0.125 moldm^{-3} nitrous oxide in 1.0 moldm^{-3} KOH/0.1 moldm^{-3} KCl at a silver electrode.

process [391]) and $D_{N_2O} = 0.80 \pm 0.04 \times 10^{-5} cm^2 s^{-1}$ (two electron process [84]). These are in good agreement with the literature values for the diffusion coefficients in this medium of $1.66 \times 10^{-5} cm^2 s^{-1}$ [392] and $0.77 \times 10^{-5} cm^2 s^{-1}$ [84] respectively.

8.2.3 The Reduction and Sensing of Gaseous Nitrous Oxide and Oxygen using an Aqueous Membrane Electrode

Figures 8.10 and 8.11 show voltammograms, obtained using the membrane electrode described above, for the reduction of a range of percentages of N_2O and O_2 respectively in gas mixtures with N_2. The limiting currents measured from these voltammograms are plotted in Figures 8.12 and 8.13 as a function of the percentage of N_2O and O_2, and a linear dependence on each can be observed. Larger currents recorded for N_2O over O_2 are attributed to the greater permeability and faster diffusion through the HDPE membrane of the former gas [84]. Thus N_2O is shown to diffuse approximately twenty times faster through 12.5μm pore HDPE than O_2 [393].

Voltammograms were then recorded for N_2O/O_2 gas mixtures. A typical example is shown in Figure 8.14 and the resulting transport–limited currents are plotted in Figure 8.15 against the percentage N_2O present in the N_2O/O_2 mixture. The limiting current for the N_2O reduction was deduced by subtraction of the O_2 current for that particular gas mixture. Once again, linear relationships between the limiting currents and percentages of N_2O and O_2 are observed.

Nitrogen is generated as a product of the reduction of N_2O [84] and therefore prolonged electrode polarisation at potentials negative of –1.20V produces tiny N_2 bubbles which occlude the working electrode and prevent the sensor from functioning [89]. Albery *et al* [90,94] overcame this problem by pulsing the potential of the working electrode, which therefore produces less N_2 and prevents bubble formation. This approach was investigated here. The pulse sequence used is shown in Figure 8.16; the potential of the silver working electrode was thus stepped from –0.7V (a potential corresponding to the transport–limited reduction of O_2 only) to –1.3V (corresponding to the reduction of N_2O and O_2). A typical series of transients thus recorded is shown in Figure 8.17 and the limiting currents for O_2 and N_2O

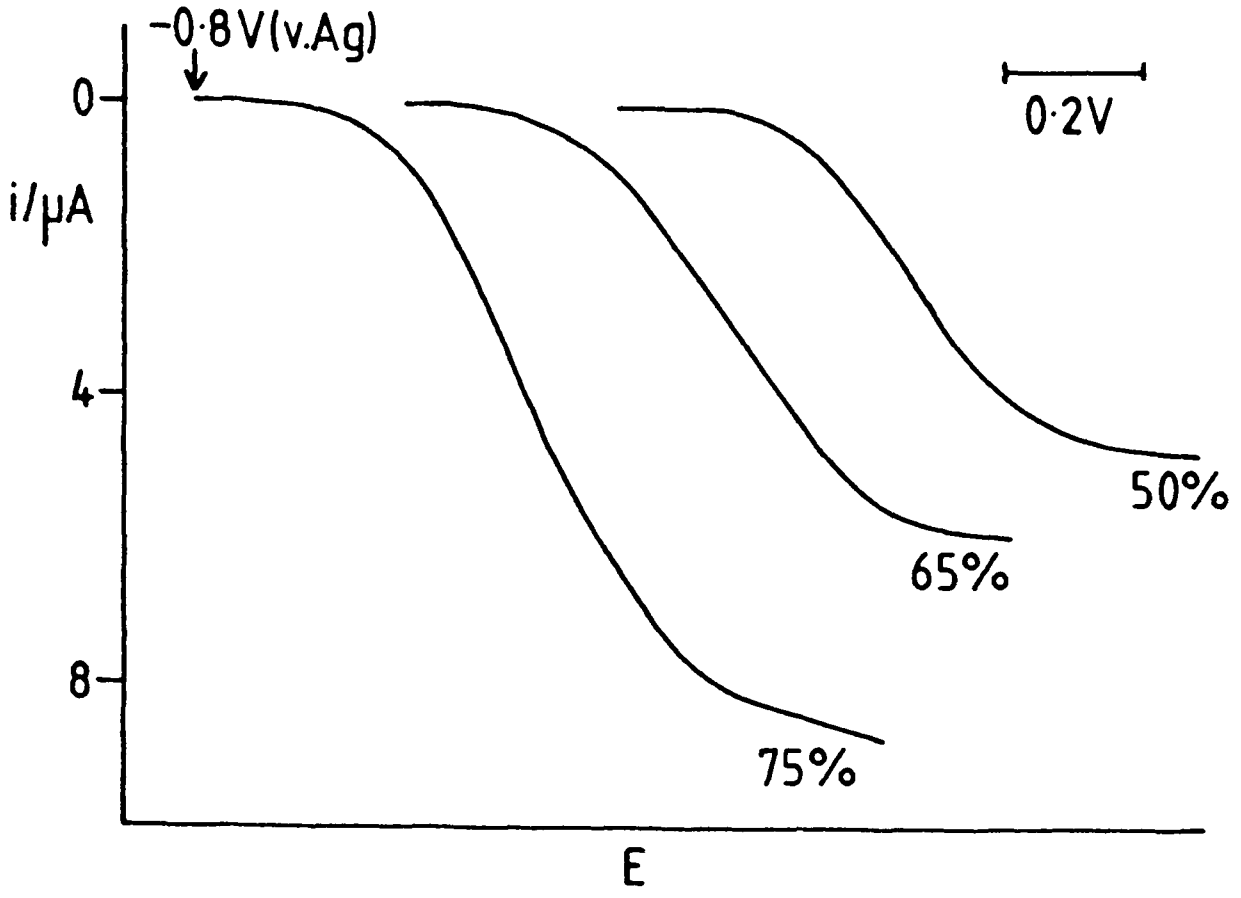


Figure 8.10: Voltammograms for the reduction of various concentrations of nitrous oxide, delivered to the membrane of the sensor illustrated in Figure 8.7.

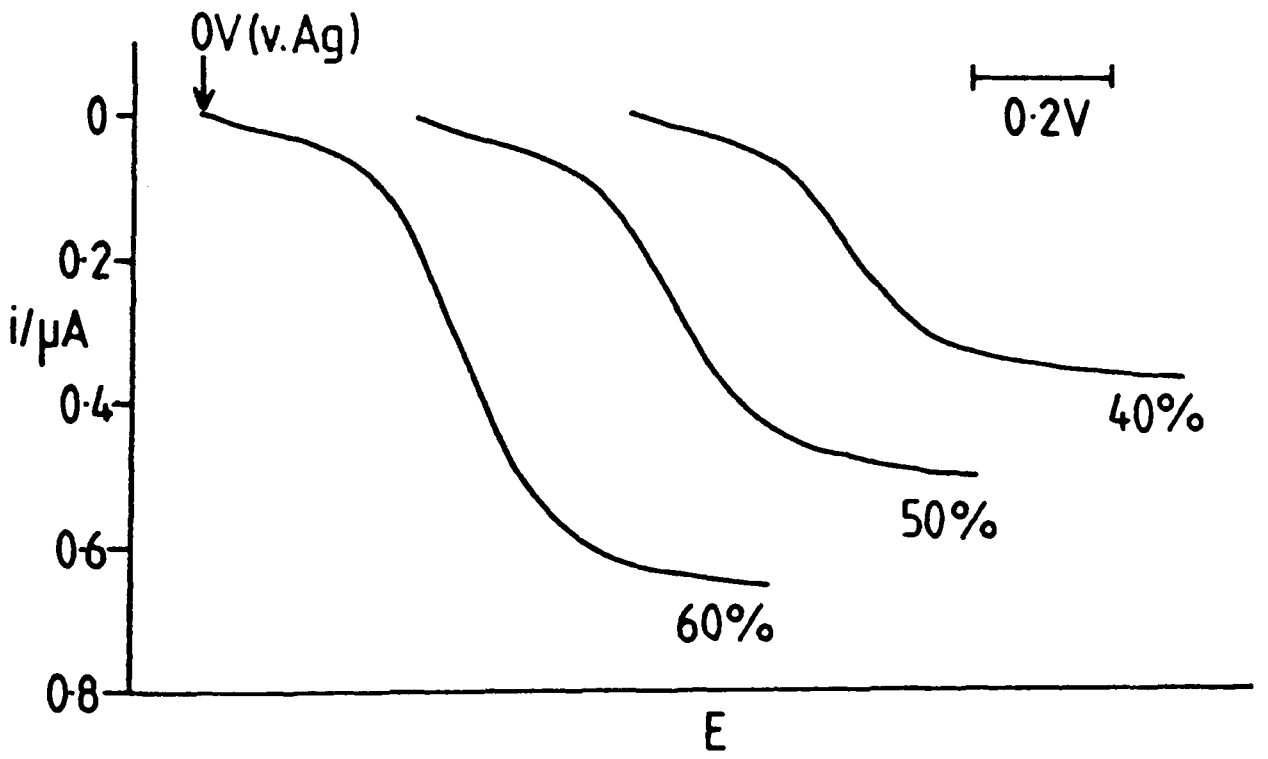


Figure 8.11: Voltammograms for the reduction of various concentrations of oxygen, delivered to the membrane of the sensor illustrated in Figure 8.7.

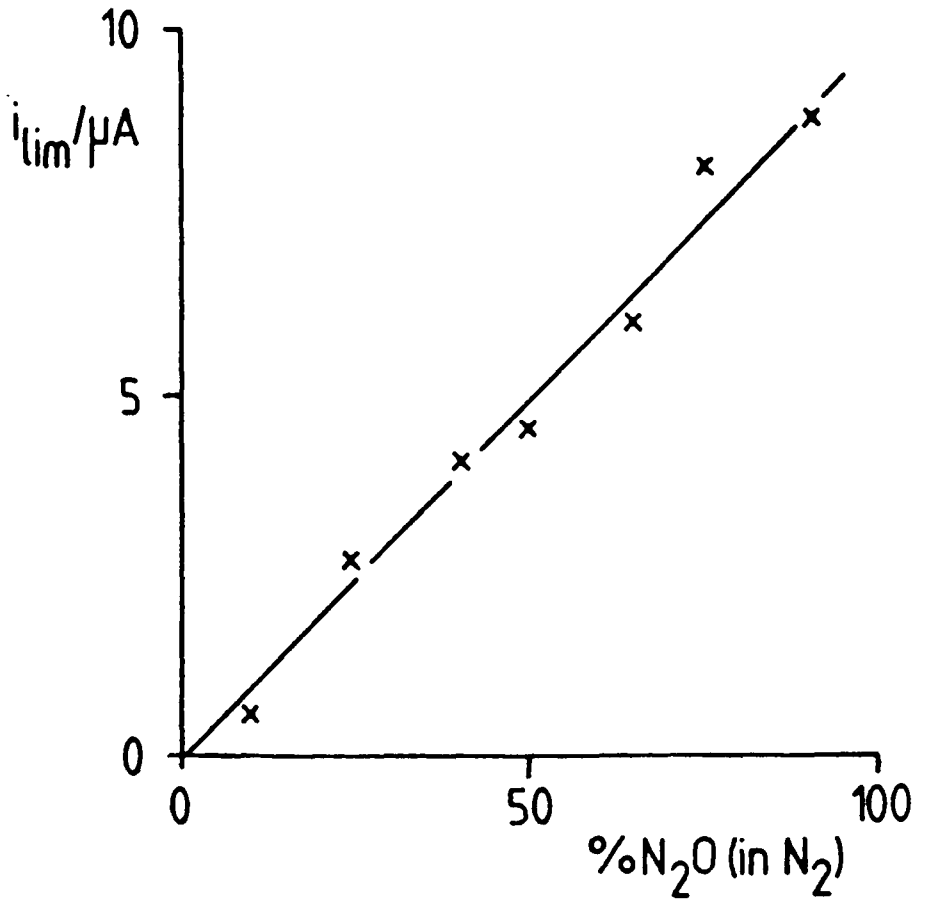


Figure 8.12: Limiting currents, determined from voltammograms such as those shown in Figure 8.10, plotted against the percentage of N_2O in the N_2O/N_2 mixture delivered to the sensor membrane.

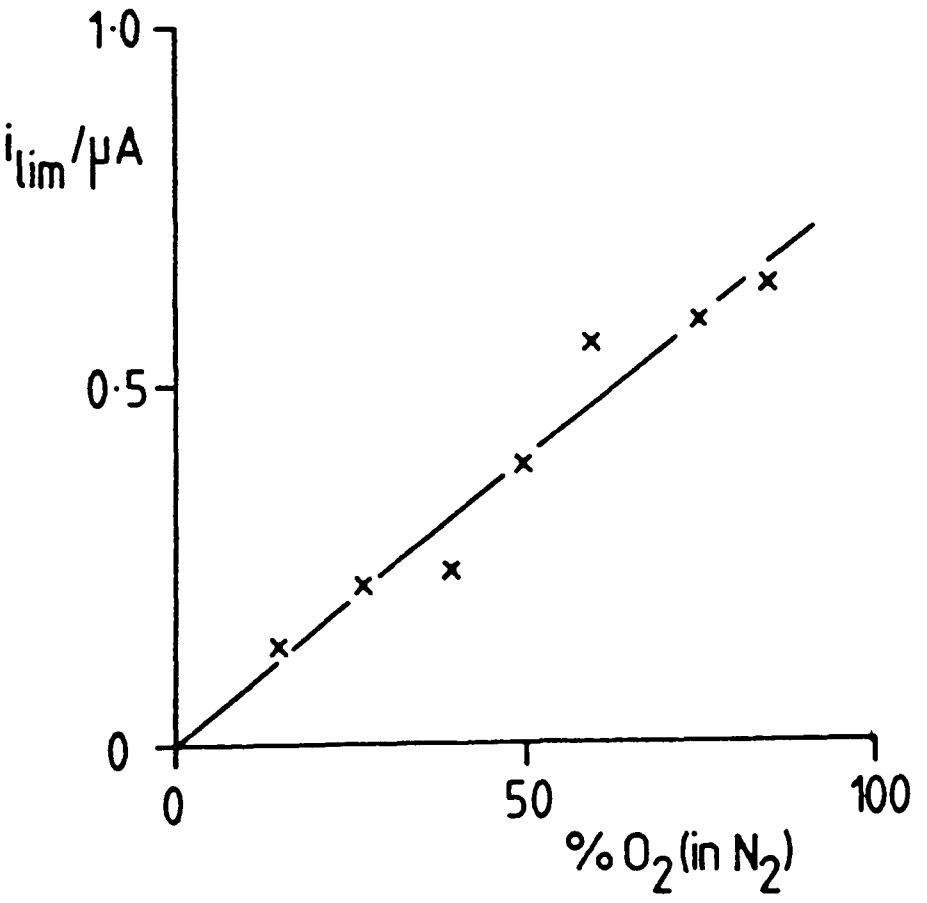


Figure 8.13: Limiting currents, determined from voltammograms such as those shown in Figure 8.11, plotted against the percentage of O_2 in the O_2/N_2 mixture delivered to the sensor membrane.

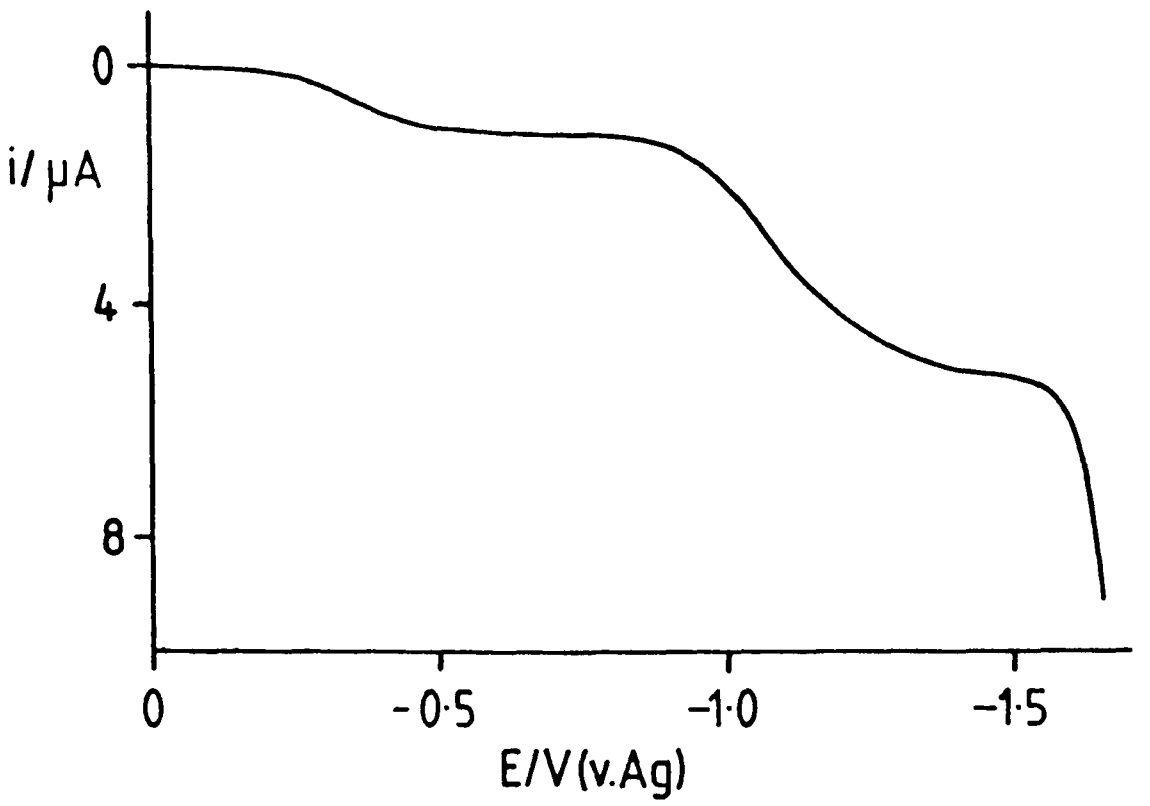


Figure 8.14: A typical voltammogram for the reduction of a N_2O/O_2 mixture (30% N_2O, 70% O_2) delivered to the sensor membrane.

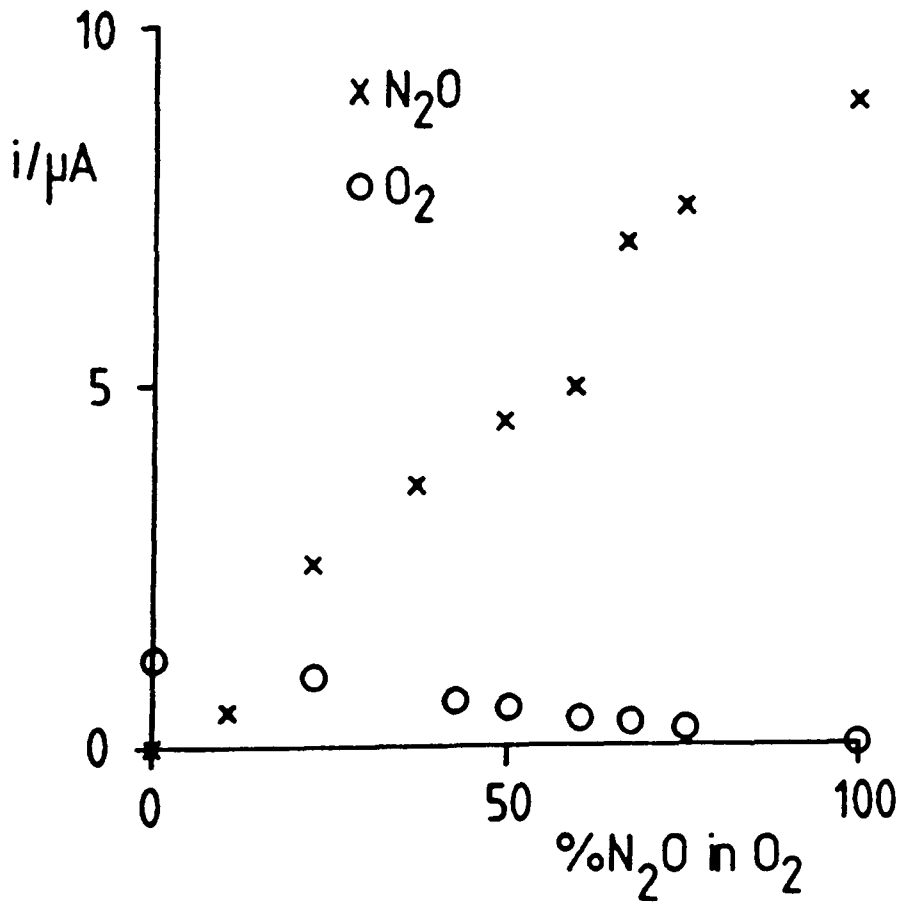


Figure 8.15: Limiting currents, determined from voltammograms such as that shown in Figure 8.14 for N_2O/O_2 mixtures, plotted as a function of $\%N_2O$ in the mixture.

(corrected for O_2) obtained from this are plotted against the percentage N_2O in the N_2O/O_2 gas mixture in Figure 8.18. These results confirm that N_2O is approximately twenty times more permeable through HDPE than O_2 and indicate clearly that the simultaneous measurement of N_2O and O_2 is feasible using an amperometric sensor of the kind described in section 8.2.1. The response time of the device is approximately twenty seconds.

In conclusion, the use of an amperometric sensor of this kind means that simultaneous detection of O_2 and N_2O is possible.

8.3 Summary

A sensor for the detection of forane, which incorporates the homogeneous mediating properties of $F^{\cdot -}$ into a conventional membrane electrode, was constructed and evaluated. In the absence of oxygen, and when operated in a pulsed potential mode, the device demonstrated a linear relationship between the steady–state current and forane concentration. A response time of approximately twenty seconds was observed when 12.5μm pore HDPE was used as a membrane material. In order to prevent an interference from oxygen dissolved in the electrolyte reservoir, continual degassing of this solution was necessary. This therefore limits the practical utility of the device.

A second sensor was constructed to simultaneously measure N_2O/O_2 and this was also shown to yield a linear response between current and gas concentration. Therefore, the use of an amperometric sensor of this kind in conjunction with a forane sensing device means that the response of the latter can be corrected for N_2O and O_2 enabling the deduction of [forane]. Respiratory breath by breath analysis is therefore feasible.

The limitations of the membrane sensor described here, namely a sluggish response and the need for electrolyte deoxygenation, led to the investigation of other means of forane detection. To this end, Chapters Nine and Ten of this thesis are concerned with the development and utility of a forane sensor based on a ChE

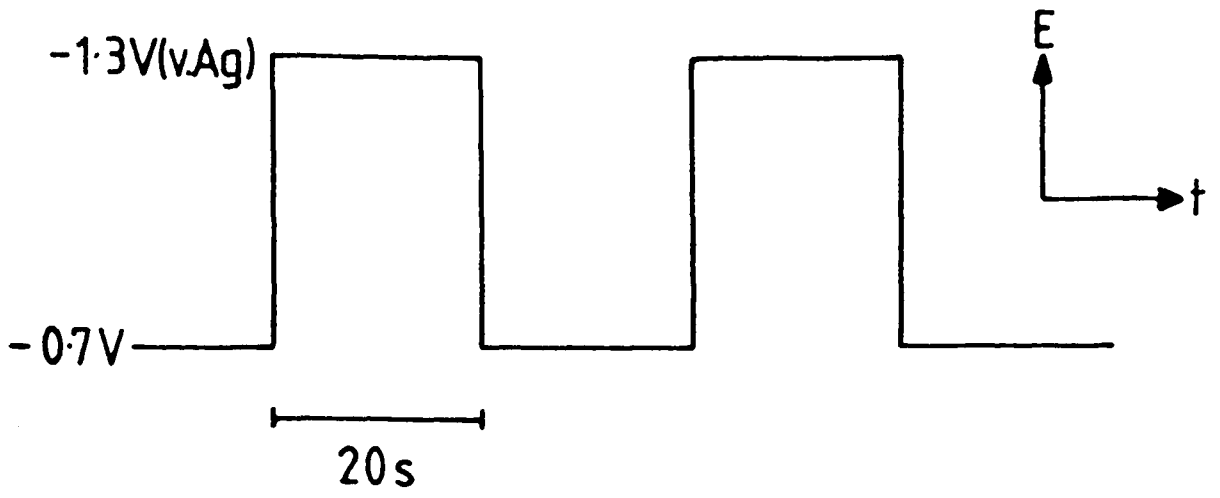


Figure 8.16: The potential–time sequence employed for the pulsed N_2O/O_2 sensor experiments.

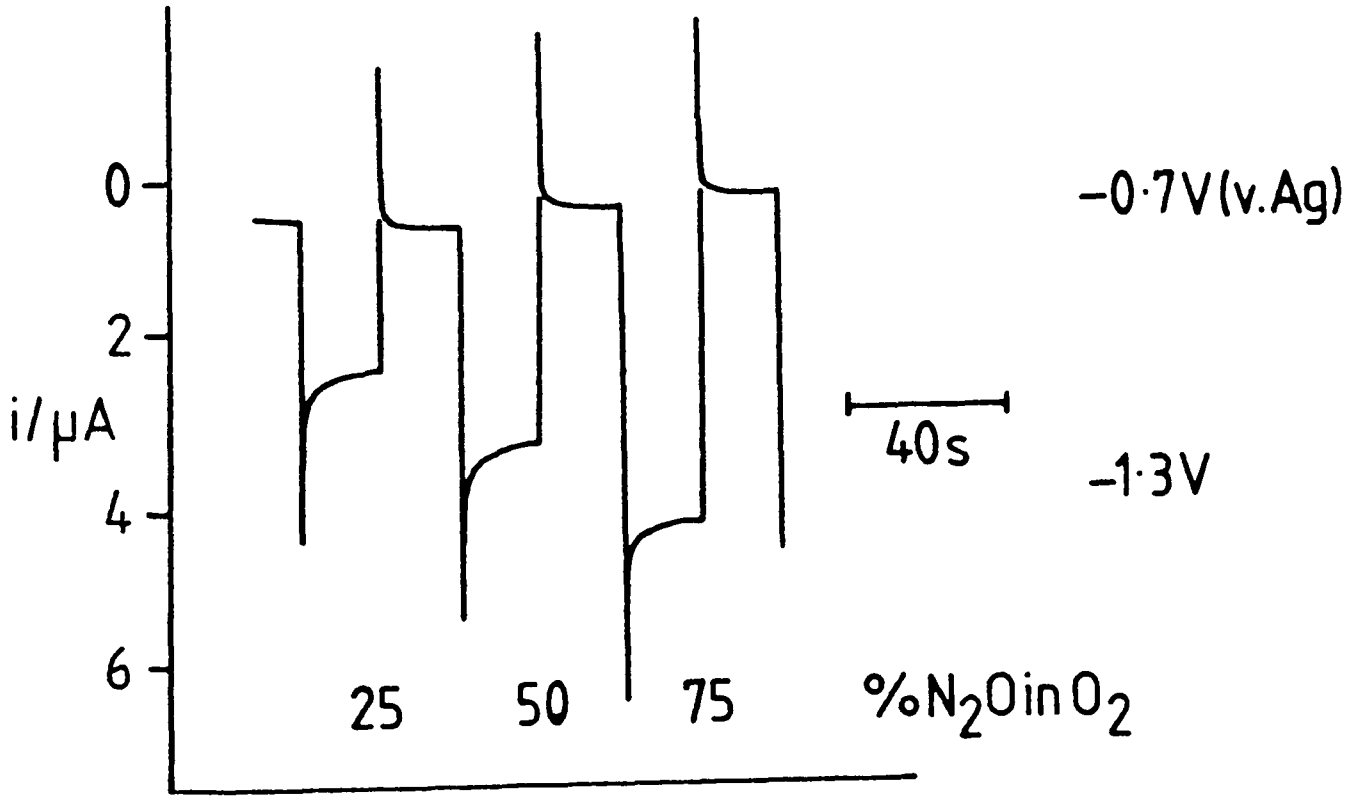


Figure 8.17: Current transients resulting from stepping the potential of the N_2O/O_2 sensor between –0.7V (reduction of O_2 only) and –1.3V v.Ag (reduction of O_2 and N_2O) for a range of N_2O : O_2 mixtures.

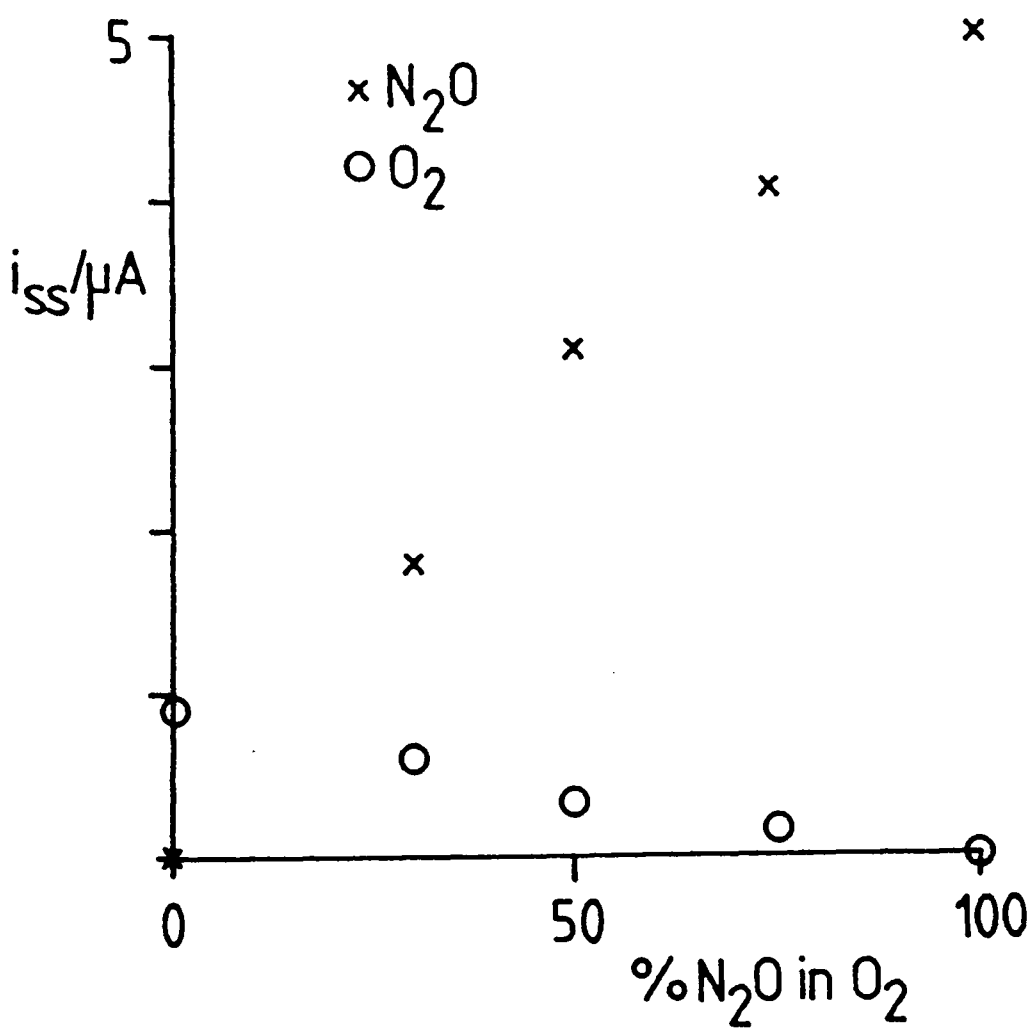


Figure 8.18: The steady–state current obtained from transients such as those shown in Figure 8.17 plotted versus $\%N_2O$.

approach.

CHAPTER NINE

THE MEDIATED REDUCTION OF FORANE AND NITROUS OXIDE AT THE CHANNEL ELECTRODE

A channel electrode, modified to facilitate the introduction of gaseous anaesthetics, will be used as the basis of the amperometric sensor to be described in Chapter Ten. Therefore, the reduction of forane and N_2O in acetonitrile using $F^{\cdot -}$ as an electrogenerated mediator is investigated at the channel electrode in this chapter. The experimental data is analysed by comparison with the theory presented in Chapter Three for the determination of steady–state currents resulting from processes involving coupled homogeneous kinetics at the ChE. Thus, electrode reaction mechanisms are assigned to the processes for the catalytic reduction of each anaesthetic. The mechanistic and kinetic deductions are compared with those found for these systems at the RDE in Chapter Seven.

9.1 Preliminary Experiments

Preliminary experiments were undertaken, using the flow system and mercury ChE cell described in Chapter Four, to investigate the one electron reduction of fluoranthene. This study served the dual purpose of confirming the hydrodynamic properties of the ChE over the range of flow rates employed [169], and enabling the depth of the channel (2h) to be calibrated from the Levich equation (equation 2.66) for the ChE [103]:

$$i_{lim} = 0.925nFw_e \left[\frac{V_f D^2 x_e^2}{h^2 d}\right]^{1/3} .[F]_\infty \qquad 9.1$$

since D_F is known from previous studies at the RDE (described in Chapter Five).

Figure 9.1 shows typical voltammograms obtained for flow rates between $4.6x10^{-3}$ and $0.135cm^3s^{-1}$ from an acetonitrile solution containing $1.00x10^{-3}moldm^{-3}$ F and 0.2 $moldm^{-3}$ TBAP. Thus $E_{1/2}$ for the reduction of F to $F^{\cdot -}$ is $-1.75\pm0.03V$ (vs. silver pseudo reference electrode). The dimensions of the mercury plated working electrode used were $w_e = 0.441cm$ and $x_e = 0.082cm$. The resulting Levich plot of i_{lim} versus $V_f^{1/3}$ is shown in Figure 9.2, and using the value of $D_F = 2.28x10^{-3}$ found at the RDE, the height of the channel was determined to be 0.041cm. The excellent straight line apparent in Figure 9.2 confirms that the hydrodynamics of the ChE are in full agreement with the predictions of the Levich equation [103] discussed in section 2.3.4 of Chapter Two. Thus, assumptions regarding the absence of lateral diffusion and edge effects [168–170] are valid over the flow rate range investigated for the ChE and flow cell employed here.

9.2 The Mediated Reduction of Forane

Figure 9.3 shows voltammograms obtained under the same experimental conditions defined above, except for the presence of increasing concentrations of forane. As expected, a catalytic increase in i_{lim} can be observed. Limiting currents were thus recorded as a function of flow rate and of the ratio of mediator to substrate. The resulting experimental data is shown in Figure 9.4. This data was analysed by comparison with the theory presented in Chapter Three for an EC'preeqm process at a channel electrode – the mechanism deduced at the RDE in Chapter Seven to be appropriate for the mediated reduction of forane by $F^{\cdot -}$. Thus "working curves" of n_{eff} versus k_{norm}(EC'preeqm), computed using the backwards implicit finite–difference approach detailed in Chapter Three, section 3.2.2.2, were calculated for the experimental ratios of $[A]_\infty/[Y]_\infty$ and from these, graphs of k_{norm}(EC'preeqm) against $V_f^{-2/3}$ were determined. A typical example of one such

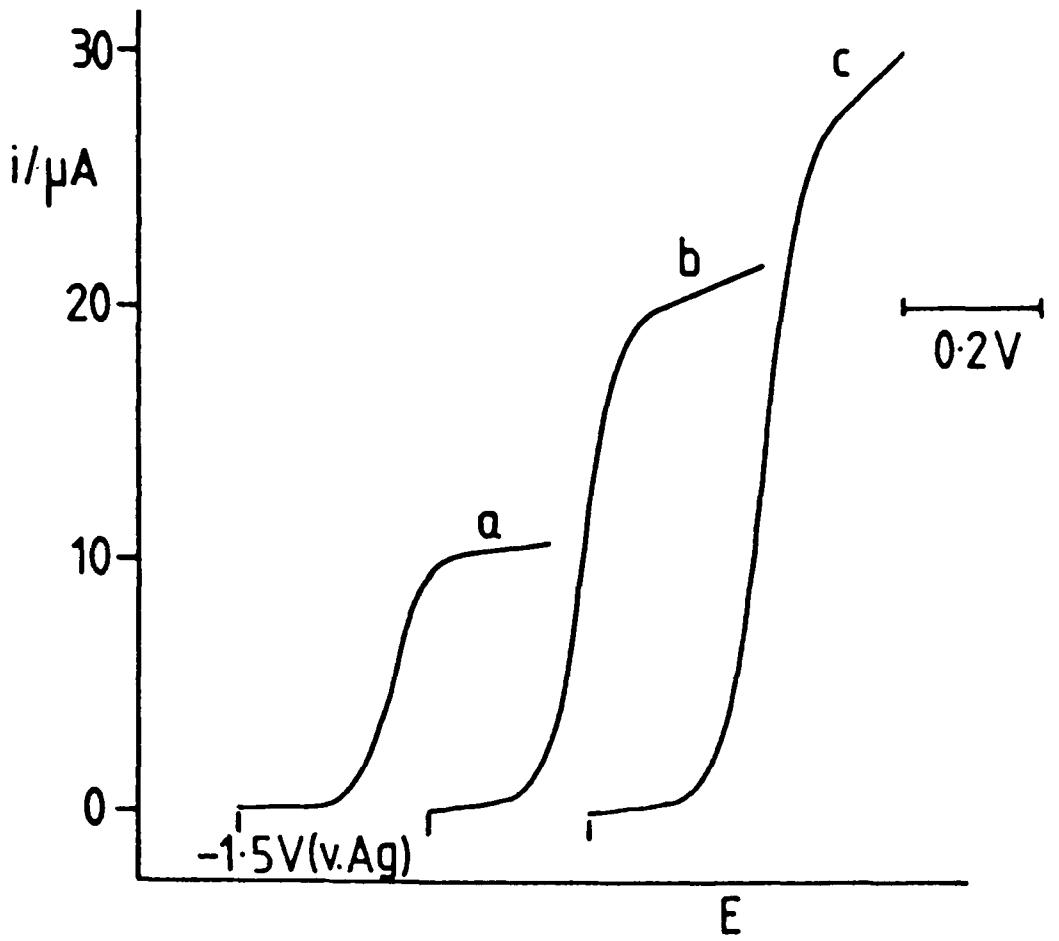


Figure 9.1: Typical ChE voltammograms for the reduction of 1.00×10^{-3} moldm^{-3} fluoranthene in acetonitrile/0.2 moldm^{-3} TBAP at a mercury electrode using flow rates of (a) 4.6×10^{-3}, (b) 3.64×10^{-2}, (c) 0.135 cm^{3}s^{-1}.

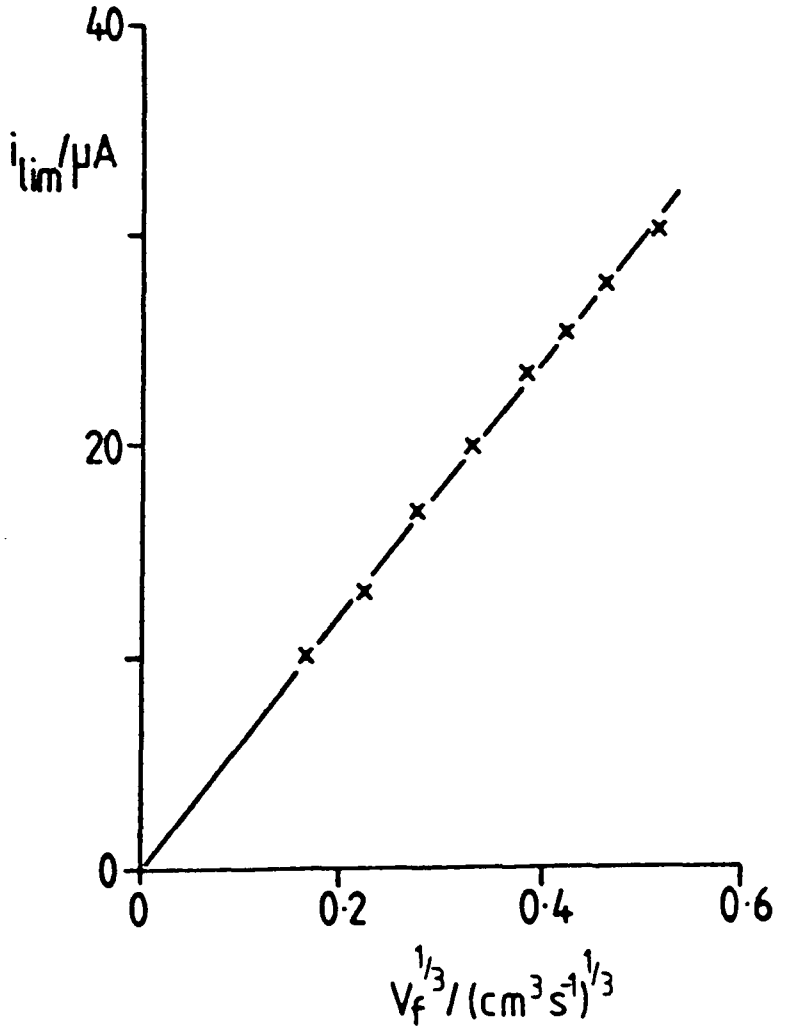


Figure 9.2: Levich plot of i_{lim} versus $V_f^{1/3}$ for the reduction of fluoranthene at the ChE. The experimental conditions were as stated in Figure 9.1.

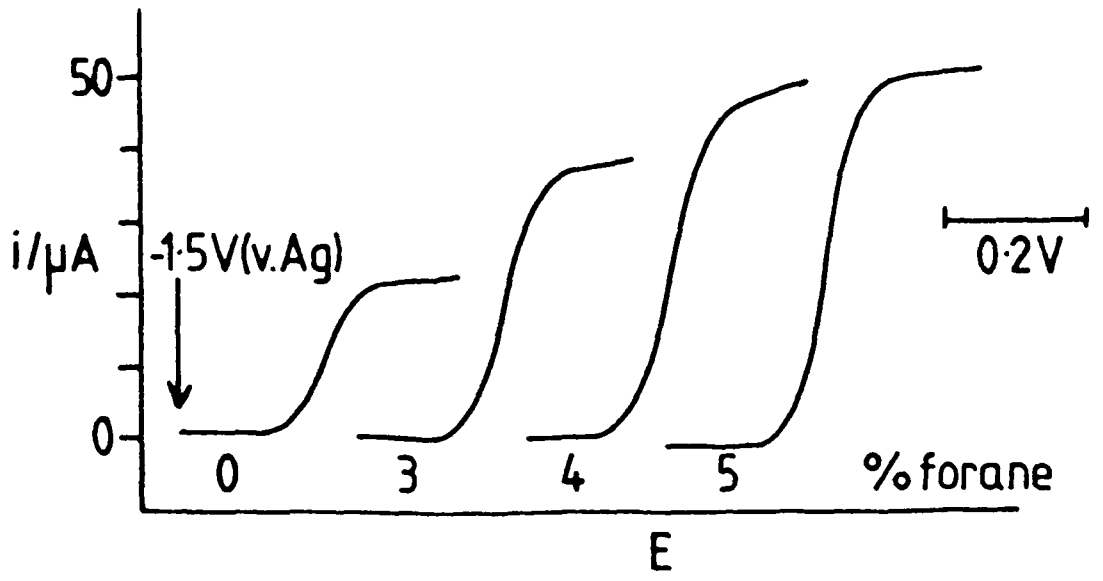


Figure 9.3: ChE voltammograms for the reduction of 1.00×10^{-3} moldm^{-3} fluoranthene in acetonitrile/0.2 moldm^{-3} TBAP in the presence of increasing forane concentrations. A mercury electrode was employed and $V_f = 3.64\times10^{-2}$ cm^{3}s^{-1}.

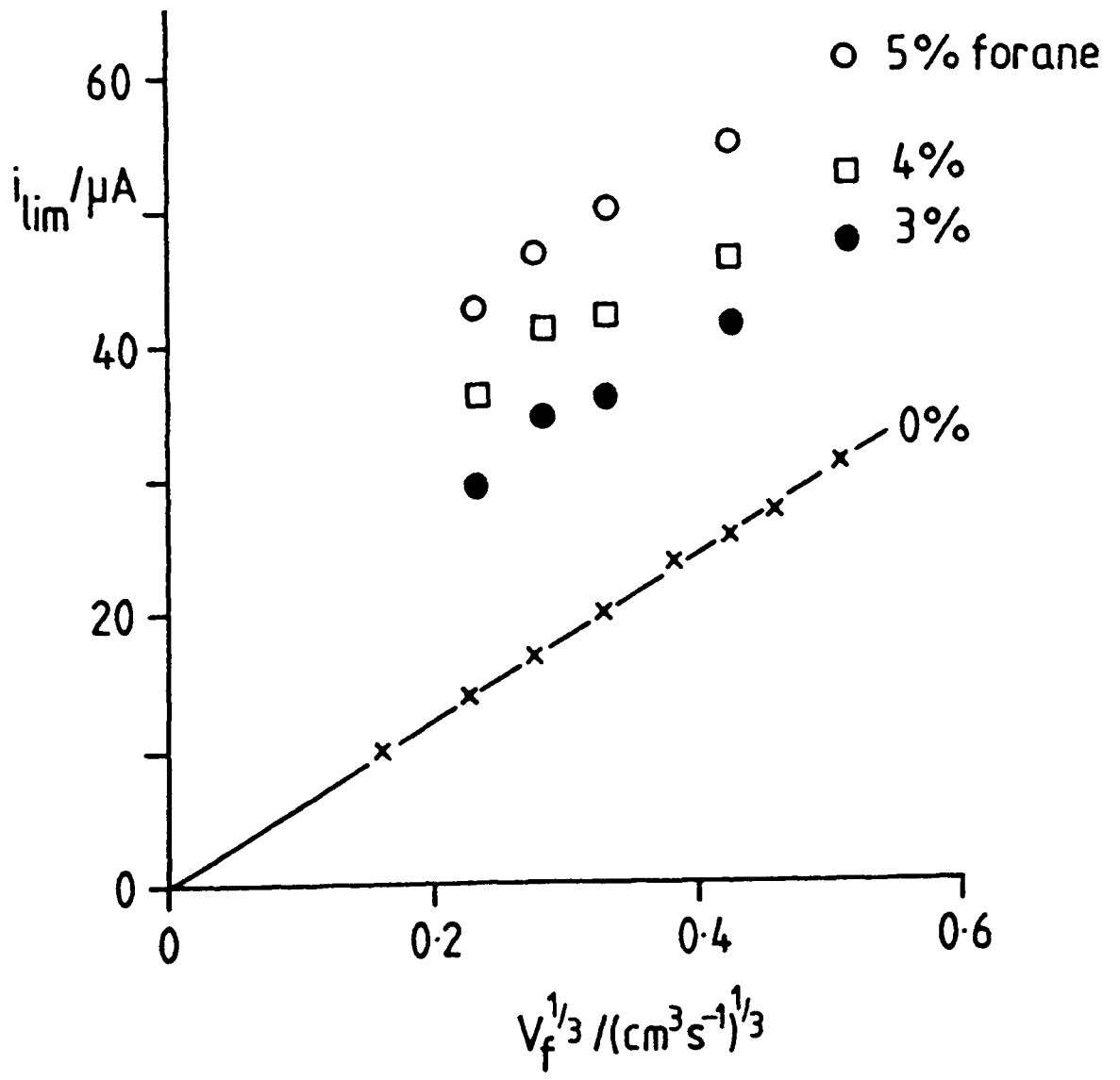


Figure 9.4: The flow rate dependence of i_{lim} for the reduction of 1.00×10^{-3} moldm^{-3} fluoranthene in the presence of a range of forane concentrations.

plot is shown in Figure 9.5. The parameter k_{norm}(EC'preeqm) for the ChE was shown in Chapter Three to be related to the flow rate by the following expression:

$$k_{norm}(EC'preeqm) = k_v K_{iv} \frac{[Y]_\infty}{[A]_\infty} \left[\frac{4h^4 d^2 x_e^2}{9DV_f^2}\right]^{1/3} \qquad 9.2$$

so that if the EC'preeqm mechanism is appropriate for this example, plots such as that shown in Figure 9.5 should be straight lines passing through the origin. Moreover, the gradients of these graphs should vary linearly with $[Y]_\infty/[A]_\infty$. Figure 9.6 demonstrates that this linear relationship is observed and the EC'preeqm mechanism can therefore be concluded to operate at the ChE during the mediated reduction of forane by $F^{\cdot -}$. Further confirmation of this reaction pathway was provided by the determination, from the slope of the line in Figure 9.6, of a value of $k_v K_{iv} = 22.7 \pm 1.5 s^{-1}$. This is in very good agreement with the corresponding value for this rate constant of $25.9 \pm 1.2 s^{-1}$ deduced at the RDE in Chapter Seven.

9.3 The Mediated Reduction of Nitrous Oxide

A similar procedure to that described above was employed to elucidate the mechanism for the mediated reduction of nitrous oxide. At the RDE, this process was shown in Chapter Seven to proceed via an EC'pure mechanism with a rate constant for the irreversible catalytic step of $k_{ii} = 115.9 \pm 4.5 s^{-1}$. Voltammograms, were recorded at the mercury ChE using a solution containing 1.0×10^{-3} F and $0.2 moldm^{-3}$ TBAP/acetonitrile in the presence of increasing concentrations of N_2O. Figure 9.7 shows n_{eff} deduced from such voltammograms plotted against $V_f^{-2/3}$. It is apparent that a catalytic process is in operation. Working curves were then generated for the appropriate values of $[Y]_\infty$ using the backwards implicit finite–difference approach described in Chapter Three, section 3.2.2.2 for an EC'pure mechanism and from these, plots of k_{norm}(EC'pure) versus $V_f^{-2/3}$ were determined. A typical example of one such graph is given in Figure 9.8. The

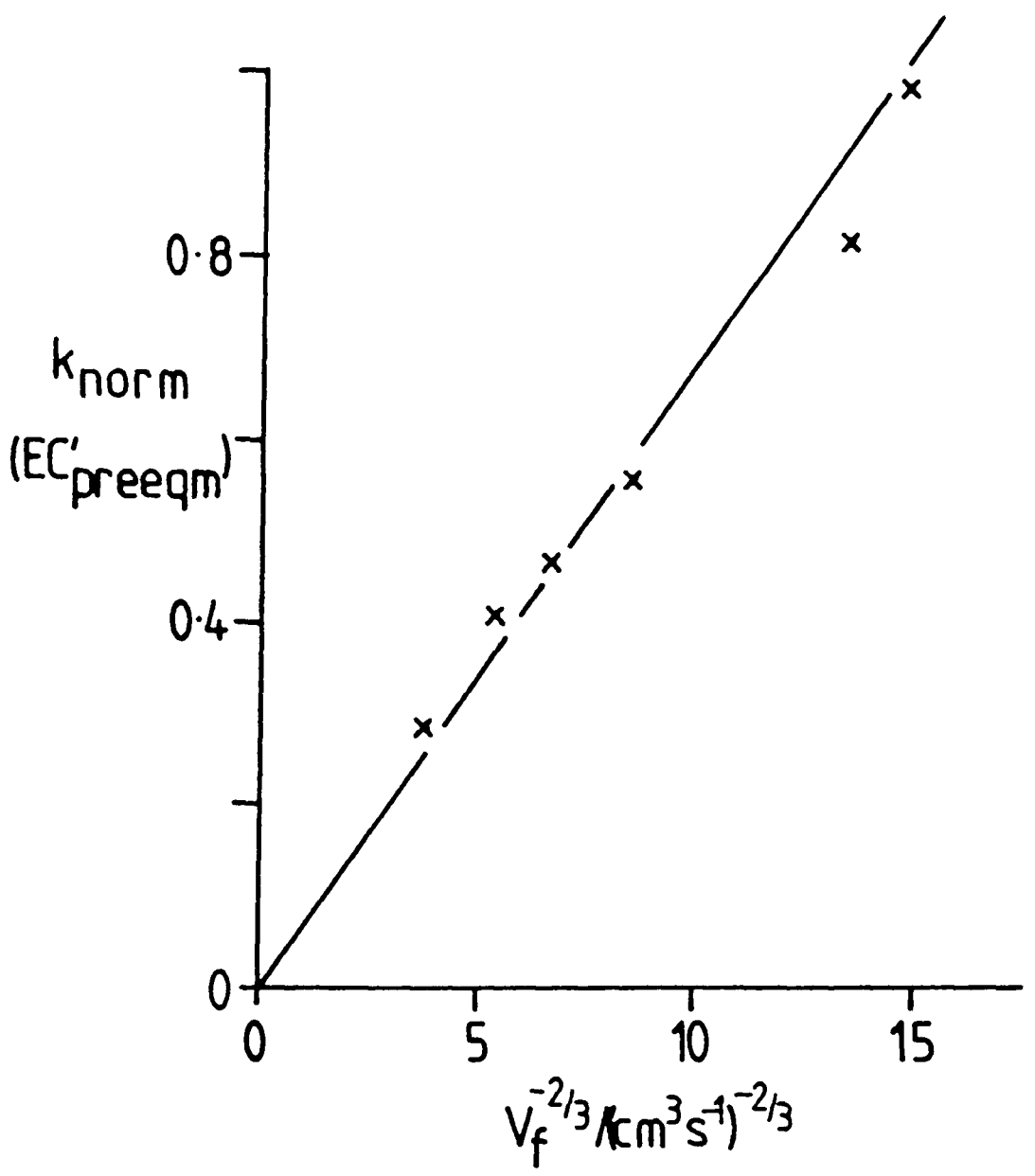


Figure 9.5: k_{norm}(EC'preeqm), deduced from the experimental n_{eff} values and appropriate working curves, versus $V_f^{-2/3}$. $[Y]_\infty/[A]_\infty$ = 2.75.

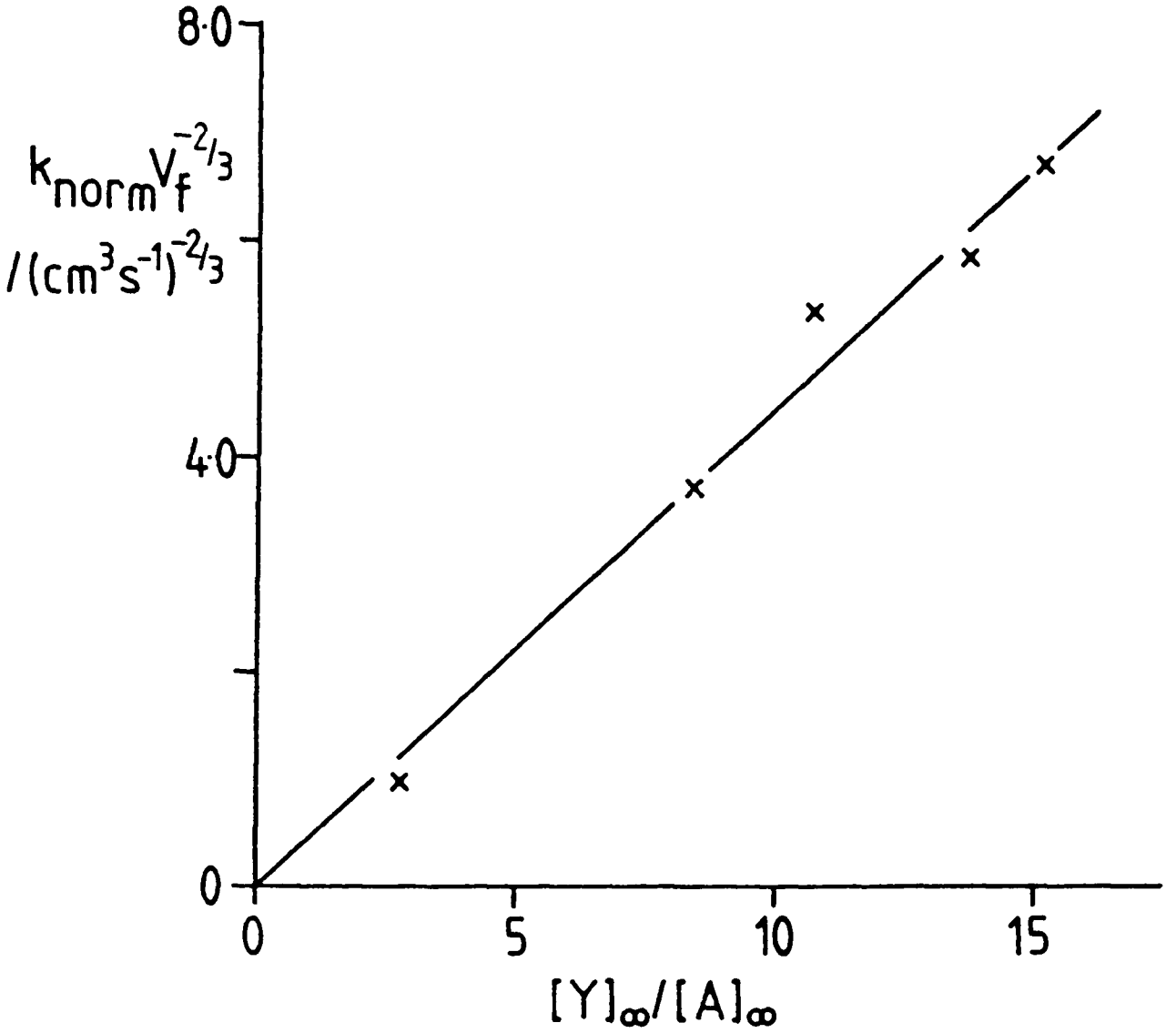


Figure 9.6: The product $V_f^{-2/3}k_{norm}$(EC'preeqm) plotted against $[Y]_\infty/[A]_\infty$.

linearity of these plots, together with the correct relationship observed between their slopes and $[Y]_\infty$ as illustrated in Figure 9.9, was taken as conclusive evidence in support of the assignment of an EC'pure mechanism. Confirmation of this reaction pathway was provided by the deduction of a value of $k_{ii} = 128 \pm 9 s^{-1}$ from the slope of the plot in Figure 9.9 which is in good agreement with that of $115.9 \pm 4.5 s^{-1}$ determined at the RDE.

It is therefore possible to conclude that the mechanistic discriminations made between the subtle nuances of the EC' reaction pathway, using steady–state measurements only at the RDE, can also be determined using a similar approach at the ChE. In addition, quantitative kinetic deductions are in very good agreement between the two hydrodynamic electrodes. The inclusion of homogeneous catalytic kinetics into the backwards implicit finite–difference approach to solving steady–state ChE electrode problems has also been experimentally verified.

Finally, the reduction of forane via electron transfer from $F^{\cdot -}$, electrogenerated at a mercury ChE, has been demonstrated and therefore the extension of this to the development of an amperometric ChE forane sensor should be feasible.

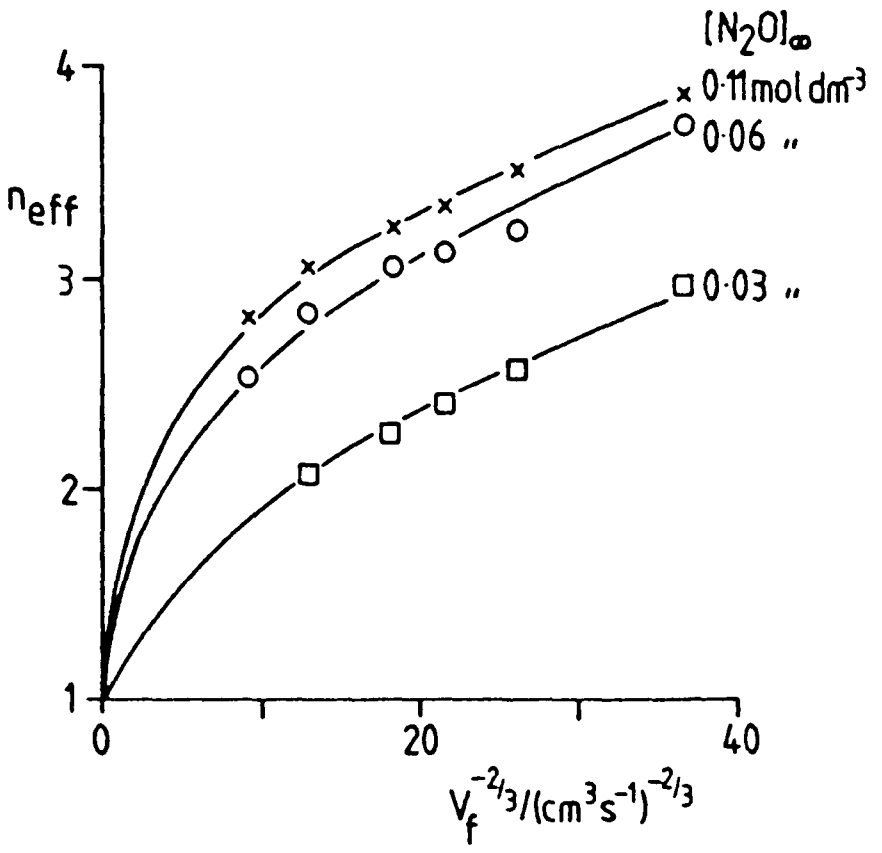


Figure 9.7: Values of n_{eff} for the reduction of 1.25×10^{-3} moldm^{-3} fluoranthene, in acetonitrile/0.02 moldm^{-3} TBAP at a mercury ChE, plotted against $V_f^{-2/3}$ in the presence of an increasing concentration of nitrous oxide.

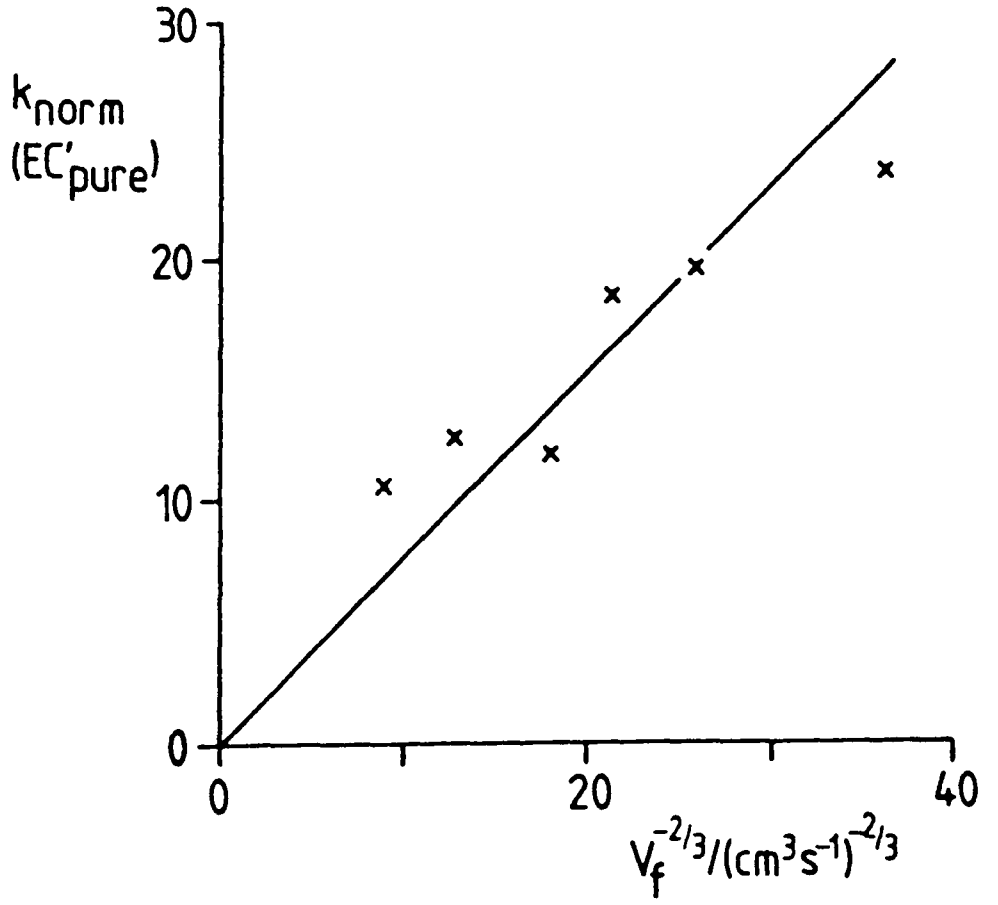


Figure 9.8: k_{norm}(EC'pure) versus $V_f^{-2/3}$ for $[F]_\infty = 1.25\times 10^{-3}$ moldm^{-3} and $[N_2O]_\infty = 0.031$ moldm^{-3}.

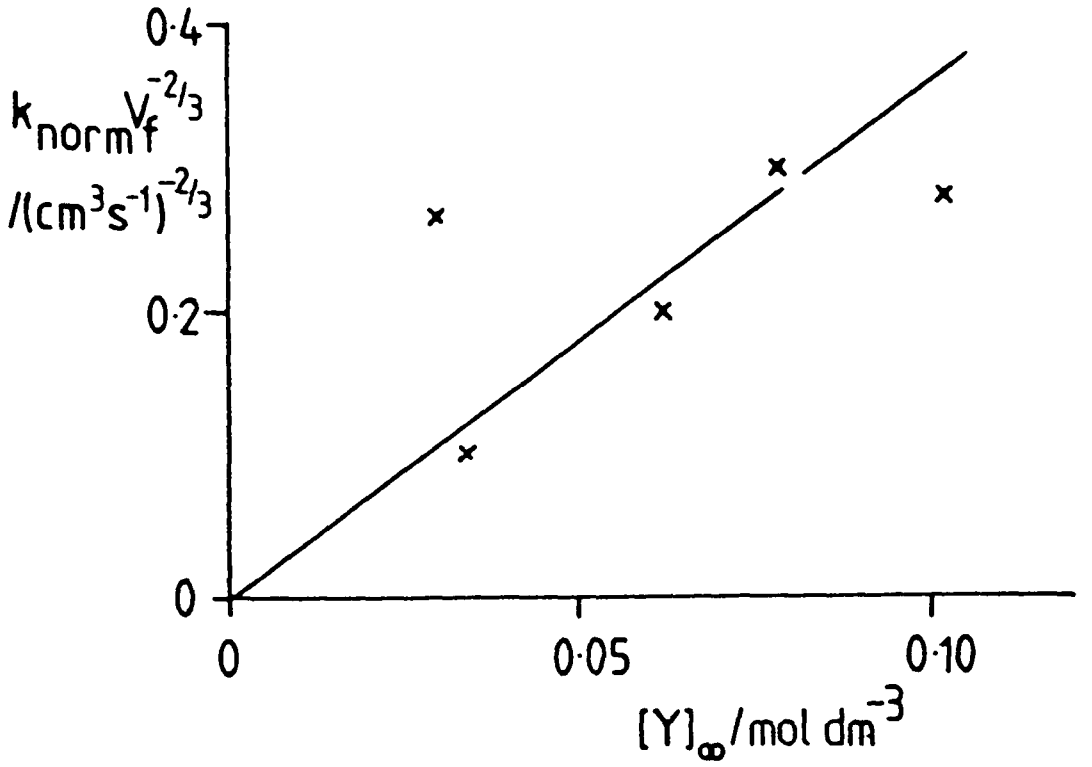


Figure 9.9: The gradients of graphs such as that presented in the previous figure plotted against $[N_2O]_\infty$, showing the linear dependence between these terms required for the assignment of an EC'pure mechanism.

CHAPTER TEN

AN AMPEROMETRIC SENSOR FOR FORANE BASED ON THE CHANNEL ELECTRODE

The mechanistic conclusions evaluated in Chapter Nine confirm that electron transfer to forane is possible at the ChE using $F^{\cdot -}$ as an electrogenerated mediator. This chapter extends this work by applying the ChE methodology to the construction of a practical amperometric sensor for forane. The design of the sensor is described and a theoretical approach to the solution of mass transport in the adapted channel cell, based on the backwards implicit finite difference method (detailed in Chapter Three), is presented.

Mechanisms for the mediated reductions of forane and N_2O, for the case when these substrates enter the channel via a high density polyethylene (HDPE) membrane, are investigated. The operation of the sensor using both voltammetric and potential pulsing methods in the presence of oxygen is also examined.

10.1 The Channel Electrode Sensor

Figure 10.1 illustrates schematically the adaptation of the conventional flow cell, described in Chapter Four, required to develop this into an anaesthetic gas sensing device. These modifications are described in the following paragraph.

The entire cell unit was constructed from teflon to prevent chemical attack from acetonitrile and the channel was 30.0mm long, 6.0mm wide and had an approximate depth of 0.4mm. The flow system, reference and counter electrode

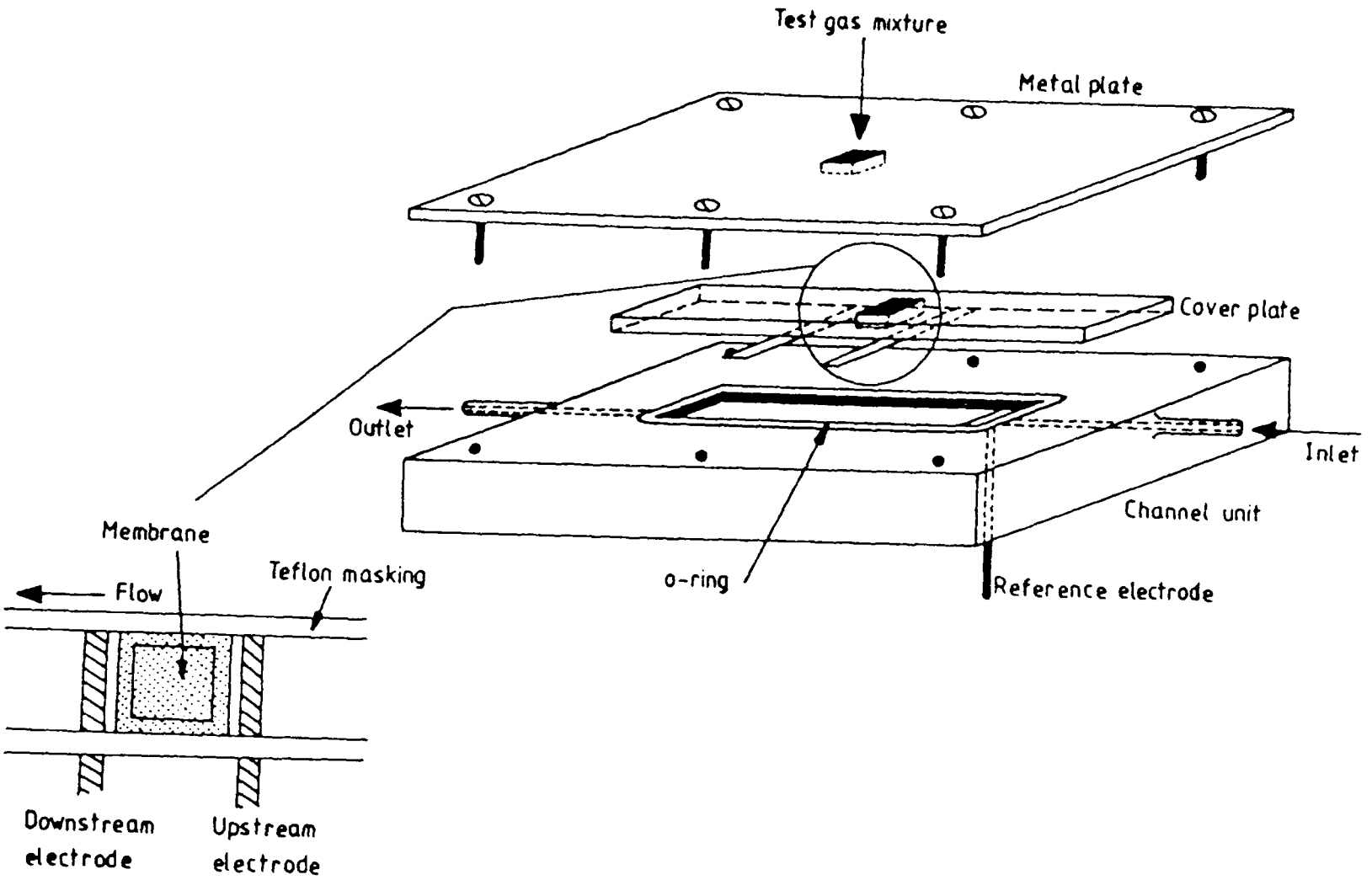


Figure 10.1: A schematic diagram of the ChE sensor showing the electrode–membrane configuration.

configuration remained unchanged from that used for conventional ChE studies and described in Chapter Four, section 4.2.2. Two copper strips (<1mm wide) served as working electrodes. The necessity for the employment of a double channel electrode [394,395] will become apparent in section 10.3.3 of this chapter. These electrodes were located approximately half way down the channel, either side of a 4.0x4.0mm square hole in the coverplate and sufficiently downstream of the entrance duct to fulfill the entry length requirement for laminar flow [162] given by equation 2.61. When the cell was assembled and sealed, this hole coincided with a matching hole in the outer steel plate. The hole in the coverplate was covered with a 12.5μm pore HDPE membrane which, along with the working electrodes, was cemented to the coverplate using low melting point wax. Prior to sealing the cell, the copper strips were polished, electroplated with mercury and measured using the procedures described in Chapter Four. Therefore, the electrode – membrane – electrode configuration was such that electrolyte solution flowed from the reservoir into the channel where it passed over the first (upstream) mercury electrode, the HDPE membrane and then the second (downstream) electrode before leaving the channel and flowing to waste. The PVC tubing (o.d. 6mm) of the carrier gas line fitted tightly into the hole in the steel plate, shown in Figure 10.1, so that gases to be sensed could be delivered to the cell via this tubing, and introduced to the channel through the membrane. Thus (0–5%) forane, (0–100%) N_2O and (0–100%) O_2 mixtures with N_2 carrier gas could reach the channel.

10.2 The Theoretical Solution of Mass Transport to the Channel Electrode Sensor

In Chapter Three, the inclusion of coupled homogeneous kinetics into the backwards implicit finite difference method for the solution of steady–state ChE problems was presented and this approach was utilised in Chapter Nine to deduce an electrode mechanism for the mediated reduction of forane by $F^{\cdot -}$. In this section, the theoretical approach is modified to account for the delivery of substrate, Y (forane), to the channel electrode via a membrane as described in section 10.1.

The coordinate system employed for the two electrode, membrane ChE is shown in Figure 10.2 and considering the system where mediator (A) enters the channel from the electrolyte reservoir, while substrate (Y) is introduced via the channel membrane, then the pertinent initial and boundary conditions are:

$x = 0$		$[Y] = 0$	$[A] = [A]_\infty$	$[B] = 0$	10.1 i
$0 < x < x_m$	$z = 0$	$[Y] = [Y]_\infty$	$[A] = [A]_\infty$	$[B] = 0$	ii
	$z = 2h$	$\frac{\partial[Y]}{\partial z} = 0$	$[A] = [A]_\infty$	$[B] = 0$	iii
$x_m < x < x_s$	$z = 0$	$\frac{\partial[Y]}{\partial z} = 0$	$[A] = [A]_\infty$	$[B] = 0$	iv
	$z = 2h$	$\frac{\partial[Y]}{\partial z} = 0$	$[A] = [A]_\infty$	$[B] = 0$	v
$x_s < x < x_e$	$z = 0$	$\frac{\partial[Y]}{\partial z} = 0$	$[A] = 0$	$\frac{\partial[B]}{\partial z} = -\frac{\partial[A]}{\partial z}$	vi
	$z = 2h$	$\frac{\partial[Y]}{\partial z} = 0$	$\frac{\partial[A]}{\partial z} = 0$	$\frac{\partial[B]}{\partial z} = 0$	vii

Examination of these boundary conditions reveals that over the membrane, and the narrow "space" between this and the downstream electrode, the concentration profile for species Y only needs to be calculated. This will be independent of the electrode reaction mechanism under investigation as this profile is "upstream" of the electrode. However, over the "downstream" electrode, the profiles of A, B and Y need to be determined and these can be calculated using the BIFD approach described in Chapter Three, section 3.2.2.2 and employed successfully in Chapter Nine. The matrix elements required [193] for the calculation of the Y concentration profile are therefore:

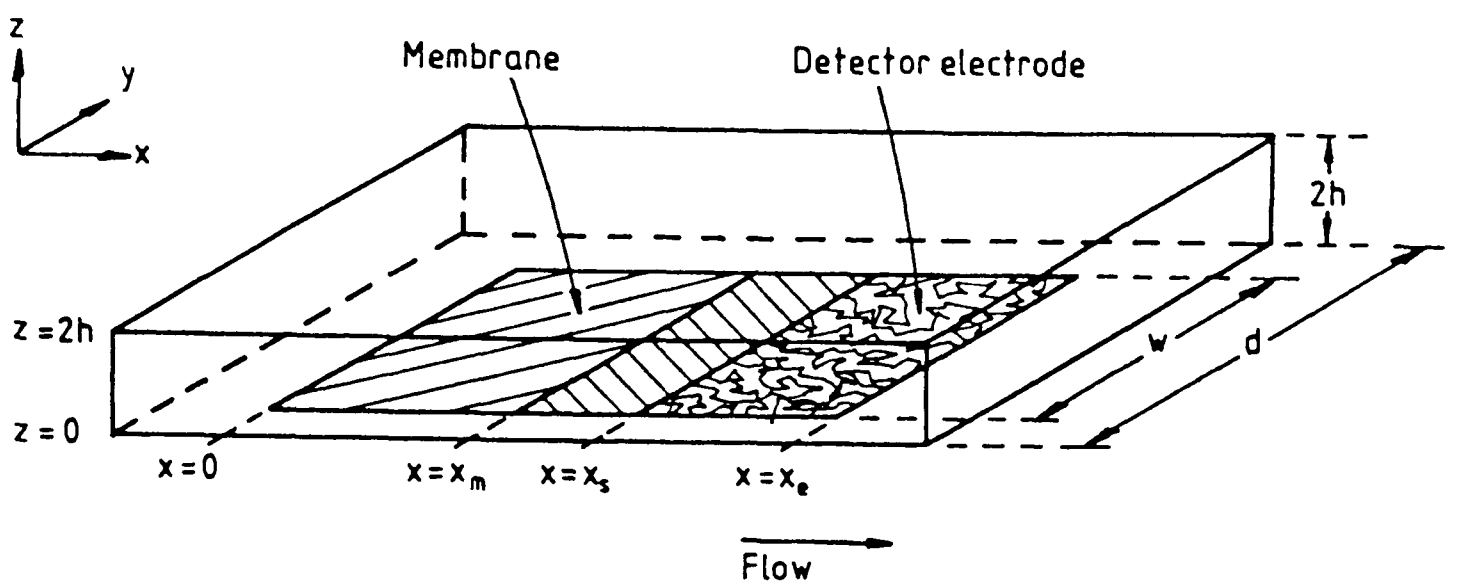


Figure 10.2: Coordinate system for the ChE sensor.

Membrane

$$g^{Y}_{j,0} = 0 \qquad j = 1,2,\ldots, J-1 \qquad 10.2\ i$$

$$d^{Y}_{1} = g^{Y}_{1,k} + \lambda^{Y}_{1} \qquad ii$$

$$d^{Y}_{j} = g^{Y}_{j,k} \qquad j = 2,3,\ldots, J-1 \qquad iii$$

$$b^{Y}_{j} = 1 + 2\lambda^{Y}_{j} \qquad j = 1,2\ldots, J-1 \qquad iv$$

Space between the Membrane and Downstream Electrode

$$g^{Y}_{j,0} = g^{Y}_{j,K_{maxmem}} \qquad j = 1,2,\ldots,J-1 \qquad 10.3\ i$$

$$d^{Y}_{j} = g^{Y}_{j,k} \qquad j = 1,2,\ldots,J-1 \qquad ii$$

$$b^{Y}_{1} = 1 + \lambda^{Y}_{1} \qquad iii$$

$$b^{Y}_{j} = 1 + 2\lambda^{Y}_{j} \qquad j = 2,3,\ldots,J-1 \qquad iv$$

Electrode

$$g^{A}_{j,0} = 1 \qquad g^{B}_{j,0} = 0 \qquad g^{Y}_{j,0} = g^{Y}_{j,K_{maxspace}} \qquad 10.4$$

where all the other electrode matrix elements for A, B and Y are given in Tables 3.4, 3.5 and 3.6, and:

$$K_{maxmem} = \frac{x_m}{\Delta x} \qquad 10.5$$

$$K_{maxspace} = \frac{x_s - x_m}{\Delta x} \qquad 10.6$$

$$K_{max} = \frac{x_e - x_s}{\Delta x} \qquad 10.7$$

Thus, employing equations 10.2 and 10.3, concentration profiles of Y over the membrane and "space" respectively were calculated using the backwards implicit finite–difference method described in Chapter Three. This provided a Y profile in the z direction at the upstream edge of the downstream electrode which was incorporated into the existing theoretical strategy for the calculation of steady–state EC' ChE problems (section 3.2.2.2). This enabled working curves of n_{eff} versus

k_{norm} to be deduced as a function of $[A]_\infty$ and $[Y]_\infty$ for each EC' mechanism, using the FORTRAN program given in Appendix 4h. The parameter k_{norm} is defined for the various EC' nuances in Table 3.7. Typical working curves, obtained using K_{max} = 2000 and J = 200, are illustrated in Figure 10.3 for the case of an EC'preeqm mechanism.

10.3 The Reduction of Forane at the Channel Electrode Sensor

10.3.1 Preliminary Experiments

The reduction of $1.0x10^{-3}moldm^{-3}$ F in an acetonitrile/$0.2moldm^{-3}$ TBAP solution thoroughly purged of O_2 was initially examined at the downstream electrode (w_e = 0.403cm, x_e = 0.065cm). The resulting limiting current data is plotted against $V_f^{1/3}$ in Figure 10.4 and Levich analysis [103] of this line, using D_F = $2.28x10^{-5}cm^2s^{-1}$ (calculated at the RDE in Chapter Five) yielded a calibrated value for the depth of the channel (2h) of 0.48mm.

10.3.2 The Mediated Reduction of Forane

The anaesthetic gas, forane (0–5%), was next introduced via the HDPE membrane using N_2 as carrier gas. Figure 10.5 shows the limiting currents, obtained from the reduction of F to $F^{\cdot -}$ at the downstream electrode, as a function of [forane] and $V_f^{1/3}$. In Chapter Nine, the mediated reduction of forane (introduced to the channel from the reservoir solution) by $F^{\cdot -}$ at the ChE was shown to proceed via an EC'preeqm mechanism with k_vK_{iv} = $22.7\pm1.5s^{-1}$. This is in excellent agreement with the mechanistic analysis deduced at the RDE in Chapter Seven. However, when the experimental data determined by forane introduction via the membrane was analysed using the theory presented above, non–linear graphs of k_{norm}(EC'preeqm) versus $V_f^{-2/3}$ resulted. These poor "fits" were attributed to an overestimation of [forane] in the channel caused by "poor" permeability of the anaesthetic through the HDPE membrane [389], i.e. $[Y]_\infty$ on the inner (channel) surface of the membrane was not equal to [Y] delivered by the carrier gas. The

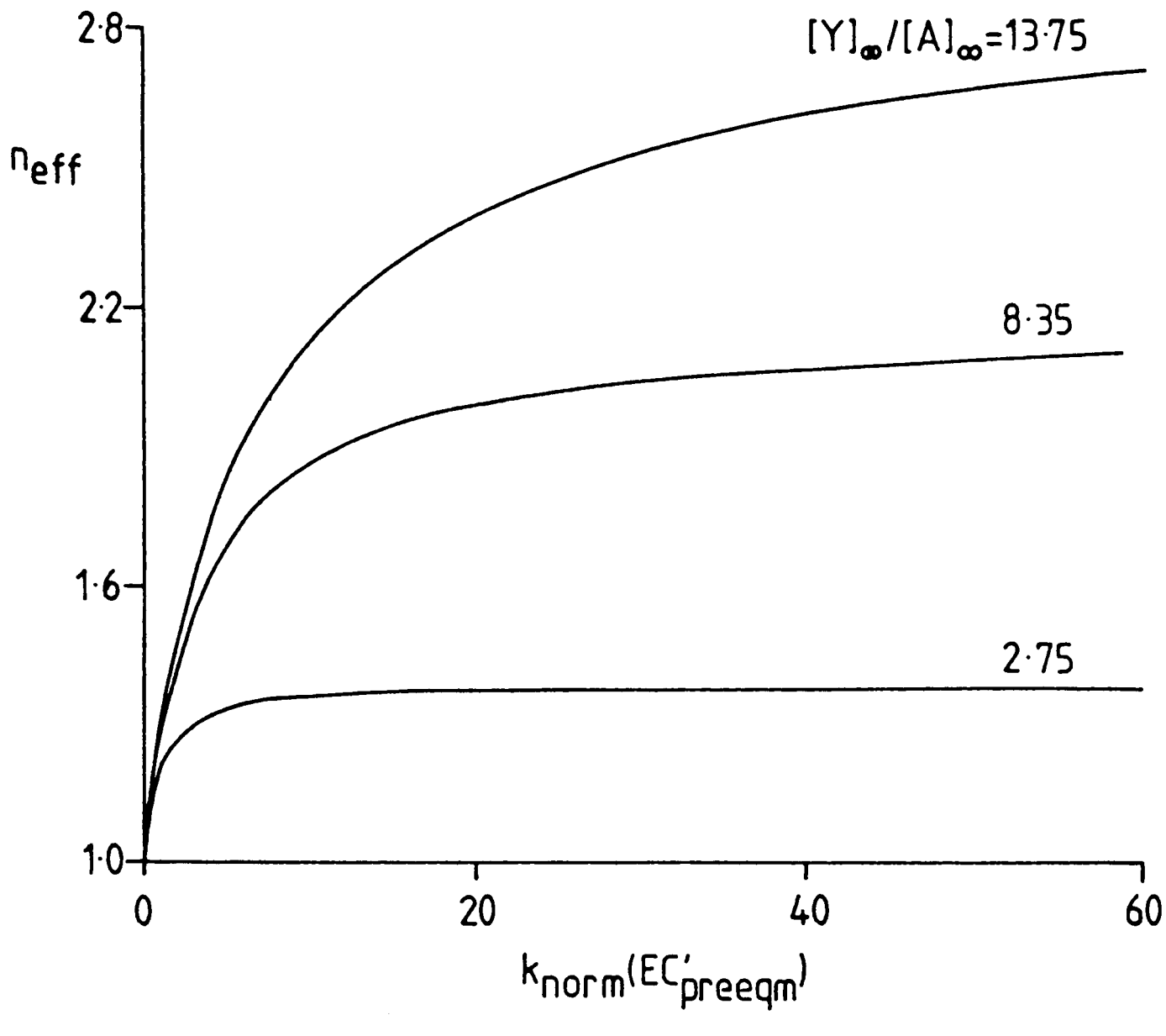


Figure 10.3: Computed steady–state working curves calculated for an EC'preeqm process at the modified ChE cell.

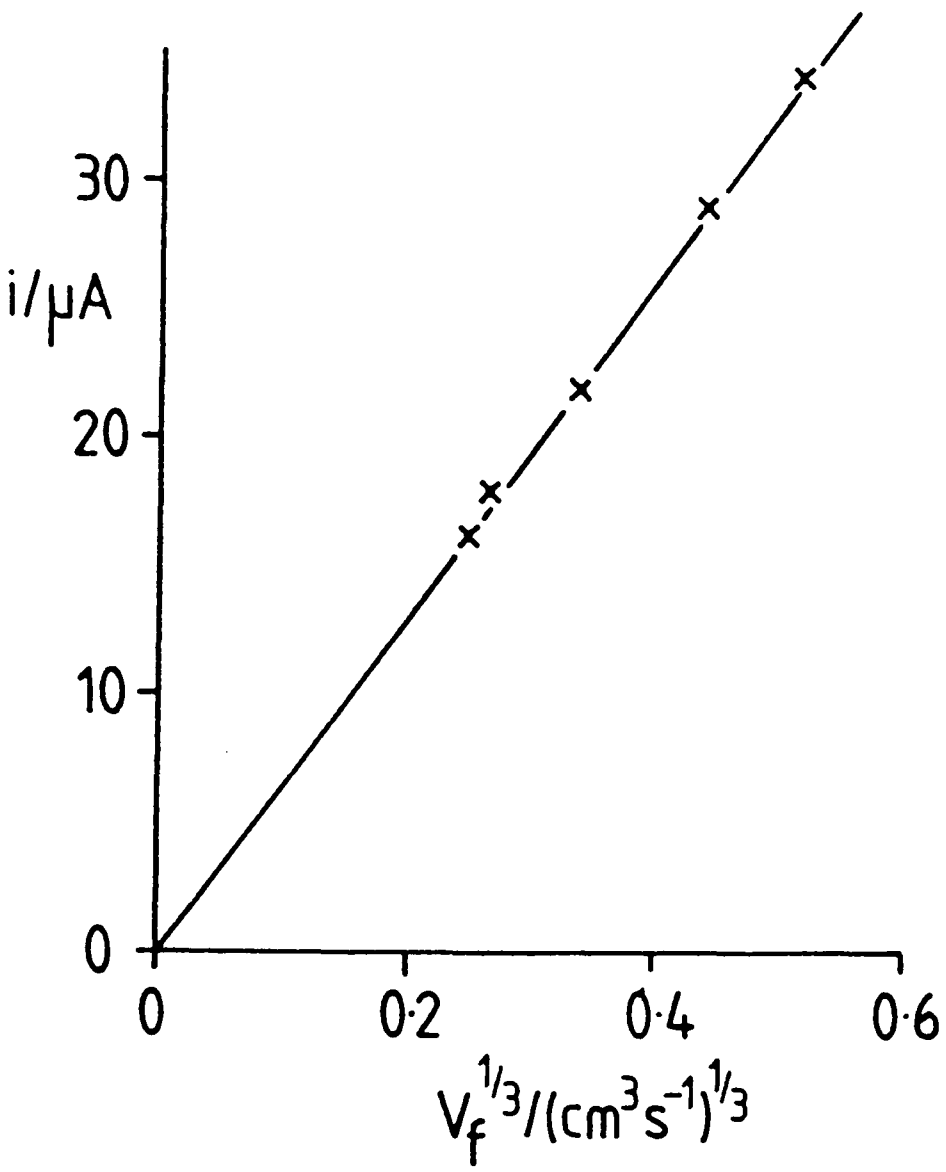


Figure 10.4: Levich plot of i_{lim} versus $V_f^{1/3}$ for the reduction of 1.0×10^{-3} moldm^{-3} fluoranthene in acetonitrile/0.02 moldm^{-3} TBAP at the ChE sensor. This straight line confirms the hydrodynamic behaviour of this channel.

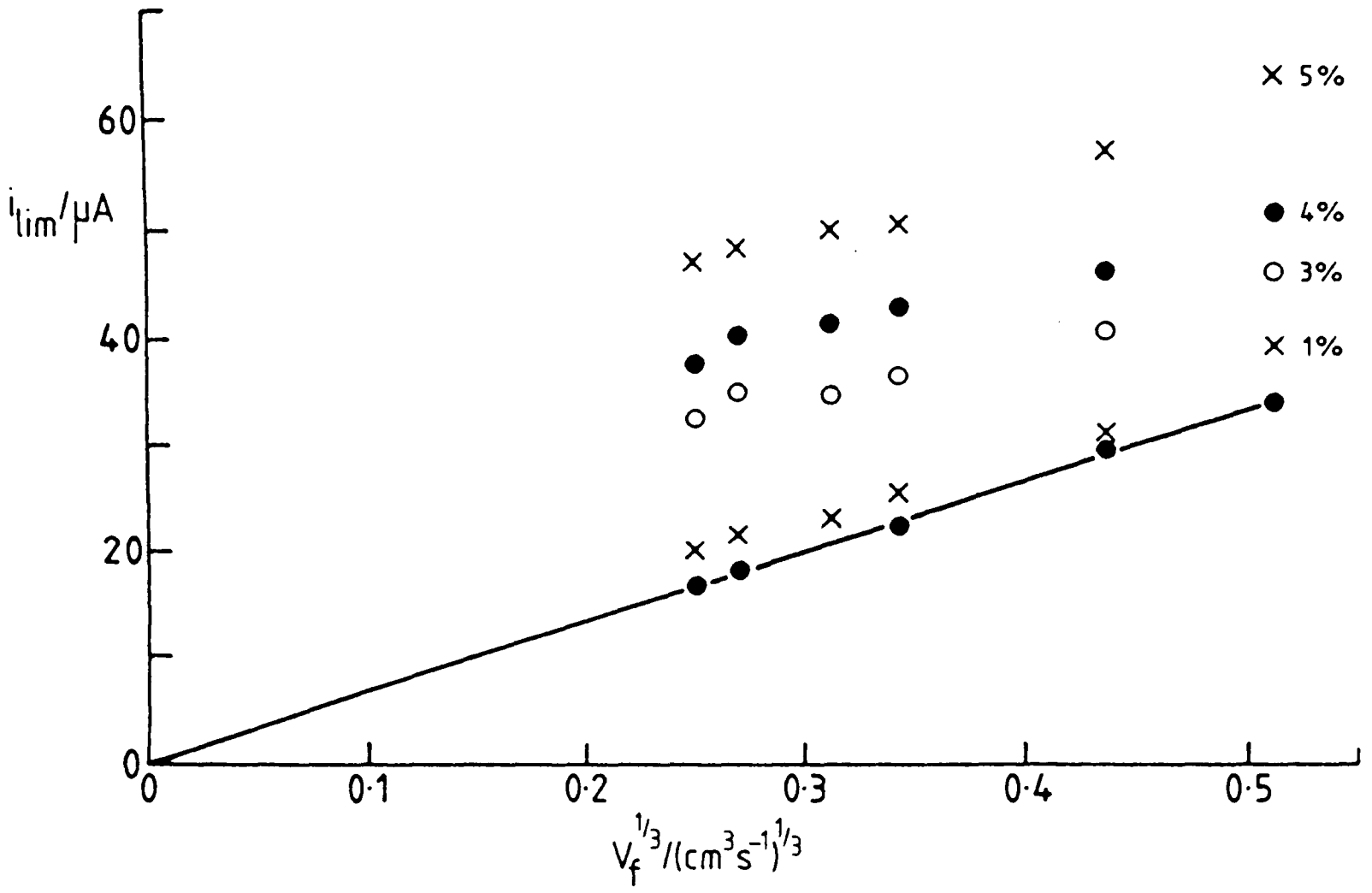


Figure 10.5: The V_f dependence of i_{lim} for the reduction of 1.0×10^{-3} moldm^{-3} fluoranthene at the ChE sensor in the presence of an increasing concentration of forane delivered to the membrane.

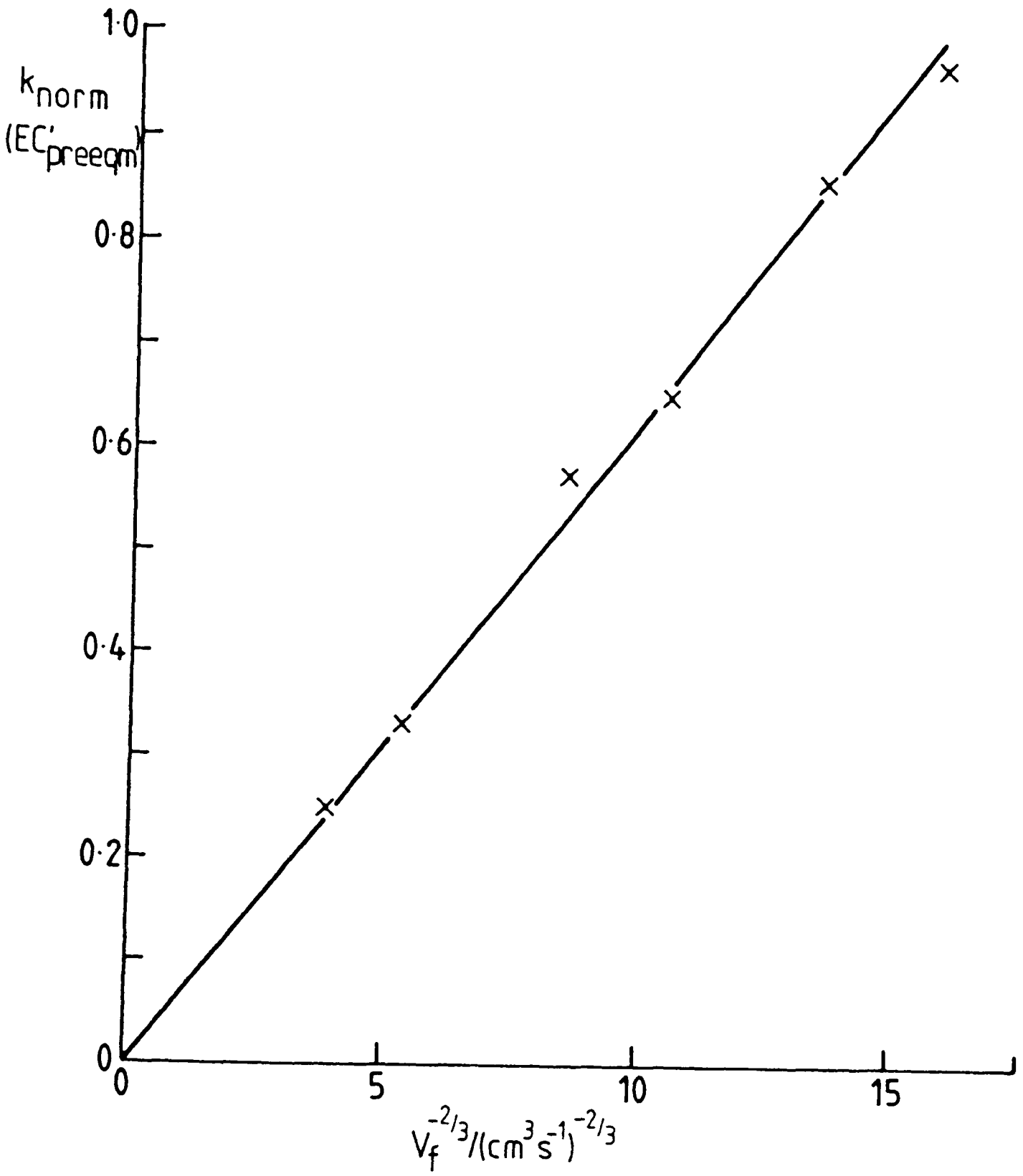


Figure 10.6: The analysis of typical catalytic current data for the fluoranthene/forane system in terms of a pre–equilibrium mechanism. The data was obtained from a solution containing 1.0×10^{-3} moldm^{-3} fluoranthene in 0.2 moldm^{-3} TBAP/acetonitrile and 2.75×10^{-3} moldm^{-3} forane.

analysis was therefore repeated with "trial and error" reductions in [forane] in the channel. It was found that when the expected [forane] was reduced by 20% (i.e. 80% transport efficiency of forane through the membrane, at any flow rate) plots of k_{norm}(EC'preeqm) versus $V_f^{-2/3}$ were in fact straight lines which passed through the origin for all $[A]_\infty$ and $[Y]_\infty$ considered. Figure 10.6 shows a typical example of one such plot. Furthermore, Figure 10.7 shows that the least squares "best fit" slopes of these graphs vary linearly with $[Y]_\infty/[A]_\infty$ as predicted by the expression defining the k_{norm}(EC'preeqm) parameter:

$$k_{norm}(EC'preeqm) = k_v K_{iv} \frac{[Y]_\infty}{[A]_\infty}\left[\frac{4h^4 d^2 x_e^2}{9DV_f^2}\right]^{1/3} \qquad 10.8$$

and the assignment of the EC'preeqm mechanism can be confirmed. Using the least squares gradient of Figure 10.7 in combination with equation 10.7, a value of $k_v K_{iv}$ = 22.0±1.8s^{-1} was deduced. This is in good agreement with the corresponding determinations for this rate constant of 25.9±1.2s^{-1} at the RDE (Chapter Seven) and 22.7±1.5s^{-1} (Chapter Nine) at the conventional ChE.

10.3.3 Interference by Oxygen

Oxygen was next introduced into the ChE flow system by removing the degassing bubbler from the solution reservoir. This solution rapidly (≈ ten minutes) became saturated with air so that reduction of O_2 at the downstream electrode masked the reduction of F. The resulting voltammogram is shown in Figure 10.8. The implications of this electrode response to the development of an amperometric sensor were discussed in Chapter Eight and no further emphasis of this problem is required here. The chemical removal of oxygen from a reservoir electrolyte was examined by Albery *et al* [396], who proposed that dihydroxy hydroanthraquinone, electrogenerated via the reduction of dihydroxy anthraquinone in aqueous solution, would react with oxygen, removing this from the bulk solution and regenerating the starting anthraquinone to maintain the supply. This approach was investigated here, using anthraquinone (AQ) in acetonitrile solvent, as a means of removing the

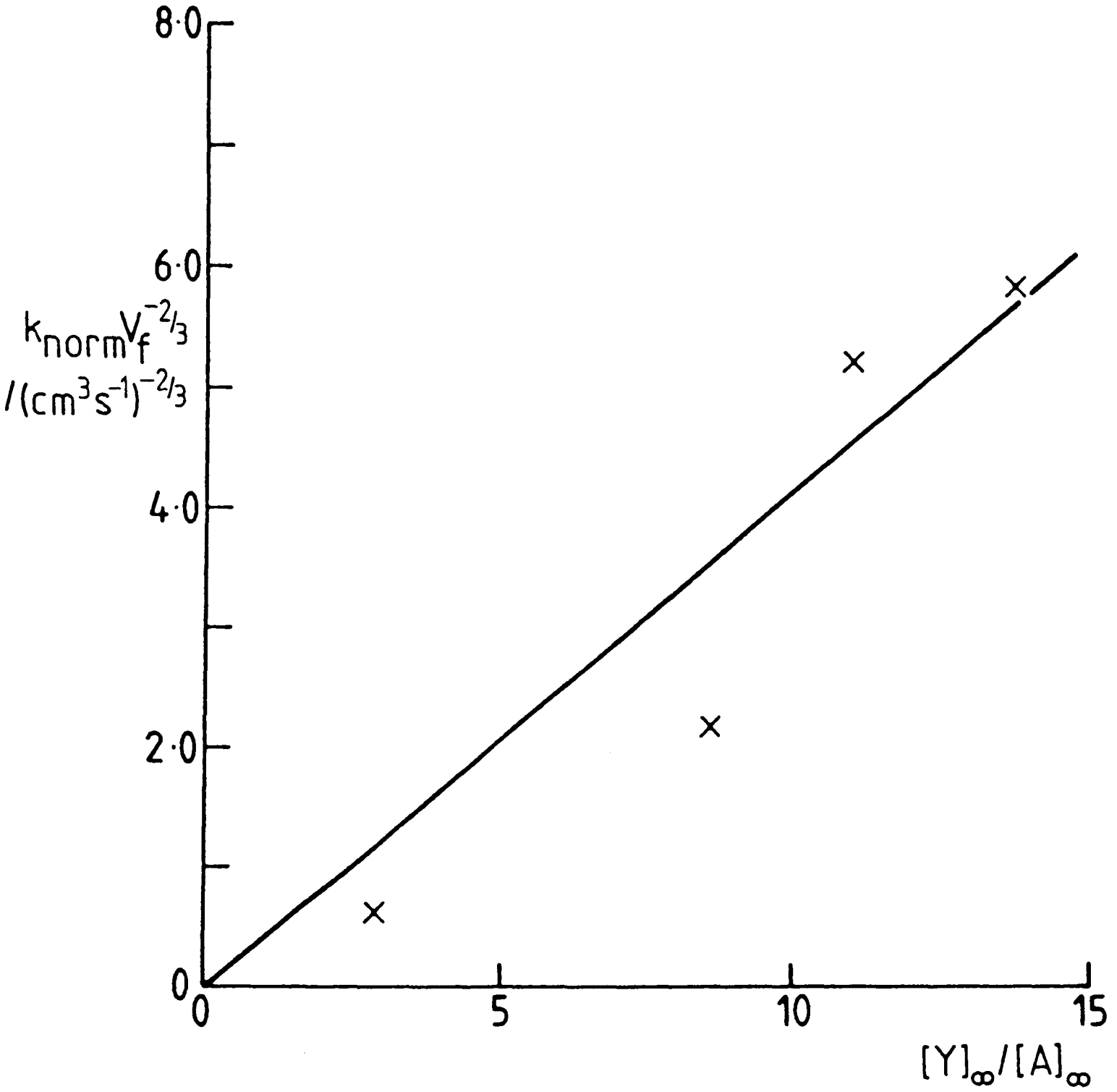


Figure 10.7: The slope of plots such as that shown in Figure 10.6 vary linearly with $[forane]_\infty/[F]_\infty$.

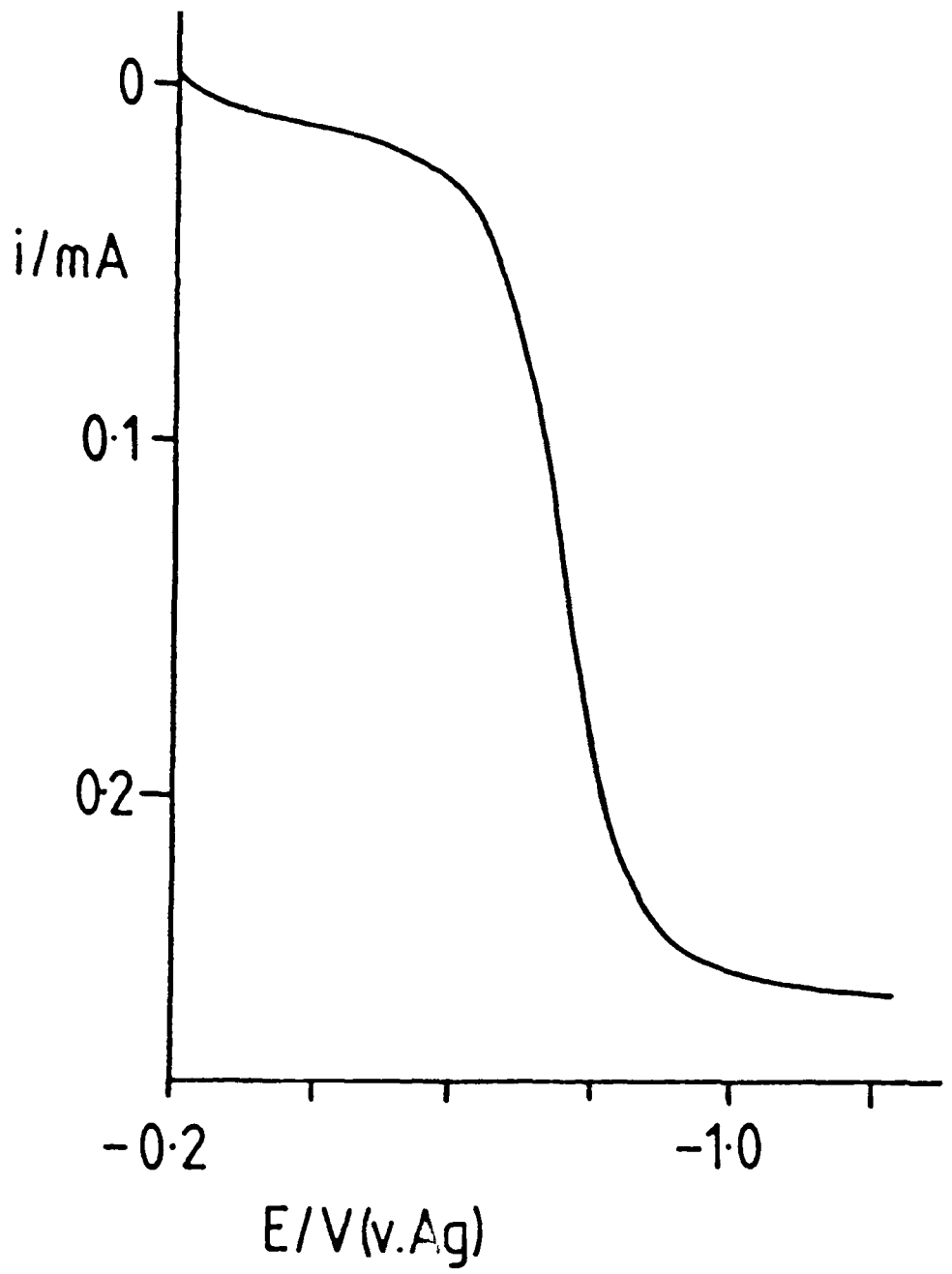


Figure 10.8: ChE sensor voltammogram for the reduction of oxygen which entered the channel when degassing ceased.

interference of oxygen from the channel electrode sensor.

Preliminary experiments were performed on a solution of 2.84×10^{-3}moldm^{-3} AQ in acetonitrile/0.1moldm^{-3} TBAP at a mercury RDE. Two reduction waves, shown in Figure 10.9, were observed with half wave potentials of -0.80 ± 0.03V and -1.35 ± 0.03V (vs. SCE). These are in good agreement with the literature values measured in acetonitrile/0.1moldm^{-3} tetraethylammonium perchlorate of -0.94V and -1.45 V (vs. SCE) respectively [361]. Levich analysis [103] of the first reduction wave produced a value for $D_{AQ} = 1.98 \pm 0.04 \times 10^{-5}$cm^{2}s^{-1}, which compares with a previous determination of 2.17×10^{-5}cm^{2}s^{-1} [362]. The two electrode processes in operation were therefore attributed to:

$$AQ + e^- \longrightarrow AQ^{\cdot -} \qquad (-0.80V)$$

and

$$AQ^{\cdot -} + e^- \longrightarrow AQ^{2-} \qquad (-1.35V)$$

The magnitudes of the limiting currents of both reduction waves were completely unchanged by the addition to the solution of 15×10^{-3}moldm^{-3} forane, 0.125 moldm^{-3} N_2O or 3.0×10^{-3}moldm^{-3} F. However, in the presence of 8×10^{-3}moldm^{-3} O_2, the limiting currents of both waves were approximately doubled, confirming the presence of a catalytic reaction with O_2 which regenerates AQ.

The electrochemistry of an acetonitrile/0.2moldm^{-3} TBAP solution containing 1.0×10^{-3}moldm^{-3} AQ and 1.0×10^{-3}moldm^{-3} F was next investigated at the downstream mercury ChE. The reservoir solution was thoroughly purged of O_2 prior to use. Three waves, shown in Figure 10.10, were apparent and these were therefore attributed to the following processes:

$$AQ + e^- \longrightarrow AQ^{\cdot -} \qquad (-0.75V)$$

$$AQ^{\cdot -}\ e^- \longrightarrow AQ^{2-} \qquad (-1.35V)$$

$$F + e^- \longrightarrow F^{\cdot -} \qquad (-1.75V)$$

Half–wave potentials are quoted against a silver pseudo reference electrode (SPRE). Levich analysis [103] of the first reduction wave (-0.75V) produced a value for D_{AQ}

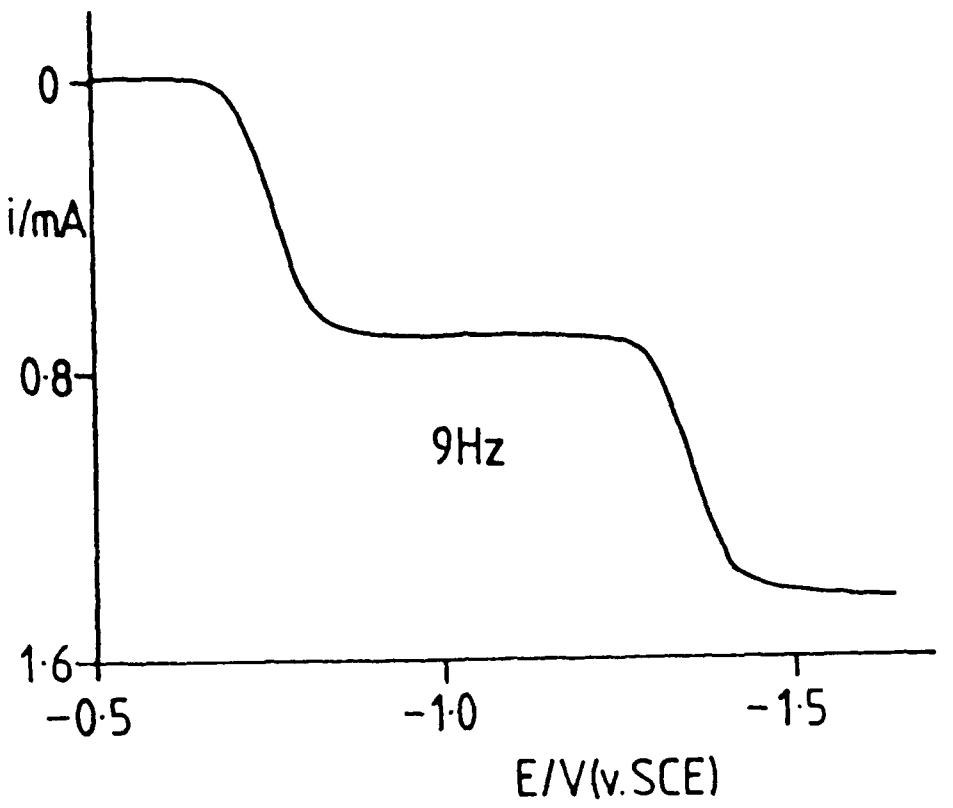


Figure 10.9: A typical RDE voltammogram for the reduction of 2.84×10^{-3} moldm^{-3} anthraquinone in acetonitrile/0.2 moldm^{-3} TBAP at a mercury electrode.

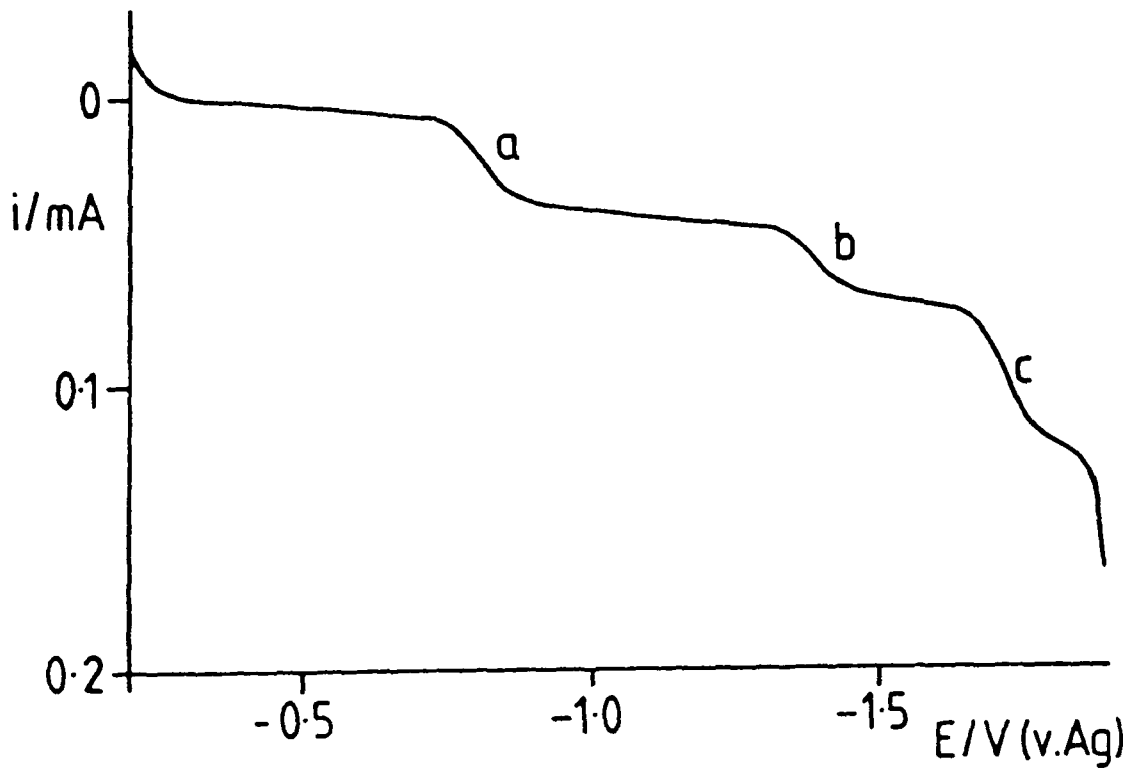


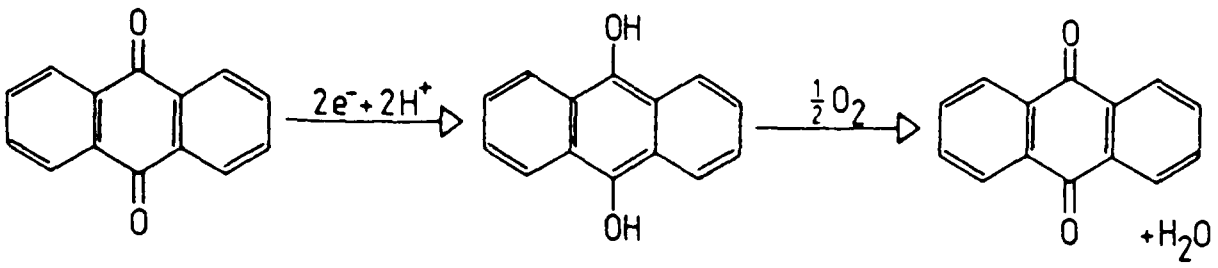
Figure 10.10: A typical ChE sensor voltammogram for the reduction of 1.0×10^{-3} moldm^{-3} anthraquinone and 1.0×10^{-3} moldm^{-3} fluoranthene in acetonitrile/0.2 moldm^{-3}, recorded in the absence of oxygen.

$= 1.86 \pm 0.05 \times 10^{-5} cm^2 s^{-1}$, which is in good agreement with that determined at the RDE of $1.98 \times 10^{-5} cm^2 s^{-1}$. The limiting current from the F (–1.75V) reduction wave ("corrected" by subtraction of i_{lim} for the two AQ reduction processes) also demonstrated a linear behaviour with $V_f^{1/3}$ and the value of $D_F = 2.25 \pm 0.03 \times 10^{-5} cm^2 s^{-1}$ determined (by Levich analysis [103] of the gradient) from this plot, is in good agreement with the value of $2.28 \times 10^{-5} cm^2 s^{-1}$ found in Chapter Five at the RDE. In addition, limiting currents from this wave, measured when 0–5% forane was added via the HDPE membrane were all within the error bars of those recorded in the absence of AQ. It is therefore possible to conclude from the above ChE and RDE experiments that the mediated reduction of forane by electrogenerated $F^{\cdot -}$ is completely unaffected by the presence of AQ.

When degassing ceased, the reduction of oxygen at the downstream electrode again completely masked the electrode processes due to AQ and F, and a current–voltage curve identical to that shown in Figure 10.8 resulted. Therefore both the "upstream" and "downstream" mercury electrode were next polarised under potentiostatic control using "ring–disc" [397] circuitry. Thus the upstream electrode ($w_e = 0.407cm$, $x_e = 0.096cm$) served as the "ring" and was held constant at a potential of –1.50V (vs. SPRE), i.e. on the limiting current of the $AQ^{\cdot -} \longrightarrow AQ^{2-}$ reduction wave, while the potential of the downstream ("disc") electrode was scanned negative from –0.5V. The voltammogram then obtained at the downstream electrode, once again revealed the three waves, corresponding to the reductions of AQ and F, observed in the absence of oxygen (shown in Figure 10.10). A reaction between AQ^{2-} generated at the upstream electrode and O_2 was concluded [396]. Moreover, the magnitude of i_{lim} for $AQ \longrightarrow AQ^{\cdot -}$ measured at the downstream electrode confirmed that no O_2 was reaching here. The i_{lim} versus $V_f^{1/3}$ data recorded at the downstream electrode gave values for D_{AQ} and D_F which were indistinguishable from these of $1.86 \times 10^{-5} cm^2 s^{-1}$ and $2.25 \times 10^{-5} cm^2 s^{-1}$ respectively, determined above.

Quantitative addition of O_2 was achieved by mixing a given percentage of O_2 with the carrier gas delivered to the HDPE membrane. Thus, 10, 20 and 50% O_2/N_2 mixtures were examined and for each ratio identical results to those described in the

previous paragraph were found; i.e. all electrochemistry at the downstream electrode indicated that no O_2 was present. The removal of O_2 was therefore attributed to the following process:



Importantly, when forane was also introduced via the membrane, the $n_{eff} - V_f - [Y]_\infty/[A]_\infty$ behaviour was indistinguishable from that obtained with degassing of the reservoir solution and shown in Figure 10.5. An EC'preeqm mechanism therefore remains in operation and the detection and successful measurement of forane in the presence of O_2 can be concluded.

10.4 The Reduction of Nitrous Oxide at the Channel Electrode Sensor

Having confirmed the success of AQ^{2-} in removing O_2 from the electrolyte solution reaching the downstream mercury electrode, the mediated reduction of N_2O was next analysed with a continual supply of 20% O_2 to the HDPE membrane. The upstream electrode remained under potentiostatic control at –1.50V (vs. SPRE) and an acetonitrile solution containing $1.0x10^{-3}moldm^{-3}$ F, $1.0x10^{-3}moldm^{-3}$ AQ and $0.2moldm^{-3}$ TBAP was used. The variation of i_{lim} with V_f was therefore measured as a function of substrate (N_2O) concentration, $[Y]_\infty$. The data is shown in Figure 10.11. Using the theory presented in section 10.2 of this chapter to solve mass transport to a membrane/ChE, working curves for the EC'pure mechanism were generated and used to determine plots of k_{norm}(EC'pure) versus $V_f^{-2/3}$. A typical example is shown in Figure 10.12, while Figure 10.13 shows a graph of the least squares "best fit" gradients of such lines, plotted against $[N_2O]$. The linear nature of the data plotted in Figures 10.12 and 10.13 demonstrates that an EC'pure mechanism is appropriate for the mediated reduction of N_2O at the membrane

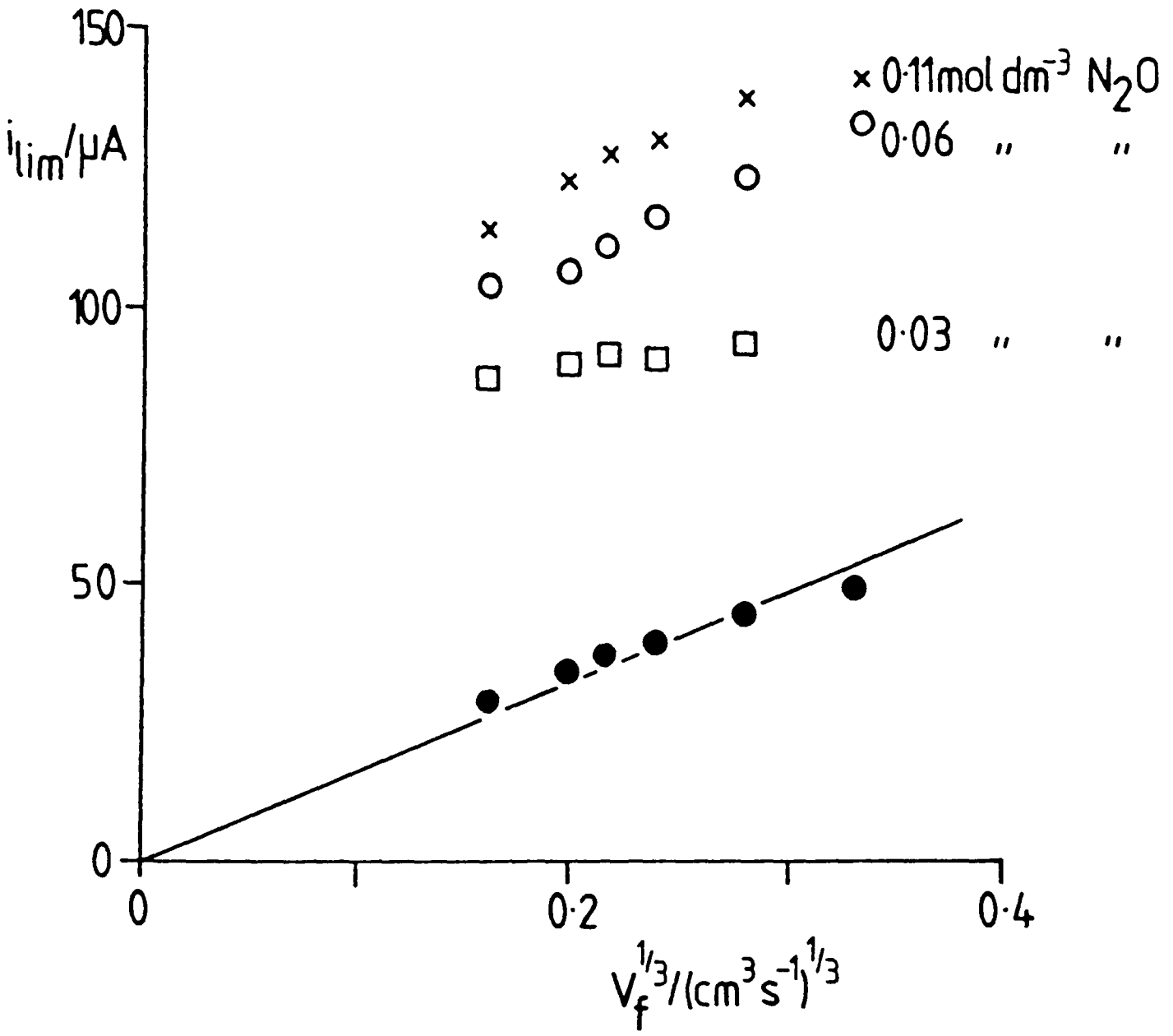


Figure 10.11: The limiting detector electrode current – flow rate data in the presence of varying concentrations of nitrous oxide applied to the membrane.

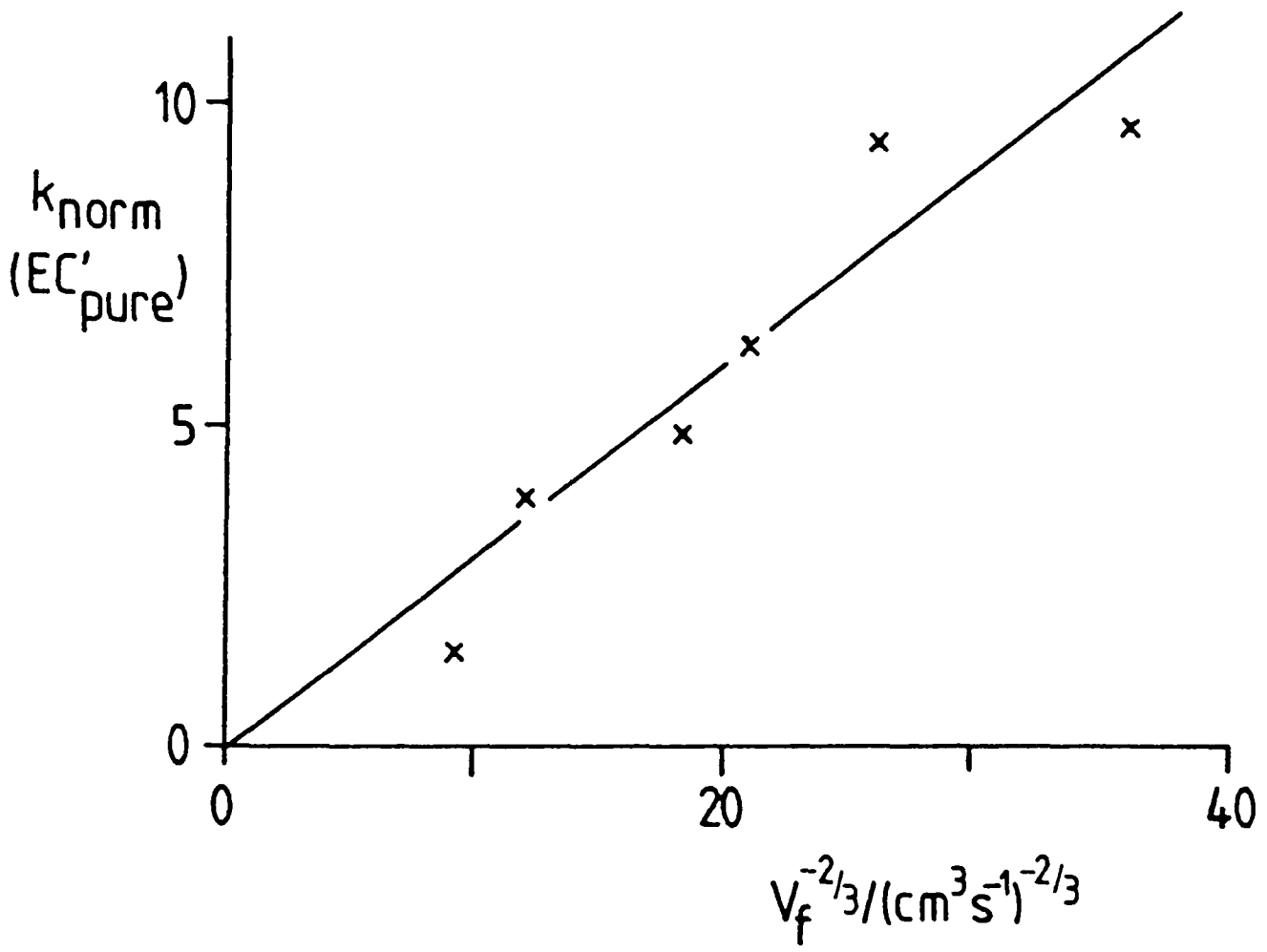


Figure 10.12: k_{norm}(EC'pure), deduced from the appropriate working curves and the measured n_{eff} values, plotted against $V_f^{-2/3}$. $[N_2O]_\infty$ = 0.063 moldm^{-3} and $[F]_\infty = 1.25\times10^{-3}$ moldm^{-3}.

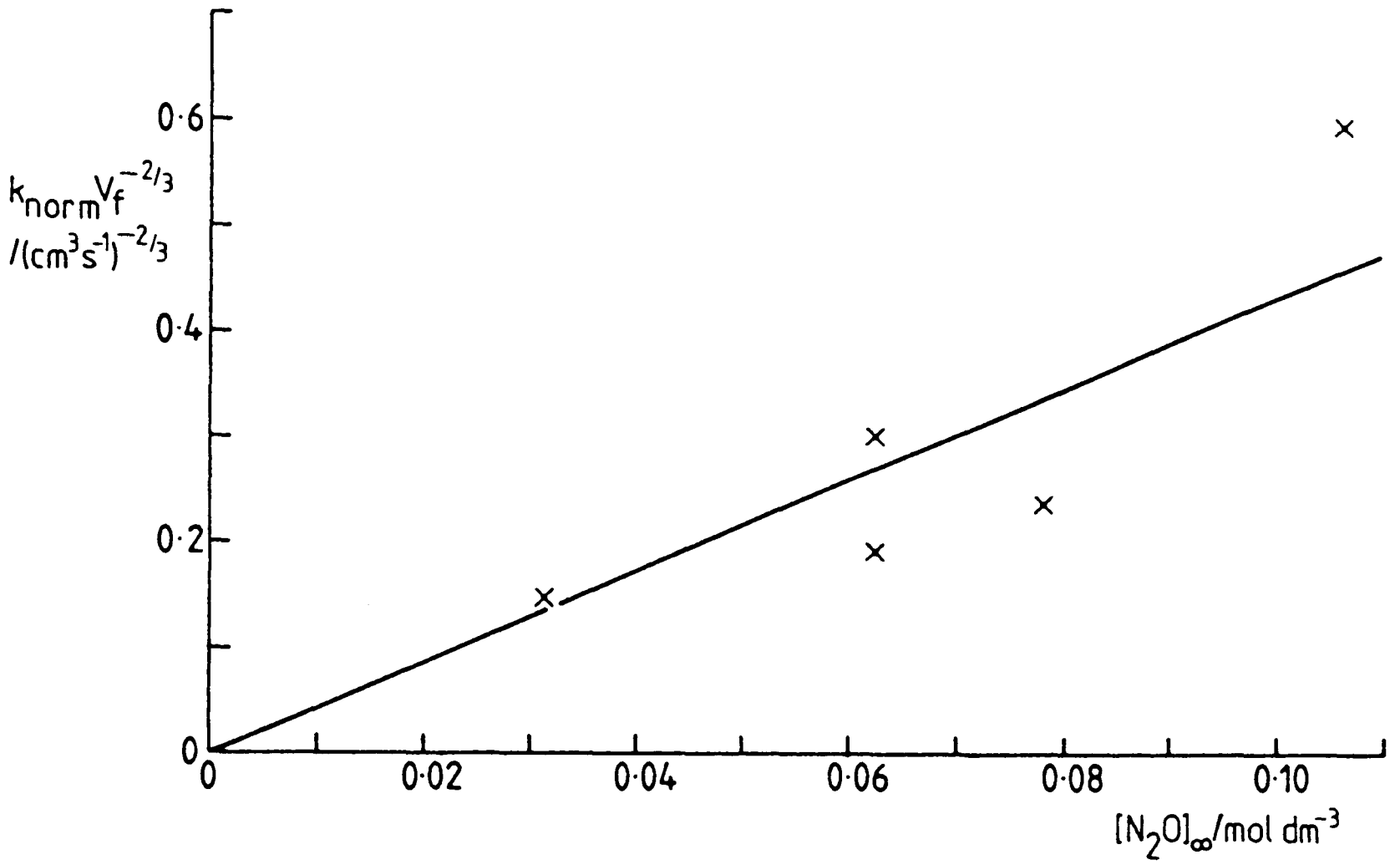


Figure 10.13: The gradients of plots such as those shown in Figure 10.12 plotted against $[N_2O]_\infty$.

mercury ChE. The gradient of Figure 10.13 enabled a value for the rate constant of the irreversible catalytic step $k_{ii} = 146 \pm 15 s^{-1}$ to be determined. This mechanistic conclusion is consistent with the previous assignments of an EC'pure mechanism determined at both the RDE (Chapter Seven) and conventional ChE (Chapter Nine) where values of $k_{ii} = 115.9 \pm 4.5 s^{-1}$ and $128 \pm 9 s^{-1}$ were found respectively. That such close agreement is observed between these separate mechanistic evaluations confirms that accurate N_2O determination is possible in the presence of O_2 using the ChE sensor.

10.5 Potential Pulsing Experiments

The reduction of N_2O in the vicinity of the downstream electrode produces N_2 as a reaction product. When this electrode is held at a reducing potential for prolonged periods, i.e. during a voltammetric potential sweep, then bubbles of N_2 form which occlude the electrode and interfere with its sensing capability. This problem was also observed at the membrane electrode and was discussed in Chapter Eight. Limited evidence of bubble formation was apparent during the voltammetric studies of the mediated reduction of N_2O presented above, particularly at low V_f where the turnover to product was large (high n_{eff}) and the solution velocity was too low to wash away any N_2 bubbles which formed.

However, if the reducing potential is applied as a series of pulses then insufficient N_2 is produced to form large bubbles [90]. Also, the resulting current transient response at the downstream electrode can be measured at a predetermined time after the beginning of each pulse, possibly before the attainment of steady–state, which has the added advantage of enabling a more sensitive determination of the anaesthetic gas concentration. This approach was applied with success in Chapter Eight to overcome the problem of N_2 bubble formation.

The current transient response of the downstream electrode to a square wave potential pulse sequence between –1.50V and –1.90V (vs. SPRE) was therefore examined, initially on the simple electron transfer ($F + e^- \longrightarrow F^{\cdot -}$) process alone

(no substrate). A pulse frequency of 0.025Hz was used which allowed the system to reach a steady–state at both potentials employed. An acetonitrile/0.2moldm^{-3} TBAP solution containing 1.0x10^{-3}moldm^{-3} F and 1.0x10^{-3}moldm^{-3} AQ was used for these experiments and the upstream electrode was once again held at a constant potential of –1.50V, enabling measurements to be made at the downstream electrode in the presence of O_2. A flow rate of 1.03x10^{-2}cm^{3}s^{-1} was used throughout.

The steady–state current found for F was identical to i_{lim} measured previously at this flow rate, confirming the consistency of the pulsing approach. 1, 2, 3 and 5% forane was next added via the HDPE membrane. The resulting transient data is shown in Figure 10.14 and the steady–state current is plotted as a function of [forane] in Figure 10.15. A linear response to forane is apparent. Figure 10.16 confirms that the steady–state current measured for a given [forane] is in excellent agreement with i_{lim} determined earlier in this chapter using a potential sweep method. The results obtained when O_2 was added to the system (up to 50%) were indistinguishable from those in Figure 10.15.

Stepping experiments were then repeated with N_2O as substrate. The experimental conditions were identical to those described above. Typical transients are shown in Figure 10.17; the "noisy" response is a result of the residual formation of tiny N_2 bubbles on the downstream electrode. The presence of such bubbles was concluded as insignificant given the excellent linear response to [N_2O] shown in Figure 10.18, recorded in the presence of up to 50% O_2.

Lastly, the response time of the sensor was investigated by adjusting the concentration of substrate during an interval at the reduction potential of the pulse cycle. The device is less sensitive to [forane] than [N_2O] since the former substrate was shown in sections 10.3 and 10.4 of this chapter to be less permeable through HDPE. Therefore the concentration of forane, delivered to the sensor via the carrier gas line and membrane, was adjusted immediately after the potential had stepped from –1.50V to –1.90V. Figure 10.19 illustrates that the transient response adjusts to the new concentration within the period of one pulse, whether [forane] is increased or decreased. An excellent response time of <10 seconds can be inferred.

In summary, the operation of the amperometric channel electrode sensor in a

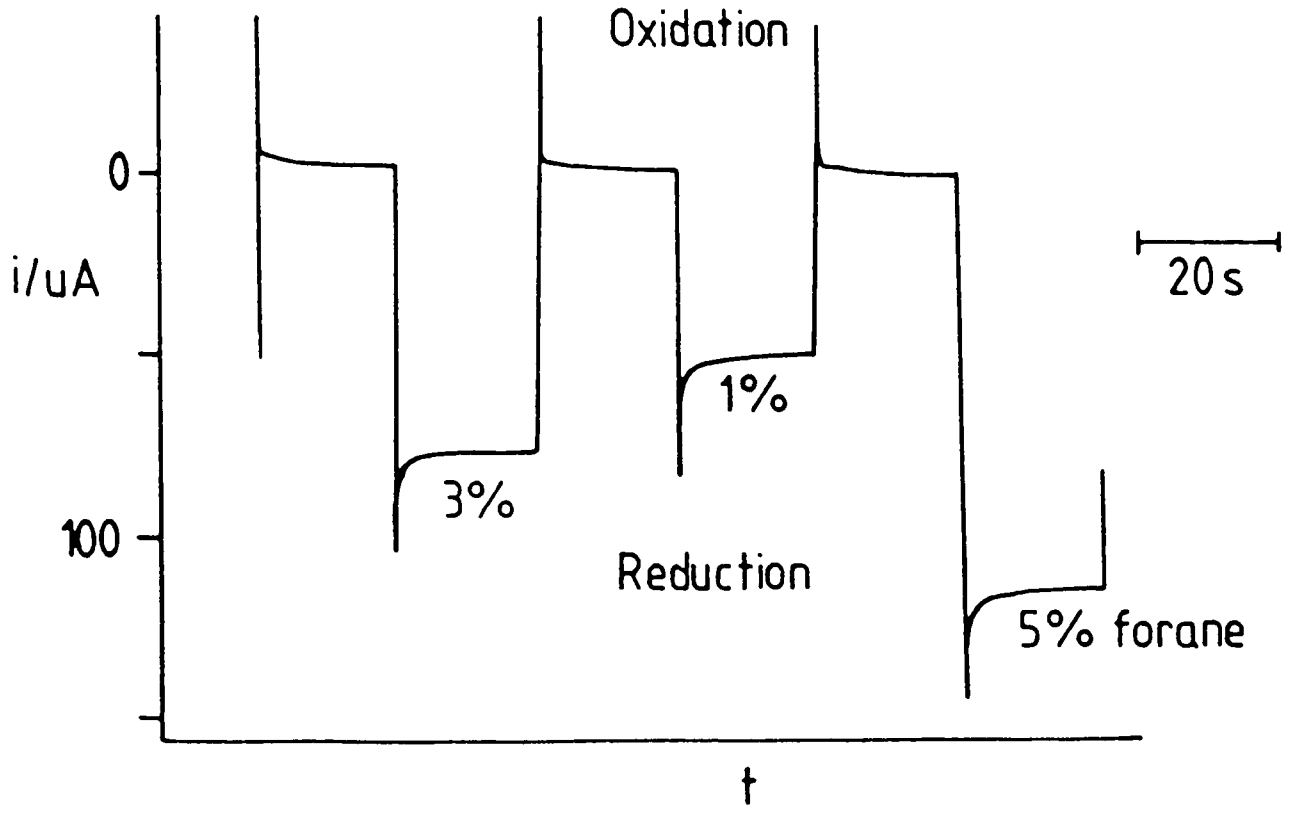


Figure 10.14: Typical current transients for the reduction of forane, obtained by pulsing the detector electrode between –1.50V and –1.90V v.Ag.

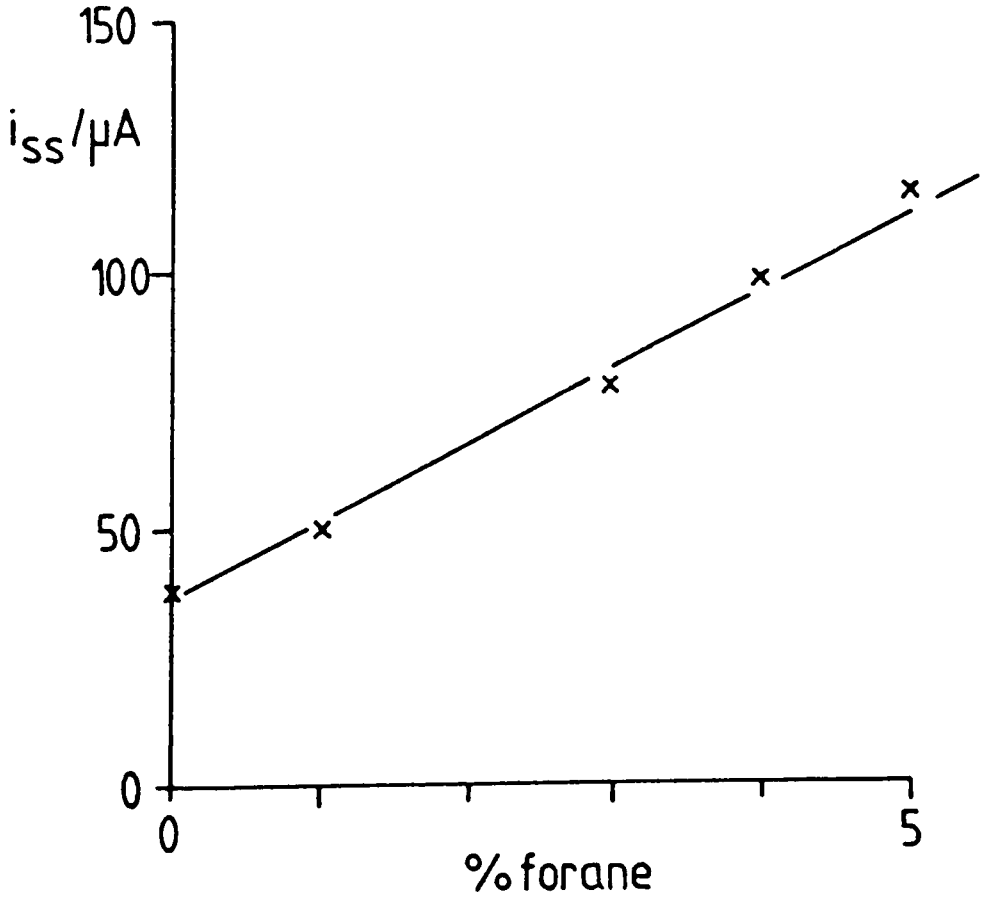


Figure 10.15: The steady–state current, measured from transients such as those shown in Figure 10.14, plotted against the concentration of forane delivered to the membrane.

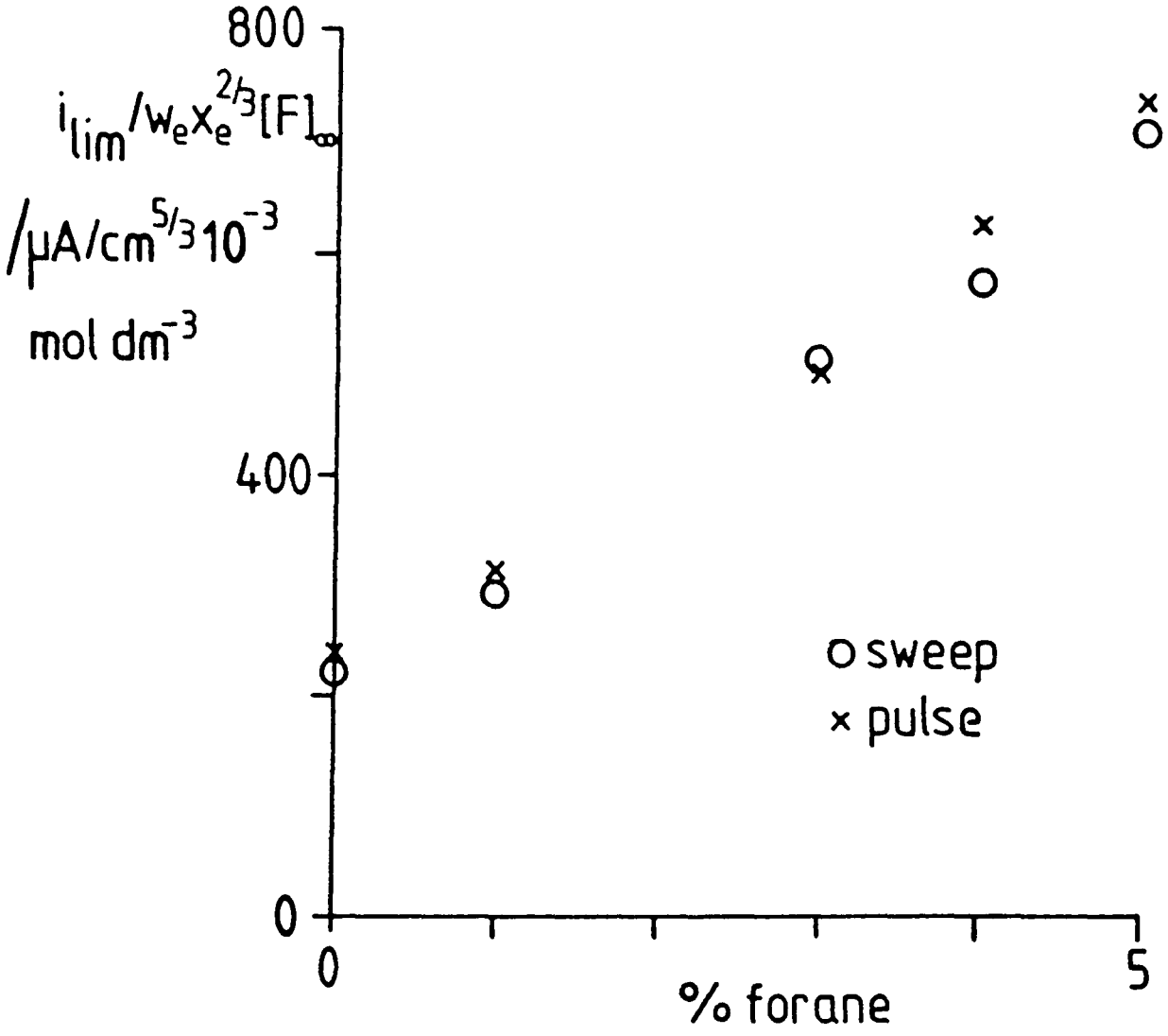


Figure 10.16: A comparison between the ChE sensor current obtained from voltammograms such as those used to produce the data presented in Figure 10.5 and from transients like those shown in Figure 10.14.

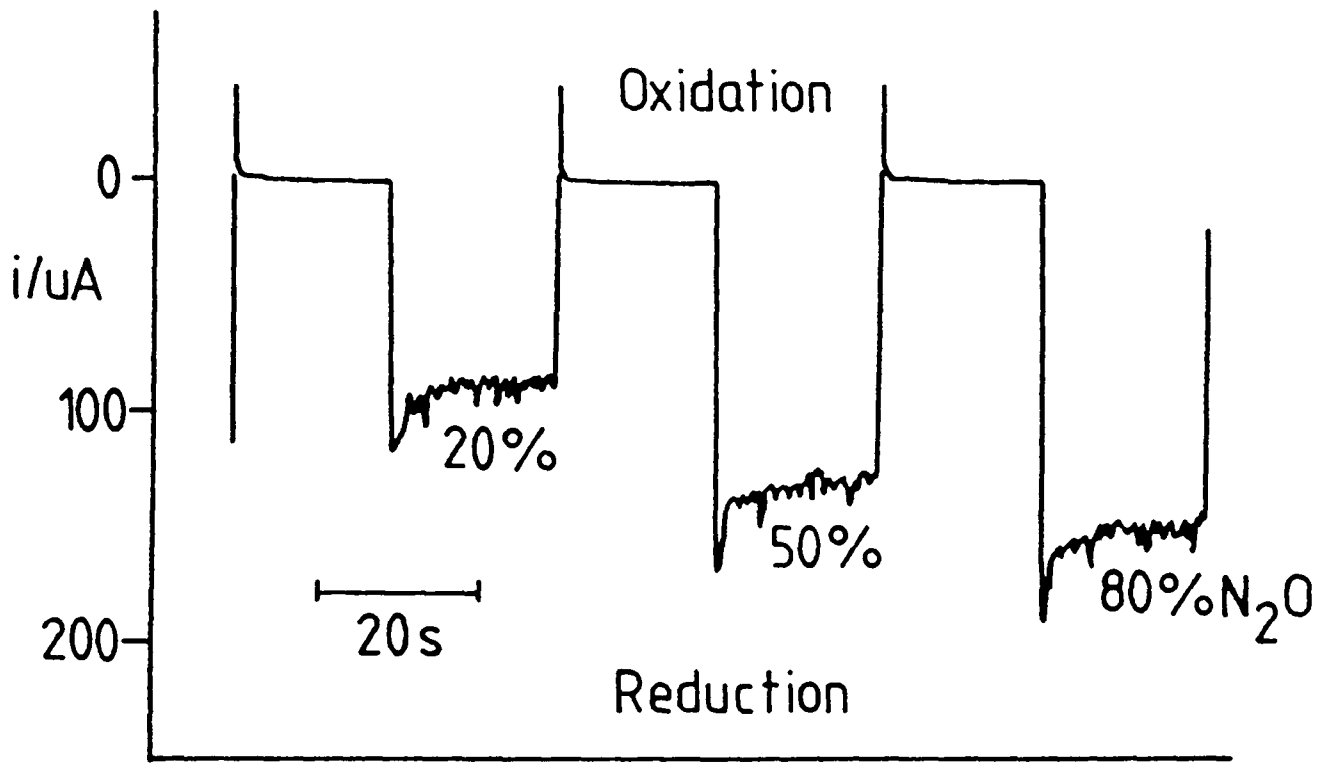


Figure 10.17: Typical current transients for the reduction of nitrous oxide, obtained by pulsing the detector electrode between –1.50V and –1.90V v.Ag.

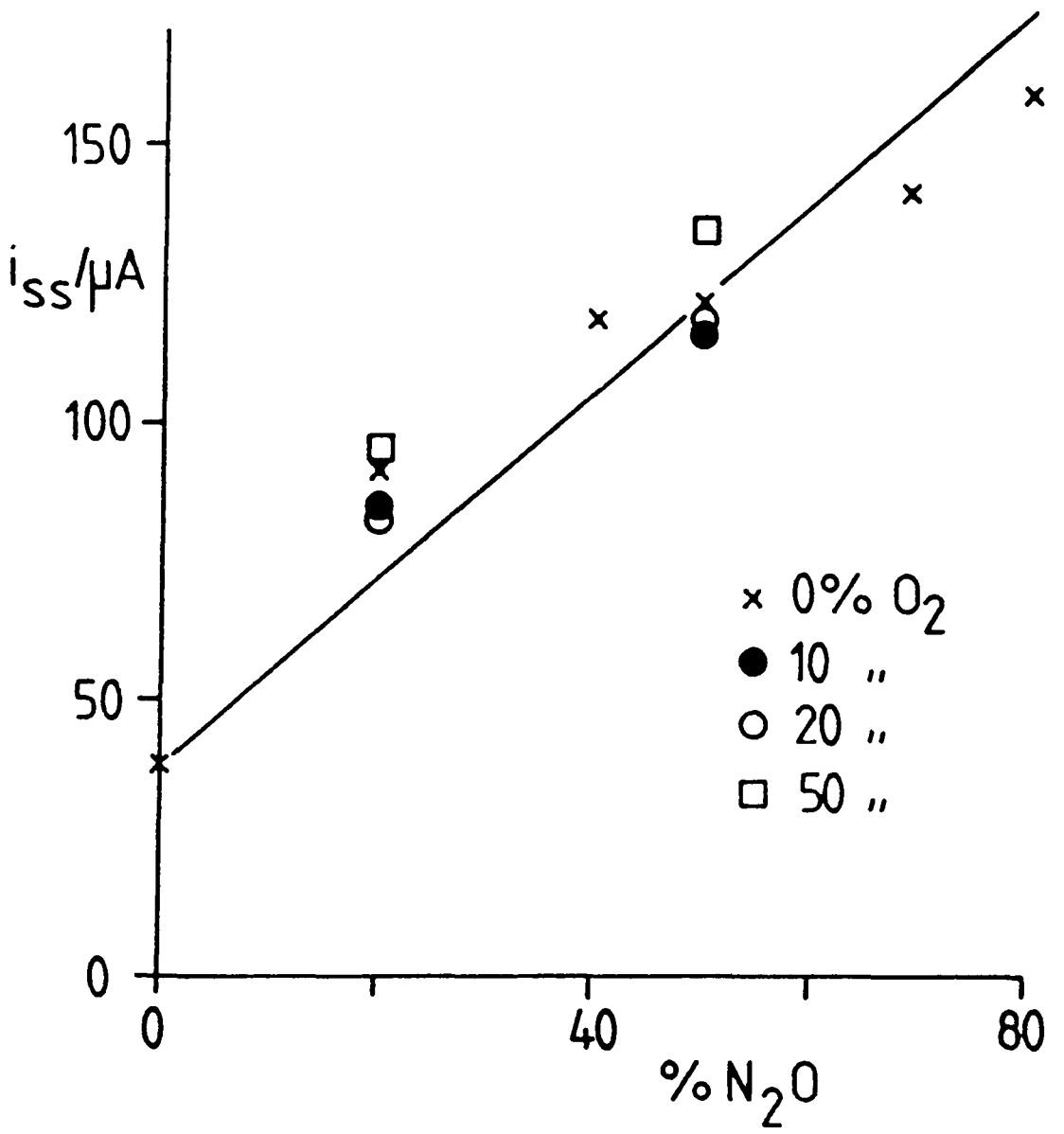


Figure 10.18: The steady–state current, measured from transients such as those shown in Figure 10.17, plotted against the concentration of nitrous oxide delivered to the membrane.

pulse potential mode, as presented in this chapter, yields a linear response to both forane and N_2O. No interference results from the presence of O_2. The merits of the device are its simplicity, sensitivity to anaesthetic detection and, in particular, a response time of under ten seconds to changes in forane concentration.

Possible improvements to the device, as it stands, might include the use of a mechanical pump to achieve solution flow, enabling the design of a miniature sensor for clinical convenience. Also, the employment of faster flow rates may further hasten the response time of the sensor.

The use of the channel electrode sensor for breath by breath respiratory forane analysis is therefore feasible.

10.6 Conclusions

The reductions of N_2O and forane, via homogeneous electron transfer from electrogenerated $F^{\cdot -}$, were demonstrated in Chapter Nine to proceed via the same electrode pathways at the ChE as previously determined (in Chapter Seven) at the RDE. In this chapter, these mechanisms were shown to remain unchanged when the gaseous anaesthetic substrates were delivered to the channel through an HDPE membrane.

The reduction of oxygen (introduced to the ChE from the electrolyte reservoir or through the carrier gas line) at the working electrode was shown to mask the current resulting from the reduction of F and therefore to prevent the determination of [forane] or [N_2O]. However, AQ^{2-} electrogenerated at the upstream electrode reacted with the dissolved O_2 and thus removed the problem of interference by this gas at the downstream electrode. Importantly, the presence of AQ was shown to have no effect on the reduction properties of the F/forane and F/N_2O systems.

Pulsing the downstream electrode from a potential where no mediator was electrogenerated, to a potential which corresponded to the transport limited current for the reduction the F, was used to overcome the problem of electrode fouling by N_2, a N_2O reduction product. The resulting transients were shown to yield

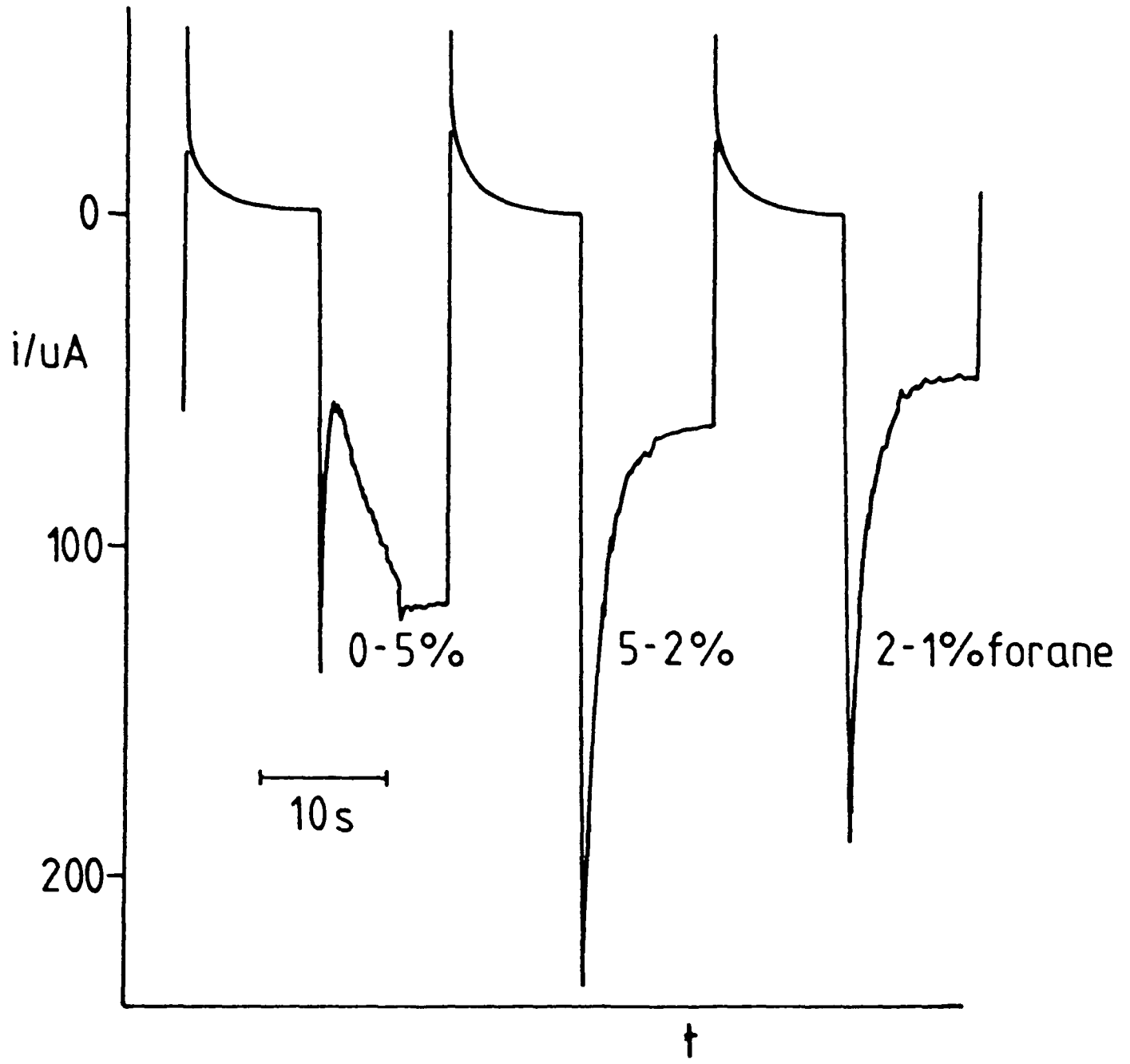


Figure 10.19: Current transients, as shown in Figure 10.14, except that the forane composition of the gas mixture was adjusted during the –1.90V v.Ag cycle of the pulse sequence.

steady–state currents which varied linearly with [forane] and [N_2O]. The response time of the device to forane detection was shown to be less than ten seconds.

As a final conclusion to this work, the ChE sensor has been demonstrated to respond linearly to both forane and N_2O in the presence of a high concentration of O_2. No limitations on the size of the device are apparent so that the sensor could be readily miniaturised, as required, for clinical convenience. Solution flow through the device would probably be best achieved by closed circuit mechanical pumping from a small electrolyte reservoir.

The use of this device in conjunction with an aqueous membrane N_2O/O_2 sensor (of the kind described in Chapter Eight) and the appropriate circuitry therefore promises fast and accurate respiratory analysis of forane, N_2O and O_2.

APPENDIX ONE

AC Impedance

The concept of impedance and the complex plane impedance diagrams arising from some simple electrical circuits are introduced in this appendix.

A1.1 AC Theory

In order to work with electrochemical cells in AC circuits, the use of some basic AC theory is necessary. The following section therefore uses the so–called phasor concept of the sinusoidal alternating current, in which voltages and currents are thought of as rotating vectors and are represented in the complex plane by an Argand diagram.

The sinusoidal voltage can be expressed as:

$$E = \Delta E \sin wt \qquad \text{A1.1}$$

where w is the angular frequency ($rads^{-1}$), E is the instantaneous voltage and ΔE is the maximum amplitude. The voltage is therefore represented as a rotating vector or phasor as illustrated in Figure A1.1. The current associated with this voltage is also sinusoidal and of the same frequency, w, but different in amplitude and phase (lagging or leading) and can be expressed as:

$$i = \Delta i \sin(wt + \varphi) \qquad \text{A1.2}$$

The rotating vectors are separated on the polar diagram by the phase angle, φ (Figure A1.1). The response of simple circuit elements to the voltage E can be seen by applying Ohm's law, which for a pure resistance of value R is:

$$E = iR \qquad \text{A1.3}$$

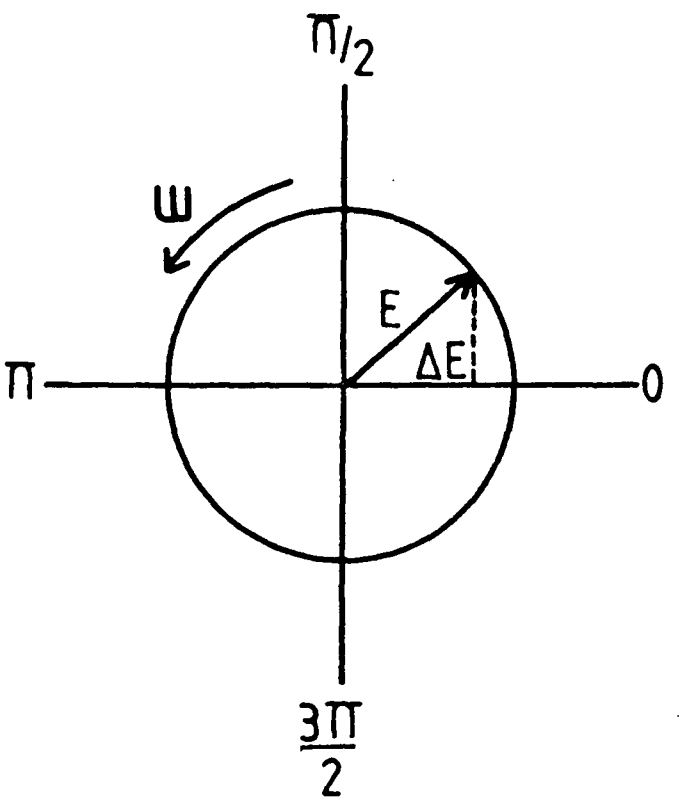


Figure A1.1: Phasor diagram for an alternating voltage $E = \Delta E \sin \omega t$ where ΔE is the maximum amplitude. The phasor is the rotating vector E.

which implies that the phase angle φ is zero. For a capacitance, C, the relationship between the potential, E, across the plates to the charge, q, residing on the plates is:

$$q = CE \qquad \text{A1.4}$$

Differentiating yields the current:

$$i = \frac{dq}{dt} = C\frac{dE}{dt} \qquad \text{A1.5}$$

which can be combined with equation A1.1 to give:

$$i = wC\Delta E \cos wt \qquad \text{A1.6}$$

or

$$i = \frac{\Delta E}{X_c} \sin(wt + \frac{\pi}{2}) \qquad \text{A1.7}$$

where $X_c = 1/wC$ and is defined as the capacitive reactance. Equation A1.7 is similar in form to the Ohm's law expression for a resistor (A1.3) but with R replaced by X_c and a phase angle of $\pi/2$ rather than zero. This phase angle is positive so the current is said to lead the voltage.

Here, it is useful to introduce "complex" notation, in which magnitudes on the ordinate axis are multiplied by $j = \sqrt{(-1)}$. The components of the phasors E and i can be represented in an Argand diagram with the real component on the abscissa and the imaginary component on the ordinate. Figure A1.2 shows equivalent representations in phasor and time axis form of the current and voltage relationship discussed above for a circuit with capacitative reactance showing a 90^0 $(\pi/2)$ phase angle. Hence, the E phasor has a phase angle of $-\pi/2$ and therefore:

$$E = -jX_c i \qquad \text{A1.8}$$

This is again similar to Ohm's law, but with a complex number, $-jX_c$, replacing

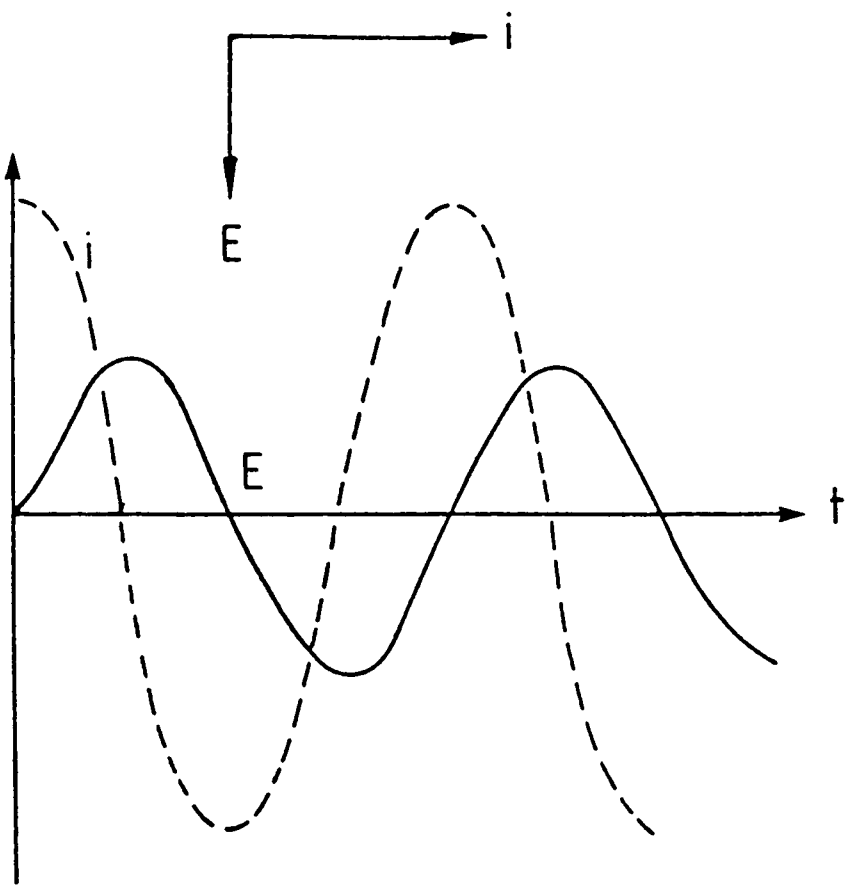


Figure A1.2: Equivalent representations in phasor and time–axis form of current and voltage relationships in a circuit with capacitative reactance showing a 90° phase angle.

resistance.

For a resistor and capacitance connected in series the sum of the voltage drops across each circuit element must sum to the total of E, so in phasor notation:

$$E = E_R + E_C$$

i.e. $$E = i(R - jX_c)$$

or $$E = iZ \qquad \text{A1.9}$$

where $Z = (R - jX_c)$ is called the impedance.

The current will no longer be in phase or 90^0 out of phase with the voltage, but can be obtained from the Argand diagram, Figure A1.3a. The phase angle is given by:

$$\tan\varphi = \frac{X_c}{R} = \frac{1}{wRC} \qquad \text{A1.10}$$

The simple relationship between complex impedance and E and i means that an alternative diagram presenting the same information can be plotted in terms of impedances (Figure A1.3b). For series circuits, the overall impedance is the vector sum of the reactances of the separate elements. The overall impedance for parallel combinations is the reciprocal of the sum of the reciprocal impedances of each circuit component.

A1.2 Impedance Measurements

One of the simplest electrochemical systems to analyse is that of a rapid reaction at its equilibrium, with no net current flowing. Under AC excitation, this net current is still zero, but the current–potential relationship is approximately linear rather than exponential (Chapter Two, section 2.1.1).

Consider the reaction:

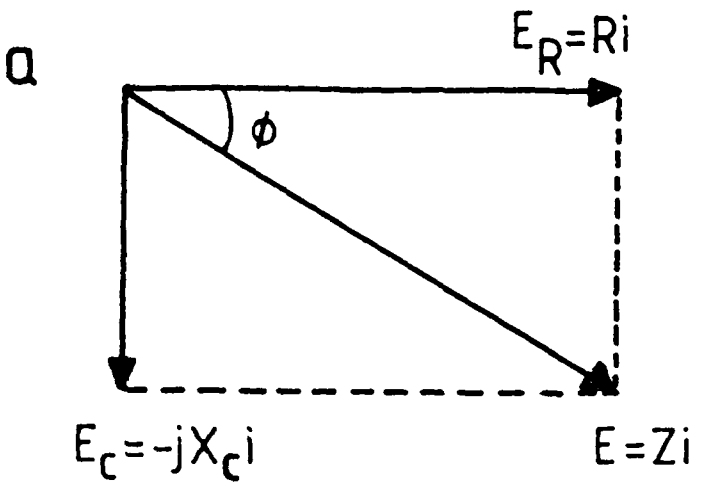
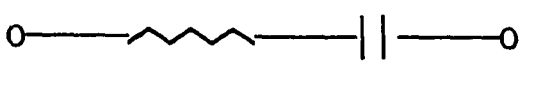


Figure A1.3: The relationship between alternating voltage across a series resistor and capacitor and the alternating current through it, represented by a) a phasor diagram, and b) an Argand diagram.

$$O + ne^- \rightleftharpoons R$$

when the AC signal is first impressed, a time–dependent diffusion layer is created and since no net current flows, a steady–state is set up after a few cycles. Assuming that the impedance can be expressed as a series combination of a resistor and a capacitor:



it is found that:

$$R_s = R_{ct} + \sigma_c / w^{1/2} \qquad \text{A1.11}$$

$$C_s = 1/(\sigma_c w^{1/2}) \qquad \text{A1.12}$$

where R_{ct} is the charge transfer resistance, C_s is the pseudo capacitance and:

$$R_{ct} = \frac{RT}{nF\, i_0} \qquad \text{A1.13}$$

and

$$\sigma_c = \frac{RT}{Z^{1/2} n^2 F^2 A D^{1/2}} \left[\frac{1}{[O]_\infty} + \frac{1}{[R]_\infty} \right] \qquad \text{A1.14}$$

Thus R_{ct} is a characteristic of the exchange current, i_0, and therefore k^0 the rate constant at equilibrium, whereas σ_c is related to the diffusional properties of the system.

The overall impedance is:

$$Z' = R_s + \frac{1}{jwC_s}$$

$$Z'' = R_{ct} + \sigma_c / w^{1/2} + \sigma_c / jw^{1/2} \qquad \text{A1.15}$$

This is the sum of two terms: a simple resistive component, which is small when i_0

is large, and a reactance, which can be regarded as a frequency dependent resistance. This special reactance is called the Warburg impedance, Z_W. If R_{ct} approaches zero, then the total impedance is:

$$|Z_W| = [(\sigma_c/w^{1/2})^2 + (\sigma_c/w^{1/2})^2]^{1/2}$$

i.e.
$$|Z_W| = (2/w)^{1/2}\sigma_c \qquad \text{A1.16}$$

Since both real and complex parts of Z_W are equal, it is characterised by a constant phase angle of $\pi/4$ (45^0), independent of frequency.

The above analysis has neglected the fact that all electrodes exhibit a capacitance, C_{dl}, the double layer capacitance, which is independent of any Faradaic reaction (which contributes C_s to the overall impedance). An uncompensated solution resistance, R_u is also present in all practical electrochemical systems. The combined effect of C_{dl} and R_u can be examined using "complex plane impedance analysis" [108].

Considering a simple circuit such as a series resistance and capacitance with an impedance $Z = R + 1/jwC$, it can be seen that the real part of Z is simply R and the imaginary part is $1/wC$. An Argand diagram of $Z = Z' + Z''$ is therefore a series of points at different w, the value of Z'' approaching zero at infinite frequency where the capacitance is effectively a short circuit (Figure 2.9). However, the graph representing a parallel combination is a semi–circle (Figure 2.11). At low frequencies, the impedance is purely resistive because the reactance of C is very large. An additional resistance in series, which might represent an uncompensated solution resistance has the effect of translating the semi–circle along the Z' axis (Figure 2.11).

A realistic model of an electrochemical cell can now be constructed by identifying C as the double layer capacitance and resolving R into the charge transfer resistance in series with the Warburg impedance (Figure 2.10). A full analysis of this series–parallel configuration, called the Randles equivalent circuit [124] has two limiting cases:

1) At low frequency as $w \rightarrow 0$:

$$Z' = R_u + R_{ct} + \sigma_c w^{-1/2}$$

$$Z'' = \sigma_c w^{-1/2} + 2\sigma_c^2 C_{dl}$$

from which $$Z'' = Z' - R_u - R_{ct} + 2\sigma_c^2 C_{dl} \qquad \text{A1.17}$$

i.e. a straight line of unit slope with an intercept on the real Z' axis of $R_u + R_{ct} - 2\sigma_c^2 C_{dl}$.

2) At high frequency, Z_W is negligible in relation to R_{ct} and the two components are:

$$Z' = R_u + \frac{R_{ct}}{1 + w^2 C_{dl}^2 R_{ct}^2} \qquad \text{A1.18}$$

$$Z'' = \frac{C_{dl} R_{ct}^2 w}{1 + w^2 C_{dl}^2 R_{ct}^2} \qquad \text{A1.19}$$

Eliminating w gives:

$$(Z' - R_u - R_{ct}/2)^2 + (Z'')^2 = (R_{ct}/2)^2 \qquad \text{A1.20}$$

which is the equation for a circle centred on $Z' = R_u + R_{ct}/2$, with a radius of $R_{ct}/2$. The plot of the whole expression for Z'' vs. Z' has the form shown in Figure 2.11, where kinetically controlled (semi–circular) and diffusion controlled (linear, unit slope) regions can be observed.

APPENDIX TWO

The Levich Equation for the Rotating Disc Electrode: Solution of Equation 2.54

Letting:

$$X = \frac{\partial[O]}{\partial w} \qquad \text{A2.1}$$

allows equation 2.54 to be written as:

$$\frac{\partial X}{\partial w} = -w^2 X \qquad \text{A2.2}$$

which upon integration gives:

$$\frac{\partial[O]}{\partial w} = \left[\frac{\partial[O]}{\partial w}\right]_{w=0} .\exp(-w^3/3) \qquad \text{A2.3}$$

Making the substitution $Y = w^3/3$ leads to:

$$\int_{[O]}^{[O]_\infty} d[O] = \left[\frac{\partial[O]}{\partial w}\right]_{w=0} .3^{-2/3} \int_0^\infty Y^{-2/3}\exp(-Y)\, dY \qquad \text{A2.4}$$

The definite integral on the right hand side of equation A2.4 is expressible in terms of the Gamma function [398]:

$$\int_0^\infty t^{x-1}e^{-t}\, dt = \sqrt{(x)} \qquad \text{A2.5}$$

and so:

$$[O]_{\infty} = \left[\frac{\partial[O]}{\partial w}\right]_{w=0} .3^{-2/3}\sqrt{(1/3)} \qquad \text{A2.6}$$

The transport limited current at the electrode is then given by:

$$i_{lim} = nFAj$$

$$= nFAD_o\left[\frac{\partial[O]}{\partial z}\right]_{z=0}$$

$$= 1.554\, nFAD_o^{2/3}\, W^{1/2}\, \nu^{-1/6}\, [O]_{\infty} \qquad \text{A2.7}$$

where F is Faradays constant and A is the area of the electrode.

APPENDIX THREE

The Levich Equation for the Channel Electrode: Solution of Equation 2.63 using the Léveque Approximation (equation 2.65)

Introducing the function:

$$\eta = \left[\frac{v_0}{D_0 hx}\right]^{1/3} z \qquad \text{A3.1}$$

leads to:

$$\frac{\partial[O]}{\partial x} = \frac{\partial[O]}{\partial \eta}\frac{\partial \eta}{\partial x} = \frac{-1}{3}\frac{\eta}{x}\frac{d[O]}{d\eta} \qquad \text{A3.2}$$

$$\frac{\partial^2[O]}{\partial z^2} = \frac{\partial[O]}{\partial \eta}\frac{\partial \eta}{\partial z}\frac{\eta}{z} = \left[\frac{v_0}{D_0 hx}\right]^{1/3}\frac{d^2[O]}{d\eta^2} \qquad \text{A3.3}$$

and thus equation 2.63 (under the Léveque approximation) may be written as:

$$\frac{d^2[O]}{d\eta^2} + \frac{2}{3}\eta^2\frac{d[O]}{d\eta} = 0 \qquad \text{A3.4}$$

with the boundary conditions (equation 2.64) becoming:

$$\eta = 0: \qquad [O] = 0 \qquad \text{A3.5 i}$$

$$\eta \to \infty: \qquad [O] = [O]_\infty \qquad \text{ii}$$

The solution to equation A3.4 follows the method described in Appendix Two and leads to:

$$[O]_\infty = \left[\frac{\partial[O]}{\partial \eta}\right]_{\eta=0}\frac{\sqrt{(1/3)}}{6} \qquad \text{A3.6}$$

The transport limited current at the ChE is then given by:

$$i_{lim} = nFw_e \int_0^1 D_o \left[\frac{\partial[O]}{\partial z}\right]_{z=0} dx \qquad \text{A3.7}$$

$$= nFw_e[O]_\infty \left[\frac{6}{\sqrt{(1/3)}}\right] \int_0^1 \left[\frac{v_0 D_0^2}{hx}\right]^{1/3} dx \qquad \text{A3.8}$$

$$= \left[\frac{9}{2}\right]^{2/3} \frac{[O]_\infty}{\sqrt{(1/3)}} nFw_e \left[\frac{v_0 D_0^2 \ l^2}{h}\right]^{1/3} \qquad \text{A3.9}$$

APPENDIX FOUR

Computer Programs

The following FORTRAN programs are listed on the microfiche below:

4a HALEF, TRANS, LESTSQR, AREA, AREADIF.

4b HALER.

4c HALECPT, HALECP, HALECPE, HALEECDA1.

4d HALHET.

4e SDECP.

4f BIE.

4g BIECP, BIECPE.

4h BIECPM, BIECPEM.



APPENDIX FIVE

The Relationship between Forward and Reverse Chronoamperograms

The purpose of this appendix is to prove that the forms of the forward and reverse transients for the case where there are no (heterogeneous or homogeneous) kinetic complications are in fact related in the special circumstances that $D_A = D_B$.

The equality of the diffusion coefficients leads to the simplification that $t^*_A = t^*_B = t$, $x_A = x_B = x$ and $w_A = w_B = w$. Thus equations 3.22 can be written as:

$$\frac{da}{dt} = \frac{\exp(-2w^3/3)}{A}\frac{d^2a}{dx^2} \qquad \text{A5.1}$$

$$\frac{db}{d(t-t')} = \frac{\exp(-2w^3/3)}{A}\frac{db^2}{dx^2} \qquad \text{A5.2}$$

If we then chose to normalise these equations as follows:

$$a - [A]_\infty = -\zeta[A]_\infty \qquad \text{A5.3}$$

and

$$b - b(t=t') = -\zeta[A]_\infty \qquad \text{A5.4}$$

then it is apparent that both transients are described by the following equation:

$$\frac{d\zeta}{dt+} = \frac{\exp(-2w^3/3)}{A}\frac{d^2\zeta}{dx^2} \qquad \text{A5.5}$$

where $t+ = t$ for the forward transient and $t+ = t - t'$ for the reverse transient. They are also described by the same boundary conditions:

$$t+ = 0 \qquad 0 < x < 1 \qquad \zeta = 0 \qquad \text{A5.6 i}$$

$$t+ > 0 \qquad x = 1 \qquad \zeta = 0 \qquad \text{ii}$$

$$t+ > 0 \qquad x = 0 \qquad \zeta = U(t+) \qquad \text{iii}$$

where $U(t+)$ is a unit step function. It thus follows that:

$$\left[\frac{d\{a - [A]_{\infty}\}}{dx}\right]_{z=0,t} = \left[\frac{d\{b - b(t+=0)\}}{dx}\right]_{z=0,t-t'} \qquad \text{A5.7}$$

where the term on the left hand side of the equation relates to the forward, and that on the right to the reverse transient. It may be seen that:

$$i_f(t) - i_r(t-t') = i_{ss} \qquad \text{A5.8}$$

where i_{ss} is the steady–state current which eventually flows at the potential E_2, and i_f and i_r relate to the currents flowing in the forward and the reverse transients.

APPENDIX SIX

The Thomas Algorithm

The Thomas Algorithm [299,300] is an efficient method by which the matrix equation:

$$[T]\{u\} = \{d\} \qquad \text{A5.1}$$

may be solved for {u}, where [T] denotes a tridiagonal matrix and {u} and {d} are vector quantities. The algorithm operates by factorising the tridiagonal matrix of $(J-1)^2$ elements:

$$[T] = \begin{bmatrix} b_1 & c_1 & 0 & & & & \\ a_2 & b_2 & c_2 & 0 & & & \\ & \ddots & \ddots & \ddots & & & \\ & & \ddots & \ddots & \ddots & & \\ 0 & & a_j & b_j & c_j & 0 & \\ & & & \ddots & \ddots & \ddots & \\ & & & & a_{J-2} & b_{J-2} & c_{J-2} \\ & & & & 0 & a_{J-1} & b_{J-1} \end{bmatrix} \qquad \text{A5.2}$$

to

$$[T] = [T_L]\,[T_U]$$

$$= \begin{bmatrix} \alpha_1 & & & & & & 0 \\ a_2 & \alpha_2 & & & & & \\ & \ddots & \ddots & & & & \\ & & \ddots & \ddots & & & \\ & & & \ddots & \ddots & & \\ & & & & a_{J-2} & \alpha_{J-2} & \\ 0 & & & & & a_{J-1} & \alpha_{J-1} \end{bmatrix} \begin{bmatrix} 1 & \beta_1 & & & & & 0 \\ & 1 & \beta_2 & & & & \\ & & \ddots & \ddots & & & \\ & & & \ddots & \ddots & & \\ & & & & \ddots & \ddots & \\ & & & & & 1 & \beta_{J-2} \\ 0 & & & & & & 1 \end{bmatrix} \qquad \text{A5.3}$$

for which α_j and β_j are readily determined:

$$\alpha_1 = b_1 \qquad \text{A5.4}$$

$$\beta_1 = c_1/\alpha_1 \qquad \text{A5.5}$$

$$\alpha_j = b_j - a_j\beta_{j-1} \qquad j = 2,3,\ldots,J-1 \qquad \text{A5.6}$$

$$\beta_j = c_j/\alpha_j \qquad j = 2,3,\ldots, J-2 \qquad \text{A5.7}$$

Writing:

$$\{f\} = [T_U]\,\{u\} \qquad \text{A5.8}$$

allows $\{d\}$ to be expressed in terms of $\{f\}$:

$$[T_L]\,\{f\} = \{d\} \qquad \text{A5.9}$$

where the elements, f_j, of $\{f\}$ are given by:

$$f_1 = d_1/\alpha_1 \qquad \text{A5.10}$$

$$f_j = (d_j - a_j f_{j-1})/\alpha_j \qquad j = 2,3,\ldots,J-1 \qquad \text{A5.11}$$

$\{f\}$ is then used to determine the elements u_j of $\{u\}$:

$$u_{J-1} = f_{J-1} \qquad \text{A5.12}$$

$$u_j = f_j - \beta_j u_{j+1} \qquad j = J-2,J-3,\ldots,1 \qquad \text{A5.13}$$

In this way $\{u\}$ is obtained from $\{d\}$.

APPENDIX SEVEN

The Synthesis of Poly(11–Vinylfluoranthene)

A6.1 Introduction

Poly(11–vinylfluoranthene) was synethised by the free radical polymerisation of the 11–vinylfluoranthene. The latter was prepared from fluoranthene via 11–acetyl–fluoranthene and 11–(1–hydroxy)ethyl–fluoranthene in the manner described below for which the following general experimental points pertain. Melting points were determined using a Kofler block. Infrared spectra were recorded as a KBr disc on a Perkin–Elmer 781 spectrophotometer. The ^{1}H NMR spectra were run at 300 MHz on a Bruker WH 300 spectrometer. Microanalyses were performed by the Dyson Perrins Laboratory. Mass spectra were measured on a VG Micromass 30F spectrometer using the in beam electron impact technique.

A6.2 11–Acetylfluoranthene

Fluoranthene was acetylated by a modification of the previous procedure [399]. Aluminium chloride (6.6 g, 0.0494 mol) was added to a solution of fluoranthene (5.0 g, 0.247 mol) in carbon disulphide (50 ml) at 0°C. Acetic anhydride (2.4 ml, 0.0247 mol) was added over a period of 30 minutes and the reaction mixture was stirred with a mechanical stirrer for seven hours at 0°C and subsequently at room temperature overnight. The brown solid was collected by filtration, washed with hexane and then treated with 3% hydrochloric acid; the residue was then extracted into ether and the resulting ether solution dried (sodium sulphate). The solvent was removed, and the reddish syrup was chromatographed (10% ethyl acetate in hexane) to give a mixture of the two monoacetyl compounds 4– and 11–acetylfluoranthene (2.1g) and the diacetyl. The mixture of the monoacetyl compounds was then separated by further chromatography (dichloromethane and hexane, 3:1) to give the faster running non–fluorescent, 4–acetylfluoranthene, (0.74 g, 13%), followed by the slower running blue fluorescent 11–acetylfluoranthene (1.2 g, 20%), together with a

further mixture of unseparated 4–acetylfluoranthene and 11–acetylfluoranthene (300mg). 11–acetylfluoranthene: m.p. 101–102°C (ref. [399]: 101–102°C) (found: C, 88.01; H, 4.76. $C_{18}H_{12}O$ requires: c, 88.43; H, 4.92%). λ_{max}(KBr): 1670cm^{-1}, ^{1}H NMR ($CDCl_3$): δ 2.72 (3H, s, Me), 7.65–7.70 (2H, t), 7.88–8.02 (6H, m) and 8.49 (1H, m). m/z (EI): 244 (M^+, 55%) and 229 (M–Me^+, 100%).

A6.3 11–(1–Hydroxy)ethyl–fluoranthene

Sodium borohydride (129 mg) in water (9 ml) was slowly added to a solution of 11–acetylfluoranthene (620 mg) in tetrahydrofuran (60 ml) at 0°C; the reaction mixture was stirred at 0°C for 2.5 hours and room temperature for 2 hours, and then cooled to 0°C and treated with ammonium chloride. The solvent was removed in vacuo to give 11–(1–hydroxy)ethyl–fluoranthene, (620 ml, 99%), recrystallised from ether hexane, m.p. 89–90°C (found: C, 87.59; H, 5.59. $C_{18}H_{14}O$ requires: C, 87.80; H, 5.69%). λ_{max}(KBr): 3500–3100 (OH)cm^{-1}, ^{1}H NMR ($CDCl_3$): δ 1.62 (3H, d, Me, J = 6.4Hz), 2.07 (1H, br s, OH), 5.05 (1H, q, J = 6.4Hz), 7.36–7.39 (1 H, m), 7.62–7.67 (2 H, m) and 7.84–7.96 (6 H, m). m/z (EI): 246 (M^+, 39%), 231 (M–Me^+, 39%), 228 (62%) and 203 (100%).

A6.4 11–Vinylfluoranthene

11–(1–Hydroxy)ethyl–fluoranthene (400 mg) in benzene (60 ml) was refluxed in the presence of toluene p–sulphonic acid (10 mg) for 3.5 hours. The reaction mixture was cooled and neutralised (solid sodium carbonate) and the solvent removed; the resulting yellow solid was dissolved in ether, washed with brine and dried (sodium sulphate). After the solvent had been removed, the yellow residue was purified by flash chromatography (neat hexane) to give 11–vinylfluoranthene, (200 mg, 54%), m.p. 102–103°C (found: C, 94.73; H, 5.42. $C_{18}H_{12}$ requires: C, 94.73; H, 5.27%). ^{1}H NMR ($CDCl_3$): δ 5.35 (1 H, dd, J = 0.6 and 10.6Hz), 5.90 (1H, dd, J = 0.2 and 17.6Hz), 6.88 (1H, dd, J = 10.6 and 17.6Hz), 7.44 (1H, dd, J = 1.6 and 7.8Hz1, 7.62–7.68 (2H, m), 7.84–8.00 (6H, m). m/z (EI): 228 (M^+, 100%).

REFERENCES

1. A.B. Dobkin, *Development of New Volatile Inhalation Anaesthetics*, Elsevier/North Holland Biomedical Press, Amsterdam, Ch. 1,2,3 and 7, (1978)

2. R.B. Dodd, *Diethyl Ether. Its Effect in the Human Body.* Ed. C. C. Thomas, Springfield, I11, Ch. 1, (1962)

3. C.M. Conway, *Brit. J. Anaesth.*, 37, (1965), 644

4. M.H. Armstrong Davison, *Brit. J. Anaesth.*, 37, (1965), 655

5. V.J. Collins, *Principles of Anesthesiology, 2nd Ed.*, Lea and Febiger, Philadelphia, Pa., (1976), pp 1461–1463

6. H.C.A. Lassen et al, *Lancet*, 1, (1956), 527

7. W.H. Konarzewski, G. Richards, S. Thompson and D.G. Nash, *Anaesthesia*, 42, (1987), 186

8. A.A. Smith, P.P. Volpitto, Z.W. Gramling, M.B. DeVore and A.B. Glassman, *Anesth. et Analg.*, 52, (1972), 1

9. R.J. Bull, *Environ. Health Perspect.*, 69, (1986), 49

10. R.M. Waters (Ed.), *Chloroform – a study after 100 years*, Univ. of Wisconsin Press, Madison, Wisc., (1951), pp 121–128

11. R.A. VanDyke and M.B. Chenoweth, *Anesthesiology*, 26, (1965), 348

12. W.J. Grant, *Medical Gases*, Aglesbury: H.M. & M. publishers, Ch. 5 and 9, (1978)

13. L.S. Goodman and A. Gilman, *The Pharmacologic Basis of Therapeutics, 4th Ed.*, Macmillan, London and Toronto, (1970), pp 292

14. I.R. Verner, *Brit. J. Anaesth.*, 37, (1965), 671

15. R.W. Virtue, R.V. Young, L.O. Lund, J.H. Vogel and R.F. Grover, *Anesthesiology*, 24, (1963), 217

16. J. Parkhouse, *Brit. J. Anaesth.*, 37, (1965), 681

17. L.W. Fabian, C.R. Stephen and M. Bourgeous–Gavardin, *Sth. Med. J.* (*Bgham, Ala.*), 49, (1956), 808

18. A.B. Dobkin and P.H. Byles, *Acta anaesth. scand.*, 6, (1962), 115

19. R.R. Johnson, T.H. Cromwell, E.I. Eiger, II, D. Cullen, W.C. Stevens and T. Joas, *Anesthesiology*, 38, (1973), 313

20. C.W. Suckling, *Brit. J. Anaesth.*, 29, (1957), 466

21. J. Raventos, *Brit. J. Pharmacol.*, 11, (1956), 394

22. C.R. Stephen and D.M. Little (Jr.), *Halothane* (*Fluothane*), Williams and Wilkins, Baltimore, Md., (1961), pp 53

23. H.L. Brennan, A.R. Hunter and M. Johnstone, *Lancet*, ii, (1957), 453

24. U.S. Department of Health and Human Services, *Cumulated Index Medicus*, 29, (1988), pp 12047–12050

25. R.L. Katz, R.S. Matteo amd E.M. Papper, *Anesthesiology*, 23, (1962), 597

26. M.H.M. Dykes, J.P. Gilbert and McPeek, *Brit.J. Anaesth.*, 44, (1972), 925

27. R.R. Johnston, E.I. Eger, II and C. Wilson, *Anesth. Analg. Curr. Res.*, 55, (1976), 709

28. J. Neuberger and R. Williams, *Br. Med J.*, 289, (1984), 1136

29. J.F. Artusio (Jr.), A. Van Poznak, R.E. Hunt, F.M. Tiers and M. Alexander, *Anesthesiology*, 21, (1960), 512

30. R.W. Virtue, L.O. Lund, M. Phelps, H.K. Vogel, H. Beckwitt and M. Heron, *Canad. Anaesth. Soc J.*, 13, (1966), 233

31. B.S. Selinsky, *Mol. Pharmacol.*, 33, (1988), 559

32. A.B. Dobkin, D.S. Kim, A.A. Levy and P.H. Byles, *Anesth. et Analg.*, 52, (1973), 317

33. J.F. Vitcha, *Anesthesiology*, 35, (1971), 4

34. A.B. Dobkin, *Studies on isoflurane (forane) anaesthesia in: Proc. VI World Congress of Anaesthesia*, Excerpta Medica, Amsterdam, (1976), pp 109

35. T.H. Corbett, *Ann. N.Y. Acad. Sci*, 271, (1976), 58

36. E.I. Eger, *Anesthesiology*, 55, (1981), 559

37. T.H. Cromwell, E.I. Eger and W.C. Stevens, *Anesthesiology*, 35, (1971), 401

38. A.B. Dobkin, P.H. Byles, H.Y. Arandia, S. Ghanooni, K. Nishioka and A.A. Levy, *Acta anaesth. scand.*, 16, (1972), 69

39. P.M. McAteer, J.A. Carter, G.M. Cooper and C. Prys Roberts, *British J. of Anaesth.*, 58, (1986), 390

40. K.R. Milligan, J.P. Howe and J.W. Dundee, *Anaesthesia*, 43, (1988), 2

41. E.I. Eger, *Anesth. Analg.*, 66, (1987), 977

42. P.H. Byles, A.B. Dobkin, J.H. Ferguson and A.A. Levy., *Canad. Anaesth. Soc. J.*, 18, (1971), 387

43. S.H. Bahlman, E.I. Eger, II and T.H. Cromwell, *Anesthesiology*, 36, (1972), 191

44. W.T. Ross, *Anaesthesiology*, 57 (suppl. 3A), (1982), A217

45. E.I. Eger, *Br. J. Anesth.*, 56, (1984), 715

46. A.B. Dobkin, D. Kim, J.K. Choi and A.A. Levy, *Canad. Anaesth. Soc. J.*, 20, (1973), 494

47. D.A. Holaday, V. Fiserova–Bergerova, I.P. Latto and M.A. Zumbiel, *Anesthesiology*, 43, (1975), 325

48. A.B. Dobkin, H.H. Borgstedt, R.F. Rohner, R.M. Kurlan and A.B. Fein, *Anesth. et Analg.*, 54, (1975), 97

49. M.H. Harper, P. Collins, B. Johnson, E.I. Eger and C. Biava, *Anesthesiology*, 56, (1982), 14 and *Anesth. Analg.*, 61, (1982), 79

50. R. Cronnelly, O. Salvatierra and N.J. Feduska, *Anesth. Analg.*, 63, (1984), 202

51. M.C. Derrington and G. Smith, *Br. J. Anesth.*, 59, (1987), 815

52. M.K. Sykes, *Br. J. Anesth.*, 59, (1987), 901

53. P. Schied, *Measurement in Clinical Respiratory Physiology*, Eds. G. Laszlo and M.F. Sudlow, Academic Press, London, Ch.7, (1983), pp 131–166

54. S. Woldring, D.C. Woolford and G. Owens, *Science*, 153, (1966), 885

55. C.E.W. Hahn and P. Foex, *Respiratory Monitoring and Intensive Care*, Ed. A.A. Spence, Clinics in Critical Care Medicine No.4, Churchill Livingstone, Edinburgh, Ch. 4, (1982), pp 56–73

56. D. Parker and D.T. Delpy, *Measurement in Clinical Respiratory Physiology*, Eds. G. Laszlo and M.F. Sudlow, Academic press, London, Ch.5, (1983), pp 75–111

57. S.M. Mastenbrook, T.A. Massaro and J.A. Demprey, *J. Applied Physiol.*, 44, (1978), 634

58. E. Pinard, J. Selaz and H. Mamo, *Med. Biol. Eng. Comput.*, 16, (1978), 59

59. L.G. Hansen, B. Jensen and J. Gronlund, *J. Med. Eng. Technol.*, 10, (1986), 11

60. G.M. Ozanne, W.G. Young, W.J. Mazzei and J.W. Severinghaus, *Anesthesiology*, 55, (1981), 62

61. C.E.W. Hahn, *Clin. Phys. Physiol. Meas.*, 8, (1987), 3

62. C.E. Whitcher, E.N. Cohen and J.R. Trudell, *Anesthesiology*, 35, (1971), 348

63. P.D. Wagner, P.F. Naumann and R.B. Laravuso, *J. Applied Physiol.*, 36, (1974), 600

64. D.W. Hill, *Gas Chromatography in Biology and Medicine*, Ed. R. Porter, J & A Churchill, London, (1969), pp 37–53

65. R.D. Dueck, M. Rathbun and P.D. Wagner, *Anesthesiology*, 49, (1978), 31

66. A. Pesenti, R. Latini, A. Riboni and L. Gattinoni, *Intensive Care Med.*, 8, (1982), 283

67. H. Kautsky, *Trans. Faraday Soc.*, 35, (1939), 216

68. J.I. Peterson, R.V. Fitzgerald and D.K. Buckhold, *Anal. Chem.*, 56, (1984), 62

69. J.I. Peterson, S.R. Goldstein and R.V. Fitzgerald, *Anal. Chem.*, 52, (1980), 864

70. O.S. Wolfbeis, H.E. Posch and H.W. Kroneis, *Anal. Chem.*, 57, (1985), 2556

71. C. Hamilton and A. Gedeon, *J. Phys. E.: Sci. Instrum.*, 19, (1986), 271

72. P. Carlsson, B. Ljungqvist, C. Allander, B. Hallen and O. Norlander, *Acta Anaesthesiol. Scand.*, 25, (1981), 315

73. H.G. Epstein and L.R. Redman, *Br. J. Anesth.*, 52, (1980), 1155

74. A.M. Wyrwicz, J.C. Schofield and C.T. Burt, *Non–invasive Probes Tissue Metab.*, (1982), 173

75. C. Nylander, R. Liedberg and T. Lind, *Sens. Actuators*, 3, (1982), 79

76. G.A. Eiceman, D.B. Shoff, C.S. Harden, A.P. Snyder, P.M. Martiney, M.E. Fleischer and M.L. Watkins, *Anal. Chem.*, 61, (1989), 1093

77. R.W. Stow, R.F. Baer and B.F. Randall, *Am. J. Physiol.*, 179, (1954), 678

78. R.W. Stow, R.F. Baer and B. Randall, *Arch. Phys. Med. Rehabil.*, 38, (1957), 646

79. L.C. Clark, *Trans. Am. Soc. Artif. Intern. Organs*, 2, (1956), 41

80. J.W. Severinghaus and A.F. Bradley, *J. Appl. Physiol.*, 13, (1958), 515

81. M.L. Heller, D.S. Imredy, P.R. Shafer and T.R. Watson, *Anesth. Analg.*, 51, (1972), 453

82. R. Huch, D.W. Lubbers and A. Huch, *Oxygen Measurements in Medicine and Biology*, Eds. J.P. Payne and D.W. Hill, Butterworths, London, Ch.9, (1975), pp 121–138

83. S.J. Isenberg and B.F. Green, *Crit. Care Med.*, 13, (1985), 683

84. W.J. Albery, W.N. Brooks, S.P. Gibson and C.E.W. Hahn, *J. Appl. Physiol.*, 45, (1978), 637

85. I. Bergman, *Ann. occup. Hyg.*, 18, (1975),53

86. R.F. Browner, G.K.E. Copeland, P.B. Stockwell and I. Bergman, *Beitrage zur Tabakforschung*, 9, (1977), 38

87. F. Kreuzer, G.A. Rogeness and P. Bornstein, *J. Appl. Physiol.*, 15, (1960), 1157

88. R. Schuler and F. Kreuzer, *Progr. Respiration Res.*, 3, (1969), 64

89. C.E.W. Hahn, W.N. Brooks, W.J. Albery and P. Rolfe, *Anaesthesia*, 34, (1979), 263

90. W.N. Brooks, C.E.W. Hahn, P. Foex, P. Maynard and W.J. Albery, *Br. J. Anaesth.*, 52, (1980), 715

91. J.W. Severinghaus, R.B. Weiskopf, M. Nishimura and A.F. Bradley, *J. Appl. Physiol.*, 31, (1971), 640

92. I.H.S. Douglas, P.J. McKenzie, I.M. Ledingham and G. Smith, *Lancet*, 2, (1978), 1370

93. W.J. Albery, C.E.W. Hahn and W.N. Brooks, *Br. J. Anaesth.*, 53, (1981), 447

94. C.E.W. Hahn, E.A.H. Hall, P. Maynard and W.J. Albery, *Br. J. Anaesth.*, 54, (1982), 681

95. K.H. Mancy, D.A. Okun and C.N. Reilley, *J. Electroanal. Chem.*, 4, (1962), 65

96. O.R. Brown and J.A. Harrison, *J. Electroanal. Chem.*, 21, (1969), 387

97. L. Eberson and H. Schafer, *Fortchr. Chem. Forsh.*, 21, (1971), 1

98. M.R. Rifi, *Organic Electrochemistry*, Ed. M.M. Baizer, Dekker, New York, (1973), pp 279–314

99. A.J. Bard and L.R. Faulkner, *Electrochemical Methods*, John Wiley and Sons, New York, (1980), pp 92–100

100. J. Tafel, *Z. Phys. Chem. Abt. A*, 50, (1905), 641

101. J. Newman, *Electroanalytical Chemistry*, Ed. A.J. Bard, Marcel Dekker, New York, Vol. 6, (1973), pp 187

102. J. Newman, *Electrochemical Systems*, Prentice–Hall, Englewood Cliffs, N.J., Ch. 11, 12, 14, 15, 16, 17 and 19, (1973)

103. V.G. Levich, *Physicochemical Hydrodynamics*, Prentice–Hall, Englewood Cliffs, N.J., Ch. 1, 2, 3, 7, 8, 9 and 10 (1962)

104. N. Ibl, *Comprehensive Treatise of Electrochemistry*, Eds. E. Yeager, J.O'M. Bockris, B.E. Conway and S. Sarangapani, Plenum Press, New York, Vol. 6, (1983), pp 1

105. Ref. 99, pp 153

106. Southampton Electrochemistry Group, *Instrumental Methods in Electrochemistry*, Ellis Horwood Ltd., (1985), pp 42–76

107. V.D. Parker, *Comprehensive Chemical Kinetics*, Eds. C.H. Bamford and R.G. Compton, Elsevier, Amsterdam, Vol. 26, (1986), pp 145

108. M. Sluyters–Rehbach and J.H. Sluyters, *Comprehensive Chemical Kinetics*, Eds. C.H. Bamford and R.G. Compton, Elsevier, Amsterdam, Vol. 26, (1986), pp 203

109. M. Fleischmann, S. Pons, D.R. Schmidt, *Ultramicroelectrodes*, Datatech Systems, Inc., Ch. 1, 4 and 5, (1987), and refs. therein

110. J. Ghoroghchian, F. Sarfarazi, T. Dribble, J. Cassidy, J.J. Smith, A. Russell, G. Dunmore, M. Fleischmann and S. Pons, *Anal. Chem.*, 58, (1986), 2278

111. J.E.B. Randles, *Trans. Faraday Soc.*, 44, (1948), 327

112. A Sevcik, *Coll. Czech. Chem. Comm.*, 13, (1958), 349

113. R.S. Nicholson and I. Shain, *Anal. Chem.*, 36, (1964), 706

114. R.S. Nicholson, *Anal. Chem.*, 37, (1965), 1351

115. H. Matsuda and Y. Ayabe, *Z. Electrochem.*, 59, (1955), 494

116. E. Laviron, *J. Electroanal. Chem.*, 52, (1974), 355, 395

117. S. Srinivasan and E. Gileadi, *Electrochim. Acta*, 11, (1966), 321

118. Ref. 99, pp 521–532

119. A.P. Brown and F.C. Anson, *Anal. Chem.*, 49, (1977), 1589

120. M.E. Laing, *D. Phil. Thesis*, Oxford University, (1988)

121. R.W. Murray, *Mater. Sci.*, 14, (1984), 145

122. D.H. Evans, *J. Phys. Chem.*, 76, (1972), 1160

123. L. Nadjo and J.M. Savéant, *J. Electroanal. Chem.*, 48, (1973), 113

124. J.E.B. Randles, *Disc. Faraday Soc.*, 1, (1947), 1

125. I. Epelboin, C. Gabrielli, M. Keddam and H. Takenouti, *Electrochim. Acta*, 20, (1975), 913

126. B.D. Cahan and C.T. Chen, *J. Electrochem. Soc.*, 129, (1982), 474

127. B.B. Damaskin, O.A. Petrii and V.V. Batrakov, *Adsorption of Organic Compounds on Electrodes*, Plenum Press, Ch. 1–10, (1971)

128. D. Schumann, *J. Electroanal. Chem.*, 17, (1968), 45

129. I. Epelboin, C. Gabrielli, M. Keddam and H. Takenouti, *Comprehensive Treatise on Electrochemistry*, Eds. J.O. Bockris, B.E. Conway and E. Yeager, Plenum Press, Vol. 4, Ch. 3, (1981), pp 151–188

130. W.J. Albery, C.C. Jones and A.R. Mount, *Comprehensive Chemical Kinetics*, Eds. R.G. Comptom amd A. Hamnett, Elsevier, Amsterdam, Vol. 29, (1989), pp129

131. C.M.A. Brett and A.M. Oliveira Brett, *Comprehensive Chemical Kinetics*, Eds. C.H. Bamford and R.G. Compton, Elsevier, Amsterdam, Vol. 26, (1986), pp 355

132. J. Heyrovsky, *Chem. Listy*, 16, (1922), 256

133. J. Newman, *J. Electrochem. Soc.*, 119, (1972), 69

134. D.–T. Chin, *J. Electrochem. Soc.*, 119, (1972), 1699

135. E. Kirowa–Eisner and E Gileadi, *J. Electrochem. Soc.*, 123, (1976), 22

136. C. Deslouis and M. Keddam, *Int. J. Heat Mass Transfer*, 16, (1973), 1763

137. D.R. Gabe and F.C. Walsh, *J. Appl. Electrochem.*, 13, (1983), 3, and refs. therein

138. E.D. Harris and A.J. Lindsey, *Analyst*, 76, (1951), 647

139. W.J. Blaedel, C.L. Olson and L.R. Sharma, *Anal. Chem.*, 35, (1963), 2100

140. H. Gerischer, I Mattes and R. Braun, *J. Electroanal. Chem.*, 10, (1965), 553

141. T.K. Ross and A.A. Wragg, *Electrochim. Acta*, 10, (1965), 1093

142. J. Yamada and H. Matsuda, *J. Electroanal. Chem.*, 44, (1973), 189

143. D.T. Chin and C.H. Tsang, *J. Electrochem. Soc.*, 125, (1978), 1461

144. H. Matsuda and J. Yamada, *J. Electroanal. Chem.*, 30, (1971), 261

145. H. Matsuda, *J. Electroanal. Chem.*, 38, (1972), 159

146. J. Yamada and H. Matsuda, *J. Electroanal. Chem.*, 30, (1971), 271

147. H. Schlichting, *Boundary–Layer Theory*, McGraw–Hill, New York, Ch. 11, (1979)

148. A.C. Riddiford, *Adv. Electrochem. Electrochem. Eng.*, 4, (1966), 47

149. V. Yu. Filinovskii and Yu. V. Pleskov, *Comprehensive Treatise of Electrochemistry*, Eds. E. Yeager, J.O.M. Bockris, B.E. Conway and S. Sarangapani, Plenum Press, New York, Vol. 9, (1984), pp 293

150. T. von Karman, *Z. Angew. Math. Mech.*, 1, (1921), 233

151. W.G. Cochran, *Proc. Cam. Phil. Soc.*, 30, (1934), 365

152. W.J. Albery and S. Bruckenstein, *J. Electroanal. Chem.*, 144, (1983), 105

153. W.H. Smyrl and J. Newman, *J. Electrochem. Soc.*, 118, (1971), 1079

154. D.P. Gregory and A.C. Riddiford, *J. Chem. Soc.*, (1956), 3756

155. K.B. Prater and R.N. Adams, *Anal. Chem.*, 38, (1966), 153

156. K.F. Blurton and A.C. Riddiford, *J. Electroanal. Chem.*, 10, (1965), 457

157. V.G. Levich, *Acta Phys.–Chim. URSS*, 17, (1942), 257

158. J. Newman, *J. Phys. Chem.*, 70, (1966), 1327

159. G.Y. Siver and N.V. Kabanov, *Zh. Fiz. Khim.*, 22, (1948), 53

160. P.R. Unwin, *D. Phil. Thesis*, Oxford University, (1989)

161. R.B. Bird, W.E. Stewart and E.N. Lightfoot, *Transport Phenomena*, Wiley, New York, (1960), pp 47

162. N. Ibl and O. Dossenbach, *Comprehensive Treatise of Electrochemistry*, Eds. E Yeager, J.O'M. Bockris, B.E. Conway and S. Sarangapani, Plenum Press, New York, Vol. 6, (1983), pp 202

163. M.A. Lévêque, *Ann. Mines Mem. Ser. 12*, 13, (1928), 201

164. W.J. Blaedel and L.N. Klatt, *Anal. Chem.*, 38, (1966), 879

165. A.A. Wragg and T.K. Ross, *Electrochim. Acta*, 12, (1967), 1421

166. A.A. Wragg, *Electrochim. Acta*, 16, (1971), 373

167. K. Aoki, K. Tokuda and H. Matsuda, *J. Electroanal. Chem.*, 217, (1987), 33

168. D.K. Cope and D.E. Tallman, *J. Electroanal. Chem.*, 188, (1985), 21

169. J.B. Flanagan and L. Marcoux, *J. Phys. Chem.*, 78, (1974), 718

170. K. Aoki, K. Tokuda and H. Matsuda, *J. Electroanal. Chem.*, 209, (1986), 247

171. I. Rousar, J. Hostomsky, J. Cezner and B. Stverak, *J. Electrochem. Soc.*, 118, (1971), 881

172. P.R. Unwin and R.G. Compton, *J. Electroanal. Chem.*, 245, (1988), 287

173. W.J. Albery, *Electrode Kinetics*, Clarendon Press, Oxford, (1975), pp 78

174. A.C. Testa and W.H. Reinmuth, *Anal. Chem.*, 33, (1961), 1320

175. See for example W.J. Albery and R.P. Bell, *Proc. Chem. Soc.*, (1963), 169

176. R.G. Compton, R.G. Harland, P.R. Unwin and A.M. Waller, *J. Chem. Soc. Faraday Trans. 1*, 83, (1987), 1261

177. B.A. Coles and R.G. Compton, *J. Electroanal. Chem.*, 127, (1981), 37

178. Ref. 99, pp 290

179. W.J. Blaedel and L.N. Klatt, *Anal. Chem.*, 39, (1967), 1065

180. C.P. Andrieux, L.Nadjo and J.M. Savéant, *J. Electroanal. Chem.*, 42, (1973), 223

181. R.G. Compton and M.B.G. Pilkington, *J. Chem. Soc. Faraday Trans. 1*, 85, (1989), 2255

182. J. Koutecky and V.G. Levich, *Dokl. Akad. Nauk SSSR*, 117, (1957), 441

183. J. Koutecky and V.G. Levich, *Zh. Fiz. Khim.*, 32, (1958), 1565

184. S. Bruckenstein and S. Prager, *Anal. Chem.*, 39, (1967), 1161

185. K. Aoki, K. Tokuda and H. Matsuda, *J. Electroanal. Chem.*, 76, (1977), 217

186. P.R. Unwin and R.G. Compton, *Comprehensive Chemical Kinetics*, Eds. R.G. Compton and A. Hamnett, Elsevier, Amsterdam, Vol. 29, Ch.6 , (1989) pp 173–290

187. C.P. Andrieux and J.M. Savéant, *Investigation of Rates and Mechanisms of Reactions. Part II* (*Techniques of Chemistry*), Ed. C.F. Bernasconi, John Wiley, New York, Vol. 6, (1986), pp 305

188. *Comprehensive Chemical Kinetics*, Eds. R.G. Compton and A. Hamnett, Elsevier, Amsterdam, Vol. 29, Ch. 1–11, (1989)

189. R.G. Compton, P.J. Daly, P.R. Unwin and A.M. Waller, *J. Electroanal. Chem.*, 191, (1985), 15

190. C. Amatore and J.M. Savéant, *J. Electroanal. Chem.*, 85, (1977), 27

191. L. Nadjo and J.M. Savéant, *J. Electroanal. Chem.*, 33, (1971), 419

192. M. Mastragastino and J.M. Savéant, *Electrochim. Acta*, 13, (1968), 751

193. R.G. Compton, M.B.G. Pilkington and G.M. Stearn, *J. Chem. Soc. Faraday Trans. 1*, 84, (1988), 2155

194. C. Amatore, M. Gareil and J.M. Savéant, *J. Electroanal. Chem.*, 147, (1983), 1

195. M. Mastragostino, L. Nadjo and J.M. Savéant, *Electrochim. Acta*, 13, (1968), 721

196. C Amatore and J.M. Savéant, *J. Electroanal. Chem.*, 102, (1979), 21

197. S.W. Feldberg, *J. Phys. Chem.*, 73, (1969), 1238

198. L.S. Marcoux, R.N. Adams and S.W. Feldberg, *J. Phys. Chem.*, 73, (1969), 2611

199. C.R. Greaves and R.G. Compton, *J. Applied Electrochem.*, in press

200. C Amatore and J.M. Savéant, *J. Electroanal. Chem.*, 107, (1980), 353

201. R.G. Compton, D. Mason and P.R. Unwin, *J. Chem. Soc. Faraday Trans. 1*, 84, (1988), 2057

202. J.D.E. McIntyre, *J. Phys. Chem.*, 71, (1967), 1196

203. W.G. Sherwood and S. Bruckenstein, *J. Electrochem. Soc.*, 125, (1978), 1098

204. S. Bruckenstein and B. Miller, *Accs. Chem. Res.*, 10, (1977), 54

205. W.J. Albery and M.L. Hitchman, *Ring–Disc Electrodes*, Clarendon Press, (1971), pp 13

206. See for example M.P. Soriaga and A.T. Hubbard, *J. Am. Chem. Soc.*, 104, (1982), 3937

207. R.G. Harland and R.G. Compton, *J. Colloid Interface Sci.*, 131, (1989), 83

208. K. Aoki, K. Tokuda and H. Matsuda, *J. Electroanal. Chem.*, 195, (1985), 229

209. T. Tsura, T. Nishimura, K. Aoki and S. Haruyana, *Denki Kagaku*, 50, (1982), 712

210. J. Robinson, *Electrochemistry* (*Specialist Periodical Report*), Ed. D. Pletcher, The Royal Society of Chemistry, London, Vol. 9, (1984), pp 101

211. 1st and 2nd International Conferences on Non–Traditional Approaches to the Study of Solid/Electrolyte Interfaces, *Surf. Sci.*, 101, (1980), *J. Electroanal. Chem.*, 150, (1983)

212. V.K.F. Chia, J.L. Stickney, M.P. Soriaga, S.D. Rosasco, G.N. Salatia, A.T. Hubbard, J.B. Benziger and K–W.P. Pang, *J. Electroanal. Chem.*, 163, (1984), 407

213. K–W.P. Pang, J.B. Benziger, M.P. Soriaga and A.T. Hubbard, *J. Phys. Chem.*, 88, (1984), 4583

214. R.L. Birke and J.R. Lombardi, *Spectroelectrochemistry: Theory and Practice*, Ed. R.A. Gale, Plenum Press, New York, (1988), pp 337

215. R.G. Compton and P.R. Unwin, *J. Electroanal. Chem.*, 205, (1986), 1

216. R.D. Allendoerfer and J.B. Carroll, *J. Mag. Res.*, 37, (1980), 497

217. R.G. Compton, D.J. Page and G.R. Searly, *J. Electroanal. Chem.*, 161, (1984), 129

218. R.G. Compton and A.R. Hillman, *Chem. in Br.*, 22, (1986), 1088

219. R.G. Compton and A.M. Waller, *Spectroelectrochemistry*, Ed. R.A. Gale, Plenum, London, Ch. 7, (1989)

220. K.B. Prater and A.J. Bard, *J. Electrochem. Soc.*, 117, (1970), 335

221. R. Caban and T.W. Chapman, *Chem. Eng. Sci.*, 36, (1981), 849

222. R.M. Machado and T.W. Chapman, *J. Electrochem. Soc.*, 134, (1987), 385

223. L.K.J. Tong, K. Liang and W.R. Ruby, *J. Electroanal. Chem.*, 13, (1967), 245

224. R.G. Compton, D. Mason and P.R. Unwin, *J. Chem. Soc. Faraday Trans. 1*, 84, (1988), 483

225. R.H. Philp, *J. Electroanal. Chem.*, 27, (1970), 369

226. Ref. 106, pp 59–68

227. R. Guidelli and D. Gozzi, *J. Electroanal. Chem.*, 14, (1967), 245

228. V. Yu Filinovskii and V.A. Kiryanov, *Dokl. Akad. Nauk SSSR*, 156, (1964), 1412

229. R.P. Buck and H.E. Keller, *Anal Chem.*, 35, (1963), 400

230. K.B. Prater and A.J. Bard, *J. Electrochem. Soc.*, 117, (1970), 207

231. S. Pons, B. Speiser and J.F. McAleer, *Electrochim. Acta*, 27, (1982), 1177

232. K. Holub, *J. Electroanal. Chem.*, 30, (1971), 71

233. J. Koutecky and R. Brdicka, *Collect. Czech. Chem. Commun.*, 12, (1947), 337

234. W. Vielstich and D. Jahn, *Z. Elektrochem.*, 64, (1960), 43

235. Z. Galus and R.N. Adams, *J. Electroanal. Chem.*, 4, (1962), 248

236. J.M. Hale, *J. Electroanal. Chem.*, 6, (1963), 187

237. J.M. Hale, *J. Electroanal. Chem.*, 8, (1964), 332

238. T. Joslin and D. Pletcher, *J. Electroanal. Chem.*, 49, (1974), 171

239. S.W. Feldberg, *J. Electroanal. Chem.*, 127, (1981), 1

240. S.W. Feldberg, M.L. Bowers and F.C. Anson, *J. Electroanal. Chem.*, 215, (1986), 11

241. R.G. Compton, M.E. Laing, D. Mason, R.J. Northing and P.R. Unwin, *Proc. R. Soc. London*, A418, (1988), 113

242. R.G. Compton, R.A. Spackman and P.R. Unwin, *J. Electroanal. Chem.*, 264, (1989), 1

243. R.G. Compton, R.J. Northing, A.M. Waller and G.W.J. Fleet, *J. Electroanal. Chem.*, 244, (1988), 203

244. M.J. Eddowes, *J. Electroanal. Chem.*, 159, (1983), 1

245. R. Caban and T.W. Chapman, *J. Electrochem. Soc.*, 124, (1977), 1371

246. S.C. Yen and T.W. Chapman, *Chem. Eng. Commun.*, 38, (1985), 159

247. S.C. Yen and T.W. Chapman, *J. Electrochem. Soc.*, 132, (1985), 2149

248. S.C. Yen and T.W. Chapman, *J. Electrochem. Soc.*, 134, (1987), 1964

249. L. Whiting and P. Carr, *J. Electroanal. Chem.*, 81, (1977), 1

250. A. Bewick, J.M. Mellor and B.S. Pons, *Electrochim. Acta*, 25, (1980), 931

251. S. Pons and P.P. Schmidt, *Electrochim. Acta*, 26, (1980), 601

252. B. Speiser, *J. Electroanal. Chem.*, 100, (1980), 69

253. S. Pons, *Can. J. Chem.*, 59, (1981), 1438

254. S. Pons, *Electrochim. Acta*, 26, (1981), 601

255. Ref. 103, pp 60–70

256. M. Danos and J. Rafelski, *Pocketbook of Mathematical Functions*, Abridged edition of "Handbook of Mathematical Functions" Eds. M. Abramowitz and I.A. Stegun, Verlag Harri Deutsch, (1984), pp 390

257. S.W. Feldberg, *Electroanalytical Chemistry*, Ed. A.J. Bard, Marcel Dekker, New York, Vol. 3, (1969), pp 199

258. D. Britz, *Digital Simulation in Electrochemistry*, Springer–Verlag, Berlin, Ch. 3, (1988), pp 28

259. R.G. Compton, R.G. Harland and R.J. Northing, *J. Chem. Soc. Faraday Trans. 1*, 85, (1989), 2273

260. C.P. Andrieux and J.M. Savéant, *J. Electroanal. Chem.*, 205, (1986), 43

261. J.M. Savéant and K.B. Su, *J. Electroanal. Chem.*, 196, (1985), 1

262. L. Nadjo, J.M. Savéant and K.B. Su, *J. Electroanal. Chem.*, 196, (1985), 23

263. C.P. Andrieux, P. Hapiot and J.M. Savéant, *J. Electroanal. Chem.*, 189, (1985), 121

264. J.M. Savéant and K.B. Su, *J. Electroanal. Chem.*, 171, (1984), 341

265. C.P. Andrieux, A. Merz, J.M. Savéant and R. Tomahogh, *J. Am. Chem. Soc.*, 113, (1984), 1957

266. C.P. Andrieux, C. Blocman, J.M. Dumas–Bouchiat, F. M'Halla and J.M. Savéant, *J. Electroanal. Chem.*, 113, (1980), 19

267. C.P. Andrieux, J.M. Dumas–Bouchiat and J.M. Savéant, *J. Electroanal. Chem.*, 113, (1980), 1

268. C.P. Andrieux, J.M. Dumas–Bouchiat and J.M. Savéant, *J. Electroanal. Chem.*, 88, (1978), 43

269. C.P. Andrieux, J.M. Dumas–Bouchiat and J.M. Savéant, *J. Electroanal. Chem.*, 87, (1978), 55

270. C.P. Andrieux, J.M. Dumas–Bouchiat and J.M. Savéant, *J. Electroanal. Chem.*, 87, (1978), 39

271. H. Lund, *J. Mol. Catal.*, 38, (1986), 203, and references cited therein

272. R.G. Compton, M.J. Day, M.E. Laing, R.J. Northing, J.I. Penman and A.M. Waller, *J. Chem. Soc. Faraday Trans. 1*, 84, (1988), 2013

273. D. Haberland and R. Landsberg, *Ber. Bunsenges Phys. Chem.*, 70, (1966), 724

274. W. Schmidt and E. Steckhan, *J. Electroanal. Chem.*, 89, (1978), 215

275. K.B. Prater and A.J. Bard, *J. Electrochem. Soc.*, 117, (1970), 1517

276. Ref. 99, pp 468–469

277. R.G. Compton and R.G. Harland, *J. Chem. Soc. Faraday Trans. 1*, 85, (1989), 761

278. R. Appelqvist, *Anal. Chim. Acta*, 180, (1986), 1 and refs therein

279. K. Tokuda, K. Aoki and H. Matsuda, *J. Electroanal. Chem.*, 80, (1977), 211

280. R.G. Compton and G.R. Sealy, *J. Electroanal. Chem.*, 145, (1983), 35

281. R.G. Compton and P.R. Unwin, *J. Electroanal. Chem.*, 206, (1986), 57

282. R.G. Compton, M.B.G. Pilkington, G.M. Stearn and P.R. Unwin, *J. Electroanal. Chem.*, 238, (1987), 43

283. J.L. Anderson and S. Moldoveanu, *J. Electroanal. Chem.*, 179, (1984), 107

284. S. Moldoveanu and J.L. Anderson, *J. Electroanal. Chem.*, 179, (1984), 119

285. J.L. Anderson and S. Moldoveanu, *J. Electroanal. Chem.*, 185, (1985), 239

286. J.L. Anderson. T.Y. Ou and S. Moldoveanu, *J. Electroanal. Chem.*, 196, (1985), 213

287. L.E. Fosdick and J.L. Anderson, *Anal. Chem.*, 58, (1986), 2481

288. L.E. Fosdick, J.L. Anderson, T.A. Baginski and R.C. Jaeger, *Anal. Chem.*, 58, (1986), 2750

289. L.E. Fosdick and J.L. Anderson, *Anal. Chem.*, 60, (1988), 156

290. J. Dutt and T. Singh, *J. Electroanal. Chem.*, 182, (1985), 259

291. T. Singh, B. Kumari and J. Dutt, *J. Electroanal. Chem.*, 190, (1985), 65

292. J. Dutt and T. Singh, *J. Electroanal. Chem.*, 207, (1986), 41

293. T. Singh, J. Dutt, B. Kumari and R.K. Dewan, *J. Electroanal. Chem.*, 238, (1987), 33

294. T. Singh and J. Dutt, *J. Electroanal. Chem.*, 196, (1985), 35

295. R.G. Compton and P.R. Unwin, *J. Electroanal. Chem.*, 264, (1989), 27

296. A.M. Waller, *D. Phil. Thesis*, Oxford University, (1987)

297. A.M. Waller and R.G. Compton, *Comprehensive Chemical Kinetics*, Eds. R.G. Compton and A. Hamnett, Elsevier, Amsterdam, Vol. 29, Ch. 7, (1988), pp 297–349

298. S. Moldoveanu and J.L. Anderson, *J. Electroanal. Chem.*, 175, (1984), 67

299. L.H. Thomas, *Watson Sci. Comput. Lab. Rept.*, Columbia University, New York, (1949)

300. L. Lapidus and G.F. Pinder, *Numerical Solutions of Partial Differential Equations in Science and Engineering*, Wiley, New York, (1982), pp 216–218

301. P.J Daly, D.J. Page and R.G. Compton, *Anal. Chem.*, 55, (1983), 1191

302. Ref. 106, Ch. 11, pp 358–359

303. S. Barnartt, *J. Electrochem. Soc.*, 99, (1952), 549

304. S. Barnartt, *J. Electrochem. Soc.*, 108, (1961), 102

305. A. Bewick, M. Fleischmann and M. Liler, *Electrochim. Acta*, 1, (1959), 83

306. Ref. 106, Ch. 11, pp 368–370

307. J. Tenygl, *Chem. Listy*, 58, (1964), 573

308. W.J. Albery, R.A. Hillman and S. Bruckenstein, *J. Electroanal. Chem.*, 100, (1979), 687

309. D.T. Sawyer, R.S. George and R.C. Rhodes, *Anal. Chem.*, 31, (1959), 2

310. Ref. 99, pp 298–308

311. *The 1170 and 1250 Families of Frequency Response Analyser*, Schlumberger–Solartron Electronic Group Ltd.

312. J.E. Wertz and J.R. Bolton, *Electron Spin Resonance*, McGraw–Hill, New York, (1986), pp 450–466

313. B.A. Coles and R.G. Compton, *J. Electroanal. Chem.*, 144, (1983), 87

314. J.F. Coetzee, *Recommended Methods for Purification of Solvents*, IUPAC, Pergamon Press, Oxford, (1982), pp 11–15

315. M.E. Peover, *Reactions of Molecules at Electrodes*, Ed. N.S. Hush, Wiley Interscience, London, Ch. 5, (1971), pp 259–283

316. R. Dietz and M.E. Peover, *Trans. Faraday Soc.*, 62, (1966), 3535

317. M.E. Peover, *Electroanalytical Chemistry*, Ed. A.J. Bard, Arnold Publishers Ltd., Vol. 2, Ch. 1, (1967), pp 1–51

318. H. Lund, M–A. Michel and J. Simonet, *Acta Chemica Scand.*, B28, (1974), 900

319. J. Simonet, M–A. Michel and H. Lund, *Acta Chemica Scand.*, B29, (1975), 489

320. H. Lund and J Simonet, *J. Electroanal. Chem.*, 65, (1975), 219

321. H.L.S. Maia, M.J. Medeiros, M.I. Montenegro, D. Court and D. Pletcher, *J. Electroanal. Chem.*, 164, (1983), 347

322. Ref. 99, Ch. 1, pp 8–14

323. L. Nyikos and T. Pajkossy, *Electrochim. Acta*, 30, (1985), 1533

324. L. Nyikos and T. Pajkossy, *Electrochim. Acta*, 31, (1986), 1347

325. T. Pajkossy and L. Nyikos, *J. Electrochem. Soc.*, 133, (1986), 2061

326. W.H. Mulder and J.H. Sluyters, *Electrochim. Acta*, 33, (1988), 303

327. M. Keddam and H. Takenouti, *Electrochim. Acta*, 33, (1988), 445

328. R. de Levie, *Electrochim. Acta*, 9, (1964), 1231

329. R. de Levie, *Electrochim. Acta*, 10, (1965), 113

330. L.C. Pauling, *The Nature of the Chemical Bond*, Cornell University Press, (1960), pp 221–264

331. B.B. Damaskin, I.P. Mishutushkina, V.M. Gerovich and R.I. Kaganovich, *Zh. Fiz. Khim.*, 38, (1964), 1797

332. M.P. Soriaga and A.T. Hubbard, *J. Am. Chem. Soc.*, 104, (1982), 2735

333. M.P. Soriaga and A.T. Hubbard, *J. Am. Chem. Soc.*, 104, (1982), 2742

334. M. Takahashi, M. Fujita and M. Ito, *Chem. Phys. Lett.*, 109, (1984), 122

335. F. Lu, S.N. Salaita, L. Laguren–Davidson, D.A. Stern, E. Wellner, D.G. Frank, N. Batina, D.C. Zapien, N. Walton and A.T. Hubbard, *Langmuir*, 4, (1988), 637

336. M.P. Soriaga, D. Song, D.C. Zapien and A.T. Hubbard, *Langmuir*, 1, (1985), 123

337. A.T. Hubbard, J.L. Stickney, M.P. Soriaga, V.K.F. Chia, S.D. Rosasco, B.C. Schardt, T. Solomun, D. Song, J.H. White and A.J. Wiechowski, *J. Electroanal. Chem.*, 168, (1984), 43

338. M.P. Soriaga, J.L. Stickney and A.T. Hubbard, *J. Molec. Catal.*, 21, (1983), 211

339. M.P. Soriaga and A.T. Hubbard, *J. Phys. Chem.*, 88, (1984), 1758

340. M.P. Soriaga and A.T. Hubbard, *J. Electroanal. Chem.*, 159, (1983), 101

341. V.K.F. Chia, J.H. White, M.P. Soriaga and A.T. Hubbard, *J. Electroanal. Chem.*, 217, (1987), 121

342. M. von Stackleberg and W.Z. Stracke, *Elektrochem.*, 53, (1949), 118

343. J. Armand, *Bull. Soc. Chim. Fr.*, (1966), 543

344. See for example A.J. Bard and A. Marz, *J. Am. Chem. Soc.*, 101, (1979), 2959 and refs. therein

345. L. Eberson and M. Ekstrom, *Acta Chemica Scand.*, B42, (1988), 113

346. T. Clark, *J. Chem. Soc. Chem. Commun.*, , (1984), 93

347. T. Clark and G. Illing, *J. Chem. Soc. Chem. Commun.*, 9, (1985), 529

348. E. Janzen and B.J. Blackburn, *J. Am. Chem. Soc.*, 91, (1969), 4481

349. M. Goledzinowski, J. Lipkowski and Z. Galus, *Elektrokhimaya*, 13, (1977), 646

350. J. Lipkowski and Z. Galus, *J. Electroanal. Chem.*, 61, (1975), 11

351. J. Lipkowski, E. Kosinska, M. Goledzinowski, J. Nieniewska and Z. Galus, *J. Electroanal. Chem.*, 59, (1975), 344

352. T. Li, H.Y. Liu and M.J. Weaver, *J. Am. Chem. Soc.*, 106, (1984), 1233

353. R. de Levie and M. Nemes, *J. Electroanal. Chem.*, 58, (1975), 123

354. R. Srinivason and R. de Levie, *J. Electroanal. Chem.*, 201, (1986), 145

355. J. Lipkowski, Cl. Buess–Herman, J.P. Lambert and L. Gierst, *J. Electroanal. Chem.*, 202, (1986), 169

356. J.T. Hupp and M.J. Weaver, *J. Am. Chem. Soc.*, 88, (1984), 1463

357. R.A. Marcus, *Private Communication*

358. D. Song, M.P. Soriaga and A.T. Hubbard, *J. Electroanal. Chem.*, 201, (1982), 2735

359. M.P. Soriaga and A.T. Hubbard, *J. Electroanal. Chem.*, 162, (1984), 143

360. M.P. Soriaga, J.H. White, A.T. Hubbard and S.E. Anderson, *J. Phys Chem.*, 87, (1983), 232

361. M.E. Peover, *J. Chem. Soc.*, (1962), 4540

362. R. Samuelson and M. Sharp, *Electrochim. Acta*, 23, (1978), 315

363. R.G. Compton, B.A. Coles, G.M. Stearn and A.M. Waller, *J. Chem. Soc. Faraday Trans. 1*, 84, (1988), 2357

364. A.H. Maki and D.H. Geske, *J. Chem. Phys.*, 33, (1960), 825

365. H. Kojima and A.J. Bard, *J. Am. Chem. Soc.*, 97, (1975), 6317

366. M.E. Peover, *Trans. Faraday Soc.*, 58, (1962), 2370

367. M. Sharp, *Electrochim. Acta*, 21, (1976), 873

368. R. Gambert and H. Baumgartel, *J. Electroanal. Chem.*, 183, (1985), 315

369. B.B. Damaskin, *J. Electroanal. Chem.*, 65, (1975), 799

370. T. Biegler and H.A. Laitinen, *J. Electrochem. Soc.*, 113, (1966), 852

371. A.N. Frumkin, O.A. Petry and N.V. Nikolaeva–Fedorovich, *Electrochim. Acta*, 8, (1963), 177

372. L. Gierst, L. Vandenberghen, E. Nicholas and A. Fraboni, *J. Electrochem. Soc.*, 113, (1966), 1025

373. W.R. Fawcett, *J. Electroanal. Chem.*, 22, (1969), 19

374. F. Gerson and J.H. Gammons, *Non–Bemzenoid Aromatics*, Ed. J.P. Snyder, Academic Press, New York, (1971), pp 81

375. L. Eberson and M. Ekstrom, *Acta Chemica Scand.*, B42, (1988), 101

376. E.K. Brickenstein and R.F. Khairutdinov, *Chem. Phys. Lett.*, 115, (1982), 176

377. L. Eberson, *Electron Transfer Reactions in Organic Chemistry*, Springer–Verlag, London, Ch. 8, (1987), pp 118–127

378. M.C.R. Symons and I.G. Smith, *J. Chem. Soc. Faraday Trans. 1*, 81, (1985), 1095

379. K.D. Snell and A.G. Keenan, *Chem. Soc. Rev.*, 8, (1979), 259

380. P. Peerce and A.J. Bard, *J. Electroanal. Chem.*, 112, (1980), 97

381. R.W. Murray, *Mater. Sci.*, 14, (1984), 145

382. D.M. Oglesby, S.H. Orwang and C.N. Reilly, *Anal. Chem.*, 37, (1965), 1312

383. D.T. Sawyer, G. Chiericato, C.T. Angelis, E.J. Nanni and T. Tsuchiya, *Anal. Chem.*, 54, (1982), 1720

384. C.P. Andrieux, P. Hapiot and J.M. Savéant, *J. Am. Chem. Soc.*, 109, (1987), 3768

385. T.A. Lorenzola, B.A. Lopez and M.C. Giordano, *J. Electrochem. Soc.*, 130, (1983), 1359

386. Ref. 377, Ch. 6, pp 86–87

387. D.T. Sawyer and J.S. Valentine, *Acc. Chem. Res.*, 14, (1981), 393

388. J.L. Roberts, T.S. Calderwood and D.T. Sawyer, *J. Am. Chem. Soc.*, 105, (1983), 7691

389. C.E.W. Hahn, *Private Communication*

390. P.M. Bungay, H.K. Lonsdale and M.N. de Pinho, *Synthetic Membranes: Science, Engineering and Applications*, D. Reidel Publishing Co., Holland, NATO ASI Series, Ch. 1, C181, (1983)

391. Ref. 106, Ch. 4, pp 139–143

392. J.P. Hoare, *Encyclopedia of Electrochemistry of the Elements,* Ed. A.J. Bard, Marcel Dekker, New York, Vol 2, Ch. 5, (1974), pp 191–382

394. H. Gerischer, I. Mattes and R. Braun, *J. Electroanal. Chem.*, 10, (1965), 553

395. R.G. Compton, G.M. Stearn, P.R. Unwin and A.J. Barwise, *J. Applied Electrochem.*, 18, (1988), 657

396. W.J. Albery and C.E.W. Hahn, *UK Patent* GB2059073B, (1984)

397. C.E.W. Hahn, A. Davis and W.J. Albery, *Respir. Physiol.*, 25, (1975), 109